External reinforced concrete beam-column joints subjected to monotonic loading

A thesis submitted in partial fulfilment of the requirements for the degree of Doctor of Philosophy (PhD)

by

Omar Algassem

Department of Civil & Environmental Engineering

Imperial College of Science, Technology and Medicine

London SW7 2AZ, United Kingdom

April 2022

This page left intentionally blank

Declaration

I hereby confirm that the work presented in this thesis is my own and conducted at the Department of Civil Engineering of Imperial College London. The other sources reported in this thesis is acknowledged herein by providing appropriate references and citations in the text describing the work of others, whether published or unpublished.

The copyright of this thesis rests with me, the author, and is made available under a Creative Commons Attribution Non-Commercial No Derivatives licence. Researchers are free to copy, distribute or transmit the thesis on the condition that they attribute it, that they do not use it for commercial purposes and that they do not alter, transform or build upon it. For any reuse or redistribution, researchers must make clear to others the licence terms of this work.

Omar Algassem

London, April 2022

Abstract

This thesis describes an investigation into the response of external reinforced concrete beam-column joints under monotonic loading. The shear force in joints is of concern since it is much higher than that in the adjacent members. The joint shear force is limited by either joint shear failure or flexural failure in the adjoining beam or column. The objectives of the research were both experimental and computational. The main experimental objectives were to study the influence of beam reinforcement detailing, column axial load and joint stirrups on joint shear strength and the mechanisms of joint shear resistance. The computational objectives were to develop a nonlinear finite element modelling procedure for external beam-column joints and to assess previously developed strut and tie (STM) and empirical design methods.

To study these parameters, the author carried out a series of tests in the Heavy Structures Laboratory at Imperial College London. Twelve external beam-column joint specimens were tested in three series of four specimens. Series 1 investigated the effect of beam reinforcement anchorage type and bend radius. Series 2 studied the effect of varying the number of joint stirrups and column axial load. Series 3 studied the provision of intermediate column bars as well as the presence and absence of joint stirrups.

The shear transfer mechanisms studied in this thesis comprise aggregate interlock, joint shear reinforcement, tension in the bend of the beam reinforcement at its intersection with the critical shear crack and flexural compression. Digital image correlation was used to determine the opening and sliding displacements of the critical shear crack within the joint of each specimen. These displacements were used to assess the contributions of aggregate interlock and joint stirrups to joint shear resistance. Detailed comparisons are presented between the predictions of the developed nonlinear finite element model and the author's test results. This assessment includes comparisons of measured and predicted load displacement responses and reinforcement strains. The predictions of various strut and tie models and empirical equations proposed by previous researchers are assessed using a large experimental database and conclusions drawn.

Acknowledgement

I would like to take this opportunity to express my gratitude to all whom supported me through this project.

In particular, I would like to thank my thesis supervisor Dr. Robert Vollum for offering his support, guidance, encouragement, knowledge, patience and kindness during my PhD. I appreciate the time invested in the detailed revisions of the chapters and endless meetings. I would also like to thank the staffs of the Heavy Structures Laboratory at Imperial College London and I am grateful for the kind help from Les Clack and Delroy Hewitt (Bob) with the process of preparing, casting and testing my various specimens.

I would like to extend my thanks to my colleagues Abobakr, Andri and Marcus for their kind advice and help during my PhD. Special gratitude also goes to my mates in office Adeyanju, Wahid, Joao and Deema for the great time I spent with them.

Furthermore, I wish to show my appreciation to the University of Hail for offering me a scholarship and the Royal Embassy of Saudi Arabia Cultural Bureau in UK for all the support I have had during my PhD.

Finally, special thanks go to my parents and my wife whom always encouraged me and supported me to do my best.

Table of Contents

Chapter 1: Introduction 32

1.1 Background 32

1.2 Research Aim and Objectives 33

1.3 Thesis Outline 34

Chapter 2: Literature Review 37

2.1 Introduction 37

2.2 Summary of previous studies on monotonically-loaded beam-column joint 37

2.2.1 Taylor [5] 37

2.2.2 Kordina [8] 43

2.2.3 Sarsam and Phipps [10] 45

2.2.4 Scott [11] 47

2.2.5 Ortiz [12] 53

2.2.6 Parker and Bullman [13] 58

2.2.7 Hamil [14] 61

2.2.8 Hegger et al [15] 69

2.2.9 Sperry et al [18&19] 72

2.3 Design of external RC beam-column joint 74

2.3.1 Calculation of joint shear force 75

2.3.2 Design code recommendations 75

2.3.3 Methods proposed by researchers 79

2.3.4 Factors influencing joint strength 82

2.4 Strut-and-Tie Modelling 86

2.4.1 Constructing STM 89

2.4.2 Model optimization 90

2.4.3 Dimensioning strut-and-tie model....91
2.4.4 Models for external beam-column joints....93
2.5 Shear Transfer Mechanism in External Beam-Column Joint....100
2.5.1 Contribution of aggregate interlock....100
2.5.2 Contribution of shear reinforcement in joint....106
2.5.3 Evaluation of crack kinematics using DIC....108
2.6 Summary of literature review....110
Chapter 3 Experimental program....112
3.1 Overview....112
3.2 General Test Description....113
3.3 Series 1 of Beam-Column Joints....114
3.4 Series 2 of Beam-Column Joints....115
3.5 Series 3 of Beam-Column Joints....118
3.6 Manufacture and curing....120
3.7 Instrumentation....122
3.7.1 General aspect....122
3.7.2 Beam-column joint setup and testing procedure....122
3.7.3 Digital image correlation (DIC) system....124
3.7.4 Linear Variable Displacement Transducers (LVDT)....128
3.7.5 Inclinometers measurements....129
3.7.6 Strain gauge position....129
3.8 Summary....135
Chapter 4 Experimental results....136
4.1 Material tests....136
4.1.1 Concrete properties....136
4.1.2 Concrete strengths for series 1....136

4.1.3 Concrete strengths for series 2 139
4.1.4 Results of batch series 3 142
4.1.5 Results of batch mix for specimen BCJ 7 145
4.1.6 Summary of concrete properties 147
4.1.7 Steel reinforcement 149
4.2 Results of BCJ tests 151
4.2.1 Overview of series 1 151
4.2.2 Failure modes and crack patterns 152
4.2.3 Load-deflection response 154
4.2.4 Concrete surface strains and crack kinematics 157
4.2.5 Reinforcement strains 164
4.3 Results of BCJ series 2 170
4.3.1 Overview of the results 170
4.3.2 Failure modes and crack patterns 170
4.3.3 Load-deflection response 172
4.3.4 Concrete surface strains and crack kinematics 175
4.3.5 Reinforcement strains 182
4.4 Results of BCJ series 3 188
4.4.1 Overview of the results 188
4.4.2 Failure modes and crack patterns 189
4.4.3 Load-deflection response 191
4.4.4 Concrete surface strains and crack kinematics 194
4.4.5 Reinforcement strains 200
4.5 Conclusion 206
Chapter 5 NON-LINEAR FINITE ELEMENT (NLFE) METHODOLOGY 208
5.1 Introduction 208

5.2 Background to nonlinear finite element analysis 208
5.2.1 Concrete material modelling 208
5.2.2 Reinforcement material modelling 221
5.2.3 Finite elements in ATENA 223
5.2.4 Iterative solution methods 225
5.3 Development of modelling procedure for external beam-column joints in ATENA....227
5.3.1 Type and size of 2D NLFEA model.....229
5.3.2 Type and size of 3D NLFEA model.....231
5.4 Material constitutive model for 2D NLFEA model 234
5.4.1 Sensitivity to the concrete elastic modulus E_c.....235
5.4.2 Sensitivity to reduction of concrete strength due to cracking (c_f) 235
5.4.3 Sensitivity to concrete tensile strength (f_t).....236
5.4.4 Sensitivity to tension stiffening stress ($\boldsymbol{\sigma}_{st}$) 237
5.4.5 Sensitivity to critical compressive displacement (w_d) 238
5.4.6 Sensitivity to fixed vs rotated crack model.....239
5.4.7 Sensitivity to bond-slip model 240
5.4.8 Summary of adopted 2D modelling parameters 241
5.5 Use of 2D model to investigate parameters varied in current test program 243
5.5.1 Effect of beam bar detailing 243
5.5.2 Effect of joint stirrups 243
5.5.3 Effect of column bars.....244
5.5.4 Effect of column axial load.....245
5.5.5 Effect of concrete strength 246
5.6 Validation of 2D NLFEA model with test results of the author and others 247
5.7 Material modelling for 3D NLFEA model 252
5.7.1 Sensitivity to the concrete elastic modulus E_c.....252

5.7.2 Sensitivity to reduction of concrete strength due to cracking (c_f) 253
5.7.3 Sensitivity to tensile fracture energy (G_f) 254
5.7.4 Sensitivity to concrete tensile strength (f_t).....255
5.7.5 Sensitivity to critical compressive displacement (w_d) 256
5.7.6 Sensitivity to fixed vs rotated crack model.....257
5.7.7 Sensitivity to bond-slip model 257
5.7.8 Summary of adopted 3D modelling parameters 261
5.8 Use of 3D model to investigate parameters varied in current test program 263
5.8.1 Effect of column axial load.....263
5.8.2 Effect of beam bar detailing 263
5.8.3 Effect of joint stirrups 264
5.8.4 Effect of column bars.....265
5.9 Validation of 3D NLFEA model with test results 266
5.10 Reviewing 2D and 3D models.....270
5.11 Summary 271
Chapter 6 Crack kinematics and Shear Transfer Actions.....272
6.1 Analysis of shear transfer actions in beam-column joint.....272
6.2 Free body diagram of each tested BCJ specimen 274
6.2.1 BCJ series 1.....275
6.2.2 BCJ series 2.....277
6.2.3 BCJ series 3.....279
6.3 Total resultant force of aggregate interlock 281
6.4 Evaluation of section forces on joint boundaries using stress-block factors.....283
6.4.1 Section analysis at beam-column interface.....285
6.4.2 Section analysis at top column 288
6.4.3 Section analysis at bottom of joint 290

6.5 Contribution of horizontal equilibrium of shear transfer mechanism 293
6.5.1 Contribution of aggregate interlock 293
6.5.2 Contribution of joint stirrups 295
6.5.3 Contribution of beam bend bar 298
6.5.4 Contribution of concrete compression zone 301
6.5.5 Relative contribution of each shear action in horizontal equilibrium 304
6.6 Summary 306
Chapter 7 Analysis of the Experimental Results and Design Recommendations 309
7.1 Introduction.....309
7.2 Assessment of NLFEA 309
7.2.1 Strain measurements in beam anchorage bars 309
7.2.2 Strain measurements in column bars 315
7.2.3 Strain measurements in joint stirrups 325
7.2.4 Summary of predicted strains with measured strains:.....330
7.2.5 Surface strain measurements at joint boundaries and strut.....331
7.3 Effect of parametric studies on strains measured around and within joint 351
7.3.1 Effect of column axial load.....352
7.3.2 Effect of beam bar detailing 353
7.3.3 Effect of shear reinforcement (specimens with U-anchorage bar) 355
7.3.4 Effect of shear reinforcement (specimens with L-anchorage bar).....357
7.3.5 Effect of intermediate column bars.....359
7.4 Evaluation of existing proposed methods for designing beam-column joint.....361
7.4.1 Evaluation of beam-column joint using empirical equations 367
7.4.2 Evaluation of beam-column joint using strut and tie method (STM).....378
7.5 Strut geometry of findings of DIC, 2D-NLFEA, section analysis and STM 386
7.5.1 Strut geometry from the findings of DIC, 2D NLFEA and section analysis 386

7.5.2 Strut geometry from proposed strut-and-tie methods 386
7.6 Evaluation of the considered empirical equations and STMs 394
7.7 Summary 395
Chapter 8: Conclusions and future work 398
8.1 Introduction 398
8.2 Background Overview 398
8.3 Description of the Experimental Program and Summary of the Test Results 400
8.4 Analysis of the Results and Shear Transfer Actions 402
8.5 Design Observations and Recommendations 404
8.6 Suggestions for Further Work 407
References 408
Appendix: Permission to reuse figures from other publications 414

List of Figures

Figure 1-1 Features of column behaviour.....32
Figure 1-2 Thesis organisation. 34
Figure 2-1: Layouts of test specimens (dimensions in mm), adapted from [5].....40
Figure 2-2 Details of Kordina's test specimens; reproduced from [8].....44
Figure 2-3 Details of Sarsam and Phipps test specimens; reproduced from [10]. 46
Figure 2-4 Layout of test specimens (dimensions in mm); reproduced from [11].....50
Figure 2-5 Details of Ortiz's test specimens; reproduced from [12]. 55
Figure 2-6 Details of Ortiz's test specimens BCJ 4, BCJ 5 and BCJ 7; reproduced from [12]. .56
Figure 2-7 Layouts of test specimens of Parker and Bullman; reproduced from [13]. 59
Figure 2-8 Details of test specimens with 210 mm deep beam; reproduced from [14]. 63
Figure 2-9 Details of test specimens with 300 mm deep beam; reproduced from [14]. 64
Figure 2-10 Details of joint stirrup positioning of first series test specimens; reproduced from [11]. 65
Figure 2-11 Details of specimens investigating stirrup positioning; reproduced from [14]. ..65
Figure 2-12 Layouts of test specimens; reproduced from [15]. 70
Figure 2-13 Parameters affecting failure load of external beam-column joint predicted by ACI provisions; reproduced from [15].....71
Figure 2-14: Layout of Sperry et al. test specimens; reproduced from [18&19]. 74
Figure 2-15: Internal and external forces in beam-column joint.....75
Figure 2-16: Effect of column intermediate reinforcement ratio; reproduced from [28] and [15] respectively.....86
Figure 2-17: D-regions with non-linear strain distribution due to loading and/or geometrical discontinuities; reproduced from [31, 32].....87
Figure 2-18 Shear transfer mechanism of external beam-column joint; reproduced from [3]. 88
Figure 2-19: Strut-and-tie model for a deep beam; adapted from [33]. 90
Figure 2-20 Basic compression fields (a) the fan; (b) the bottle; (c) the prism; reproduced from [31, 32]. 92
Figure 2-21 (a) Smeared node and concentrated node & (b) Non-hydrostatic node; reproduced from [34]. 93

Figure 2-22 Strut-and-tie model; reproduced from [12]. 94
Figure 2-23: Softened strut-and-tie model; reproduced from [37].....96
Figure 2-24 Ratios of force distribution among mechanisms; reproduced from [37]. 96
Figure 2-25: Softened strut-and-tie model; reproduced from [37].....97
Figure 2-26: STM for external beam-column joint, reproduced from [39]. 100
Figure 2-27 Walraven two-phase model: a) layout of test specimen, b) Sphere particles intersected by a crack plane; and c) Contact area during shear displacement; reproduced from [41]. 101
Figure 2-28 Stresses acting on the surface of aggregate particles; reproduced from [41]...102
Figure 2-29 The fundamental contact modes for varying the radius R of the spherical particle; reproduced from [41]. 103
Figure 2-30 Comparison between experimental values and the model results; reproduced from [41]. 103
Figure 2-31 Fit curves of experimental test results; reproduced from [45]. 104
Figure 2-32 Stepped rigid plastic bond behaviour proposed by Sigrist; reproduced from [49]. 107
Figure 2-33 Bond and shear reinforcement response at and between cracks: (a) Prior to yielding; (b) after yielding; adapted from [49]. 107
Figure 2-34 DIC results obtained from existed studies for measuring crack kinematics; reproduced from [53]. 109
Figure 2-35 DIC results obtained from existed studies for evaluating concrete surfaces strains; reproduced from [50]. 109
Figure 3-1 Series 1 of beam-column joint specimens.....115
Figure 3-2 series 2 of beam-column joint specimens. 117
Figure 3-3 Third series of beam-column joint specimens. 119
Figure 3-4 Beam-column joint wooden moulds. 120
Figure 3-5 Assembled steel reinforcement cages inside the moulds before casting. 121
Figure 3-6 Attaching strain gauges to steel reinforcement. 121
Figure 3-7 Casting and curing concrete procedure. 122
Figure 3-8 Roller bearing support at column base. 123
Figure 3-9 Testing rig configuration. 124
Figure 3-10 Digital image correlation (DIC) 125

Figure 3-11 Typical virtual gauges along the critical crack for specimen BCJ 4. 126
Figure 3-12 Measurements for calculation of crack kinematics: (a) undeformed configuration; (b) deformed configuration; reproduced from [40]. 127
Figure 3-13 Linear variable displacement transducers (LVDT) and DCT locations. 128
Figure 3-14 Inclinometers locations in BCJ specimens. 129
Figure 3-15 Column bars strain gauges locations for specimens with or without 1 joint stirrup. 130
Figure 3-16 Column bars strain gauges locations for specimens with 2 joint stirrups or more. 130
Figure 3-17 U-anchorage beam bars strain gauges locations for specimens with standard bend radius 131
Figure 3-18 U-anchorage beam bars strain gauges locations for specimens with large bend radius 132
Figure 3-19 L-anchorage beam bars strain gauges locations for specimens with standard bend radius 132
Figure 3-20 L-anchorage beam bars strain gauges locations for specimens with large bend radius 133
Figure 3-21 Joint stirrup strain gauges locations in BCJ specimens. 134
Figure 3-22 locations of strain gauges in BCJ 12 with six joint stirrups. 134
Figure 4-1 Concrete cube compressive strength development– series 1. 137
Figure 4-2 Concrete cube compressive strength development – series 2. 140
Figure 4-3 Concrete cube compressive strength development – series 3. 143
Figure 4-4 Coupon test instrumentation 149
Figure 4-5 Stress-strain relationship for steel bars size 10, 16 and 25 mm. 150
Figure 4-6 Minimum manrdel diameter for bends, hooks and loops reinforcement (reproduced from EC2 [23]) 151
Figure 4-7 Failure modes and crack patterns of series 1: (a) specimen BCJ 1; (b) specimen BCJ 2; (c) specimen BCJ 3; and (d) specimen BCJ 4. 153
Figure 4-8 Load-deflection response: (a) Specimen BCJ 1; (b) Specimen BCJ 2; (c) Specimen BCJ 3; (d) Specimen BCJ 4. 155
Figure 4-9 Horizontal deflection recorded from LVDTs for first series: (a) Specimen BCJ 1; (b) Specimen BCJ 2; (c) Specimen BCJ 3; (d) Specimen BCJ 4. 156

Figure 4-10 Inclinometer's readings for first series: (a) Specimens BCJ 1; (b) Specimens BCJ 2; (c) Specimens BCJ 3; (d) Specimens BCJ 4. 157
Figure 4-11 Typical virtual gauges along the critical crack (specimen BCJ 4). 158
Figure 4-12 Results of crack opening and sliding along the joint height of first series: (a) Crack opening; (b) crack sliding. 159
Figure 4-13 Crack kinematics for specimen BCJ 1. 160
Figure 4-14 Crack kinematics for specimen BCJ 2. 161
Figure 4-15 Crack kinematics for specimen BCJ 3. 162
Figure 4-16 Crack kinematics for specimen BCJ 4. 163
Figure 4-17 Front column bar strain measurements: (a) Specimen BCJ 1; (b) Specimen BCJ 2; (c) Specimen BCJ 3; (d) Specimen BCJ 4.....165
Figure 4-18 Front column bar strain distribution: (a) Specimen BCJ 1; (b) Specimen BCJ 2; (c) Specimen BCJ 3; (d) Specimen BCJ 4.....165
Figure 4-19 Back column bar strain measurements: (a) Specimen BCJ 1; (b) Specimen BCJ 2; (c) Specimen BCJ 3; (d) Specimen BCJ 4.....166
Figure 4-20 Back column bar strain distribution: (a) Specimen BCJ 1; (b) Specimen BCJ 2; (c) Specimen BCJ 3; (d) Specimen BCJ 4.....167
Figure 4-21 Beam anchorage bar strain measurements: (a) Specimen BCJ 1; (b) Specimen BCJ 2; (c) Specimen BCJ 3; (d) Specimen BCJ 4.....168
Figure 4-22 Beam anchorage bar strain distribution: (a) Specimen BCJ 1; (b) Specimen BCJ 2; (c) Specimen BCJ 3; (d) Specimen BCJ 4.....169
Figure 4-23 Joint shear reinforcement strain measurements: (a) Specimen BCJ 1; (b) Specimen BCJ 2; (c) Specimen BCJ 3; (d) Specimen BCJ 4. 169
Figure 4-24 Failure modes and crack patterns of second series: (a) specimen BCJ 5; (b) specimen BCJ 6; (c) specimen BCJ 7; and (d) specimen BCJ 8. 172
Figure 4-25 Load-deflection response: (a) Specimen BCJ 5; (b) Specimen BCJ 6; (c) Specimen BCJ 7; (d) Specimen BCJ 8. 173
Figure 4-26 Horizontal deflection recorded from LVDTs for second series: (a) Specimen BCJ 5; (b) Specimen BCJ 6; (c) Specimen BCJ 7; (d) Specimen BCJ 8. 174
Figure 4-27 Inclinometer's readings for second series: (a) Specimens BCJ 5; (b) Specimens BCJ 6; (c) Specimens BCJ 7; (d) Specimens BCJ 8. 175

Figure 4-28 Results of crack opening and sliding along the joint height of second series: (a) Crack opening; (b) crack sliding. 177
Figure 4-29 Crack kinematics for specimen BCJ 5. 178
Figure 4-30 Crack kinematics for specimen BCJ 6. 179
Figure 4-31 Crack kinematics for specimen BCJ 7. 180
Figure 4-32 Crack kinematics for specimen BCJ 8. 181
Figure 4-33 Front column bar strain measurements: (a) specimen BCJ 5; (b) specimen BCJ 6; (c) specimen BCJ 7; and (d) specimen BCJ 8. 183
Figure 4-34 Front column bar strain distribution: (a) specimen BCJ 5; (b) specimen BCJ 6; (c) specimen BCJ 7; and (d) specimen BCJ 8. 183
Figure 4-35 Back column bar strain measurements: (a) specimen BCJ 5; (b) specimen BCJ 6; (c) specimen BCJ 7; and (d) specimen BCJ 8. 184
Figure 4-36 Back column bar strain distribution: (a) specimen BCJ 5; (b) specimen BCJ 6; (c) specimen BCJ 7; and (d) specimen BCJ 8. 185
Figure 4-37 Beam anchorage bar strain measurements(a) specimen BCJ 5; (b) specimen BCJ 6; (c) specimen BCJ 7; and (d) specimen BCJ 8. 186
Figure 4-38 Beam anchorage bar strain distribution: (a) specimen BCJ 5; (b) specimen BCJ 6; (c) specimen BCJ 7; and (d) specimen BCJ 8. 187
Figure 4-39 Joint shear reinforcement strain measurements: (a) specimen BCJ 5; (b) specimen BCJ 6; (c) specimen BCJ 7; and (d) specimen BCJ 8.....188
Figure 4-40 Failure modes and crack patterns of third series: (a) specimen BCJ 9; (b) specimen BCJ 10; (c) specimen BCJ 11; and (d) specimen BCJ 12.....191
Figure 4-41 Load-deflection response: (a) Specimen BCJ 9; (b) Specimen BCJ 10; (c) Specimen BCJ 11; (d) Specimen BCJ 12. 192
Figure 4-42 Horizontal deflection recorded from LVDTs for third series: (a) Specimen BCJ 9; (b) Specimen BCJ 10; (c) Specimen BCJ 11; (d) Specimen BCJ 12.....193
Figure 4-43 Inclinometer's readings for third series: (a) Specimen BCJ 9; (b) Specimen BCJ 10; (c) Specimen BCJ 11; (d) Specimen BCJ 12.....194
Figure 4-44 Results of crack opening and sliding along the joint height of third series: (a) Crack opening; (b) crack sliding. 195
Figure 4-45 Crack kinematics for specimen BCJ 9. 196
Figure 4-46 Crack kinematics for specimen BCJ 10. 197

Figure 4-47 Crack kinematics for specimen BCJ 11. 198
Figure 4-48 Crack kinematics for specimen BCJ 12. 199
Figure 4-49 Front column bar strain measurements: (a) Specimen BCJ 9; (b) Specimen BCJ 10; (c) Specimen BCJ 11; (d) Specimen BCJ 12.....201
Figure 4-50 Front column bar strain distribution: (a) Specimen BCJ 9; (b) Specimen BCJ 10; (c) Specimen BCJ 11; (d) Specimen BCJ 12.....201
Figure 4-51 Back column bar strain measurements: (a) Specimen BCJ 9; (b) Specimen BCJ 10; (c) Specimen BCJ 11; (d) Specimen BCJ 12.....202
Figure 4-52 Back column bar strain distribution: (a) Specimen BCJ 9; (b) Specimen BCJ 10; (c) Specimen BCJ 11; (d) Specimen BCJ 12.....203
Figure 4-53 Beam anchorage bar strain measurements(a) Specimen BCJ 9; (b) Specimen BCJ 10; (c) Specimen BCJ 11; (d) Specimen BCJ 12. 204
Figure 4-54 Beam anchorage bar strain distribution: (a) Specimen BCJ 9; (b) Specimen BCJ 10; (c) Specimen BCJ 11; (d) Specimen BCJ 12.....205
Figure 4-55 Joint shear reinforcement strain measurements: (a) Specimen BCJ 9; (b) Specimen BCJ 10; (c) Specimen BCJ 11; (d) Specimen BCJ 12. 206
Figure 5-1 Components of stress and strain state; reproduced from [58].....210
Figure 5-2 compressive stress-strain curve; reproduced from [58]. 211
Figure 5-3 Softening displacement law in compression; reproduced from [58].....211
Figure 5-4 Biaxial failure function for concrete in 2D model; reproduced from [58]. 212
Figure 5-5 Elliptic function; reproduced from [61]. 213
Figure 5-6 Compressive hardening/softening and compressive characteristic length; reproduced from [58]. 214
Figure 5-7 Stages of crack opening; reproduced from [58]. 214
Figure 5-8 Tensile softening and characteristic length; reproduced from [58]. 215
Figure 5-9 Definition of localization bands for L_t and L_C; reproduced from [58].....216
Figure 5-10 Compressive strength reduction of cracked concrete; reproduced from [58]. .217
Figure 5-11 Tension stiffening factor in ATENA; reproduced from [58].....218
Figure 5-12 Discrete crack propagation; reproduced from [66].....218
Figure 5-13 Rotating crack model and stress and strain law; reproduced from [58].....219
Figure 5-14 Fixed crack model and stress and strain state; reproduced from [58]. 220
Figure 5-15 Shear retention factor; reproduced from [58]. 221

Figure 5-16 The stress-strain law for reinforcement; reproduced from [58].....222
Figure 5-17 Bond law by BIGAJ [71]; reproduced from [58].....223
Figure 5-18 Geometry of CCIsoTruss elements; reproduced from [58]. 224
Figure 5-19 Geometry of 2D plane and 3D solid elements; reproduced from [58]. 225
Figure 5-20 Solving set of non-linear equations: a) Full Newton-Raphson method and b) modified Newton-Raphson method; reproduced from [58].....226
Figure 5-21 The Arc-length method; reproduced from [58]. 227
Figure 5-22 Finite element mesh size 2D models.....229
Figure 5-23(b) Results of 2D mesh refinement process; using square mesh in ATENA. 230
Figure 5-24 Finite element mesh size system.....232
Figure 5-25 Finite element mesh for experimental beam-column joint dimensions.....232
Figure 5-26 Results of 3D mesh refinement process.....233
Figure 5-27 Finite element mesh size 3D models.....234
Figure 5-28 Material constitutive model for 2D NLFEA model: sensitivity to modulus of elasticity (E_c).....235
Figure 5-29 Material constitutive model for 2D NLFEA model: sensitivity to reduction of concrete strength due to cracking (c_f).....236
Figure 5-30 Material constitutive model for 2D NLFEA model using BCJ 11: sensitivity to concrete tensile strength (F_t).....237
Figure 5-31 Material constitutive model for 2D NLFEA model: sensitivity to tenson stiffening (σ_{st}).....238
Figure 5-32 Material constitutive model for 2D NLFEA model using BCJ 11: sensitivity to critical compressive displacement (w_d).....239
Figure 5-33 Material constitutive model for 2D NLFEA model: sensitivity to fixed vs rotated crack model.....239
Figure 5-34 Material constitutive model for 2D NLFEA model: sensitivity bond-slip model 241
Figure 5-35 Material constitutive model for 3D NLFEA model: sensitivity to bond-slip model 241
Figure 5-36 Validation of 2D model to experimental test parameters: effect of beam bar detailing. 243
Figure 5-37 Validation of 2D model to experimental test parameters: effect of joint stirrups with U-anchorage bar. 244

Figure 5-38 Validation of 2D model to experimental test parameters: effect of joint stirrups with L-anchorage bar. 244
Figure 5-39 Validation of 2DD model to experimental test parameters: effect of column intermediate bar. 245
Figure 5-40 Validation of 2D model to experimental test parameters: effect of column axial load. 246
Figure 5-41 Validation of 2D model to experimental test parameters: effect of concrete strength. 247
Figure 5-42 Validation of 2D model with Author's tests. 248
Figure 5-43 Validation of 2D model with Ortiz tests 250
Figure 5-44 Validation of 2D model with Ortiz and Author tests. 252
Figure 5-45 Material constitutive model for 3D NLFEA model: sensitivity to modulus of elasticity (E_c) 253
Figure 5-46 Material constitutive model for 3D NLFEA model: sensitivity to reduction of concrete strength due to cracking (c_f) 254
Figure 5-47 Material constitutive model for 3D NLFEA model: sensitivity to tensile fracture energy (G_f) 254
Figure 5-48 Material constitutive model for 3D NLFEA model using BCJ 11: sensitivity to concrete tensile strength (f_t) 255
Figure 5-49 Material constitutive model for 3D NLFEA model using BCJ 5: sensitivity to concrete tensile strength (ft) 255
Figure 5-50 Material constitutive model for 3D NLFEA model using BCJ 11: sensitivity to critical compressive displacement (w_d) 256
Figure 5-51 Material constitutive model for 3D NLFEA model using BCJ 5: sensitivity to critical compressive displacement (wd) 256
Figure 5-52 Material constitutive model for 3D NLFEA model: sensitivity to fixed vs rotated crack model 257
Figure 5-53 Application of bond-slip model on steel reinforcements 258
Figure 5-54 Crack width and principal strain of 3D model using specimen BCJ 11. 259
Figure 5-55 Crack width and principal strain of 3D model using specimen BCJ 2. 260
Figure 5-56 Material constitutive model for 3D NLFEA model: sensitivity bond-slip model 261

Figure 5-57 Validation of 3D model to experimental test parameters: effect of column axial load. 263
Figure 5-58 Validation of 3D model to experimental test parameters: effect of beam bar detailing. 264
Figure 5-59 Validation of 3D model to experimental test parameters: effect of joint stirrups with U-anchorage bar. 264
Figure 5-60 Validation of 3D model to experimental test parameters: effect of joint stirrups with L-anchorage bar. 265
Figure 5-61 Validation of 3D model to experimental test parameters: effect of joint stirrups with U-anchorage bar. 265
Figure 5-62 Validation of 3D model with Author tests 267
Figure 5-63 Validation of 3D model with Ortiz tests 268
Figure 5-64 Validation of 3D model with Ortiz and Author tests 270
Figure 6-1 Horizontal equilibrium of shear transfer actions in a free body diagram of a beam-column joint. 273
Figure 6-2 Vertical equilibrium of shear transfer actions in a free body diagram of a beam-column joint. 274
Figure 6-3 Horizontal equilibrium of shear transfer actions of series 1. 276
Figure 6-4 Horizontal equilibrium of shear transfer actions of series 2. 278
Figure 6-5 Horizontal equilibrium of shear transfer actions of series 3. 280
Figure 6-6 Resultant force of aggregate interlock. 283
Figure 6-7 Stress-block factors; reproduced from [33]. 284
Figure 6-8 Stress-strain relationship used in the section analysis 284
Figure 6-9 Comparison of predicted and measured moment-curvature responses; reproduced from [33]. 285
Figure 6-10 Concrete and steel forces acting on beam-column interface. 286
Figure 6-11 Predicted and measured strains in steel reinforcement at beam-column interface. 287
Figure 6-12 Concrete and steel forces acting at top column. 288
Figure 6-13 Predicted and measured strains in steel reinforcement at top column. 290
Figure 6-14 Concrete and steel forces acting at bottom column. 291
Figure 6-15 Predicted and measured strains in steel reinforcement at bottom column. 292

Figure 6-16 Results of aggregate interlock in horizontal direction for series 1. 293
Figure 6-17 Results of aggregate interlock in horizontal direction for series 2. 294
Figure 6-18 Results of aggregate interlock in horizontal direction for series 3. 295
Figure 6-19 Joint stirrups contribution results for series 1. 296
Figure 6-20 Joint stirrups contribution results for series 2. 297
Figure 6-21 Joint stirrups contribution results for series 3. 298
Figure 6-22 Contribution of beam bend bar for series 1. 299
Figure 6-23 Contribution of beam bend bar for series 2. 300
Figure 6-24 Contribution of beam bend bar for series 3. 301
Figure 6-25 Contribution of concrete compression zone for series 1. 302
Figure 6-26 Contribution of concrete compression zone for series 2. 303
Figure 6-27 Contribution of concrete compression zone for series 3. 304
Figure 6-28 Shear transfer mechanism in horizontal direction. 306
Figure 7-1 Measured and predicted strains of series 1; beam anchorage bar. 311
Figure 7-2 Measured and predicted strains of series 2; beam anchorage bar. 313
Figure 7-3 Measured and predicted strains of series 3; beam anchorage bar. 314
Figure 7-4 Measured and predicted strains of series 1; front column bars. 316
Figure 7-5 Measured and predicted strains of series 2; front column bars. 318
Figure 7-6 Measured and predicted strains of series 3; front column bars. 320
Figure 7-7 Measured and predicted strains of series 1; back column bars. 321
Figure 7-8 Measured and predicted strains of series 2; back column bars. 323
Figure 7-9 Measured and predicted strains of series 3; back column bars. 325
Figure 7-10 Measured and predicted strains of series 1; joint stirrups. 326
Figure 7-11 Measured and predicted strains of series 2; joint stirrups. 328
Figure 7-12 Measured and predicted strains of series 3; joint stirrups. 329
Figure 7-13 Virtual DEMC gauges at joint boundaries and in the strut; DIC vs 2D NLFEA. ...332
Figure 7-14 Sensitivity analysis at gauge 4 for gauge length of 50, 75 and 100 mm; DIC vs 2D NLFEA. 332
Figure 7-15 Strains at top joint for BCJ series 1; DIC vs 2D NLFEA. 334
Figure 7-16 Strains at top joint for BCJ series 2; DIC vs 2D NLFEA. 335
Figure 7-17 Strains at top joint for BCJ series 3; DIC vs 2D NLFEA. 336
Figure 7-18 Strains at bottom joint for BCJ series 1; DIC vs 2D NLFEA. 338

Figure 7-19 Strains at bottom joint for BCJ series 2; DIC vs 2D NLFEA. 339
Figure 7-20 Strains at bottom joint for BCJ series 3; DIC vs 2D NLFEA. 340
Figure 7-21 Strains at beam-column interface for BCJ series 1; DIC vs 2D NLFEA. 341
Figure 7-22 Strains at beam-column interface for BCJ series 2; DIC vs 2D NLFEA. 342
Figure 7-23 Strains at beam-column interface for BCJ series 3; DIC vs 2D NLFEA. 343
Figure 7-24 Diagonal gauges position in joint; DIC and 2D NLFEA. 344
Figure 7-25 Strains in first row of diagonal gauges for BCJ series 1; DIC vs 2D NLFEA. 345
Figure 7-26 Strains in first row of diagonal gauges for BCJ series 2; DIC vs 2D NLFEA. 346
Figure 7-27 Strains in first row of diagonal gauges for BCJ series 3; DIC vs 2D NLFEA. 347
Figure 7-28 Strains in second row of diagonal gauges for BCJ series 1; DIC vs 2D NLFEA. ... 349
Figure 7-29 Strains in second row of diagonal gauges for BCJ series 2; DIC vs 2D NLFEA. ... 350
Figure 7-30 Strains in second row of diagonal gauges for BCJ series 3; DIC vs 2D NLFEA. ... 351
Figure 7-31 Effect of column load; DIC vs 2D NLFEA. 353
Figure 7-32 Effect of beam bar detailing; DIC vs 2D NLFEA. 355
Figure 7-33 Effect of shear reinforcement for specimens with U-anchorage type; DIC vs 2D NLFEA. 357
Figure 7-34 Effect of shear reinforcement for specimens with L-anchorage type; DIC vs 2D NLFEA. 359
Figure 7-35 Effect of intermediate column bars; DIC vs 2D NLFEA. 361
Figure 7-36 Results of empirical equation proposed by Hegger et al. [15]. 369
Figure 7-37 Results of measured to predicted failure load for Hegger et al [15] empirical method. 370
Figure 7-38 Results of empirical equation proposed by Vollum & Newman [24]. 371
Figure 7-39 Results of measured to predicted failure load for Vollum & Newman [24] empirical method. 372
Figure 7-40 Results of empirical equation proposed by Bakir and Boduroğlu [25]. 373
Figure 7-41 Results of measured to predicted failure load for Bakir and Boduroğlu [25] empirical method. 374
Figure 7-42 Results of empirical equation proposed by Hassan and Mohele [26]. 375
Figure 7-43 Results of measured to predicted failure load for Hassan and Mohele [26] empirical method. 375
Figure 7-44 Results of STM proposed by Hassan and Mohele [26]. 380

Figure 7-45 Results of measured to predicted failure load of STM for Hassan and Mohele [26]. 380
Figure 7-46 Results of STM proposed by Hwang et al [38].....381
Figure 7-47 Results of measured to predicted failure load of STM for Hwang et al [38]. 382
Figure 7-48 Results of STM proposed by Vollum and Parker [39].....383
Figure 7-49 Results of measured to predicted failure load of STM for Vollum and Parker [39]. 383
Figure 7-50 Strut geometry from the findings of DIC, 2D NLFEA and section analysis; specimens in series 1. 388
Figure 7-51 Strut geometry from the findings of DIC, 2D NLFEA and section analysis; specimens in series 2. 389
Figure 7-52 Strut geometry from the findings of DIC, 2D NLFEA and section analysis; specimens in series 3. 390
Figure 7-53 Strut geometry from the findings of STM; specimens in series 1. 391
Figure 7-54 Strut geometry from the findings of STM; specimens in series 2. 392
Figure 7-55 Strut geometry from the findings of STM; specimens in series 3. 393
Figure 7-56 Demerit point classification of external beam-column joints for different design methods. 395

List of Tables

Table 2-1 Details of Taylor's test specimens, adapted from [5]. 41
Table 2-2 Taylor's test results, adapted from [5] 42
Table 2-3 Details of Kordina's test specimens; adapted from [8]. 44
Table 2-4 Results of Kordina's test specimens; adapted from [8]. 45
Table 2-5 Details of Sarsam and Phipps test specimens; adapted from [10]. 47
Table 2-6 Results of Sarsam and Phipps test specimens; adapted from [10]. 47
Table 2-7 Details of Scott's test specimens; adapted from [11]. 51
Table 2-8 Results of Scott's test specimens; adapted from [11]. 52
Table 2-9 Details of Ortiz test specimens; adapted from [12]. 57
Table 2-10 Results of test specimens; adapted from [12]. 57
Table 2-11 Details of test specimens of Parker and Bullman; adapted from [13]. 60
Table 2-12 Results of test specimens of Parker and Bullman; adapted from [13]. 60
Table 2-13 Details of Hamil first series test specimens; adapted from [14]. 66
Table 2-14 Details of Hamil remaining series test specimens; adapted from [14]. 67
Table 2-15 Results Hamil's test specimens for series one; adapted from [14]. 68
Table 2-16 Results of exterior test specimens; adapted from [15]. 71
Table 2-17 Details of test specimens for Sperry et al.; adapted from [18&19]. 74
Table 2-18 Values of γ for beam-to-column – ACI-ASCE Committee 352-05; adapted from [16] 76
Table 2-19 Values of γ for beam-to-column – ACI-ASCE Committee 352-02; adapted from [17]. 77
Table 2-20 Shear reinforcement coefficient factor $\alpha 2$; adapted from [15]. 81
Table 3-1 Series 1 of beam-column joint steel reinforcement detail and column axial load 114
Table 3-2 Series 2 of beam-column joint steel reinforcement detail and column axial load 116
Table 3-3 Series 3 of beam-column joint steel reinforcement detail and column axial load 118
Table 4-1 Concrete strength development using cubes (100 mm^3) – series 1. 136
Table 4-2 Compressive cube strength (100 mm^3) – series 1. 137
Table 4-3 Compressive cylinder strength (100 x 200 mm) – series 1. 138
Table 4-4 Tensile cylinder strength (150 x 300 mm) – series 1. 138
Table 4-5 Compressive and tensile strength for BCJ specimens - series 1. 139

Table 4-6 Concrete strength development using cubes (100 mm^3) – series 2.....139
Table 4-7 Compressive cube strength (100 mm^3) – series 2. 140
Table 4-8 Compressive cylinder strength (100 x 200 mm) – series 2.....141
Table 4-9 Tensile cylinder strength (150 x 300 mm) – series 2. 141
Table 4-10 Compressive and tensile strength for BCJ specimens - series 2.....142
Table 4-11 Concrete strength development using cubes (100 mm^3) – series 3.....142
Table 4-12 Compressive cube strength (100 mm^3) – series 3. 143
Table 4-13 Compressive cylinder strength (100 x 200 mm) – series 3.....144
Table 4-14 Tensile cylinder strength (150 x 300 mm) – series 3. 144
Table 4-15 Compressive and tensile strength for BCJ specimens - series 3.....145
Table 4-16 Concrete mix design.....145
Table 4-17 Concrete strength development using cubes (100 mm^3) – BCJ 7. 146
Table 4-18 Compressive cube strength (100 mm^3) – BCJ 7.....146
Table 4-19 Compressive cylinder strength (100 x 200 mm) – BCJ 7.....146
Table 4-20 Tensile cylinder strength (150 x 300 mm) – BCJ 7.....147
Table 4-21 Compressive and tensile strength for BCJ specimens – BCJ 7.....147
Table 4-22 Concrete compressive and tensile strength of tested BCJ specimens 148
Table 4-23 Longitudinal and transverse steel reinforcement properties used in experimental tests.....149
Table 4-24 Summary of experimental results for first series. 151
Table 4-25 Maximum crack opening and sliding of BCJ specimens in series 1 at maximum load. 158
Table 4-26 Summary of experimental results for series 2.....170
Table 4-27 Maximum crack opening and sliding of BCJ specimens in second series at maximum load. 176
Table 4-28 Summary of experimental results for third series.....189
Table 4-29 Maximum crack opening and sliding of BCJ specimens in third series at maximum load. 194
Table 5-1 Parameters for defining the bond strength-slip relationship for ribbed bars (ATENA manual [58]).....223
Table 5-2 Default concrete constitutive model parameters in ATENA for 2D and 3D models. 228

Table 5-3 Number of quadrilateral mesh elements 230
Table 5-4 Number of hexahedral mesh elements 233
Table 5-5 2D chosen parameters input for 2D model 242
Table 5-6 Summary of validation of 2D model with Author tests: measured/predicted failure load from ATENA.....249
Table 5-7 Summary of validation of 2D model with Ortiz tests: measured/predicted failure load from ATENA.....251
Table 5-8 Summary of 2D model measured/predicted failure load from ATENA.....251
Table 5-9 Chosen parameters input for 3D model. 262
Table 5-10 Summary of validation of 3D model with Author tests: measured/predicted failure load from ATENA.....267
Table 5-11 Summary of validation of 3D model with Ortiz tests: measured/predicted failure load from ATENA.....269
Table 5-12 Summary of 3D model measured/predicted failure load from ATENA.....269
Table 7-1 Spacing between DEMEC gauges above and below the joint; DIC and 2D NLFEA. 332
Table 7-2 Spacing between DEMEC gauges at beam-column interface; DIC and 2D NLFEA.333
Table 7-3 Angle of diagonal gauges; DIC and 2D NLFEA. 333
Table 7-4 Experimental database of external beam-column joints (1/5). 362
Table 7-5 Experimental database of external beam-column joints (2/5). 363
Table 7-6 Experimental database of external beam-column joints (3/5). 364
Table 7-7 Experimental database of external beam-column joints (4/5). 365
Table 7-8 Experimental database of external beam-column joints (5/5). 366
Table 7-9 The parameters used in the proposed design methods.....367
Table 7-10 Results of proposed empirical equations (1/2). 376
Table 7-11 Results of proposed empirical equations (2/2). 377
Table 7-12 Results of proposed STMs (1/2).....384
Table 7-13 Results of proposed STMs (2/2).....385
Table 7-14 Demerit point classification of proposed methods 395

List of Symbols

Symbol

θ	Angle that direct strut makes to horizontal.
A_{sje}	The effective area of joint stirrups which is assumed to be positioned within the upper two thirds of beam depth.
A_{str}	Effective area of the diagonal compressive strut.
A_x	Projected contact areas in x-directions for a unit crack area (walraven [41]).
A_y	Projected contact areas in y-directions for a unit crack area (walraven [41]).
b_b	Beam width.
b_c	Column width.
b_e	Effective beam width; taken as $0.5(b_c + b_b)$.
BCJ	Beam-column joint.
BF	Beam flexural failure.
C_b	Flexural compressive force in beam extreme fibre.
C_{se}	Flexural compressive force in outer column bars at upper joint boundary.
C_{si}	Flexural compressive force in inner column bars at lower joint boundary.
C_{ce}	Flexural compressive force in inner column bars & concrete at lower joint boundary.
C_{ci}	Flexural compressive force in outer column bars & concrete at lower joint boundary.
C_{comp}	Horizontal force of concrete compression zone.
C_d	Diagonal compression force in strut.
c_f	reduction factor of concrete strength due to cracking (used in ATENA).
d_b	Flexure effective depth in beam.
d_c	Flexure effective depth in column.

DP	Demerit point assigned for a specific design method.
DIC	Digital image correlation used to obtain relative displacements.
E_c	Young's modulus of concrete.
f_c'	Concrete compressive cylinder strength.
f_{cu}	Concrete compressive cube strength.
f_t	Concrete Tensile strength.
f_y	Yield stress of steel reinforcement.
G_f	Fracture energy to a specific crack width.
h_b	Beam depth.
h_c	column depth.
H_{c1}/ H_{c1}	The height of top/lower columns.
JS	Joint shear failure.
K	strut-and-tie index
κ	A factor that considers the effect of column axial load.
L	The distance of beam load from column face.
M_b	Beam moment at front column face.
M_{col}	Column moment above/below joint.
N_{col}	Column axial load applied in upper column.
NLFEA	Non-linear finite element analysis.
R_d	Ratio of diagonal compression force resisted by diagonal mechanism.
R_h	Ratio of diagonal compression force resisted by horizontal mechanism.
R_v	Ratio of diagonal compression force resisted by vertical mechanism.
STM	Sturt-and-tie method.
SG	Strain gauge attached to steel reinforcement.
T_b	Flexural tensile force in beam tension steel reinforcement.
T_{si}	Flexural tensile force in inner column bars at upper joint boundary.

T_{se}	Flexural tensile force in outer column bars at lower joint boundary.
$T_{b,hor}$	Horizontal force in the bend of beam anchorage bars.
$\sum T_s$	Total shear reinforcement horizontal force.
V_{agg}	Resultant force of aggregate interlock force.
$V_{agg,hor}$	Horizontal resultant force of aggregate interlock.
$V_{agg,\ vert}$	Vertical resultant force of Aggregate interlock.
V_b	Beam vertical shear force.
V_c	Concrete resistance in joint.
V_{col}	Column horizontal shear force.
V_{comp}	Vertical force of concrete compression zone.
V_j	Joint shear strength ($V_j = T_b - V_c$).
V_s	Shear reinforcement resistance in joint.
w	*Crack width.*
w_d	Plastic displacement in concrete cylinder.
ζ	Concrete softening coefficient.
ε_d	Principal compressive strain in joint.
ε_r	Principal tensile strain in joint.
ε_0	Concrete cylinder strain at peak stress.
ρ	Ratio of shear reinforcement in joint.
σ_d	Principal compressive stress in strut.
σ	Normal stress on the crack surface (walraven [41]).
σ_{pu}	Matrix yielding strength (walraven [41]).
σ_{st}	Tension stiffening stress (used in ATENA).
τ	Shear stress on the crack surface (walraven [41]).
μ	Coefficient of friction (walraven [41]).

Δ Crack slip.

Δp Deformation increment due to loading increment in Full Newton-Raphson Method (used in ATENA).

λ_i A new loading factor used in Arc-Length method to provide additional degree of freedom associated with the loading level (used in ATENA).

ν Poisson's ratio.

Chapter 1: Introduction

This chapter provides a brief background to the research, addresses the research question, states the research aim and objectives and outlines the description of the thesis chapters.

1.1 Background

Multi-storey reinforced concrete framed structures consisting of beams framing into columns are built in many countries of the world. Typically, the beams support either insitu concrete slabs or alternatively one-way spanning precast concrete slabs. Joints arise in such structures at the intersections of beams (horizontal elements) and columns (vertical elements). Dependent on their location, joints are classified as internal, external or corner. This thesis is concerned with the design and behaviour of external joints which arise around the perimeter of a building. Joints are potentially critical regions because the joint shear force is very high compared with the shear force in the adjacent columns as shown in Figure 1-1. The joint shear force arises from moment transfer from the beam to the column and equals the difference between the tensile force in the beam flexural reinforcement and the shear force in the column. The joint shear force can be sufficient to cause diagonal cracking, which reduces joint stiffness and, in the limit, causes joint failure. The joint shear strength can be enhanced by the provision of horizontal links and vertical reinforcement bars within the joint.

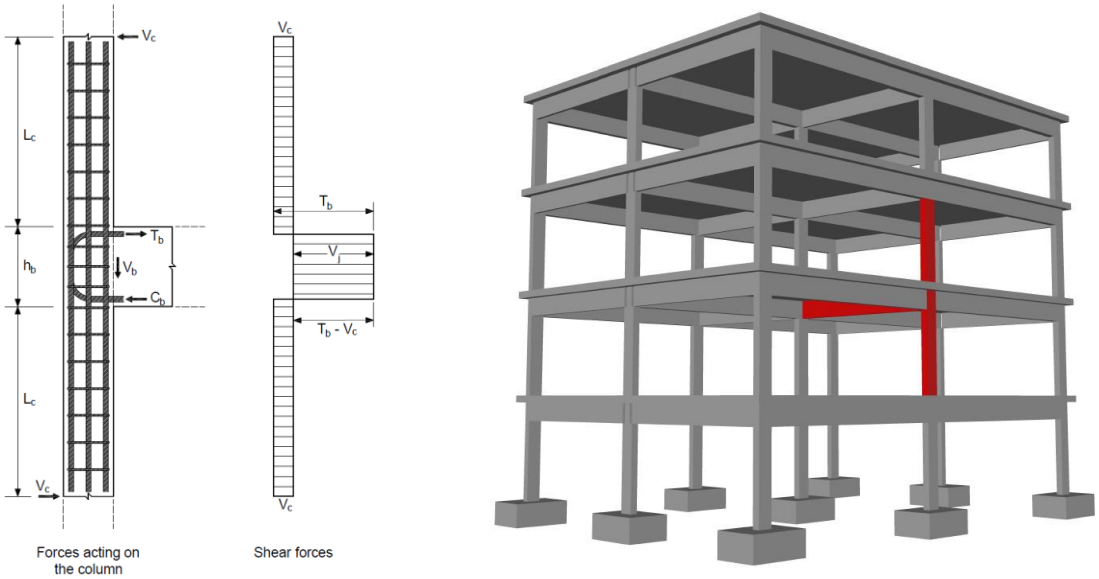

a) Forces acting on joint b) External joints in framed structures

Figure 1-1 Features of column behaviour.

Seismically loaded beam-column joints have been the subject of much research since joint failure is of major concern in structures built in seismic regions [1], [2], [3] and [4]. Whilst beam-column joint failure is common in buildings subject to seismic loading, joint failure under monotonic loading is seldom reported even though beam-column joints are often not designed in UK practice. Consequently, experimental studies into the behaviour of monotonically loaded beam-column joints are much fewer than studies into seismically loaded connections. Where available, existing studies of beam-column connections tend to focus on joint strength with little or no information reported on specimen deformation which is needed for the validation of nonlinear finite element models. Information on joint stiffness is also needed for assessment of moment redistribution from the column into the span following joint cracking. Furthermore, little attention has been given to the study of shear transfer mechanisms in cracked beam-column joints.

1.2 Research Aim and Objectives

The thesis aims to develop an improved understanding of the influence of reinforcement detailing and column axial load on the behaviour and shear strength of external beam-column joints. Emphasis is placed on the study of shear transfer through cracked concrete within the joint. The research methodology involves assessment of existing test data, nonlinear finite element modelling and laboratory testing. The main objectives of this research are as follows:

- To develop a database of previously tested monotonically loaded external beam-column joints
- To experimentally investigate the influence on joint shear strength of beam reinforcement anchorage type and bend radius, joint stirrups, column axial load and intermediate column bars.
- To use digital Image Correlation (DIC) to study the joint shear deformation and crack kinematics, by monitoring displacements and cracks pattern occurring in the joint surface.
- To assess the relative contributions of aggregate interlock and joint shear reinforcement in transferring shear through the critical diagonal crack in the tested beam-column joints.
- To develop and calibrate a nonlinear finite element analysis (NLFEA) modelling procedure for external beam-column joints.

- To assess the accuracy of existing mechanically based and strut and tie models for determining joint shear strength.
- To develop refined guidance for the design and detailing of external beam-column joints.

1.3 Thesis Outline

The thesis consists of eight chapters as shown in Figure 1-2 and described below.

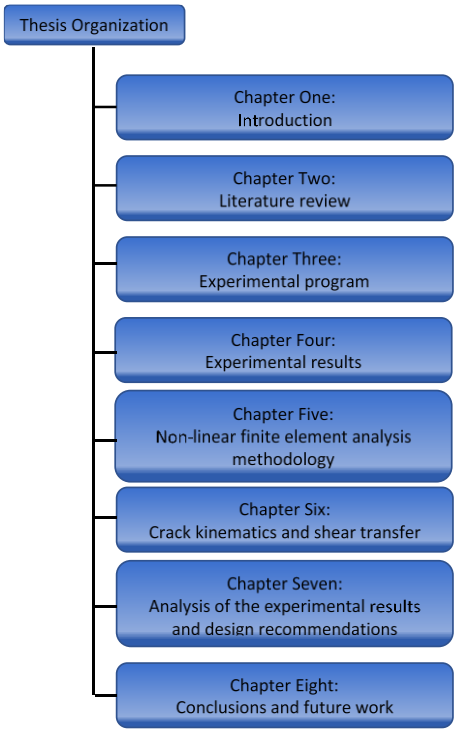

Figure 1-2 Thesis organisation.

Chapter 1. Introduction

This current chapter provides a brief background to the research, states the research aim and objectives and outlines the content of each chapter.

Chapter 2. Literature Review

Previous experimental studies into monotonically loaded external beam-column joints are summarised as well as pertinent design methods proposed by previous researchers. These include purely empirical methods, analytically based methods and strut-and-tie models. Codified design methods are also reviewed. Methods for assessing shear transfer through cracked concrete are also reviewed.

Chapter 3. Experimental Program

This chapter describes the experimental program carried out by the author in the Heavy Structures Laboratory at Imperial College London. In total, twelve beam-column joint specimens were tested in three sets of four. Each set of four tests was designed to investigate a different parameter, such as beam reinforcement anchorage detail, though the three sets are also linked. Details are given of the experimental methodology. In particular, the chapter describes the manufacturing process, test configurations, instrumentation and the procedures used to obtain crack kinematics using the DIC system.

Chapter 4. Experimental Results

This chapter presents the experimental results. The first part of the chapter summarises the material properties of the concrete and the reinforcement used. The second provides a detailed description of the behaviour of the tested specimens. This includes the global load-deflection response, failure modes and crack patterns, the surface strain of the concrete and the reinforcement strain gauge readings.

Chapter 5. Nonlinear Finite Element Analysis Methodolgy

This chapter comprises three parts. The first part reviews the main features of the nonlinear finite element analysis (NLFEA) and describes the basic constitutive models and solution procedures available in the adopted software. Selected experimental results from this program and the literature are used in the second part to calibrate the NLFEA and to assess the sensitivity of the model to several parameters. Finally, a proposed modelling procedure is selected on the basis of comparison of experimentally observed and predicted load-deflection responses and crack patterns. The proposed modelling procedure is subsequently validated by modelling various tested specimens that were not used in the calibration of the modelling procedure.

Chapter 6. Crack kinematics and Shear Transfer Actions

This chapter describes the development of joint cracking and subsequent failure for each test. Shear transfer actions are evaluated by studying the relative contributions to joint shear strength of aggregate interlock, shear reinforcement, intermediate column bars, concrete compression zone and bend of beam bar.

Chapter 7. Analysis of the Experimental Results and Design Recommendations

Results obtained from the experimental program are used in this chapter to assess the current provisions in design codes regarding joint shear strength of specimens without and with joint shear reinforcement. An analysis is carried out to assess the outcomes from using the developed STM and various empirical design equations from the literature. The results from this analysis are then compared with the results of refined nonlinear finite element analysis and the author's test results.

Chapter 8. Conclusions and Future Work

This chapter provides a summary of the research, highlights key conclusions and provides recommendations for further work.

Chapter 2: Literature Review

Relevant literature is explored in this chapter; this includes a summary of previous studies on beam-column joints under monotonic loading, some guidance on design of external beam-column joint using codes of practice, design methods proposed by previous researchers employing both empirical and mechanically based methods such as strut-and-tie modelling. Research into mechanisms of shear transfer through cracked concrete is also reviewed.

2.1 Introduction

This chapter reviews previous research into the behaviour and design of external reinforced concrete beam-column joints. Many studies have been carried out to assess the behaviour of beam column joints under seismic loading [1], [2], [3] and [4]. Previous studies into joint failure of monotonically loaded beam-column joints are more limited with insufficient attention given to joint deformation and its influence on frame behaviour. A common omission in the reporting of experimental tests of monotonically loaded beam-column joints is the load-displacement relationship, which is important for the development of improved methods for the analysis of joint behaviour and refinement of NLFEA models. Shear transfer mechanisms in beam-column joints have been extensively studied for seismic loading, but much less so for monotonically loaded joints. Furthermore, experimental details, such as the stiffness of the horizontal prop provided at the beam end, are not always reported causing modelling difficulties.

Design methods for monotonically loaded beam-column joints are reviewed. The review includes various empirical models proposed by researchers, as well as mechanically based models including strut and tie models.

2.2 Summary of previous studies on monotonically-loaded beam-column joint

2.2.1 Taylor [5]

Taylor tested twenty-six small scale external beam-column joint specimens under monotonic loading with a constant axial load applied to the column. As shown in Figure 2-1, the specimens had a column height of 1420 mm with a cross-section of 140 mm x 140 mm. The beam had a length of 500 mm with a cross-section of either 100 mm x 125 mm or 100 mm x

200 mm. The beam was loaded at a distance of 470 mm away from the column face. Details of the test parameters including concrete strength, reinforcement ratio of beam and column and strut type are given in Table 2-1. The concrete compressive strength varied between 21 MPa and 60 MPa. A variety of bar diameters (6 mm, 8 mm, 10 mm and 16 mm) were used for the beam flexural tension reinforcement. The columns were reinforced longitudinally with four bars having a diameter of 16 mm. Stirrups were installed in the beam and column at a spacing of 100 mm and 145 mm respectively. The beam tension reinforcement was anchored into the column with either a 90-degree hook (bent up or down) or a 180-degree U bar. All the specimens, except one, had one stirrup in the joint. One specimen had three joint stirrups (B3/41/24). Column loads were either 60 kN or 240 kN. In some tests, the beam end was attached to a prop (thrust) to prevent side sway, having a stiffness of either ($\frac{AE}{L}$ = 110 kN/mm or 890 kN/mm). The results of Taylor's test are shown in Table 2-2 and summarized as follows:

- Provision of a prop at beam end allowed the joint to reach its full capacity by allowing the lower column (closing side of joint) to resist greater bending moment than the upper column (opening side of joint), which caused an increase in the joint shear strength.
- Taylor concluded that diagonal cracking is likely to occur under service loading in joints with the geometry used in series A to E for beam flexural ratios greater than 2.0%. Even though the crack widths were less than the limit of 0.3 mm given by the then UK code of practice CP 110 [6], Taylor recommended that joints should be designed to avoid diagonal cracking under service loads.
- Taylor suggested that the diagonal joint cracking load can be calculated with either a rigorous finite element analysis or an approximate principal stress analysis. He estimated the joint shear stress at diagonal cracking to be:

$$v_c = 0.67 \sqrt{f_t^2 + f_c f_t} \qquad (2\text{-}1)$$

Where f_t represents the concrete tensile strength and f_c is the compressive stress in the upper column ($f_c = N/b_c h_c$, where N is the column load and b_c/h_c are the column breadth and height respectively). A similar equation, but with f_t replaced by the shear resistance provided by concrete (v_c), is adopted in the superseded BS8110 design code [7] for cases where it is considered necessary to prevent shear cracking prior to the design ultimate limit state.

- The bending moment carried by the upper and lower column was evaluated by Taylor. Based on his results he suggested designing the lower column for 70% of the beam moment and the upper column for 50% of the beam moment.
- Taylor concluded that reducing the column axial load to 60 kN showed no evidence of weakening the joint strength.
- In BCJ specimens with low beam flexural reinforcement ratios, failure was due to the formation of a plastic hinge near the column face. However, specimens with high reinforcement ratios failed due to diagonal cracking in the joint region.
- Joint behaviour was adversely affected by anchoring the beam reinforcement with L-bars having their vertical leg projecting up into the column. Joint performance improved for beam reinforcement consisting of L-bars with the vertical leg bent down into the column below or U-bars.
- Increasing the number of joint stirrups to three in specimen B3/41/24 did not increase the joint ultimate strength. Taylor likened this behaviour to diagonal compression failure in over reinforced deep beams where the presence of beam stirrups does not influence the ultimate shear capacity.

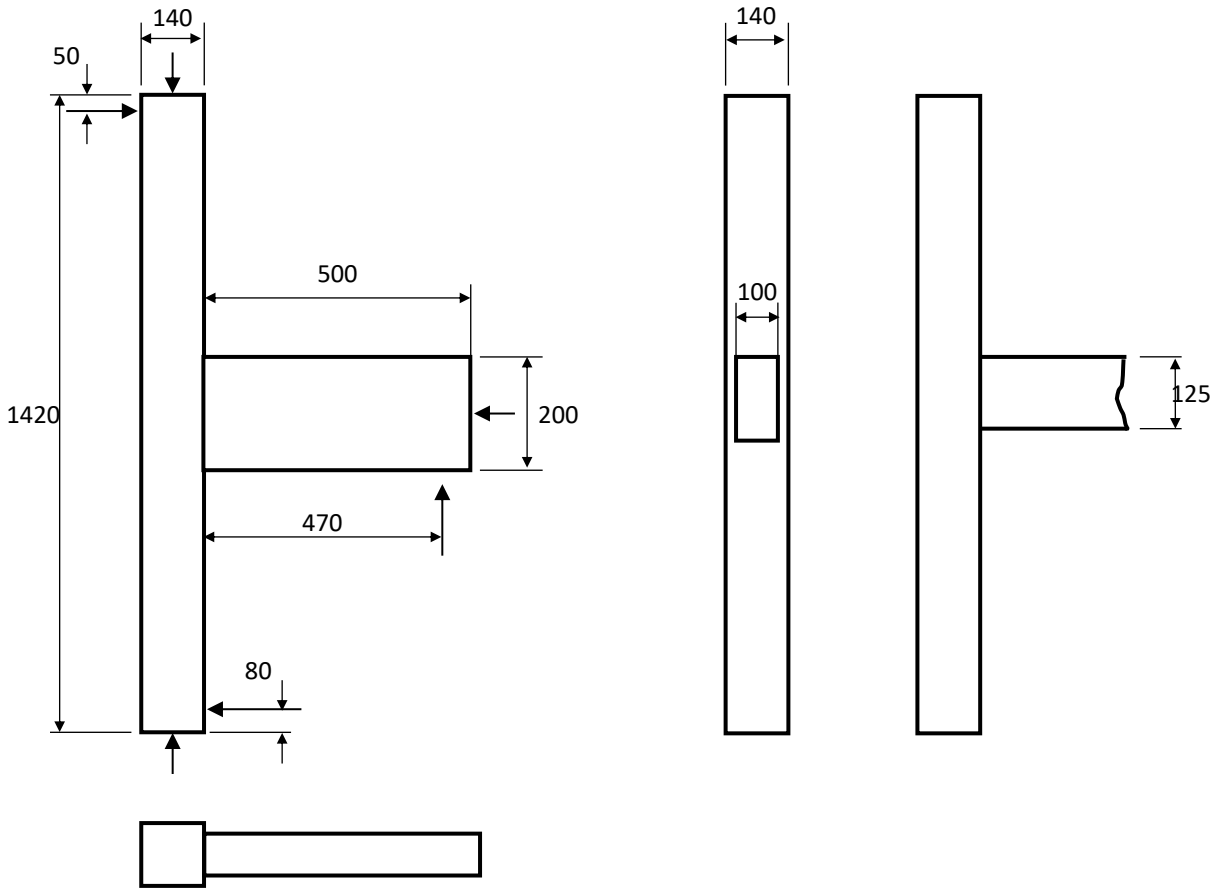

Figure 2-1: Layouts of test specimens (dimensions in mm), adapted from [5].

Table 2-1 Details of Taylor's test specimens, adapted from [5].

Specimen	Series	Variable	Strut type	Beam reinforcement ratio %	Column reinforcement ratio %	Concrete strength (MPa)
P1/41/24	P	Preliminary	1	2.4	4.1	33.0
P2/41/24			2	2.4	4.1	29.0
P2/41/24A			2	2.4	4.1	46.5
P1/41/09			1	0.9	4.1	37.0
A3/41/24	A	Beam steel percentage	3	2.4	4.1	27.0
A3/41/13			3	1.3	4.1	45.0
A3/41/09			3	0.9	4.1	43.5
A3/41/06			3	0.6	4.1	27.5
B3/41/24	B	Number of joint stirrups	3	2.4	4.1	22.0
C3/41/24X	C	Beam steel detail	3	2.4	4.1	50.5
C3/41/24BY			3	2.4	4.1	31.7
C3/41/13Y			3	1.3	4.1	28.2
C3/41/24Y			3	2.4	4.1	59.5
D3/41/24	D	Column load	3	2.4	4.1	53.0
D3/41/13			3	1.3	4.1	55.5
D3/41/09			3	0.9	4.1	42.5
D3/41/06			3	0.6	4.1	21.0
E3/41/24A	E	Beam thrust	-	2.4	4.1	42.8
E3/41/24B			-	2.4	4.1	44.5
E3/41/24C			-	2.4	4.1	41.6
F3/41/24A	F	Beam thrust, steel ratio, column load, all with small beam size	3	2.3	4.1	37.2
F3/41/16A			3	1.6	4.1	21.1
F3/41/24B			3	2.3	4.1	34.2
F3/41/16B			3	1.6	4.1	23.9
F3/41/24C			-	2.3	4.1	34.4
F3/41/16C			-	1.6	4.1	37.7

Note: 1. **X** indicates vertical leg of L-bar anchored into upper column.
2. **Y** represents U-bar detail
3. the letters **A**, **B** and **C** in some specimens refer to repeat of similar specimens.
4. strut type **1** refers to no prop; **2** denotes a prop with stiffness AE/L of 110 x 10^3 kN/mm; and **3** indicates a prop stiffness AE/L of 890 x 10^3 kN/mm.

Table 2-2 Taylor's test results, adapted from [5].

Specimen	Column load (kN)	Beam thrust (kN)	Concrete strength (MPa)	M_{flex} (kN.m)	M_d (kN.m)	M_u (kN.m)	Failure mode
P1/41/24	240	0	33	26.7	14	18.8	JS
P2/41/24	240	13.4	29	25.2	11.7	18.8	JS
P2/41/24A	240	20.6	46.5	29.9	16.43	25.25	JS
P1/41/09	240	0	37	13.3	12.28	17.54	BF
A3/41/24	240	7.2	27	24.2	11.69	18.71	JS
A3/41/13	240	15.4	45	21.6	18.71	22.39	BF
A3/41/09	240	7.3	43.5	14.6	11.7	12.90	BF
A3/41/06	240	8.3	27.5	9.3	-	12.80	BF
B3/41/24	240	6.8	22	20.9	11.72	16.31	JS
C3/41/24X	240	2.13	50.5	30.4	14.61	16.08	JS
C3/41/24BY	240	4.9	31.7	22.8	11.69	15.49	JS
C3/41/13Y	240	8.3	28.2	15.9	14.41	14.41	JS
C3/41/24Y	240	14.3	59.5	31.7	19.88	24.20	JS
D3/41/24	60	14.0	53	30.8	16.37	26.95	JS
D3/41/13	60	9.1	55.5	20.6	12.86	20.64	BF
D3/41/09	60	14.5	42.5	14.0	14.03	15.96	BF
D3/41/06	60	5.8	21	8.85	-	10.17	BF
E3/41/24A	240	5.0*	42.8	28.9	11.69	14.41	JS
E3/41/24B	240	2.5*	44.5	29.0	16.37	16.37	JS
E3/41/24C	240	15.0*	41.6	28.7	18.71	21.66	JS
F3/41/24A	240	3.9	37.2	7.72	9.94	10.03	BF
F3/41/16A	240	4.2	21.1	4.95	-	8.24	BF
F3/41/24B	240	4.6	34.2	7.48	7.6	9.82	BF
F3/41/16B	240	3.2	23.9	5.50	7.31	7.77	BF
F3/41/24C	60	2.5	34.4	7.46	-	10.14	BF
F3/41/16C	60	2.5	37.7	5.80	-	7.98	BF

Note: 1. beam thrust values with * indicate constant thrust throughout test.
2. **JS** indicates joint shear failure; **BF** indicates beam flexural failure.
3. absence of values of diagonal cracking moment (M_d) denotes beam failure occurred prior to joint cracking.

2.2.2 Kordina [8]

Kordina [8] tested a series of 10 reinforced concrete beam-column joint specimens. The parameters studied were type of beam anchorage detail, column axial load, type of joint reinforcement, beam depth and the ratio of reinforcement in beam and joint. The dimensions of the specimens are shown in Figure 2-2 and summarised in Table 2-3. The column height was 3000 mm for all specimens. The beam load was located at a distance of 1100 mm away from the centre line of the column. Results for specimen RE1 were not reported by Kordina. The concrete strength was measured using 200 mm cubes and the concrete cover to the main steel bars was 25 mm. The concrete strengths in Table 2-3 are equivalent values for a 150 mm concrete cube as determined by Vollum [9]. Three types of beam anchorage bar were investigated including L-anchorage bars bent down into the column, U-anchorage bars and anchorage by plates at the back of column. The stirrup diameter used in this study was 8 mm. The study also investigated the use of diagonal ties and horizontal U-bars placed in the joint to strengthen its capacity. Details of the specimens and failure loads are given in Table 2-4. The following observations were made by Kordina:

- Anchoring the beam reinforcement with L-bars and the use of anchorage plates at the back face of the column were satisfactory. U-anchorage bars performed better when additional capping U-bars were placed in the lower column since this provides an overlapping splice in the joint.
- If U-anchorage bars are used, Kordina recommends providing hairpin stirrups within the joint over the beam depth. He also observed that placing a diagonal bar across the opening corner of the joint controlled the crack width there.
- Due to the large number of parameters varied in a relatively few tests it is difficult to isolate the influence of each parameter and hence draw firm conclusions from the test program.

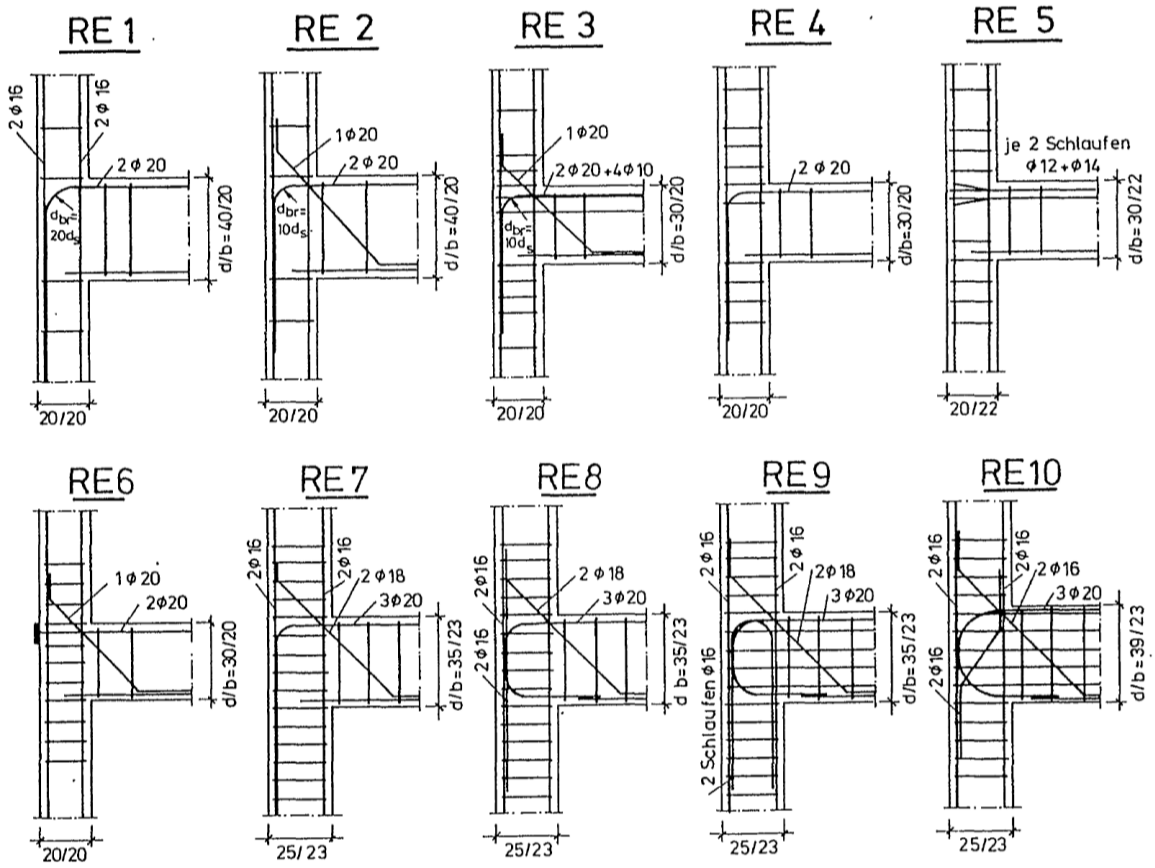

Figure 2-2 Details of Kordina's test specimens; reproduced from [8].

Table 2-3 Details of Kordina's test specimens; adapted from [8].

Specimen	Column steel	Beam steel	Joint stirrups	Anchorage type	Yield strength T16 (MPa)	Yield strength T20 (MPa)
RE2	4T16	2T20	-	L	420	420
RE3	4T16	2T20+2T10	1T10UB*	L	420	420
RE4	4T16	2T20	1T8	L	420	420
RE5	4T16	2T12+2T10	-	P	420	420
RE6	4T16	2T20	3T8	P	490	463
RE7	4T16	3T20	4T8	L	454	448
RE8	4T16	3T20	4T8	U	454	464
RE9	4T16	3T20	4T8UB	U	406	454
RE10	4T16	3T20	5T8UB	U	440	459

Note: 1. ***UB** denotes extra U-bars used in joint.

2. **L** indicates L-anchorage bars; **U** indicates U-anchorage bars; and **P** denotes anchorage by plate.

Table 2-4 Results of Kordina's test specimens; adapted from [8].

Specimen	Beam depth (mm)	Column load (kN)	Failure load (kN)	Equivalent 150 mm concrete cube strength (MPa)
RE2	400	240	67	31.6
RE3	300	400	80	50.5
RE4	300	51	51	40.3
RE5	300	46	46	36.9
RE6	300	213	66	39.5
RE7	350	650	117	32.1
RE8	350	525	105	35
RE9	350	770	110	35.6
RE10	390	551	100	29.7

Note: The equivalent concrete cube strength is taken from Vollum [9].

2.2.3 Sarsam and Phipps [10]

Five large-scale beam-column joints were tested to investigate parameters including column axial load, provision of joint stirrups and beam shear span (a_v/d_b). The dimensions of test specimens are shown in Figure 2-3 and given in Table 2-5. The beam flexural reinforcement consisted of L-bars with the vertical leg bent down into the column. The bend radius was three times the beam bar diameter. Joint stirrups with diameter of 8 mm were installed in all the specimens except EX2 which had no joint shear reinforcement. The shear span from the load to the column face was around 1420 mm apart from specimens EX3 and EX4 where the spans were 663 mm and 881 mm, respectively. The specimens were cast in two stages using different concrete strengths. The beam and lower column were cast first. The next day the top column was cast with a different concrete strength. The column axial stress was increased from around 9.5 MPa to 27.6MPa in specimen EX5 to study the effect of column axial load on failure mode. Specimen EX2, without joint shear reinforcement, failed in joint shear while the remaining specimens exhibited beam flexural failure. The test results are given in Table 2-6. The following observations were made by Sarsam and Phipps:

- Up to joint cracking there was no difference in behaviour between specimens with and without joint stirrups. However, the joint stirrups became effective after joint

cracking. The provision of joint stirrups in specimen EX1 caused an increase of the joint stiffness when compared with specimen EX2 without shear reinforcement in joint.

- Only specimen EX2 failed in joint shear so the tests only give limited information on joint shear strength. However, the joint shear strength was not adversely affected in test EX5 by the increase in axial column stress from around 8.5 MPa to 27.6 MPa.
- An empirical equation was proposed to predict the joint shear stress at joint cracking.

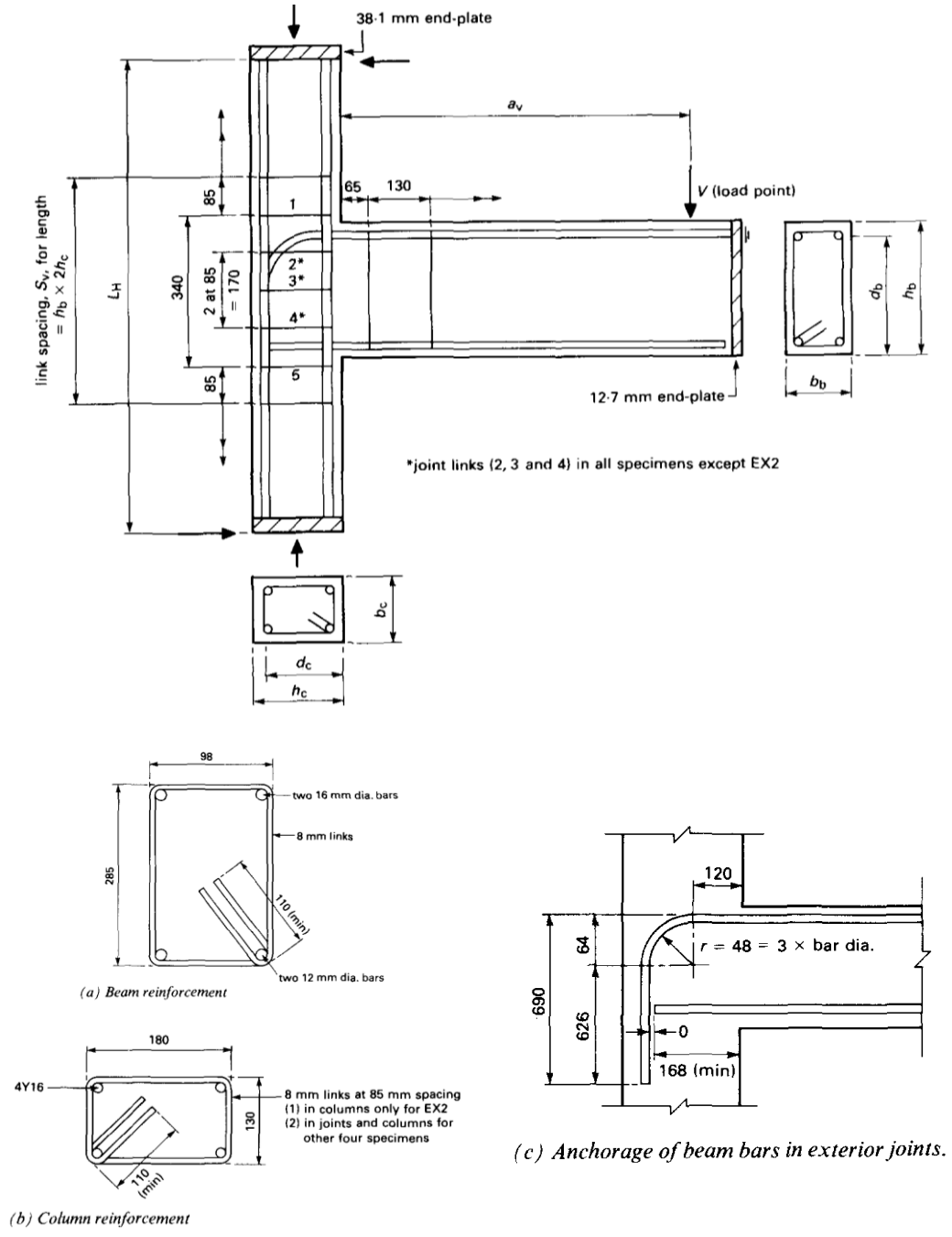

Figure 2-3 Details of Sarsam and Phipps test specimens; reproduced from [10].

Table 2-5 Details of Sarsam and Phipps test specimens; adapted from [10].

Specimen	a_v (mm)	b_b (mm)	h_b (mm)	b_c (mm)	h_c (mm)	d_c (mm)	L_H (mm)
EX1	1422	152	303	155	205	173	1531
EX2	1422	152	305	157	204	172	1536
EX3	661	152	305	157	204	172	1532
EX4	883	152	305	157	204	172	1537
EX5	1419	152	305	157	206	173	1535

Table 2-6 Results of Sarsam and Phipps test specimens; adapted from [10].

Specimen	f_{cu} (MPa)	f'_c (MPa)	Column stress (MPa)	V_{crack} (kN)	V_{ult} (kN)	Failure mode
EX1	69	56	9.39	125	181	F
EX2	66	54	9.52	123	172	J
EX3	53	41	9.47	111	161	F
EX4	66	49	9.72	113	173	F
EX5	65	49	27.64	121	170	F

2.2.4 Scott [11]

Fifteen reinforced concrete beam-column joint specimens were tested under monotonic loading to observe the effects of reinforcement detailing, beam reinforcement ratio and column axial load. The column had a cross-section of 150 x 150 mm and a height of 1700 mm. It was reinforced with 4-16 mm longitudinal bars and 6 mm stirrups spaced at 150 mm above and below the joint. Two beam depths (210 mm and 300 mm) were tested. The beam length and width were 850 mm and 100 mm respectively, as shown in Figure 2-4. The concrete compressive strength varied between 41 MPa and 62 MPa while the tensile strength ranged from 2.1 MPa to 3.4 MPa. The tested beam tension reinforcement ratios were 1.0%, 1.3% and

1.9% with reinforcement consisting of either 12 mm or 16 mm diameter bars. Two 12 mm diameter bars were provided at the bottom of beams reinforced with L-bars. The yield strength of the reinforcement was 575 MPa for bar size 12 mm and 525 MPa for bar size 16 mm. Beam tension bars were anchored into the column by bending the L-bars up, down or using U-bars. The vertical L-bar leg length was the minimum recommended by BS8110 [7], except for a couple of specimens (C1 and C4) which had longer legs to investigate its effect. Details of the specimens are given in Table 2-7. Reinforcement strains were measured by installing closely spaced strain gauges internally in the reinforcing bars, providing the capability of reading strains up to failure. The column was subjected to an axial load of either 50 kN or 275 kN (representing a full-size structure under working loads). A prop was installed at the beam end in order to control the lateral sway. The results of test specimens are given in Table 2-8 and summarized as follows:

- Bond stress distributions were determined from the reinforcement strain distributions. Up to initial joint cracking, force was transferred from the reinforcement to the surrounding concrete mainly by bond stress around the first bend in the beam tension bars. After joint cracking, strains measured around the bend and in the vertical leg of bent down L-bars indicated a large reduction in bond stresses at the bend which resulted in an increase of tensile force in the vertical leg. U-bars transferred load into the concrete via bond stresses at the first bend (top bend) and in the vertical leg. As tension developed further around the U-bar with increasing load, bond stresses developed around the second bend (bottom bend) and in the bottom horizontal leg though this was counterbalanced by compressive flexural strains resulting from beam bending.
- Additionally, the method of internally strain gauging the steel reinforcement allowed the calculation of bearing stress at bends in the beam reinforcement. The calculated bearing stresses were observed to be higher than permitted by BS8110 [7]. To tolerate high bearing stresses, Scott suggested providing additional joint stirrups instead of using large radius bend.
- Reducing the column load from 275 kN to 50 kN changed the failure mode from beam flexure to joint shear failure in specimens having 12 mm beam tension bars. It was observed that the strain in the column reinforcement was compressive throughout

the test for specimens with high column load while tensile strains developed in specimens with low column load with flexural cracks forming above and below the joint.

- The failure mode of the specimens with 16 mm diameter beam bars was unaffected by the column axial load with all specimens failing in joint shear.
- Increasing the length of vertical leg had no influence on the joint failure capacity or mode.
- In specimens with bent down L-bars, tension extended to the end of vertical leg at failure, except for specimen C4 with a longer vertical leg which developed tensile strain up to mid-height of the vertical leg.
- In specimens reinforced with 16 mm diameter beam bars, the difference between the failure load and the joint cracking load was greatest in specimens with low column axial load. This difference was not observed in specimens with 12 mm beam tension bars where beam flexural failure occurred for high column loads.
- Similarly to Taylor, Scott found that the detailing of beam tension steel bent down and U-bar performed better than the beam bars bent up into the column which is undesirable in practical joint design.

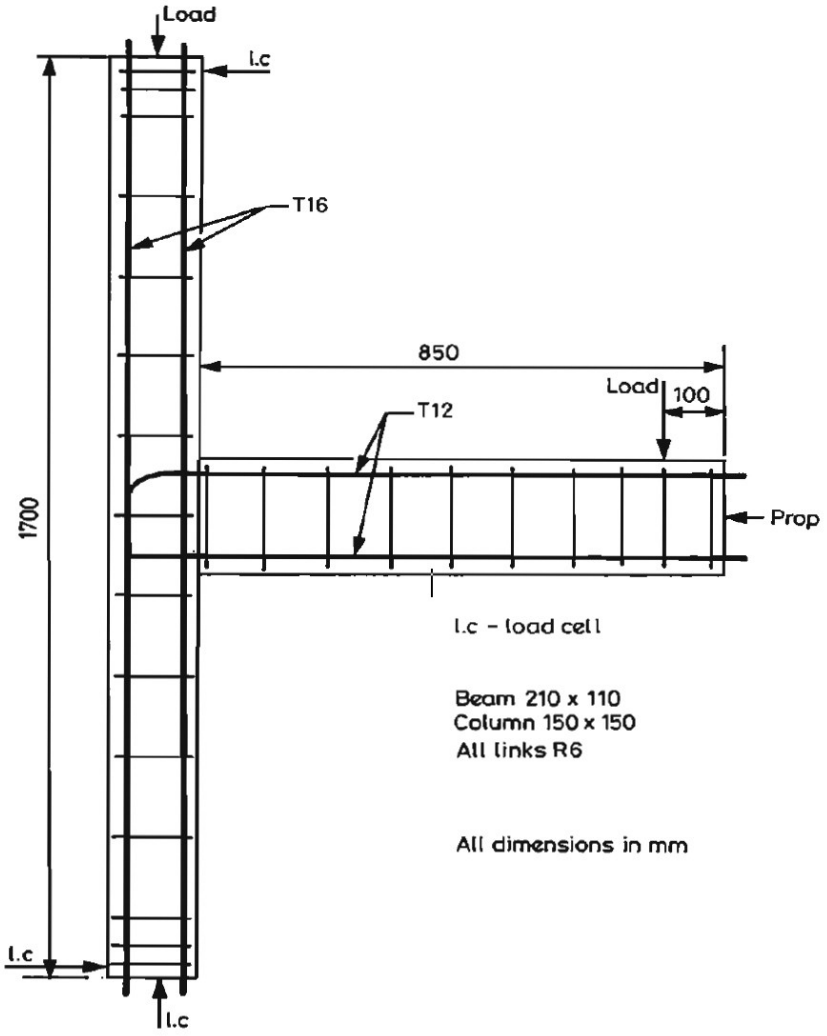

Figure 2-4 Layout of test specimens (dimensions in mm); reproduced from [11].

Table 2-7 Details of Scott's test specimens; adapted from [11].

Specimen	Beam depth (mm)	Beam tension reinforcement size (mm)	Beam tension reinforcement percent (%)	Concrete cube strength (MPa)	Concrete tensile strength (MPa)
C1	210	2T12	1.0	49.9	2.5
C1A	210	2T12	1.0	60.0	2.7
C1AL	210	2T12	1.0	41.7	2.1
C2	210	2T12	1.0	61.7	3.2
C3	210	2T12	1.0	45.0	3.1
C3L	210	2T12	1.0	44.4	2.6
C4	210	2T16	1.9	51.8	3.2
C4A	210	2T16	1.9	55.4	3.0
C4AL	210	2T16	1.9	44.7	2.4
C5	210	2T16	1.9	41.3	2.8
C6	210	2T16	1.9	49.8	2.6
C6L	210	2T16	1.9	57.3	2.8
C7	300	2T16	1.3	44.0	3.0
C8	300	2T16	1.3	55.6	3.4
C9	300	2T16	1.3	44.9	3.0

Table 2-8 Results of Scott's test specimens; adapted from [11].

Specimen	Detailing type	Column load (kN)	Failure mode	Beam failure load (kN)	Concrete cube strength (MPa)
C1	A	275	B	26.2	49.9
C1A	A	275	B	26.8	60.0
C1AL	A	50	J	22.0	41.7
C2	B	275	J	21.5	61.7
C3	C	275	B	25.9	45.0
C3L	C	275	J	21.6	44.4
C4	A	275	J	29.7	51.8
C4A	A	275	J	31.8	55.4
C4AL	A	50	J	28.3	44.7
C5	B	275	J	13.8	41.3
C6	C	275	J	21.8	49.8
C6L	C	50	J	26.0	57.3
C7	A	275	J	32.0	44.0
C8	B	275	J	27.3	55.6
C9	C	275	J	27.9	44.9

Note: 1. **A** denotes beam reinforcement bent down into column (L-bar).
2. **B** denotes beam reinforcement bent up into column (L-bar).
3. **C** denotes beam reinforcement bent into U-bar.

2.2.5 Ortiz [12]

Ortiz tested seven exterior large-scale beam-column joint specimens. The study investigated several parameters including bend radius, column load and number of joint stirrups. As shown in Figure 2-5 and Figure 2-6, the column had a height of 2400 mm and a depth of 300 mm. The beam had a length of 1300 mm with a depth of 400 mm. The width of the beam and column was 200 mm. The beam was loaded at a distance of 1050 mm from column face for BCJ 1 and 1100 mm from column face for the remaining of BCJ specimens. The concrete cube strength varied between 41 MPa and 47 MPa. All specimens had beam tension bars size 16 mm bending down into the column with a radius of 65 mm or 130 mm. The vertical leg of the L-bars used for the beam reinforcement varied between 220 mm and 420 mm. Beam compression bar size was 8 mm. Columns were reinforced with six, eight or ten 16 mm diameter bars corresponding to reinforcement ratios of 2.01%, 2.68% and 3.35% respectively. The reinforcement yield strength was 720 MPa for longitudinal reinforcement and 556 to 571 MPa for shear reinforcement. Specimens were tested with no, one, three and four joint stirrups. The column axial load was either zero or 300 kN. Details and results of test specimens are given in Table 2-9 and Table 2-10. The geometry of the BCJ specimens tested in this thesis was chosen to be similar to that of the Ortiz specimens, but the column depth was reduced from 300 mm to 250 mm to study the effect of increasing the joint aspect ratio. There is also some overlap of the parameters investigated in the test programs of Ortiz and this thesis. The similarity of the tested specimens allows a direct comparison of the results to be made. The following observations were made by Ortiz:

- Joint shear failure occurred in six specimens with the remaining specimen (BCJ7) failing in beam flexure. Change in failure mode from joint shear to flexure was due to the increase in number of joint stirrups.
- Increasing the column load from 0 to 300 kN in tests BCJ 5 to BCJ 7 had no effect on the joint shear strength but increased the load at joint cracking. The influence of column axial load was ambiguous because Ortiz varied many parameters for the number of tests. For example, the anchorage length of beam reinforcement was reduced from 420 mm in BCJ 1 and BCJ 3 (without column load) to 290 mm in BCJ 5 and BCJ 6 with column load of 300 kN making it difficult to draw comparative conclusions.

- Joint stirrups increased joint shear strength if positioned between the beam tension reinforcement and the top of the flexural compressive zone in the beam. Additionally, increasing the number of joint stirrups increased joint shear resistance significantly.
- Increasing the beam bar bend radius from 65 mm in BCJ 1 to 130 mm in BCJ 3, both without joint stirrups and no upper column axial load, prevented crushing of the diagonal strut in the radius of the bend. However, the failure load was 118 kN in both specimens. The same failure load was also observed in specimens BCJ5 and BCJ6 with column axial load of 300 kN and bend radii of 65 mm and 130 mm respectively.
- In most specimens, a diagonal crack propagated from the centre of the joint to the column reinforcement above the joint from where it extended along the outside column bars. This led to spalling of the concrete cover to the outside column bars which resulted in joint failure.
- Strains in the beam bars were greatest in the straight portion of the bars up to the start of the bend.

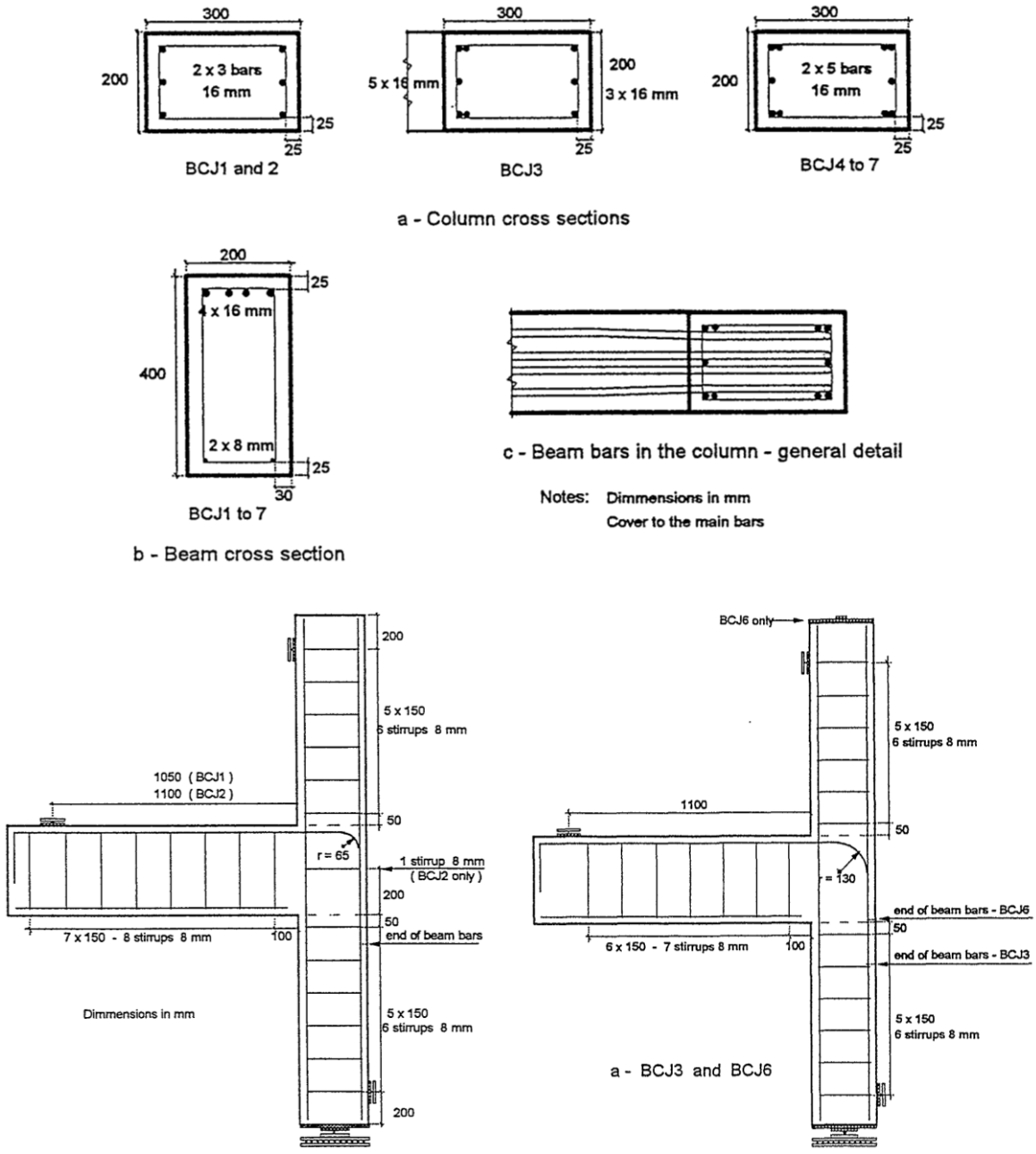

Figure 2-5 Details of Ortiz's test specimens; reproduced from [12].

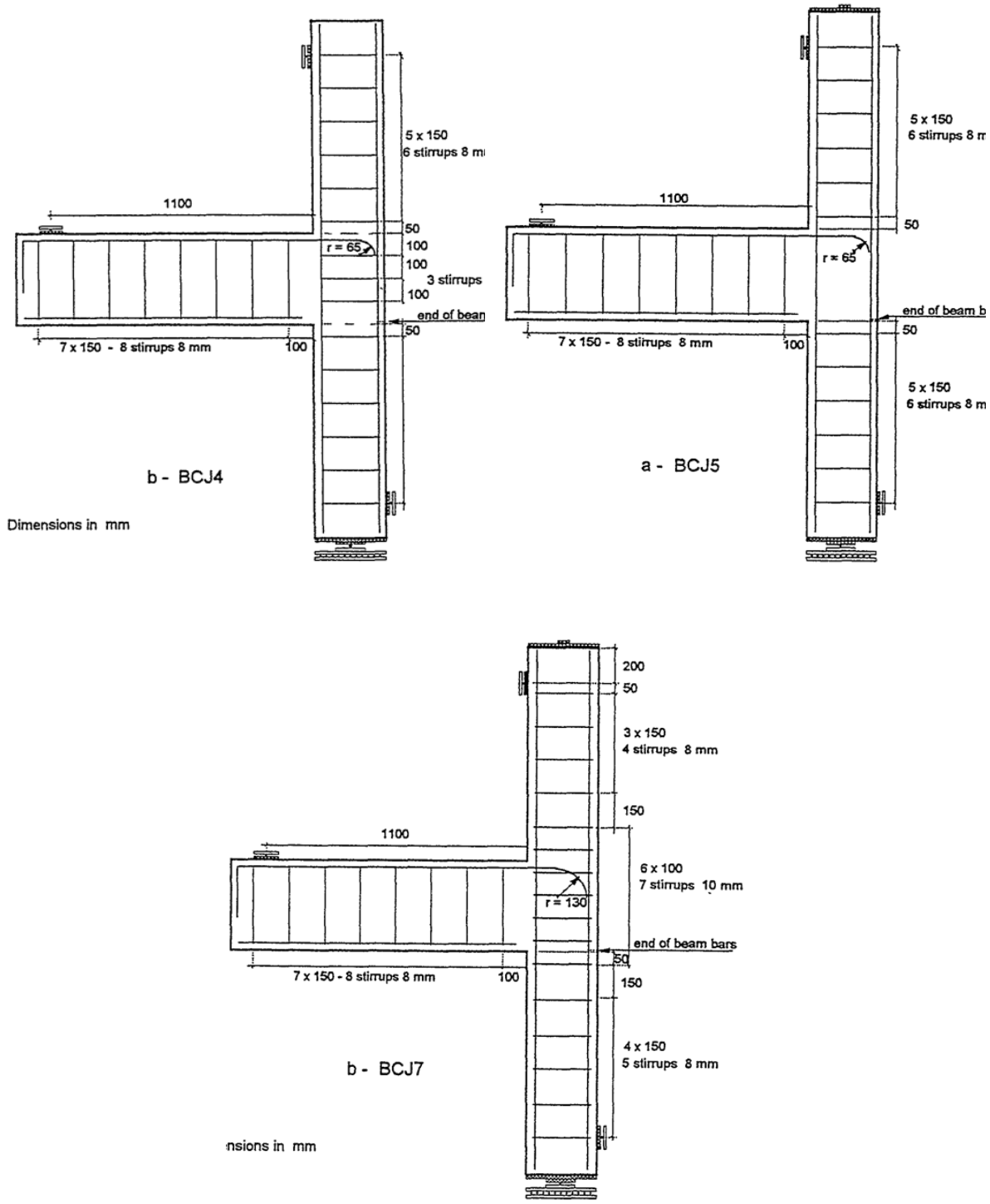

Figure 2-6 Details of Ortiz's test specimens BCJ 4, BCJ 5 and BCJ 7; reproduced from [12].

Table 2-9 Details of Ortiz test specimens; adapted from [12].

	Specimen	Bar size (mm)	Total area (mm^2)	Reinforce-ment percentage (%)	Yield strength (MPa)	Bend radius (mm)	Straight anchorage (mm)
Beam reinforce-ment.	BCJ 1 & 2	16	804	1.1	720	65	420
	BCJ 3	16	804	1.1	720	130	420
	BCJ 4 & 5	16	804	1.1	720	65	290
	BCJ 6 & 7	16	804	1.1	720	130	290
Column reinforce-ment.	BCJ 1 & 2	16	1206	2.01	720	-	-
	BCJ 3	16	1608	2.68	720	-	-
	BCJ 4 to 7	16	2010	3.35	720	-	-
Joint stirrups	BCJ 2	8	101	0.13	571	-	-
	BCJ 4	8	302	0.38	571	-	-
	BCJ 7	10	402	0.50	571	-	-

Table 2-10 Results of test specimens; adapted from [12].

Specimen	Concrete cylinder strength (MPa)	Column load (kN)	Top Reaction (kN)	Bottom Reaction (kN)	Beam load at failure (kN)
BCJ 1	34	0	70.8	70.8	118
BCJ 2	38	0	78.1	78.1	125
BCJ 3	33	0	73.8	73.8	118
BCJ 4	34	0	81.3	81.3	130
BCJ 5	38	300	68.6	68.6	115
BCJ 6	35	300	68.7	68.7	115
BCJ 7	35	300	102.9	102.9	170

2.2.6 Parker and Bullman [13]

Twelve large-scale beam-column joints were tested by Parker and Bullman [13]. The study investigated the effect of longitudinal reinforcement ratio in the beam and column, provision of joint stirrups and column axial load. The column height was 2000 mm with a cross-section of 300 x 300 mm. The beam was 500 mm deep and 250 mm wide. Details of the specimens are shown in Figure 2-7. The column axial load was varied between 0 and 600 kN. Four longitudinal reinforcement bars with diameter of either 16 mm, 25 mm or 32 mm were used in the column. The beams were reinforced with two bent down L-bars with diameter of 25 mm or 32 mm. The size of stirrups used in joint was 12 mm. The yield strength of the column bars varied between 485 MPa and 580 MPa while the yield strength of beam tension bars varied between 485 MPa and 570 MPa. The concrete strength used in this study ranged from 46 MPa to 56 MPa. The details of test specimens are given in Table 2-11. The spacing between joint stirrups was either 100 mm or 150 mm. The results of test specimens are summarised in Table 2-12. The following comments were observed by Parker and Bullman from the test results:

- The effect of column axial load was investigated and the results showed that the mode of failure changed from column hinging to either joint shear failure or beam hinging, when column axial load was increased. It was also observed that increasing the column load led to an increase in joint shear strength.
- Presence of joint stirrups enhanced the joint shear strength. Specimens 5A to 5f with joint shear reinforcement had larger failure loads than specimens 4a to 4f without shear reinforcement. Joint shear strength increased with increasing number of joint stirrups.
- The column reinforcement ratio was a significant factor in determining the ultimate strength of the joint.

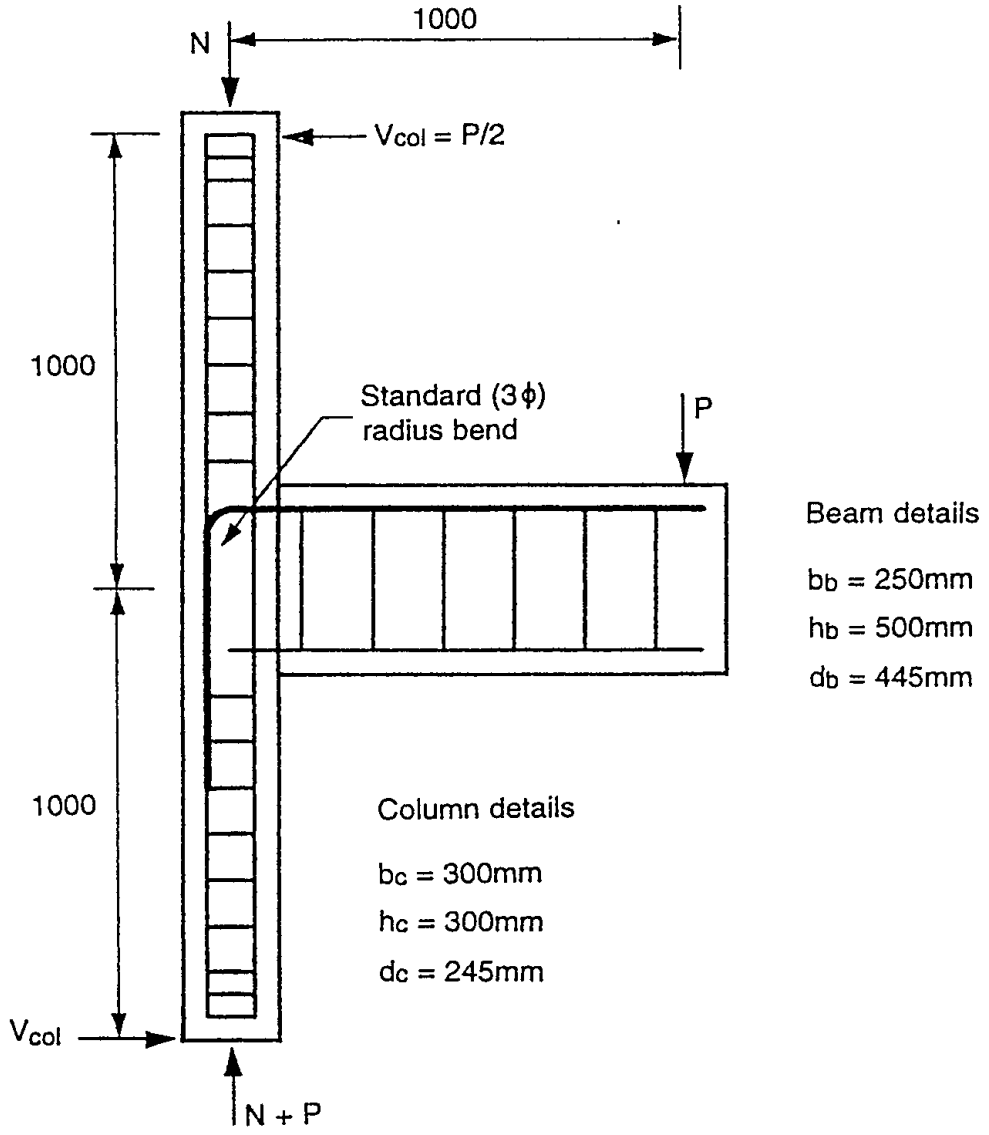

Figure 2-7 Layouts of test specimens of Parker and Bullman; reproduced from [13].

Table 2-11 Details of test specimens of Parker and Bullman; adapted from [13].

Specimen	Column steel (MPa)	Beam steel (MPa)	Stirrups (MPa)	Concrete cube strength (kN)
4a	550	570	560	49
4b	550	570	560	49
4c	550	570	560	46
4d	550	570	560	49
4e	550	570	560	50
4f	550	570	560	47
5a	485	485	480	53
5b	485	485	480	54
5c	485	485	480	54
5d	485	515	480	54
5e	485	515	480	56
5f	485	515	480	54

Table 2-12 Results of test specimens of Parker and Bullman; adapted from [13].

Specimen	Column steel	Beam steel	Joint stirrups	Column load (kN)	Failure load (kN)	Failure mode
4a	4T16	2T25	-	0	118	CF
4b	4T16	2T25	-	300	138	JS
4c	4T16	2T25	-	570	170	JS
4d	4T32	2T25	-	0	150	JS
4e	4T32	2T25	-	300	160	JS
4f	4T32	2T25	-	600	183	JS
5a	4T25	2T25	T12@150	0	213	CF
5b	4T25	2T25	T12@150	300	236	JS
5c	4T25	2T25	T12@150	600	242	BF
5d	4T25	2T32	T12@100	0	226	CF
5e	4T25	2T32	T12@100	300	295	CF
5f	4T25	2T32	T12@100	600	322	JS

Note: 1. **CF** denotes flexural failure in upper column.
2. **BF** indicates beam flexural failure.
3. **JS** refers to joint shear failure.

2.2.7 Hamil [14]

Seventy small-scale reinforced concrete beam-column joint specimens were tested of which 49 were monotonically loaded with the remainder cyclically loaded. The monotonic test programme included 16 specimens of which 8 specimens were cast with normal concrete strength and 8 specimens with high concrete strength. These specimens investigated beam anchorage type, number of joint stirrups and concrete strength. The monotonic test programme was extended, and 4 extra series were added including 11 specimens investigating joint stirrup positioning, 8 specimens investigating joint aspect ratio, 9 specimens investigating fibre reinforced concrete and 5 specimens investigating anchorage and shear plates. The column dimensions were 1700 mm high, 150 mm wide and 150 mm deep. The upper column axial load was 50 kN for specimens with normal concrete strength and 100 kN for specimens with high concrete strength. Specimen C6LN1 had an upper column load of 100 kN (series one), and a repeat of specimen C6LN1 was tested with a column load of 50 kN which is denoted as C6LN1(r). The beam had a length of 840 mm, a cross-section of 110 mm x 210 mm and was loaded 750 mm away from column face. Details of these specimens are shown in Figure 2-8. The beam depth was increased to 300 mm in the series investigating joint aspect ratio. Details of this series are shown in Figure 2-9. The beam tension steel bars were anchored into column by bending the bars 90-degree down or 180-degree (U-bar). The column in all specimens had four 16 mm steel bar diameter and 6 mm plain stirrups spaced at 150 mm centres. Beams with L-bars were reinforced with two 16 mm bars at the top and two 12 mm diameter bars at the bottom. The beam shear reinforcement consisted of 6 mm smooth stirrups at spacing of 100 mm. Normal-strength concrete with a compressive strength varying between 46 MPa and 64 MPa and high-strength concrete with a compressive strength ranging from 119 MPa to 130 MPa were used in this investigation. All steel reinforcement had a specified yield strength of 500 MPa. The internally gauging technique of Scott was used in this study, allowing detailed measurements of strain along the bars up to failure. The number of joint stirrups was either one, three or five. The stirrup positioning of first series specimens and specimens investigated stirrup positioning are shown in Figure 2-10 and Figure 2-11. The details and results of these specimens are given in Table 2-13 to Table 2-15. A prop with diameter of 40 mm was installed at the beam end to prevent sidesway. Conclusions from series one (16 specimens) cast from normal and high-strength concrete were as follows:

- The number of joint stirrups had no influence on the joint shear force at initial joint cracking. This was observed in specimens with normal and high-strength concrete. The beam anchorage detail influenced the joint shear force at initial joint cracking. Specimens with U-bar anchorage had higher resistance to joint cracking than specimens with L-anchorage detail. Hamil commented that the increase of joint strength at initial joint cracking in specimens with U-bar beam steel detail may be due to higher volumetric ribbed steel within the joint region.
- A significant increase in joint capacity was observed as the number of joint stirrups was increased from none to five. This was seen in specimens made with both normal and high-strength concrete. Specimens with both normal and high-strength concrete showed larger joint shear strength when L-bar beam reinforcement anchorage, rather than U-bar, was used.
- Specimens cast from normal strength concrete failed in joint shear while using high-strength concrete changed the failure mode in five specimens from joint shear failure to beam flexural failure. This change in failure mode was observed in specimens having L-anchorage bar and specimen C6LH5 (having 5 joint stirrups and U-bar detail).
- The vertical leg of L-bars used to anchor beam tension reinforcement transferred the beam force into the lower column while U-bar anchorages transferred the beam force into the joint region where the majority of this load was observed around the first bend. Hamil suggested that this was the reason of why specimens having U-anchorage bar had lower joint strength than specimens with L-bar beam detail.
- The beam tension steel bars in specimens C4ALN1 and C4ALN3, with normal strength concrete, yielded at the column face. In the companion high strength specimens C4ALH1 and C4ALH3, yielding of the beam tension bars penetrated into the column for a distance of around 200 mm from column face causing significant tension forces in the vertical legs.
- The test results showed larger bearing stress in specimens with L-anchorage detail for both normal and high strength specimens than calculated with equation (50) of BS 8110 [7] ($\sigma_{b(lim)} = 2\, f_{cu}/[1 + 2(\sigma/a_b)]$). However, lower values were observed for specimens having U-bar beam detail for both normal and high-strength concrete.

- Positioning joint stirrups near and above the beam tension bars increased the joint shear strength. This changed the failure mode from joint shear in C4ALN3 to beam flexure failure in specimens C4ALN3C and C4ALN3D all with three joint stirrups.

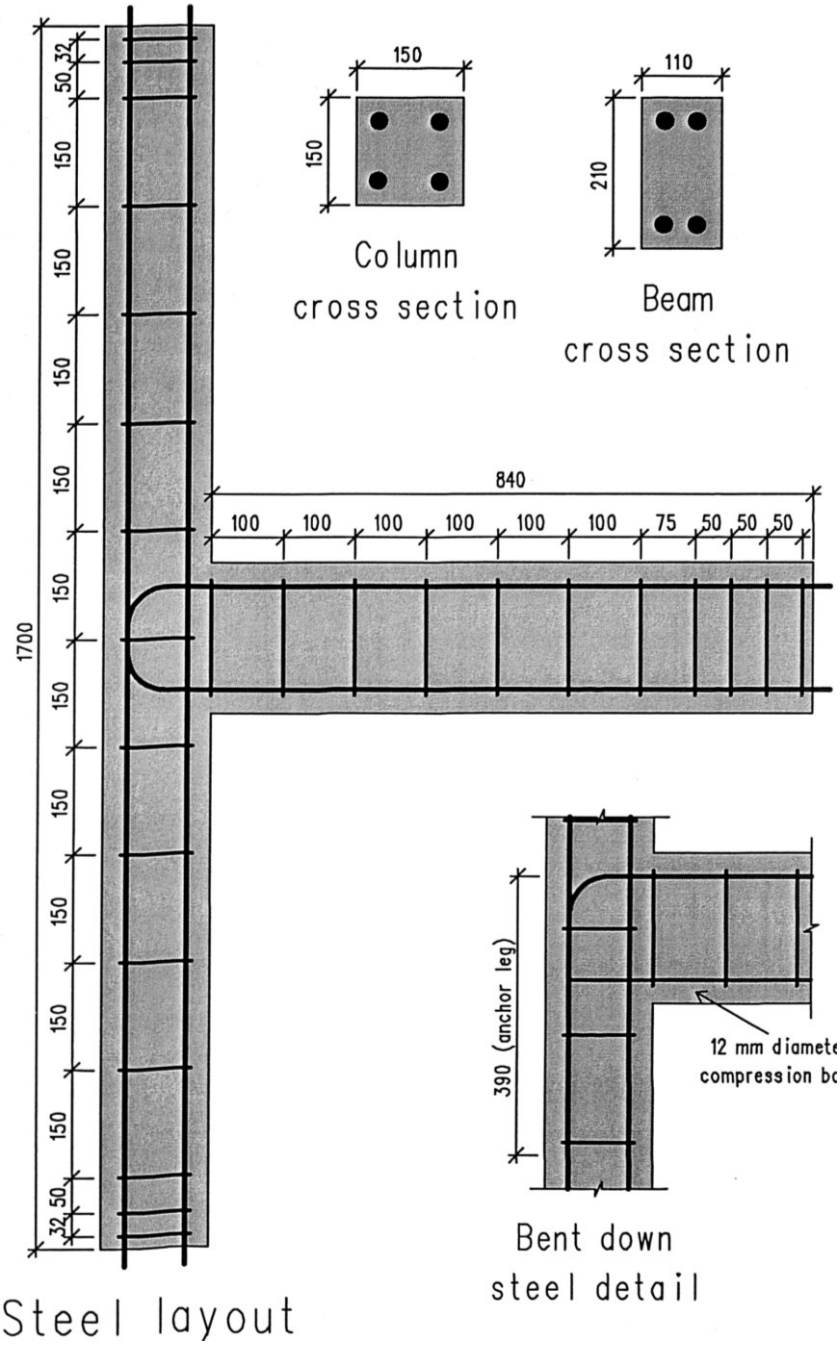

Figure 2-8 Details of test specimens with 210 mm deep beam; reproduced from [14].

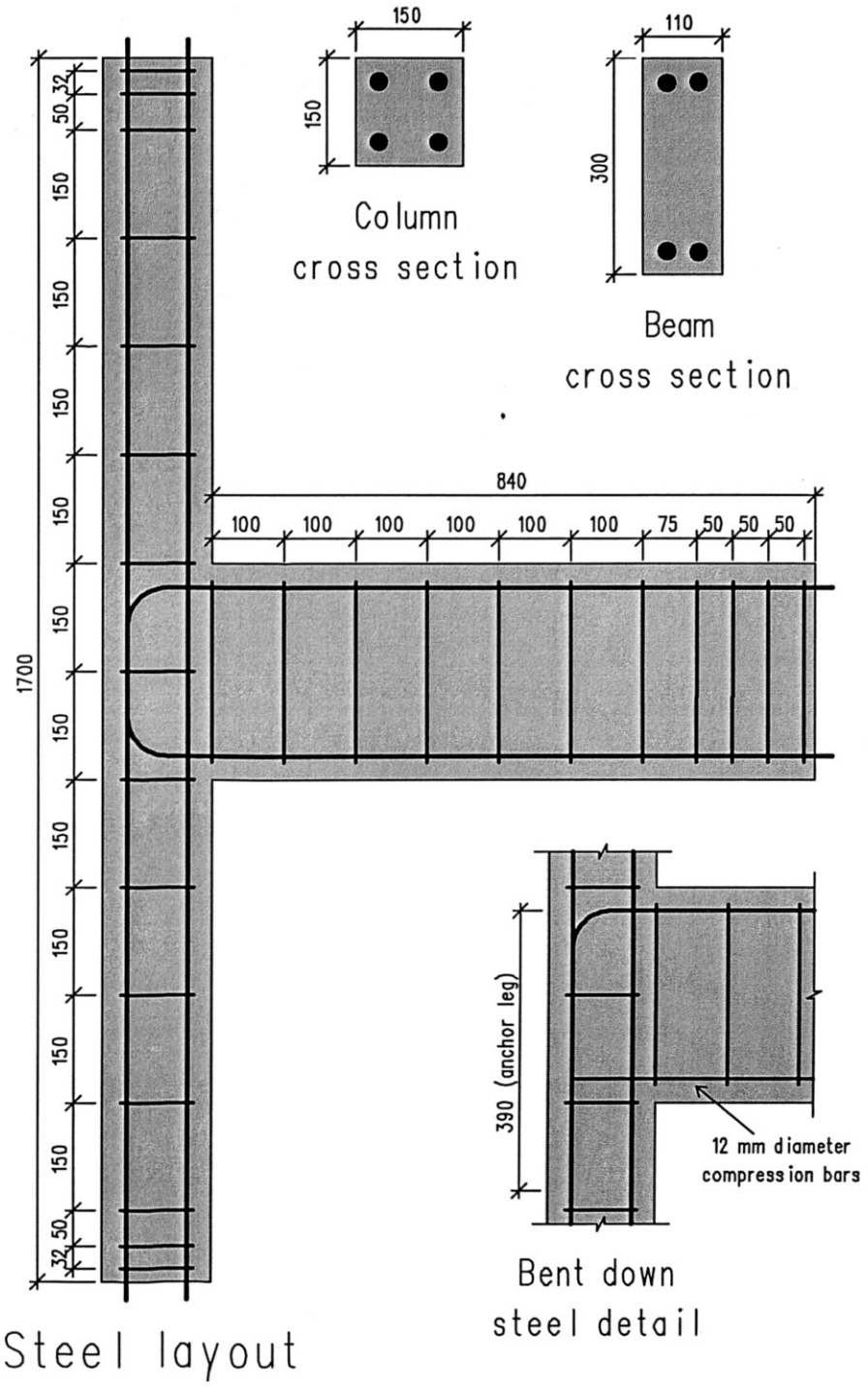

Figure 2-9 Details of test specimens with 300 mm deep beam; reproduced from [14].

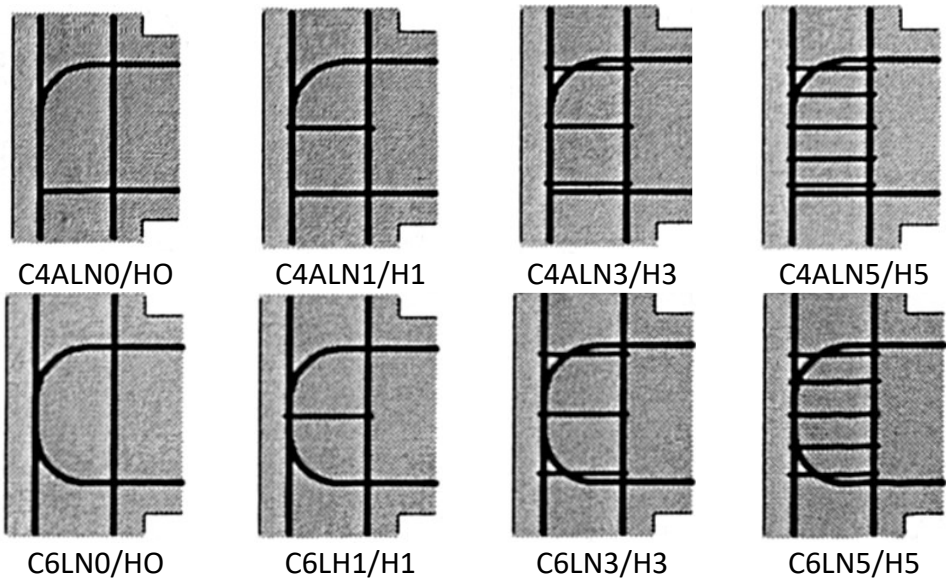

Figure 2-10 Details of joint stirrup positioning of first series test specimens; reproduced from [14].

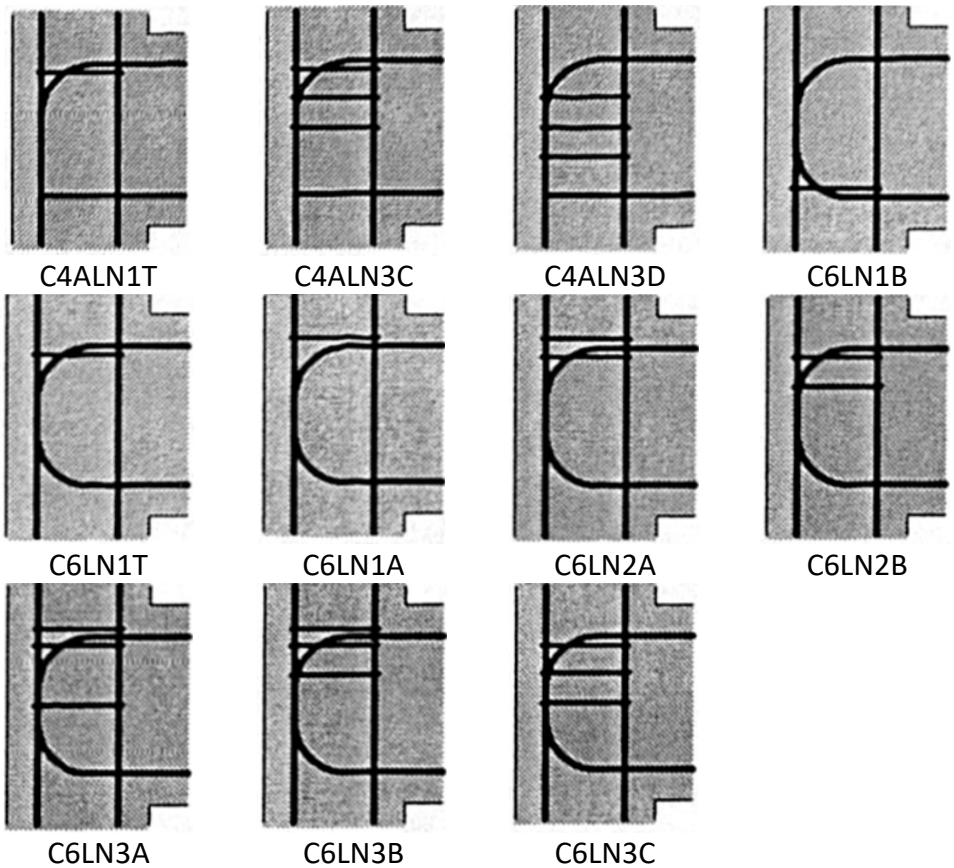

Figure 2-11 Details of specimens investigating stirrup positioning; reproduced from [14].

Table 2-13 Details of Hamil first series test specimens; adapted from [14].

Specimen	Beam depth (mm)	Beam tension reinforcement size (mm)	Number of joint stirrups	Concrete cube strength (MPa)	Concrete tensile strength (MPa)
Specimens with normal concrete strength					
C4ALNO	210	2T16	0	53	2.7
C4ALN1	210	2T16	1.0	57	3.4
C4ALN3	210	2T16	3.0	52	2.9
C4ALN5	210	2T16	5.0	63	3.2
C6LNO	210	2T16	0	64	3.4
C6LN1	210	2T16	1.0	64	3.3
C6LN3	210	2T16	3.0	61	3.2
C6LN5	210	2T16	5.0	46	2.7
Specimens with high concrete strength					
C4ALHO	210	2T16	0	130	4.9
C4ALH1	210	2T16	1.0	119	3.7
C4ALH3	210	2T16	3.0	132	5.5
C4ALH5	210	2T16	5.0	123	5
C6LHO	210	2T16	0	126	4.7
C6LH1	210	2T16	1.0	127	4.9
C6LH3	210	2T16	3.0	121	3.7
C6LH5	210	2T16	5.0	125	5.2

Note: 1. Specimens denoted **C6** had U-anchorage bar and specimens denoted **C4** had L-anchorage bar.

2. letter **N** in specimen denotation represents specimens with normal concrete strength; **H** denotes specimens with high concrete strength.
3. Numbers (0, 1, 3 and 5) at the end of specimen numbering refer to number of joint stirrups.

Table 2-14 Details of Hamil remaining series test specimens; adapted from [14].

Specimen	Beam depth (mm)	Beam tension reinforcement size (mm)	Number of joint stirrups	Concrete cube strength (MPa)	Concrete tensile strength (MPa)
Specimens investigating stirrup positioning					
C4ALN1T	210	2T16	1.0	50	3.3
C4ALN3C	210	2T16	3.0	56	3.2
C4ALN3D	210	2T16	3.0	59	3.4
C6LN1B	210	2T16	1.0	49	3.2
C6LN1T	210	2T16	1.0	50	3.2
C6LN1A	210	2T16	1.0	61	3.2
C6LN2A	210	2T16	2.0	64	3.4
C6LN2B	210	2T16	2.0	64	3.3
C6LN3A	210	2T16	3.0	58	3.1
C6LN3B	210	2T16	3.0	65	3.7
C6LN3C	210	2T16	3.0	60	3.3
Specimens investigating joint aspect ratio					
C7LNO	300	2T16	0	48	2.6
C7LN1	300	2T16	1.0	47	2.7
C7LN3	300	2T16	3.0	50	3.4
C7LN5	300	2T16	5.0	50	3.3
C9LNO	300	2T16	0	51	3.3
C9LN1	300	2T16	1.0	48	3.4
C9LN3	300	2T16	3.0	46	3
C9LN5	300	2T16	5.0	44	3.4
Specimens investigating steel fiber					
C4ALO4SF	210	2T16	0	45	4.5
C4AL15SF	210	2T16	0	47	3.8
C4AL23SF	210	2T16	0	55	4.7
C4ALO4LF	210	2T16	0	42	4.2
C4AL15LF	210	2T16	0	50	4.6
C4AL23LF	210	2T16	0	56	4.2
C4AL38LF	210	2T16	0	52	4.7
C6L04SF	210	2T16	0	54	3.2
C6L04LF	210	2T16	0	42	4.5
Additional specimens					
C6LN1(r)	210	2T16	1.0	61	3.2
C6LN1AE	210	2T16	1.0	55	3.1
C4PLNO	210	2T16	0	54	3.1
C6LNP4	210	2T16	Shear plate	58	3
C6PLNP4	210	2T16	Shear plate	51	3.2

Table 2-15 Results Hamil's test specimens for series one; adapted from [14].

Specimen	Detailing type	Column load (kN)	Beam failure load (kN)	Concrete cube strength (MPa)	Failure mode
Specimens with normal concrete strength					
C4ALNO	L	50	26.5	53	J
C4ALN1	L	50	33.5	57	J
C4ALN3	L	50	35.2	52	J
C4ALN5	L	50	39.5	63	J
C6LNO	U	50	23.9	64	J
C6LN1	U	100	24.6	64	J
C6LN3	U	50	28.7	61	J
C6LN5	U	50	33.9	46	J
Specimens with high concrete strength					
C4ALHO	L	100	43.2	130	F
C4ALH1	L	100	43.4	119	F
C4ALH3	L	100	45.6	132	F
C4ALH5	L	100	48.6	123	F
C6LHO	U	100	36.1	126	J
C6LH1	U	100	37.1	127	J
C6LH3	U	100	41.2	121	J
C6LH5	U	100	51.4	125	F

Note: 1. Letter **U** denotes U-anchorage bar and letter **L** denotes L-anchorage bar.
2. letter **J** refers to joint shear failure; letter **F** denotes beam flexural failure.

2.2.8 Hegger et al [15]

Fifteen beam-column joints, eight external and seven internal, were monotonically tested. Details of these specimens are shown in Figure 2-12.The main parameters investigated were joint aspect ratio (h_{beam}/h_{col}), compressive concrete strength (f'_c), beam reinforcement ratio and detailing, column longitudinal reinforcement ratio, and shear reinforcement. The exterior beam-column joints had two anchorage details, either 180-degree hooked bar or headed bar. The column height from top support to lower support was 1660 mm with a cross section of 150 mm x (200 mm or 240 mm deep). The beam was 150 mm wide by either 300 mm or 400 mm deep and was loaded 850 mm away from the column face. The concrete compressive strength ranged from 39 MPa to 87 MPa. The beam tension bars were a pair of 20 mm or 25 mm bars, except for specimen RK2 having extra diagonal steel reinforcement of 20 mm diameter. The columns were reinforced with four 16 mm diameter longitudinal bars, except for specimen RK2 having extra U-bar No. 20 inside the joint. Four hairpin stirrups of either 8 mm or 10 mm diameter were positioned in the joint. The joint aspect ratios (h_{beam}/h_{col}) considered in this study were 1.25, 1.50 and 2.0. An axial load of 500 kN was applied to the upper column in all specimens. The results and details of this study are given in Table 2-16. A database of 200 tests (including internal and external monotonically loaded joints) from the literature was used to assess the validity of the ACI-ASCE recommendations. The results of tests on external beam-column joint specimens are as follows:

- The beam anchorage detail influenced joint shear strength. Headed bars showed better performance than 180-degree hooked bars, with joint shear strength increased by 20% relative to hooked bars.
- The authors calculated joint shear strength using the ACI-ASCE 352 [16, 17] provisions which were found to be conservative. In comparison to 180-degree hooked bars, the degree of conservatism of the ACI-ASCE provisions increased for specimens with headed bars where the ratio of ($V_{j,Test}/V_{n,ACI}$) increased from 1.33 for specimen RK4 to 1.53 for specimen RK5. A reduction in degree of conservatism to ACI provisions was observed when (h_{beam}/h_{col}) ratio increased. The ratio of ($V_{j,Test}/V_{n,ACI}$) decreased from 1.33 to 1.0 for specimens RK4 (h_{beam}/h_{col} = 1.5) and RK7 (h_{beam}/h_{col} = 2.0) respectively.
- External beam-column joint specimens having (h_{beam}/h_{col} = 1.25) failed due to beam hinging and specimens with joint aspect ratio more than 1.25 failed in joint shear. This

indicated that joint shear strength reduces as joint aspect ratio (h_{beam}/h_{col}) increases, as shown in Figure 2-13(b).

- The ACI-ASCE provisions [16,17] require a minimum of at least two layers of joint stirrups. The tests with two or more joint stirrups showed conservative results with ACI-ASCE 352 [17] requirements. However, ACI provisions were on the unsafe side when the ratio of joint stirrups was less than 0.5% as shown in Figure 2-13(c).
- Test results showed a significant increase in joint strength as column reinforcement ratio increases. The ACI formula, unfortunately, did not consider the effect of column longitudinal reinforcement ratio when evaluating joint shear resistance force.
- A model was developed for design applications, taking into consideration the parameters investigated in the study. The model showed good agreement with the experimental tests and 200 tests from the literature.

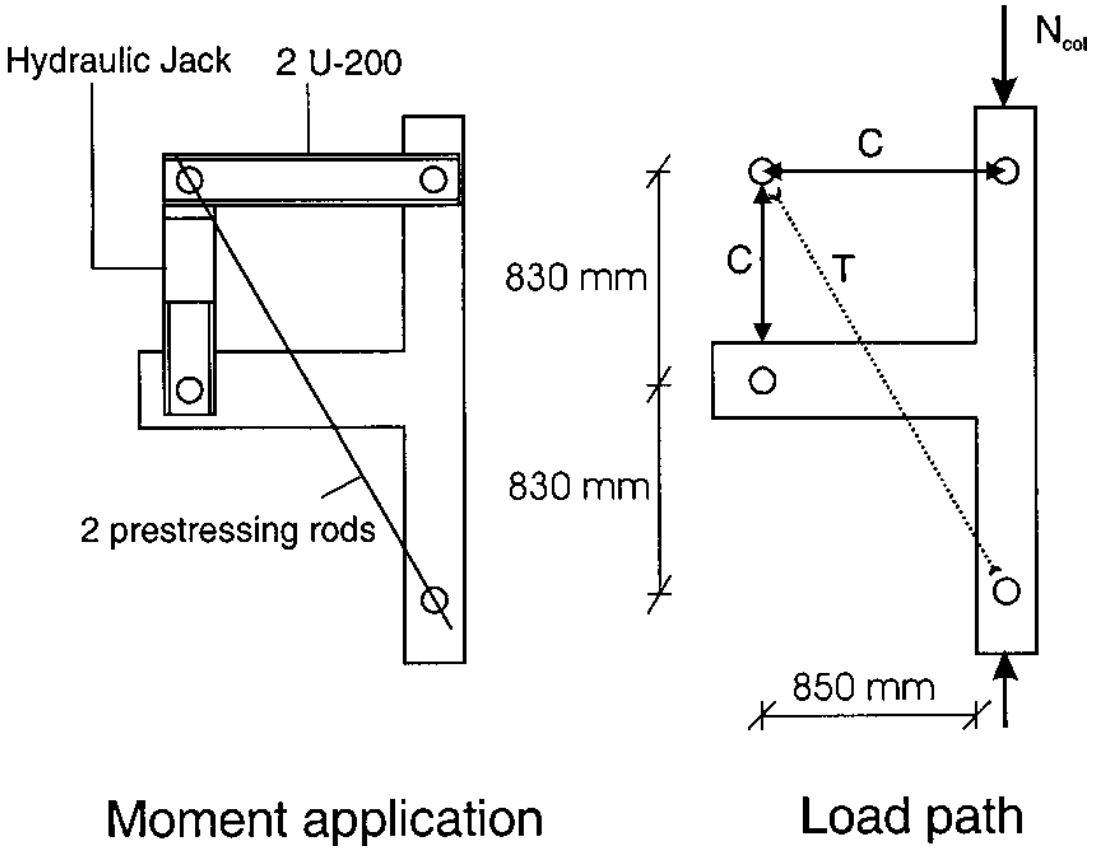

Figure 2-12 Layouts of test specimens; reproduced from [15].

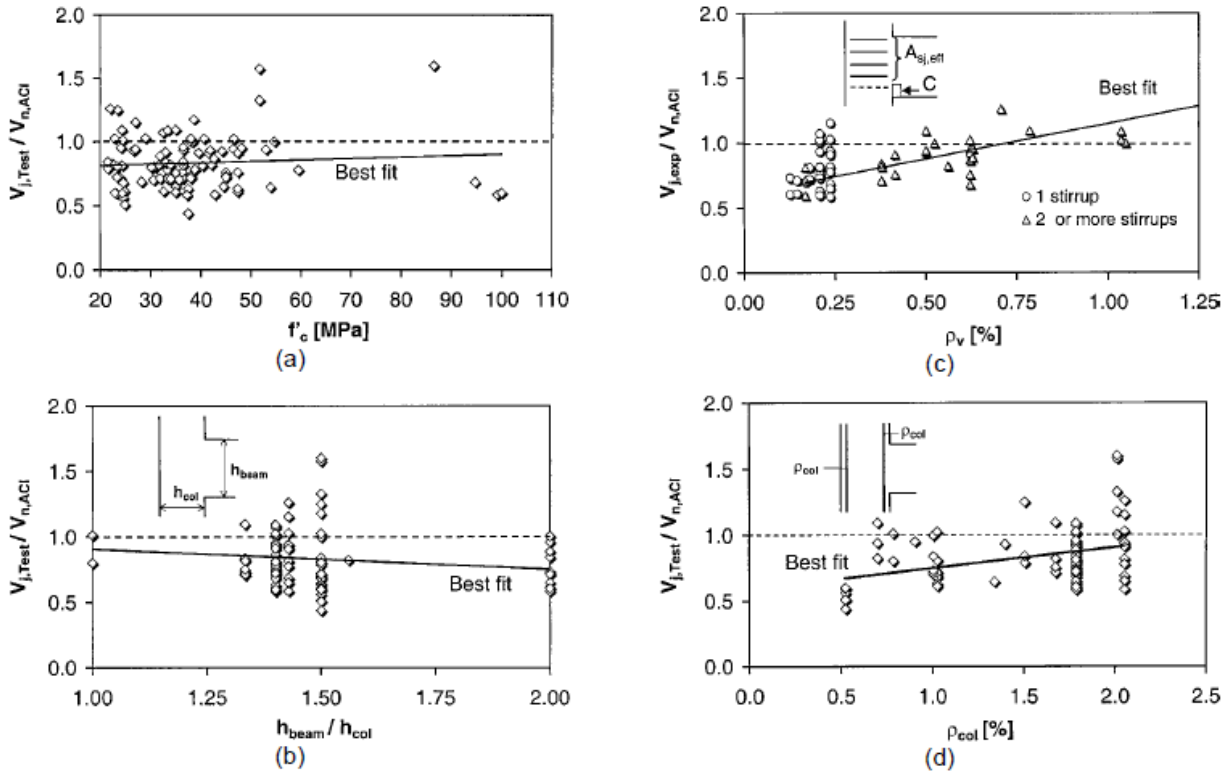

Figure 2-13 Parameters affecting failure load of external beam-column joint predicted by ACI provisions; reproduced from [15].

Table 2-16 Results of exterior test specimens; adapted from [15].

Test*	h_{beam}/h_{col}	f_c', MPa	Beam tension reinforcement	Column reinforcement	Stirrups hairpins	V_jTest, kN	V_nACI, kN	$\frac{V_jTest}{V_nACI}$
RK1	1.25	57.9	2 No. 20	2 x No. 16 + 2 No. 16	4 No. 10	374	341.0	1.10
RK2	1.25	57.4	2 No. 20 + 1 No. 20 diagonal	2 x 2 No. 16 + U bar No. 20	4 No. 8	417	339.6	1.23
RK3	1.25	57.2	2 No. 20	2 x 2 No. 16 + 2 No. 16	4 No. 10	402	339.0	1.19
RK4	1.50	51.7	2 No. 20	2 x 2 No. 16 + 2 No. 16	4 No. 10	357	268.6	1.33
RK5	1.50	54.9	2 No. 25	2 x 2 No. 16 + 2 No. 16	4 No. 10	423	276.7	1.53
RK6	1.50	86.5	2 No. 25	2 x 2 No. 16 + 2 No. 16	4 No. 10	556	347.4	1.60
RK7	2.00	54.7	2 No. 20	2 x 2 No. 16 + 2 No. 16	4 No. 10	277	276.2	1.00
RK8	1.50	38.6	2 No. 20	2 x 2 No. 16 + 2 No. 16	4 No. 10	273	232.1	1.18

*Configuration = RK1 RK2 RK3 RK4 RK5 RK6 RK7 RK8

Note: Width of beam = width of column = 150 mm; h_{beam} = 300 mm for all beams except for RK7 h_{beam} = 400 mm; h_{col} = 240 mm for RK1 to RK3 = 200 mm for RK4 to RK8; N_{col} = 500 kN; and type of failure = beam failure for RK1 to RK3, joint failure for RK4 to RK8.

2.2.9 Sperry et al [18&19]

Three hundred and thirty-seven reinforced hooked bar pullout specimens were conducted in this study. The tested specimens are reviewed here since they have similarities to external beam-column joints. Investigated parameters included the number of hooked bars per specimen, bar diameter, side cover, amount of confining reinforcement, hooked bar spacing, hook bend angle, hook placement and embedment length. The layouts and details of the test specimens are given in Figure 2-14 and Table 2-17. The development length of the hooked bars was calculated according to ACI 318-14. Concrete compressive strength varied between 30 MPa and 114 MPa. Hooked bars were either normal-strength steel ASTM A615 (f_y = 550 MPa) or high-strength steel A1035 (f_y = 830 MPa). Three US bar diameters were chosen in this investigation No.5 (d_b = 15.875 mm), No.8 (d_b = 25.4 mm) and No.11 (d_b = 35.81 mm). Columns were reinforced longitudinally and transversely with normal-strength steel ASTM A615, with side cover ranging from 38 to 102 mm. Two hundred and seventy-six specimens were cast with a pair of hooked bars spaced at 203 mm for specimens with hooked bars No.5, at 305 mm for specimens with hooked bars No.8 and at 419 mm for specimens with hooked bars No.11. The rest of the specimens had more than two hooked bars for all bar sizes. The joint was reinforced with stirrups of size No.3 (d_b = 9.525 mm) with one hoop, two hoops or spaced at $3d_b$. The hooked bars had a bend angle of either 90-degree or 180-degree, with embedment length ranging from 89 mm to 286 mm for bar No.5, 147 to 495 mm for bar No.8 and 257 to 668 mm for bar No.11. A constant axial load was applied to the column from the beginning of the test. The magnitude of the column load depended on the column cross-section dimensions. Specimens with hooked bars No.5 and No.8 had column loads of 133 kN and 356 kN respectively (with axial stress ranging from 0.53 to 7.17 MPa) while other specimens with hooked bars No.11 had a constant axial stress of 1.93 MPa. The results of this study are as follows:

- The anchorage strength of specimens with bars No.5 and No.8 bars (d_b = 15.875 mm and 25.4 mm respectively) compared well with the ACI 318-14 provisions [20] for hooked bars but the anchorage strength of specimens with bar No.11 bars (d_b = 35.81 mm) was over estimated.
- Five failure modes were observed: front pullout, front blowout, side splitting, side blowout and tail kickout. The front and side failure were considered the main failure

of most specimens while the tail kickout was a secondary failure with either front or side failure.

- The blowout failure caused spalling of concrete on either the front or side face of the column. In the pullout failures, a cone of concrete pulled out from the front column face along with the hooked bar. The tail kickout failure exposed the vertical leg of the hooked bar by pushing the concrete cover off the back column face.
- In most specimens, slip occurred along the straight part of the bar before the first bend, resulting in bearing at the bend becoming the primary bar anchorage.
- A regression analysis technique based on dummy variables was used in order to evaluate the development length of hooked bar provided by ACI 318-14 [20]. The analysis showed that the effect of concrete compressive strength, confining reinforcement in joint and the strengths of larger hooked bar diameters is overestimated by ACI 318-14 [20].
- The ratio of the measured tensile force to the predicted tensile resistance ($F_s/F_{s,ACI}$) increased when shear reinforcement was added to the joint. However, the ratio $F_s/F_{s,ACI}$ became progressively unsafe with increasing anchorage bar size and concrete compressive strength. This indicates that ACI 318-14 [20] formula should be adjusted to reflect more accurately the effects of parameters investigated in this study.

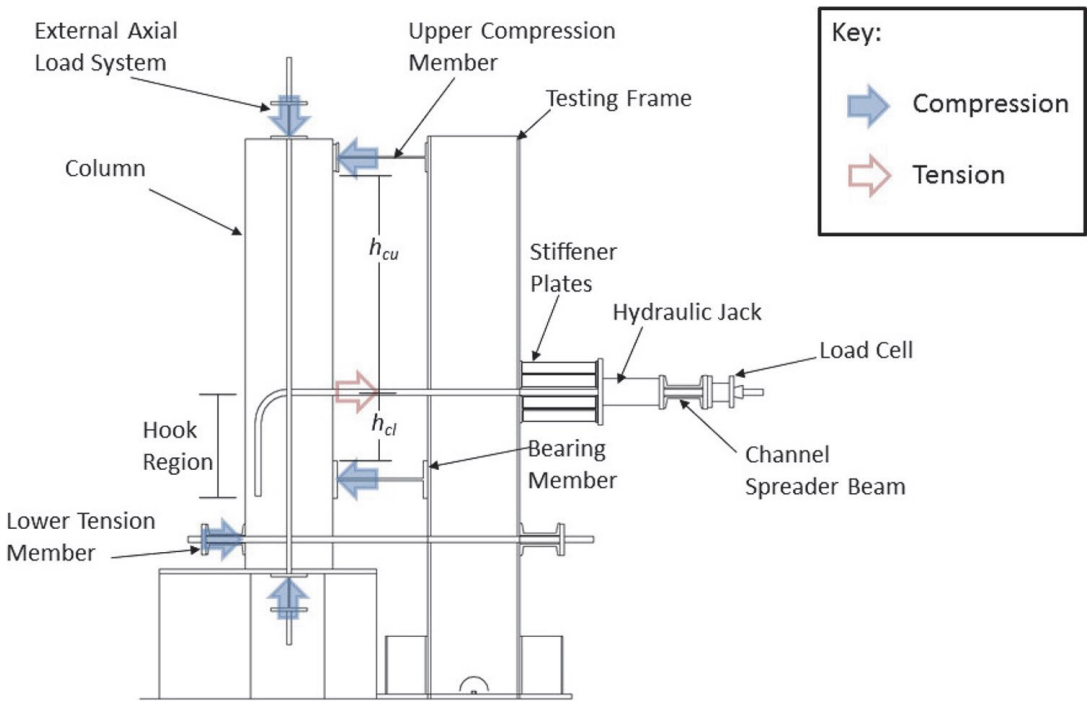

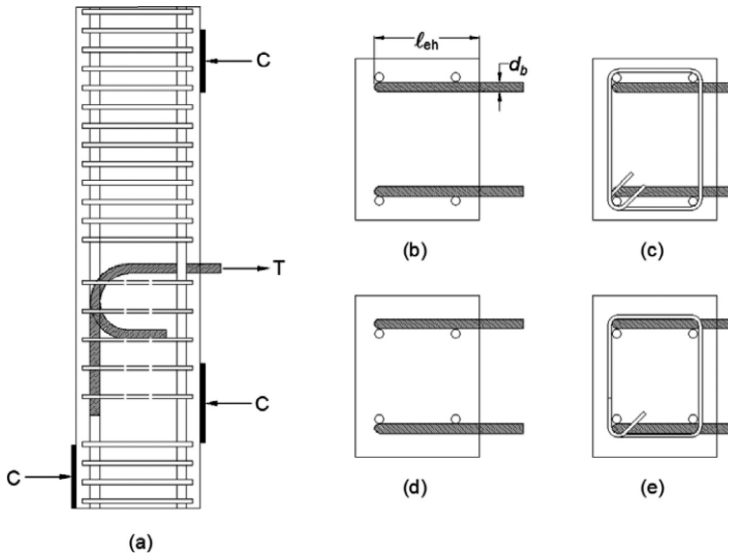

Size of hooked bar	No. 5 (No. 16)	No. 8 (No. 25)	No. 11 (No. 36
Specimen height, in.	54	54	96
Distance from center of hook to top of bearing member flange, h_{ci}, in.*	5-1/4	10	19-1/2
Distance from center of hook to bottom of upper compression member flange, h_{co}, in.*	18-1/2	18-1/2	48-1/2

Figure 2-14: Layout of Sperry et al. test specimens; reproduced from [18&19].

Table 2-17 Details of test specimens for Sperry et al.; adapted from [18&19].

Bar size	ASTM designation	Yield strength, ksi*	Tensile strength, ksi*	Nominal diameter, in.	Average rib spacing, in.	Average rib height		Gap width		Relative rib area‡
						A†, in.	B‡, in.	Side 1, in.	Side 2, in.	
5	A1035	119.5	162.5	0.625	0.391	0.038	0.034	0.200	0.175	0.073
8	A615	94.0	128.3	1	0.666	0.059	0.056	0.146	0.155	0.073
8	A1035§	120.0‖	168.0‖	1	0.666	0.059	0.056	0.146	0.155	0.073
8	A1035#	122.0‖	168.0‖	1	0.686	0.068	0.065	0.186	0.181	0.084
8	A1035**	129.0	167.3	1	0.666	0.056	0.059	0.146	0.155	0.073
11	A615	88.2	122.1	1.41	0.894	0.080	0.074	0.204	0.196	0.069
11	A1035	131.0	165.7	1.41	0.830	0.098	0.088	0.248	0.220	0.085

*Tests performed as part of this study. †Per ASTM A615, A706. ‡Per ACI 408R-03. ‖From mill report. §Heat 1. #Heat 2. **Heat 3.

Notes: 1 in. = 25.4 mm; 1 ksi = 6.89 MPa.

2.3 Design of external RC beam-column joint

The design procedure of external beam-column joints typically consists of the following steps:

- Calculate the design joint shear force (V_{jd}).
- Determine the effective joint shear area in accordance with the adopted design code (e.g. equations (2-3), (2-4) and (2-6)).
- Check that the design joint shear strength is greater than the design joint shear force. The design joint shear strength is the sum of the contributions of the concrete and joint stirrups. If the maximum possible shear resistance is exceeded the joint geometry or concrete strength should be changed.
- Ensure adequate anchorage of beam flexural reinforcement in the joint.

2.3.1 Calculation of joint shear force

In general, a frame analysis should be carried out to obtain the design moments in the beam and column. However, as shown in Figure 2-15, the beam moment at the face of the column in a typical test specimen is calculated as $M_b = P. L$ where L is the distance from the centre of the load to the column face. The column moments at the top and bottom of the joint are calculated from the horizontal reactions at the column ends (e.g. $M_{col,upper} = V_{col} . H_{c1}$). As shown in Figure 2-15, the joint shear force is given by the difference between the tensile force in the beam flexural reinforcement and the shear force in the upper column ($V_j = T – V_{col}$).

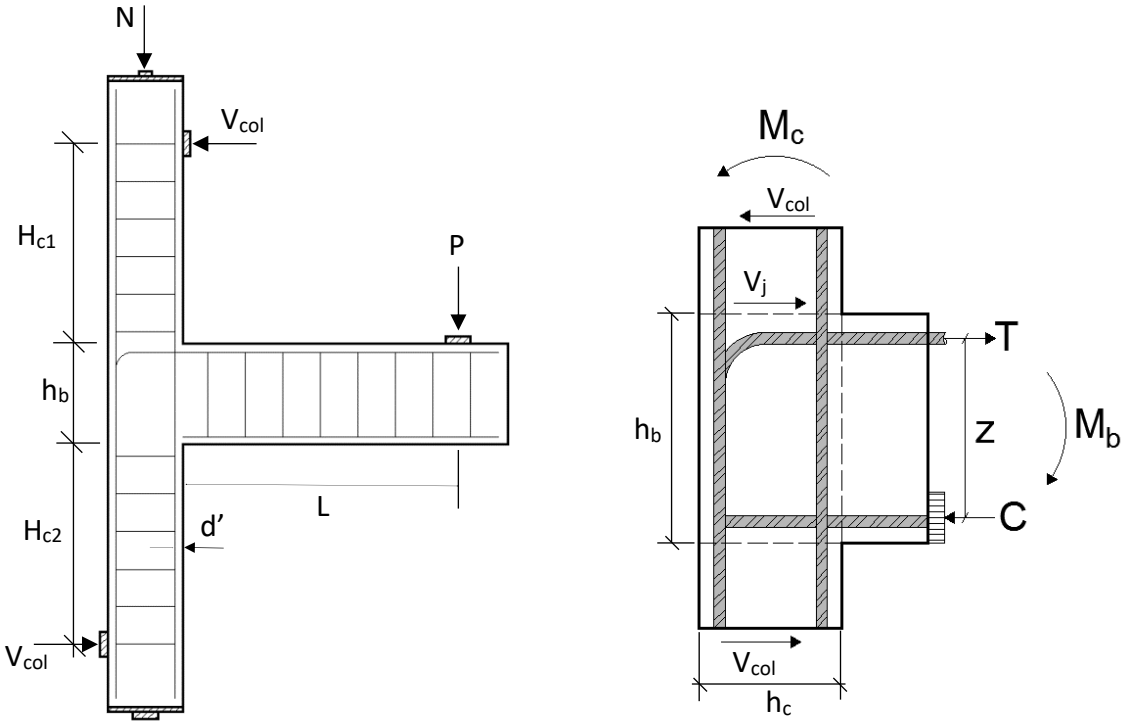

Figure 2-15: Internal and external forces in beam-column joint

2.3.2 Design code recommendations

2.3.2.1 ACI/ASCE Committee 352-05 [16]

ACI/ASCE Committee 352 [16] provides recommendations for the design of monotonically loaded internal and external beam-column joints. These recommendations include member proportions, adequate confinement in the joint core, control of joint shear stress, ratio of column-to-beam flexural strength at the connection, development of reinforcing bars and details of columns and beams framing into the joint. ACI/ASCE Committee 352-05 [16] categorises beam-column joints as follows:

- Type 1 is a moment-resisting connection designed on the basis of strength without taking into account special ductility requirements (joints in typical frame designed to resist gravity and normal wind loads), satisfying ACI 318 [21] strength requirements.
- Type 2 is a connection joining members that are required to dissipate energy through inelastic deformation (induced by earthquake motions, high winds, or blast effects).

The ultimate joint shear resistance is obtained using equation (2-2), where the constant 0.083 is a factor used to convert the equation from psi to MPa, h_c is the depth of the column, b_j is the effective joint width and f_c' is the concrete compressive strength. Because the research studies at that time (1985) had limited concrete strength, equation (2-2) is unsuitable for concrete compressive strength larger than 42 MPa. The constant γ is a factor given in Table 2-18 which is based on the joint classification and joint type.

$$V_c = 0.083\,\gamma\sqrt{f_c'}\,b_j h_c \tag{2-2}$$

The effective joint width b_j is determined from the beam width b_b and column width $b_c$using equation (2-3). The effective joint width b_j should not be taken as greater than the beam width b_b plus one half of the column depth h_c on each side of the beam.

$$\begin{aligned} if\ b_b\ > b_c\,, then\ b_j = b_c \\ if\ b_b\ \leq b_c\,, then\ b_j = (b_c + b_b)/2 \end{aligned} \tag{2-3}$$

Table 2-18 Values of γ for beam-to-column – ACI-ASCE Committee 352-05; adapted from [16]

	Joint classification		
Joint type	(a)Interior	(b)Exterior	(c)Corner
1	**24**	20	15
2	20	15	12

2.3.2.2 ACI/ASCE Committee 352-02 [17]

The recommendations provided by ACI/ASCE Committee 352-02 (2002) [17] are similar to those adopted in ACI/ASCE Committee 352-05 (1985) [16]. The nominal joint shear strength is calculated using equation (2-2). The constant γ is a factor given in Table 2-19

which is based on the connection classification and type. The only difference with the ACI/ASCE Committee 352-02 [16] recommendations is in the determination of effective joint depth b_j which is calculated using equation (2-4). b_b and b_c are the beam and column width, h_c is the column depth and m is the slope used to define the joint effective width transverse to the direction of shear. The value of m should be taken as 0.3 for joints where the eccentricity between the beam centerline and the column centroid exceeds $b_c/8$ and 0.5 for all other cases. The term (m . $h_c/2$) should not be larger than the extension of the column beyond the edge of the beam.

$$b_j = min\left(\frac{b_b + b_c}{2}; b_b + \sum \frac{m\,.\,h_c}{2};\ b_c\right) \quad (2\text{-}4)$$

Table 2-19 Values of γ for beam-to-column – ACI-ASCE Committee 352-02; adapted from [17].

Classification	Connection type	
	1	2
A. Joints with a continuous column		
A.1 Joints effectively confined on all four vertical faces	24	20
A.2 Joints effectively confined on three vertical faces or on two opposite vertical faces	20	15
A.3 Other cases	15	12
B. Joints with a discontinuous column		
B.1 Joints effectively confined on all four vertical faces	20	15
B.2 Joints effectively confined on three vertical faces or on two opposite vertical faces	15	12
B.3 Other cases	12	8

For joint shear reinforcement, ACI-ASCE Committee 352-02 [17] recommends providing at least two layers of transverse reinforcement between top and bottom levels of beam tension bars. The spacing from center-to-center of shear reinforcement should be 300 mm for joints resisting gravity loads and 150 mm for joints subjected to non-seismic lateral loads. Additionally, the transverse reinforcement should satisfy Section 7.10 of ACI 318 [21].

2.3.2.3 Eurocode 8 [22]

EC2 [23] does not give formulae for the design of beam-column joints though guidance is given in EC8 [22] for seismically loaded connection. EC8 [22] states that “The diagonal compression induced in the joint by the diagonal strut mechanism shall not exceed the

compressive strength of concrete in the presence of transverse tensile strains". In the absence of a more precise model EC8 provides the following equation for evaluating the shear strength of external and internal joints:

$$V_{jhd} \leq \eta . f_{cd} \sqrt{1 - \frac{\nu_d}{\eta}} . b_j . h_{jc}$$
$$\eta = \alpha \left(1 - \frac{f_{ck}}{250}\right) \quad (2\text{-}5)$$

Where h_{jc} represents the distance between extreme layers of column reinforcement, b_j is the effective joint width, ν_d is the normalised axial force in the column above the joint [$\nu_d = N_{Ed}/(A_c . f_{cd})$], and f_{ck} is concrete strength in MPa. The parameter α should be taken as 0.6 for internal joints and 0.48 for external joint corresponding to 80% of joint shear strength of internal joints. To obtain the effective joint width, the following expression are used:

a) $if\ b_c > b_w;\ b_j = min\{b_c; (b_w + 0.5 . h_c\}$
b) $if\ b_c \leq b_w;\ b_j = min\{b_w; (b_c + 0.5 . h_c\}$ (2-6)

Where b_c and b_w are the column and beam width and h_c is the column depth.

EC8 requires adequate confinement (both horizontal and vertical) of the joint to be provided, to limit the maximum diagonal tensile stress of concrete max σ_{ct} to f_{ctd}. In the absence of a more precise model, the following expression can be used to determine the required area of horizontal hoops:

$$\frac{A_{sh} . f_{ywd}}{b_j . h_{jw}} \geq \frac{(\frac{V_{jhd}}{b_j . h_{jc}})^2}{f_{ctd} + \nu_d . f_{cd}} - f_{ctd} \quad (2\text{-}7)$$

Where:

A_{sh} is the total area of the horizontal hoops;

h_{jw} is the distance between the top and the bottom reinforcement of the beam;

h_{jc} is the distance between extreme layers of column reinforcement;

f_{ctd} is the design value of the tensile strength of concrete, in accordance with EN 1992:2004 [23];

V_{jhd} is taken as ($V_{jhd} = \gamma_{Rd} . A_{s1} . f_{yd} - V_c$) for exterior joint;

A_{s1} is the area of the beam top reinforcement;

γ_{Rd} is a factor account for overstrength and should be not less than 1.2;

V_c is the shear force in the column above joint.

2.3.3 Methods proposed by researchers

Research has shown that joint strength is affected by a large number of parameters including concrete strength, joint geometry, beam reinforcement ratio, beam anchorage reinforcement type and bend radius, joint shear reinforcement area and position, column load and intermediate column bars if present. Many of the parameters that influence joint strength are not considered in design standards. Some previous researchers proposed empirical methods for designing beam-column joints but codes of practice have not generally taken these recommendations into account. Vollum and Newman [24] proposed a simple design method for external joints with and without stirrups. Their method realistically predicts the strength of many previous tests and is more accurate than the design methods given by EC 8 [22] and ACI/ASCE Committee 352 [16, 17] due to inclusion of the effect of joint aspect ratio (h_b/h_c). Sperry et al. [18, 19] studied the effect of high strength concrete, large steel bar size and high strength steel on hooked bar anchorage. They found that the equation for anchorage development length of a hooked bar in ACI 318-14 [20] overestimated the response of beam-column joint constructed with high strength materials and larger steel bar size. Hegger et al. [15] suggested that the longitudinal column reinforcement parameter significantly influences joint strength and that ACI 318 [21] should be amended to take this effect into account. The following sections provide details of these and other methods proposed by researchers for evaluating joint shear strength.

2.3.3.1 Vollum and Newman [24]

Vollum and Newman [24] developed a simple empirical method for the design of external beam-column joints without and with stirrups. The method was derived from consideration of previously tested monotonically loaded specimens. Several parameters were studied including concrete strength, detailing of beam flexural reinforcement anchorage, joint shear reinforcement and joint aspect ratio. The following equations (2-8) to (2-10) were proposed to evaluate the joint shear resistance.

$$V_j = V_c + (A_{sje} f_y - \alpha b_e h_c \sqrt{f_c'}) \quad (2\text{-}8)$$

$$V_c = 0.642\beta(1 + 0.555\left(2 - \frac{h_b}{h_c}\right))b_e h_c \sqrt{f_c'} \quad (2\text{-}9)$$

$$V_j < 0.97 b_e h_c \sqrt{f_c'}(1 + 0.555\left(2 - \frac{h_b}{h_c}\right)) < 1.33 b_e h_c \sqrt{f_c'} \quad (2\text{-}10)$$

The joint shear strength is calculated using equation (2-8), where V_c is the joint shear strength without stirrups and $A_{sje} f_y$ is the yield capacity of the effective joint shear reinforcement. The parameter A_{sje} is the cross-sectional area of shear reinforcement in the joint, which is located within the top five-eighths of beam depth under the beam tension bars. The coefficient α accounts for the fact that shear reinforcement increases joint shear strength by less than the yield capacity of the shear reinforcement. $b_e$and h_c are the joint effective width and column depth respectively. The factor β in equation (2-9) accounts for beam anchorage detailing and is taken as 1.0 for joints with L-bars and 0.9 for joints with U-bars. Equation (2-10) defines the maximum possible joint shear strength.

2.3.3.2 Bakir and Boduroğlu [25]

An empirical model was developed which accounts for several parameters affecting joint shear strength. A database of past tests was used to determine the influence of parameters including concrete strength, column reinforcement ratio, beam bar anchorage type and ratio, joint aspect ratio and joint stirrup ratio. Joint shear strength is estimated by combining the contributions of concrete (V_c) and shear reinforcement (V_s) as follows:

$$V_j = V_c + A_{sje} f_y \quad (2\text{-}11)$$

$$V_j = 0.71\beta(100\frac{A_{sb}}{b_b\, d_b})^{0.4289}\left(\frac{h_b}{h_c}\right)^{-0.61}\left(\frac{h_c + h_b}{2}\right)h_c\sqrt{f_c} + \alpha A_{sje} f_y \quad (2\text{-}12)$$

The factor β is for anchorage bar detailing including 0.85 for joints with U-anchorage bar and 1.0 for joints with L-anchorage bar. Factor A_{sb} is the total area of beam anchorage bars and A_{sje} is the area of the shear reinforcement in joint. The effect of joint aspect ratio is considered in the empirical model as (h_b/h_c). The factor α represents the joint stirrup ratio as 0.664 for joints with low amount of stirrups, 0.6 for joint with medium amount of stirrups and 0.37 for joints with high amount of stirrups. Joint stirrup ratio is evaluated as ($A_{sje}/b_j\, h_c$), where a stirrup ratio less than 0.003 refers to low amount of stirrups, between 0.003 and

0.0055 indicated medium amount of stirrups and higher than 0.0055 assigned to high amount of stirrups.

2.3.3.3 Hegger et al. [15]

Hegger et al. proposed a semi-empirical model which is appropriate for design applications. The model considers various parameters influencing joint behaviour including concrete strength, beam anchorage detail, joint aspect ratio and column longitudinal reinforcement ratio. The joint shear resistance was determined as the sum of the concrete resistance (V_c) and shear reinforcement resistance (V_s), as given in equation (2-13). This contribution can be calculated using the equations in (2-14). The factors A, B and C in the concrete resistance (V_c) equation are determined from the equations in (2-15).

$$V_n = V_c + V_s \tag{2-13}$$

$$V_c = \alpha_1 .\ A\ .B\ .C\ .b_j\ .h_{col} \quad ; \quad V_s = \alpha_2 .\ A_{sj.eff}\ .f_y \tag{2-14}$$

$$A = 1.2 - 0.3\frac{h_{beam}}{h_{col}},\ B = 1.0 - \frac{\rho_{col}-0.5}{7.5},\ C = 2(f_c')^{1/3} \tag{2-15}$$

These factors represent joint aspect ratio, column longitudinal reinforcement ratio and concrete compressive strength respectively. Factor α_1 is the effect of anchorage bar detail and can be taken as 0.85 for U-bar detail, 0.95 for L-bar detail and 1.0 for headed bars. Parameter α_2 is the shear reinforcement efficiency factor as given in Table 2-20.

Table 2-20 Shear reinforcement coefficient factor α_2; adapted from [15].

Anchorage type	Hairpins	Closed stirrups
90-degree bend or headed bars	0.7	0.6
180-degree bend bars	0.6	0.5

An upper limit was set to determine the maximum shear capacity that the joint can resist. This limit depends on the anchorage type of beam reinforcement, column load and joint aspect ratio. The following equation (2-16) represent the upper limit of shear force resistance in joint.

$$V_{max} = \gamma_1 .\ \gamma_2 .\ \gamma_3 .0.25 .\ f_c' .\ b_j .\ h_{col} \leq 2V_c \tag{2-16}$$

$$\gamma_2 = 1.5 - 1.2\frac{\sigma_{col}}{f_c'} \leq 1.0 \tag{2-17}$$

$$\gamma_3 = 1.9 - 0.6\frac{h_{beam}}{h_{col}} \leq 1.0 \tag{2-18}$$

The factors γ_1, γ_2 and γ_3 are for the anchorage efficiency of beam bars, column load and joint aspect ratio respectively. The factor $\gamma_1$is equal to 1.0 for bend bars and 1.2 for headed bars. The remaining factors γ_2 and γ_3 are calculated from equations (2-17) and (2-18).

2.3.3.4 Hassan and Mohele [26]

This empirical model gives the shear capacity of exterior beam-column connections without transverse reinforcement. The model accounts for various parameters influencing joint shear capacity including joint aspect ratio, column axial load, and concrete strength. The empirical model was based upon a database of laboratory existed test results for external and corner beam-column joints without shear reinforcement within the joint. The empirical expression for joint shear strength is as follows:

$$V_j = 0.91 \sqrt{\frac{h_c}{h_b}}\, \kappa\, b_j\ h_c \sqrt{f_c'} \qquad (2\text{-}19)$$

$$\kappa = 1 + \frac{4}{9}\left[\frac{P}{f_c'\, A_g} - 0.15\right] \qquad 1.0 \le \kappa \le 1.2 \qquad (2\text{-}20)$$

The term (h_c/h_b) is the inverse of joint aspect ratio and κ considers the effect of column axial load. The normalized column axial stress ($P\ /f_c'\ A_g$) enhances joint strength if more than 0.2 which gives a low limit of κ with a value of 1.0. The increase in joint strength due to compression in the column is limited to a multiple of κ = 1.2 as given in equation (2-20). The parameter b_j is the effective joint width.

2.3.4 Factors influencing joint strength

2.3.4.1 Effects of column load

High column loads enhance joint behaviour by increasing the first cracking load and preventing the upper column from failing in flexure. The influence of column load on joint strength is less clear. Taylor [5] tested twenty-six beam-column joint specimens with a variety of investigated parameters including column load. The study showed low column load allowed the joint to sustain more beam moment when compared with similar specimens subjected to high axial load. Scott [11] made detailed measurements of reinforcement strain using internally gauged bars. He found that increasing the column load could change the failure mode from joint shear to beam flexure with larger strains measured in the column

reinforcement for high column load. In addition, flexural failure in upper column was prevented in some of Parker & Bullman's [13] specimens by increasing the column load.

On the other hand, Ortiz [12] tested seven reinforced concrete beam-column joint specimens with and without column load. Increasing the axial column stress from zero to 5 MPa had no effect on joint performance in terms of failure load and crack pattern. This may be due to applying low axial stress on column (5 MPa normal stress against 12.2 MPa normal stress in the studies of Taylor [5] and Scott [11]).

2.3.4.2 Effects of bend radius

According to EC2 [23], a minimum mandrel diameter is required for bent bars to avoid failure of concrete inside the bend and damage to reinforcement. It is recommended that bars have a minimum mandrel diameter of four times the bar diameter (if bar diameter is less than or equal to 16 mm) or seven times the bar diameter (if bar diameter is greater than 16 mm).

To study the effect of bend radius, Ortiz [12] studied beam-column joint with two different bend radius (65 mm and 130 mm). The results showed two specimens with same column load of 300 kN and no joint stirrups failed at same applied load, but a crushing of the strut occurred when a bend radius of 65 mm was used. However, the column load was not high enough to influence the joint behaviour (5 MPa normal stress against 12.2 MPa normal stress in Taylor [5] and Scott [11] studies). Further tests are required to properly investigate the effect of varying the bend radius on joint shear strength.

2.3.4.3 Effects of beam tension reinforcement ratio

Increasing the beam reinforcement ratio can cause the failure mode to change from beam flexure to joint failure as found by Scott [11] for his specimens with low column load. Taylor [5] investigated the effect of reinforcement ratio for different column loads. Diagonal cracking followed by shear failure occurred as the beam tension bar ratio increased indicating that the joint failure mode is significantly influenced by beam steel reinforcement ratio.

The 337 anchorage tests of Sperry et al [18, 19] simulate external beam-column joints with a variety of parameters. The failure load increased as the bar size was increased due to an improvement in anchorage strength. The crack patterns also changed as reinforcement ratio increased showing severe cracking as hooked bars became larger, leading to a loss of bond stress and slip of the straight portion of the beam anchorage bars.

2.3.4.4 Effects of reinforcing detail

Anchorage of reinforcement plays a crucial role in determining joint strength. It is found that reinforcement bent up (90-degree) is not effective compared to beam reinforcement bent down (90-degree) and back (180-degree). Taylor [5] and Scott [11] found anchorage reinforcement bent up was not adequate for beam-column joint. In addition, they reported that anchorage reinforcement bent down performed better than the one bent back.

Recent studies showed that headed bars are a good alternative to hooked bars when the anchorage development length cannot be achieved due to small measurement in column depth. A research study conducted by Hegger et al [15] found that headed bars increased the load bearing capacity of beam-column joint by 20% when compared with hooked bars (specimens RK4 vs. RK5). Chun et al [27] found that headed bars provided sufficient anchorage to joint, making it adequate alternative option for replacing hooked bars; however, in regard to failure mode hooked bars resisted additional load compared to headed bars, after diagonal cracking propagated to top of joint. More studies on headed bars are required for external beam-column joints.

2.3.4.5 Effects of shear reinforcement

Previous studies found that shear reinforcement significantly enhances joint shear strength. Ortiz [12] used three different shear reinforcement ratios (one stirrup, three stirrups and four stirrups). Joint strength increased with increasing number of joint stirrups. It also changed the failure mode from shear into beam flexure failure when four shear stirrups were used in joint. Hamil [14] and Hegger et al [15] also found that joint stirrups played an important factor in improving joint shear strength. Although stirrups enhance joint shear strength there is a limit to the increase in shear resistance. For example, Taylor [5] found no increase in joint strength for a specimen with three joint stirrups in in comparison to his specimens having only one joint stirrup.

2.3.4.6 Effects of beam end prop

Most researchers have tested statically determinate specimens like that shown in Figure 2-15. However, researchers like Taylor [5] and Scott [11] introduced a prop at the beam end to prevent sidesway and represent the other half of the frame structure.

Taylor [5] used two different prop stiffness in his experimental program and found the lower column (closing corner) sustained more moment from the beam than the upper column (opening corner). On this basis, he proposed designing the closing corner for 70% of the beam moment and the opening corner for 50% of beam moment. He also found increasing prop stiffness increased the maximum prop force. However, the ultimate load was not affected by changing the prop stiffness.

2.3.4.7 Effects of column intermediate reinforcement

Previous studies [15][28] suggest that the provision of intermediate column reinforcement enhances joint shear strength, and this enhancement increases significantly with increasing intermediate column bar area.

A study of seismically loaded beam-column joints conducted by Wong and Kuang [28] investigated a variety of parameters including column intermediate reinforcement. The column had four main reinforcement bars of diameter 25 mm. The reinforcement was locally increased to six and eight bars by adding intermediate column bars at mid-height of the column. Increasing the column intermediate reinforcement ratio from 0%, 0.35% to 0.7% improved the joint shear strength by 24% and 33%, as shown in Figure 2-16(a). Moreover, adding column intermediate reinforcement above a ratio of 0.8% provided no further enhancement in joint strength.

Hegger et al [15] also found joint strength to depend on the column reinforcement with the joint shear strength increasing significantly as the column reinforcement ratio was increased from 0.5% to 2.0% as shown in Figure 2-16(b).

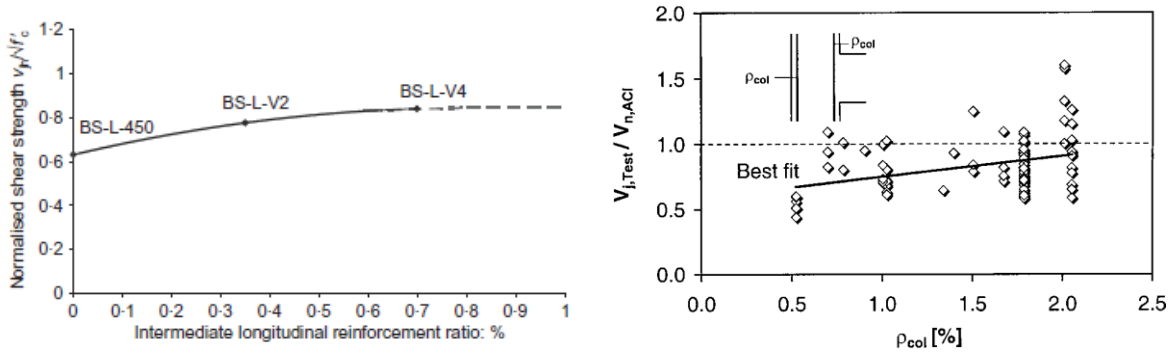

a) Column intermediate reinforcement b) Column reinforcement

Figure 2-16: Effect of column intermediate reinforcement ratio; reproduced from [28] and [15] respectively.

2.3.4.8 Effects of joint aspect ratio (h_b/h_c)

Various researchers [15, 24-26] have studied the influence of joint aspect ratio on joint shear strength. The studies show that joints with aspect ratio (h_b/h_c) ranging between 1 and 2 tend to fail in shear while flexural failure occurs in joints with aspect ratio (h_b/h_c) less than 1.

This is reflected in the work of Hegger et al. [15] who studied the influence of joint aspect ratio experimentally. They found joint shear strength to reduce as the joint aspect ratio (h_b/h_c) was increased. They found that beam-column joints with h_b/h_c = 1.25 tended to fail due to beam hinging, whereas specimens with joint aspect ratio more than 1.25 failed in joint shear. This reduction in joint strength due to joint aspect ratio can be seen in Figure 2-13(b). The significance of joint aspect ratio on joint shear strength is reflected in its inclusion in the design methods of [15, 24-26].

2.4 Strut-and-Tie Modelling

The strut and tie method (STM) is an application of the truss analogy originally developed by Ritter [29] and Mörsch [30]. Schlaich and Schafer [31, 32] introduced the concept of dividing the structure into B-regions, where plane sections remain plane, and D-regions where the strain distribution is not linear due to geometry or loading. Corners in frames, openings and near concentrated load/supports are examples of D-regions as shown in Figure 2-17. Typical examples of structural members with D-regions are corbels, deep beams, pile caps and beam-column joints. Theoretically, the STM is justified by the lower bound theorem of plasticity which requires the internal stress distribution in a structure to be in equilibrium and concrete and reinforcement not to be overstressed.

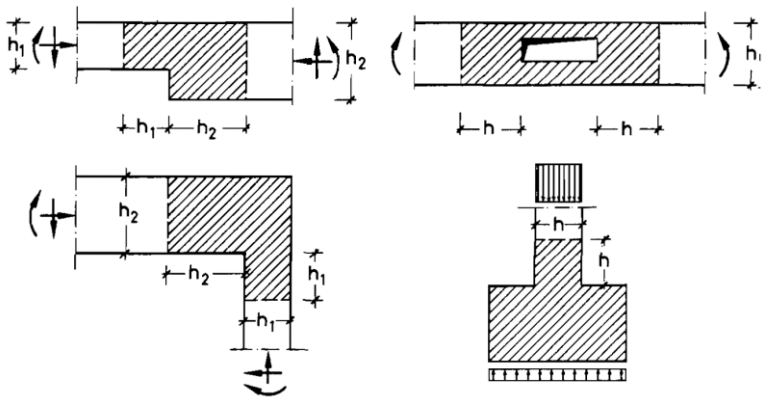

a) Geometrical discontinuity

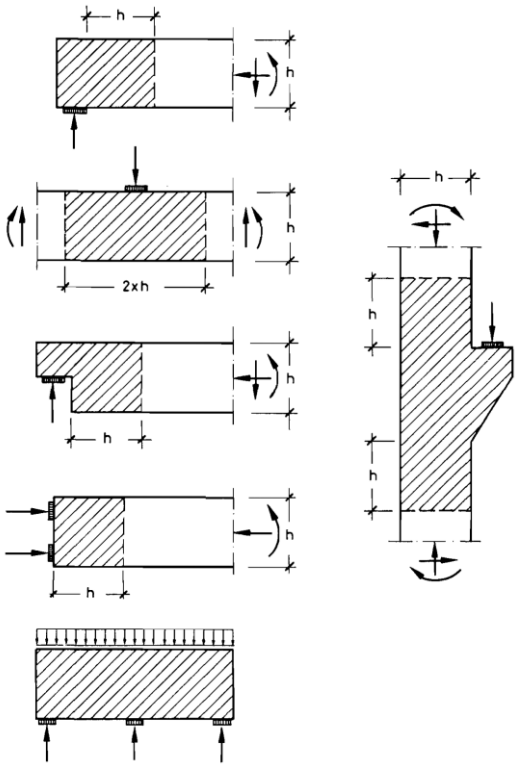

b) Loading and/or geometrical discontinuity

Figure 2-17: D-regions with non-linear strain distribution due to loading and/or geometrical discontinuities; reproduced from [31, 32].

Prior to cracking the stress distribution is largely elastic. When cracks form, the elastic stresses are disturbed due to the re-orientation of the internal forces and reinforcement is needed to transfer tension through cracks. Forces in D regions are assumed to be resisted by compression in the concrete (called compressive strut) and tension in the reinforcement (called tension ties). Struts and ties intersect at nodes.

Previous research into beam-column joints tested under monotonic loads only provides a limited description of the mechanisms of shear transfer through the joint. Park and Paulay [2]

introduced the concept of a diagonal strut mechanism coupled with a truss mechanism as shown in Figure 2-18. A diagonal strut mechanism is developed between the bend in the beam bars and the flexural compression force in the diagonally opposite corner of the joint. The truss mechanism comprises a uniform inclined compressive stress field which requires vertical and horizontal ties for equilibrium.

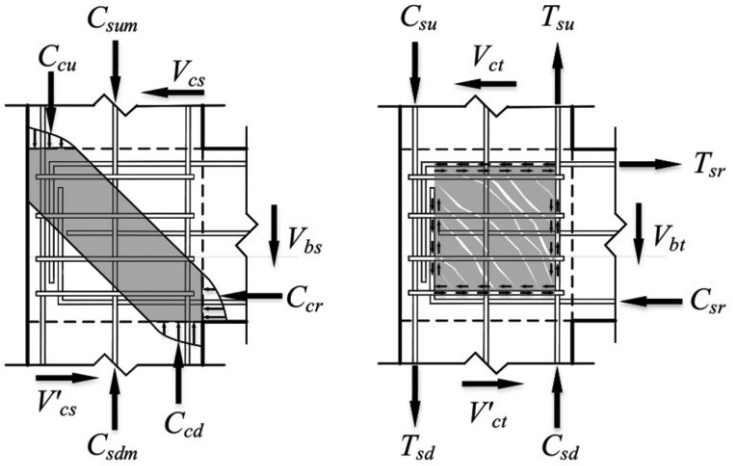

Figure 2-18 Shear transfer mechanism of external beam-column joint; reproduced from [3].

The strength of the strut mechanism is dependent mainly on the concrete compressive strength which reduces as the transverse tensile strain, perpendicular to the direction of the strut, increases. Additionally, the angle of the strut depends considerably on the magnitude of column axial load. If the column axial load is low, the angle of the inclined strut forms parallel with the joint diagonal. The angle of inclined strut becomes steeper as the column axial load increases. The changing of strut angle with increasing column load is analogous to the steepening of the diagonal crack as the column load increases.

The truss mechanism is mobilized by the development of bond stresses in the beam and column longitudinal reinforcement passing through the joint. To sustain the inclined compression field within a joint, the horizontal and vertical forces at joint core boundaries need to be resisted and maintained. The provision of joint stirrups and column intermediate bars passing through the joint equilibrate the vertical and horizontal components of the inclined compressive stress field at the boundaries of the core. The strength of the truss mechanism is dependent on the tensile yield strength of joint shear reinforcement crossing the plane of shear failure. This mechanism relies upon good bond between the joint

boundaries and the beam and column longitudinal reinforcement. If bond deterioration occurs, the truss mechanism diminishes resulting in the joint shear force being resisted dominantly by the diagonal strut mechanism. In this case, the joint shear reinforcement acts only as a confinement to the core of joint which enhances the efficiency of concrete and joint performance [4].

2.4.1 Constructing STM

The strut-and-tie method is a powerful tool for modelling regions like beam-column joints where plane sections do not remain plane. The following procedure can be used to develop a STM:

1. Define and isolate the B-regions, where plane sections remain plane, and D-regions. B-regions are designed using normal beam theory following codes of practice while D-regions are designed using STM. The size of the D-regions can be evaluated by St Venant's principle, which is used as a quantitative guide, so that the engineer can reach a satisfactory decision.
2. Build a truss system comprising struts, ties and nodes to represent the flow of forces through the D-region. Calculate the member forces in the truss as shown in Figure 2-19.
3. Design the structural members of the STM by dimensioning the truss members to resist the design forces based on code provisions. The stresses in the struts, ties and nodes should not exceed the material strengths of the elements.
4. If the constructed STM is statically indeterminate, the member forces can be determined from consideration of the relative stiffness of members or an assumed failure mechanism.
5. Iteration may be needed to optimise the constructed STM.

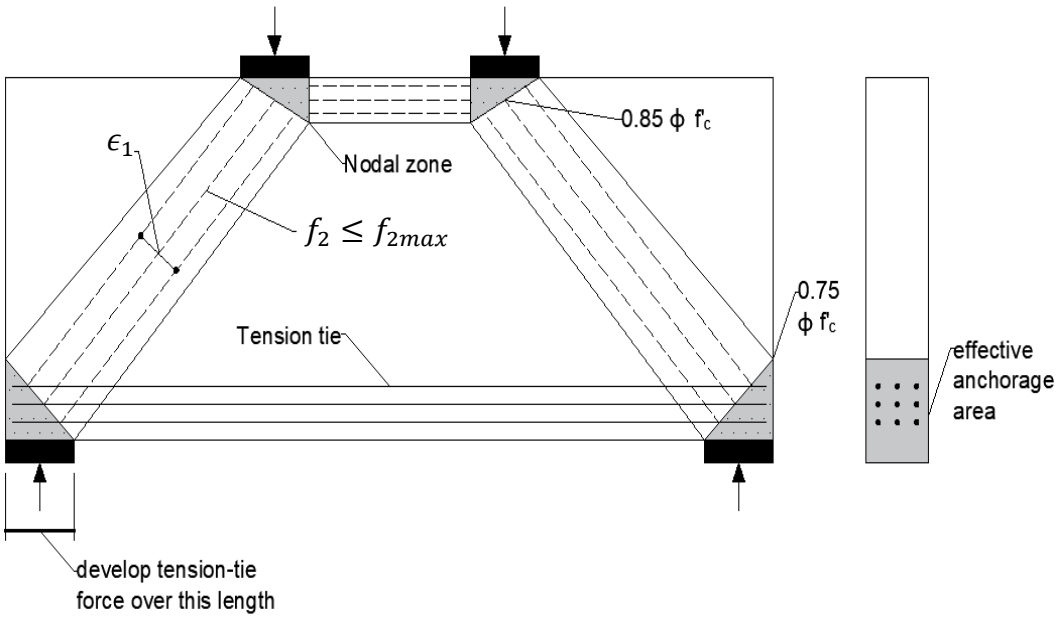

a) Flow of forces

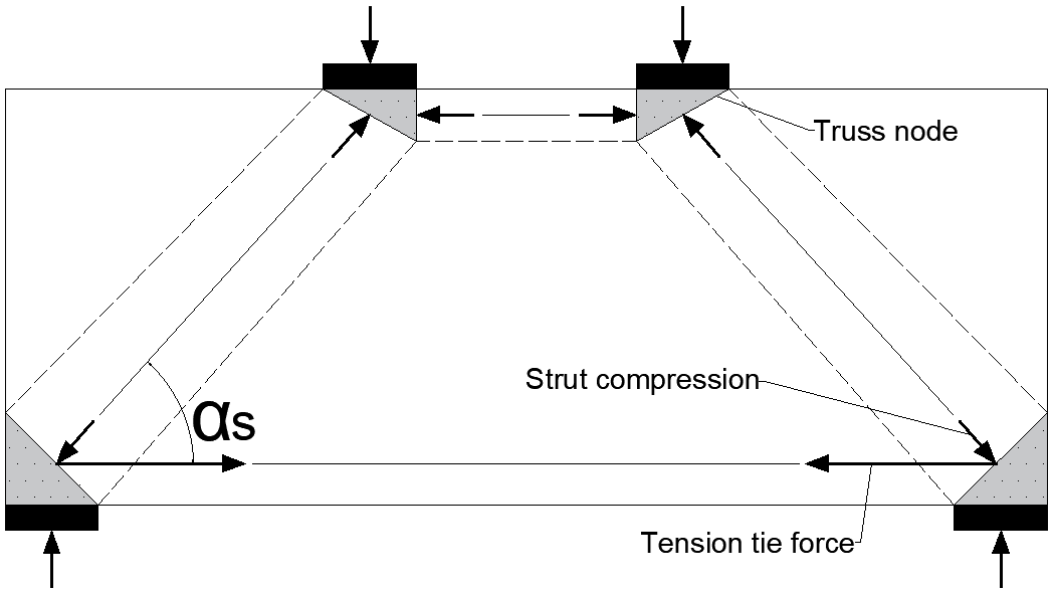

b) Truss model

Figure 2-19: Strut-and-tie model for a deep beam; adapted from [33].

2.4.2 Model optimization

An iterative procedure can be used to optimise STM by minimising strain energy. Normally no unique STM exists causing doubt about the efficiency of the selected model. According to Schlaich and Scahfer [31, 32], the model with least and shortest reinforcement ties is best because reinforcement ties are more deformable than concrete struts. Besides, loads attempt to follow the stiffest path with least deformation. The STM geometry can be optimized through an iteration process in which strain energy is minimised. This can be achieved by using the following expression:

$$\sum F_i \, l_i \, \epsilon_{mi} = \text{minimum} \quad (2\text{-}21)$$

Where F_i is the force in strut or tie, l_i is the length of member and ϵ_{mi} is the mean strain of a member. The concrete strut contribution can be neglected due to the ability of reinforcement ties to deform much more than concrete.

2.4.3 Dimensioning strut-and-tie model

Dimensioning the STM consists of sizing the struts, ties and nodes. The following sections describe in detail the dimensioning of struts, ties and nodes.

2.4.3.1 Struts

There are three shapes of struts that can be used in developing a STM: prismatic struts, bottle struts and fan-shaped struts. A prismatic strut is a compressive stress field in which the stress trajectories are parallel to each other as shown Figure 2-20. Prismatic stress fields are typically found in B-regions while fan- and bottle-shaped stress fields arise in D-regions occurring commonly at concentrated loads and supports. Both the fan-shaped and prismatic stress fields have no tensile transverse stresses since the stress field trajectories are straight. However, the bottled-shape stress fields develop significant tensile transverse stresses due to the curvature shape of the compressive stress trajectories. The strength of a prismatic strut, without transverse tension, is similar to the concrete cylinder strength, whereas the strength of the fan- and bottle-shape struts is lower due to the development of tensile transverse stresses away from the strut ends leading to transverse splitting. Cracks forming due to tensile transverse stresses reduce the strut strength and cause an early failure of the strut. consequently, a proper amount of reinforcement should be provided to control these crack widths. The strength of the strut is also influenced by the angle formed between struts and ties. According to Schlaich and Schafer [31, 32], strain incompatibility at nodes occurs if the angle between struts and ties is very low. Furthermore, it is suggested by Collins & Mitchell [33] that the effective strut strength is dependent on the strain in the tie and the angle between strut and tie.

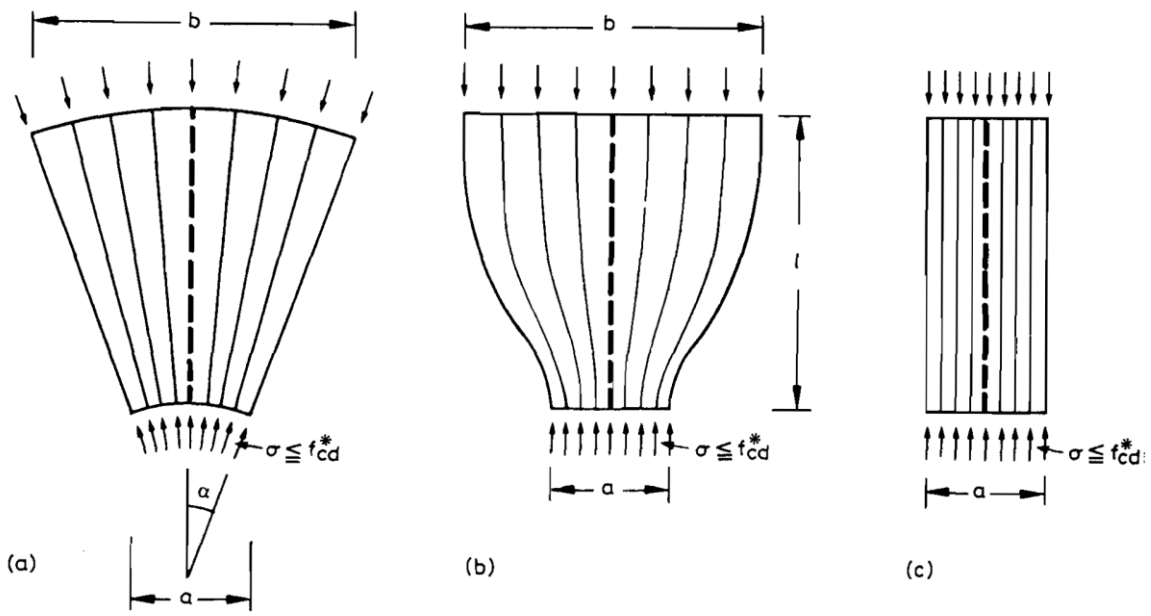

Figure 2-20 Basic compression fields (a) the fan; (b) the bottle; (c) the prism; reproduced from [31, 32].

2.4.3.2 Reinforcement ties

Tie forces are normally carried by reinforcement positioned at the centreline of the tie force. Distributed reinforcement should be used to control cracking in areas where secondary tension develops. Ties should be fully anchored at nodes with hooks provided where the available straight anchorage is insufficient for bar anchorage. For nodes with high concentrated stresses, tensile reinforcement is best provided in several layers to facilitate bar anchorage and increase node dimensions.

2.4.3.3 Nodes

Nodes are the regions where struts and ties intersect or struts change direction. Nodes are classified as either smeared (continuous) nodes or concentrated (singular) nodes as shown in Figure 2-21(a). Smeared nodes comprise regions where wide stress fields join each other or regions with a tie composed of smeared reinforcement. Concentrated nodes arise at the intersection of concentrated struts and ties and typically occur under loading or support plates. EC2 classifies nodes as CCC (3 compressive struts), CCT (2 compressive struts and 1 tie), and CTT (1 compressive strut and 2 ties). EC2 allows CCC nodes to be designed as either hydrostatic or non-hydrostatic in accordance with Schlaich et al [31, 32]. Stresses are equal on all node-to-strut interfaces of hydrostatic nodes but this is not always feasible due to geometrical constraints. Non-hydrostatic nodes, as shown in Figure 2-21 (b), are more commonly used in structural design.

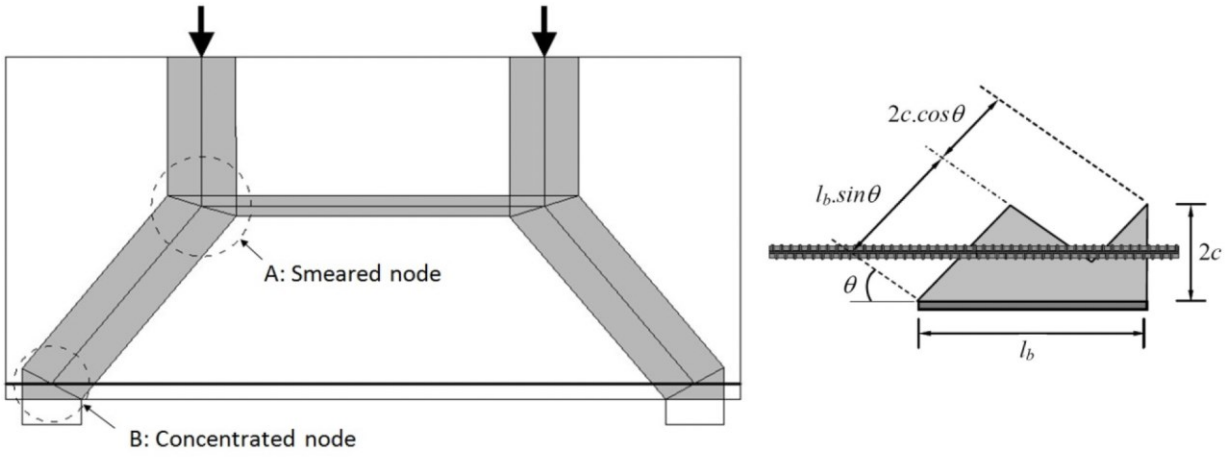

(a) Smeared node and concentrated node (b) Non-hydrostatic node

Figure 2-21 (a) Smeared node and concentrated node & (b) Non-hydrostatic node; reproduced from [34].

2.4.4 Models for external beam-column joints

Various researchers have proposed STM for the design of external beam-column joints as described below.

2.4.4.1 Ortiz [12]

Ortiz developed a STM for external beam-column joints without and with joint stirrups. The inclined strut carries the joint shear force (the difference between tensile force in beam reinforcement and the shear force in upper column) across the joint as shown in Figure 2-22 (a). The strength of the inclined strut σ_d is determined with equation (2-22) from CEB Mode Code 1990 [35]. As shown in Figure 2-22 (b) and (c), the width of the inclined strut is evaluated using equations (2-23) and (2-24). To calculate the diagonal strut strength and shear strength without joint stirrup, equations (2-25) and (2-26) should be used. If joint stirrups are present, the strut width is increased by an amount dw given by equation (2-27) as shown in Figure 2-22 (c). The increased strut width corresponds to the shear force resisted by joint stirrups. Thus, the diagonal strut strength and shear strength with joint stirrup can be evaluated with equations (2-28) and (2-29). To solve this model, an iterative procedure should be used to determine the joint shear strength.

$$\sigma_d = 0.6\, f_c \left(1 - \frac{f_c}{250}\right) \quad (2\text{-}22)$$

$$w_i = 0.45\, W \quad (2\text{-}23)$$

$$W = h_c\, sin\theta + s\, cos\, \theta \quad (2\text{-}24)$$

$$D = \sigma_d \, b_c \, w_i \tag{2-25}$$

$$V_j = \sigma_d \, b_c \, w_i \cos\theta \tag{2-26}$$

$$dw = \frac{\delta D}{f_c \, b_c} = \frac{A_{sjh} \, f_{yj}}{\cos\theta} \frac{1}{f_c \, b_c} \tag{2-27}$$

$$D = \sigma_d \, b_c \, (w_i + dw) \tag{2-28}$$

$$V_j = \sigma_d \, b_c \, w_i \cos\theta + A_{sjh} \, f_{yj} \tag{2-29}$$

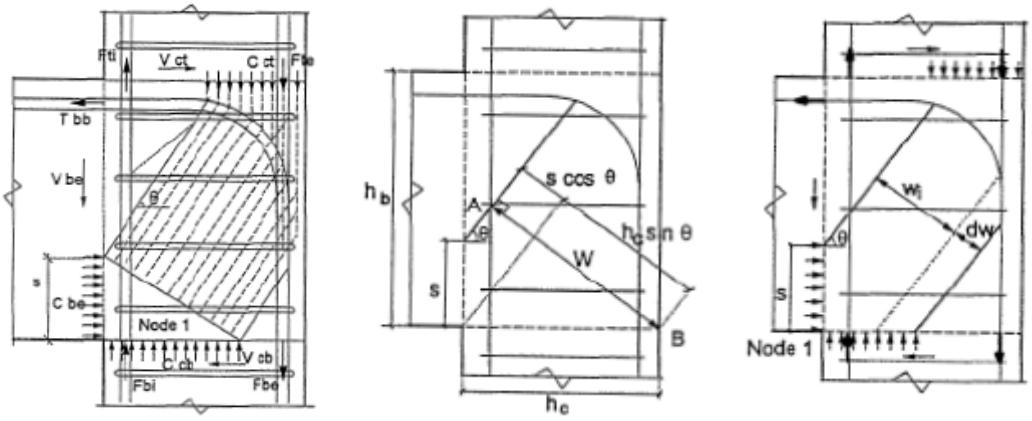

(a) (b) (c)

Figure 2-22 Strut-and-tie model; reproduced from [12].

2.4.4.2 Hwang and Lee [36]

Hwang and Lee [37] first proposed a design model for external and internal beam-column joints in 1999. The model was subsequently simplified in 2002 [36]. The proposed model, which is statically indeterminate, satisfies equilibrium, compatibility and constitutive law of materials of cracked reinforced concrete. As shown in Figure 2-23, shear equilibrated by a diagonal compressive strut, a horizontal tie force and a vertical tie force. Since the forces meeting at a node must be in equilibrium, the horizontal and vertical joint shear strength can be evaluated using equation (2-30). The statically indeterminate tie-force F_h and F_v can be determined using the formulas (2-31) and (2-32), where either vertical or horizontal tie is absent or yielded. γ_h and γ_v are the fraction of horizontal and vertical shear transferred by the horizontal and vertical ties. The nominal diagonal compressive strength (C_d) is defined in equation (2-33). The components of horizontal and vertical shear force V_h and V_v are defined as ($D\cos\theta : F_h : F_v \; cot\;\theta = R_d : R_h : R_v$) and ($D\sin\theta + F_h \tan\theta + F_v = R_d : R_h : R_v$). These are evaluated using the simplified factor (K) developed to obtain the maximum beneficial effect of the ties forces in increasing the shear strength. This factor can be estimated by using

equation (2-34). The relative contributions of R_d, R_h and R_v are defined in equation (2-35). The sum of the relative contributions equals one as shown in Figure 2-24. To check whether the ultimate strength is reached, the compressive forces in the diagonal, flat, and steep struts shown in Figure 2-23 are checked using equation (2-36). The softened stress-strain relationship for concrete is evaluated using equation (2-37) which is applicable for compressive strengths ranging between 20 and 100 MPa. The concrete cylinder strain (ε_0) corresponding to maximum concrete strength (f_c') can be determined using equation (2-38). The ultimate joint shear strength arises when $\sigma_d = \xi f_c'$ and $\varepsilon_d = \xi \varepsilon_0$. For simplicity, the softening coefficient (ξ) is approximiated to ($\xi = 3.35/\sqrt{f_c'} \leq 0.52$) by assuming constant values of average principal strains in the *d*- and *r*- directions ($\varepsilon_d = -0.001$ and $\varepsilon_r = 0.005$).

$$V_v = C_d \sin\theta \ and \ V_h = C_d \cos\theta \ ; \frac{V_v}{V_h} = \frac{l_v}{l_h} = \tan\theta \tag{2-30}$$

$$F_h = \gamma_h \times V_h \text{ where, } \gamma_h = \frac{2\tan\theta - 1}{3} \text{ for } 0 \leq \gamma_h \leq 1 \tag{2-31}$$

$$F_v = \gamma_v \times V_v \text{ where, } \gamma_v = \frac{2\cot\theta - 1}{3} \text{ for } 0 \leq \gamma_v \leq 1 \tag{2-32}$$

$$C_d = K\zeta f_c' A_{str} \ ; \ A_{str} = a_s \times b_j \ ; \ a_s = \left(0.25 + 0.85\frac{N_{col}}{A_g f_c'}\right) h_c \tag{2-33}$$

$$K = \frac{R_d + R_h + R_v}{R_d + R_h\left(1 - \frac{sin^2\theta}{2}\right) + R_v\left(1 - \frac{cos^2\theta}{2}\right)} \geq 1 \tag{2-34}$$

$$R_d = \frac{(1-\gamma_h)(1-\gamma_v)}{1-\gamma_h\gamma_v}, R_h = \frac{\gamma_h(1-\gamma_v)}{1-\gamma_h\gamma_v}, \text{ and } R_v = \frac{\gamma_v}{1-\gamma_h\gamma_v} \tag{2-35}$$

$$-\sigma_{max} = \frac{1}{A_{str}}\left\{-D + \frac{F_h}{\cos\theta}\left(1 - \frac{sin^2\theta}{2}\right) + \frac{F_v}{\sin\theta}\left(1 - \frac{cos^2\theta}{2}\right)\right\} \tag{2-36}$$

$$\sigma_d = \xi f_c'\left[2\left(\frac{\varepsilon_d}{\xi\varepsilon_0}\right) - \left(\frac{\varepsilon_d}{\xi\varepsilon_0}\right)^2\right] \text{ for } \left(\frac{\varepsilon_d}{\xi\varepsilon_0}\right) \leq 1, \text{ and } \xi = \frac{5.8}{\sqrt{f_c'}}\frac{1}{\sqrt{1+400\varepsilon_r}} \leq \frac{0.9}{\sqrt{1+400\varepsilon_r}} \tag{2-37}$$

$$\varepsilon_0 = -0.002 - 0.001\left(\frac{f_c' - 20}{80}\right) for \ 20 \leq f_c' \leq 100 \tag{2-38}$$

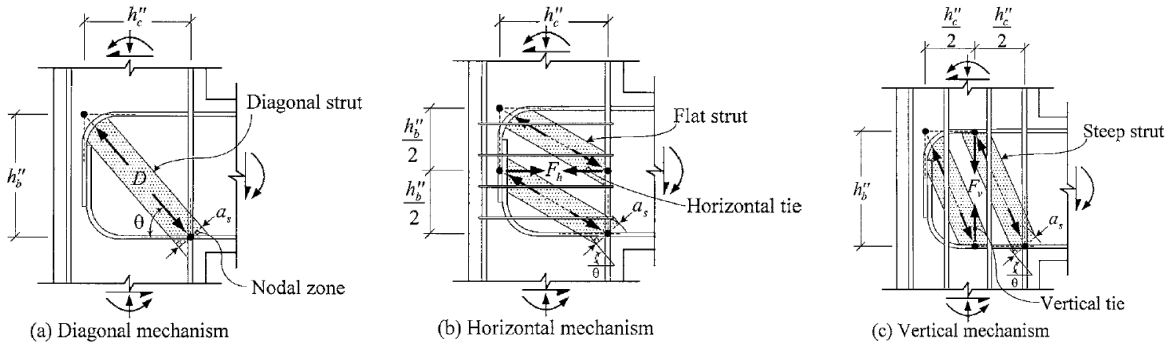

Figure 2-23: Softened strut-and-tie model; reproduced from [37].

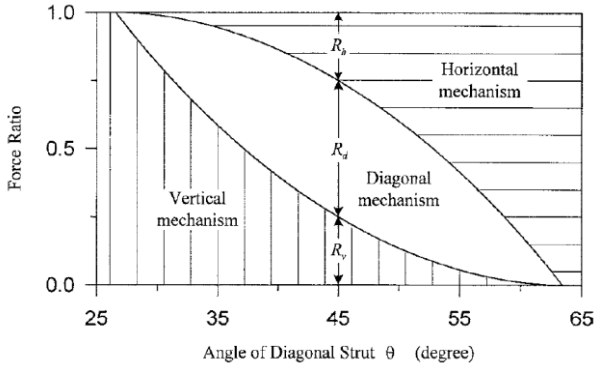

Figure 2-24 Ratios of force distribution among mechanisms; reproduced from [37].

2.4.4.3 Hwang et al. [38]

The proposed model is for deep beams, corbels, squat walls, and beam-column joints. This model is a development and simplification of Hwang and Lee's [36] 2002 softened truss model. The proposed model satisfies equilibrium, compatibility and constutive laws of cracked reinforced concrete. The proposed model is statically indeterminate. As shown in Figure 2-25, joint shear is equilibrated by a diagonal compressive strut, horizontal tie force and vertical tie force ($C_d = D + F_h/\cos\theta + F_v/\sin\theta$). The nominal diagonal compression strength is limited using equation (2-39). The factors (softening coefficient, effective area of nodal zone and the strut-and-tie index) in the equation are calculated using equations (2-40) and (2-41). The horizontal and vertical shear reinforcements ratio (ρ) is calculated using equation (2-42). This method was shown to give better predictions of joint shear strength than ACI 318-14 [20].

$$C_d = K\zeta f_c' A_{str}$$

where, ζ: softening coefficient of cracked reinforced concrete. (2-39)

A_{str}: effective area on the nodal zone of the diagonal strut.

$$A_{str} = a_s \times b_j \;;\; \zeta = \frac{3.35}{\sqrt{f_c'}} \leq 0.52 \;;\; K = tan^A + cot^A - 1 + 0.14B \leq 1.64 \quad (2\text{-}40)$$

$$a_s = \left(0.25 + 0.85\frac{N}{A_g f_c'}\right) h_c \;;\; A = 12\frac{\rho f_y}{f_c'} \leq 1 \;;\; B = 30\frac{\rho f_y}{f_c'} \leq 1 \;; \quad (2\text{-}41)$$

$$b_j = \frac{b_b + b_c}{2}$$

$$\theta \geq 45\ degrees, \rho = \rho_h \;\&\; f_y = f_{yh} \;; \theta < 45\ degrees;\ \rho = \rho_v \;; f_y = f_{yv} \quad (2\text{-}42)$$

$$\theta = tan^{-1}\left(\frac{l_v}{l_h}\right)$$

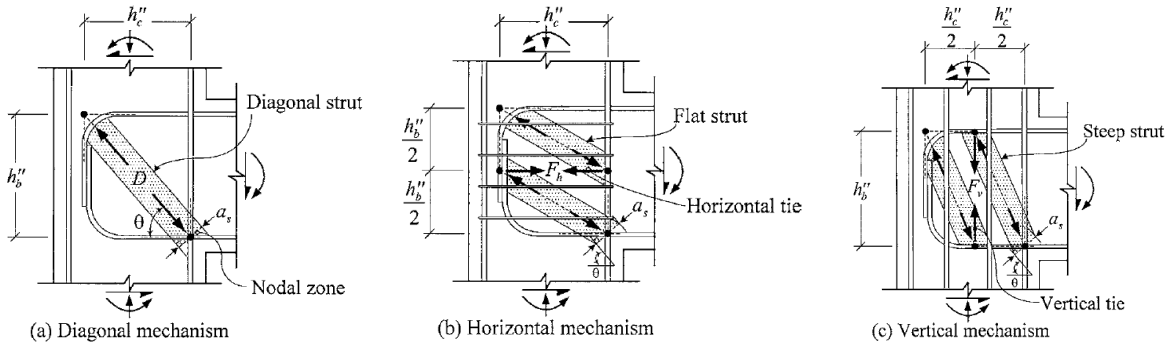

Figure 2-25: Softened strut-and-tie model; reproduced from [37].

2.4.4.4 Vollum and Parker [39]

Vollum and Parker developed a rational STM for the design of external beam-column joints. The model is derived from the strut and tie rules given in EC2 (EN 1992-1, 2004)[23]. The joint shear strength is expressed in terms of the geometry of the nodes as shown in Figure 2-26 and can be determined using the following formula.

$$V_j = b_e k v' f_{cd}(x - y) \quad \text{, where } b_e = \frac{b_b + b_c}{2} \leq \frac{0.85}{0.6} b_b \quad (2\text{-}43)$$

The effective joint width b_e should not exceed the upper limit set to limit the compressive stress in the beam, which is taken as 0.85(1-f_{ck}/250)f_{ck}/γ_c. The concrete design strength given in EC2 were adopted as illustrated in the equation below.:

$$kv' f_{cd} = k\left(1 - \frac{f_{ck}}{250}\right) f_{ck}/\gamma_c \quad (2\text{-}44)$$

The coefficient k was taken as 0.6 as used for the web of beams with shear reinforcement. The maximum moment developed in the beam at the column face is transferred through the joint into the upper and lower columns. Thus, the width of the node x_c shown in Figure 2-26 (a) is equal to half the column width to maximise the moment transferred into the columns

at joint boundaries. This moment transferred into upper and lower column through the diagonal strut can be calculated as follows:

$$M_{col} = 0.125\, b_e h_c^2\, v\, f_{ck} \tag{2-45}$$

The model accounts for the provision of joint stirrups as shown in in Figure 2-26 (b). As recommended by Vollum and Newman [24], joint stirrups are assumed to be effective in increasing the joint strength if placed with the top 5/8^{ths} of the beam depth below the beam tension bars. The centroid of joint stirrups is assumed to be at mid-height of the beam and the increase of the moment capacity of column at top and bottom of the beam is influenced by the joint stirrups. This increase in the moment capacity can be estimated from the following expression:

$$\Delta M = (2d_c - h_c)\Delta T \tag{2-46}$$

ΔT is the half the vertical force transferred from the inclined strut into the internal and external column bars. This force ΔT is obtained as follows:

$$\Delta T = 0.5\, T_{syd}\, \cot\emptyset$$
$$\text{Where, } T_{syd} = A_{sw}\, f_{yd} \tag{2-47}$$

A_{sw} is the area of joint shear stirrup within the top 5/8^{ths} of the beam depth below the anchorage tension bar. The coefficient cotØ and the node dimensions are calculated from geometry using the following equations:

$$\cot\emptyset = (d_b + 0.5x - 2y - z)/(2d_c - h_c + w)$$
$$x = d_b\left(1 - \sqrt{\left(1 - \frac{2M_b}{b_e d_b^2 v f_{cd}}\right)}\right) \le 0.5h_b$$
$$y = M_b\left(1 + \frac{0.5h_c}{L_b}\right)/(L_c b_e v f_{cd}) \tag{2-48}$$
$$w = 2\Delta T/(b_e\, v\, f_{cd}) \le 0.5\, h_{col}$$
$$z = T_{syd}/(b_e\, v\, f_{cd})$$

Where L_c is the distance between the points of contraflexure in the upper and lower columns, L_b is the distance to the point of contraflexure in the beam from the column face and M_b is the moment in the beam at the column face. The maximum permissible joint shear force is limited in accordance with EC2 [23] as follows:

$$V_{jdmax} \le 0.45\, v f_{cd}\, b_c\, d_c/\gamma_m \tag{2-49}$$

The coefficients b_c and d_c depict the column width in the plane of the joint and the effective depth of the column respectively.

$$\begin{gathered} \Delta T = 0.5\ (-b + \sqrt{(b^2 - 4c)}) \\ b = 0.5(2d_c - h_c)vf_{cd}b_e \\ c = -0.25T_{syd}(h^* - z)vf_{cd}b_e \\ h^* = d_b + 0.5x - 2y \end{gathered} \quad (2\text{-}50)$$

The maximum moment transferred into the joint at the beam face is given by:

$$M_b = 2(M_{col} + \Delta M)/(1 - (1 + 0.5h_c/L_b)(d_b + 0.5x - y)/L_c \quad (2\text{-}51a)$$

$$M_b = 2(M_{col} + \Delta M)/(1 - (1 + 0.5h_c/L_b)\ d_b/L_c \quad (2\text{-}51b)$$

M_b can be calculated iteratively as follows:

- Step 1: calculate ΔT with equation (2-50) assuming $h^* - z = d_b$.
- Step 2: calculate $M_{col} + \Delta M$ with equations (2-45) and (2-46) respectively.
- Step 3: calculate M_b with equation (2-51b) in the first iteration and with equation (2-51a) subsequently.
- Step 4: calculate the node dimensions x and y with equations (2-48) in terms of M_b from step 3.
- Step 5: recalculate ΔT with equation (2-50) and the current value of h*.
- Step 6: repeat steps 2–5 until values of M_b from successive iterations converge.

The proposed method was validated with existing experimental data.

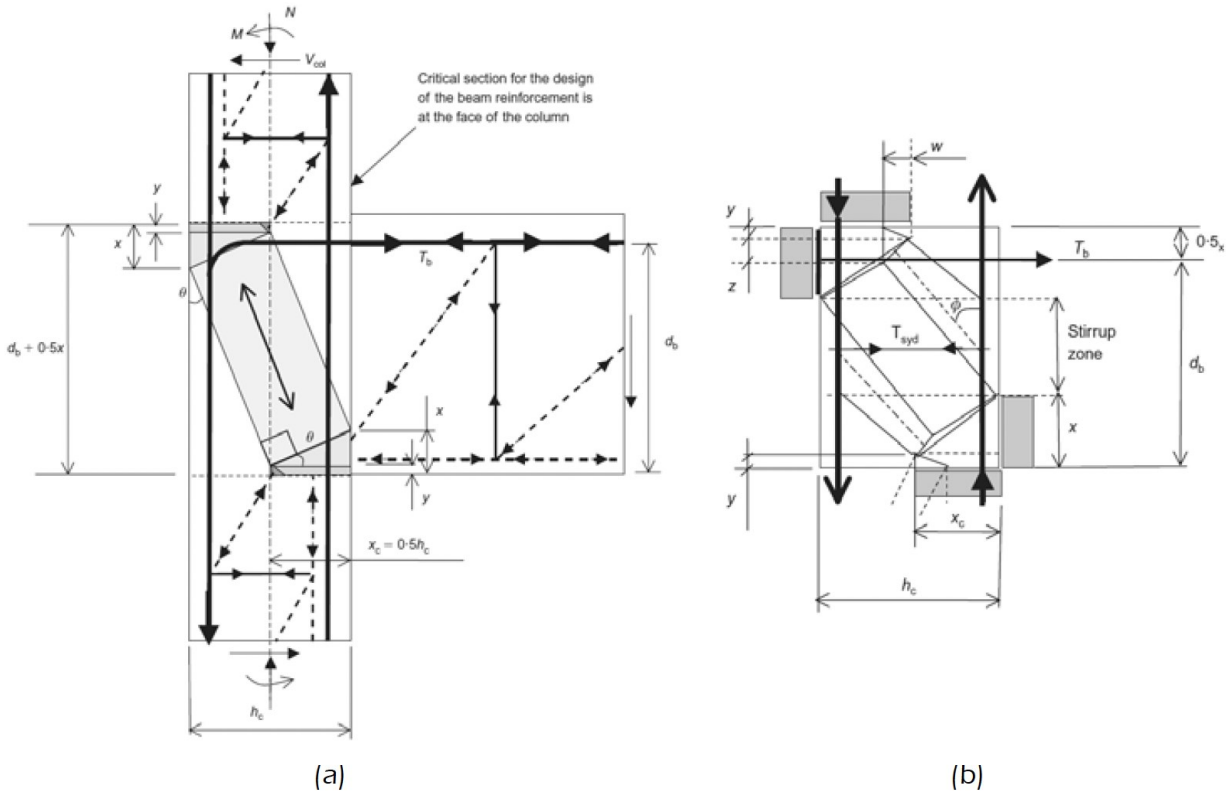

Figure 2-26: STM for external beam-column joint, reproduced from [39].

2.5 Shear Transfer Mechanism in External Beam-Column Joint

Shear transfer actions in reinforced concrete beams have been widely studied by many researchers. These studies show that shear is resisted in cracked reinforced concrete beams through a combination of aggregate interlock, dowel action, flexural compression zone, shear reinforcement and residual tensile stress. Chapter 6 assesses the contributions of aggregate interlock and shear reinforcement to the joint shear strength of the specimens tested in this campaign. The influences of dowel action and residual tensile stress are neglected in this research for reasons explained in chapter 6.

2.5.1 Contribution of aggregate interlock

Joint shear failure is associated with the formation of a critical diagonal crack within the joint. The current research assesses shear transfer through this crack via aggregate interlock. According to Campana et al. [40], aggregate interlock is influenced by several parameters including crack width, crack slip, maximum aggregate size, crack normal stress and concrete strength. Various constitutive relationships for aggregate interlock are in the literature. These

relationships can be categorized as either empirical or physically based. Physically based models calculate shear resistance as a function of the contact between the crack surfaces. Examples of such models are those of Walraven [41] and Li et al. [42]. Empirically based models are derived by curve fitting the results of push-off tests. Empirically based models include those of Walraven and Reinhardt [43], Hamadi and Regan [44], Bazant and Gambarova [45] and Gambarova and Karakoc [46].

2.5.1.1 Walraven two-phase model [41]

This is a theoretically based model which was validated using experimental results from push-off tests. Shear transfer in cracked concrete was studied by testing pre-cracked push-off specimens as shown in Figure 2-27(a). The model considers load transfer through a crack plane in a two-phase material consisting of mortar (cement paste with fine sand) and coarse aggregate particles. To simplify the analysis, the aggregate particles are assumed to be spherical particles intersected by the crack face as shown in Figure 2-27(b). Shear displacement across the crack plane causes plastic deformation to occur at the contact area in the surrounding mortar as shown in Figure 2-27(c). This deformation produces normal and shear stresses, parallel and perpendicular to the surface of the spherical particles as shown in Figure 2-28.

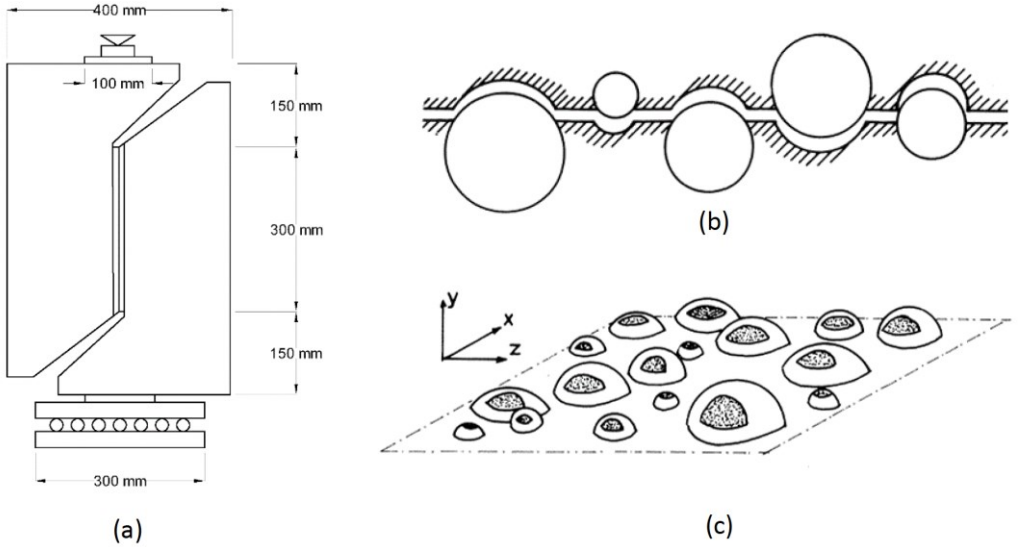

Figure 2-27 Walraven two-phase model: a) layout of test specimen, b) Sphere particles intersected by a crack plane; and c) Contact area during shear displacement; reproduced from [41].

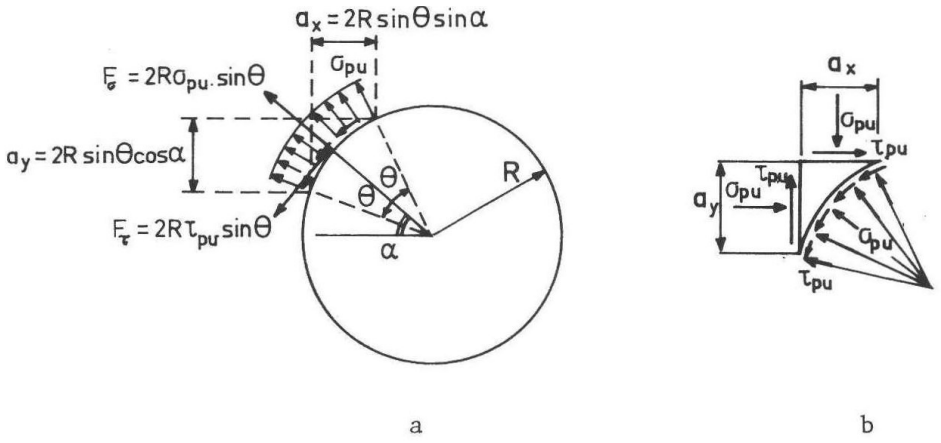

Figure 2-28 Stresses acting on the surface of aggregate particles; reproduced from [41].

The model is dependent upon several parameters including maximum aggregate size, total aggregate volume, crack width and crack slip. It relates the normal and shear stresses to the displacement components (Δ and *w*) as given in the following expression:

$$\sigma = \sigma_{pu}(A_x - \mu \times A_y) \quad (2\text{-}52)$$

$$\tau = \sigma_{pu}(A_y - \mu \times A_x) \quad (2\text{-}53)$$

The parameters A_x and A_y are the projected contact areas in x and y-directions for a unit crack area of 1 mm^2 and they depend on the displacement components (Δ and *w*). The factor μ is a coefficient of friction acting between aggregate particles and mortar. The parameter σ_{pu} is the matrix yielding strength (taken as 6.39× $f_{cc}^{0.56}$MPa). Two cases are considered for calculating the normal and shear stresses (Case A and Case B). These depend on whether the magnitude of the crack slip (Δ) is less or greater than the crack width (*w)*. As shown in Figure 2-29, the two cases represent the growing contact phase and maximum contact phase, which depends mainly on the radius of aggregate particle. The growing phase represents the first contact between aggregate particles and mortar, whereas maximum contact phase means that there is no more increase in contact area between the two materials.

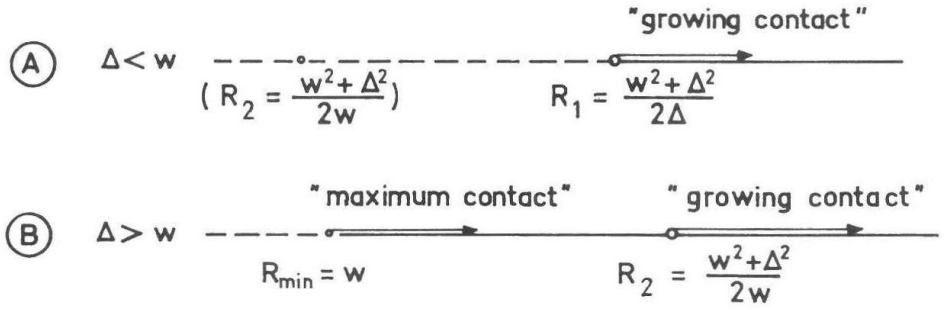

Figure 2-29 The fundamental contact modes for varying the radius R of the spherical particle; reproduced from [41].

Figure 2-30 shows good agreement between the experimental results of Walraven and theoretical results for various crack widths.

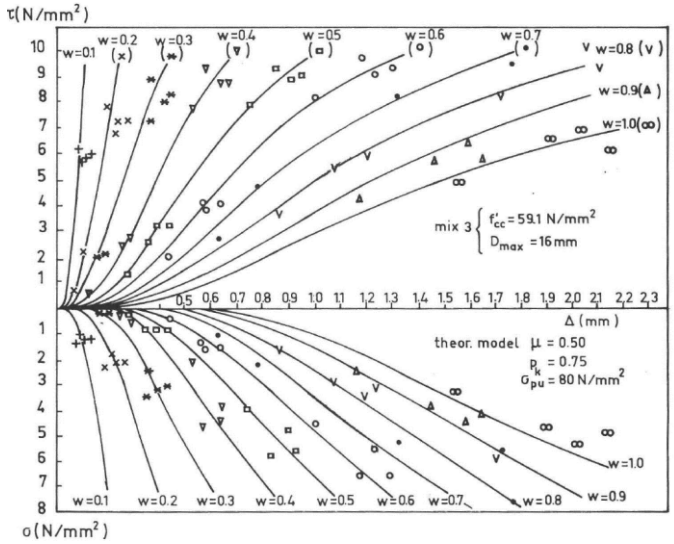

Figure 2-30 Comparison between experimental values and the model results; reproduced from [41].

2.5.1.2 The Rough Crack model (Bazant and Gambarova [45] & Gambarova and Karakoç [46])

A semi-empirical crack model was developed by Bazant and Gambarova [45]. The model neglects the effects of dowel action and kinking of steel reinforcement in a crack. Subsequently, Gambarova and Karakoç [46] improved the formulation of the relationship between stress and crack displacements by considering the effects of confinement and aggregate size. In the model of Bazant and Gambarova [45], shear transferred through cracks depends primarily upon the displacement ratio ($r = s/w$). The model accounts for concrete compressive strength (f'c), crack width (w), crack slip (s), maximum aggregate diameter (D_{max}) and concrete tensile strength (f_t). The shear resistance is assumed to reduce to zero, due to

loss of contact, at a crack width of $D_{max}/2$. The defining equations of the model of Bazant and Gambarova are as follows:

$$\tau_{cr} = \tau_u r \frac{a_3 + a_4|r|^3}{1 + a_4 r^4} \tag{2-54}$$

$$\sigma_{cr} = -\frac{a_1}{w}(a_2|f_t|)^p \tag{2-55}$$

$$\text{Where, } r = \frac{s}{w}\,;\ \tau_u = \tau_0 \frac{a_0}{a_0 + w^2}\,;\ \tau_0 = 0.245 f_c'\,;\ a_0 = 0.01 D_{max}\,;$$

$$a_1 = 5.34 \times 10^{-4}\,;\ a_2 = 145\,;\ a_3 = \frac{2.45}{\tau_0}\,;\ a_4 = 2.44\left(1 - \frac{4}{\tau_0}\right)\,; \tag{2-56}$$

$$p = 1.3\left(1 - \frac{0.231}{1 + 0.185w + 5.63w^2}\right)$$

τ_u depicts the maximum shear stress and τ_0 is the limiting shear stress when w = 0. As shown in Figure 2-31, the model predictions compare well with the test data of Paulay and Loeber [47].

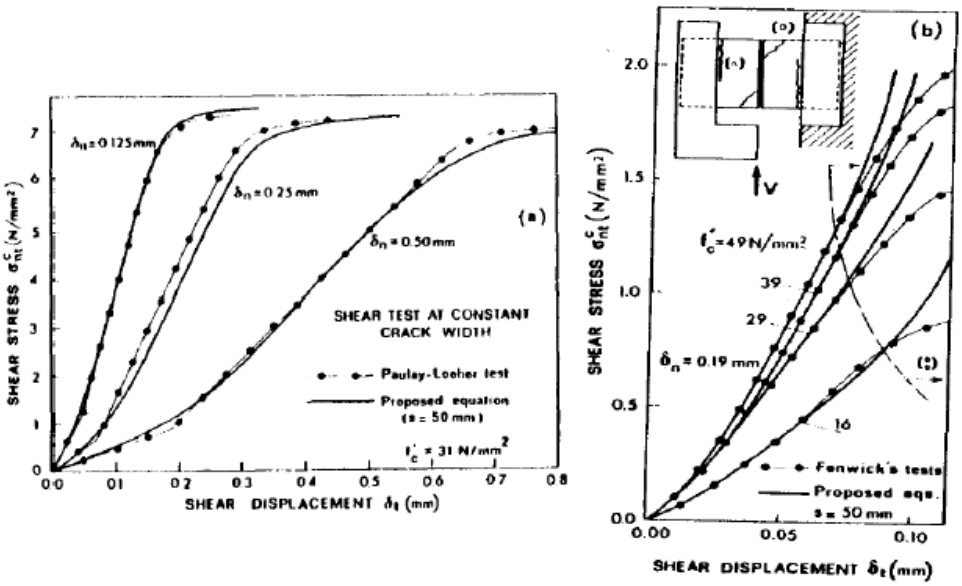

Figure 2-31 Fit curves of experimental test results; reproduced from [45].

The formulation of Gambarova and Karakoç [46] is as follows:

$$\tau_{cr} = \tau_0 \left(1 - \sqrt{\frac{2w}{D_{max}}}\right) r\, \frac{a_3 + a_4|r|^3}{1 + a_4 r^4} \tag{2-57}$$

$$\sigma_{cr} = -a_1 a_2 \sqrt{w} \frac{r}{(1+r^2)^{0.25}} f_t \quad (2\text{-}58)$$

$$\text{Where, } \tau_0 = 0.25 f_c' \text{ ; } a_1 a_2 = 0.62 \text{ ; } a_3 = \frac{2.45}{\tau_0} \text{ ; } a_4 = 2.44(1 - \frac{4}{\tau_0}) \quad (2\text{-}59)$$

2.5.1.3 Hamadi and Regan model [44]

Hamadi and Regan developed an empirical model for shear transfer through aggregate interlock from regression analysis of push-off test data. The shear stress is assumed to be linearly proportional to s/w up to a maximum shear stress τ_u. The model distinguishes between natural aggregate concrete and expanded clay aggregate since cracks passed around the natural gravel aggregate but through the expanded clay aggregate. The equations below represent the formulation used in this model.

$$\tau_{cr} = \frac{k}{w} s \quad (2\text{-}60)$$

$$\tau_{ult} = c + \mu\sigma \quad (2\text{-}61)$$

The parameter k is 5.4 N/mm^2 for gravel aggregate and 2.7 N/mm^2 for expanded clay aggregate. For natural gravel aggregate, c and μ have values of 4 N/mm^2 and 0.7 N/mm^2 respectively.

2.5.1.4 Contact Density Model (CDM)

Li et al. [42] developed a contact density model for aggregate interlock from analysis of contact density probability functions $\Omega\,(\theta)$. The model divides the crack plane into a number of contact units with different inclinations ranging from -$\pi/2$ to $\pi/2$. The following equations describe the mathematical formulation for this model.

$$\tau_{cr} = \int_{-\pi/2}^{\pi/2} \sigma_{con}\ k\,(w)\,.A_t\,\Omega\,(\theta)\,.sin\theta\,.d\theta \quad (2\text{-}62)$$

$$\sigma_{cr} = \int_{-\pi/2}^{\pi/2} \sigma_{con}\ k\,(w)\,.A_t\,\Omega\,(\theta)\,.cos\theta\,.d\theta \quad (2\text{-}63)$$

in which σ_{con} is the contact stress which was determined using a elasto-perfectly plastic model. $k\,(w)$ is the effective ratio of the contact area and depicts the contact stage along the crack. This parameter becomes effective when the crack (w) is wide enough in comparison with the roughness of the crack plane. $\Omega\,(\theta)$ is a contact density function. It is defined by a trigonometric formula that depends upon the grading, strength, size and type of aggregate

particles. A_t is the surface area which is assumed to be 1.27 time of the section of crack surface. This model was simplified on the basis of this contact density model of Li et al. [42] and Soltani [48] in which the crack stress is dependent upon the displacement ratio ($r = s/w$). The following expression is the formulation for the simplified model.

$$\tau_{cr} = 3.83\, f_c'^{(\frac{1}{3})}\, \frac{r^2}{1+r^2} \tag{2-64}$$

$$\sigma_{cr} = 3.83\, f_c'^{1/3} \left[\frac{\pi}{2} - cot^{-1}r - \frac{r}{1+r^2}\right] \tag{2-65}$$

2.5.2 Contribution of shear reinforcement in joint

Sigrist [49] developed a model for obtaining the stress in reinforcement crossing a crack in terms of the crack width. A stepped rigid plastic bond behaviour is assumed to occur at the interface between concrete and reinforcement before and after yielding of stirrup, as shown in Figure 2-32. Prior to yielding, it is assumed that the bond stress is constant and equal to twice the concrete tensile strength ($\tau_{b0} = 2\, f_{ct}$). After yielding, the bond stress is assumed to reduce to the tensile strength of concrete ($\tau_{b0} = f_{ct}$). The tensile force in the reinforcement decreases away from a crack due to load being transferred into the surrounding concrete through bond. The corresponding distributions of bond stress and reinforcement stress are shown in Figure 2-33. The crack width is determined from integration of the reinforcement strain distribution as shown below.

$$w = 2\int_0^L \varepsilon_s\, dx \tag{2-66}$$

Where, L is the effective length over which slip occurs.

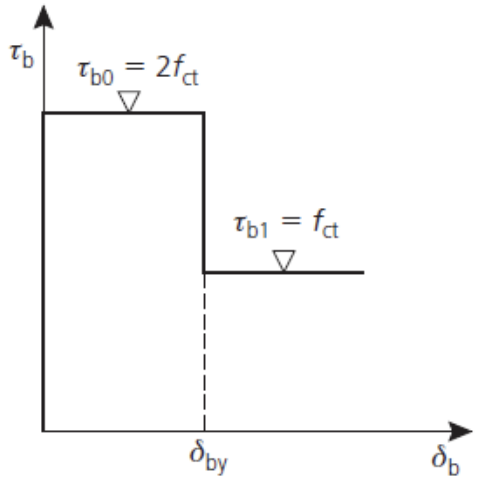

Figure 2-32 Stepped rigid plastic bond behaviour proposed by Sigrist; reproduced from [49].

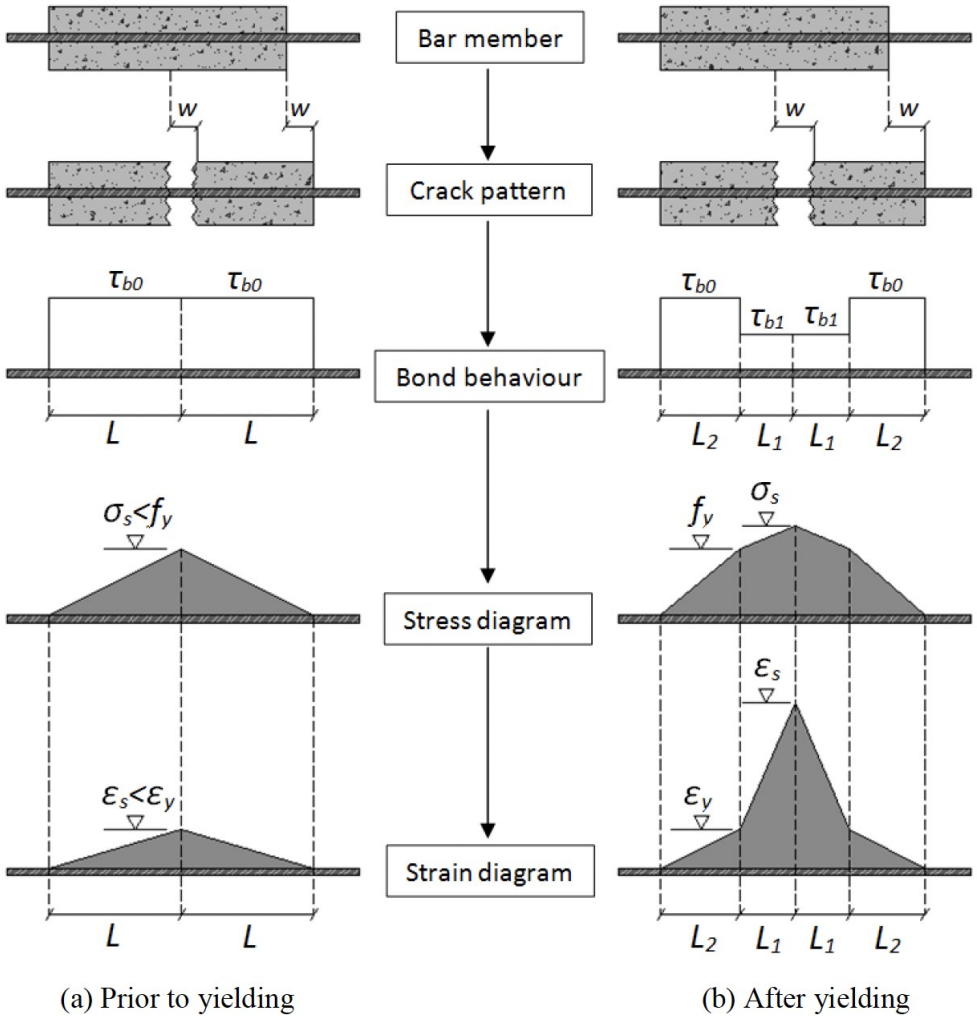

Figure 2-33 Bond and shear reinforcement response at and between cracks: (a) Prior to yielding; (b) after yielding; adapted from [49].

Shear reinforcement response in elastic stage:

Prior to yielding of shear reinforcement, the bond stress is assumed constant and equal to ($\tau_{b0} = 2\ f_{ct}$). The effective length over which slip occurs is calculated as follows:

$$L = \frac{\sigma_s\ A_{sw}}{\pi\ \emptyset\ \tau_{b0}} \tag{2-67}$$

The stress in the reinforcement can be determined in terms of the crack width as follows:

$$\sigma_s = \sqrt{\frac{2\pi\ E_s\ \emptyset\ f_t}{A_{sw}}.w} \tag{2-68}$$

Shear reinforcement response in plastic stage:

After yielding of reinforcement, the bond stress is assumed to reduce to a constant value equal to the concrete tensile strength ($\tau_{b0} = f_{ct}$), over an effective length, subject to slip between steel and concrete, equal to the sum of L_1 and L_2 given by:

$$L_1 = \frac{(\sigma_s - f_y)\ A_{sw}}{\pi\ \emptyset\ \tau_{b1}} \tag{2-69}$$

$$L_2 = \frac{f_y\ A_{sw}}{\pi\ \emptyset\ \tau_{b0}} \tag{2-70}$$

The crack width (w) can be found using the following equation which is obtained by integration of the reinforcement strain over L_1 plus L_2:

$$\sigma_s = \frac{2}{A_{sw}}\left(\frac{f_y^2}{2\pi\ E_s\ \emptyset\ \tau_{b0}} + \frac{(\sigma_s - f_y)^2}{2\pi\ E'\ \emptyset\ \tau_{b1}} + \frac{\sigma_s.\ f_y}{2\pi\ E_s\ \emptyset\ \tau_{b1}} - \frac{f_y^2}{\pi\ E_s\ \emptyset\ \tau_{b1}}\right) \tag{2-71}$$

σ_s is greater than the yield stress of reinforcement and can be estimated from equation (2-71) if the crack width (w) is known. The parameter E' is the post-peak stiffness of steel reinforcement and its value can be estimated from bar tensile test.

2.5.3 Evaluation of crack kinematics using DIC

Shear transfer through cracks depends on the crack kinematics which can be determined using DIC which is a non-contact measurement tool utilising digital photogrammetry. The technique is described in detail in Chapter 3. DIC has been used by researchers such as Cavagnis et al [50], Cavagnis et al [51] and Elwakeel et al. [52] to track concrete surface strains

and crack kinematics in reinforced concrete beams loaded in shear. Once determined, the crack kinematics can be used to determine the shear transfer through cracks as illustrated in Figure 2-34 and Figure 2-35 from [50, 53].

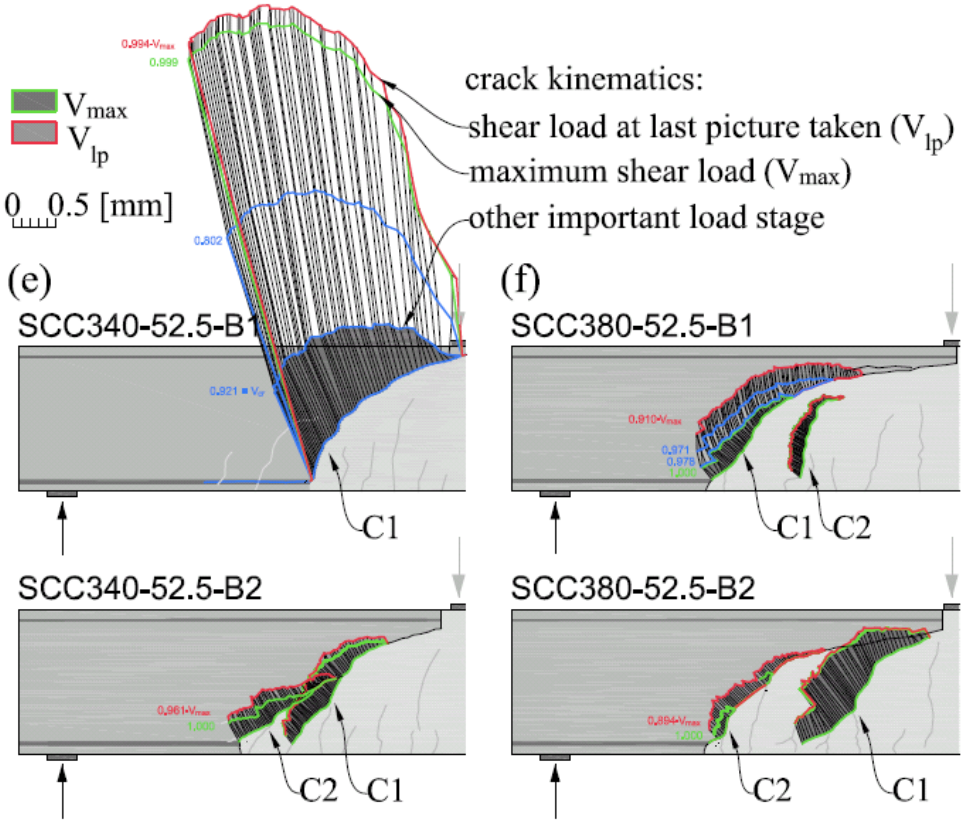

Figure 2-34 DIC results obtained from existed studies for measuring crack kinematics; reproduced from [53].

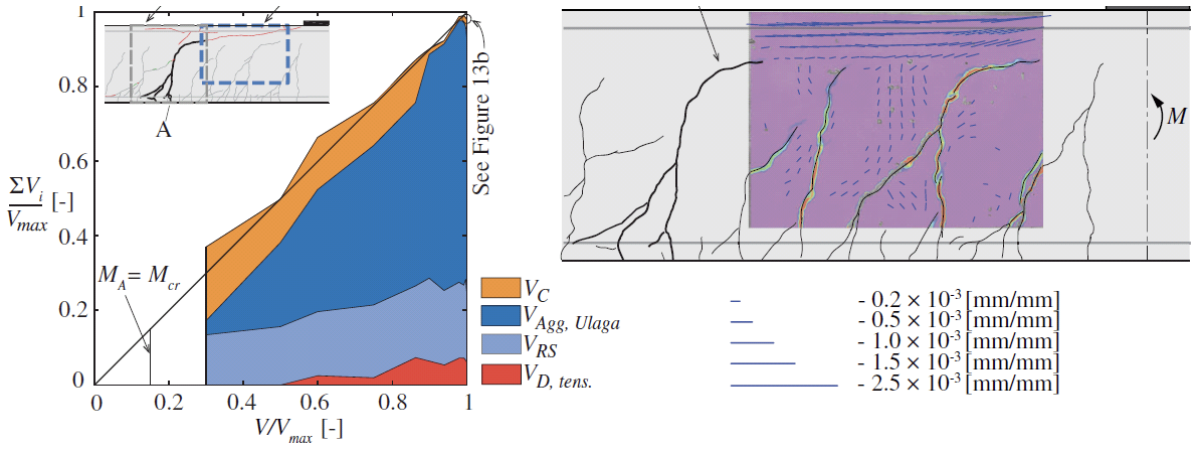

Figure 2-35 DIC results obtained from existed studies for evaluating concrete surfaces strains; reproduced from [50].

2.6 Summary of literature review

This chapter reviews the behaviour and design of monotonically loaded external beam column joints which are less researched than seismically loaded connections. The chapter starts by summarising previous experimental studies into monotonically loaded beam-column joints. It goes onto describe various design methods for external beam-column joints from the literature. These models are classified as either empirical or analytically based. The basis of strut and tie modelling is described as well as its application to external beam-column joints by several researchers. Shear transfer through aggregate interlock is also discussed. The key conclusions and observations of this chapter are outlined below in the order they appear:

- Several previous studies suggest that high column axial load plays a crucial role in improving joint behaviour and can change the failure mode from beam and upper column flexure to joint shear failure.
- The influence of column load on joint strength is less clear because most of previous studies showed different joint response when column axial load increased. Some previous experiments resulted in a reduction of joint shear strength or an increase in joint shear strength when column load increased.
- Increasing the bend radius reduces the bearing stresses inside the bend of the beam reinforcement. The effect of this on joint shear strength is unclear so is investigated further in this thesis.
- The horizontal and vertical joint reinforcement (stirrups and intermediate column bars) improve joint strength as the reinforcement ratio increases.
- Code provisions for anchorage reinforcement tend to underestimate the maximum tensile force that can be developed. In the case of beam column joints, this can result in the joint shear stress being underestimated.
- The lack of reporting of load-displacement curves in previously tested monotonically loaded external beam-column joints prevents accurate assessment of NLFEA models.
- Various researchers have proposed rational design methods for external beam-column joints but this is not reflected in codes of practice like ACI 318 and EC2.
- Two main mechanisms are reported in the literature for transferring shear force through joints. In the absence of joint shear reinforcement, shear is resisted by an inclined compressive strut. The addition of shear reinforcement gives rise to a

secondary truss mechanism in which an inclined compressive stress field is equilibrated by horizontal and vertical reinforcements consisting of joint stirrups and intermediate column bars.

- Four models for evaluating aggregate interlock are described in this chapter. Both empirical and physically based models are considered. The crack models of Walraven model [41] and Li et al. model [42] are derived from considerations of contact area during shear displacement. The empirical crack models are derived from curve fitting test results by studying the crack stress relationships. Examples include the models of Walraven and Reinhardt [43], Hamadi and Regan [44], Bazant and Gambarova [45] and Gambarova and Karakoc model [46].
- The Sigrist model [49] for calculating reinforcement stress in terms of crack width is described in detail and the formulae used in this model are summarised.
- Crack kinematics can be determined using Digital Image Correlation (DIC) of which further details are given in Chapter 3.
- Shear transfer mechanisms in beam-column joints have not been studied in detail for monotonically loaded external beam-column joints.

Chapter 3 Experimental program

This chapter describes the experimental program carried out by the author in the Heavy Structures Laboratory in the Department of Civil & Environmental Engineering at Imperial College London. Three series of external beam-column joints were tested to investigate the influence of detailing of beam reinforcement, joint shear reinforcement, column intermediate bars and column axial load. The chapter describes the manufacturing process, loading configuration, instrumentation and the procedures used to obtain the crack kinematics with Digital Image Correlation (DIC).

3.1 Overview

Shear in beam-column joints has been a topic of interest for many years. This research focuses on the design and behaviour of external beam-column joints in framed structures. Joints are potentially critical regions in reinforced concrete frame structures since the joint shear stress is very high compared with the shear stress in adjacent members. Joints are loaded in shear due to moment transfer from beam to column. This mechanism causes diagonal cracking to occur in joints, which reduces joint stiffness and, in the limit, causes joint failure. The shear response of beam-column joint has been studied by many researchers in the past including Taylor [5], Scott [11], Ortiz [12], Hamil [14], Hegger et al [15] and Sperry et al [18, 19].

Failures of beam-column joints are not widely reported for non-seismic loading possibly due to redistribution of moment from support to span after diagonal joint cracking. The majority of research into beam-column joints has focussed on seismic behaviour. Unlike cyclic tests, most previous tests on monotonically loaded beam-column joints only report the failure load and not the joint shear deformation which influences the development of column moments in framed structures. A further limitation of the available experimental data on monotonically loaded specimens is the small scale of the tested specimens. An exception to this is the seven large scale tests of Ortiz [12] on external beam-column joints, which are considered as the basis of designing the tested BCJ specimens in this thesis.

Analysis of test data show that joint strength is affected by a large number of parameters including concrete strength, joint geometry, the effect of beam reinforcement ratio, beam anchorage reinforcement type and bend radius, joint shear reinforcement area and position, column load and intermediate column bars if present. Anchorage of reinforcement plays a

crucial role in improving joint strength with details used including 90-degree bends (bent up/down L-bar) and 180-degree bends (U-bar). Providing shear reinforcement in joints enhances joint shear strength. However, tests show that there is a limit to the increment in joint shear strength that can be achieved by providing joint shear reinforcement. The influence of column axial load has been investigated by various researchers including Scott [11] and Ortiz [12]. These studies show that the influence of axial load on joint behaviour is complex and not fully understood. Increasing the column axial load delays diagonal joint cracking and dependent on the magnitude of the axial load and may prevent failure of the upper column in flexure prior to beam or joint failure. However, test data on the influence of column axial load on joint shear strength are inconclusive meriting further investigation. The provision of intermediate column reinforcement enhances joint shear strength with the enhancement increasing significantly with increasing intermediate column bar area, according to Hegger et al [15].

The aim of this research is to study the behaviour of isolated external beam-column joint specimens. The data gathered in the test programme give insight into the parameters influencing joint shear strength and deformation. The latter is significant for the assessment of moment redistribution from edge columns into the span in framed structures. Downwards moment redistribution at external columns reduces the joint shear force and hence the required area of joint shear reinforcement.

Digital Image Correlation (DIC) was used to record the joint shear deformation and crack kinematics as described in this chapter. Strain measurements obtained with the DIC also help identify the orientation and width of the diagonal strut in the joint.

3.2 General Test Description

Twelve geometrically identical beam-column joint specimens were tested in the Heavy Structures Laboratory at Imperial College London. These were designed based on the dimensions of the BCJ specimens tested in Ortiz study. The specimens were tested in three groups of four. The column of each specimen measured 2300 mm long by 250 mm deep by 225 mm wide. The beam measured 1300 mm long by 400 mm deep by 225 mm wide. Series 1 was designed to study the effect of the anchorage of beam reinforcement in the joint. The beam reinforcement was anchored into the column with both L-anchorage and U-anchorage.

The bend radius was either standard (3.5ϕ) or large (6ϕ) according to EC2 [23]. Series 2 investigated the influence of varying the column axial load on the joint failure mode and strength. Upper column loads of 300 kN, 600 kN and 900 kN were considered. The column load 300 kN (5.3 MPa) was used to match the column load used in Ortiz tested specimens in order to investigate the effect of each experimental parameters and compare the results with the tested specimens of this research. It was decided to increase the column load to 600 kN and 900 kN (10.7 MPa and 16 MPa respectively) to study the effect of column load on joint behaviour. These loads were applied at the start of the test and maintained constant during the test. Series 3 was designed to investigate the influence of joint shear reinforcement and intermediate column bars.

3.3 Series 1 of Beam-Column Joints

Four specimens were constructed with different reinforcement detailing. The flexural tension steel in the beam consisted of 2B25 bars. Specimens BCJ 1 and BCJ 2 were constructed with L-anchorage reinforcement, whereas BCJ 3 and BCJ 4 had U-anchorage reinforcement. A standard bend radius (r = 3.5 ϕ = 87.5 mm) was provided in BCJ 1 and BCJ 3 while a large bend radius (r = 6ϕ = 150 mm) was used in BCJ 2 and BCJ 4 as shown in Figure 3-1. The aim of increasing the bend radius was to reduce the bearing stress in the radius of the bend which can be critical for standard radius bends according to EC2. Two 16 mm diameter bars were provided in the flexural compression zone of the beam in the specimens with L-bars. Four longitudinal bars of 25 mm diameter were used in the column. Stirrups of 10 mm in diameter were provided in the beam at 200 mm centres and in the column at 135 mm centres. The joint shear reinforcement consisted of three stirrups spaced at 75 mm centres. Hanger bars of diameter 10 mm were placed in the corners of the beam links as shown in Figure 3-1. The reinforcement detailing is summarised in Table 3-1.

Table 3-1 Series 1 of beam-column joint steel reinforcement detail and column axial load

Specimen	Column Reinf.	Beam Reinf.	Anchorage type	Bend radius (mm)	Joint stirrups	column load (kN)
BCJ 1	4B25	2B25	L	87.5	3B10	300
BCJ 2	4B25	2B25	L	150	3B10	300
BCJ 3	4B25	2B25	U	87.5	3B10	300
BCJ 4	4B25	2B25	U	150	3B10	300

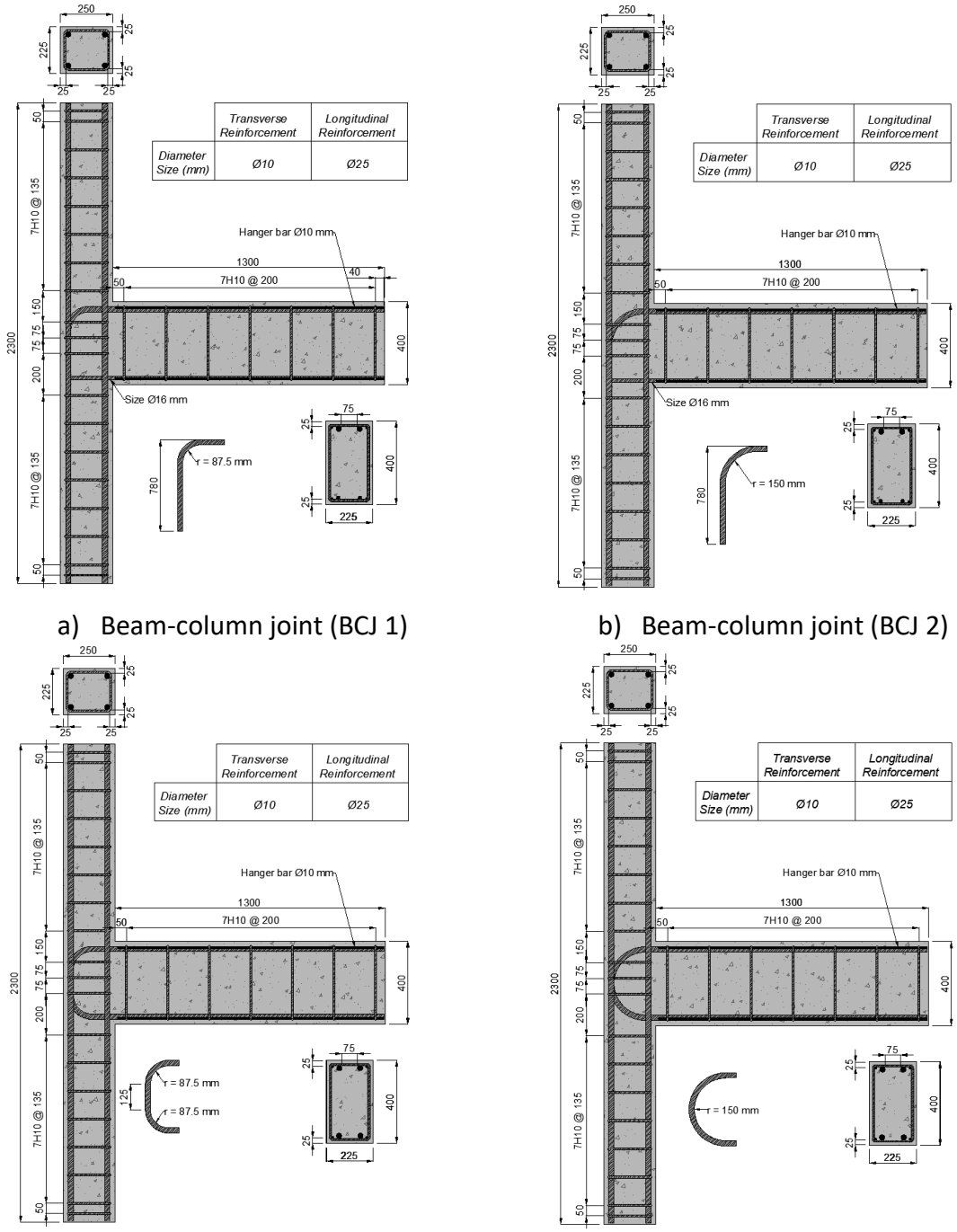

a) Beam-column joint (BCJ 1) b) Beam-column joint (BCJ 2)

c) Beam-column joint (BCJ 3) d) Beam-column joint (BCJ 4)

Figure 3-1 Series 1 of beam-column joint specimens.

3.4 Series 2 of Beam-Column Joints

Four beam-column joint specimens were tested in Series 2 which investigated the effect on joint shear strength of column axial load and joint shear reinforcement. The upper column axial load was chosen to be 300 kN, 600 kN and 900 kN. The columns of all four specimens were reinforced with four 25 mm diameter bars. The beams of the specimens were reinforced

with 25 mm diameter, standard radius (r = 87.5 mm) U-bars apart from BCJ 7 where the flexural tension reinforcement consisted of two 25 mm diameter, large radius (r = 150 mm) L-bars. Two 16 mm diameter bars were placed in the flexural compression zone. The stirrup arrangement in the beam and columns above and below the joint were the same as in Series 1. BCJ 6 and BCJ 8 had three joint stirrups spaced at 75 mm centres like Series 1 while the other two specimens had only 1 stirrup at the middle of joint. Additional links were provided at the column ends to control potential bursting stresses as shown in Figure 3-2. Hanger bars size 10 mm were placed in the corners of the beam stirrups for anchorage and to control cracking as shown in Figure 3-2. The reinforcement detailing is summarised in Table 3-2.

Table 3-2 Series 2 of beam-column joint steel reinforcement detail and column axial load

Specimen	Column Reinf.	Beam Reinf.	Anchorage type	Bend radius (mm)	Joint stirrups	column load (kN)
BCJ5	4B25	2B25	U	87.5	1B10	300
BCJ6	4B25	2B25	U	87.5	3B10	600
BCJ 7	4B25	2B25	L	150	1B10	300
BCJ8	4B25	2B25	U	87.5	3B10	900

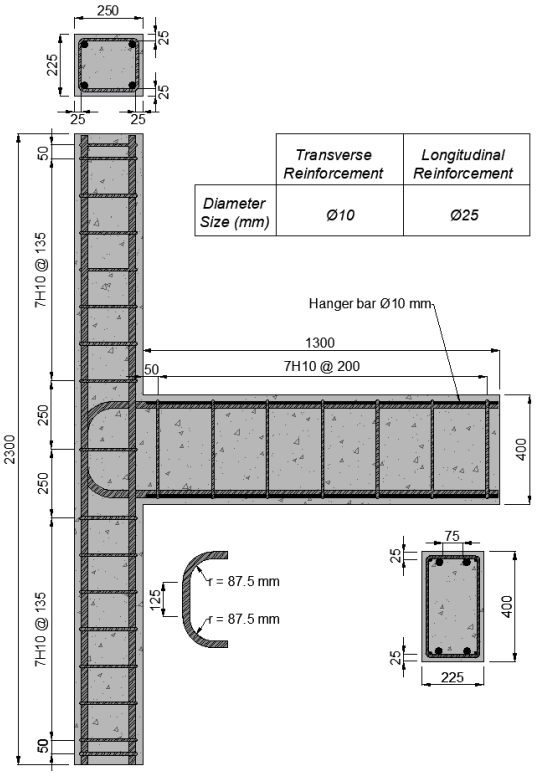

a) Beam-column joint (BCJ 5)

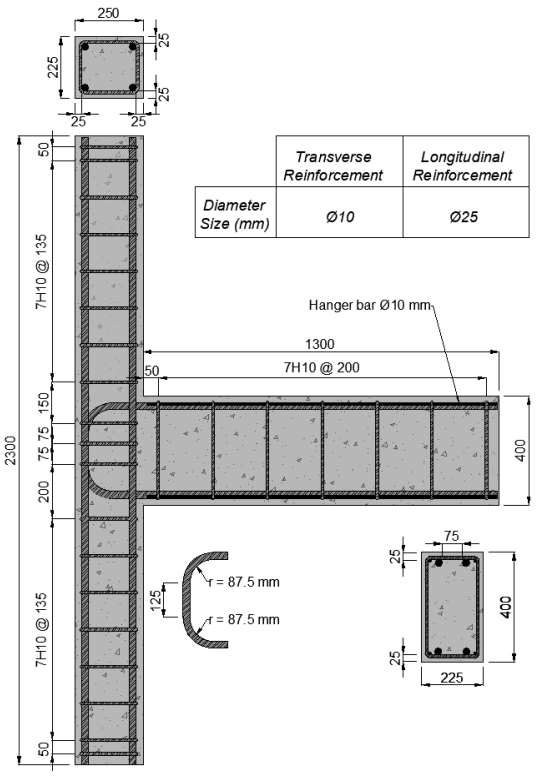

b) Beam-column joint (BCJ 6)

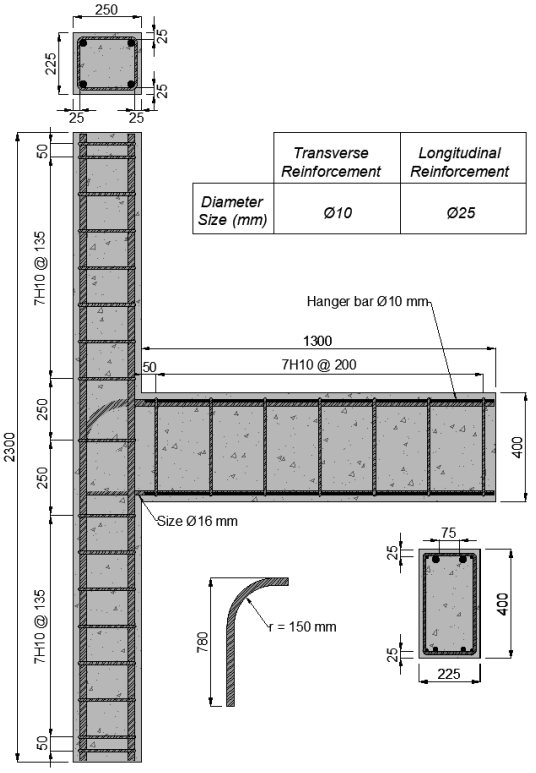

c) Beam-column joint (BCJ 7)

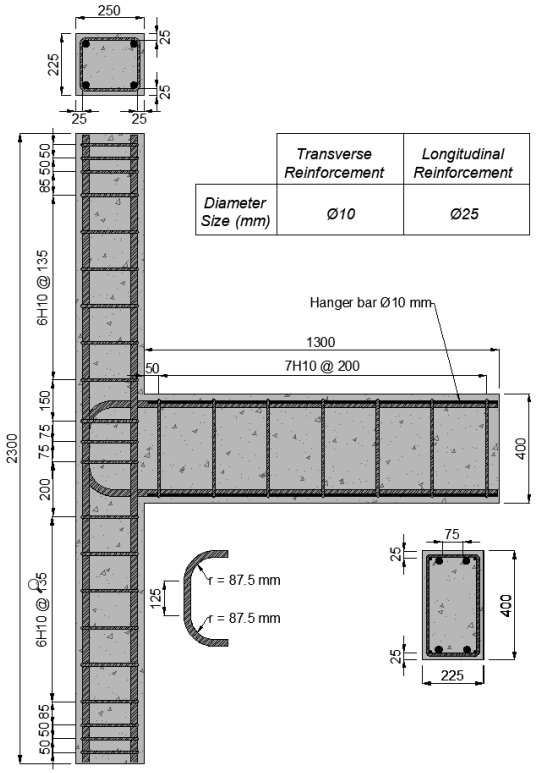

d) Beam-column joint (BCJ 8)

Figure 3-2 series 2 of beam-column joint specimens.

3.5 Series 3 of Beam-Column Joints

Four BCJ specimens were tested in Series 3 to study the influence on joint shear strength of joint shear reinforcement and intermediate column bars. The number of joint stirrups investigated were none, two, three and six as shown in Figure 3-3. The number of 25 mm diameter column bars was increased from four to six in BCJ 10 to prevent flexural failure. The other specimens had four 25 mm column bars as in the Series 1 and 2. The flexural reinforcement in specimens BCJ 10 and BCJ 12 consisted of two 25 mm diameter L-bars in tension and two straight 16 mm bars in compression. The L-bars in BCJ 10 and BCJ 12 had a large bend radius of 150 mm. The other BCJ specimens were reinforced with 25 mm diameter U-bars with a standard bend radius of 87.5 mm. The stirrup arrangement in the beam and column were the same as in Series 1 and 2. The reinforcement detailing is summarised in Table 3-3.

Table 3-3 Series 3 of beam-column joint steel reinforcement detail and column axial load

Specimen	Column Reinf.	Beam Reinf.	Anchorage type	Bend radius (mm)	Joint stirrups	column load (kN)
BCJ 9	4B25	2B25	U	87.5	2B10	300
BCJ 10	6B25	2B25	L	150	3B10	300
BCJ 11	4B25	2B25	U	87.5	NO	300
BCJ 12	4B25	2B25	L	150	6B10	300

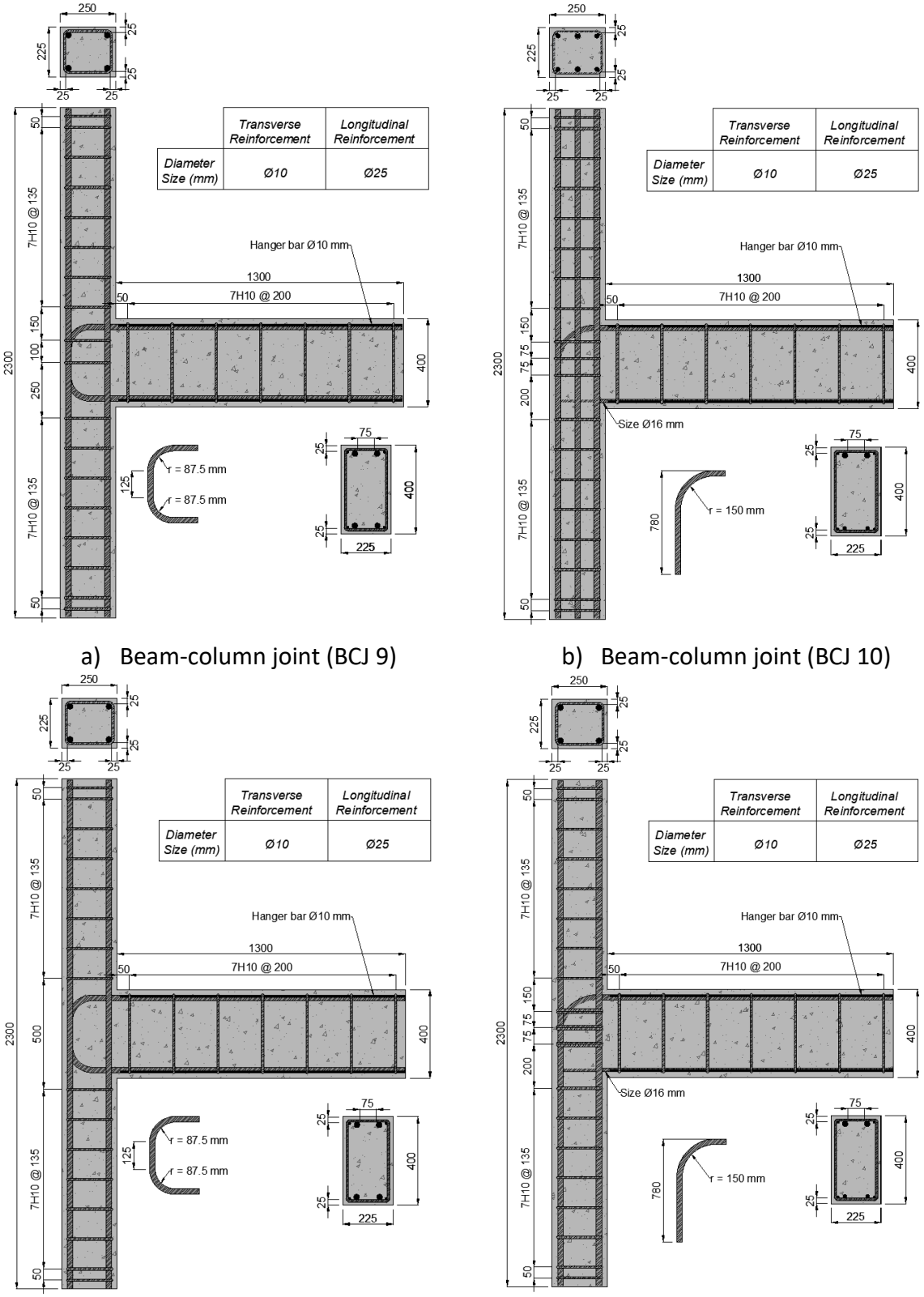

a) Beam-column joint (BCJ 9) b) Beam-column joint (BCJ 10)

c) Beam-column joint (BCJ 11) d) Beam-column joint (BCJ 12)

Figure 3-3 Third series of beam-column joint specimens.

3.6 Manufacture and curing

The specimens were cast on their sides in plywood moulds as shown in Figure 3-4. All three series of specimens were cast from ready mix concrete using the same formwork. The inside face of the moulds was rubbed with mould oil prior to each casting to prevent the formwork becoming stuck to the concrete.

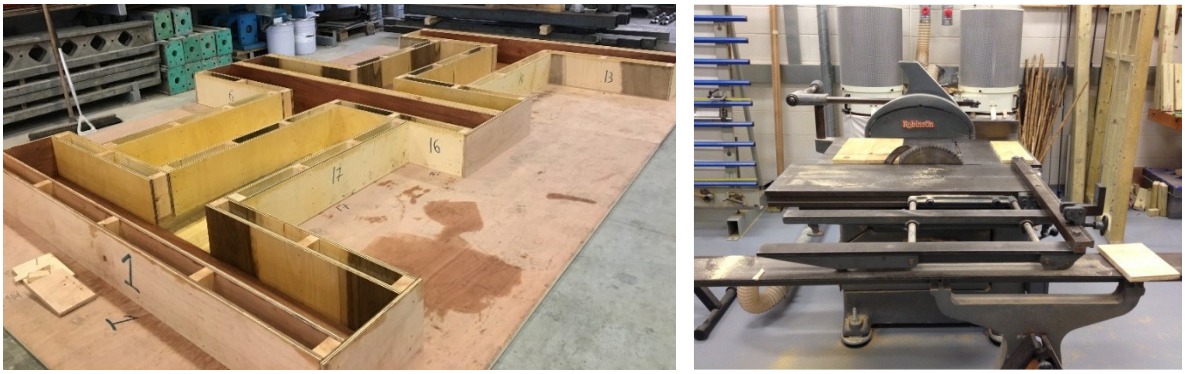

Figure 3-4 Beam-column joint wooden moulds.

The reinforcement was delivered in a single batch for all the specimens and stored in the laboratory until needed. The reinforcement cages for the beam and column were assembled separately with the main flexural reinforcement projecting from the column as shown in Figure 3-5. Strain gauges were installed after assembling the steel reinforcement cages. This involved locally grinding away the seam along the sides of the reinforcement bars as shown in Figure 3-6 to make the surface flat for installing the strain gauge. After grinding, the ground surface was cleaned using acetone and MNA5-2 neutralizer to remove any dirt or grease as shown in Figure 3-6. The strain gauge was then glued onto the rebar surface and coated with an epoxy resin for protection during concrete casting. When the process of attaching strain gauges to steel reinforcement was completed, the steel cages were placed inside the timber moulds prior to casting the concrete as shown in Figure 3-5.

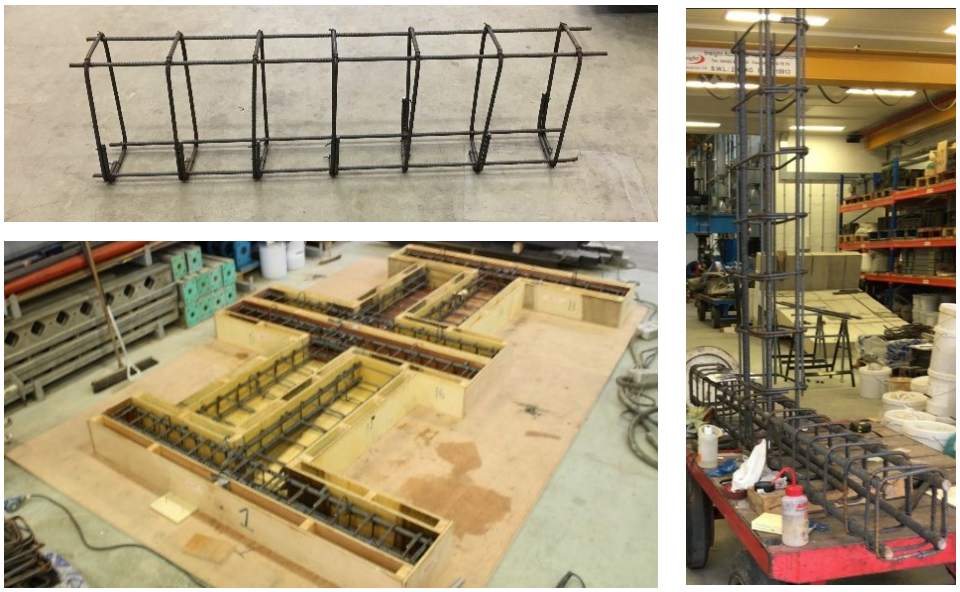

Figure 3-5 Assembled steel reinforcement cages inside the moulds before casting.

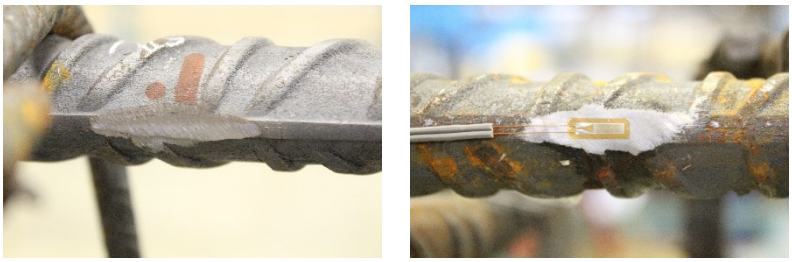

Figure 3-6 Attaching strain gauges to steel reinforcement.

The specimens were cast in three batches of four from ready-mixed concrete. The concrete was poured into the moulds from an upright concrete skip with a central discharge hose. Eighteen cubes (100 x 100 x 100 mm), twelve cylinders (100 x 150 mm) and twelve cylinders (150 x 300 mm) were cast with each batch. Half of the specimens were cured in water and the rest were cured in air as shown in Figure 3-7. A vibrator was used to compact the concrete in the BCJ specimens while the control specimens were cast on a vibrating table. The specimens were covered with polythene sheets until they were demoulded. The BCJ specimens were stripped after two days while the control specimens were demoulded on the next day. To keep adequate moisture levels for proper curing, the BCJ specimens were watered three times per week and covered by wet hessian and polythene sheets.



Figure 3-7 Casting and curing concrete procedure.

3.7 Instrumentation

3.7.1 General aspect

The instrumentation during the tests consisted of:

- Digital image correlation (DIC) system.
- Strain gauges attached to steel reinforcement.
- Linear variable displacement transducers (LVDT).
- Inclinometers.

The following sections describe the instrumentation in detail.

3.7.2 Beam-column joint setup and testing procedure

The specimens were loaded in an internal reaction frame as shown in Figure 3-9. The ends of the columns were restrained horizontally in the plane of the specimen with steel supports fixed to the top and bottom of the frame. The base of the column was supported on a roller bearing which allowed horizontal movement as shown in Figure 3-8. The column was loaded from the top with a hydraulic jack through a pinned connection that allowed rotation. The beam was loaded with a second hydraulic jack.

At the start of the series 1 tests, the upper column axial load was applied gradually until it reached 300 kN. After that, the column axial load was held constant, and the beam load was increased at a rate of 1 mm/min until the maximum load was reached. The same loading procedure was adopted for specimens BCJ 5 and BCJ 7 of series 2, and series 3, which all had an upper column load of 300 kN.

In tests BCJ6 and BCJ8 with higher upper column loads of 600 kN and 900 kN respectively, the column was observed to rotate backwards as the axial load was increased above 300 kN. To prevent this, a nominal beam load of between 1 kN and 2 kN was applied before increasing the column load above 300 kN. In addition, an angle section was attached to the rig (see Figure 3-9) to prevent excessive backwards rotation of the top of the column in the event of the specimen becoming unstable during application of the upper column load. Load cells were used to determine the reactions at the top and bottom column horizontal supports.

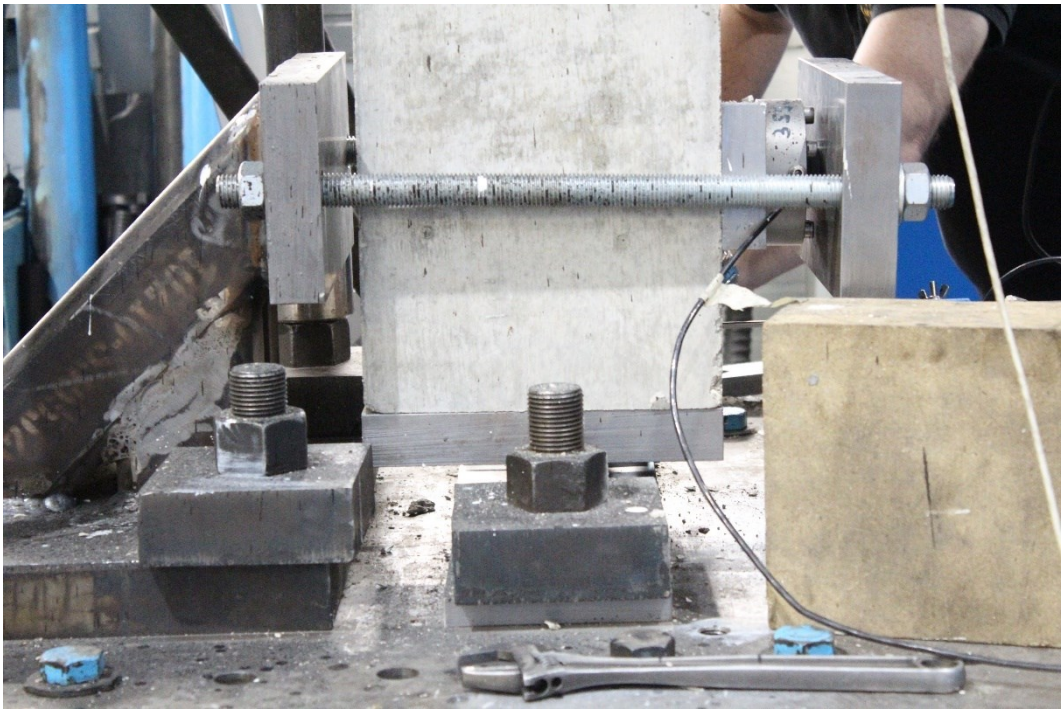

Figure 3-8 Roller bearing support at column base.

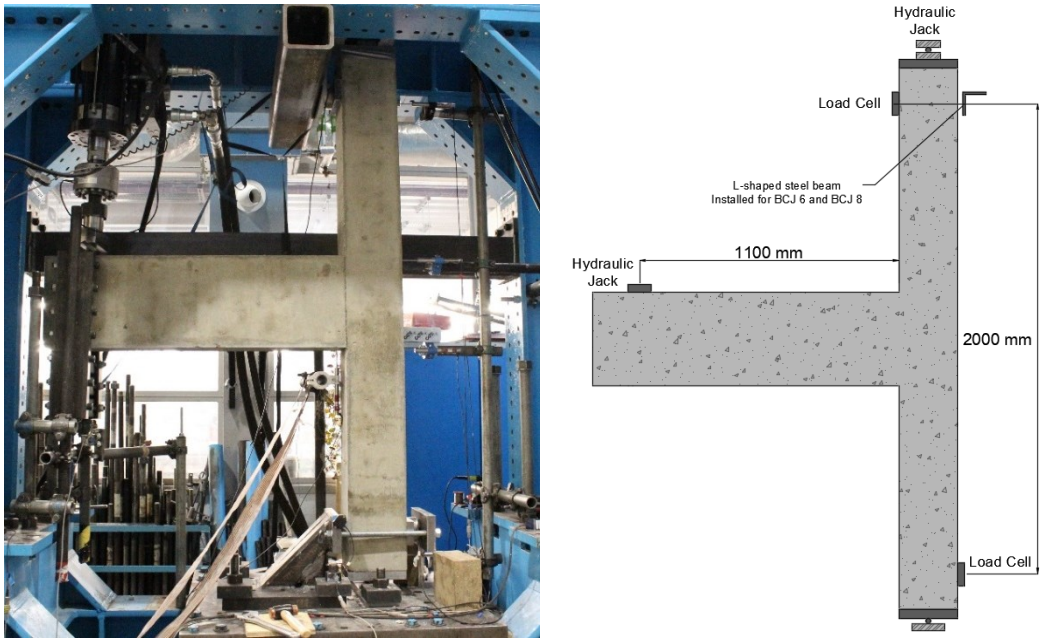

Figure 3-9 Testing rig configuration.

3.7.3 Digital image correlation (DIC) system

Digital image correlation (DIC) was used to observe the crack development during the tests. DIC is a photogrammetric measurement system that enables full field surface displacement measurements of an object. This method involves three major steps: (1) surface preparation with speckle pattern; (2) recording images of the planar joint surface before and after deformation via cameras and (3) using a computer program to process the acquired images and to obtain the displacement and strain measurements. In comparison to conventional methods for measuring displacements, DIC technique provides a low-cost and accurate method for measuring surface strain.

The LaVision's Strain Master (LaVision [54, 55]) DIC system was used in this investigation. The DIC system is composed of a central control unit that manages two high-resolution cameras with lighting components and a laptop connected to the central control unit to process the displacement measurements. Two high-resolution cameras were placed with their optical axis perpendicular to the joint surface, as shown in Figure 3-10. Prior to the test, the joint surface was painted white and a random black speckle pattern was applied with a spray can. The size of speckle pattern ranged between 0.3 – 0.4 mm, based on the area of interest of the joint. From the laptop, the user can control all features of the data acquisition during the test and measure the displacement and strain in the surface of the joint. The distance from the

specimen to the cameras ranged between 1400 mm and 1600 mm, depending on the size of the area of interest.

During the test, the La Vision's Davis software recorded images from the two high-resolution cameras at a specified rate of an image every 2 seconds. The images taken from the monitored area are divided into small overlapping subsets so that the full field displacement can be calculated. The strain and displacement measurements are obtained by comparing the deformations in the images before and after loading.

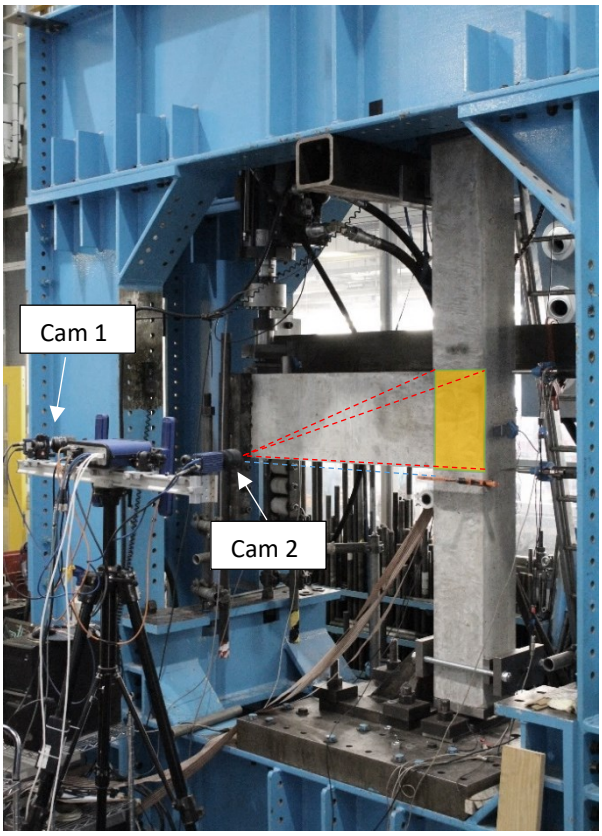

Figure 3-10 Digital image correlation (DIC)

To measure crack propagation and crack kinematics, a theoretical methodology developed by Campana et al. [40] was used in a MATLAB code developed by Elwakeel A. [56]. The displacement field data was extracted from the DIC software and used in the MATLAB code to determine the opening and sliding displacements of selected cracks in the joint surface. The accuracy of these calculations is dependent upon the positioning of a pair of virtual DEMEC gauges placed perpendicular to each other across the considered crack as shown in Figure 3-11. There are limits for gauges locations which need to be checked visually to make sure the gauges placed on a proper location. These limits are as follows:

- The gauge should cross the considered crack and be within the joint boundaries.
- The gauge end-points at the top and bottom of the crack should be within the joint boundaries.
- The gauge length or location should not cross more than one crack.
- If a secondary crack is close to the critical crack, the gauge was shifted to the left or right of the critical crack and its length was reduced if it still crossed the critical crack.
- The gauge length was reduced if it crossed the back face of the joint.

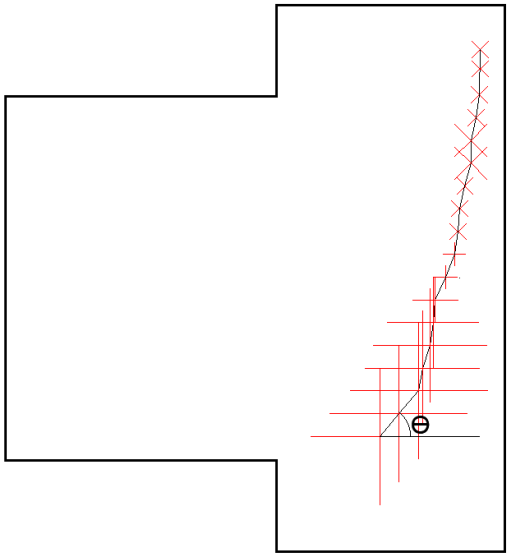

Figure 3-11 Typical virtual gauges along the critical crack for specimen BCJ 4.

The crack opening and sliding displacements are determined from the relative displacements of points f_1 and f_2 in Figure 3-12b. These relative displacements are determined from the displacement fields $w_1(x,y)$ and $w_2(x,y)$ of the two idealized rigid bodies to either side of the crack as shown in Figure 3-12. The displacement fields $w_1(x,y)$ and $w_2(x,y)$ are calculated in terms of the displacements of points P_1 to P_4 in Figure 3-12 which are given by the DIC. As shown by Campana et al. [40] the crack opening and sliding displacements at point *f* can be calculated as follows:

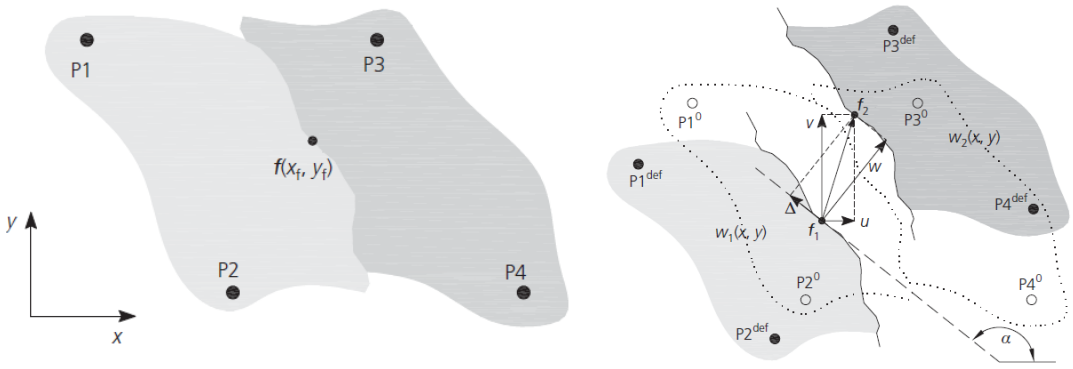

a) Undeformed configuration b) Deformed configuration

Figure 3-12 Measurements for calculation of crack kinematics: (a) undeformed configuration; (b) deformed configuration; reproduced from [40].

$$w_1(x,y) = \begin{cases} a_{1-} e_1 x \\ b_{1+} e_1 y \end{cases} \tag{3.1}$$

$$w_2(x,y) = \begin{cases} a_{2-} e_2 x \\ b_{2+} e_2 y \end{cases} \tag{3.2}$$

Where:

$$\begin{bmatrix} a_1 \\ b_1 \\ e_1 \end{bmatrix} = (A_1^T . A_1)^{-1} . (A_1^T . c_1) \tag{3.3}$$

$$\begin{bmatrix} a_2 \\ b_2 \\ e_2 \end{bmatrix} = (A_2^T . A_2)^{-1} . (A_2^T . c_2) \tag{3.4}$$

$$A_1 = \begin{bmatrix} 1 & 0 & -P1_y^0 \\ 0 & 1 & P1_x^0 \\ 1 & 0 & -P2_y^0 \\ 0 & 1 & P2_x^0 \end{bmatrix} \text{ and } A_2 = \begin{bmatrix} 1 & 0 & -P3_y^0 \\ 0 & 1 & P3_x^0 \\ 1 & 0 & -P4_y^0 \\ 0 & 1 & P4_x^0 \end{bmatrix} \tag{3.5}$$

$$c_1 = \begin{bmatrix} P1_x^{def} & -P1_x^0 \\ P1_y^{def} & -P1_y^0 \\ P2_x^{def} & -P2_x^0 \\ P2_y^{def} & -P2_y^0 \end{bmatrix} \text{ and } c_2 = \begin{bmatrix} P3_x^{def} & -P3_x^0 \\ P3_y^{def} & -P3_y^0 \\ P4_x^{def} & -P4_x^0 \\ P4_y^{def} & -P4_y^0 \end{bmatrix} \tag{3.6}$$

After calculating $w_1(x,y)$ and $w_2(x,y)$, the relative displacement (δ) between points f_1 and f_2, (see Figure 3-12 (b)), is given by the difference between the two displacement fields $w_1(x_f, y_f)$ and $w_2(x_f, y_f)$, as presented in the equation below.

$$\delta = \begin{bmatrix} u \\ v \end{bmatrix} = w_2(x_f, y_f) - w_1(x_f, y_f) \tag{3.7}$$

This method is suitable for calculating crack opening and sliding in beam-column joint if the four points of virtual DEMEC gauge are intersected by a critical crack and the two concrete bodies are relatively rigid. By knowing the displacement field on joint surface, the crack opening and sliding can then be calculated using equation 3.8.

$$\begin{bmatrix} s \\ w \end{bmatrix} = \begin{bmatrix} cos\ \alpha & sin\ \alpha \\ -sin\ \alpha & cos\ \alpha \end{bmatrix} . \delta \quad (3.8)$$

3.7.4 Linear Variable Displacement Transducers (LVDT)

Five linear variable displacement transducers (LVDT) were used to measure displacements. The horizontal deflections at the bottom and top ends of the column were monitored with LVDT1 and LVDT4 which were placed 40 mm and 90 mm away from the bottom and top column ends respectively as shown in Figure 3-13. A pair of LVDTs was also installed on the back face of the column at the top and bottom of the beam (LVDT2 and LVDT3) to measure horizontal deflection. The distance between LVDT2 and LVDT3 was 400 mm. LVDT5 was placed under the beam, 25 mm away from the column face, to measure the vertical deflection of the beam at the joint. Taken together, LVDT2, LVDT3 and LVDT5 provide insight into the deformation and rotation of the joint. To measure beam deflection, a displacement cable transducer (DCT) was placed at 200 mm away from beam end to record the beam deflection. The positions of the LVDTs and the DCT are shown Figure 3-13.

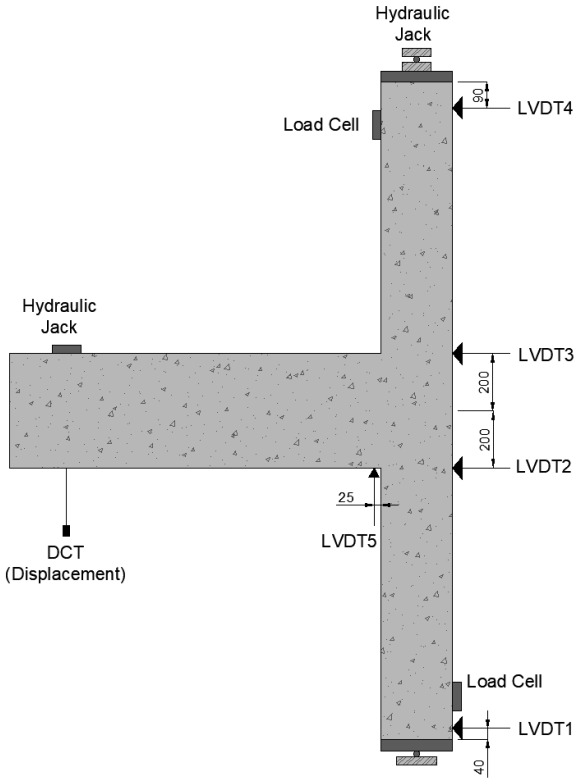

Figure 3-13 Linear variable displacement transducers (LVDT) and DCT locations.

3.7.5 Inclinometers measurements

The rotation of the joint and beam were measured with two inclinometers. One inclinometer was placed on the back of the column at mid-depth of the beam. The other inclinometer was placed at a distance of 350 mm away from beam end as shown in Figure 3-14. The working range of this device was from -60° to +60°. This device was used to record the rotation of joint and beam to provide a better understanding of the failure modes.

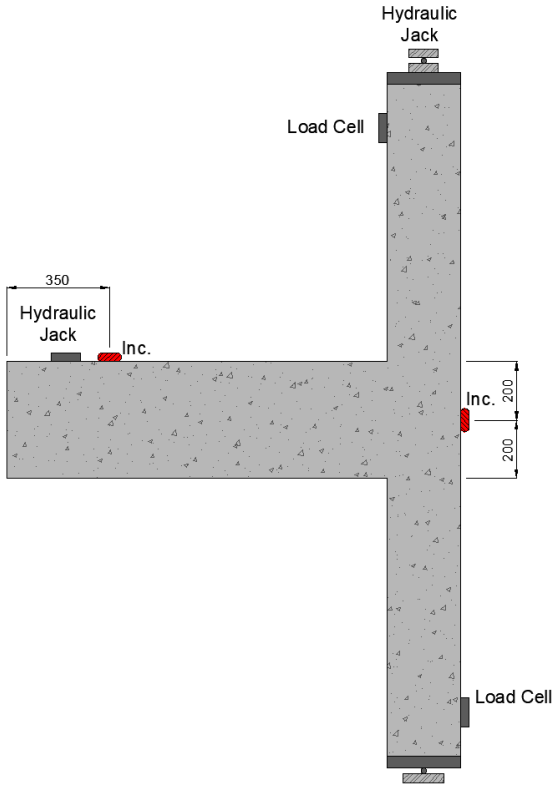

Figure 3-14 Inclinometers locations in BCJ specimens.

3.7.6 Strain gauge position

Strain gauges used in this experimental program had a gauge length of 5mm. The type of strain gauge was YFLA-5-F-1LJC-F by Tokyo Sokki Kenkyuijo Co. Ltd. The strain gauge had an electrical resistance of 119.8±0.5Ω and a gauge factor of 2.1±0.2%. To measure strains along steel reinforcement, every BCJ specimen was installed with twenty strain gauges in different locations of column bars, anchorage beam bars and joint stirrups.

In columns, strain gauges were placed along one internal and one exterior reinforcement bar. Twelve strain gauges were used in BCJ specimens without and with one joint stirrup. Pairs of strain gauges were positioned on the column bars at the joint corners whereas only single strain gauges were placed at other locations as shown in Figure 3-15. Ten strain gauges were

attached to the column bars in BCJ specimens with more than one joint stirrup. In these specimens, gauges were mounted singly on column bars apart from on the inner bar at the top of the joint as shown in Figure 3-16. Strain gauges were uniformly distributed along the column bars at a spacing of 200 mm.

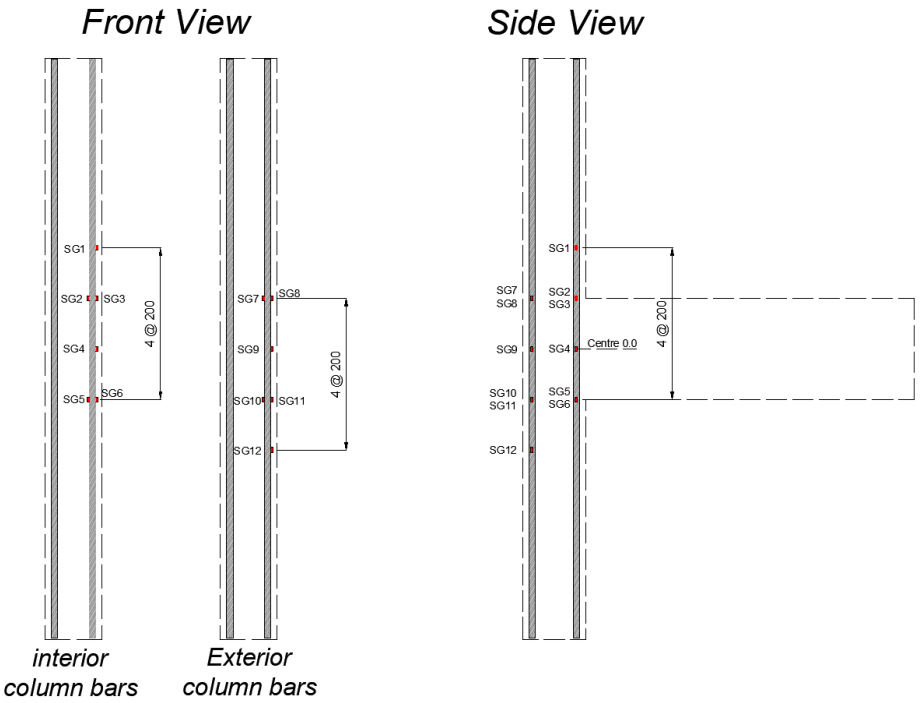

Figure 3-15 Column bars strain gauges locations for specimens with or without 1 joint stirrup.

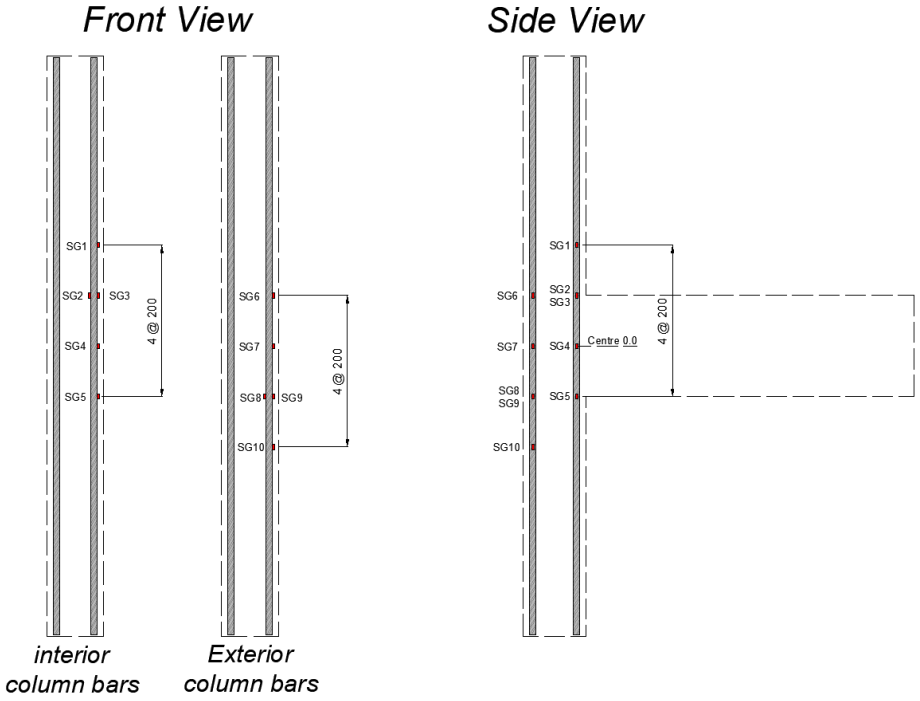

Figure 3-16 Column bars strain gauges locations for specimens with 2 joint stirrups or more.

Strains in beam anchorage bars were measured using seven strain gauges distributed along the bars at different spacings depending on the type of anchorage and size of bend radius. For U-anchorage beam bars, strain gauges were distributed within the joint around the complete U-bend. The locations of the strain gauges varied dependent on whether a standard or large beam anchorage bars was used. The locations of strain gauges in BCJ specimens with standard bend radius are shown in Figure 3-17, including both BCJ specimens with one joint stirrup or more. Positions of strain gauges in BCJ specimens with large bend radius are shown in Figure 3-18. For L-anchorage beam bars, the strain gauges were placed along anchorage bar starting from the column face and ending at the middle of vertical leg of anchorage reinforcement. The positioning of the strain gauges in BCJ specimens with standard bend radius are shown in Figure 3-19 while the positions of gauges in specimens with large radius bends are shown in Figure 3-20.

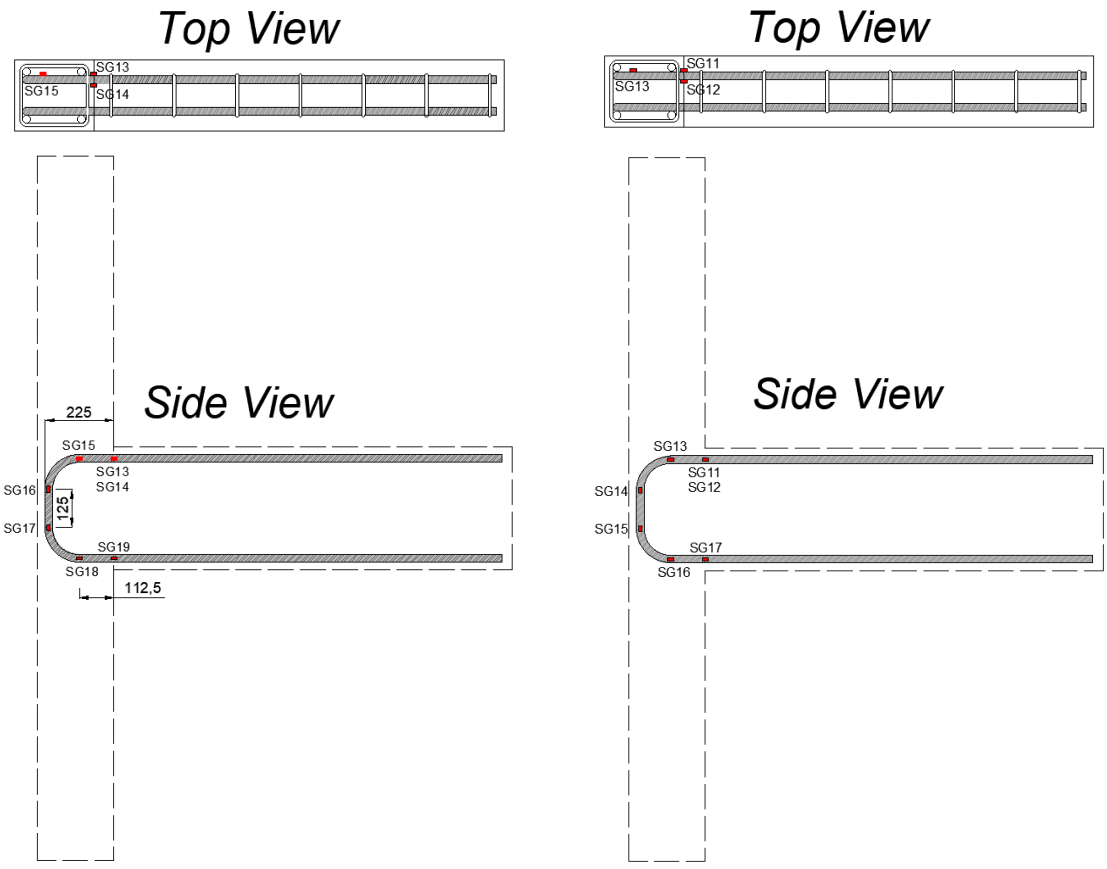

a) BCJ specimens with or without 1 stirrup. b) BCJ specimens with 2 stirrups or more.
Figure 3-17 U-anchorage beam bars strain gauges locations for specimens with standard bend radius.

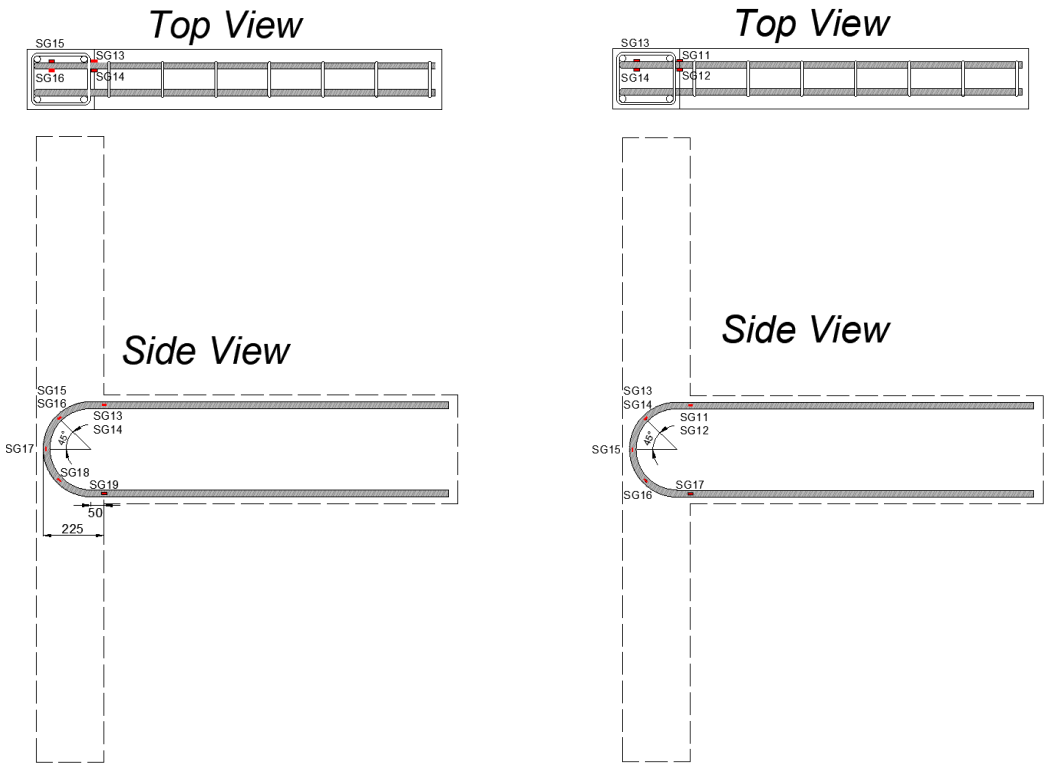

a) BCJ specimens with or without 1 stirrup. b) BCJ specimens with 2 stirrups or more.
Figure 3-18 U-anchorage beam bars strain gauges locations for specimens with large bend radius.

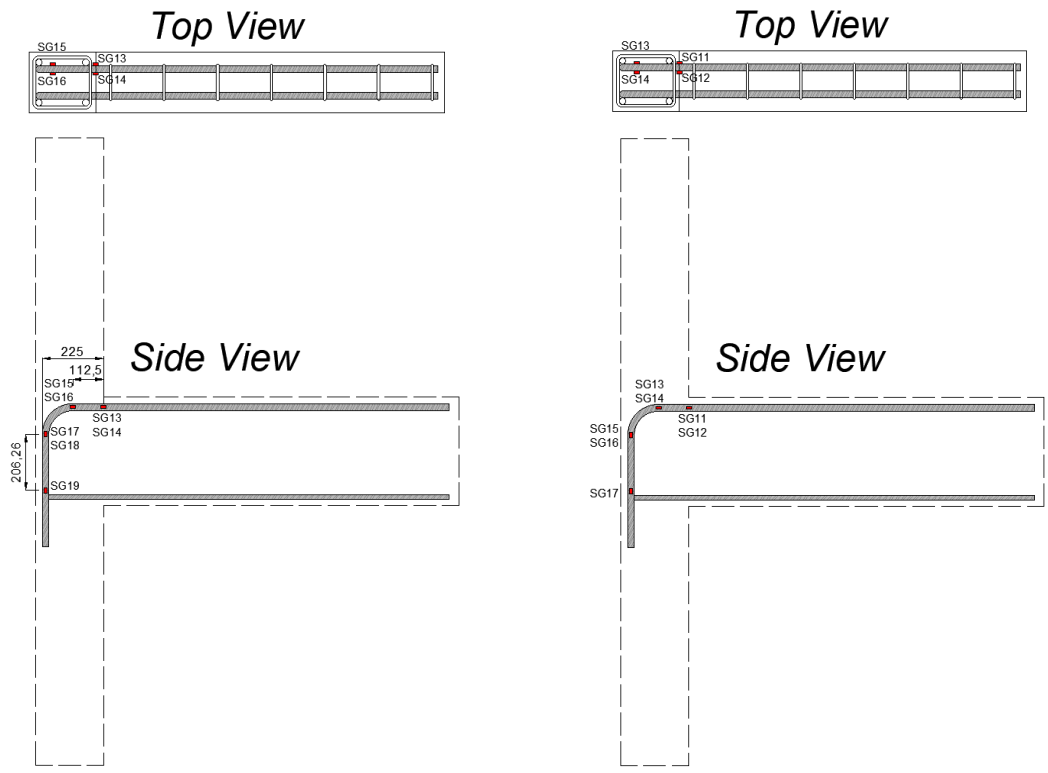

a) BCJ specimens with or without 1 stirrup. b) BCJ specimens with 2 stirrups or more.
Figure 3-19 L-anchorage beam bars strain gauges locations for specimens with standard bend radius.

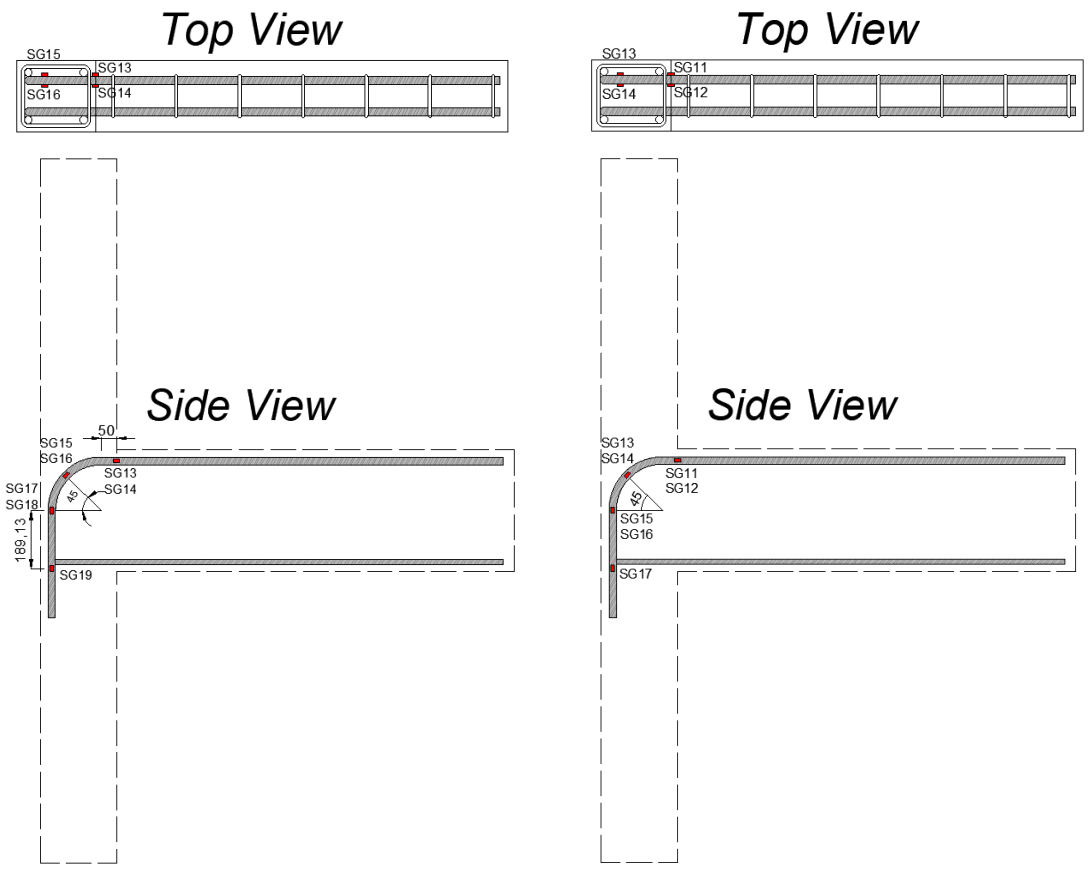

a) BCJ specimens with or without 1 stirrup. b) BCJ specimens with 2 stirrups or more.
Figure 3-20 L-anchorage beam bars strain gauges locations for specimens with large bend radius.

Strains were also measured in the joint stirrups. The gauges were positioned midway along one of the stirrup legs running parallel to the beam bars as shown in Figure 3-21. In specimen BCJ 12 with six joint stirrups positioned in three groups of two, strain gauges were only fixed to one stirrup in each pair as shown in Figure 3-22.

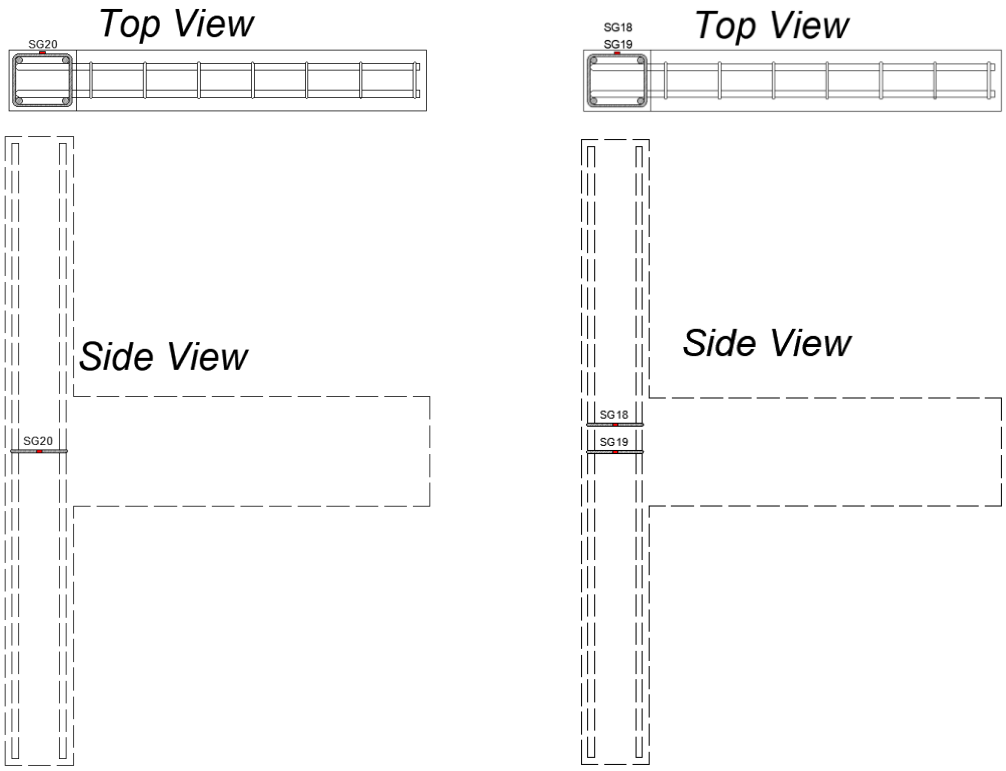

a) BCJ specimens with or without 1 stirrup. b) BCJ specimens with 2 stirrups or more.
Figure 3-21 Joint stirrup strain gauges locations in BCJ specimens.

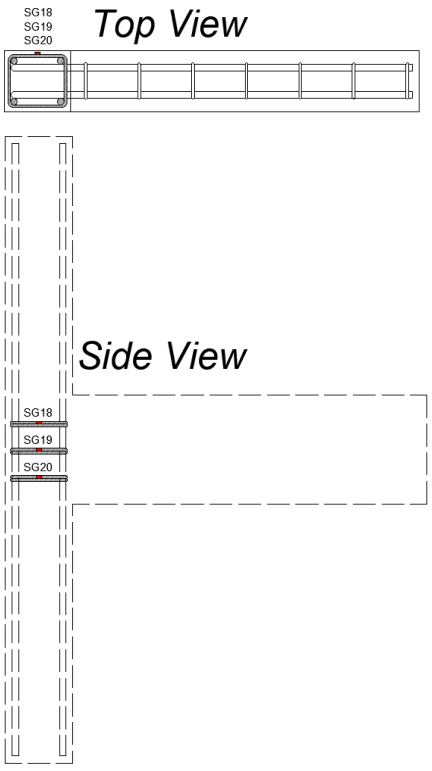

Figure 3-22 locations of strain gauges in BCJ 12 with six joint stirrups.

3.8 Summary

The chapter describes the test specimens and testing procedure carried out by the author in the Heavy Structures Laboratory at Imperial College London. Results of the tests are presented in Chapter 4. Twelve beam-column joint specimens were tested in this experimental program. All the BCJ specimens had the same geometry with a column dimension of (2300 mm long, 250 mm deep and 225 mm wide) and a beam dimension of (1300 mm long, 400 mm deep and 225 mm wide). The BCJ specimens were designed to study a number of significant parameters influencing joint shear strength. Series 1 studied the influence of beam reinforcement anchorage type and bend radius on the mode of failure and joint shear strength. Series 2 investigated the influences of column axial load on joint strength for two different joint stirrup arrangements. Series 3 studied the influence on joint strength of increasing the number of joint stirrups and intermediate column bars.

To assess the influence of these parameters on the shear transfer mechanisms, Digital Image Correlation (DIC) was used to record the joint shear deformation and crack kinematics, by monitoring displacements and cracks pattern occur in the joint surface. To determine the global deformation of the BCJ specimens, LVDTs were provided at different locations on the column, beam and joint. Strains in the steel reinforcement were measured using electrical resistance strain gauges. Additionally, inclinometers were used to record the rotation of the joint and beam end.

Chapter 4 Experimental results

This chapter presents all the experimental results. These comprise the results of the material tests on concrete and reinforcement as well as tests on the beam-column connections. The latter include the global load-deflection response, failure modes and crack patterns, the surface strain of the concrete and reinforcement strain gauge readings.

4.1 Material tests

4.1.1 Concrete properties

Ready-mixed concrete was used to cast the BCJ specimens. The concrete had a specified strength class C30/37 with maximum coarse aggregate size of 10 mm and consistency Class S3. Concrete compressive strength was established from tests on concrete cylinders (100 x 200 mm) and concrete cubes (100 x 100 x 100 mm). The split cylinder test (150 x 300 mm cylinder) was utilized to measure concrete tensile strength. The results of these tests are summarised below.

4.1.2 Concrete strengths for series 1

A total of 42 control specimens were cast made up of 18 cubes (100 mm^3), 12 cylinders (100 x 200 mm) and 12 cylinders (150 x 300 mm). Half of the specimens were cured in water at 20° C with the remainder cured in air alongside the BCJ specimens. The compressive strength development was assessed by testing single cubes cured in water at ages of 14 and 21 days, as shown in Table 4-1.

Table 4-1 Concrete strength development using cubes (100 mm^3) – series 1.

Testing date	Age at testing date	Cured in	Strength (MPa)
21-June	14	Water	32.4
28-June	21	Water	35.4

Typically, three air cured and three water cured cubes were tested on the same day as each BCJ specimen. The results are given in Table 4-2. The development of compressive cube strength is plotted in Figure 4-1 for series 1. The strengths of the air and water cured cubes were similar except at 39 days when the strength of the air cured cubes was greatest. This result appears to be an anomaly.

Table 4-2 Compressive cube strength (100 mm^3) – series 1.

Specimen	Test date	Age [days]	Cured in	Strength (MPa)	Average strength (MPa)
BCJ 1	11-July	34	Air	43.3	38.3
				37.7	
				44.0	
			Water	38.4	38.4
BCJ 2	16-July	39	Air	41.7	41.5
				43.0	
				39.8	
			Water	38.4	36.2
				31.3	
				38.9	
BCJ 3	18-July	41	Air	23.0	37.9
				41.8	
				41.9	
			Water	38.0	38.3
				37.2	
				39.8	

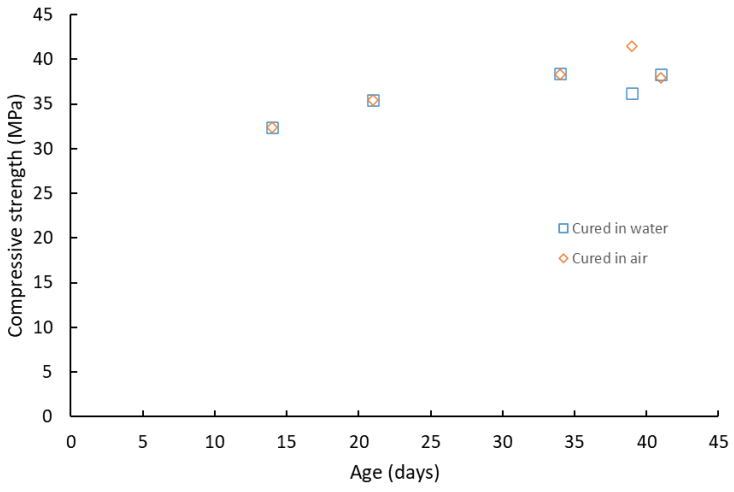

Figure 4-1 Concrete cube compressive strength development– series 1.

Three air cured and three water cured concrete cylinders were tested for compressive strength (100 x 200 mm) and tensile strength (150 x 300 mm) alongside specimens BCJ 1 and BCJ 4. The resulting compressive and tensile strengths are presented in Table 4-3 and Table 4-4 respectively. The in-situ concrete strength of the tested BCJ specimens is assumed to be

that of the air cured specimens. Linear interpolation was used to estimate the concrete strength compressive and tensile strengths of BCJ 2 and BCJ 3 at the time of testing. The resulting concrete strengths for each specimen in series 1 are summarised in Table 4-5.

Table 4-3 Compressive cylinder strength (100 x 200 mm) – series 1.

Specimen	Test date	Age [days]	Cured in	Strength [MPa]	Average strength [MPa]
BCJ 1	11-July	34	Air	33.0	33.7
				32.4	
				35.7	
			Water	30.8	32.4
				32.5	
				33.8	
BCJ 4	23-July	46	Air	34.2	32.9
				33.0	
				31.5	
			Water	35.2	34.6
				33.6	
				34.8	

Table 4-4 Tensile cylinder strength (150 x 300 mm) – series 1.

Specimen	Test date	Age [days]	Cured in	Strength [MPa]	Average strength [MPa]
BCJ 1	11-July	34	Air	4.1	3.9
				3.4	
				4.3	
			Water	4.5	4.2
				4.2	
				3.9	
BCJ 4	23-July	46	Air	4.3	4.3
				3.8	
				4.8	
			Water	4.6	4.1
				4.1	
				3.5	

Table 4-5 Compressive and tensile strength for BCJ specimens - series 1.

Specimen ID	Casting date	Testing date	Age at testing	f'_c (MPa)	f_t (MPa)
BCJ 1	07-June	11-July	34	33.7	3.90
BCJ 2		16-July	39	33.4	4.07
BCJ 3		18-July	41	33.2	4.13
BCJ 4		23-July	46	32.9	4.30

4.1.3 Concrete strengths for series 2

A total of 42 control specimens were cast in this batch comprising 18 cubes (100 mm^3), 12 cylinders (100 x 200 mm) and 12 cylinders (150 x 300 mm). Half of the specimens were cured in water with the remainder cured in air alongside the BCJ specimens. The early age compressive strength development was assessed by testing single cubes cured in water at ages of 14 and 21 days, as shown in Table 4-6.

Table 4-6 Concrete strength development using cubes (100 mm^3) – series 2.

Testing date	Age at testing date	Cured in	Strength (MPa)
30-Aug	14	Water	26.9
06-Sep	21	Water	27.9

The same procedure was used to determine the concrete compressive and tensile concrete strengths as for series 1. The age at testing and measured cube, compressive cylinder and split cylinder strengths are given in Table 4-7, Table 4-8 and Table 4-9. A plot of the development of compressive cube strength with time (in days) is presented in Figure 4-2. The plot shows that the cubes cured in air had slightly higher compressive strengths than those cured in water.

Table 4-7 Compressive cube strength (100 mm^3) – series 2.

Specimen	Test date	Age [days]	Cured in	Strength (MPa)	Average strength (MPa)
BCJ 5	08-Oct	53	Air	33.89	35.1
				34.0	
				37.4	
			Water	31.2	31.2
BCJ 6	10-Oct	55	Air	36.7	36.7
				36.5	
				36.8	
			Water	33.4	33.0
				32.8	
				32.9	
BCJ 8	17-Oct	62	Air	34.8	35.2
				35.0	
				35.9	
			Water	31.3	32.0
				32.6	
				32.2	

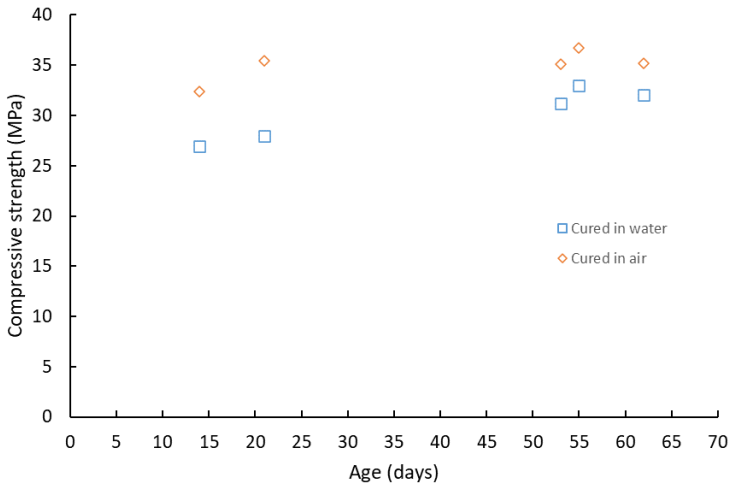

Figure 4-2 Concrete cube compressive strength development – series 2.

Table 4-8 Compressive cylinder strength (100 x 200 mm) – series 2.

Specimen	Test date	Age [days]	Cured in	Strength [MPa]	Average strength [MPa]
BCJ 5	08-Oct	53	Air	26.6	27.0
				27.9	
				26.6	
			Water	29.6	29.1
				29.7	
				28.2	
BCJ 8	17-Oct	62	Air	27.8	26.8
				26.3	
				26.3	
			Water	19.5	25.9
				28.2	
				29.9	

Table 4-9 Tensile cylinder strength (150 x 300 mm) – series 2.

Specimen	Test date	Age [days]	Cured in	Strength [MPa]	Average strength [MPa]
BCJ 5	08-Oct	53	Air	4.0	3.8
				3.5	
				3.9	
			Water	4.1	3.9
				3.9	
				3.7	
BCJ 8	17-Oct	62	Air	4.0	4.1
				3.8	
				4.5	
			Water	4.1	3.8
				3.6	
				3.8	

The in-situ concrete compressive and tensile strengths are presented in Table 4-10. As for series 1, the concrete compressive and tensile strengths for BCJ 6 were found by linearly interpolating between the strengths of BCJ 5 and BCJ 8. Unfortunately, specimen BCJ 7 failed while the column load was being increased to 900 kN due to a sudden rotation of the

specimen within the rig which caused shear failure within the joint. This BCJ specimen was recast with laboratory mixed concrete as described in section 4.1.5.

Table 4-10 Compressive and tensile strength for BCJ specimens - series 2.

Specimen ID	Casting date	Testing date	Age at testing	f'_c (MPa)	f_t (MPa)
BCJ 5	16-Aug	08-Oct	53	27	3.8
BCJ 6		10-Oct	55	26.9	3.9
BCJ 8		17-Oct	62	26.8	4.1

4.1.4 Results of batch series 3

Fifty-four control specimens were cast in this series. Twenty-four cubes (100 mm^3) and eighteen cylinders (100 x 200 mm) were cast for measuring concrete compressive strength. Twelve cylinders (150 x 300 mm) were cast to obtain concrete tensile strength. Half of the control samples were cured in water and the remainder in air alongside the BCJ specimens. The early age concrete strength development was measured by testing single water cured cubes on the 14th and 21st day, as shown in Table 4-11.

Table 4-11 Concrete strength development using cubes (100 mm^3) – series 3.

Testing date	Age at testing date	Cured in	Strength (MPa)
14-Nov	14	Water	54.3
21-Nov	21	Water	56.8

Three air cured cubes were tested on the day of testing of each specimen, except for BCJ 12 where only two air cured cubes were tested. Additionally, three cubes water cured cubes were tested for each specimen apart from BCJ 9 where only one cube was tested. The age of testing and measured cube strengths is presented in Table 4-12. The development of compressive cube strength with time is presented in Figure 4-3. The plot shows the compressive strengths of air cured cubes were greater than water cured samples.

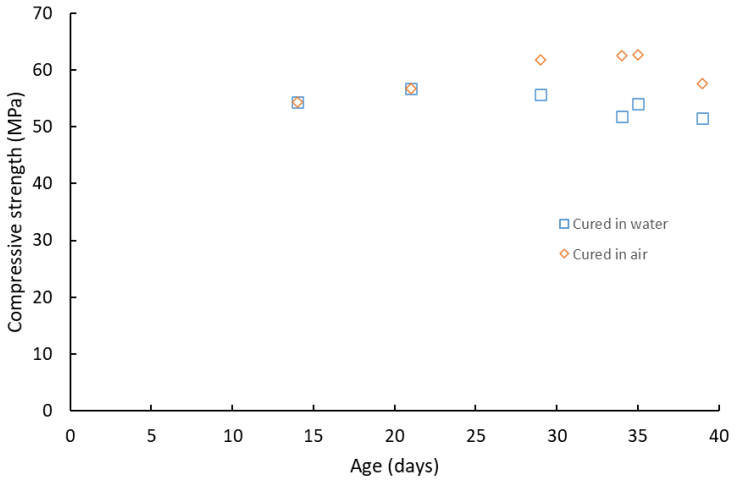

Figure 4-3 Concrete cube compressive strength development – series 3.

Table 4-12 Compressive cube strength (100 mm^3) – series 3.

Specimen	Test date	Age [days]	Cured in	Strength (MPa)	Average strength (MPa)
BCJ 9	29-Nov	29	Air	62.8	61.8
				62.6	
				59.8	
			Water	55.7	55.7
BCJ 10	05-Dec	35	Air	66.2	62.7
				63.3	
				58.5	
			Water	53.6	54.0
				58.6	
				50.0	
BCJ 11	04-Dec	34	Air	63.8	62.6
				61.9	
				62.2	
			Water	43.3	51.8
				54.7	
				57.4	
BCJ 12	09-Dec	39	Air	63.9	57.7
				51.5	
			Water	61.0	51.6
				54.4	
				39.3	

Three air cured and three water cured cylinders were tested for compressive (100 x 200 mm) and split cylinder tensile (150 x 300 mm) strength on the day of testing BCJ 9 and BCJ 12. Additionally, three air cured cylinders were tested for compressive strength alongside BCJ10

and BCJ11. The resulting compressive and tensile strengths are presented in Table 4-13 and Table 4-14.

Table 4-13 Compressive cylinder strength (100 x 200 mm) – series 3.

Specimen	Test date	Age [days]	Cured in	Strength (MPa)	Average strength (MPa)
BCJ 9	29-Nov	29	Air	49.9	51.3
				52.1	
				51.9	
			Water	43.4	45.4
				47.5	
				45.4	
BCJ 10	05-Dec	35	Air	51.6	51.1
				50.6	
				51.2	
BCJ 11	04-Dec	34	Air	47.2	48.9
				51.3	
				48.1	
BCJ 12	09-Dec	39	Air	52.2	49.9
				52.2	
				45.2	
			Water	36.3	41.9
				42.6	
				46.9	

Table 4-14 Tensile cylinder strength (150 x 300 mm) – series 3.

Specimen	Test date	Age [days]	Cured in	Strength [MPa]	Average strength [MPa]
BCJ 9	29-Nov	29	Air	4.5	5.5
				6.5	
				5.7	
			Water	5.2	5.3
				5.5	
				5.2	
BCJ 12	09-Dec	39	Air	5.3	5.4
				6.7	
				4.1	
			Water	5.2	5.1
				5.3	
				4.7	

The in-situ concrete compressive and tensile strengths are presented in Table 4-15. For concrete tensile strength, linear interpolation was used to calculate the concrete tensile strengths of BCJ 10 and BCJ 11.

Table 4-15 Compressive and tensile strength for BCJ specimens - series 3.

Specimen ID	Casting date	Testing date	Age at testing	f'_c (MPa)	f_t (MPa)
BCJ 9	31-Oct	29-Nov	29	51.3	5.50
BCJ 10		05-Dec	35	51.1	5.44
BCJ 11		04-Dec	34	48.9	5.45
BCJ 12		09-Dec	39	49.9	5.40

4.1.5 Results of batch mix for specimen BCJ 7

Concrete with a nominal strength of C40/50 was mixed in *the Heavy Structures Laboratory at Imperial College London* for BCJ7. The concrete mix design is presented in Table 4-16 with weights given in kg/m^3 of concrete. A total of twenty control samples were cast for this batch including cubes and cylinders. Eight cubes (100 mm^3) and six cylinders (100 x 200 mm) were cast to measure the concrete compressive strength. Six cylinders (150 x 300 mm) were cast to obtain the concrete tensile strength. Half the total of control samples was cured in air alongside the BCJ specimens, and the remaining samples were cured in water. The development of early age strength of the concrete on the 14th and 21st day was measured by testing two water cured cubes as shown in Table 4-17.

Table 4-16 Concrete mix design.

Component	Weight [kg/m$_3$]
CEM I	360.0
Water	200.8
Gravel 10mm	1042.5
Sand	826.7
W/C Ratio	0.55
Chemical admixture: Sika® ViscoFlow® 1000	0.3% of cement weight

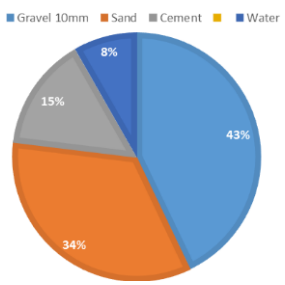

Table 4-17 Concrete strength development using cubes (100 mm^3) – BCJ 7.

Testing date	Age at testing date	Cured in	Strength (MPa)
27-Nov	14	Water	46.5
04-Dec	21	Water	46.5

To measure concrete compressive and tensile strength, six control samples (3 samples cured in water and 3 cured in air) were tested on the testing date of BCJ 7. The age and results of compressive and tensile strengths of concrete are presented in Table 4-18, Table 4-19 and Table 4-20. The in-situ concrete compressive and tensile strengths are summarised in Table 4-21.

Table 4-18 Compressive cube strength (100 mm^3) – BCJ 7.

Specimen	Test date	Age [days]	Cured in	Strength [MPa]	Average strength [MPa]
BCJ 7	11-Dec	28	Air	48.4	48.1
				47.1	
				48.7	
			Water	44.5	45.3
				42.5	
				48.8	

Table 4-19 Compressive cylinder strength (100 x 200 mm) – BCJ 7.

Specimen	Test date	Age [days]	Cured in	Strength [MPa]	Average strength [MPa]
BCJ 7	11-Dec	28	Air	39.9	39.9
				40.1	
				39.9	
			Water	41.9	41.4
				41.5	
				40.8	

Table 4-20 Tensile cylinder strength (150 x 300 mm) – BCJ 7.

Specimen	Test date	Age [days]	Cured in	Strength [MPa]	Average strength [MPa]
BCJ 7	11-Dec	28	Air	5.6	5.3
				5.7	
				4.5	
			Water	5.0	4.6
				4.2	
				4.7	

Table 4-21 Compressive and tensile strength for BCJ specimens – BCJ 7.

Specimen ID	Casting date	Testing date	Age at testing	f'_c (MPa)	f_t (MPa)
BCJ 7	13-Nov	11-Dec	29	39.9	5.3

4.1.6 Summary of concrete properties

To conclude, the concrete properties were measured by testing control samples cast with the beam-column joint specimens. Concrete compressive strength was obtained by testing concrete cylinders (100 x 200 mm) and concrete cubes (100 x 100 x 100 mm). Concrete tensile strength was obtained by testing concrete cylinders (150 x 300 mm). The compressive cylinder and split cylinder tensile strengths were measured for each batch of concrete at the time of testing the first and last BCJ specimens in each series. In addition, cubes were tested alongside all specimens. Half of the control samples were cured in air alongside the BCJ specimens with the other half cured in water. The in-situ concrete compressive and tensile strengths of the BCJ specimens were assumed to equal the strengths of the air cured control samples. Linear interpolation was used to determine the concrete strengths of BCJs in cases where air cured cylinder strengths were not tested. The results of the concrete properties, compressive and tensile strengths, are summarised in Table 4-22.

Table 4-22 Concrete compressive and tensile strength of tested BCJ specimens

	Specimen	Concrete Cylinder Strength	
		f_c' (MPa)	f_t (MPa)
First series	**BCJ 1**	33.7	3.9
	BCJ 2	33.4	4.1
	BCJ 3	33.2	4.1
	BCJ 4	32.9	4.3
Second series	**BCJ 5**	27.0	3.8
	BCJ 6	26.9	3.9
	BCJ 7	39.9	5.3
	BCJ 8	26.8	4.1
Third series	**BCJ 9**	51.3	5.5
	BCJ 10	51.1	5.4
	BCJ 11	48.9	5.5
	BCJ 12	49.9	5.4

4.1.7 Steel reinforcement

The beam-column joint specimens were reinforced with bar diameters of 10 mm, 16 mm and 25 mm. In order to measure the tensile strength of each bar size, 400 mm long offcuts were taken from each batch of reinforcement and tested under displacement control at a rate of 5 mm/min. The strains in the coupons were recorded using a digital video extensometer. The testing arrangement is shown in Figure 4-4. The average yield strength, modulus of elasticity, maximum tensile strength and maximum strain were determined from the measured stress-strain relationships as shown in Figure 4-5 for each bar diameter. The yield strength was calculated using the 0.2% offset rule. The reinforcement properties are summarized in Table 4-23.

Table 4-23 Longitudinal and transverse steel reinforcement properties used in experimental tests.

Bar size (mm)	$f_{yk,0.2}$ **(MPa)**	E_s **(GPa)**	f_{tk} **(MPa)**	ε_1 **(%)**
25	550	181	666	9.78
16	534	189	638	8.71
10	515	190	615	6.74

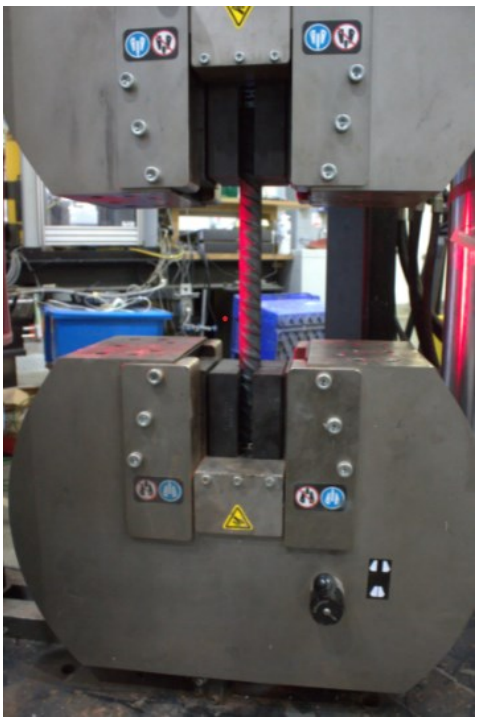

Figure 4-4 Coupon test instrumentation

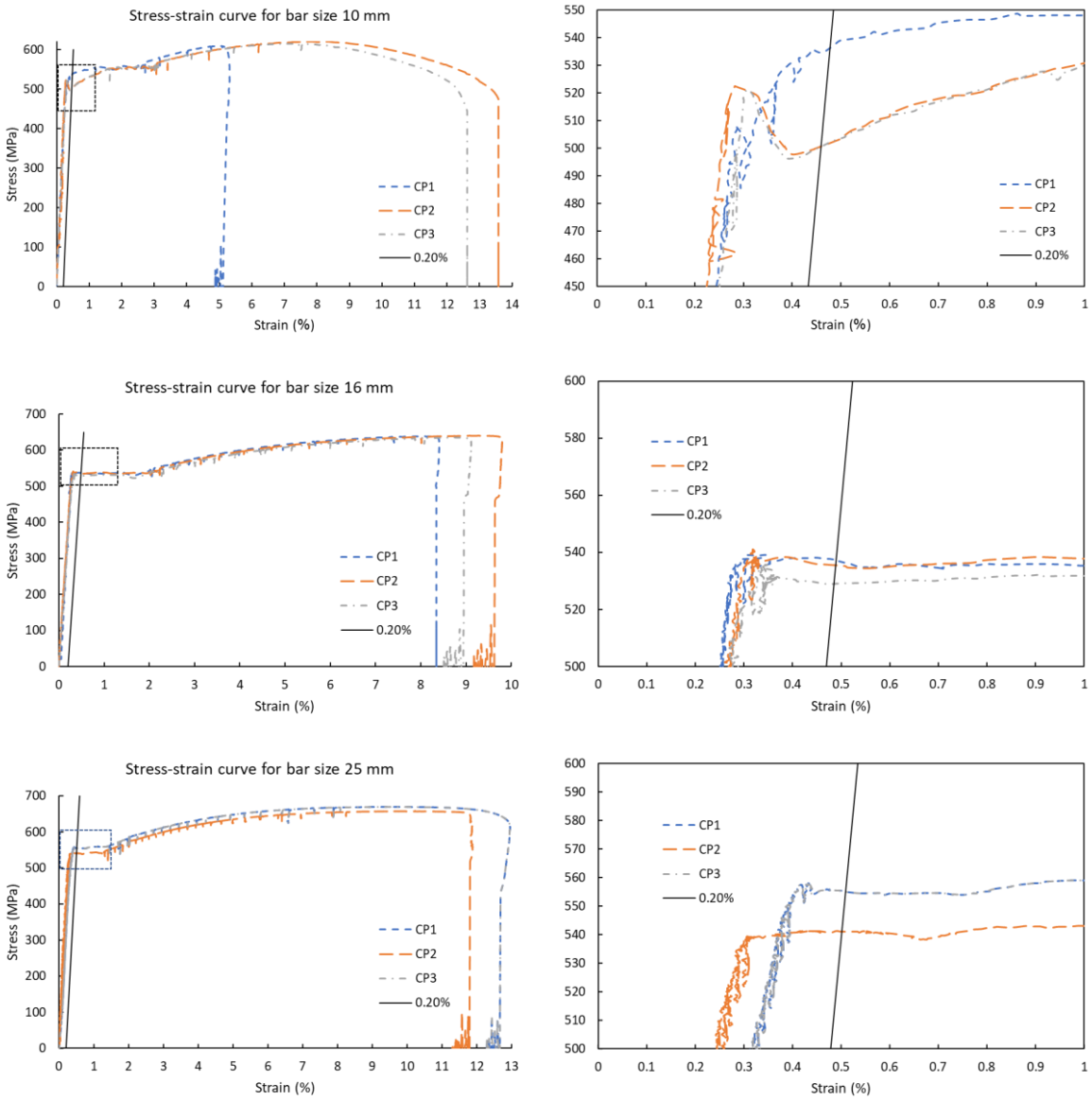

a) Stress-strain curves b) Zoom in on yield plateau areas

Figure 4-5 Stress-strain relationship for steel bars size 10, 16 and 25 mm.

4.2 Results of BCJ tests

The results of each series of tests are presented in the following sections.

4.2.1 Overview of series 1

Specimens BCJ 1, BCJ 2, BCJ 3 and BCJ 4 were designed to investigate the effect on joint shear strength of beam reinforcement anchorage type and bend radius. Specimens BCJ 1 and BCJ 2 had L-anchorage type with bend radius of 87.5 mm for BCJ 1 and 150 mm for BCJ 2. U-anchorage type was used in BCJ 3 and BCJ 4 with bend radius of 87.5 mm for BCJ 3 and 150 mm for BCJ 4. The minimum bend radius was calculated using the EC2 recommendations for minimum mandrel diameter presented in Table 8.1N as shown in Figure 4-6. All the specimens of series 1 had three joint stirrups and were loaded with an upper column axial load of 300 kN. At the beginning of each test, the column axial load was increased gradually until it reached 300 kN and after which the beam load was increased to failure whilst maintaining the upper column load. All the specimens in this series failed in joint shear. The maximum beam loads and corresponding column end reactions are presented in Table 4-24. Due to friction at the bottom bearing, the measured horizontal reaction was less at the bottom of the column than the top.

Table 8.1N: Minimum mandrel diameter to avoid damage to reinforcement

a) for bars and wire

Bar diameter	Minimum mandrel diameter for bends, hooks and loops (see Figure 8.1)
$\phi \leq 16$ mm	4ϕ
$\phi > 16$ mm	7ϕ

b) for welded bent reinforcement and mesh bent after welding

Minimum mandrel diameter	
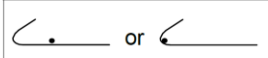	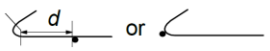
5ϕ	$d \geq 3\phi$: 5ϕ $d < 3\phi$ or welding within the curved zone: 20ϕ

Note: The mandrel size for welding within the curved zone may be reduced to 5ϕ (AC1) where the welding is carried out in accordance with (AC2) EN ISO 17660.(AC2)(AC1)

Figure 4-6 Minimum manrdel diameter for bends, hooks and loops reinforcement (reproduced from EC2 [23])

Table 4-24 Summary of experimental results for first series.

Specimen	f'_c (MPa)	f_t (MPa)	Column load (kN)	Top Reaction (kN)	Bottom Reaction (kN)	Beam load at first crack (kN)	Beam Failure Load (kN)
BCJ 1	33.7	3.9	300	92	74	63	132.8
BCJ 2	33.4	4.1	300	96	74	58	139.7
BCJ 3	33.2	4.1	300	78	62	60	120.8
BCJ 4	32.9	4.3	300	77	58	55	118.8

4.2.2 Failure modes and crack patterns

The failure mode and final crack patterns in specimens BCJ 1, BCJ 2, BCJ 3 and BCJ 4 are shown in Figure 4-7. All the BCJ specimens in this series failed in shear through the formation of an inclined crack which extended from the bottom left to top right corner of the joint. In some specimens, this crack extended along the back column bars above the joint causing spalling of concrete cover in the upper column. A noticeable crack also appeared at the interface between the beam and column in all the BCJ specimens. This crack extended diagonally into the joint prior to typically becoming vertical.

Specimens BCJ 1 and BCJ 2 were nominally identical apart from the L-bar anchorage bend radius. A standard bend radius of 87.5 mm was used in BCJ 1 and a large bend radius of 150 mm was used in BCJ 2. Specimen BCJ 1 initially cracked at the centre of the joint at a load of 63 kN, (see 1st crack in Figure 4-7 (a)). This crack widened and extended as the beam load was increased. Further cracks developed as the load was increased. The joint failed in shear at a beam load of 132.8 kN due to the extension of the 1st crack from the bottom left hand corner to the top right hand corner of the joint. As shown in Figure 4-7 (a), this crack increased in width along its length from a minimum at the bottom of the beam. The crack extended up into the column above the joint and led to spalling of cover in the upper column. Specimen BCJ 2 initially cracked at the centre of joint at a beam load of 58 kN. Several additional cracks formed within the joint as the load was increased. BCJ2 failed at 139.7 kN due to the formation of two major diagonal cracks within the joint. These additional two cracks (which are depicted 2nd and 3rd in Figure 4-7 (b)) extended upwards from around the bottom left corner of the joint, with cracks 1st and 2nd merging at peak load. As shown in Figure 4-7 (b), both cracks 1st and 2nd extended to the back face of the joint causing the cover to spall after the peak load was reached. Crack 3rd, which extended into the upper column, widened along its length from a minimum at the bottom end where it meets the 2nd crack.

Specimens BCJ 3 and BCJ 4 were nominally identical apart from the radius of the U-bar. A standard bend radius of 87.5 mm and a large bend radius of 150 mm were used in BCJ 3 and BCJ 4 respectively. The first crack in specimen BCJ 3 appeared around the centre of joint when the load reached 60 kN. After that, this crack grew and extended as beam load was increased with secondary cracks (including crack 2nd) forming parallel with this crack and spreading over the joint width. Around peak load the 1st crack stopped from extending and 2nd crack

continued to grow and extend. BCJ3 failed in joint shear at 120.8 kN due to the formation of a diagonal 2nd crack which extended from the inside bottom corner of the joint to the outside top corner. As shown in Figure 4-7 (c), this crack caused the concrete cover to spall away at the back of the upper column. Specimen BCJ 4 showed a first crack above the centre of joint when the beam load reached 55 kN. Further cracks (2nd and 3rd) appeared as loading was increased. The joint failed in shear at a load of 118.8 kN due to the formation of a diagonal crack (crack 2nd and 3rd joining each other) which extended from the bottom inner corner of the joint to the top outer corner. As shown in Figure 4-7 (d), the crack widened along its length from a minimum at the bottom end. It ran to the back of the joint and up into the upper column causing concrete to spall away from the back of the column after the peak load was reached.

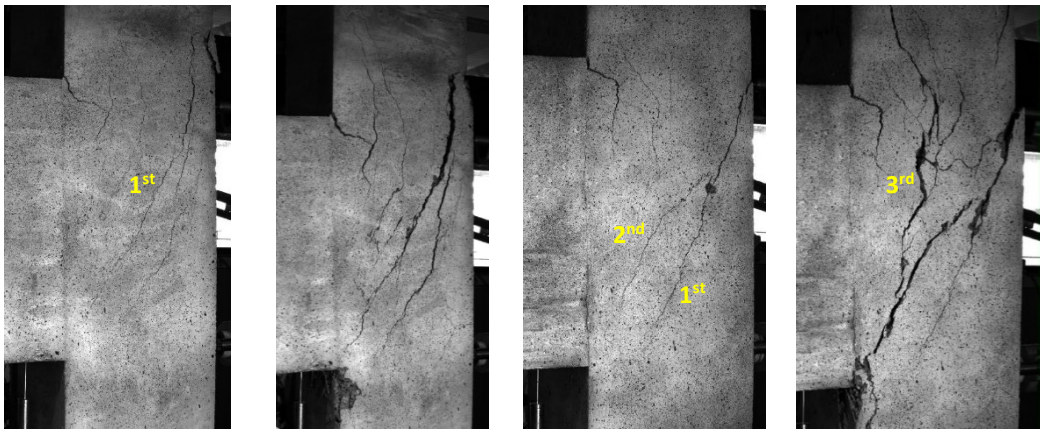

Peak load Post-peak load Peak load Post-peak load

a) Specimen BCJ 1 b) Specimen BCJ 2

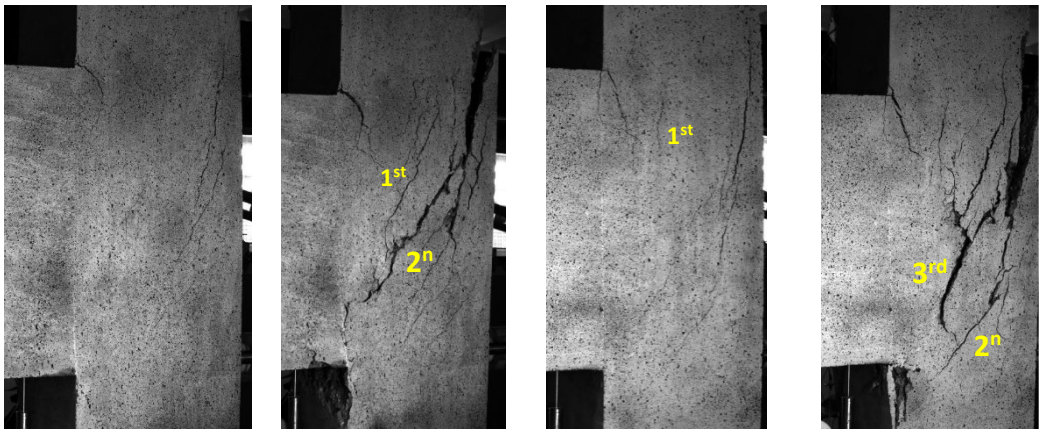

Peak load Post-peak load Peak load Post-peak load

c) Specimen BCJ 3 d) Specimen BCJ 4

Figure 4-7 Failure modes and crack patterns of series 1: (a) specimen BCJ 1; (b) specimen BCJ 2; (c) specimen BCJ 3; and (d) specimen BCJ 4.

4.2.3 Load-deflection response

A displacement cable transducer (DCT) was placed at 200 mm away from beam end to monitor the beam deflection in each specimen as shown in Figure 3-13. The top and bottom reactions were also recorded by installing load cells at column ends as shown in Figure 3-13. The load-deflection responses of first series are shown in Figure 4-8. Due to friction at the bottom end of the column, the horizontal reaction was greater at the top than bottom end of the column as shown in Figure 4-8. The tests were stopped at a beam end deflection of around 70 mm when the joint was severely damage.

The test results show that the beam reinforcement anchorage type plays a significant role in determining the joint shear strength. Specimens BCJ 1 and BCJ 2 with L-anchorage type were able to resist greater shear forces than BCJ 3 and BCJ 4 due to the use of L-anchorage type. Specimens BCJ 3 and BCJ 4 with U-anchorage type had relatively little effect on joint shear strength. The effect of increasing the bend radius was to slightly increase the strength of BCJ2 with L-bars compared with its companion BCJ1. Conversely, increasing the U-bar radius in BCJ4 slightly reduced its strength compared with BCJ3 with standard bend radius U-bar.

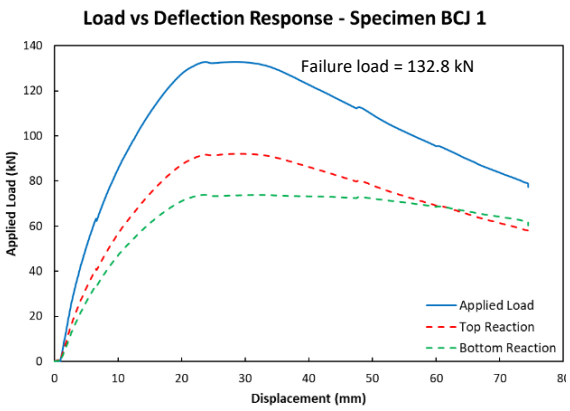

a) Load-deflection response for BCJ 1

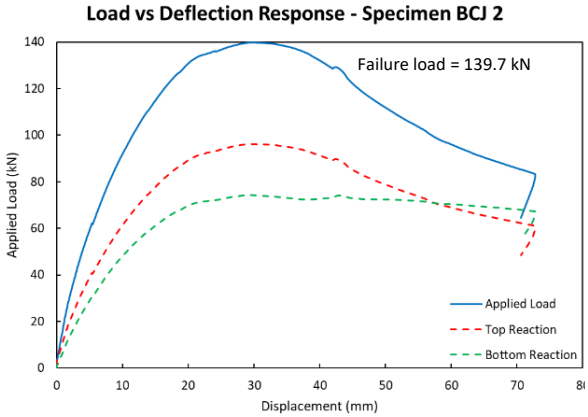

b) Load-deflection response for BCJ 2

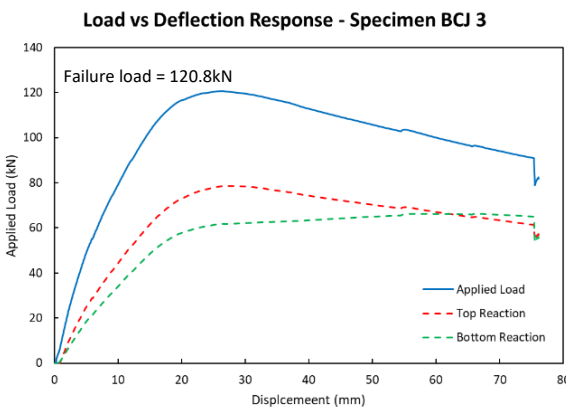

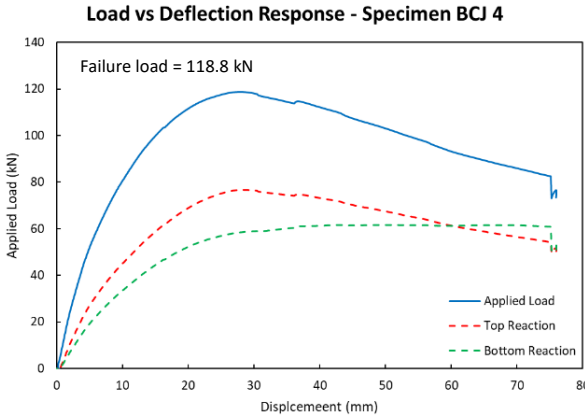

c) Load-deflection response for BCJ 3 d) Load-deflection response for BCJ 4

Figure 4-8 Load-deflection response: (a) Specimen BCJ 1; (b) Specimen BCJ 2; (c) Specimen BCJ 3; (d) Specimen BCJ 4.

The horizontal displacement of the back face of the column was measured with four LVDTs positioned at the top and bottom ends of the column, and at the top and bottom of the joint, as shown in Figure 3-13. The distances of the LVDTs from the bottom end of the column were as follows; LVDT1, 40 mm; LVDT2, 950 mm (bottom of joint); LVDT3, 1350 mm (top of joint), and LVDT4, 2210 mm (top of column). The horizontal displacements recorded by the LVDTs are shown in Figure 4-9 for the first series at 50 kN, 70kN, 90 kN, 110 kN and failure. The difference between the displacements at LVDT1 and LVDT4 results from global rotation of the specimen.

Specimens BCJ 1, BCJ 2 and BCJ 3 had relatively large displacements at LVDT1 (base of column) compared with BCJ 4 where displacements were below 1 mm. The displacement response at LVDT2, at the bottom of the joint, varied with BCJ 1 and BCJ 2 having positive displacements (towards beam) at higher loads and BCJ 3 and BCJ 4 gave negative readings up to failure load. The failure load displacement at LVDT 3 was greatest for specimen BCJ 2.

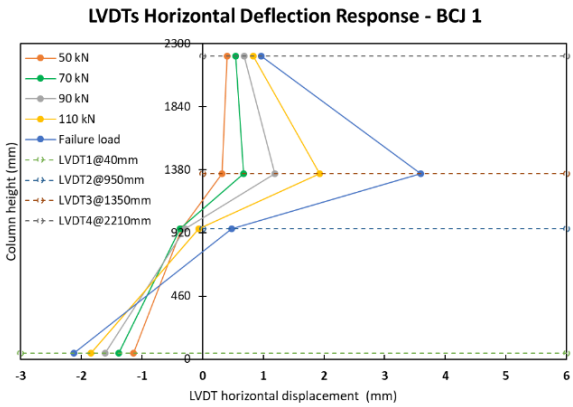

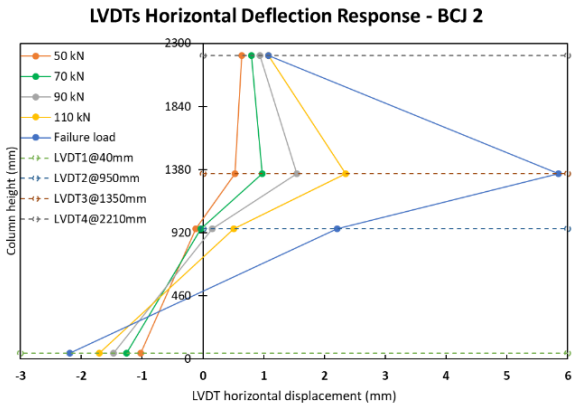

a) LVDTs response for BCJ 1 b) LVDTs response for BCJ 2

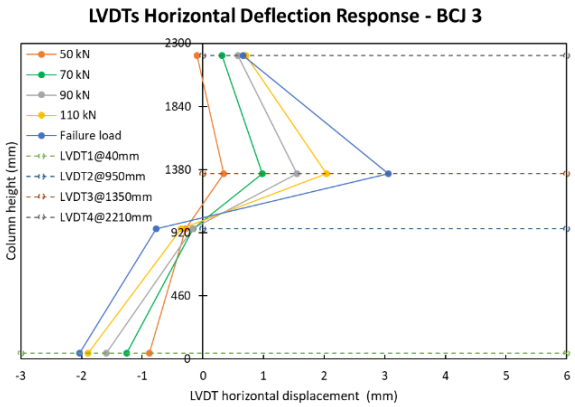

c) LVDTs response for BCJ 3

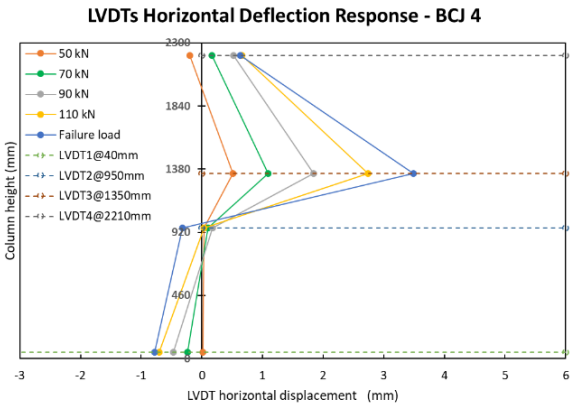

d) LVDTs response for BCJ 4

Figure 4-9 Horizontal deflection recorded from LVDTs for first series: (a) Specimen BCJ 1; (b) Specimen BCJ 2; (c) Specimen BCJ 3; (d) Specimen BCJ 4.

As shown in Figure 3-14, inclinometers were used to measure the rotation of the joint and beam in each specimen. One inclinometer was installed at mid height of the beam at the back of joint while the other one was positioned at a distance of 350 mm from the beam end. The results of inclinometers readings for series 1 are shown in Figure 4-10.

The presence of cracks in the back of joint disrupted the inclinometer from reading the exact global joint rotation, especially near failure. Thus, the horizontal deflection readings from LVDT2 and LVDT3 were utilized to measure the joint rotation. As shown in Figure 4-10, the inclinometer and LVDT rotations agreed well up to the peak load.

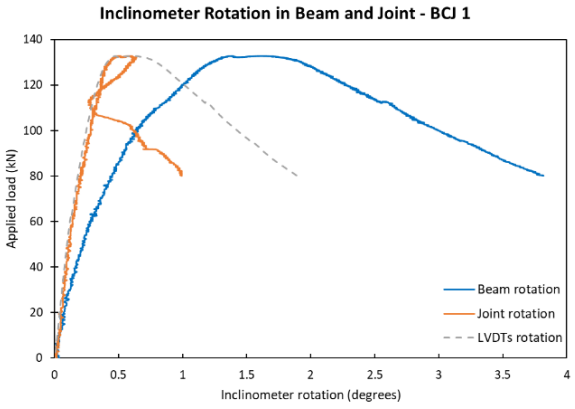

a) Inclinometer response for BCJ 1

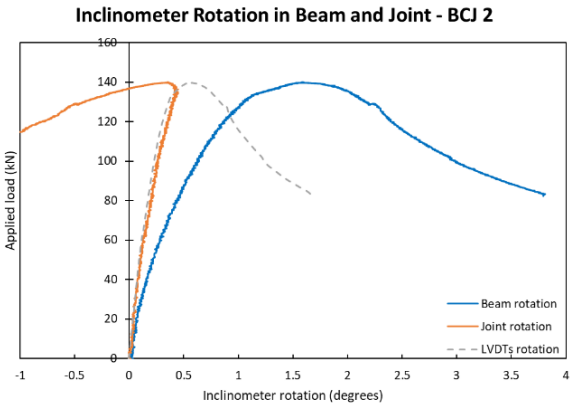

b) Inclinometer response for BCJ 2

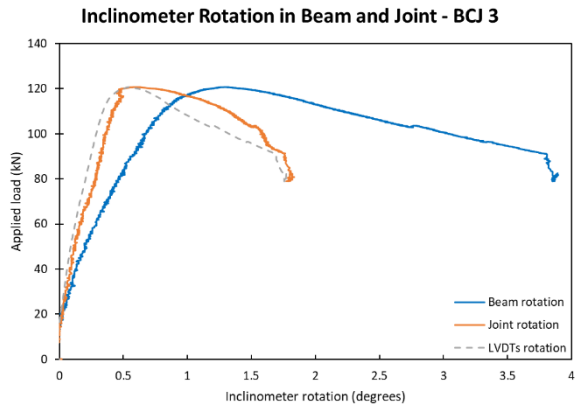

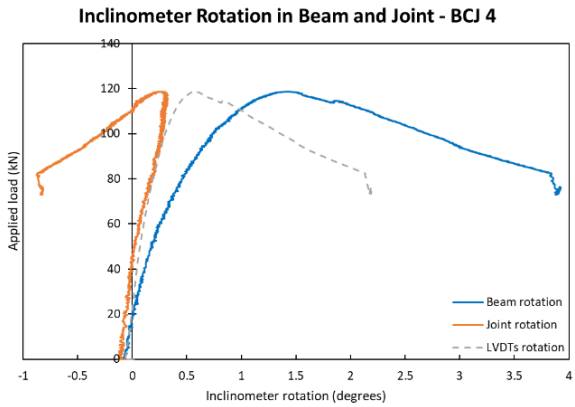

c) Inclinometer response for BCJ 3 d) Inclinometer response for BCJ 4

Figure 4-10 Inclinometer's readings for first series: (a) Specimens BCJ 1; (b) Specimens BCJ 2; (c) Specimens BCJ 3; (d) Specimens BCJ 4.

4.2.4 Concrete surface strains and crack kinematics

Digital image correlation (DIC) was used to measure displacements within the joint surface. Pairs of orthogonal virtual DEMEC gagues were distributed along the critical crack at intervals of 25 mm as shown in Figure 4-11 in order to obtain the crack opening and sliding displacements. The gauge length was varied from 25 mm to 150 mm, depending on the proximity of neighbouring cracks. The gauges were oriented horizontally and vertically for crack angles less than 75-degrees to the horizontal and at 45-degrees otherwise because the vertical gauge end-points would be located at or close to the critical crack dirction due to the steep angle. Limits were also taken into consideration when gagues end-points lied within the joint boundaries (especially near the back side of joint) or crossed other cracks closed to the critical crack. These limits should be avoided in the analysis to ensure the validity of the results and a modification of gauge length or location should be carried out by shifting the gauge to the left or right of critical crack and reducing the gauge length if it crosses the back side of joint or other cracks.

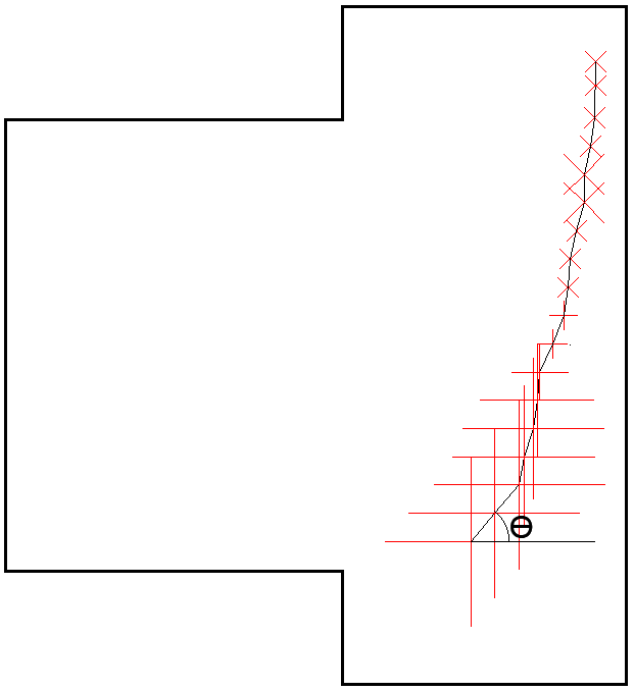

Figure 4-11 Typical virtual gauges along the critical crack (specimen BCJ 4).

Crack opening and sliding were determined at $0.1P_u$ intervals of loading (where P_u represents the failure load of each specimen). Table 4-25 shows the maximum crack opening and sliding displacements along the critical crack at the failure load. It also presents the position of maximum crack opening and sliding with the crack orientation angle. The angle of the critical crack rotation was measured as counter-clockwise from the horizontal axis as shown in Figure 4-11.

Table 4-25 Maximum crack opening and sliding of BCJ specimens in series 1 at maximum load.

Specimen	Max. opening (mm)	Height (mm)	Angle (Degrees)	Max. sliding (mm)	Height (mm)	Angle (Degrees)
BCJ 1	1.54	350	79.1	0.68	300	43.9
BCJ 2	2.87	350	73.8	1.70	300	58.1
BCJ 3	2.10	300	84.2	1.41	250	80.8
BCJ 4	3.12	400	83.4	2.31	425	85.8

**The beam bar detailing and bend radius include: BCJ 1 (L-anchorage type with standard bend radius), BCJ 2 (L-anchorage type with large bend radius), BCJ 3 (U-anchorage type with standard bend radius) and BCJ 4 (U-anchorage type with large bend radius); all specimens had three joint stirrups and 300 kN column load.*

The crack opening and sliding displacements over the joint height are shown in Figure 4-12. These results are at failure load of each specimen. Specimens with large bend radius in

anchorage bars (BCJ2 and BCJ4) exhibited larger crack opening and sliding displacements than specimens with standard radius bends (BCJ1 and BCJ3). Additionally, L-anchorage type in specimens BCJ 1 and BCJ 2 had smaller crack opening and sliding displacements than their companion specimens BCJ3 and BCJ4 with U-anchorage type.

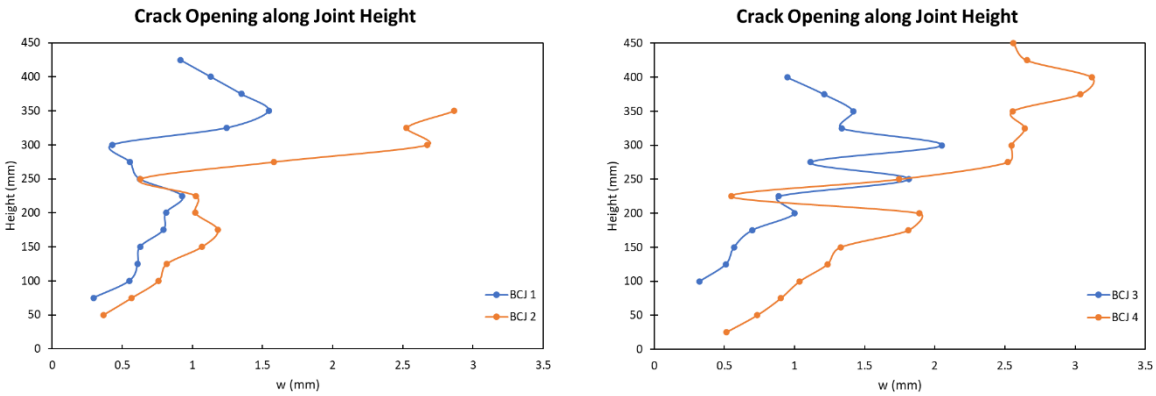

a) Cracks opening results for specimens BCJ 1, BCJ 2, BCJ 3 and BCJ 4

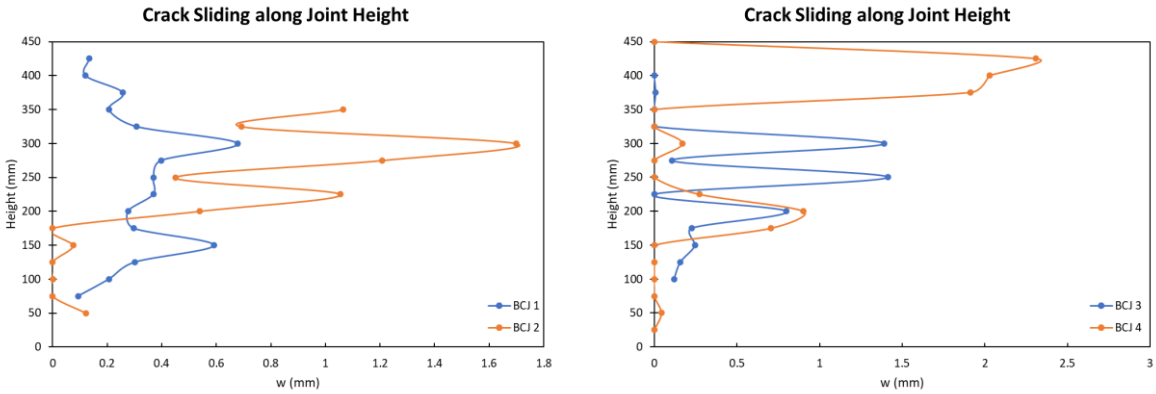

b) Cracks sliding results for specimens BCJ 1, BCJ 2, BCJ 3 and BCJ 4

Figure 4-12 Results of crack opening and sliding along the joint height of first series: (a) Crack opening; (b) crack sliding.

The results of the crack kinematics calculations for the BCJ specimens of series 1 are presented in Figure 4-13 to Figure 4-16. The figures show the variation with load of the crack opening and sliding displacements at various positions over the joint height. Sliding only developed in specimens BCJ 3 and BCJ 4 with U-anchorage type at 90% of the failure load, whereas the crack sliding displacements in the specimens with L-anchorage type gradually increased from 40% of the failure load. It is noticeable that the values of (s/w) are large in specimens with L-anchorage type in comparison with specimens with U-anchorage type.

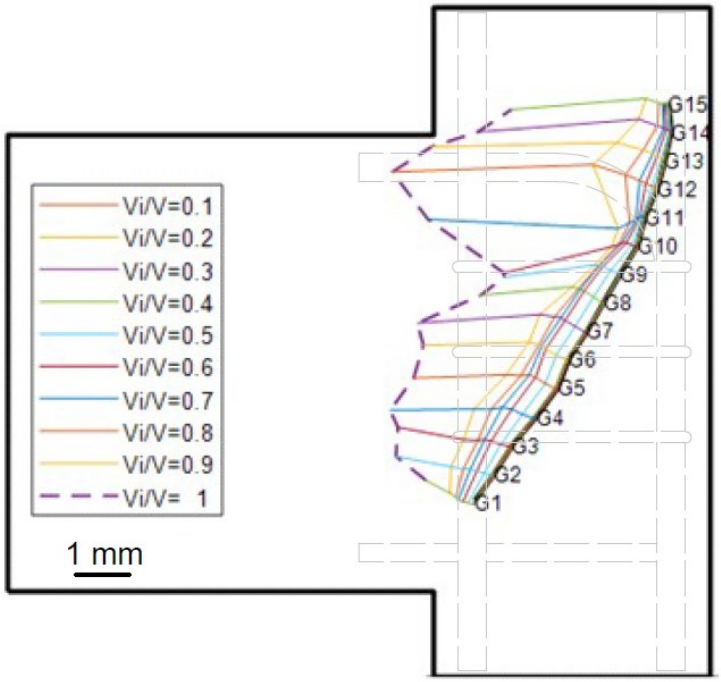

a) Crack kinematics

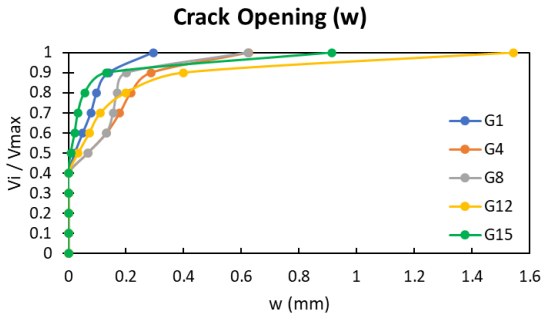

b) Crack opening

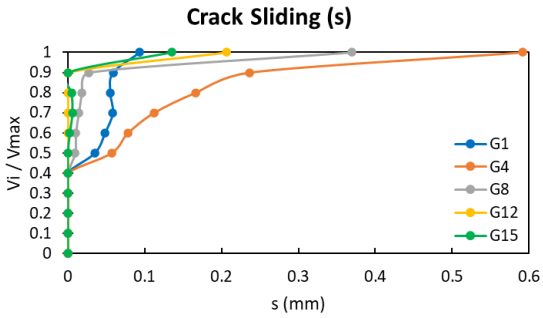

c) Crack sliding

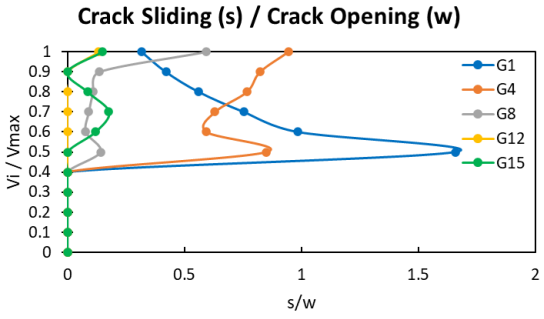

d) Crack sliding / crack opening

Figure 4-13 Crack kinematics for specimen BCJ 1.

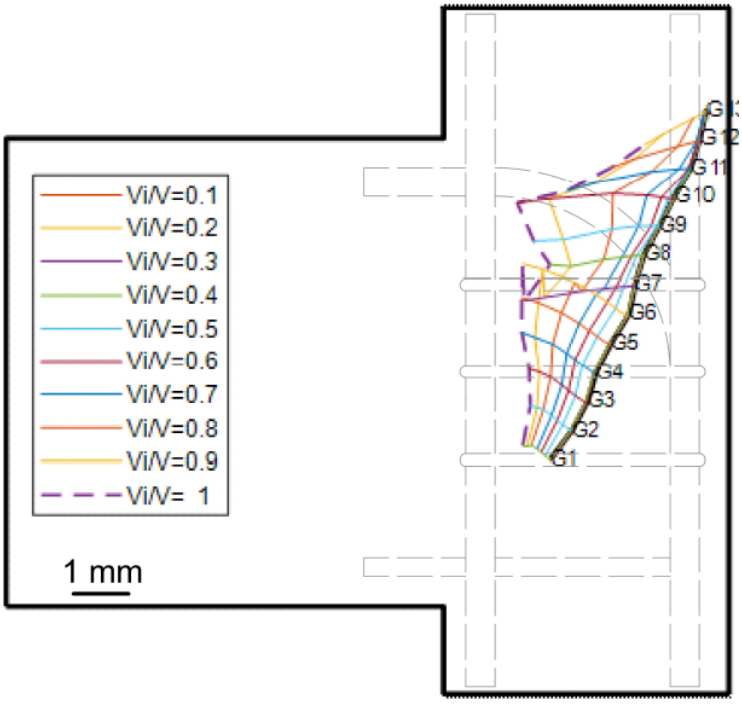

a) Crack kinematics

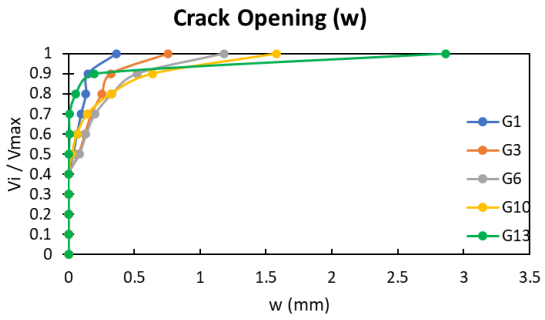

b) Crack opening

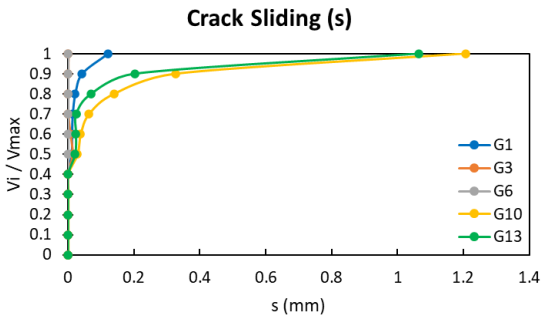

c) Crack sliding

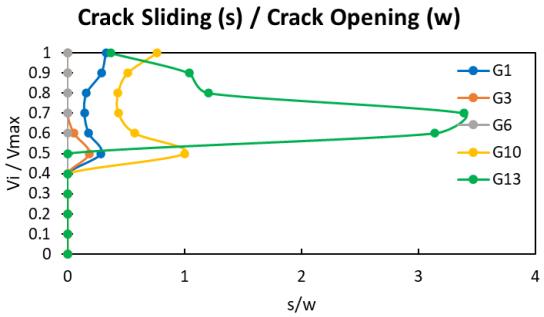

d) Crack sliding / crack opening

Figure 4-14 Crack kinematics for specimen BCJ 2.

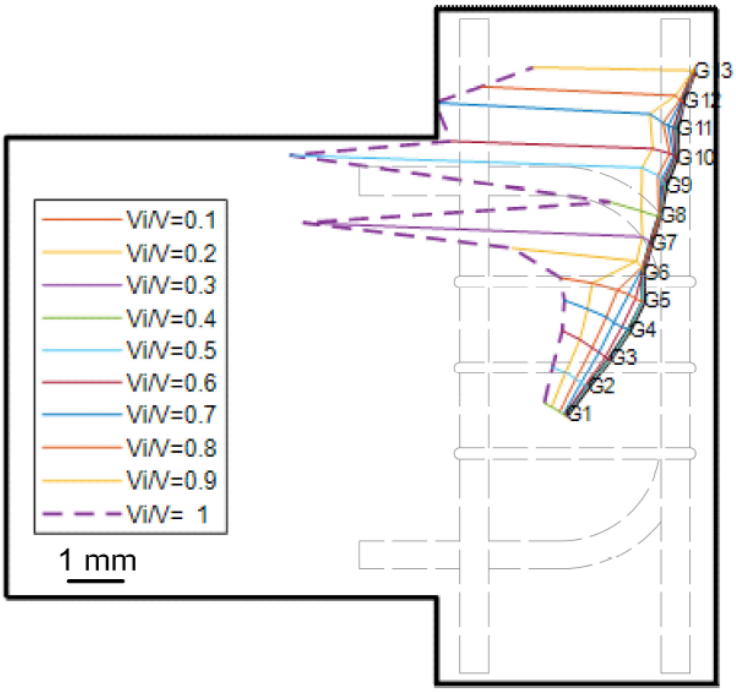

a) Crack kinematics

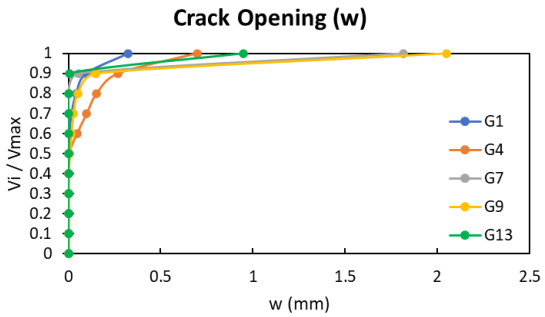

b) Crack opening

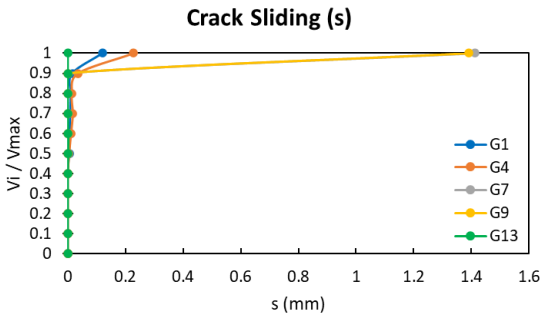

c) Crack sliding

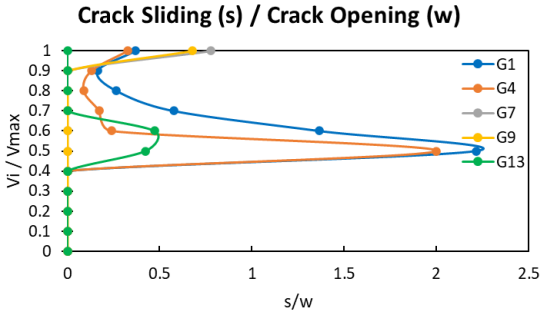

d) Crack sliding / crack opening

Figure 4-15 Crack kinematics for specimen BCJ 3.

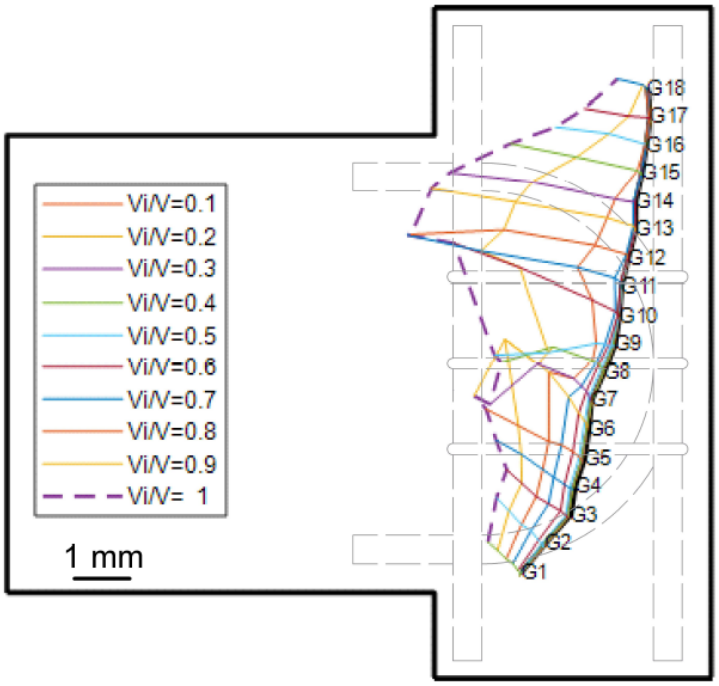

a) Crack kinematics

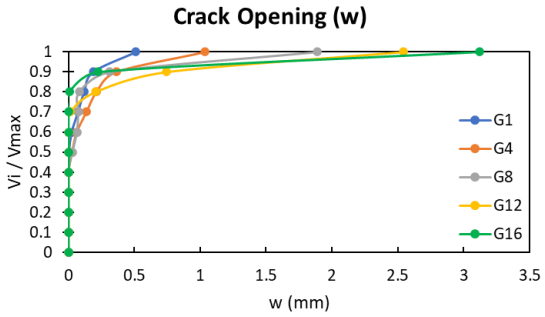

b) Crack opening

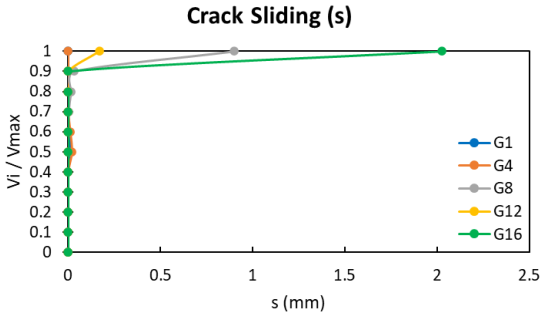

c) Crack sliding

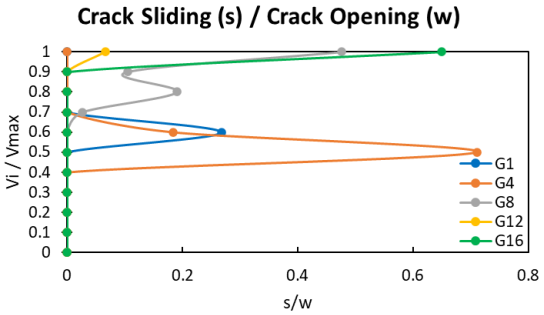

d) Crack sliding / crack opening

Figure 4-16 Crack kinematics for specimen BCJ 4.

4.2.5 Reinforcement strains

Strain gauges were installed on the longitudinal and shear reinforcement of all the specimens in this series. The strain gauges were located near to joint boundaries and inside the joint (including column bars, beam anchorage bars and joint stirrups). The locations of strain gauges are shown in Figure 3-15 to Figure 3-22. Readings at some gauges are not reported due to the gauge being damaged during the casting process.

The strains in the inner column bars (SG 1 to SG 5) are shown in Figure 4-17. A pair of strain gauges (SG 2 and SG 3) was provided at the top of joint as this strain is particularly important for the determination of the width of the compressive stress block in the upper column. Gauges SG 1, SG 4 and SG 5 were mounted singly. The strain values in the back column bar were measured from the strain gauges (SG 6 to SG 10). A pair of strain gauges (SG 8 and SG 9) and single gauges (SG 6, SG 7 and SG 10) were placed on the back column bar. The results of strain gauges readings are shown in Figure 4-19. The SG 7 in specimen BCJ 2 was broken before testing the specimen. Additionally, strain distributions along column bars were plotted for front and back bars as show in Figure 4-18 and Figure 4-20. The strain distributions represent the first crack load (blue dotted line) and failure load (orange dotted line).

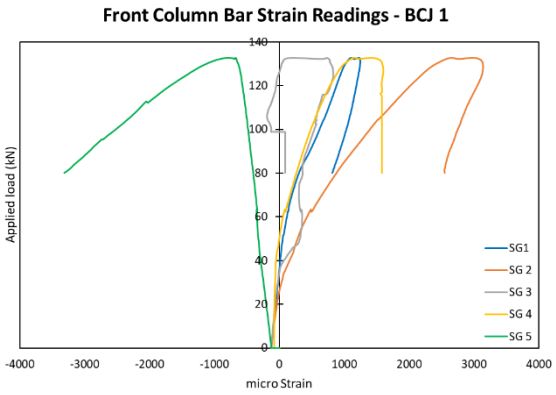

a) Strain gauge response for BCJ 1

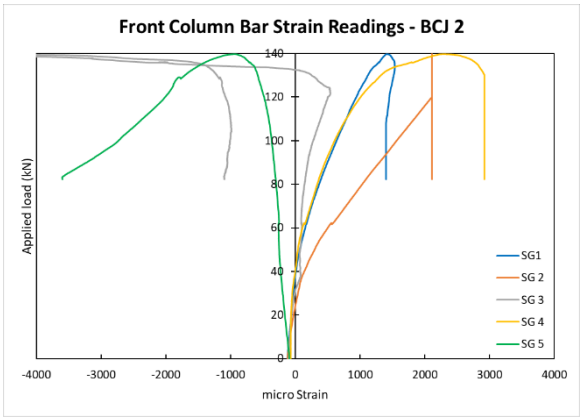

b) Strain gauge response for BCJ 2

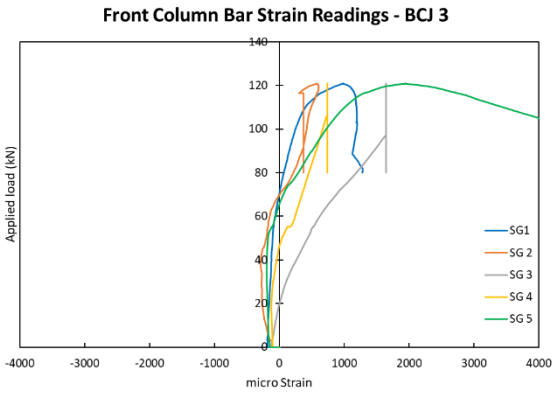

c) Strain gauge response for BCJ 3

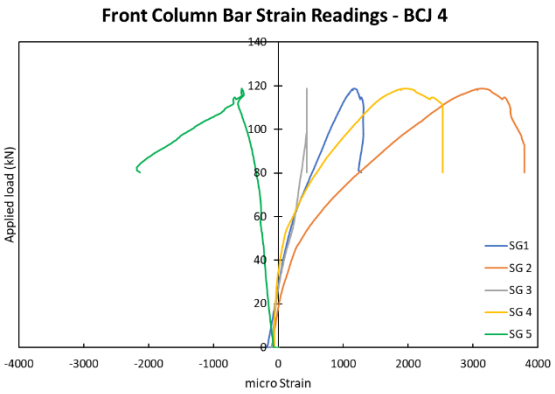

d) Strain gauge response for BCJ 4

Figure 4-17 Front column bar strain measurements: (a) Specimen BCJ 1; (b) Specimen BCJ 2; (c) Specimen BCJ 3; (d) Specimen BCJ 4.

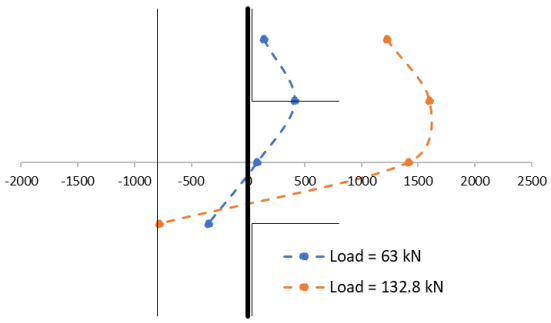

a) Strain distribution for BCJ 1

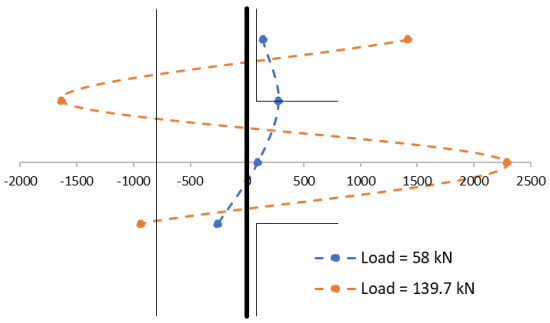

b) Strain distribution for BCJ 2

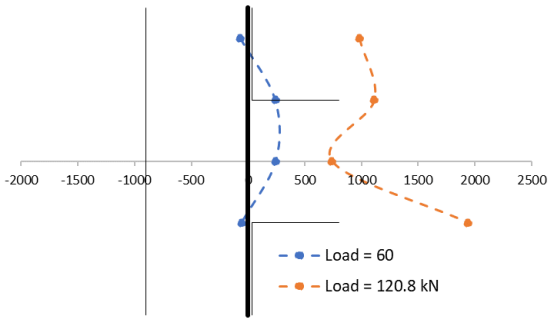

c) Strain distribution for BCJ 3

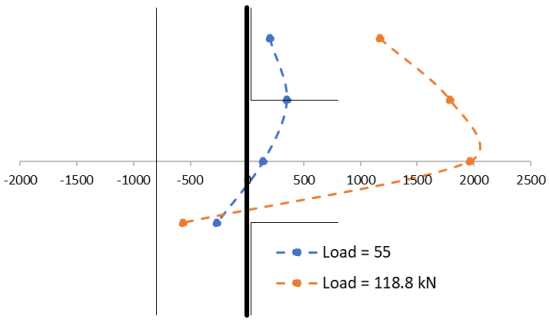

d) Strain distribution for BCJ 4

Figure 4-18 Front column bar strain distribution: (a) Specimen BCJ 1; (b) Specimen BCJ 2; (c) Specimen BCJ 3; (d) Specimen BCJ 4.

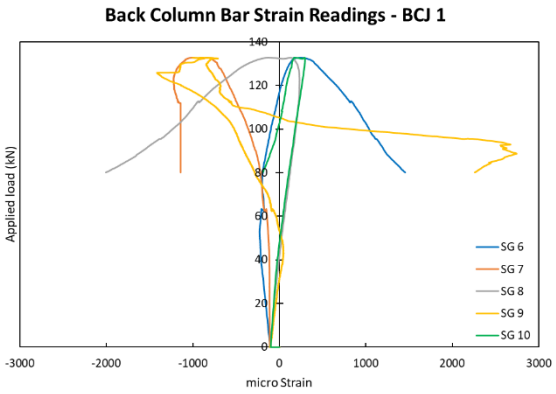

a) Strain gauge response for BCJ 1

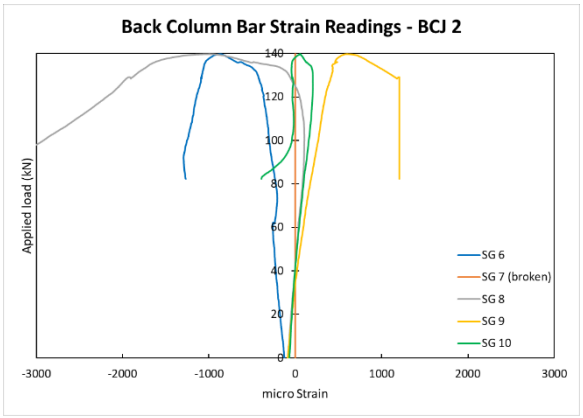

b) Strain gauge response for BCJ 2

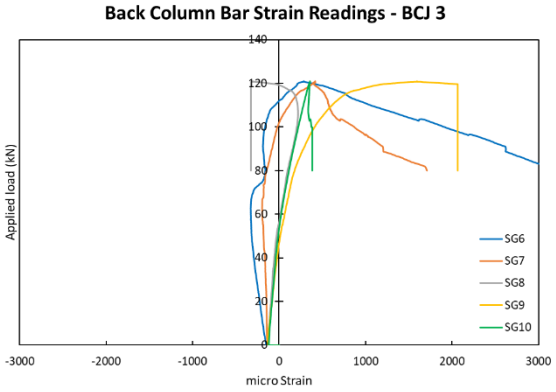

c) Strain gauge response for BCJ 3

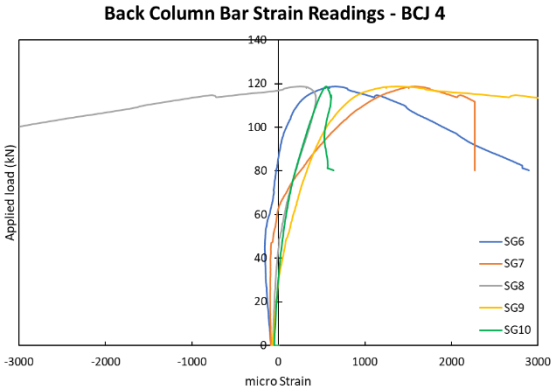

d) Strain gauge response for BCJ 4

Figure 4-19 Back column bar strain measurements: (a) Specimen BCJ 1; (b) Specimen BCJ 2; (c) Specimen BCJ 3; (d) Specimen BCJ 4.

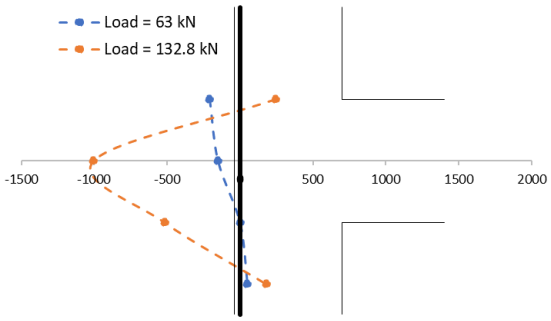

a) Strain distribution for BCJ 1

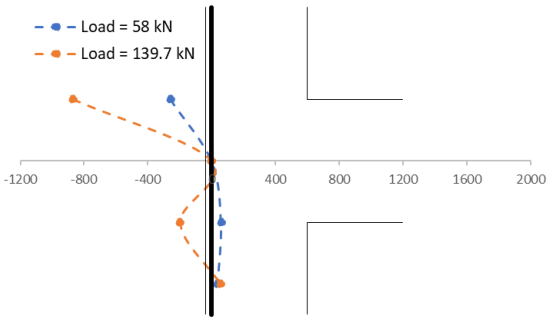

b) Strain distribution for BCJ 2

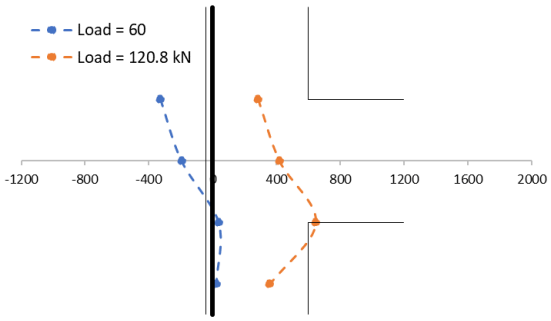

c) Strain distribution for BCJ 3

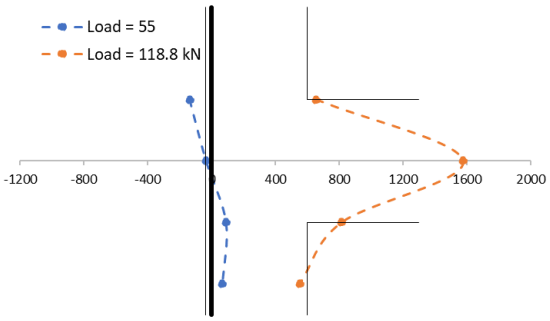

d) Strain distribution for BCJ 4

Figure 4-20 Back column bar strain distribution: (a) Specimen BCJ 1; (b) Specimen BCJ 2; (c) Specimen BCJ 3; (d) Specimen BCJ 4.

The strain gauge measurements in beam anchorage reinforcement are shown in Figure 4-21. The number and location of strain gauges used in this series are shown in Figure 3-17 to Figure 3-20. Before testing, strain gauge SG 17 was broken in specimen BCJ 2 and gauges SG 13 and SG 16 were broken in specimen BCJ 3. The results of strain gauge readings in joint stirrups are shown in Figure 4-23. Specimen BCJ 1 had faulty strain readings in SG 18 when loading exceeded 80 kN. The strain distributions along the beam anchorage bar are shown in Figure 4-22. The strain distributions were plotted outside the beam bar for tensile strains and inside the beam bar for compressive strains. The strain distributions were taken at first crack load and failure load of each specimen.

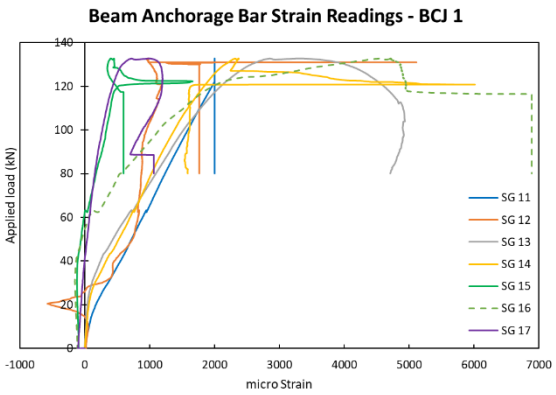

a) Strain gauge response for BCJ 1

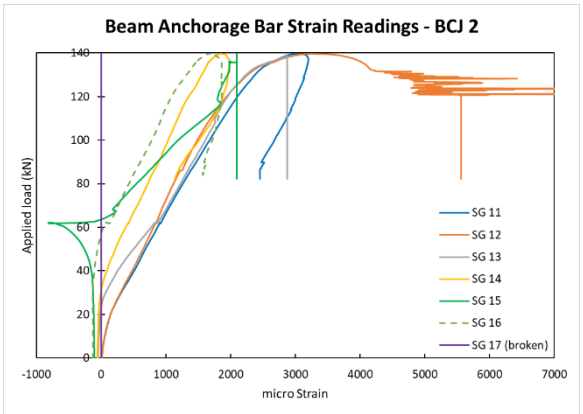

b) Strain gauge response for BCJ 2

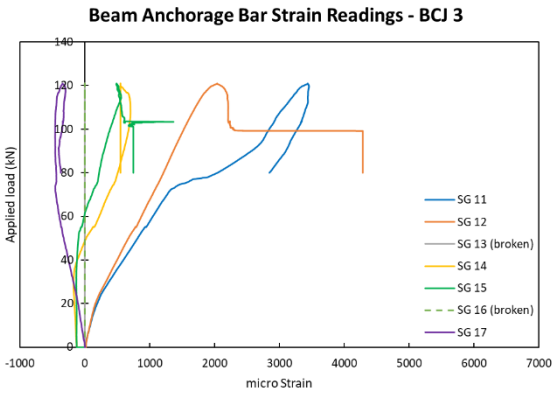

c) Strain gauge response for BCJ 3

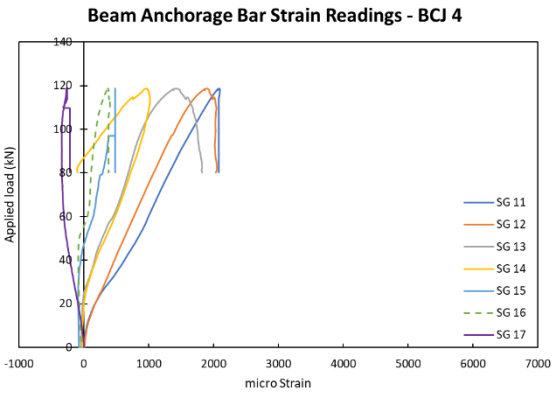

d) Strain gauge response for BCJ 4

Figure 4-21 Beam anchorage bar strain measurements: (a) Specimen BCJ 1; (b) Specimen BCJ 2; (c) Specimen BCJ 3; (d) Specimen BCJ 4.

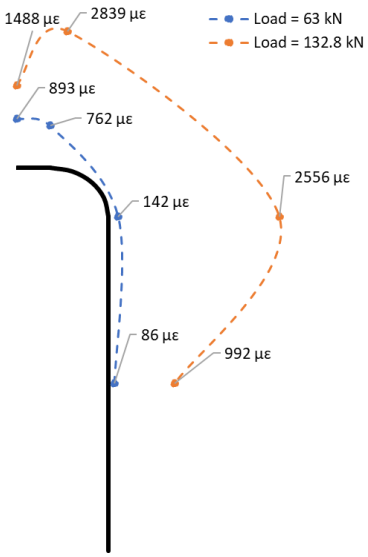

a) Strain distribution for BCJ 1

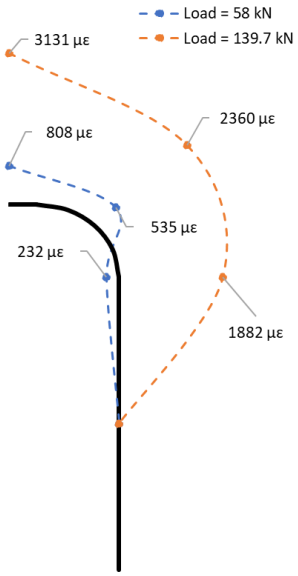

b) Strain distribution for BCJ 2

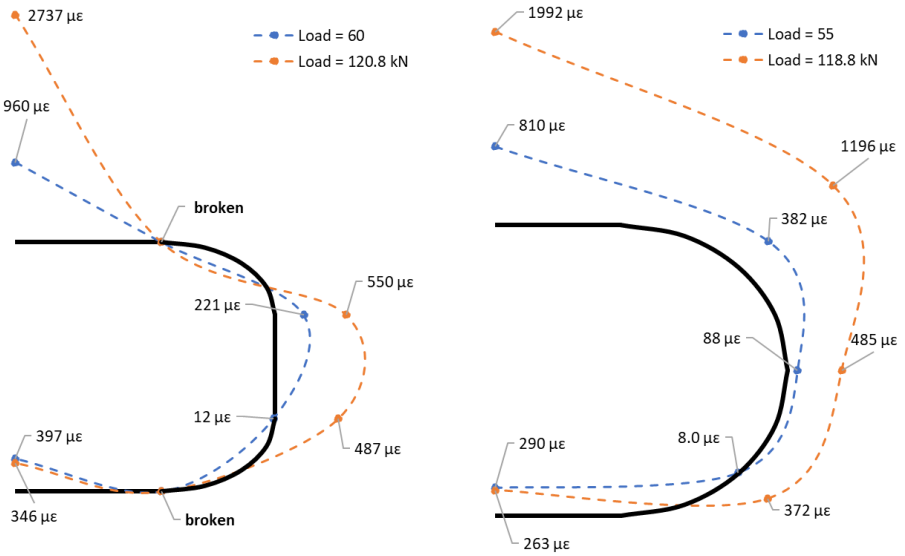

c) Strain distribution for BCJ 3 d) Strain distribution for BCJ 4

Figure 4-22 Beam anchorage bar strain distribution: (a) Specimen BCJ 1; (b) Specimen BCJ 2; (c) Specimen BCJ 3; (d) Specimen BCJ 4.

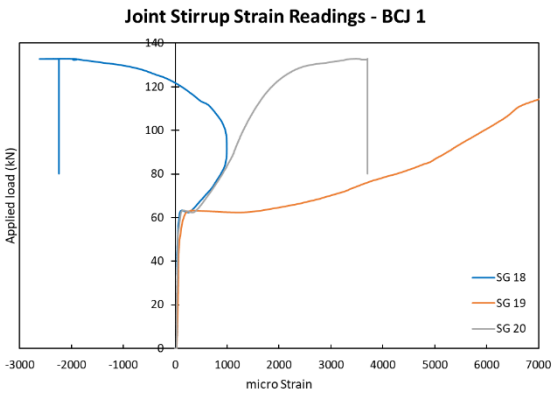

a) Strain gauge response for BCJ 1

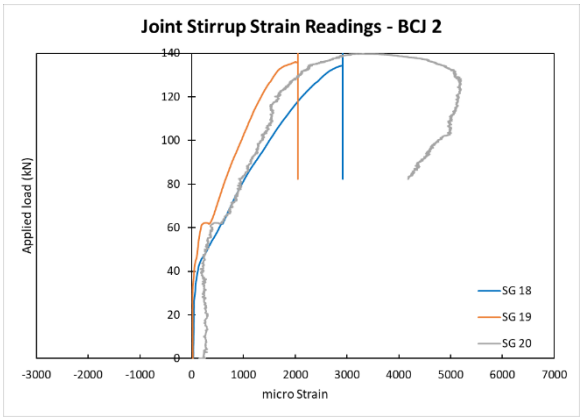

b) Strain gauge response for BCJ 2

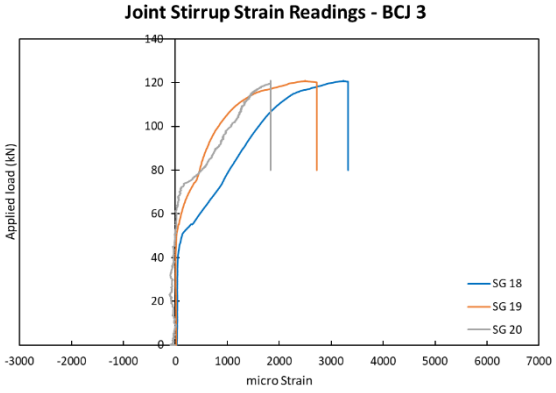

c) Strain gauge response for BCJ 3

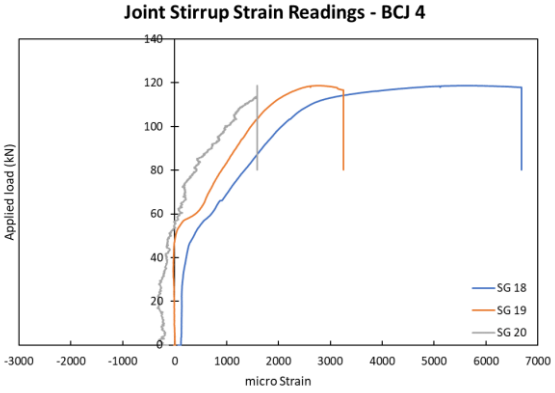

d) Strain gauge response for BCJ 4

Figure 4-23 Joint shear reinforcement strain measurements: (a) Specimen BCJ 1; (b) Specimen BCJ 2; (c) Specimen BCJ 3; (d) Specimen BCJ 4.

4.3 Results of BCJ series 2

4.3.1 Overview of the results

Series 2 studied the influence on joint behaviour of high column axial load in specimens with one (BCJ 5 and BCJ 7) and three joint stirrups (BCJ 6 and BCJ 8). Increased upper column loads of 600 kN and 900 kN were applied to specimens BCJ 6 and BCJ 8 respectively. The beam anchorage type used in this series was L-anchorage type for specimen BCJ 7 and U-anchorage type for the remainder of the specimens. A large bend radius of 150 mm was used in specimen BCJ 7 and the remaining three specimens were anchored with a standard bend radius of 87.5 mm. All four BCJ specimens failed in shear due to the formation of a critical diagonal crack which extended from the bottom left corner of the joint into the upper column. The measured failure loads, column end reaction and concrete strengths of these specimens are shown in Table 4-26.

The experimental results in Table 4-26 show that increasing the column load increased the load at which diagonal cracking first occurred in specimens BCJ 6 and BCJ 8 relative to specimen BCJ 5. The failure load decreased when the axial column load was increased from 600 kN in BCJ 6 (111.5 kN) to 900 kN in BCJ 8 (107.9 kN) but the reduction in strength does not appear significant. Reducing the number of joint stirrups reduced the joint strength of BCJ 5 as expected. When comparing the results of series 1 and 2, the lower concrete strength of series 2 should be noted.

Table 4-26 Summary of experimental results for series 2.

Specimen	f'_c (MPa)	f_t (Mpa)	Column load (kN)	Top Reaction (kN)	Bottom Reaction (kN)	Beam load at first crack (kN)	Beam Failure Load (kN)
BCJ 5	27.0	3.8	300	53	42	45	81.1
BCJ 6	26.9	3.9	600	75	54	65	111.5
BCJ 7	39.9	5.3	300	86	68	60	127.6
BCJ 8	26.8	4.1	900	80	39	85	107.9

4.3.2 Failure modes and crack patterns

The failure mode and final crack patterns of this series are shown in Figure 4-24. All the BCJ specimens failed in shear with an inclined crack extending from bottom left corner to top right corner of the joint. This crack widened significantly towards the end of the test and resulted in significant spalling of the concrete from the back of the upper column. In all specimens, a

crack formed at the interface between the beam and column. This crack was longer in BCJ 7 than the other specimens.

The initial crack (1st crack) appeared in specimen BCJ 5 at the centre of joint when the load reached 45 kN. As beam load increased, this crack extended further and secondary cracks (including 2nd crack) also formed within the joint approached bottom left corner and right top corner. At failure, 1st and 2nd crack extended diagonally and joined each other near top column. Both cracks reached the upper column causing a shear failure of joint at a load of 81.1 kN. As shown in Figure 4-24 (a), after the peak load the cracks became wider and split the concrete into two parts above the joint. Specimen BCJ 6 first cracked (1st) near the centre of the joint when the beam load reached 65 kN. As the load increased, an inclined crack (2nd) formed parallel to 1st crack and extended gradually up to the peak load. At peak load, a 3rd crack appeared and joined 1st crack at the tip of crack causing a shear failure of joint at a load of 111.5 kN. As shown in Figure 4-24 (b), the concrete in post peak load spalled away at the back of joint and in the upper column due to the extension of the critical diagonal cracks (1st, 2nd, and 3rd).

Cracking (depicted 1st) first occurred in the joint of specimen BCJ 7 at the centre of joint when the load reached 60 kN. As the load was increased, the 1st crack extended diagonally, and a 2nd crack formed parallel to the first crack. The vertical crack at beam-column interface extended downwards into the joint in a diagonal as the load was increased. The joint failed in shear at a load of 127.6 kN. After the peak load, the 2nd crack joined with a vertical crack in the beam at the face of the joint causing a piece of concrete to spall off as shown in Figure 4-24 (c). Specimen BCJ 8 first cracked (1st) at the centre of joint when the load reached 85 kN along with a vertical crack formed near beam face before the first crack load was reached. The 1st crack extended and joined another inclined crack (2nd) as the load increased. These two critical inclined cracks became larger and their length increased extending from bottom left corner to top right corner of joint, causing a shear failure mode at a load of 107.9 kN. During the post-peak load, concrete spalled away from the back of joint concrete as shown in Figure 4-24 (d).

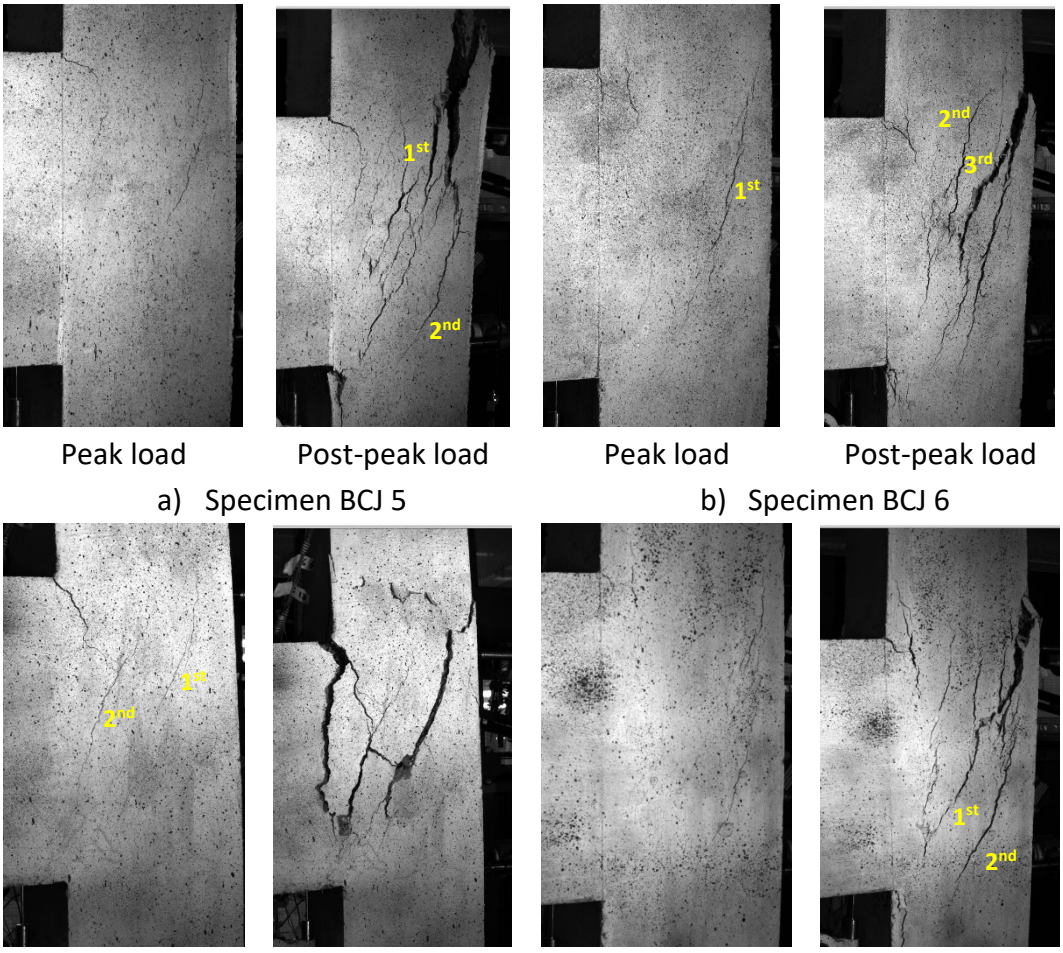

Peak load Post-peak load Peak load Post-peak load

a) Specimen BCJ 5 b) Specimen BCJ 6

Peak load Post-peak load Peak load Post-peak load

c) Specimen BCJ 7 d) Specimen BCJ 8

Figure 4-24 Failure modes and crack patterns of second series: (a) specimen BCJ 5; (b) specimen BCJ 6; (c) specimen BCJ 7; and (d) specimen BCJ 8.

4.3.3 Load-deflection response

The load-deflection results for series 2 are shown in Figure 4-25. As discussed, for the first series, the measured column top reaction was greater than the bottom reaction because of friction forces acting on the bearing at the bottom end of the column. In this series, tests were stopped when the deflection of the beam exceeded a displacement of 60 mm, except for specimen BCJ 7 which exceeded a displacement of 80 mm. Increasing the column axial load from 600 kN in BCJ 6 to 900 kN in BCJ 8 only marginally affected the failure load which was 111.5 kN for BCJ 6 and 107.9 kN for BCJ 8. Specimens BCJ 5 and BCJ 7 with only one joint stirrup had lower shear joint strengths than the comparable specimens in series 1.

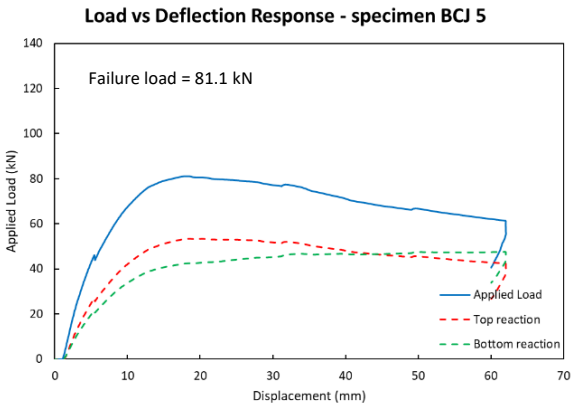

a) Load-deflection response for BCJ 5

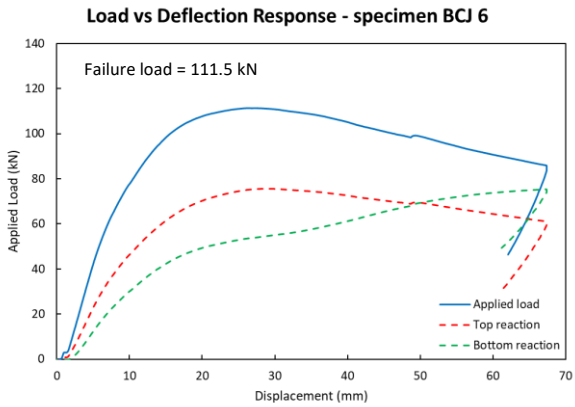

b) Load-deflection response for BCJ 6

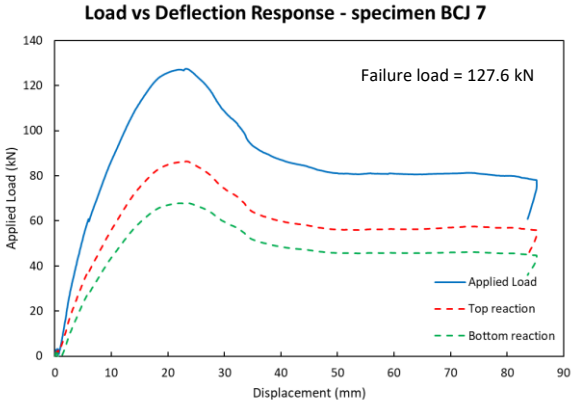

c) Load-deflection response for BCJ 7

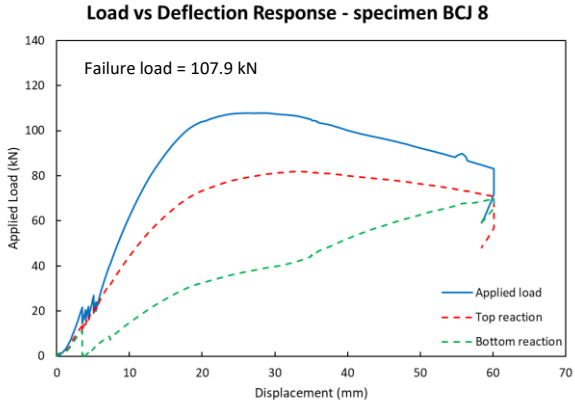

d) Load-deflection response for BCJ 8

Figure 4-25 Load-deflection response: (a) Specimen BCJ 5; (b) Specimen BCJ 6; (c) Specimen BCJ 7; (d) Specimen BCJ 8.

The horizontal displacements, in the plane of the specimen, from the LVDTs at the ends of the column and the top and bottom of the joint are shown in Figure 4-26. The results are presented at 50 kN, 70kN, 90 kN, 110 kN and failure for BCJ 6 and BCJ 7. Different levels of loading were used in BCJ 5 and BCJ 8 because the failure load was smaller in comparison with the other specimens.

LVDT1 at the base of the column recorded similar displacements in specimen BCJ 5, BCJ 7 and BCJ 8, but very small displacements were measured in BCJ 6. The deflection measurements from LVDT2 at the bottom of the joint showed large displacement values in BCJ 8 and displacements lower than 1 mm were recorded in the other specimens. Specimens BCJ 6 and BCJ 7 showed higher values of deflection recorded in LVDT 3 at the top of the joint and displacements lower than 2 mm were measured in specimens BCJ 5 and BCJ 8. LVDT4 at the top of the column recorded displacements more than 1 mm in specimens BCJ 7 and BCJ 8 while in the other two specimens the displacement values were lower. The displacements at

LVDTs 1 and 4, at the bottom and top ends of the column respectively, arise from global rotation of the test specimen in the test rig.

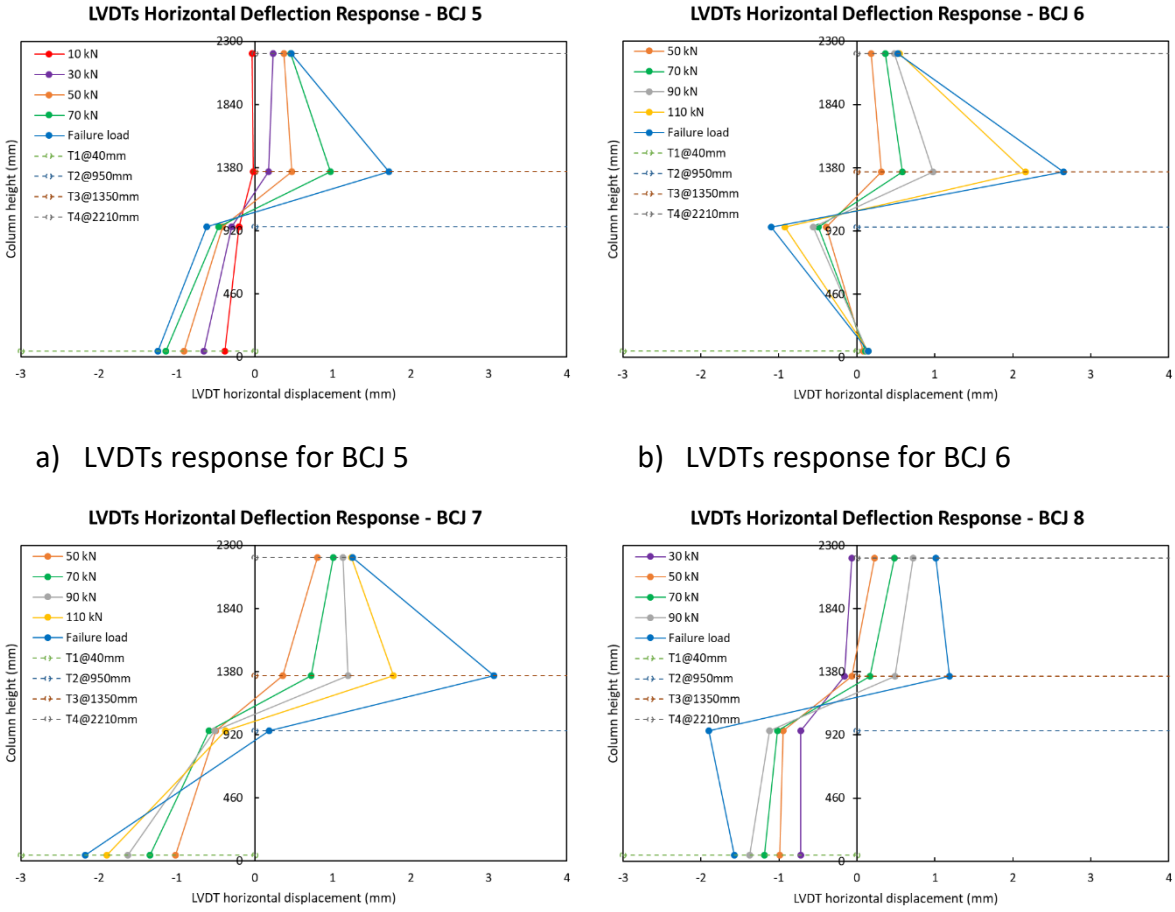

a) LVDTs response for BCJ 5

b) LVDTs response for BCJ 6

c) LVDTs response for BCJ 7

d) LVDTs response for BCJ 8

Figure 4-26 Horizontal deflection recorded from LVDTs for second series: (a) Specimen BCJ 5; (b) Specimen BCJ 6; (c) Specimen BCJ 7; (d) Specimen BCJ 8.

Inclinometers were installed on the back of the column at beam mid-height and near the beam end as shown in Figure 3-14. The inclinometer at the back of the joint was disrupted from reading the exact rotation values due to spalling of the cover zone subsequent to failure. Therefore, the deflection measurements taken from LVDT2 and LVDT3 were also used to obtain the joint rotation. The results of these readings agreed with the inclinometer measurements installed in joint up to peak load after which the readings diverged due to spalling of cover at the back of the column. The results of inclinometers and LVDTs measurement values for second series are shown in Figure 4-27.

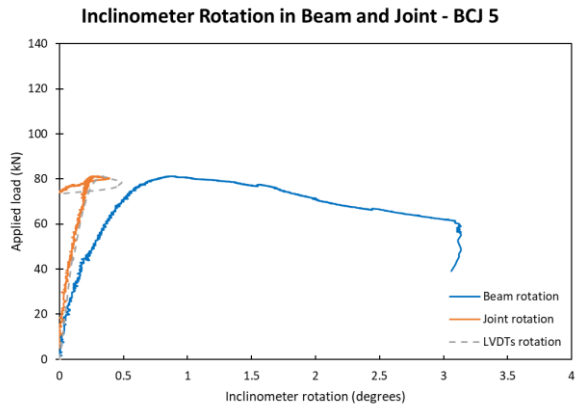

a) Inclinometer response for BCJ 5

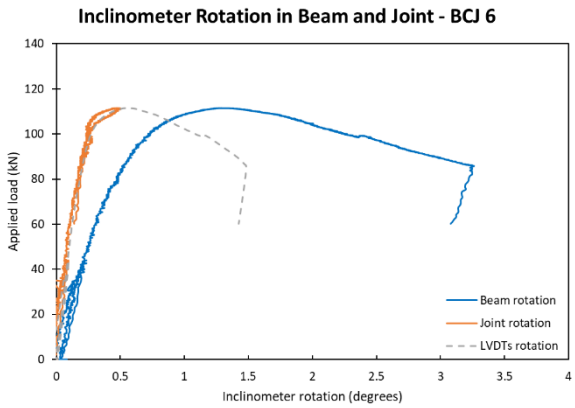

b) Inclinometer response for BCJ 6

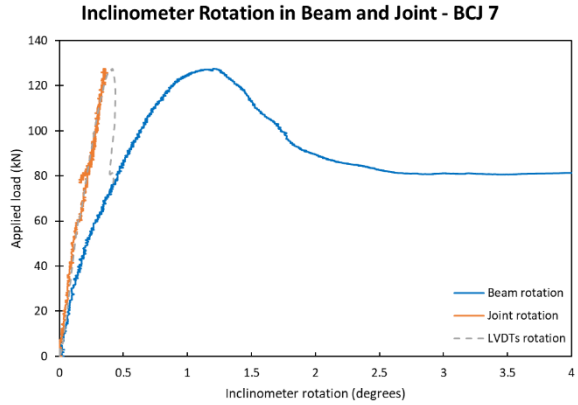

c) Inclinometer response for BCJ 7

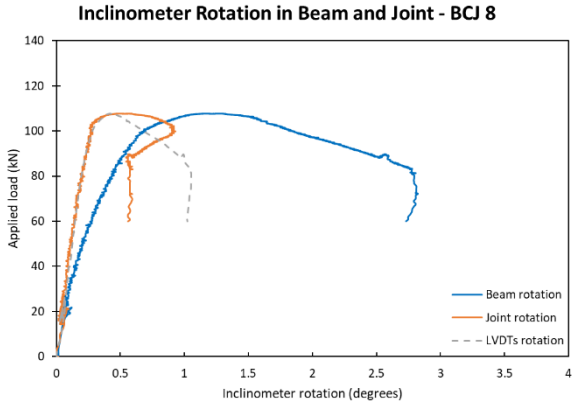

d) Inclinometer response for BCJ 8

Figure 4-27 Inclinometer's readings for second series: (a) Specimens BCJ 5; (b) Specimens BCJ 6; (c) Specimens BCJ 7; (d) Specimens BCJ 8.

4.3.4 Concrete surface strains and crack kinematics

The procedure followed in series 1 is also applied to series 2 by utilizing the DIC technique to measure the crack kinematics. The distribution of virtual DEMEC gagues along the critical crack is similar to Figure 4-11 for series 1. Similar limits were also taken into consideration to be avoided in the analysis to ensure the validitiy of the results. Crack opening and sliding displacements were determined at different loading levels, and the results of maximum crack opening and sliding displacements at failure load are presented in Table 4-27 and Figure 4-28. The angle of the critical crack rotation was measured counter-clockwise from the horizontal axis.

Table 4-27 Maximum crack opening and sliding of BCJ specimens in second series at maximum load.

Specimen	Max. opening (mm)	Height (mm)	Angle (Degrees)	Max. sliding (mm)	Height (mm)	Angle (Degrees)
BCJ 5	1.14	400	81.2	0.76	375	79.8
BCJ 6	1.63	275	75.0	1.72	275	75.0
BCJ 7	1.00	325	84.4	0.35	225	56.8
BCJ 8	1.70	325	70.2	1.65	325	70.2

**The column load and number of joint stirrups include: BCJ 5 (300 kN axial load with one joint stirrup), BCJ 6 (600 kN axial load with three joint stirrups), BCJ 7 (300 kN axial load with one joint stirrup) and BCJ 8 (900 kN axial load with three joint stirrups); all specimens had U-anchorage bar with standard radius except for BCJ 7 with L-anchorage bar and large bend radius.*

All these specimens had three joint stirrups and standard radius U-bars. The maximum crack opening and sliding tended to occur near mid-height of the joint. The crack opening and sliding displacements at peak load were least in BCJ 5 and BCJ 7 despite them having only one joint stirrup. Both these specimens had upper column axial loads of 300 kN. However, BCJ 7 failed at a significantly greater beam load than BCJ 5 due to its greater concrete strength and use of large radius L-bars compared with standard radius-bars in BCJ 5.

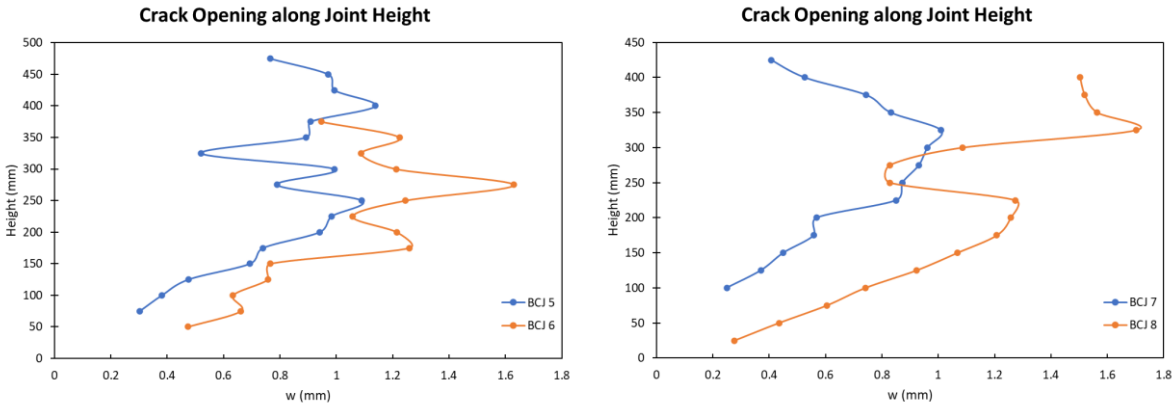

a) Cracks opening results for specimens BCJ 5, BCJ 6, BCJ 7 and BCJ 8

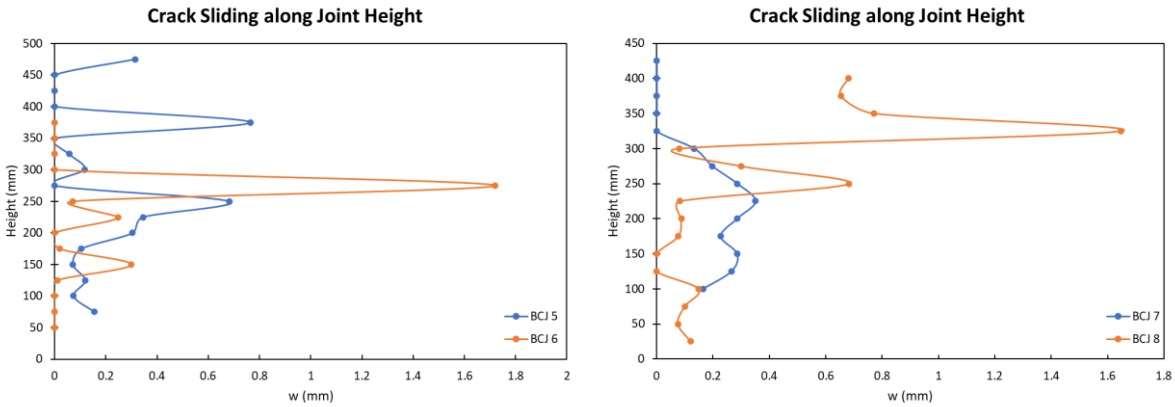

b) Cracks sliding results for specimens BCJ 5, BCJ 6, BCJ 7 and BCJ 8

Figure 4-28 Results of crack opening and sliding along the joint height of second series: (a) Crack opening; (b) crack sliding.

Figure 4-29 to Figure 4-32 present the crack opening and sliding results for series 2. Crack widths were greatest around mid-height of joint. Crack displacements developed from around 50% of the failure load and at failure load. Specimens BCJ 5 and BCJ 7 with column axial load of 300 kN showed a gradual increase in crack opening and sliding displacements as load increased to failure load. However, a sudden increase in crack opening and sliding occurred near failure in specimens with high column load (BCJ 6 and BCJ 8). The ratio of crack sliding to crack opening is also plotted against load stages for each specimen. Specimen BCJ 8 had the largest value of (s/w) and specimen BCJ 7 the least.

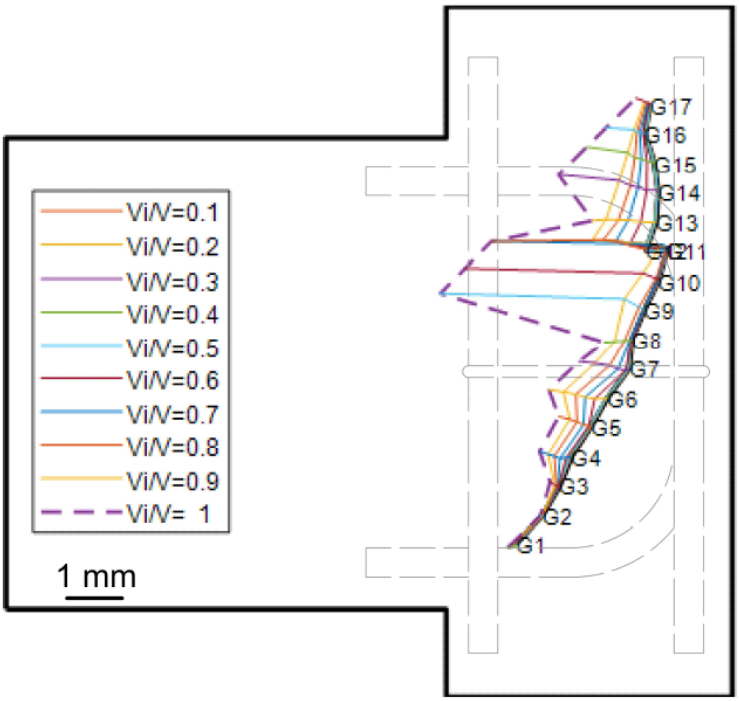

a) Crack kinematics

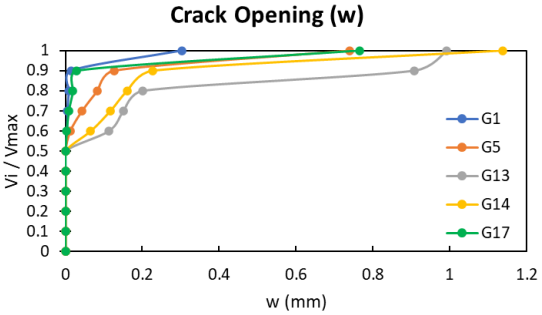

b) Crack opening

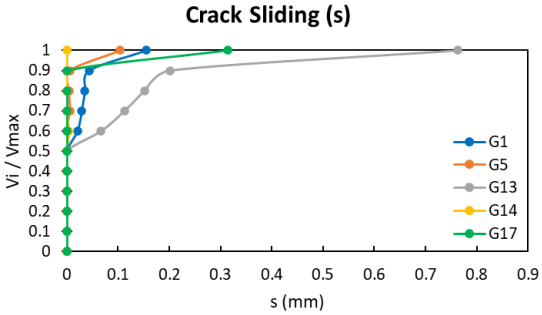

c) Crack sliding

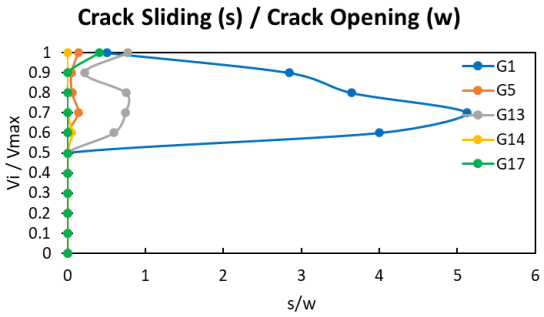

d) Crack sliding / crack opening

Figure 4-29 Crack kinematics for specimen BCJ 5.

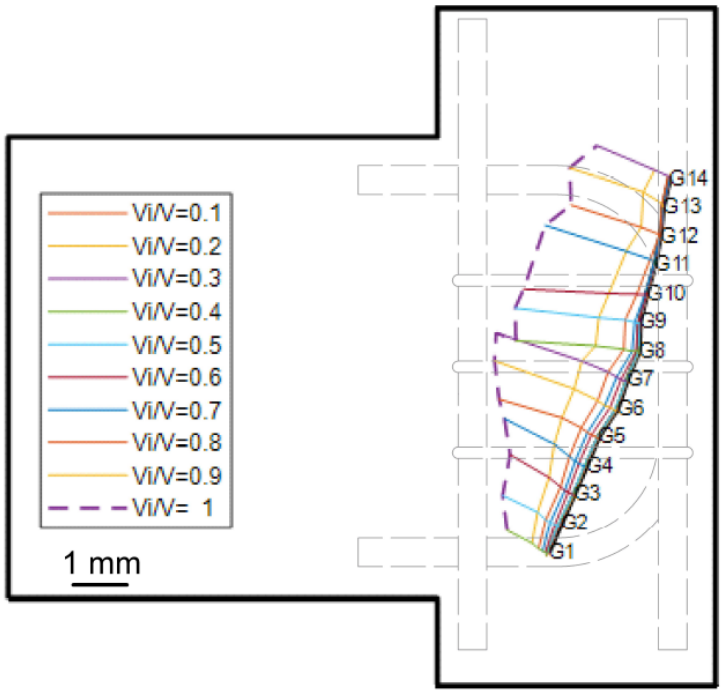

a) Crack kinematics

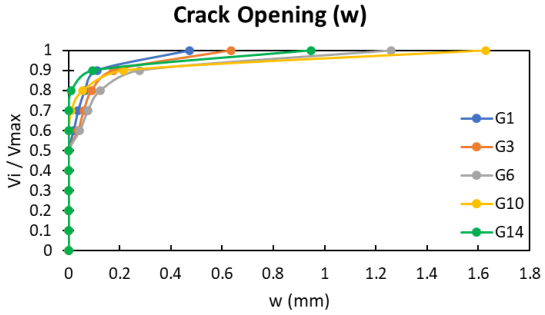

b) Crack opening

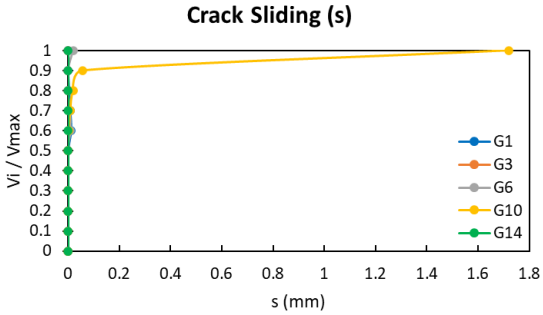

c) Crack sliding

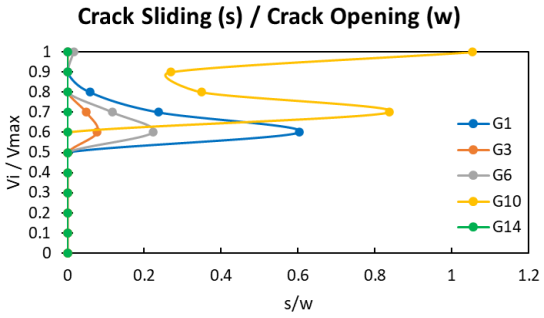

d) Crack sliding / crack opening

Figure 4-30 Crack kinematics for specimen BCJ 6.

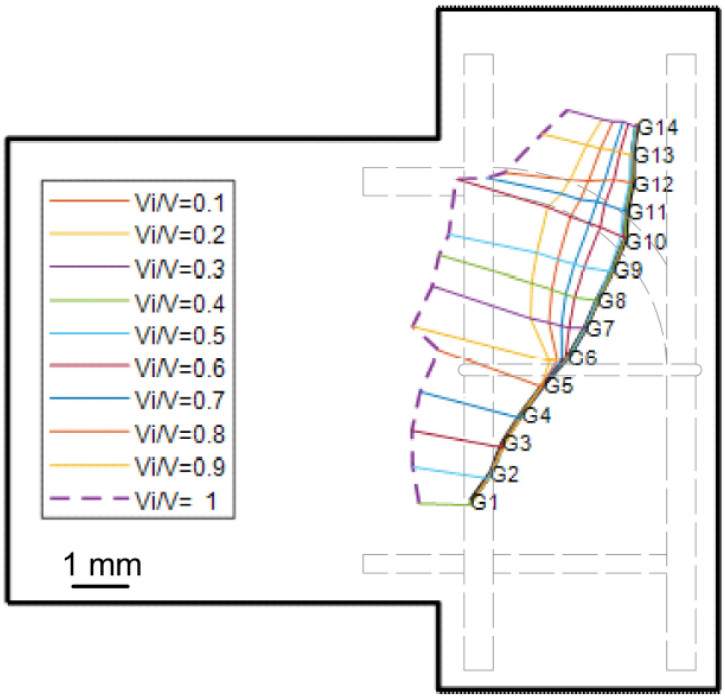

a) Crack kinematics

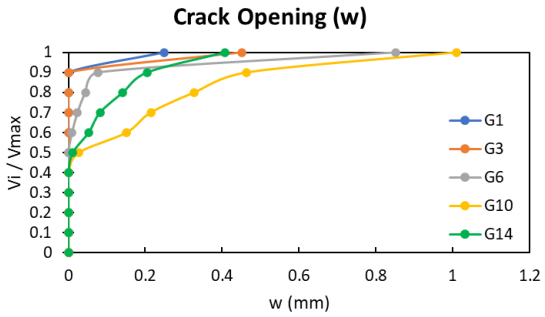

b) Crack opening

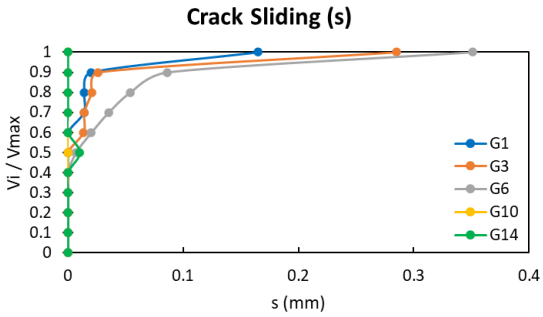

c) Crack sliding

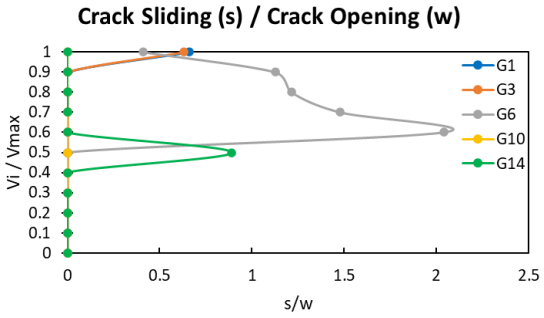

d) Crack sliding / crack opening

Figure 4-31 Crack kinematics for specimen BCJ 7.

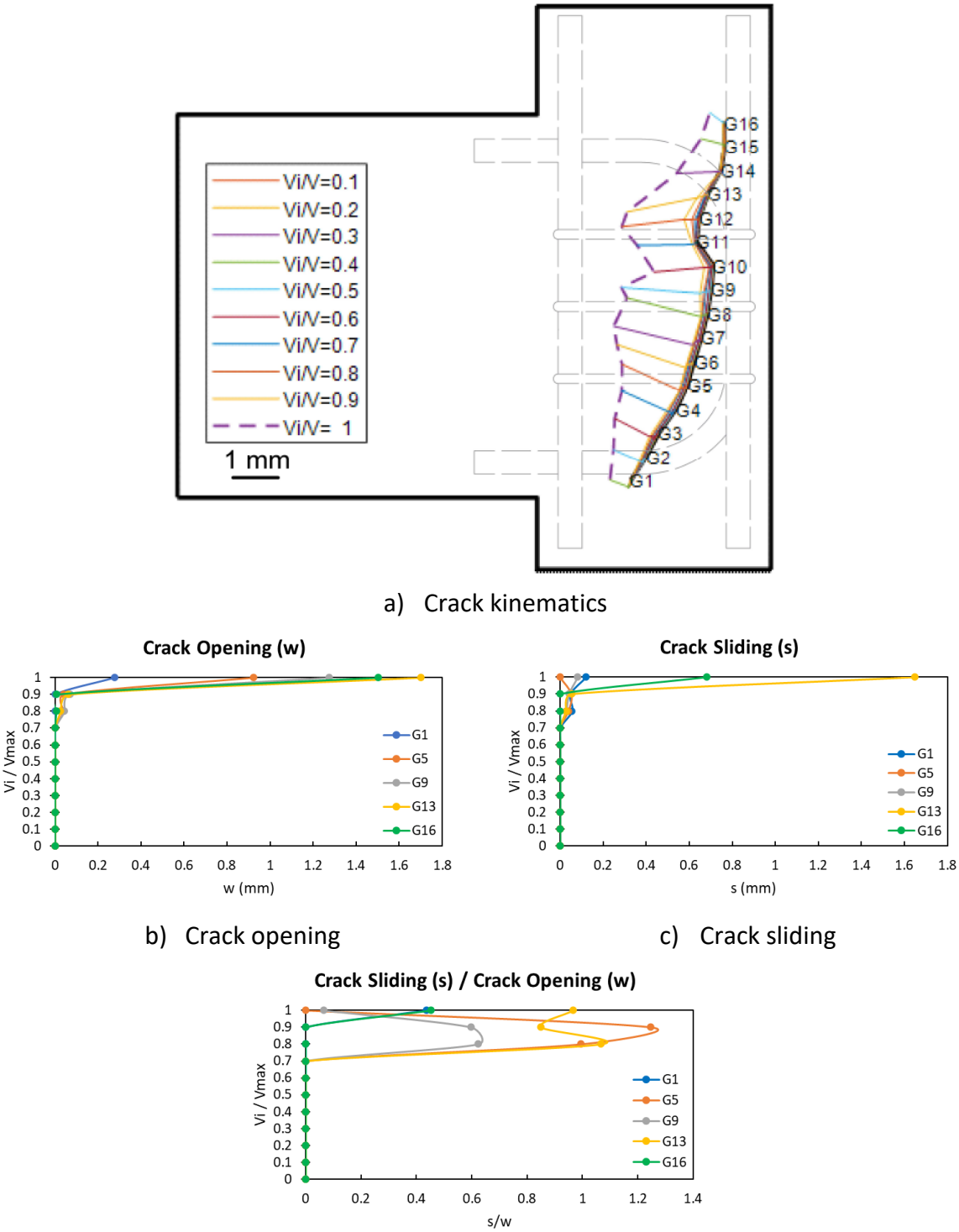

a) Crack kinematics

b) Crack opening

c) Crack sliding

d) Crack sliding / crack opening

Figure 4-32 Crack kinematics for specimen BCJ 8.

4.3.5 Reinforcement strains

As shown in Figure 3-15 to Figure 3-22, strain gauges were placed along the longitudinal and joint shear reinforcement similarly to the series 1. Strain gauges were placed on the beam and column bars near to joint boundaries and inside joint including column bars, beam anchorage bars and joint stirrups. A few gauges gave faulty readings or were broken during the casting process.

The strains measured in the inner column bars are shown in Figure 4-33. Specimens BCJ 6 and BCJ 8 had five strain gauges (SG 1 to SG 5) and specimens BCJ 5 and BCJ 7 had six strain gauges (SG 1 to SG 6). For specimens with high column load, a pair of strain gauges (SG 2 and SG 3) were placed on one of the inner column bars at the top of the joint. Single gauges were used elsewhere (SG 1, SG 4 and SG 5). For specimens with only one joint stirrup, pairs of gauges were positioned on one of the inner column bars at the top (SG 2 and SG 3) and bottom (SG 5 and SG 6) of the joint. Gauges SG 1 and SG 4 were single gauges. SG 1 was broken in BCJ 5 and both SG 2 and SG 3 were broken in BCJ 8. These strains were distributed along the front and back column bars considering two load cases including joint cracking load (blue dotted line) and failure load (orange dotted line), as shown in Figure 4-34 and Figure 4-36.

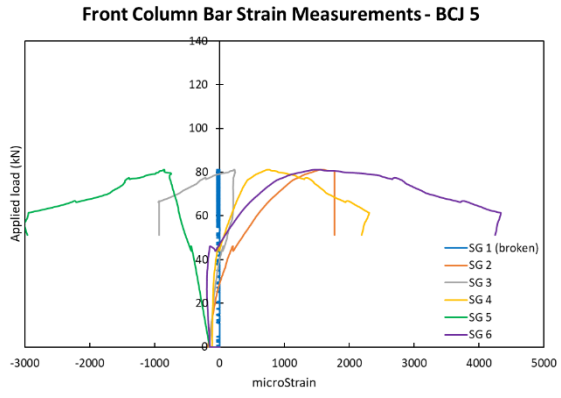

a) Strain gauge response for BCJ 5

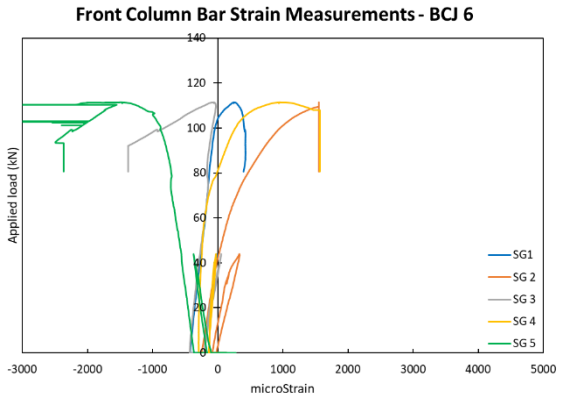

b) Strain gauge response for BCJ 6

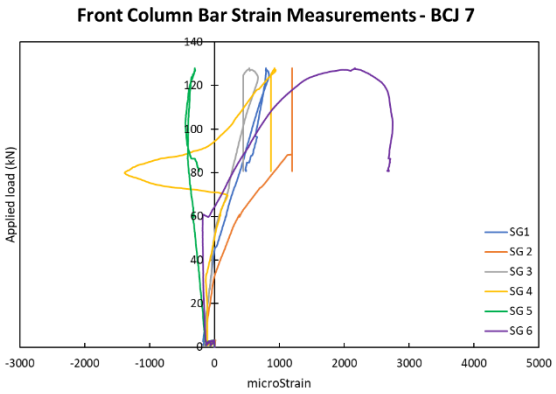

c) Strain gauge response for BCJ 7

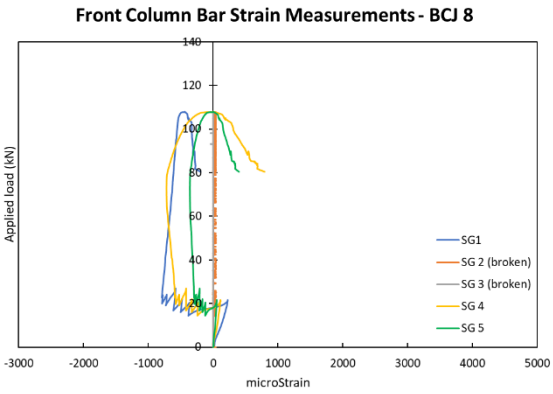

d) Strain gauge response for BCJ 8

Figure 4-33 Front column bar strain measurements: (a) specimen BCJ 5; (b) specimen BCJ 6; (c) specimen BCJ 7; and (d) specimen BCJ 8.

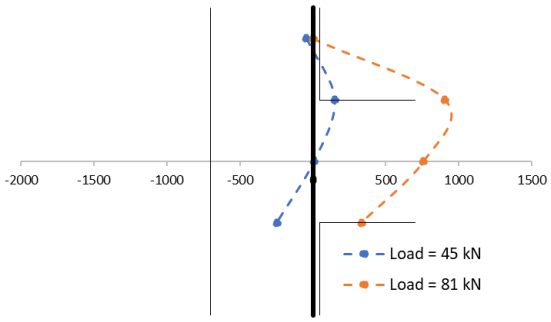

a) Strain distribution for BCJ 5

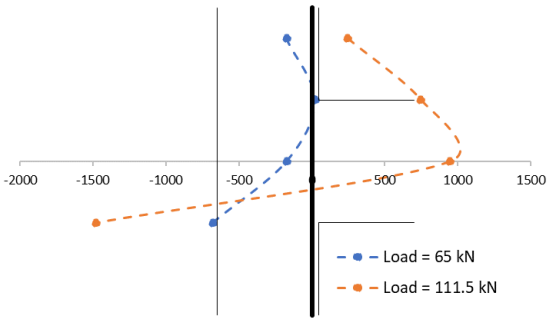

b) Strain distribution for BCJ 6

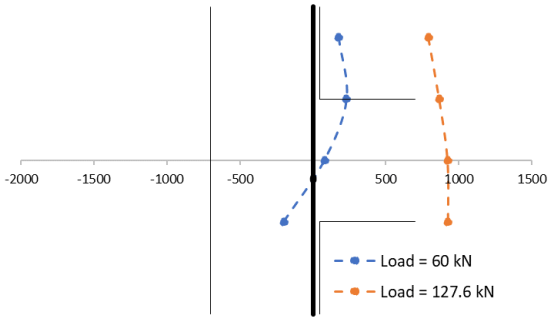

c) Strain distribution for BCJ 7

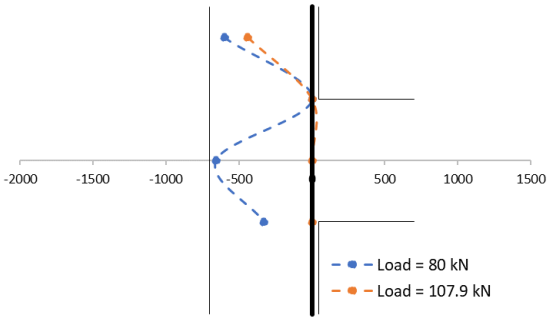

d) Strain distribution for BCJ 8

Figure 4-34 Front column bar strain distribution: (a) specimen BCJ 5; (b) specimen BCJ 6; (c) specimen BCJ 7; and (d) specimen BCJ 8.

Strains in the outer column bars were measured using a combination of single and paired strain gauges. The results of strain gauges readings are shown in Figure 4-35. A pair of strain gauges (SG 8 and SG 9) and single gauges (SG 6, SG 7 and SG 10) were used in specimens BCJ

6 and BCJ 8 while single gauges (SG 9 and SG 12) and pair gauges of the rest of gauges were placed in the other specimens. SG 10 in specimen BCJ 5 and BCJ 6 was broken, and SG 11 in specimen BCJ 5 was also broken before testing the specimen.

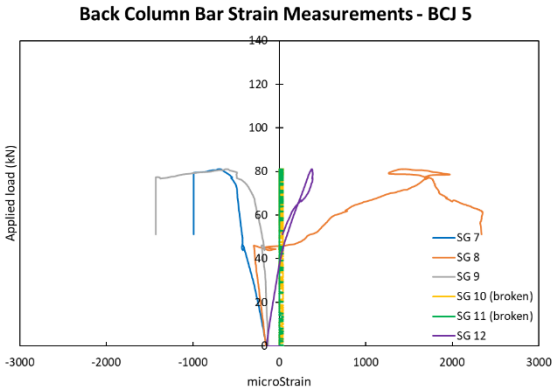

a) Strain gauge response for BCJ 5

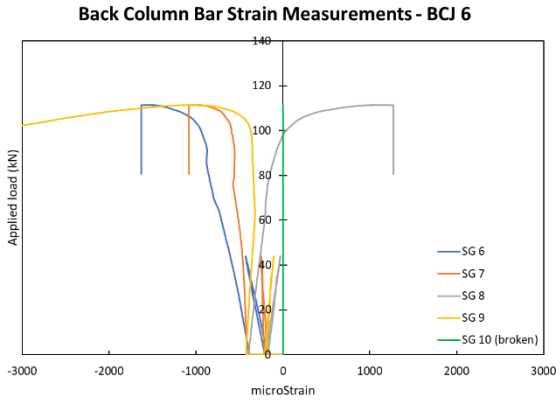

b) Strain gauge response for BCJ 6

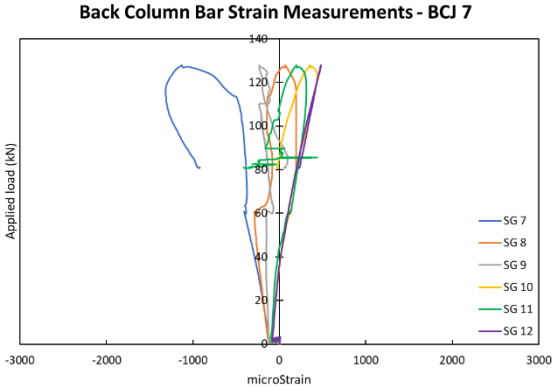

c) Strain gauge response for BCJ 7

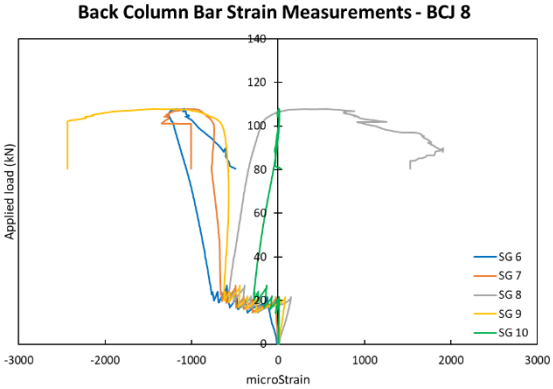

d) Strain gauge response for BCJ 8

Figure 4-35 Back column bar strain measurements: (a) specimen BCJ 5; (b) specimen BCJ 6; (c) specimen BCJ 7; and (d) specimen BCJ 8.

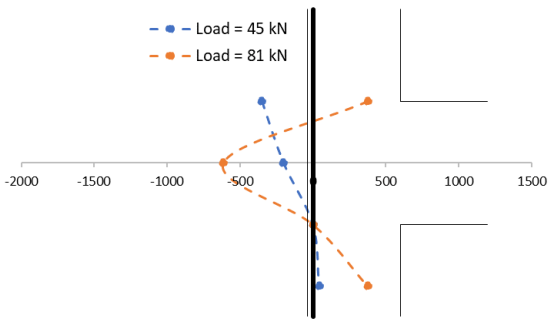

a) Strain distribution for BCJ 5

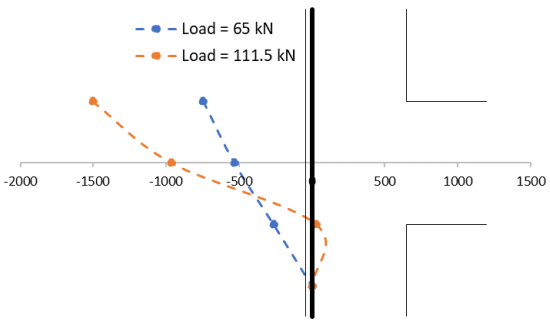

b) Strain distribution for BCJ 6

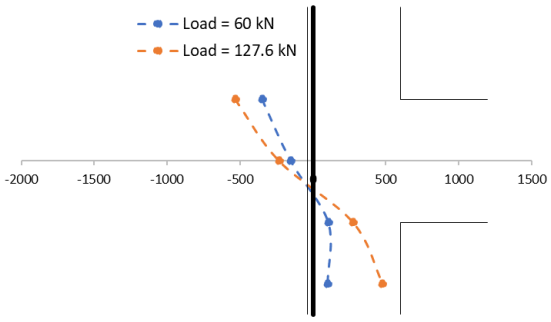

c) Strain distribution for BCJ 7

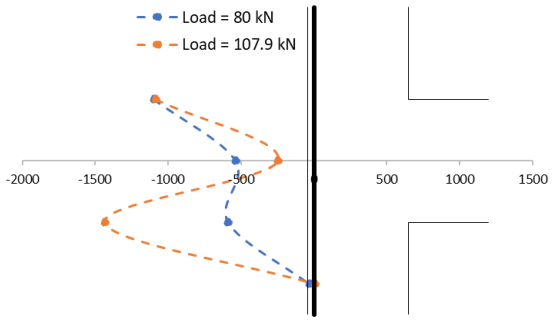

d) Strain distribution for BCJ 8

Figure 4-36 Back column bar strain distribution: (a) specimen BCJ 5; (b) specimen BCJ 6; (c) specimen BCJ 7; and (d) specimen BCJ 8.

Strains along the beam anchorage reinforcement are presented in Figure 4-37. Some strain gauges are labelled as broken in Figure 4-37 illustrating the strain gauge was broken before testing the specimen. Number and location of strain gauges used in this series are shown in Figure 3-17 to Figure 3-20. Specimen BCJ 5 had one broken gauge (SG 14) and three strain gauges (SG 17, SG 18 and SG 19) in specimen BCJ 7 were broken too. Two strain gauges were damaged before testing specimen BCJ 8 (SG 13 and SG 15). The measurements of these strains were used along the beam anchorage bar as strain distributions shown in Figure 4-38. The strain distributions were plotted using two load cases including first crack load and peak load. Tensile strains were plotted outside the beam anchorage bar, whereas compressive strains were on the inside.

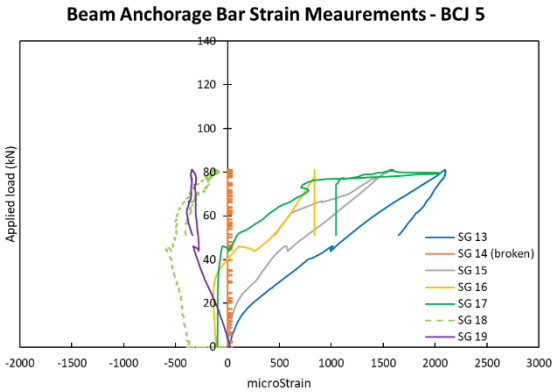

a) Strain gauge response for BCJ 5

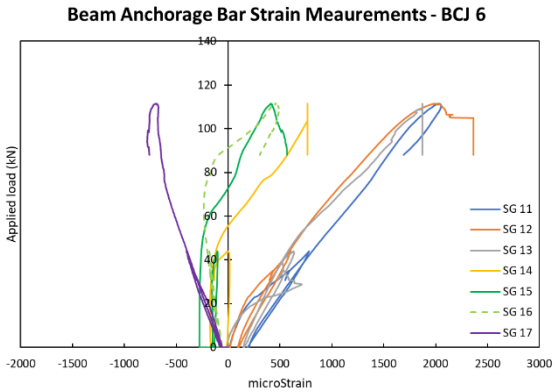

b) Strain gauge response for BCJ 6

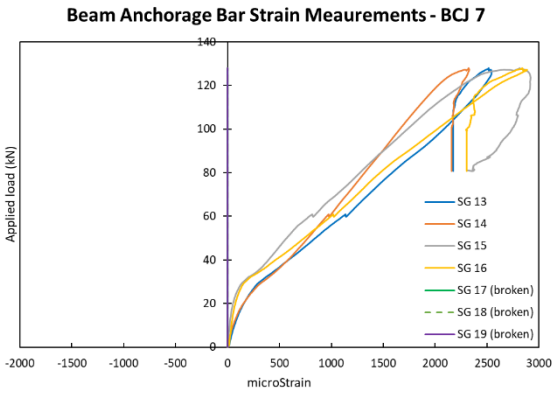

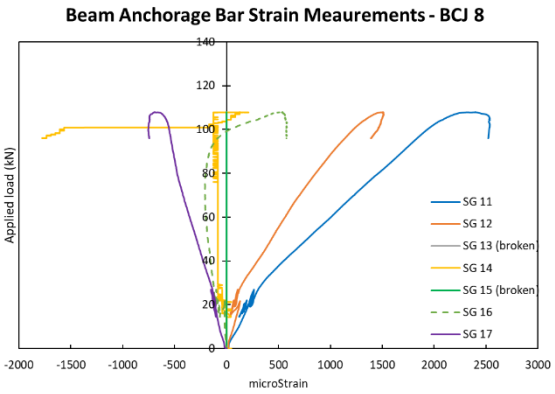

c) Strain gauge response for BCJ 7 d) Strain gauge response for BCJ 8

Figure 4-37 Beam anchorage bar strain measurements(a) specimen BCJ 5; (b) specimen BCJ 6; (c) specimen BCJ 7; and (d) specimen BCJ 8.

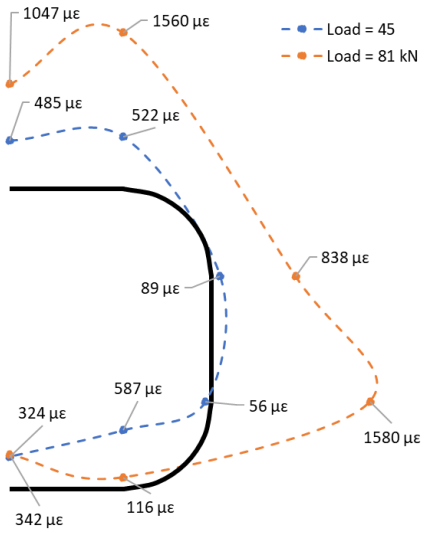

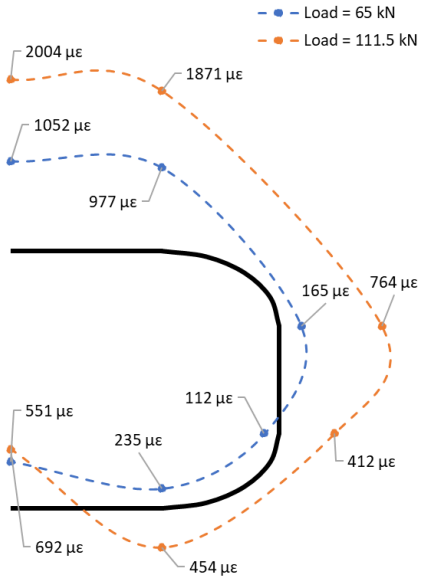

a) Strain distribution for BCJ 5 b) Strain distribution for BCJ 6

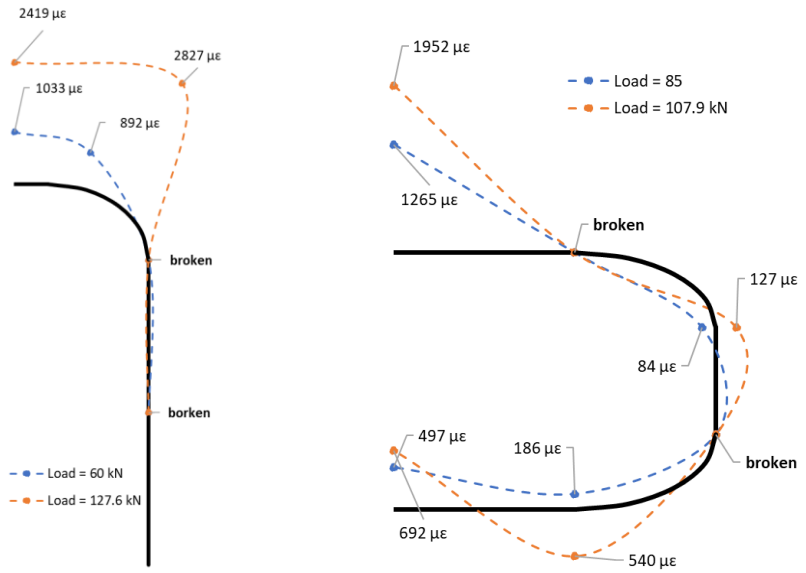

c) Strain distribution for BCJ 7 d) Strain distribution for BCJ 8

Figure 4-38 Beam anchorage bar strain distribution: (a) specimen BCJ 5; (b) specimen BCJ 6; (c) specimen BCJ 7; and (d) specimen BCJ 8.

Strains in joint stirrups were measured using a single strain gauge in specimens BCJ 5 and BCJ 7, and with three strain gauges in specimens BCJ 6 and BCJ 8. The results of these strain gauges are shown in Figure 4-39. Broken strain gauges were found in Specimens BCJ 6 and BCJ 7 while faulty strain readings were recorded in specimen BCJ 5.

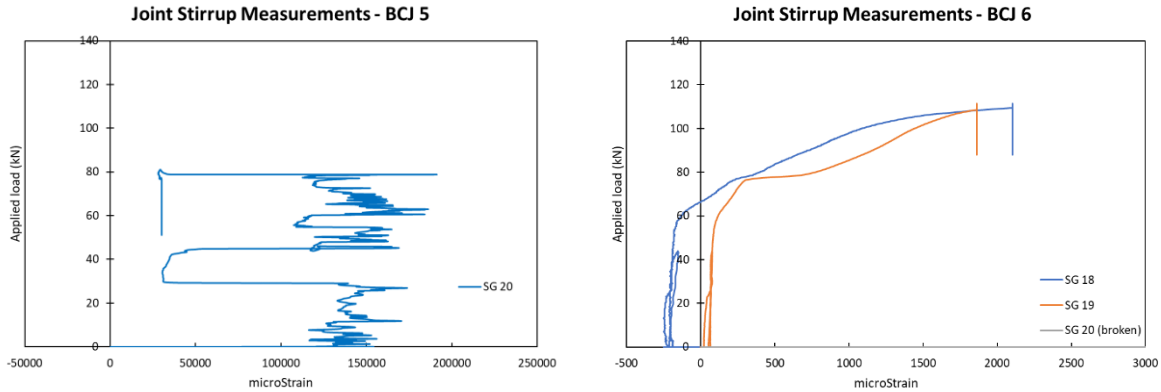

a) Strain gauge response for BCJ 5 b) Strain gauge response for BCJ 6

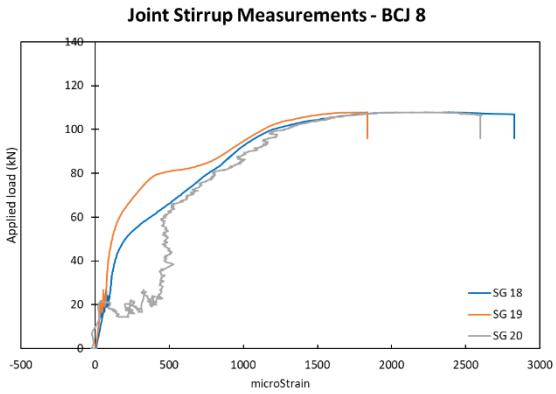

c) Strain gauge response for BCJ 8

Figure 4-39 Joint shear reinforcement strain measurements: (a) specimen BCJ 5; (b) specimen BCJ 6; (c) specimen BCJ 7; and (d) specimen BCJ 8.

4.4 Results of BCJ series 3

4.4.1 Overview of the results

Series 3 studied the effect of increasing the number of joint stirrups, the presence of intermediate column bars and the absence of joint stirrups. All the specimens were loaded with an upper column axial load of 300 kN. The test begun by increasing the column axial load gradually until it reached 300 kN. Subsequently, the column axial load was held constant and the beam was gradually loaded to failure. BCJ 9, with two joint stirrups, and BCJ 11, without joint stirrups, had standard U-anchorage type. L-anchorage type with large bend radius of 150 mm was used in BCJ 10 and BCJ 12. Intermediate column bars were provided in BCJ 10 while three pairs of two 10 mm diameter joint stirrups were provided in BCJ 12. BCJ 9 and BCJ 11 failed in shear due to the formation of a wide diagonal shear crack which ran from the bottom left corner of joint to the upper right corner. The peak load in specimens BCJ 10 and BCJ 12 was limited by the flexural capacity of the beam. In these specimens, a wide vertical crack formed at the beam-column interface with relatively few shear cracks appearing in the joint. The diagonal shear cracks in the joint of BCJ 10 and BCJ 12 were narrower than in specimens BCJ 12 than BCJ 10. The experimental results are summarised in Table 4-28 which shows the maximum beam load and corresponding column end reactions.

Table 4-28 Summary of experimental results for third series

Specimen	f'_c (MPa)	f_t (MPa)	Column load (kN)	Top Reaction (kN)	Bottom Reaction (kN)	Beam load at first crack (kN)	Beam Failure Load (kN)
BCJ 9	51.3	5.5	300	94	67	70	139.7
BCJ 10	51.1	5.4	300	125	97	90	181.2
BCJ 11	48.9	5.5	300	67	52	65	101.9
BCJ 12	49.9	5.4	300	124	93	80	184.6

4.4.2 Failure modes and crack patterns

The final crack patterns of each beam-column joint in this series are shown in Figure 4-40. Failure in this series was either due to joint shear or beam flexural failure. Specimens BCJ 9 and BCJ 11 failed in joint shear as a result of a critical diagonal crack extending from the bottom left joint corner to the top right joint corner. BCJ 10 and BCJ 12 had some diagonal cracking in the joint but also a wide flexural crack passing through the beam-column interface. In specimens BCJ 9 and BCJ 11, the critical crack passed through the joint and extended to the back column bars above the joint and spalled the concrete off.

Before reaching the first diagonal crack load of BCJ 9, a vertical crack appeared at the beam-column interface at a load of 22 kN. Specimen BCJ 9 initially cracked (labelled as 1st) at the centre of joint at a beam load of 70 kN. Subsequently, this crack became wider and extended as the beam load was increased. Additionally, secondary inclined cracks (including 2nd and 3rd cracks) formed parallel to the first crack. BCJ 9 failed in shear at a beam load of 139.7 kN due to the formation of a wide diagonal shear crack. As shown in Figure 4-40 (a), the critical cracks extended into the upper column causing spalling of concrete above the joint near the end of the test. Specimen BCJ 11 initially cracked below the centre of joint around at a beam load of 65 kN, which is depicted as (1st). As the load increased, this crack propagated diagonally, and multiple cracks (2nd and 3rd cracks) appeared in parallel to the first crack. At 101.9 kN, a major diagonal crack formed in the joint causing failure consisting of both the 2nd and 3rd cracks. The crack ran from the bottom inside corner of the joint into the upper column near its back face. As shown in Figure 4-40 (c), this critical crack became very wide and caused spalling of the concrete at the back of the joint in post peak load.

Diagonal cracking (depicted as 1st) initially occurred near the centre of the joint in BCJ 10 at around 90 kN. With increasing load, this crack grew and extended diagonally across the joint,

and other secondary cracks (including 2nd crack) formed in parallel to the first crack. A vertical crack also developed at the beam-column interface before first crack load was reached which widened and became longer as the load was increased. The test was stopped at a displacement of around 50 mm when the beam load had plateaued at 181.2 kN due to yielding of the beam reinforcement at the column face. As shown in Figure 4-40 (b), there was some significant diagonal cracking in the joint at this load with the widest crack extending vertically into the upper column along the outer column bars.

Specimen BCJ 12 initially cracked (1st) in the joint at 80 kN below the centre of the joint. This crack extended from the inner bottom corner of the joint to the centre of joint. As the load was increased, the 1st crack stopped extending and a 2nd crack appeared parallel to the first crack. Subsequently, further cracks formed in the joint. A vertical crack formed at the beam-column interface before the first crack load was reached and it grew gradually as load increased. The test was stopped at a displacement of around 50 mm just prior to which the beam load reached a maximum of 184.6 kN. As shown in Figure 4-40 (d), the vertical crack at the beam-column interface was very wide at the end of the test indicating extensive yield of beam flexural reinforcement, and 1st crack width was very small which made it difficult to be seen in the photograph. Reaching of the peak load of 184.6 kN was accompanied by the formation of an additional crack within the joint.

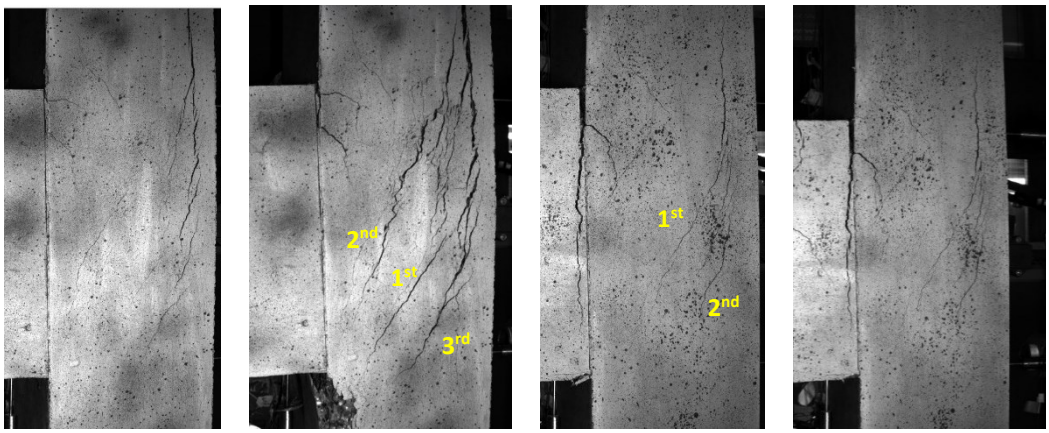

Peak load Post-peak load Peak load Post-peak load

a) Specimen BCJ 9 b) Specimen BCJ 10

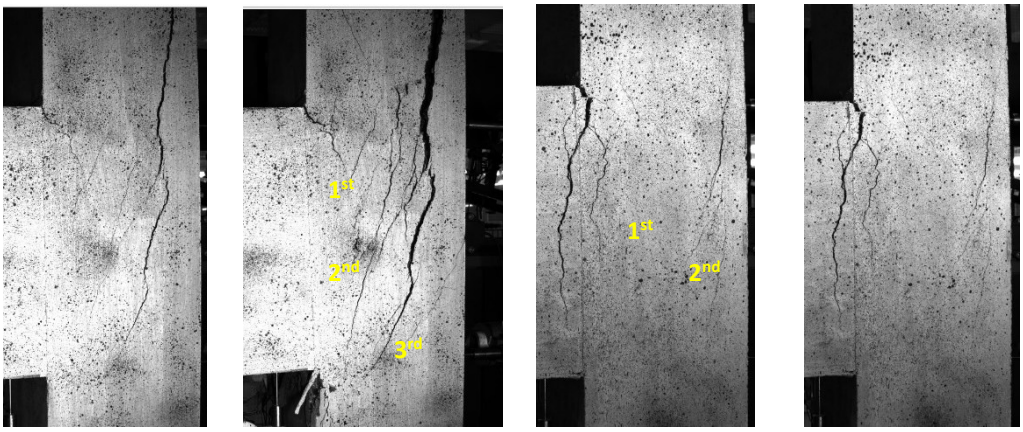

Peak load Post-peak load Peak load Post-peak load

c) Specimen BCJ 11 d) Specimen BCJ 12

Figure 4-40 Failure modes and crack patterns of third series: (a) specimen BCJ 9; (b) specimen BCJ 10; (c) specimen BCJ 11; and (d) specimen BCJ 12.

4.4.3 Load-deflection response

The load-deflection results as well as the top and bottom column reactions are shown for series 3 in Figure 4-41. The top reaction values were larger than in bottom reaction due to the presence of friction in the bearing at the bottom column. In this series, the test was ended when the displacement exceeded 50 mm in specimens BCJ 9 and BCJ 10 and after exceeding a displacement of 40 mm in BCJ 11 and BCJ 12.

Reinforcing the joint with vertical and horizontal reinforcements and increasing the number of joint stirrups improved the joint behaviour significantly. The provision of joint stirrups and mid-column reinforcements in specimen BCJ 10 and increasing the number of joint stirrups in specimen BCJ 12 enhanced the failure load and changed the failure mode to flexure. As expected, BCJ 11 with no joint stirrups failed at the least beam load.

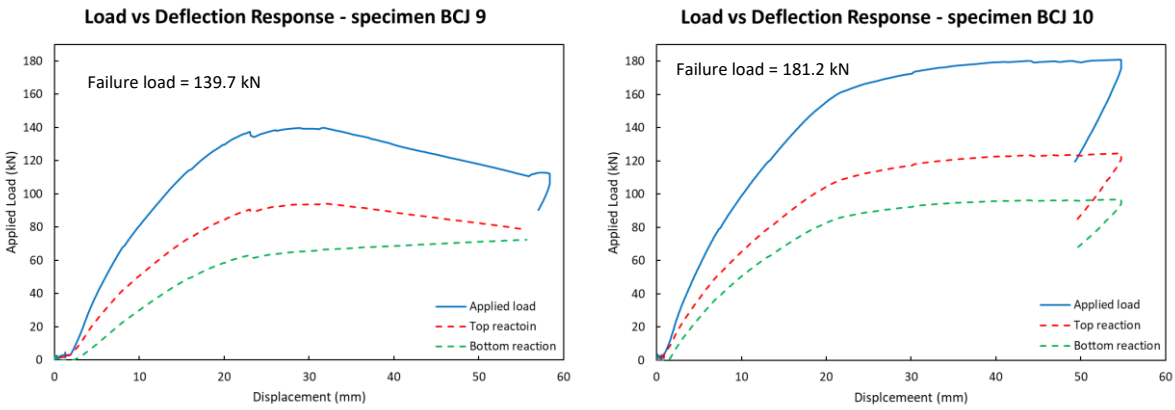

a) Load-deflection response for BCJ 9 b) Load-deflection response for BCJ 10

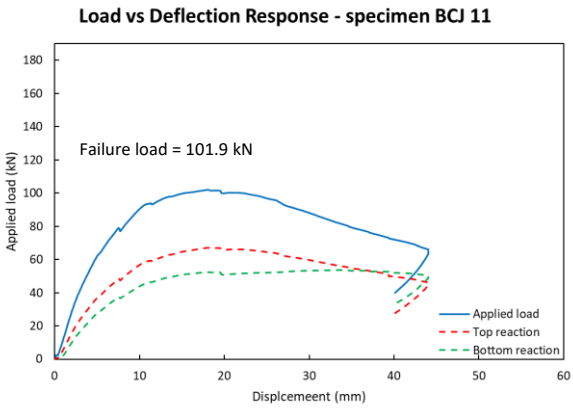

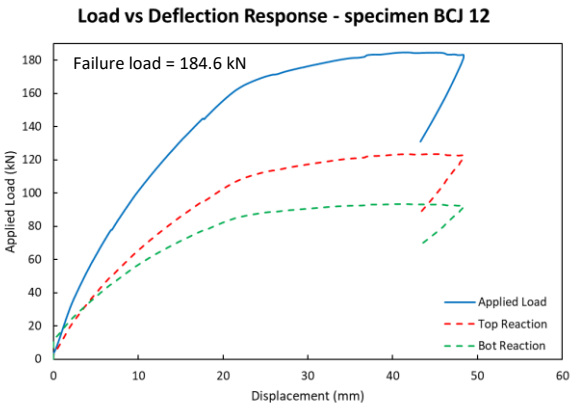

c) Load-deflection response for BCJ 11 d) Load-deflection response for BCJ 12

Figure 4-41 Load-deflection response: (a) Specimen BCJ 9; (b) Specimen BCJ 10; (c) Specimen BCJ 11; (d) Specimen BCJ 12.

The horizontal displacements measured by the four LVDTs installed at on the back face of the column at the column ends and joint corners are shown in Figure 4-42. Five different levels of loading (50 kN, 70kN, 90 kN, 110 kN and failure load of each specimen) are presented for specimens BCJ 9, BCJ 10 and BCJ 12 while loadings of (30 kN, 50 kN, 70kN, 90 kN and failure load) are presented for BCJ 11. The distance from the base of column was 40 mm for LVDT1, 950 mm (bottom of beam) for LVDT2, 1350 mm (top of beam) for LVDT3, and 2210 mm for LVDT4.

Relatively, large displacements were recorded in specimens BCJ 10 and BCJ 12 especially at failure, whereas small displacements were monitored in specimens BCJ 9 and BCJ 11. LVDT3 showed highest deflection values in specimens BCJ 10, BCJ 11 and BCJ 12 while extremely small displacements were recorded in BCJ 9 except for the displacement value at failure load. The lateral movement in BCJ 11 at top column end, measured from LVDT1, was very small when compared with the other specimens.

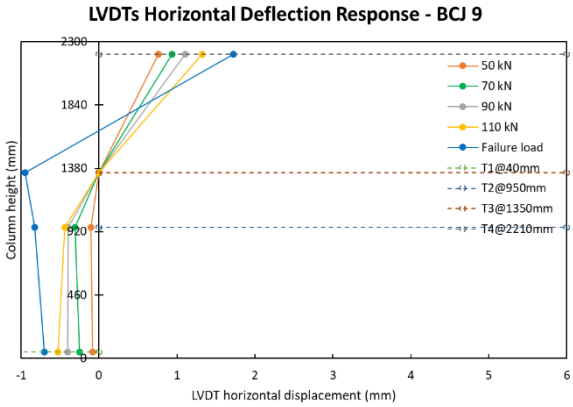

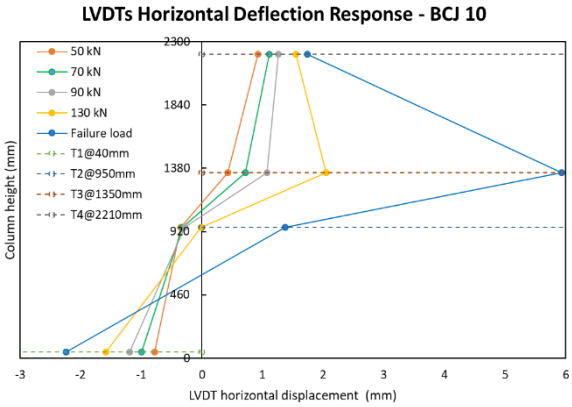

a) LVDTs response for BCJ 9 b) LVDTs response for BCJ 10

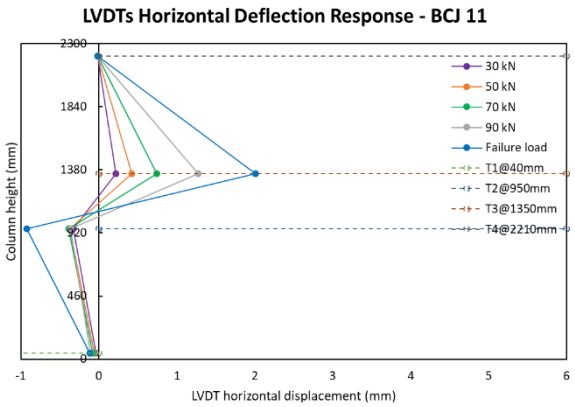

c) LVDTs response for BCJ 11

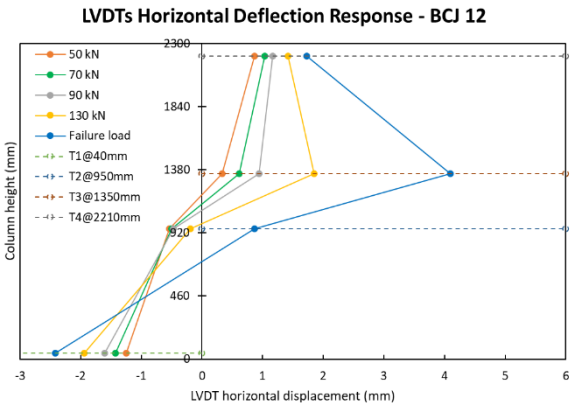

d) LVDTs response for BCJ 12

Figure 4-42 Horizontal deflection recorded from LVDTs for third series: (a) Specimen BCJ 9; (b) Specimen BCJ 10; (c) Specimen BCJ 11; (d) Specimen BCJ 12.

The results of the two inclinometers set to measure the rotation of the joint and beam are shown in Figure 4-43. Due to the presence of cracks on the back of joint, the inclinometer was disrupted from reading the exact rotation values so the horizontal deflection measurements from LVDT2 and LVDT3 were utilized to measure the joint rotation. The joint rotations derived from the LVDT measurements agreed very well with the joint inclinometer measurements up to peak load in BCJ 10 and BCJ 11. Agreement is less good in BCJ 9 due to spalling of the cover zone.

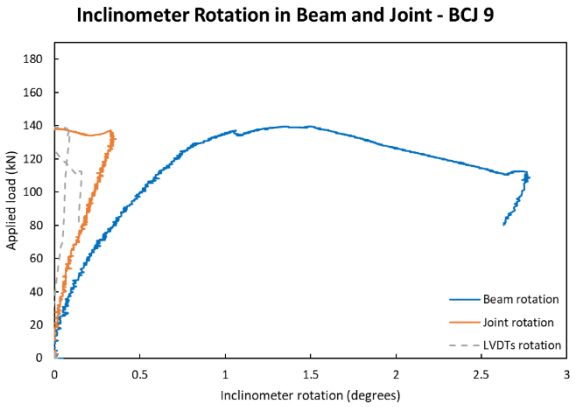

a) Inclinometer response for BCJ 9

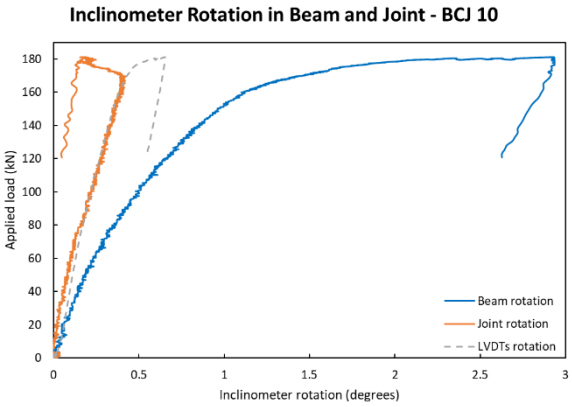

b) Inclinometer response for BCJ 10

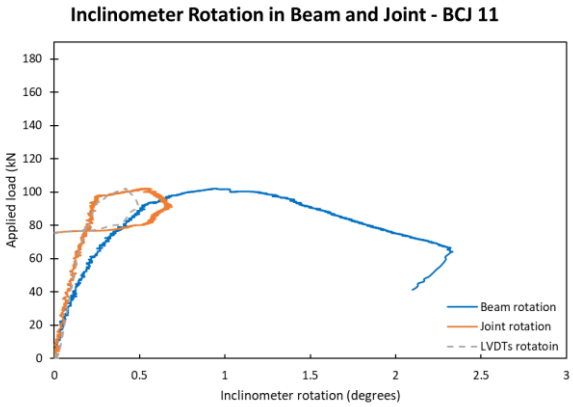

c) Inclinometer response for BCJ 11

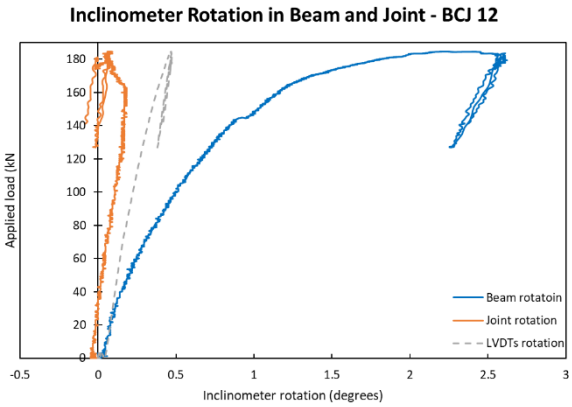

d) Inclinometer response for BCJ 12

Figure 4-43 Inclinometer's readings for third series: (a) Specimen BCJ 9; (b) Specimen BCJ 10; (c) Specimen BCJ 11; (d) Specimen BCJ 12.

4.4.4 Concrete surface strains and crack kinematics

The procedure followed in series 1 and 2 to determine the crack kinematics was also applied to this series. Similar distribution of virtual DEMEC gagues along the critical crack used in the previous series was used in this series as shown in Figure 4-11. The results of maximum crack opening and sliding displacements at failure load are presented in Table 4-29. Limits were also taken into account in the analysis to ensure the validitiy of the results as followed in first and second series. To note, the angle of the critical crack rotation was measured as counter-clockwise from the horizontal axis.

Table 4-29 Maximum crack opening and sliding of BCJ specimens in third series at maximum load.

Specimen	Max. opening (mm)	Height (mm)	Angle (Degrees)	Max. sliding (mm)	Height (mm)	Angle (Degrees)
BCJ 9	3.96	425	90.0	1.76	375	87.0
BCJ 10	2.81	275	74.9	0.51	275	74.9
BCJ 11	2.40	400	77.3	1.36	425	79.9
BCJ 12	2.37	275	86.7	1.90	275	86.7

** The beam bar detailing and bend radius include: BCJ 9 (U-anchorage type with standard bend radius and two joint stirrups), BCJ 10 (L-anchorage type with large bend radius and three joint stirrups), BCJ 11(U-anchorage type with standard bend radius and no joint stirrup) and BCJ 12 (L-anchorage type with large bend radius and three double joint stirrups); all specimens had column load of 300 kN.*

The crack opening and sliding displacements over the joint height were determined at the failure load and their results are shown in Figure 4-44. Specimen BCJ 9 had the widest crack

width while specimen BCJ 12 had the smallest crack opening displacement. Specimen BCJ 11 had a gradual increase in crack opening as position of DEMEC gauge became near the center of joint, whereas the other specimens had varied crack width along the crack. Specimens BCJ 9 and BCJ 12 recorded large crack sliding displacements near the center of joint and specimen BCJ 10 had the lowest value of crack sliding.

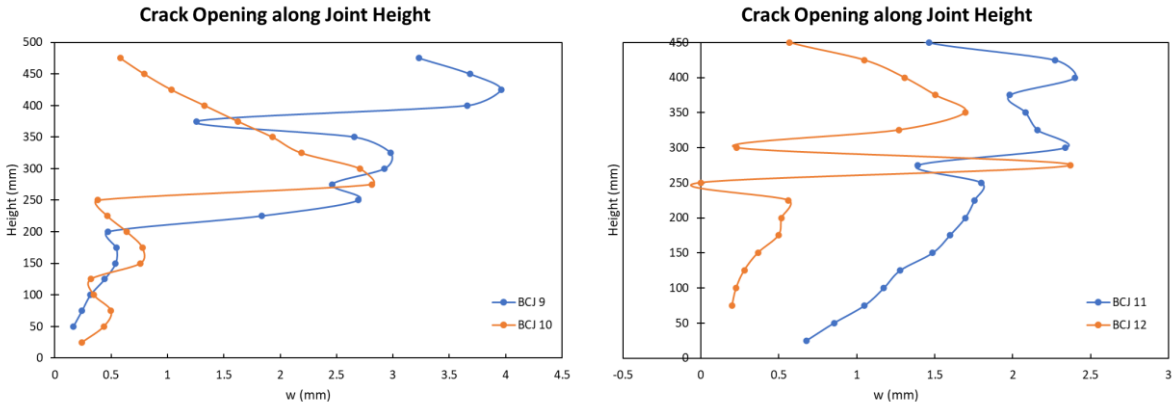

a) Cracks opening results for specimens BCJ 9, BCJ 10, BCJ 11 and BCJ 12

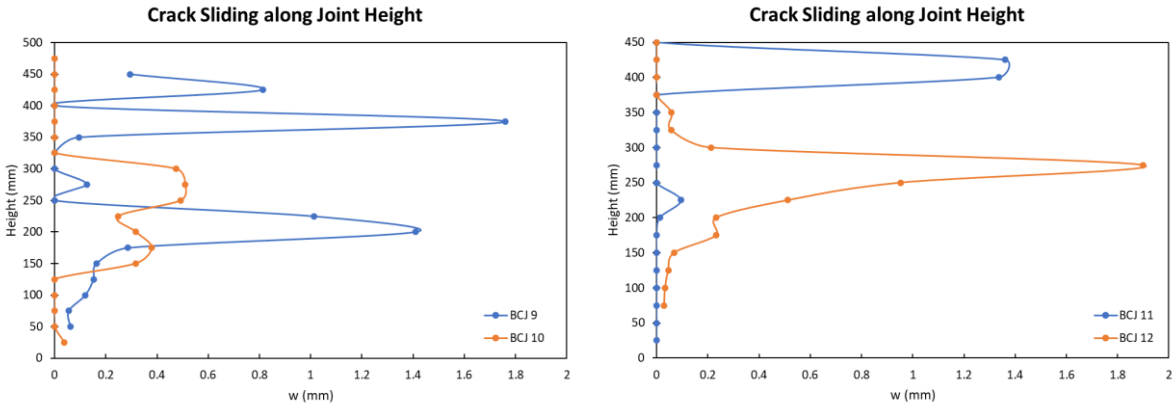

b) Cracks sliding results for specimens BCJ 9, BCJ 10, BCJ 11 and BCJ 12

Figure 4-44 Results of crack opening and sliding along the joint height of third series: (a) Crack opening; (b) crack sliding.

The crack kinematics results of this series are presented in Figure 4-45 to Figure 4-48. The results show crack opening and sliding displacements for some specific gauges in each specimen as well as the crack kinematics along the critical crack. A sudden increase in crack sliding displacement was observed near the failure load in most of the BCJ specimens, especially after 80% of failure load. The crack opening displacements were detectable after 70% of failure load in specimens BCJ 9 and BCJ 11 while the other specimens had readable crack opening displacements from 40% of failure load to peak load. A plot showing the change of crack sliding over crack opening during load stages of each specimen was also shown in

Figure 4-45 to Figure 4-48. The values of (s/w) were minor in specimen BCJ 9 and remarkable in the other specimens.

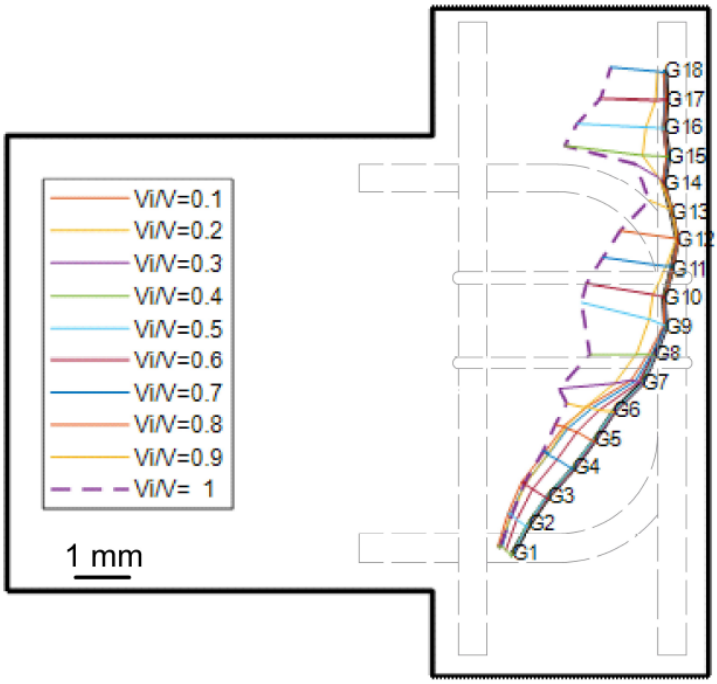

a) Crack kinematics

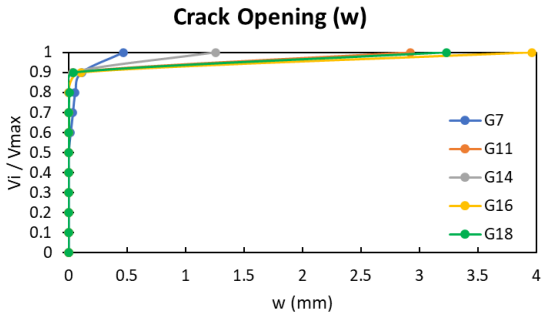

b) Crack opening

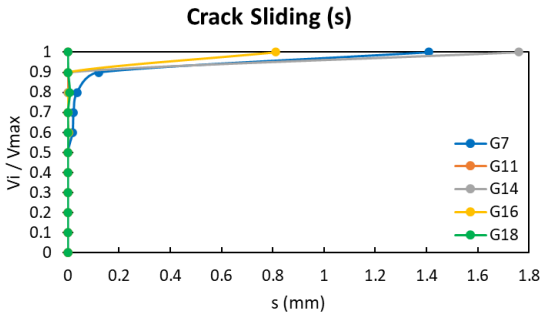

c) Crack sliding

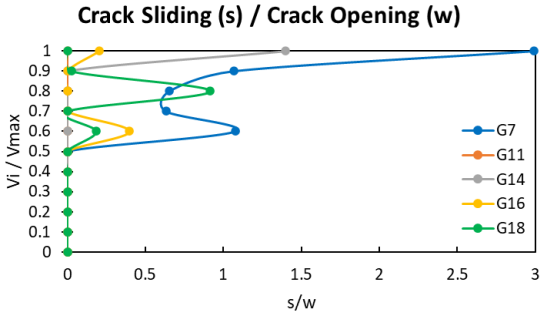

d) Crack sliding / crack opening

Figure 4-45 Crack kinematics for specimen BCJ 9.

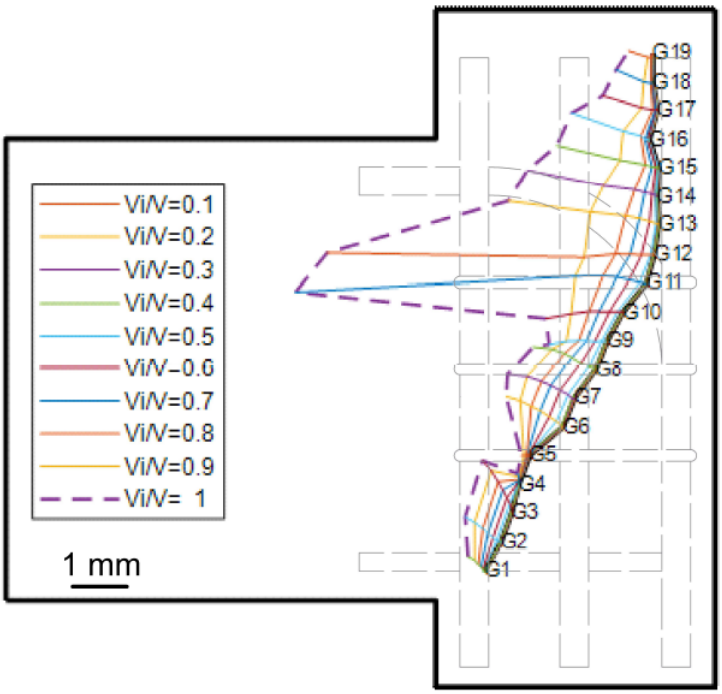

a) Crack kinematics

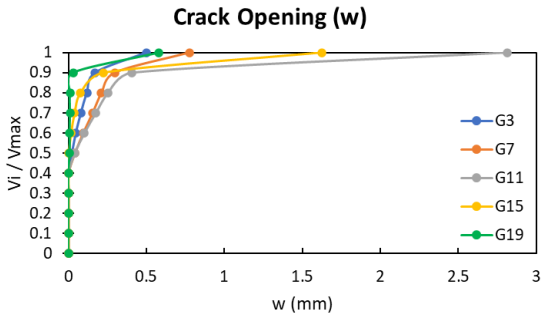

b) Crack opening

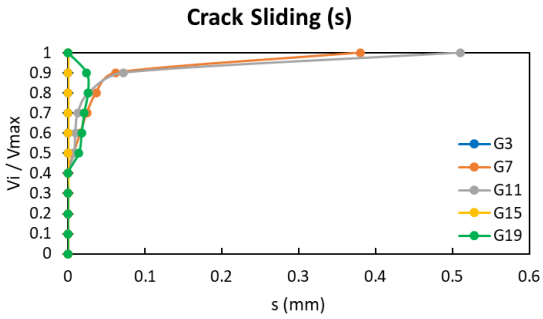

c) Crack sliding

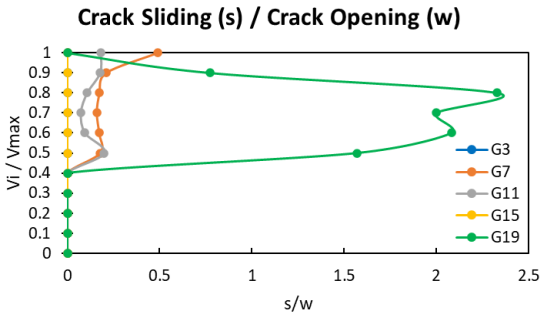

d) Crack sliding / crack opening

Figure 4-46 Crack kinematics for specimen BCJ 10.

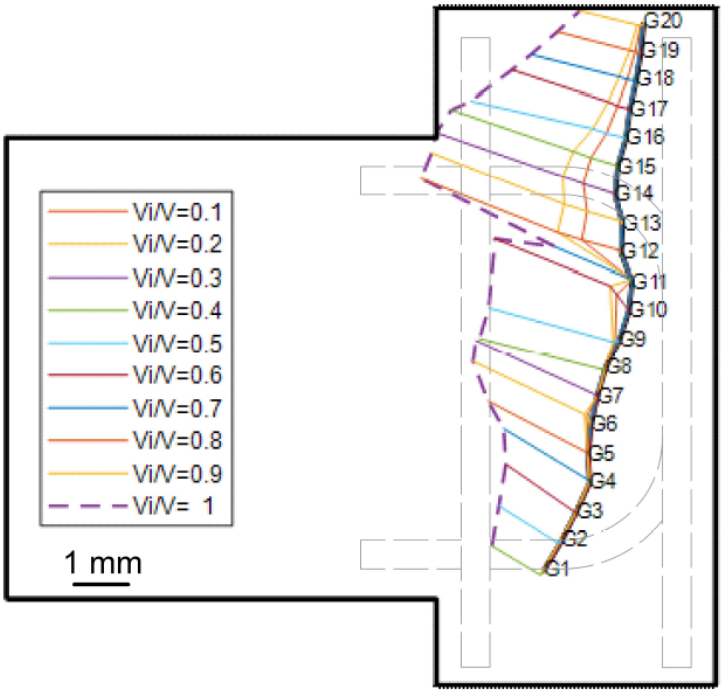

a) Crack kinematics

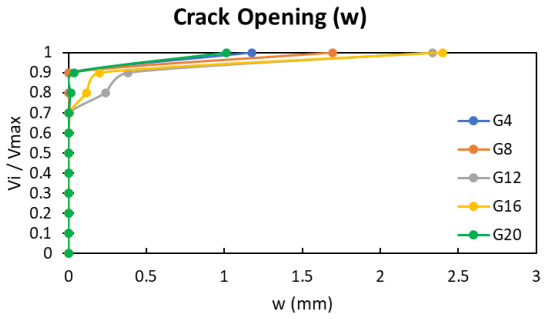

b) Crack opening

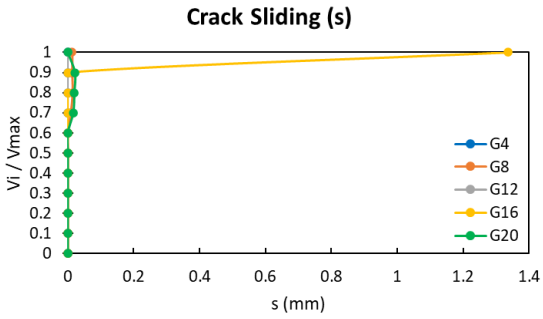

c) Crack sliding

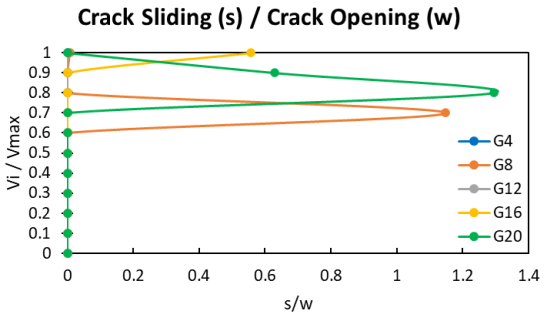

d) Crack sliding / crack opening

Figure 4-47 Crack kinematics for specimen BCJ 11.

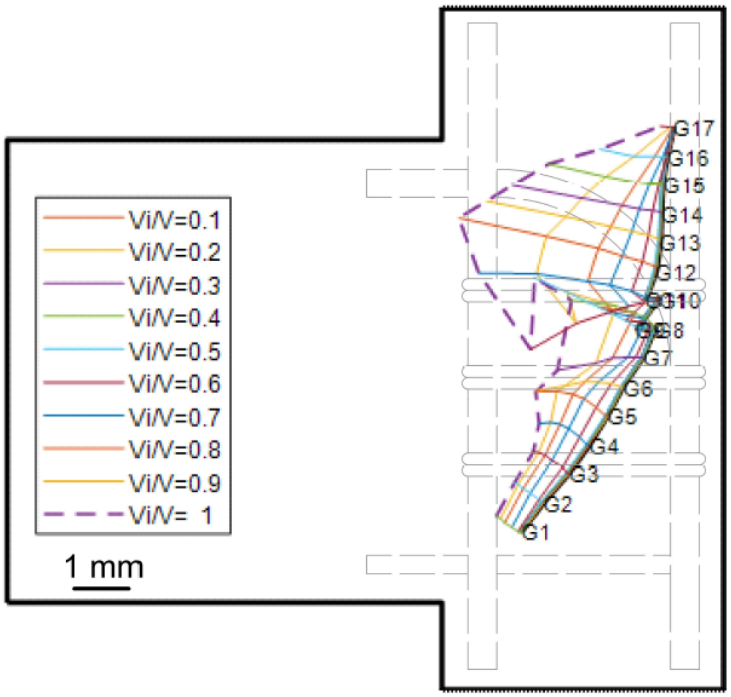

a) Crack kinematics

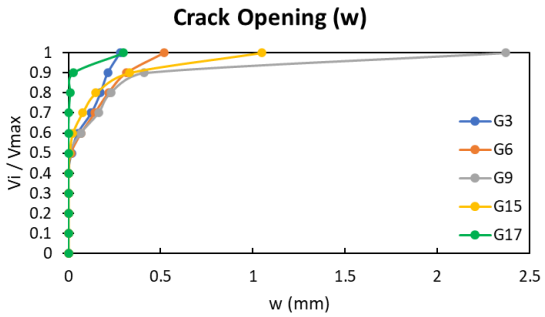

b) Crack opening

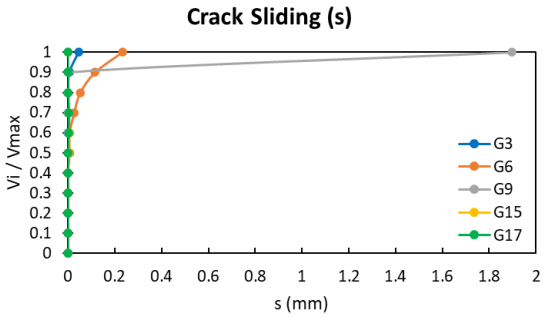

c) Crack sliding

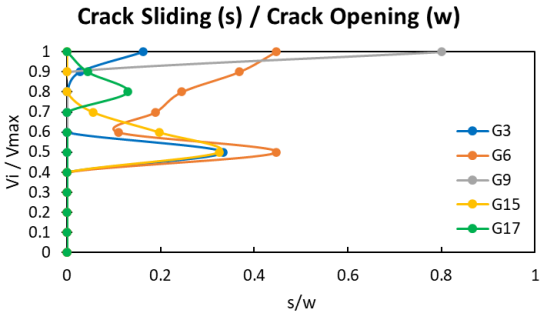

d) Crack sliding / crack opening

Figure 4-48 Crack kinematics for specimen BCJ 12.

4.4.5 Reinforcement strains

The column bars, beam anchorage bars and joint stirrups were instrumented with strain gauges in each specimen in this series. The strain gauges were distributed at specific locations of reinforcements at positions near to joint boundaries and inside joint as shown in Figure 3-15 to Figure 3-22. Some specimens had broken gauges due to pouring the concrete in the moulds during casting process or faulty readings during test process.

In the inner column bar, a pair of strain gauges (SG 2 and SG 3) were used at the location of maximum moment in specimens (BCJ 9, BCJ 10 and BCJ 12), and single gauges were used in SG 1, SG 4 and SG 5. Specimen BCJ 11 had six strain gauges (SG 1 to SG 6) due to the absence of joint stirrups. Pair of strain gauges were used at joint top corner (SG 2 and SG 3) and joint bottom corner (SG 5 and SG 6) and the rest of gauges were single, as shown in Figure 3-15. The results of strain gauges in front column bars are shown in Figure 4-49. The strain readings from SG 3 looked dubious in specimen BCJ 12. In the back column bar, six strain gauges (SG 7 to SG 12) were used in specimen BCJ 11 and five strain gauges (SG 6 to SG 10) were installed in the other specimens. The results of strain gauges measurements are presented in Figure 4-51. Specimen BCJ 9 had broken strain gauges (SG 7 and SG 10) before testing the specimen. Faulty strain measurements were observed in specimen BCJ 10 (from SG 9). From these strain measurements, strain distributions were plotted along the front and back column bars at first crack load (represented by blue dotted line) and failure load (using blue dotted line) as shown in Figure 4-50 and Figure 4-52.

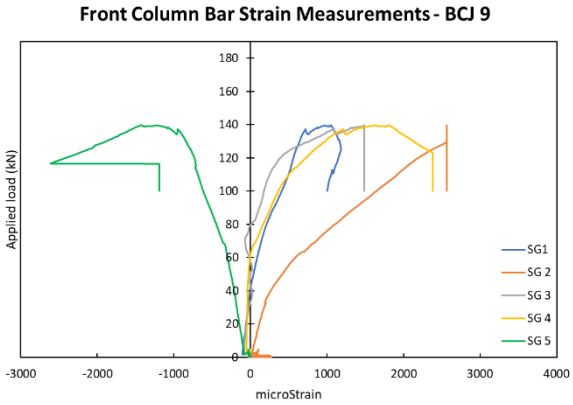

a) Strain gauge response for BCJ 9

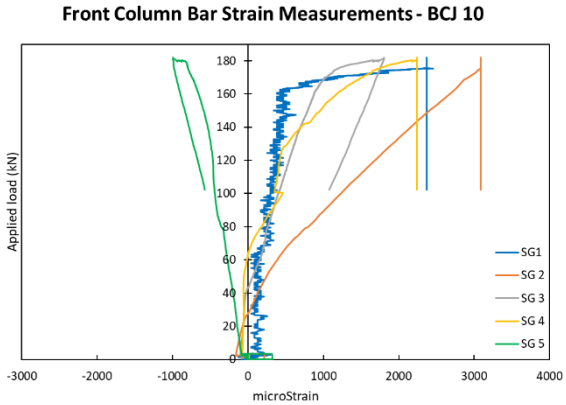

b) Strain gauge response for BCJ 10

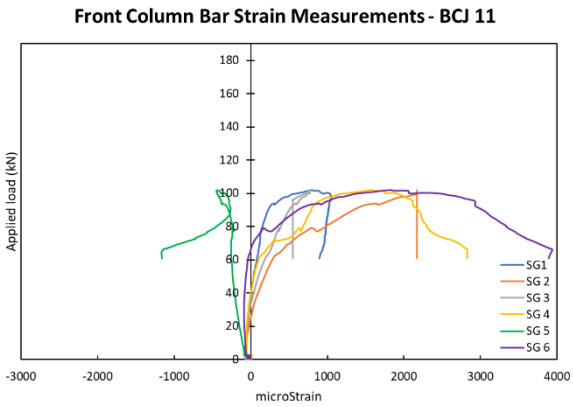

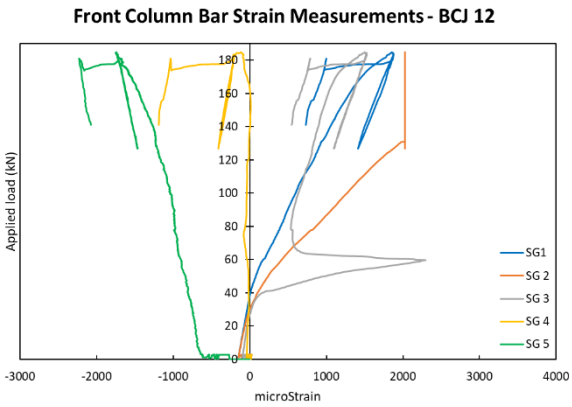

c) Strain gauge response for BCJ 11 d) Strain gauge response for BCJ 12

Figure 4-49 Front column bar strain measurements: (a) Specimen BCJ 9; (b) Specimen BCJ 10; (c) Specimen BCJ 11; (d) Specimen BCJ 12.

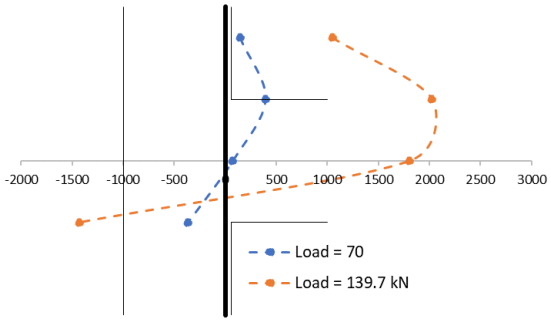

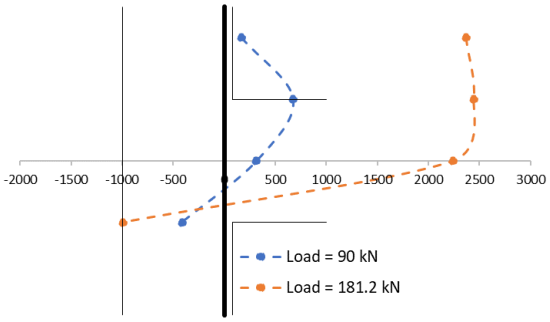

a) Strain distribution for BCJ 9 b) Strain distribution for BCJ 10

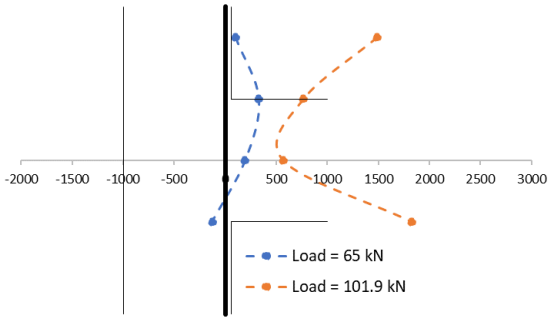

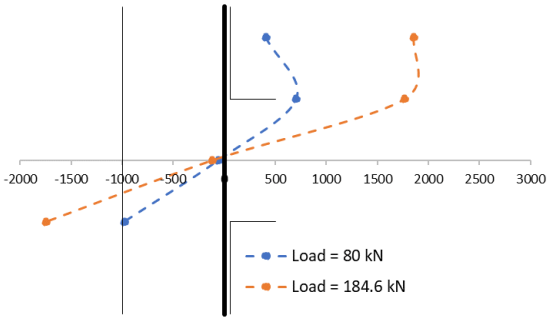

c) Strain distribution for BCJ 11 d) Strain distribution for BCJ 12

Figure 4-50 Front column bar strain distribution: (a) Specimen BCJ 9; (b) Specimen BCJ 10; (c) Specimen BCJ 11; (d) Specimen BCJ 12.

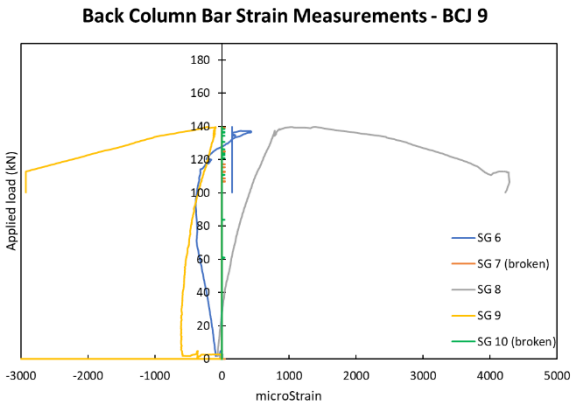

a) Strain gauge response for BCJ 9

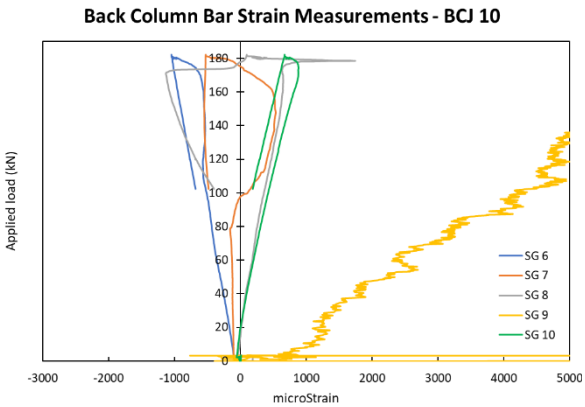

b) Strain gauge response for BCJ 10

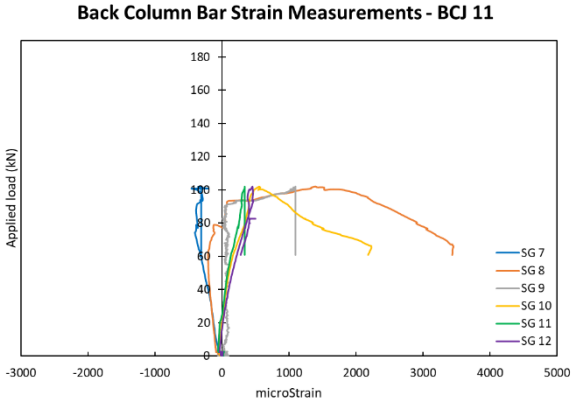

c) Strain gauge response for BCJ 11

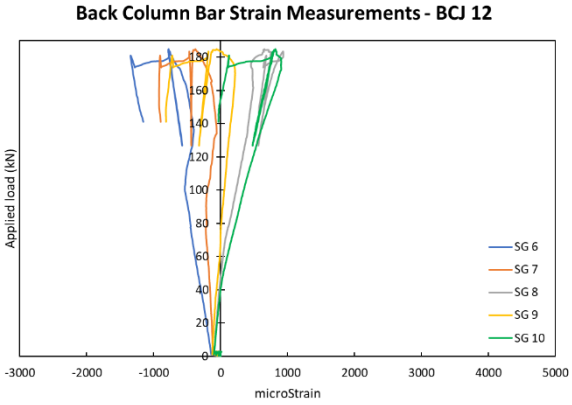

d) Strain gauge response for BCJ 12

Figure 4-51 Back column bar strain measurements: (a) Specimen BCJ 9; (b) Specimen BCJ 10; (c) Specimen BCJ 11; (d) Specimen BCJ 12.

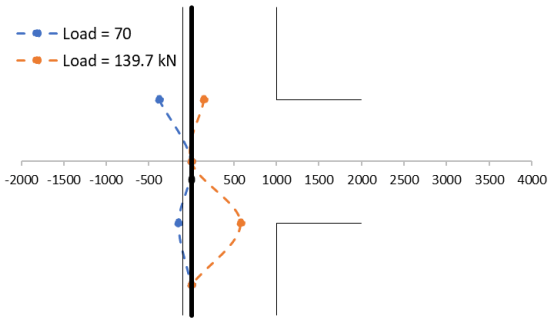

a) Strain distribution for BCJ 9

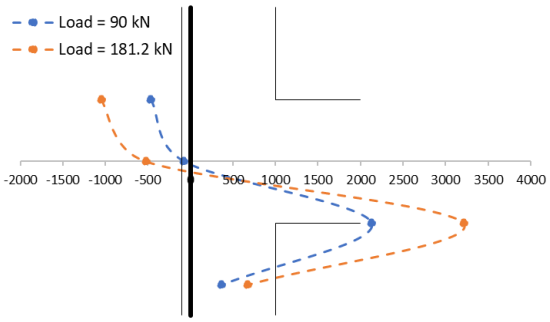

b) Strain distribution for BCJ 10

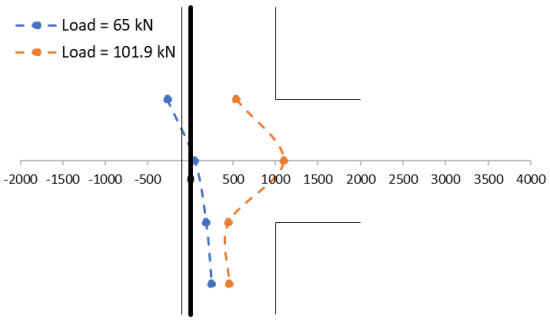

c) Strain distribution for BCJ 11

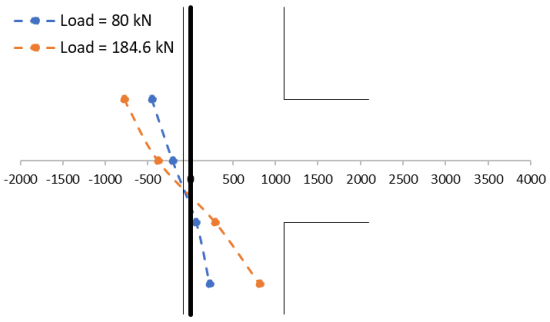

d) Strain distribution for BCJ 12

Figure 4-52 Back column bar strain distribution: (a) Specimen BCJ 9; (b) Specimen BCJ 10; (c) Specimen BCJ 11; (d) Specimen BCJ 12.

The strains in beam anchorage reinforcement were measured and the results are shown in Figure 4-53. The strain gauges' location and labels used in this series are shown in Figure 3-17 to Figure 3-20. Some broken strain gauges were found in all specimens: SG 13 and SG 15 in specimen BCJ 9, SG 12 in specimen 10, SG 14 in specimen BCJ 11 and SG 15 in specimen BCJ 12. These strain gauges were broken before testing the specimens. Some faulty strain gauges were also observed in specimen BCJ 9 (SG 14), BCJ 10 (SG 14), specimen BCJ 11 (SG 15) and specimen BCJ 12 (SG 13). Strain distributions were also plotted along the beam anchorage bar representing the first crack load and failure load. Strain distributions outside the bars represent tensile strains while inside the bars are for compressive strains, as shown in Figure 4-54.

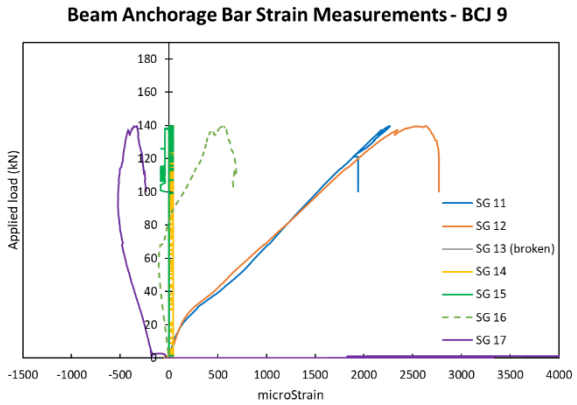

a) Strain gauge response for BCJ 9

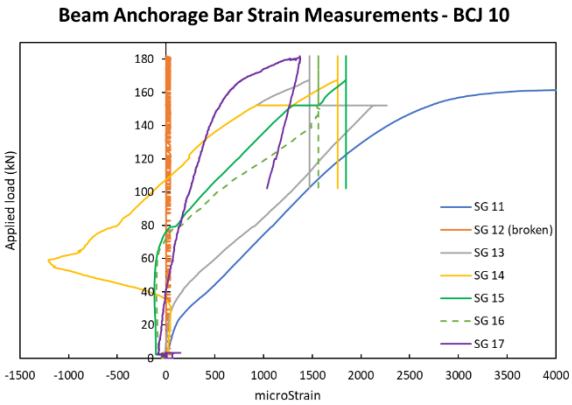

b) Strain gauge response for BCJ 10

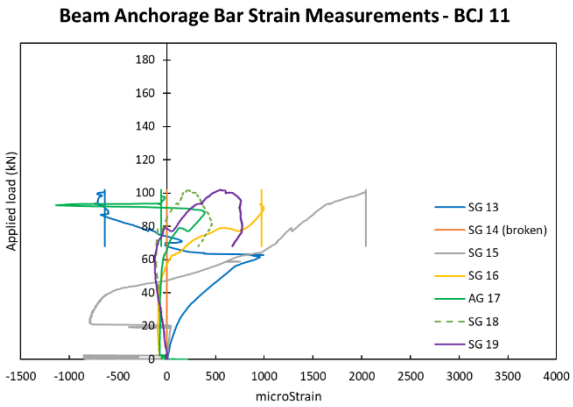

c) Strain gauge response for BCJ 11

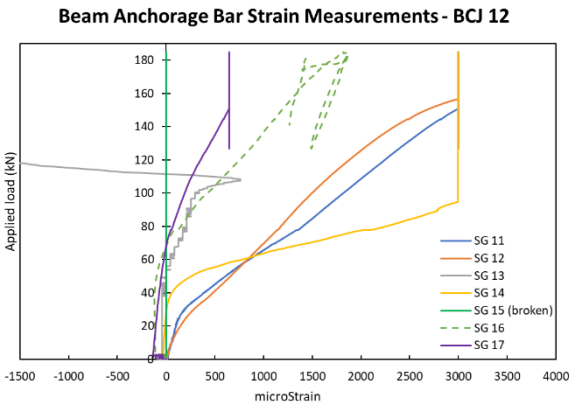

d) Strain gauge response for BCJ 12

Figure 4-53 Beam anchorage bar strain measurements(a) Specimen BCJ 9; (b) Specimen BCJ 10; (c) Specimen BCJ 11; (d) Specimen BCJ 12.

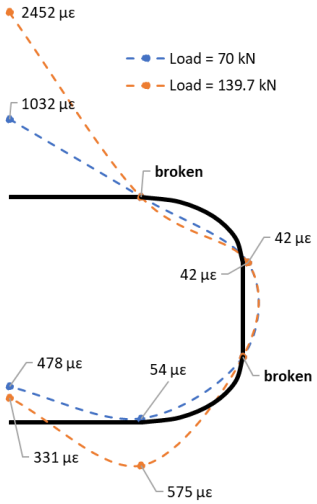

a) Strain distribution for BCJ 9

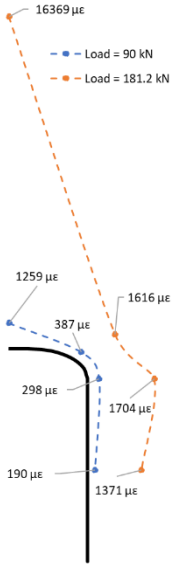

b) Strain distribution for BCJ 10

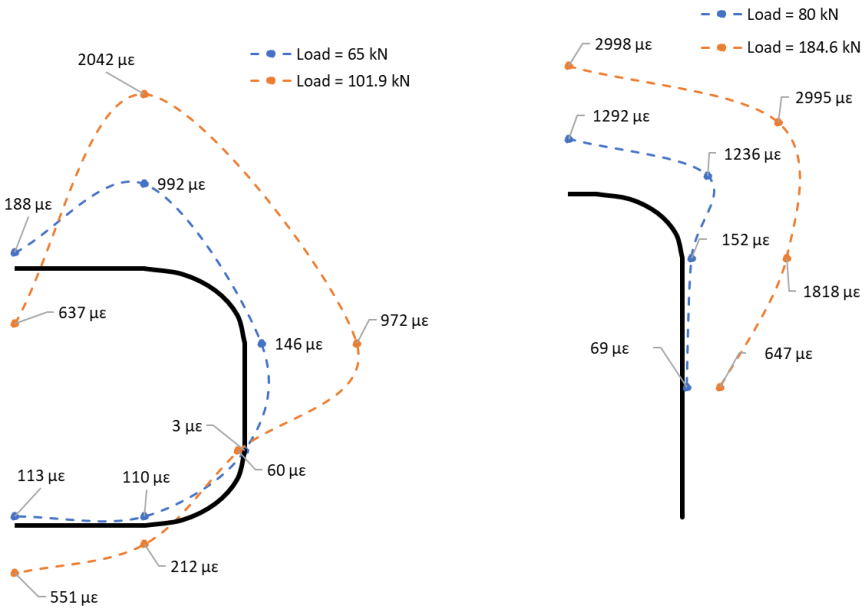

c) Strain distribution for BCJ 11 d) Strain distribution for BCJ 12

Figure 4-54 Beam anchorage bar strain distribution: (a) Specimen BCJ 9; (b) Specimen BCJ 10; (c) Specimen BCJ 11; (d) Specimen BCJ 12.

Strain gauges were placed on joint stirrups in each specimen, except for BCJ 11 without joint stirrup. The results of strain gauge measurements are shown in Figure 4-55. Only one broken strain gauge was found in specimen BCJ 12 (SG 19). Faulty strain gauges were also observed in specimen BCJ 10 (SG 20) and specimen 12 (SG 12 and SG 20). Unfortunately, none of the stirrup strain gauges in specimen BCJ 12 functioned. Thus, those strain gauges will not be used in chapter 7 (analysis of the results). For specimen BCJ 9, the strain gauges recorded large strain values at early stage of test, and hence are considered dubious.

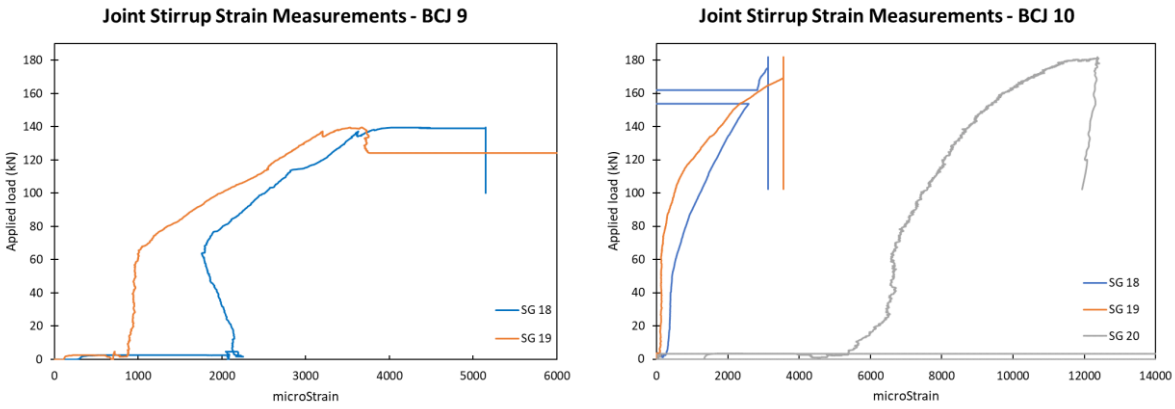

a) Strain gauge response for BCJ 9 b) Strain gauge response for BCJ 10

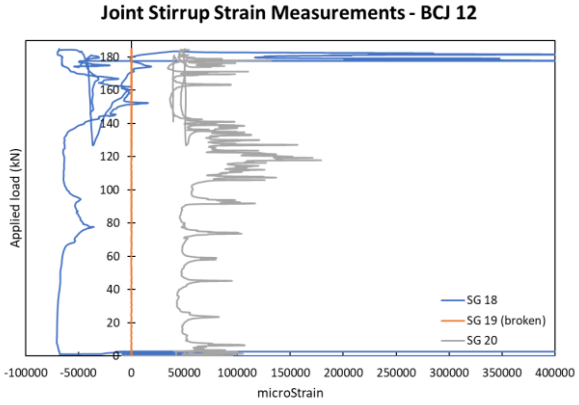

c) Strain gauge response for BCJ 12

Figure 4-55 Joint shear reinforcement strain measurements: (a) Specimen BCJ 9; (b) Specimen BCJ 10; (c) Specimen BCJ 11; (d) Specimen BCJ 12.

4.5 Conclusion

Twelve beam-column joint specimens were fabricated and tested in *the Heavy Structures Laboratory at Imperial College London*. The specimens were grouped into three series: series 1 was designed to study the effect of anchorage type and anchorage bend radius, series 2 studied the influence of column axial load on joint strength and series 3 investigated the presence and absence of joint stirrups as well as the use of intermediate column bars.

The three series were cast with ready-mixed having a Consistency Class S3 with a strength class of C30/37 and coarse aggregate of maximum size 10 mm. Forty-two control specimens, comprising cubes and cylinders, were cast to determine the compressive and tensile strength of concrete in each series. Eighteen cubes (100 x 100 x 100 mm), twelve cylinders (100 x 150 mm) and twelve cylinders (150 x 300 mm) were cast with each batch. Half the specimens were cured in water and the rest were cured in air.

The results of the BCJ tests are presented in terms of failure modes and crack patterns, load-deflection response, horizontal deflection recorded from LVDTs, joint and beam rotation measured using inclinometers, crack kinematics extracted from DIC technique and strain values in reinforcements.

Unfortunately, specimen BCJ 7 of series 2 failed during application of the upper column load due to a testing rig malfunction. This specimen was replaced with a new specimen cast from

laboratory batched concrete having a nominal strength of C40/50 subsequent to casting series 3.

Series 1 provides information on the influence of beam reinforcement anchorage type on joint behaviour. L-anchorage type enhanced the joint shear strength considerably when compared to U-anchorage type. Use of a large radius bend increased the joint strength of specimens with L-bars but not U-bars where the best results were obtained with standard bend radius.

Series 2 studied the effect of column axial load on joint strength. Increasing the column load from 300 kN to 900 kN increased the load at first diagonal cracking but had minimal influence on joint shear strength in specimens with both one and three joint stirrups. As expected, joint shear strength increased with increasing number of joint stirrups.

Series 3 showed that the provision of intermediate column bars significantly increased joint shear strength and changed the failure mode from joint shear to beam flexure. Doubling the joint shear reinforcement from three to six joint stirrups, without intermediate column bars, significantly improved the joint response and changed the failure mode from joint shear to flexure.

Chapter 5 NON-LINEAR FINITE ELEMENT (NLFE) METHODOLOGY

This chapter comprises three parts. The first part describes the constitutive models and solution procedures adopted in the analyses carried out in this thesis. Secondly, 2D and 3D modelling procedures are developed for external beam-column joints on the basis of sensitivity studies. Finally, the adopted modelling procedure is used to model the beam-column joints tested in this program as well as those of Ortiz [12]. The 3D modelling procedure is shown to predict the experimentally observed response well.

5.1 Introduction

An objective of this research is to simulate the response of external reinforced concrete beam-column joints using NLFEA. The commercial software package ATENA-Gid [57] was used for nonlinear finite element analysis. In ATENA, model development was carried out with Gid v11.0.8 while analysis and post-processing was carried out in ATENA Studio v5.0.3.

The finite element model was calibrated in a sensitivity study focussed on specimen BCJ 11 from this program. The study investigated the sensitivity of the predicted response to the element size and the input parameters adopted in the modelling of concrete and bond slip. Both 2D and 3D NLFEA models were studied. The parametric studies considered the effects of:

- Concrete compressive strength.
- Column axial load.
- Beam anchorage reinforcement: bend radius and anchorage type.
- Joint shear reinforcement.
- Column intermediate bars.

5.2 Background to nonlinear finite element analysis

The following sections describe the adopted concrete constitutive models, finite element type, and solution methods for both 2D and 3D analysis.

5.2.1 Concrete material modelling

For 2D modelling, the concrete constitutive model used in ATENA is depicted “SBETA”. The model is a plane stress model. A smeared approach is adopted for modelling cracks and

distributed reinforcement. The constitutive model is based on stiffness and is described by the following equation:

$$s = De, s = \{\sigma_x, \sigma_y, \tau_{xy}\}^T, e = \{\varepsilon_x, \varepsilon_y, \gamma_{xy}\}^T \quad (5\text{-}1)$$

Where s is a stress vector, D is a material stiffness matrix and e is a strain vector. The stress components of plane stress state and strain components represent the stress and strain vectors as shown in Figure 5-1. The definition of the material stiffness matrix depends on whether the concrete is uncracked concrete (isotropic material) or cracked (orthotropic material). The material stiffness matrix for the isotropic material is defined as shown in equation (5-1a). When the concrete is cracked, ATENA defines the material stiffness matrix as for an orthotropic material. The matrix is obtained based on a coordinate system which is coincident with the crack direction (either fixed or rotated crack). The formulation of this matrix is expressed in equation (5-1b). The Poisson's ratios (υ) is eliminated in the orthotropic material and a symmetry relation ($\upsilon_{12}E_2 = \upsilon_{21}E_1$) is used instead by assuming $\upsilon_{21} = \upsilon$ for isotropic material and $\upsilon_{12} = (E_1/E_2)\upsilon$ for orthotropic material. The total material stiffness matrix is then formulated as the sum of material stiffness of concrete and smeared reinforcement ($D = D_c + \sum_{i=1}^{n} D_{si}$), where D_{si} can be determined using equation (5-1c). The parameter p_i is the reinforcement ratio and defined as $p_i = (A_S/A_c)$. The elastic modulus of concrete is defined as E_1 and E_2 while the elastic modulus of reinforcement represents E_{si}. The angle β_i is determined between the x-axis and reinforcement direction.

$$D_c = \frac{E}{1-\upsilon^2}\begin{bmatrix} 1 & \upsilon & 0 \\ \upsilon & 1 & 0 \\ 0 & 0 & \dfrac{1-\upsilon}{2} \end{bmatrix} \quad (5\text{-}1a)$$

$$\begin{Bmatrix} \varepsilon_1 \\ \varepsilon_2 \\ \gamma \end{Bmatrix} = \begin{bmatrix} \dfrac{1}{E_1} & -\dfrac{\upsilon_{21}}{E_2} & 0 \\ -\dfrac{\upsilon_{12}}{E_1} & \dfrac{1}{E_2} & 0 \\ 0 & 0 & \dfrac{1}{G} \end{bmatrix} \begin{Bmatrix} \sigma_1 \\ \sigma_2 \\ \tau \end{Bmatrix} \quad (5\text{-}1b)$$

$$D_{si} = p_i E_{si} \begin{bmatrix} \cos(\beta_i)^4 & \cos(\beta_i)^2 \sin(\beta_i)^2 & \cos(\beta_i)^3 \sin(\beta_i) \\ \cos(\beta_i)^2 \sin(\beta_i)^2 & \sin(\beta_i)^4 & \cos(\beta_i) \sin(\beta_i)^3 \\ \cos(\beta_i)^3 \sin(\beta_i) & \cos(\beta_i) \sin(\beta_i)^3 & \cos(\beta_i)^2 \sin(\beta_i)^2 \end{bmatrix} \quad (5\text{-}1c)$$

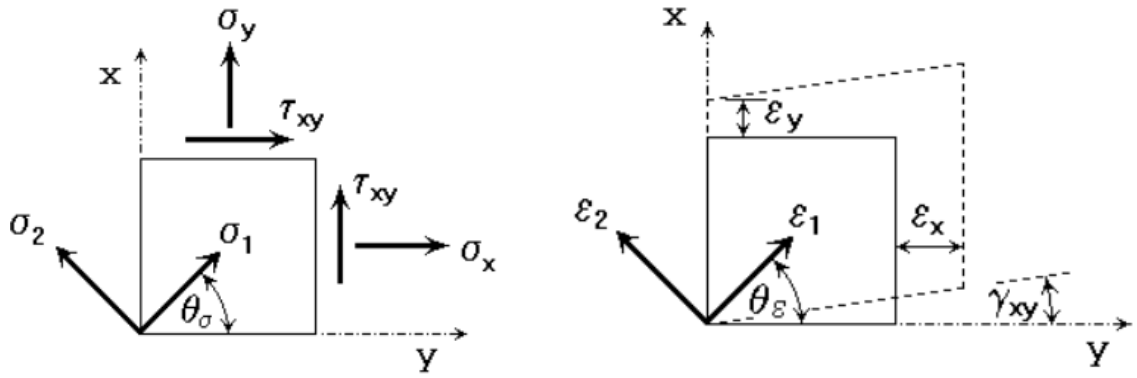

a) Components of plane stress state b) Components of strain state

Figure 5-1 Components of stress and strain state; reproduced from [58].

For 3D analysis, ATENA provides several concrete models of which "CC3D Nonlinear Cementitious2" is used in this research. This model combines tensile (fracturing) and compressive (plastic) behaviour. A mapping algorithm is used for integration of constitutive equations. This allows the combination of constitutive model (fracture and plastic) to be formulated separately. The model is able to simulate cracking and crushing of concrete under high confinement.

5.2.1.1 Compressive behaviour

2D NLFEA model:

The ascending and descending branches of concrete compressive behaviour are formulated separately in "SBETA". The ascending branch is formulated using equation 5-2 below from CEB-FIP Model Code 90 [35]. The stress-strain relationship, which is illustrated in in Figure 5-2, is appropriate for normal and high strength concrete.

$$\sigma_c^{ef} = f_c'^{ef} \frac{kx - x^2}{1 + (k-2)x} \, , x = \frac{\varepsilon}{\varepsilon_c} \, , k = \frac{E_0}{E_c} \, , E_c = \frac{f_c'^{ef}}{\varepsilon_c} \qquad (5\text{-}2)$$

Where σ_c^{ef} is the concrete compressive stress, $f_c'^{ef}$ is concrete effective compressive strength, k is shape parameter, x is normalized strain, ε is strain, ε_c is strain at peak stress, E_0 is the initial elastic modulus and E_c is the secant elastic modulus at peak stress.

The descending branch is defined using the fictitious compression plane model. In this model, the compressive stress is assumed to reduce linearly from the peak stress to zero at a plastic displacement (w_d). The model is based on tests carried out by Van Mier [59].

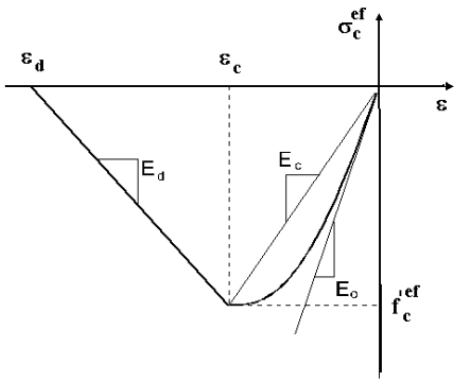

Figure 5-2 compressive stress-strain curve; reproduced from [58].

As shown in Figure 5-3, concrete compression failure is localized in a plane normal to the compressive principal stress direction. The softening part of the stress-strain relationship is determined from two points: the peak stress of the curve and the compressive strain ε_d at zero stress (end of curve). The compressive strain ε_d is calculated in terms of the plastic displacement (w_d) and a band size L_d as follows:

$$\varepsilon_d = \varepsilon_c + \frac{w_d}{L_d} \tag{5-3}$$

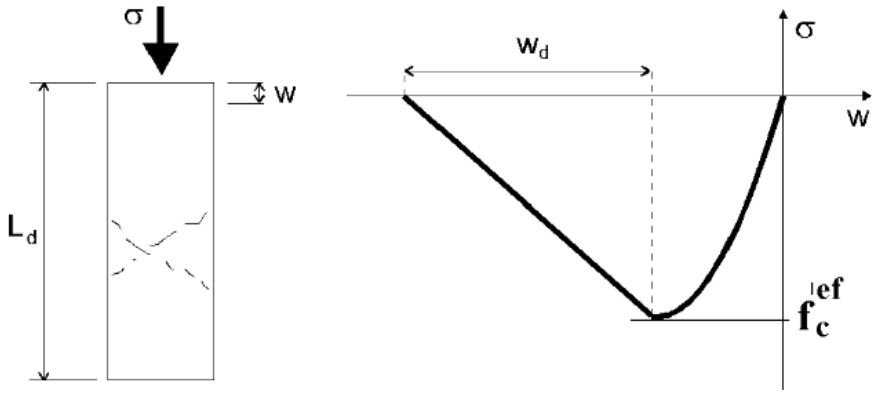

Figure 5-3 Softening displacement law in compression; reproduced from [58].

SBETA utilizes the biaxial stress failure criterion of Kupfer et al. [60] as shown in Figure 5-4. In the compression-compression stress state, the assumption of a proportional stress path is used to predict the strength of concrete and the failure criterion can be determined from the following equation:

$$f_c^{'ef} = \frac{1 + 3.65a}{(1+a)^2} f_c' \, , a = \frac{\sigma_{c1}}{\sigma_{c2}} \tag{5-4}$$

Where σ_{c1} and σ_{c2} are the principal stresses in concrete and f_c' is the uniaxial cylinder strength. In the tension-compression stress state, the failure criterion extends linearly from point $\sigma_{c1} = 0$ and $\sigma_{c2} = f_c'$ into the tension-compression stress region having linearly decreasing strength. This failure criterion can be determined using the following equation:

$$f_c'^{ef} = f_c' r_{ec}\,,\; r_{ec} = (1 + 5.3278\frac{\sigma_{c1}}{f_c'})\,,\; 1.0 \geq r_{ec} \geq 0.9 \qquad (5\text{-}5)$$

Where r_{ec} is the reduction factor of the compressive strength in the principal direction 2 due to tensile stress in the principal direction 1.

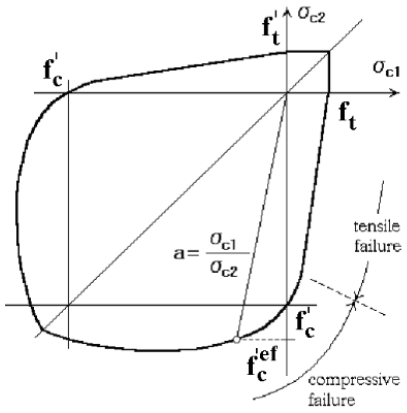

Figure 5-4 Biaxial failure function for concrete in 2D model; reproduced from [58].

3D NLFEA model:

The "CC3D Nonlinear Cementitious2" model was adopted for 3D modelling of concrete. The models utilises the Menetrey-William failure surface [61] for concrete under triaxial stress. The model is defined in terms of the hydrostatic stress (ξ_s), deviatoric stress (ρ_s) and deviatoric polar angle (θ_s). The compression failure criterion in "CC3D Nonlinear Cementitious2" model combines plasticity for concrete crushing with a fracture model for concrete cracking. The failure criterion is defined as follows:

$$F(\xi_s, \rho_s, \theta_s) = \left[\sqrt{1.5}\frac{\rho_s}{f_c}\right]^2 + m\left[\frac{\rho_s}{\sqrt{6}f_c} r(\theta_s, \mathrm{e}) + \frac{\xi}{\sqrt{3}f_c}\right] - c = 0 \qquad (5\text{-}6)$$

Where,

$$r(\theta_s, \mathrm{e}) = \frac{4(1-\mathrm{e}^2)cos^2\theta_s + (2\mathrm{e}-1)^2}{2(1-\mathrm{e}^2)cos\theta_s + (2\mathrm{e}-1)[4(1-\mathrm{e}^2)cos^2\theta_s + 5\mathrm{e}^2 - 4\mathrm{e}]^{\frac{1}{2}}} \qquad (5\text{-}7)$$

$$m = 3\left[\left(\frac{f_c^2 - f_t^2}{f_c\, f_t}\right)\left(\frac{\mathrm{e}}{\mathrm{e}+1}\right)\right] \qquad (5\text{-}8)$$

The parameters (ξ_s, ρ_s, θ_s) in equation (5-6) are Heigh-Vestergaard coordinates representing the failure surface for concrete. The main parameters in equation (5-6) are the concrete compressive strength (f_c), concrete tensile strength (f_t) and the eccentricity (e) which describes the out-of-roundness of the failure surface. The eccentricity lies between 0.5 (for sharp corners) and 1.0 (for a circular failure surface), as shown in Figure 5-5. Hardening-softening is controlled by the parameter (c), given by equation (5-9).

$$c = (\frac{f_c(\mathcal{E}_{eq}^p)}{f_c})^2 \tag{5-9}$$

The expression $f_c(\mathcal{E}_{eq}^p)$ represents the hardening-softening law defined by equation (5-10). The behaviour of uniaxial stress-strain law is described by an elliptical and linear curve as shown in Figure 5-6(a). The ascending branch is obtained by the following equation:

$$\sigma = f_{co} + (f_c - f_{co})\sqrt{1 - (\frac{\mathcal{E}_c - \mathcal{E}_{eq}^p}{\mathcal{E}_c})^2} \tag{5-10}$$

Where f_{co} is the onset of the non-linear behaviour and $\mathcal{E}_c$ is the strain at peak concrete compressive strength (f_c). For concrete softening, the descending branch in Figure 5-6(b) is defined as a linear curve based on displacement (w_d) to express the energy required for crushing. Based on the experimental work of Van Mier [59], the recommended value of w_d is 0.5 mm for normal concrete.

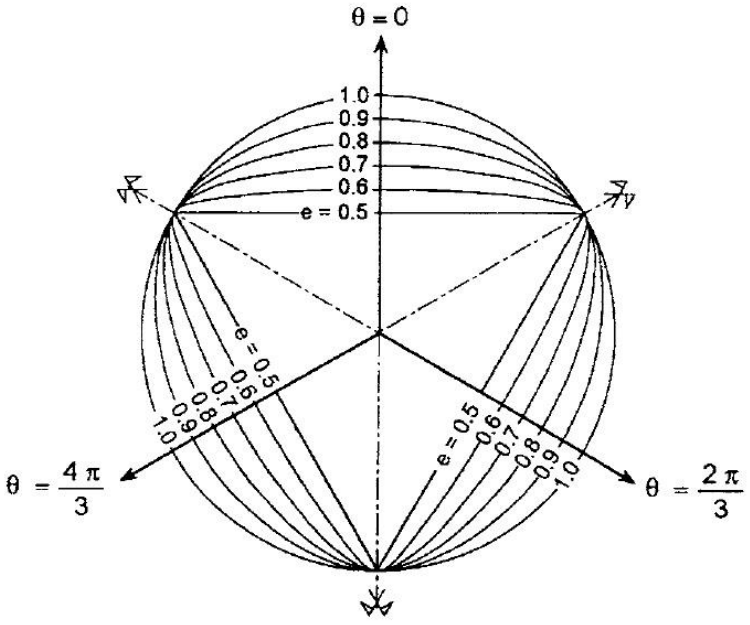

Figure 5-5 Elliptic function; reproduced from [61].

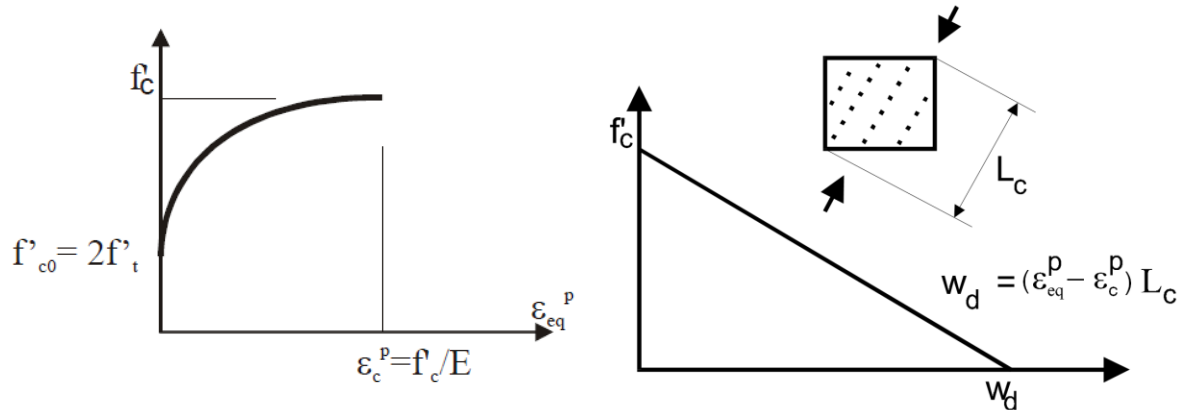

a) Compressive hardening b) Softening branch

Figure 5-6 Compressive hardening/softening and compressive characteristic length; reproduced from [58].

5.2.1.2 Tensile behaviour

The tensile fracture process of crack formation comprises three stages. Concrete is uncracked in the first phase. Cracking occurs when the tensile stress reaches the concrete tensile strength and a "process zone" develops. In this stage, the tensile stress on the crack face reduces progressively to zero with increasing crack width. Finally, the tensile stress is released completely, and crack opening continues without presence of tensile stress. These stages are presented in Figure 5-7.

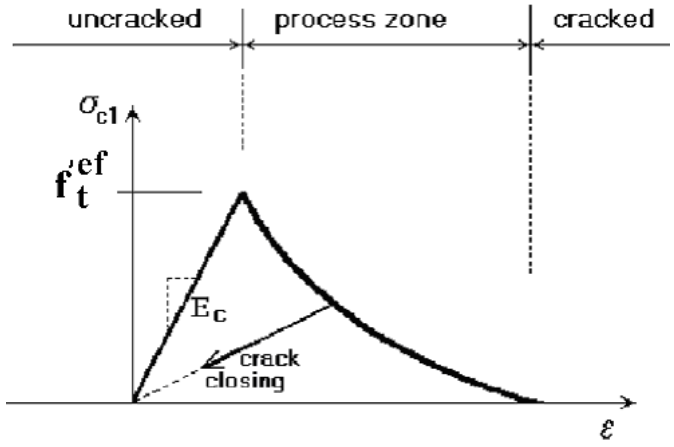

Figure 5-7 Stages of crack opening; reproduced from [58].

2D NLFEA model:

Before cracking, the response is assumed to be linear elastic and stress is calculated using equation (5-11) in which E_c depicts the elastic modulus of concrete, $f_t^{'ef}$ is the maximum effective tensile strength and ε^{eq} is the tensile strain at the effective tensile stress (σ_c^{ef}). After cracking, the process of crack opening requires an amount of energy to be absorbed

while the crack transmit tensile stress. This energy is depicted as the fracture energy (G_f) and equals the amount of energy absorbed per unit area during the fracture process as illustrated in Figure 5-8. Based on the model of Hordijk [62], the tensile softening response is calculated using equation (5-12).

$$\sigma_c^{ef} = E_c\, \varepsilon^{eq}\ ,\ 0 \le \sigma_c' \le f_t'^{ef} \tag{5-11}$$

$$\frac{\sigma_c'}{f_t'^{ef}} = \left\{1 + (c_1 \frac{w_t}{w_{tc}})^3\right\} \exp\left(-c_2 \frac{w_t}{w_{tc}}\right) - \frac{w_t}{w_{tc}}(1 + c_1^3)\exp\,(-c_2) \tag{5-12}$$

Where,

$$w_t = \varepsilon^f L_t,\ \ w_{tc} = 5.14 \frac{G_f}{f_t'^{ef}},\quad c_1 = 3,\quad c_2 = 6.93 \tag{5-13}$$

$f_t'^{ef}$ is the effective tensile strength of concrete and σ_c' is the stress perpendicular to the crack. w_t is used to determine the crack opening displacement calculated from total value of fracturing strain perpendicular to the crack. ε^f represents the inelastic cracking strains and L_t is the characteristic length. w_{tc} is considered as the crack opening at the end of the tensile fracture process. c_1 and c_2 are constants.

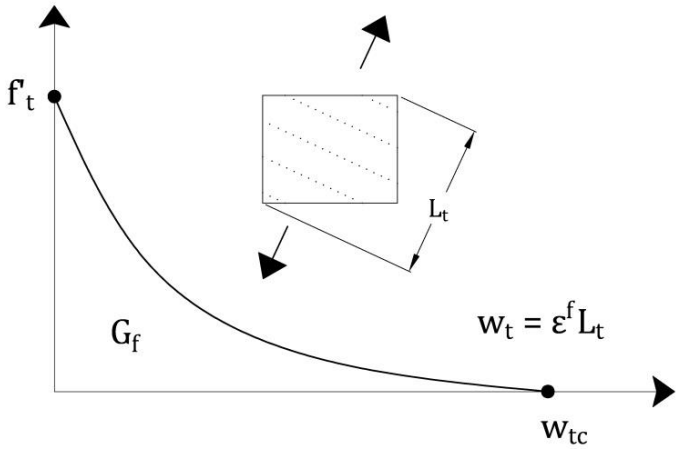

Figure 5-8 Tensile softening and characteristic length; reproduced from [58].

3D NLFEA model:

A similar procedure is used in 3D models to SBETA, but tensile strain is related to the crack band size and crush band size (L_t and L_C) as illustrated in Figure 5-9. The strain value used to obtain the tensile strength is calculated using the following equation:

$$\tilde{\varepsilon}_1^f = \varepsilon_1^f, \text{ if } \varepsilon_1^f < \varepsilon_{loc}^f$$
$$\tilde{\varepsilon}_1^f = \varepsilon_{loc}^f + (\varepsilon_1^f - \varepsilon_{loc}^f)\frac{L_t}{L_c} \text{ if } \varepsilon_1^f \geq \varepsilon_{loc}^f \quad (5\text{-}14)$$

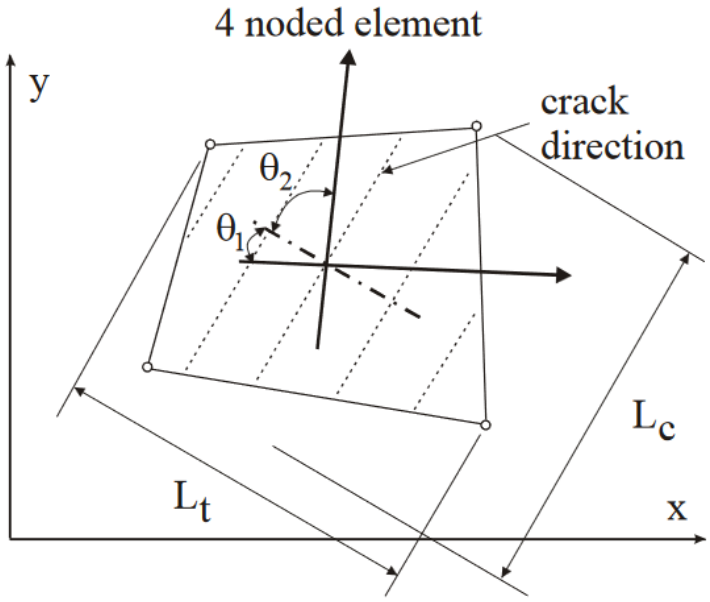

Figure 5-9 Definition of localization bands for L_t and L_C; reproduced from [58].

5.2.1.3 Interaction of tensile and compressive behaviour

2D NLFEA model:

The concrete compressive strength is reduced when cracking occurs in the perpendicular direction in accordance with the recommendations of the Modified Compression Field Theory (Vecchio and Collins [63]). In SBETA, this relationship is defined using the Gauss function which allows the user to adjust the maximum softening factor r_c between 1 and c, as shown in Figure 5-10, where c is the maximal strength reduction. The reduced concrete strength is defined as follows:

$$f_c'^{ef} = r_c f_c', r_c = c + (1-c)e^{-(128\varepsilon_u)^2} \quad (5\text{-}15)$$

Where $f_c'^{ef}$ is the reduced concrete strength and ε_u is the principal tensile strain in concrete in transverse direction.

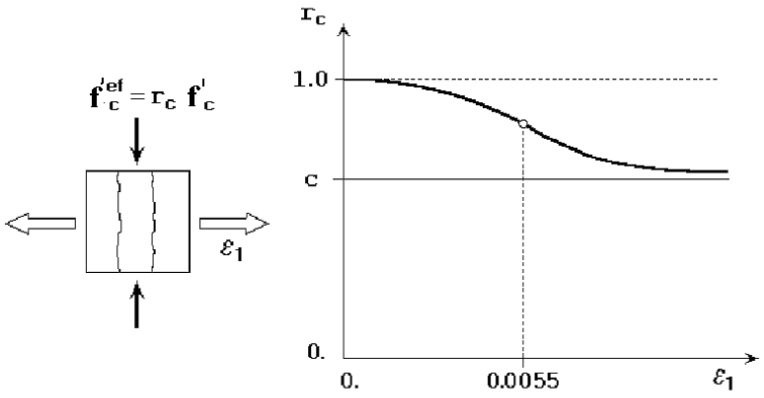

Figure 5-10 Compressive strength reduction of cracked concrete; reproduced from [58].

3D NLFEA model:

The reduction of concrete compressive strength is a function of a combination of plastic and fracture models. The interaction between these two models considers the reduction of tensile strength after concrete crushing (ε_1) and of compressive strength when cracking occurs (r_c). This interaction is similar to the interaction of tensile and compressive behaviour in SBETA. The reduction of compressive strength is calculated using the following equation proposed by Vecchio and Collins [63]:

$$f_c^{'ef} = r_c f_c' \, , r_c = \frac{1}{0.8+170\,\varepsilon_1} \, , r_c^{lim} \leq r_c \leq 1.0 \qquad (5\text{-}16)$$

5.2.1.4 Tension stiffening

2D NLFEA model:

In cracked reinforced concrete, the concrete between cracks contributes to the steel reinforcement stiffness in resisting the development of crack opening. ATENA simulates this mechanism, which is depicted tension stiffening, by limiting the residual concrete tensile stress after cracking to a multiple (c_{ts}) of the tensile strength as shown in Figure 5-11. The CEB-FIP Model Code [35] recommends a default value for c_{ts} equal to 0.4.

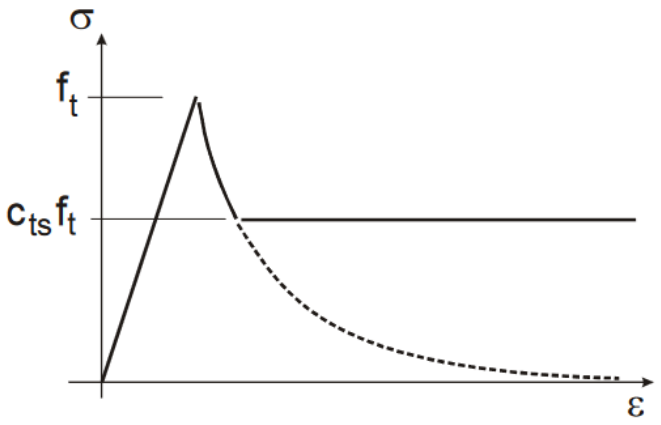

Figure 5-11 Tension stiffening factor in ATENA; reproduced from [58].

3D NLFEA model:

Similarly to SBETA, a factor (c_{ts}) is applied in 3D models to limit the residual tensile strength in concrete after cracking as shown in Figure 5-11.

5.2.1.5 Crack modelling

The dominant techniques used in NLFEA to model fracture process of concrete are the discrete and smeared crack approaches. The discrete crack model was first introduced by Ngo and Scordelis [64] who simulated the response of simply supported reinforced concrete beams under three-point loading. The discrete crack technique separates the concrete elements on either side of the crack when the crack forms. As the crack grows during loading, the node at the crack tip is split into two nodes when the nodal force at the crack tip reaches the maximum tensile strength of concrete. This causes the crack to propagate to the next node as shown in Figure 5-12. The main drawback of this method is the high computational cost and complexity of code required for the remeshing process (Cervera and Chiumenti [65]).

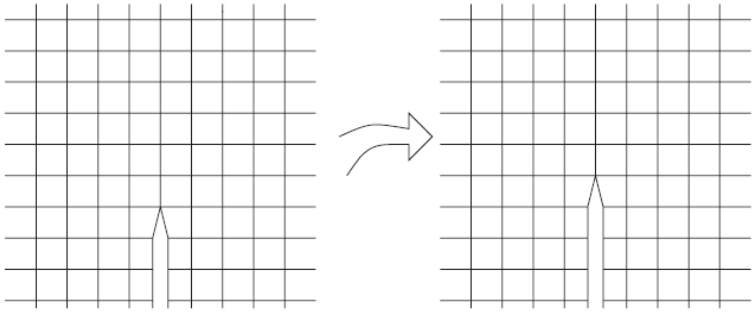

Figure 5-12 Discrete crack propagation; reproduced from [66].

The smeared crack approach was proposed initially by Rashid [67] for modelling cracks in prestressed concrete pressure vessels. The method is based on computational continuum

mechanics. The criteria for crack propagations rely upon failure criteria expressed in terms of stress or strain (Bažant and Planas [68]). The mechanical properties (stress and stiffness) are reduced when the tensile stress exceeds the tensile strain at sampling points. Cracks form as a number of failure planes distributed within an area or volume of an element. The smeared crack approach is widely accepted and is adopted in ATENA. The crack formation process in the smeared crack approach can be simulated with either a rotating crack or a fixed crack model.

2D NLFEA model:

Rotating crack model

The rotating crack model was introduced independently by Vecchio and Collins [63] and Crisfield et al. [69]. The main concept of this approach is that the direction of principal strain axes rotates in conjunction with the direction of principal stress axes. The rotating crack model avoids the need to consider shear stress on the crack face and depends only on principal stresses parallel and perpendicular to crack as shown in Figure 5-13. Consequently, the crack direction rotates simultaneously with the principal strain axes. To ensure the co-axiality of the principal strain axes with the material axes, the tangent shear modulus (G_t) is calculated according to Crisfield et al. [69] as follows:

$$G_t = \frac{\sigma_{c1} - \sigma_{c2}}{2(\varepsilon_1 - \varepsilon_2)} \tag{5-17}$$

where σ_{c1} and σ_{c2} are the principal stress in direction-1 and -2 while ε_1 and ε_2 are the principal strain in direction-1 and -2. Direction-1 is perpendicular to the crack and direction-2 is parallel to the crack plane as shown in Figure 5-13. An example of the application of this model is the Modified Compression Field Theory (Vecchio and Collins [63]), which adopts the concept of co-axiality.

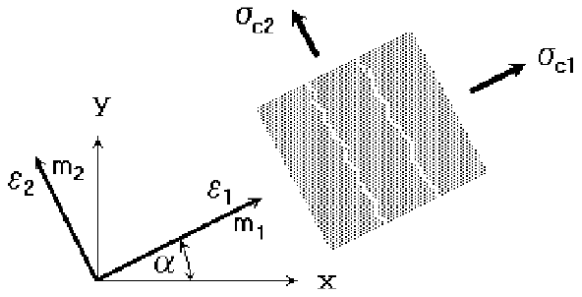

Figure 5-13 Rotating crack model and stress and strain law; reproduced from [58].

Fixed crack model

The direction of principal strain and stress coincide before cracking. After cracking, the concept of orthotropy is introduced. At the moment of crack initiation, the crack direction is obtained by the principal stress direction. As further loading is applied, the direction of the crack is fixed and represents the material axis of the orthotropy. Consequently, the principal strain axes rotate independently of the axes of orthotropy. This mechanism produces a shear stress on the crack plane as shown in Figure 5-14.

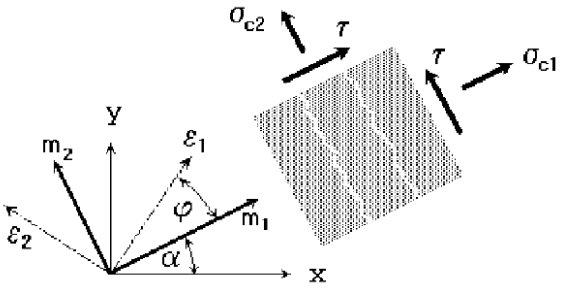

Figure 5-14 Fixed crack model and stress and strain state; reproduced from [58].

The shear modulus is reduced with increasing strain perpendicular to the crack (see Figure 5-15) using the approach of Kolmar [70]. The following equation is used to calculate the shear modulus:

$$G = r_g G_c \, , r_g = c_3 \frac{-\ln\left(\frac{1000\varepsilon_u}{c_1}\right)}{c_2} \text{ and } G_c = \frac{E_c}{2(1+v)} \tag{5-18}$$

Where.

$$c_1 = 7 + 333(p - 0.005), c_2 = 10 - 167(p - 0.005), 0 \leq p \leq 0.02 \tag{5-19}$$

r_g is the shear retention factor, G is the reduced shear modulus and G_c represents the initial concrete shear modulus, E_c is the initial elastic modulus, v is the Poisson's ratio and ε_u is the strain normal to the crack. c_1 and c_2 are defined in terms of the reinforcement ratio p crossing the crack direction, c_3 is scaling factor defined by the user (by default this parameter is equal to 1.0). The reinforcement ratio p includes all the reinforcement transformed normal to the crack plane.

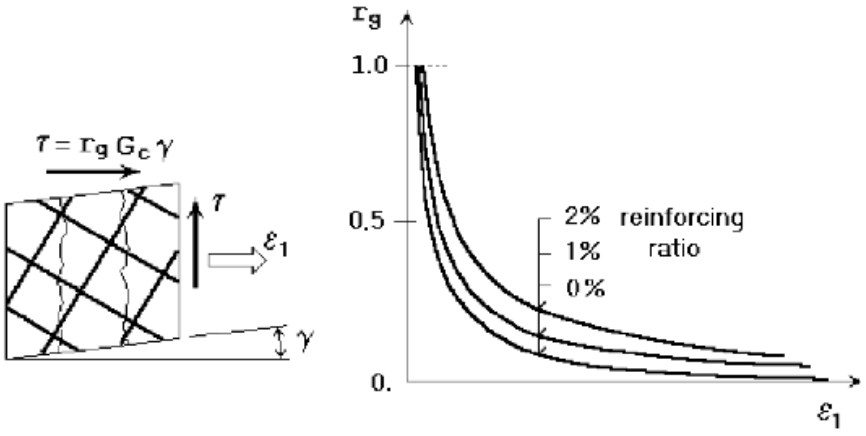

Figure 5-15 Shear retention factor; reproduced from [58].

3D NLFEA model:

Rotating crack model

Similarly to SBETA, CC3D Nonlinear Cementitious2 provides a rotated crack option in which the principal strain axes are coincident with the principal stress axes.

Fixed crack model

As in SBETA, the principal strain axes of the fixed crack model rotate independently of the axes of orthotropy after cracking occurs. The shear strength of cracked concrete is calculated in accordance with the Modified Compression Field of Vecchio and Collins [63] as follows:

$$v_{ci} = \frac{0.18\sqrt{f_c'}}{0.31 + \frac{24w}{a_g + 16}} \quad (5\text{-}20)$$

Where f_c' is the concrete compressive strength and w is the maximum crack width and a_g is the maximum aggregate size.

5.2.2 Reinforcement material modelling

Reinforcement can be modelled in ATENA as either smeared or discrete. Smeared reinforcement is uniformly distributed over an entire concrete element area for which an average stress-strain relationship is obtained for the composite material. Discrete reinforcement is modelled with 1-D truss elements in this research using embedded reinforcement. The technique links the nodes of the bar elements to the displacement of the underlying solid elements. Bond slip can be simulated with embedded reinforcement in both 2D and 3D models by inserting bond elements between the embedded bar elements and solid

elements. The “CCReinforcement" model is used for the constitutive relationships for both models (smeared and discrete approach), including same formulation of stress-strain relationship in all types of reinforcement. This model provides a bilinear or multi-linear law as shown in Figure 5-16. The multi-linear law comprises four stages allowing to model the steel behaviour in terms of elastic state, yield plateau, hardening and fracture. In default, ATENA considers the reinforcement bar as perfectly bonded to the adjacent solid element. If bond-slip model is required, the user can use any of the three types of bond-slip models including CEB-fib Model Code [35], slip law by Bigaj [71] and a user defined bond-slip law.

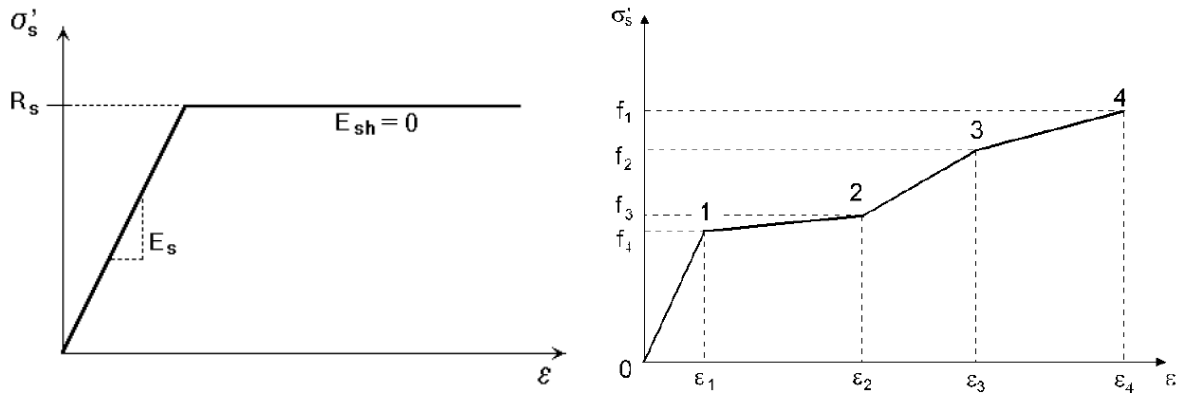

a) bilinear stress-strain law b) multi-linear stress-strain law

Figure 5-16 The stress-strain law for reinforcement; reproduced from [58].

In this research, the Bigaj model [71] was used due to the accuracy observed in simulating the modelled beam-column joints. Additionally, the Bigaj model has fewer options in ATENA than the other two models mentioned earlier. The bond quality, concrete cubic compressive strength and reinforcement bar radius are the main inputs in the Bigaj model which is illustrated in Figure 5-17. Points 1 to point 4 in Figure 5-17 are defined using Table 5-1, where the stress-slip relationship is related to the bond quality and concrete type.

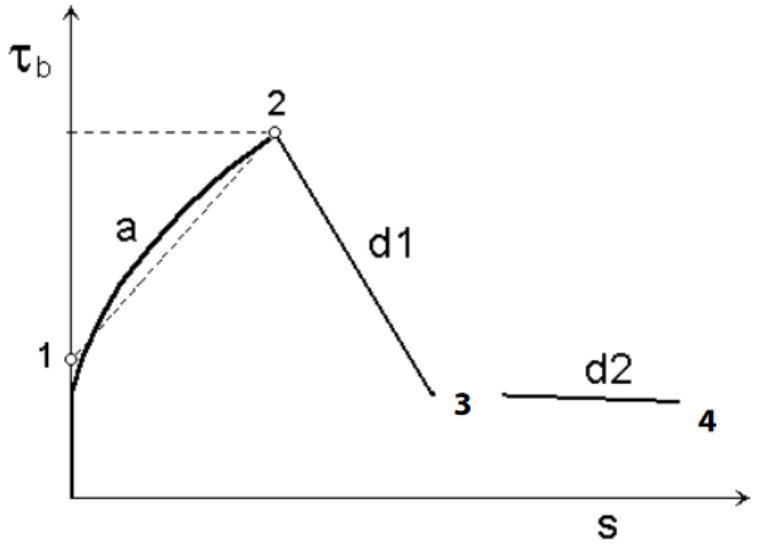

Figure 5-17 Bond law by BIGAJ [71]; reproduced from [58].

Table 5-1 Parameters for defining the bond strength-slip relationship for ribbed bars (ATENA manual [58]).

Concrete Type	Bond quality		Point 1	Point 2	Point 3	Point 4
$f_c^{'} < 60$	Excelent	s / D	0.000	0.020	0.044	0.480
		$\tau_b / \sqrt{0.8\, f_{cu}^{'}}$	0.500	3.000	0.700	0.000
	Good	s / D	0.000	0.030	0.047	0.480
		$\tau_b / \sqrt{0.8\, f_{cu}^{'}}$	0.500	2.000	0.700	0.000
	Bad	s / D	0.000	0.040	0.047	0.480
		$\tau_b / \sqrt{0.8\, f_{cu}^{'}}$	0.500	1.000	0.700	0.000
$f_c^{'} > 60$	Excelent	s / D	0.000	0.012	0.030	0.340
		$\tau_b / \sqrt{0.88\, f_{cu}^{'}}$	0.600	2.500	0.900	0.000
	Good	s / D	0.000	0.020	0.030	0.340
		$\tau_b / \sqrt{0.88\, f_{cu}^{'}}$	0.600	1.900	0.900	0.000
	Bad	s / D	0.000	0.025	0.030	0.340
		$\tau_b / \sqrt{0.88\, f_{cu}^{'}}$	0.600	1.100	0.900	0.000

5.2.3 Finite elements in ATENA

ATENA provides 2D plane stress elements, 3D solid elements and special elements (for modelling springs, external cables, and gaps). Isoparametric formulation with linear or quadratic interpolation functions is implemented in almost all elements in ATENA. The Gauss

integration scheme is used in most elements to integrate the element stiffness matrix. In this research, three types of elements were used. In 2D models, truss elements and 2D plane stress elements were used. 3D solid elements and truss elements were used in 3D models. Truss elements depicted “CCIsoTruss” (see Figure 5-18) were used for both 2D and 3D analyse in this research.

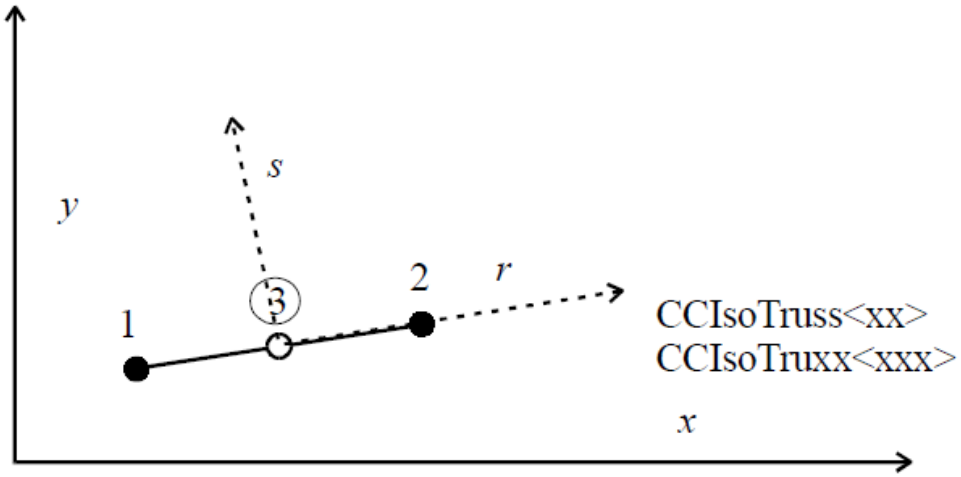

Figure 5-18 Geometry of CCIsoTruss elements; reproduced from [58].

Plane triangular elements and plane quadrilateral elements are available in ATENA. These are depicted “CCIsoTriangle” and “CCIsoQuad” respectively as presented in Figure 5-19(a). For 3D solid elements, two types of elements are provided in ATENA: tetrahedral elements “CCIsoTetra” and brick elements “CCIsoBrick” as shown in Figure 5-19(b). ATENA also provides a 3D solid wedge element depicted “CCIsoWedge”, but this was not used in the current research.

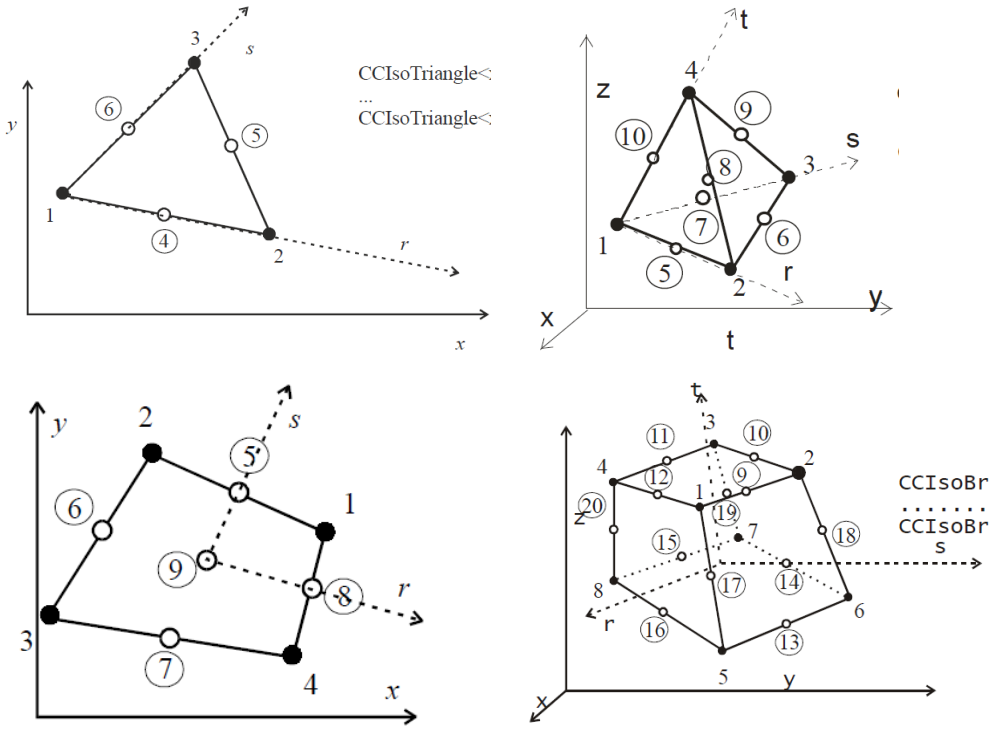

a) 2D plane elements b) 3D solid elements

Figure 5-19 Geometry of 2D plane and 3D solid elements; reproduced from [58].

5.2.4 Iterative solution methods

Several methods are available in ATENA for solving non-linear equations. These methods are based on the concept of incremental step by step analysis. The main iterative solution methods used in ATENA are Full Newton-Raphson, Modified Newton-Raphson and Arc-Length method.

5.2.4.1 Full Newton-Raphson Method

The Full Newton-Raphson method can be expressed as follows:

$$K(p)\,\Delta p = q - f(p) \tag{5-21}$$

Where q is the vector of total applied joint loads, $f(p)$ is the vector of internal joint forces and Δp is the deformation increment due to loading increment, which represents out-of-balance forces during a load increment. Parameter p represents the deformation of structure prior to load increment while $K(p)$ is the stiffness matrix which is evaluated at each iteration. Because this method is based on the concept of incremental step by step analysis, the iterative procedures continue until the specified convergence criteria are satisfied. The available convergence criteria relate to deformations, out-of-balance forces, out-of-balance energy

and maximum components of out-of-balance forces. The concept of Full Newton-Raphson method for the solution of non-linear equations is shown in Figure 5-20(a).

5.2.4.2 Modified Newton-Raphson Method

From a computation perspective, recalculating the stiffness matrix $K(p_{i-1})$ at each iteration as done in the full Newton-Raphson method is very time-consuming. The Modified Newton-Raphson method was developed to save time by using the stiffness matrix obtained at the first iteration of each step as shown in Figure 5-20 (b). Thus, each iteration requires less calculation time but typically converges more slowly than the full Newton-Raphson method. In comparison to Full Newton-Raphson method, the Modified Newton-Raphson method requires more iterations to reach the solution.

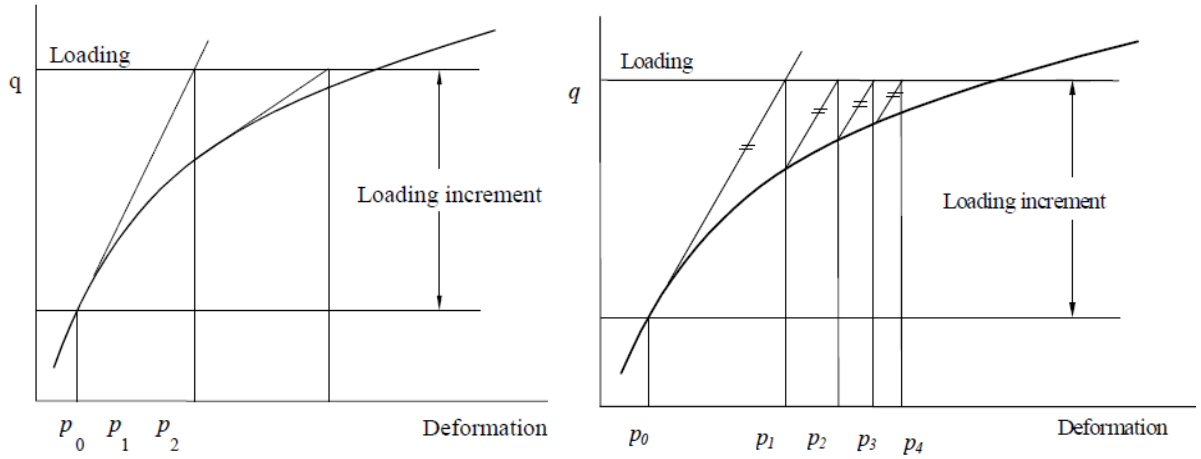

a) Full Newton-Raphson method b) Modified Newton-Raphson method

Figure 5-20 Solving set of non-linear equations: a) Full Newton-Raphson method and b) modified Newton-Raphson method; reproduced from [58].

5.2.4.3 Arc-Length Method

One of the drawbacks of using Newton-Raphson methods is their inability to solve stability problems where structures undergo either snap back or snap through behaviour. The arc-length method is able to trace the complete equilibrium path by iterating both the displacement and the load vector. This method was originally proposed by Wempner [72] and Riks [73] and has subsequently become very popular. It is well established for geometric and material non-linearity. The main concept of the arc-length method is to ensure that the solution path remains within the last converged equilibrium point, by fixing the loading and displacement conditions at the end of a step. This can be performed by introducing an

additional constraint equation (an additional degree of freedom associated with the loading level), by adding a new loading factor (λ_i) to equation (5-21) as given in equation (5-22).

$$K(p)\,\Delta p = \lambda_i q - f(p) \tag{5-22}$$

Additionally, a scalar η is a variable introduced by the Line-search method. When convergence problems arise such as near bifurcation and extreme points, the Line-search method is used in a combination with Arc-Length method to accelerate solutions in cases of well-behaved load deformation relationships or to damp possible oscillations. The arc-length method is shown in Figure 5-21. In this study, the arc-length method is adopted to simulate the response of beam-column joint specimens. A load control method was used in this research with number of iterations limited to 30 for each load step. The convergence tolerance was set at 1% for displacement, residual, and absolute residual error as well as at 0.1% for energy error.

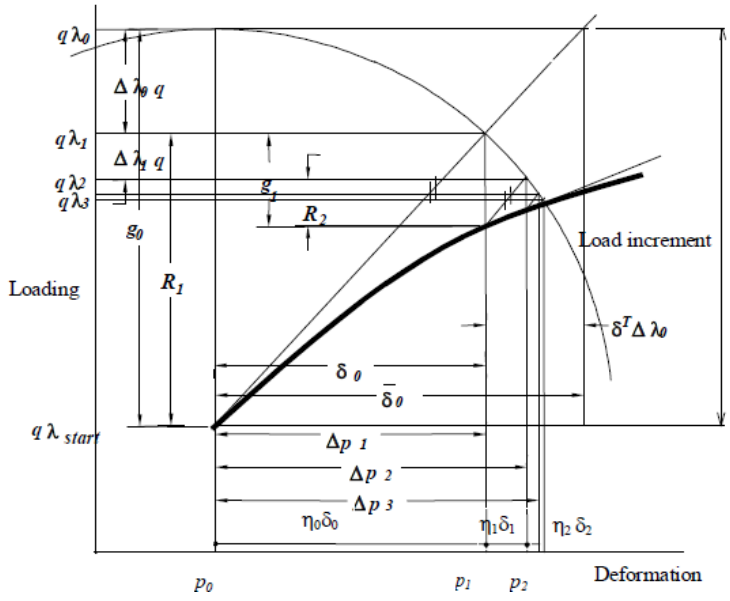

Figure 5-21 The Arc-length method; reproduced from [58].

5.3 Development of modelling procedure for external beam-column joints in ATENA

This section describes the development of the adopted modelling procedure for external-beam column joints. The section considers the choice of element type, element size and material parameters.

Table 5-2 shows the default parameters used for concrete and steel reinforcement for both 2D and 3D models. It also presents the loading procedure and convergence used in ATENA. A

bilinear stress strain relationship was used for reinforcement. Initially, perfect bond was assumed between concrete and steel reinforcement. A force controlled (static) loading procedure was adopted in conjunction with the arc-length solution procedure.

The next section describes the development of the adopted finite element meshing procedure for 2D and 3D analysis. A rotating crack model was used unless stated otherwise.

Table 5-2 Default concrete constitutive model parameters in ATENA for 2D and 3D models.

Parameter	Function/reference
Concrete constitutive model	
Concrete cylinder strength	f_c' = 0.85 f_{cu} f_{cu} = defined by the user
Concrete elastic modulus (E_c)	$E = (6000 - 15.5 f_{cu})\sqrt{f_{cu}}$
Concrete Tensile strength (f_t)	$f_t = 0.24\, fcu^{2/3}$
Concrete fracture energy factor (G_f)	$G_f = 0.000025\, f_t$
Concrete ductility (w_d)	Default value = -0.0005 m
reduction of concrete strength due to cracking (c_f)	0.8 f_c'
Poisson's ratio (ν)	0.2
Tension stiffening stress (σ_{st})	σ_{st} = 0
Maximum aggregate size	d_{agg} = specified by user
Crack model	Rotated crack = 0; Fixed crack = 1
Reinforcement bar model	
Stress-strain relationship	Bilinear
Bond-slip model	Perfect bond
Loading procedure and convergence	
Loading procedure	Force controlled
Iteration method	Arc-length method

5.3.1 Type and size of 2D NLFEA model

5.3.1.1 Type of finite element mesh

Specimen BCJ1 of Ortiz [12] with concrete compressive strength of 34 MPa was modelled in the mesh sensitivity study. Linear 4-node quadrilateral plane stress elements were used for concrete and linear triangular elements for steel plates. Reinforcement was modelled with truss using the embedded reinforcement technique.

5.3.1.2 Size of finite element mesh

The mesh was initially generated automatically using GiD. The maximum element size was progressively refined from 100 mm^2 to 6 mm^2. The resulting unstructured mesh is shown in Figure 5-22. The results of the analysis are presented in Figure 5-23(a)&(b). As shown in Figure 5-23(b), a further mesh refinement was carried out using square elements. Comparison of Figures 5-23(a) and 5-23(b) shows that the differences between the results obtained with the unstructured and square element meshes are relatively minor. Square elements were used to determine the concrete surface strains for comparison with the DIC results and discussed in chapter 7. Table 5-3 summarises the number of elements used in each model. An element size of 25 mm^2 was selected for subsequent analyses since reducing the element size further resulted in greater computational time but small differences in peak load.

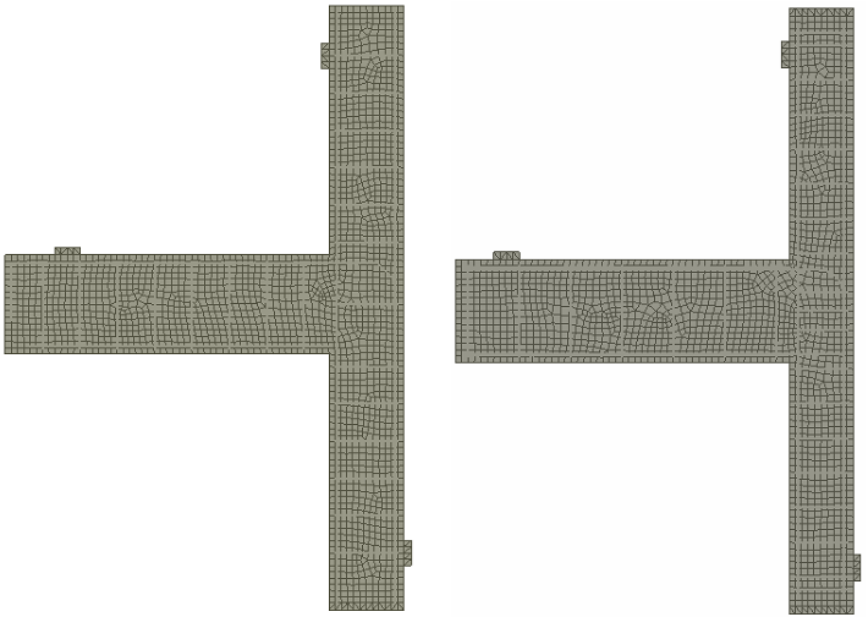

a) Ortiz BCJ1 b) Tested specimen

Figure 5-22 Finite element mesh size 2D models

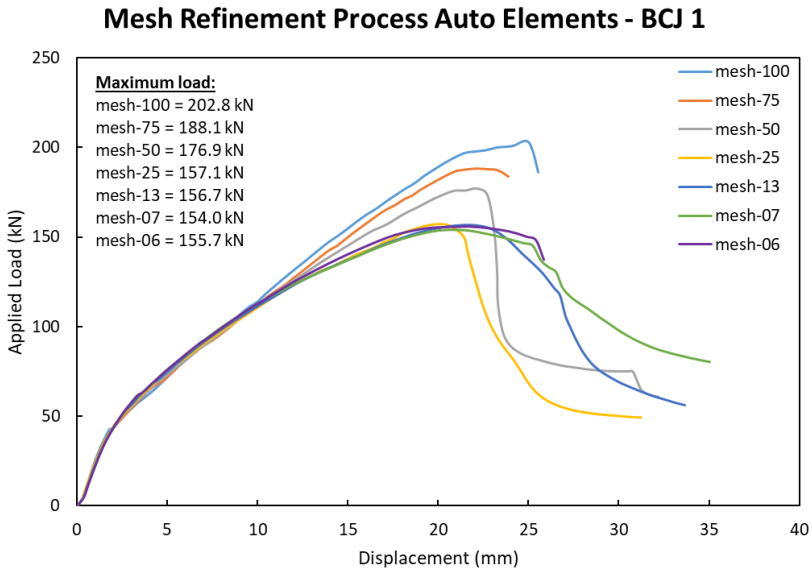

Figure 5-23(a) Results of 2D mesh refinement process; using automatic mesh in ATENA.

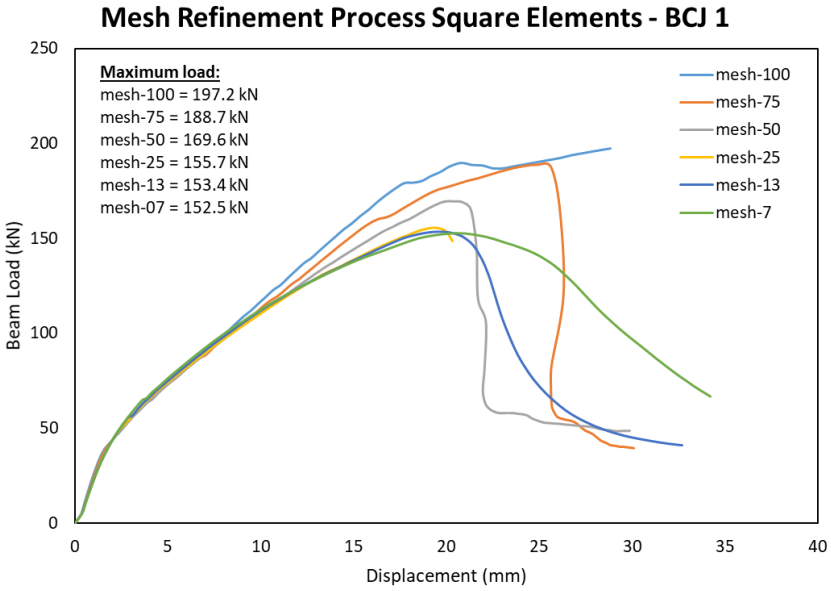

Figure 5-23(b) Results of 2D mesh refinement process; using square mesh in ATENA.

Table 5-3 Number of quadrilateral mesh elements

Model	Number of quadrilateral mesh elements	
	Ortiz [12]	Tested specimens
Mesh-100	174	162
Mesh-75	265	248
Mesh-50	501	468
Mesh-25	2,032	1,805
Mesh-13	7,780	7,048
Mesh-07	27,260	25,907
Mesh-06	39,572	35,322

5.3.2 Type and size of 3D NLFEA model

5.3.2.1 Type of finite element mesh

Linear 8-noded hexahedral elements were used for concrete while steel plates were meshed with linear tetrahedral elements. Steel reinforcement was meshed with line elements using the embedded reinforcement technique.

5.3.2.2 Size of finite element mesh

The size of the adopted hexahedral elements was related to the geometry of the beam-column joints being modelled. Following the approach of Hamil [14], the total number of brick elements was minimised without losing the functionality of the model, by refining the mesh in the joint and a small part of beam to better capture the true behaviour of the joint. This technique made the calculations faster and more efficient, by focusing on the joint instead rather the entire structural model. The technique splits the beam-column joint into two mesh size elements: dense mesh element (located in joint and one-quarter of beam length) and coarse mesh element (located in top column, bottom column and the remaining of three-quarters of beam length). The size of dense mesh element is half size of coarse mesh element. Initially, specimen BCJ 1 of Ortiz [12] was modelled as shown in Figure 5-24. The joint and one-quarter of the beam length were modelled with dense mesh elements. The remaining structural elements were meshed with coarse elements having twice the size of the fine elements. The dense mesh of elements was used in in the beam adjacent to the joint in order to better capture the structural response at the beam-column interface. A master slave method was used to model the contact surface between 3D volume objects (beam, column and supports). Nodes in the coarser faced mesh were the masters, while the nodes on the other face were controlled by kinematic equations as fixed-contact surface. The meshing procedure is illustrated in Figure 5-25 for the geometry of the specimens tested in this project. The elements used in the joint and one-quarter of beam length (1300 mm × 1/4 = 325 mm) were dense mesh elements while the elements in columns and three-quarters of beam length (1300 mm × 3/4 = 975 mm) were coarse mesh elements.

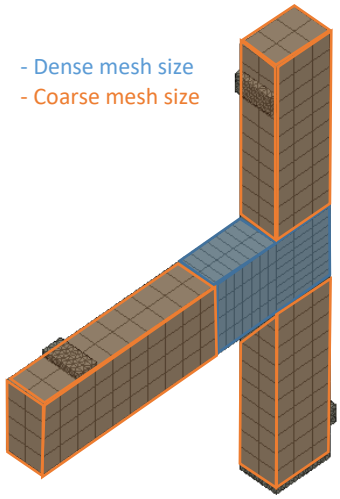

Figure 5-24 Finite element mesh size system

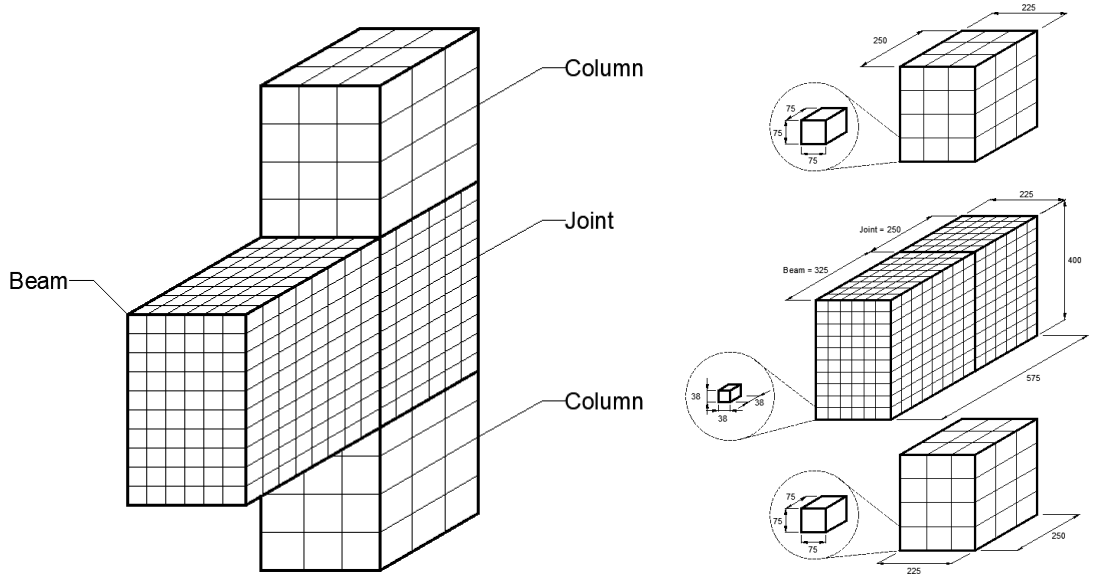

a) Beam-column joint mesh size (C75/D38)

b) Mesh size calculation (C75/D38)

Figure 5-25 Finite element mesh for experimental beam-column joint dimensions.

Results on mesh refinement are reported here for specimen BCJ 11 from this program. Details of the specimen are given in Chapters 3 and 4. Element sizes of 100, 75, 50, 40 and 30 mm^3 were used in the mesh refinement process. The coarse element size was reduced from 100 mm^3 in steps of 25 mm^3 to an element size of 50 mm^3. Subsequently, the element size was reduced in steps of 10 mm^3 until no further drop in resistance occurred as shown in Figure 5-26. The mesh refinement process followed a sequence of divisions by C100/D50, C75/D38, C50/D25, C40/D20 and C30/D15 where the number represents the mesh element size, and the letter is related to the coarse mesh element (C) and dense mesh element (D). Table 5-4

and Figure 5-27 present the finally adopted mesh arrangements used for analysis of the test specimens of Taylor [5], Ortiz [12], Hamil [14] and this program. Steel plates were meshed with 25 mm^3 tetrahedral elements. Reinforcement was modelled with 1-D truss elements using the embedded reinforcement option.

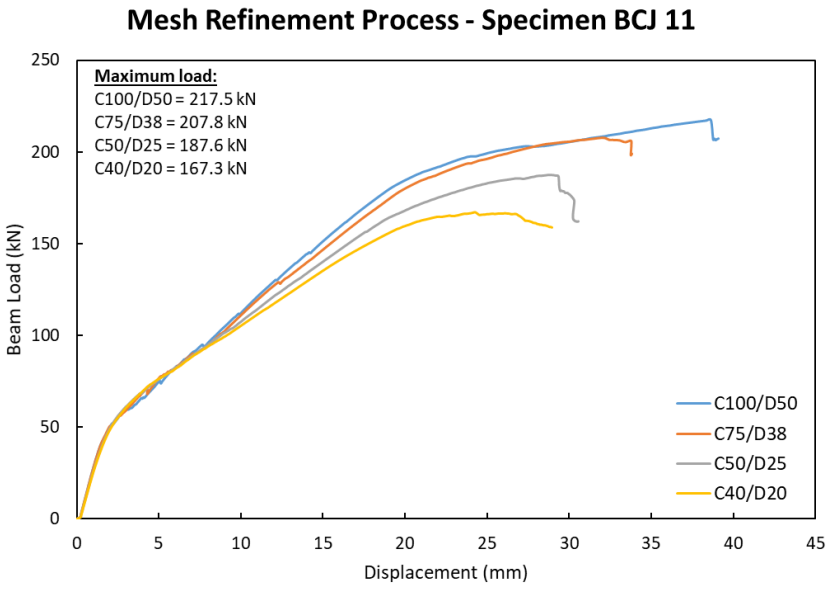

Figure 5-26 Results of 3D mesh refinement process

Table 5-4 Number of hexahedral mesh elements

Model	Number of hexahedral mesh elements			
	Taylor [5]	Ortiz [12]	Hamil [14]	Tested specimens
C100/D50	30	304	100	316
C75/D38	111	774	188	681
C50/D25	400	2400	510	2506
C40/D20	910	4800	1174	4592
C30/D15	1808	-	2580	-

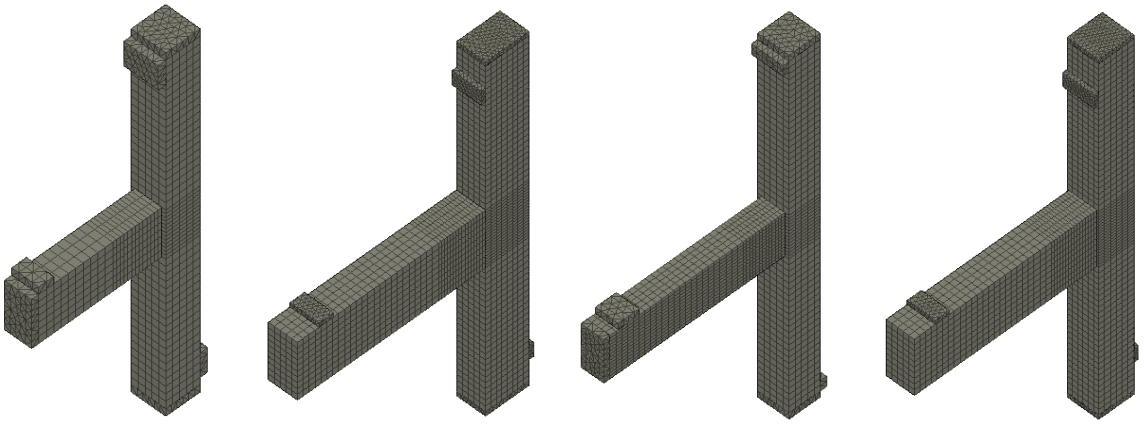

a) Taylor [5] b) Ortiz [12] c) Hamil [14] d) Tested specimens

Figure 5-27 Finite element mesh size 3D models

5.4 Material constitutive model for 2D NLFEA model

This section describes the analysis carried out to study the sensitivity of the 2D analysis to the input parameters of the concrete constitutive model. The parameters studied in the study were concrete modulus of elasticity (E_c), reduction of concrete strength due to cracking (c_f), tension stiffening (σ_{st}), concrete tensile strength (f_t), fixed vs rotated crack model, critical compressive displacement (w_d) and bond-lip model. The rest of parameters were taken as the default values in ATENA, as presented in Table 5-2. Specimen BCJ 11 from the author's experimental tests was used for calibrating these parameters. The specimen was chosen because it had no joint stirrups. It was anticipated that this gives a better understanding of the effect of varying the inputs to the concrete constitutive model than modelling specimens with joint stirrups. The concrete compressive strength of BCJ 11 was 48.9 MPa. The finite element mesh used in the model was mesh-25 for beam/column from Table 5-3 and 1-D truss element for steel reinforcement. The sensitivity analysis was carried out by sequentially changing one parameter at a time. Initially, default values were used for the other parameters. Once a suitable value had been chosen for a parameter, that value was selected and another sensitivity analysis was carried out for the next considered parameter. This procedure was repeated until all the model parameters had been selected. It is worth mention that plane-stress model was used in the 2D NLFEA model, taking no considerations of the effect of out-of-plane behaviour in the tested specimens.

5.4.1 Sensitivity to the concrete elastic modulus E_c

Initially, a sensitivity analysis was carried out to study the effect of the concrete modulus of elasticity on strength and stiffness. The default value of ATENA for modulus of elasticity was multiplied by a reduction factor of 75%, 50% and 25%. The results are plotted in Figure 5-28 which shows that reducing the modulus of elasticity improves the initial stiffness of the load-displacement response. It was decided to use a reduction factor of 75% since the initial stiffness of the load-displacement response is not affected by other parameters such as tension stiffening (σ_{st}) and concrete tensile strength (f_t).

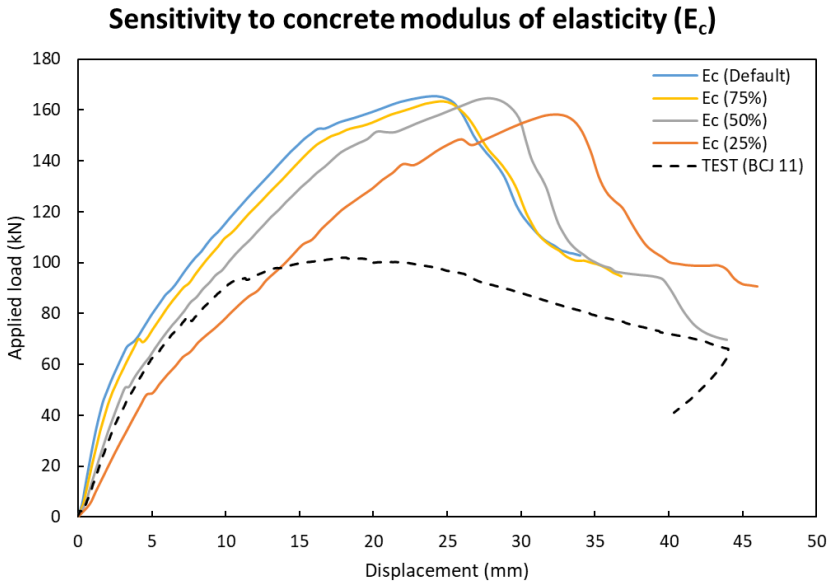

Figure 5-28 Material constitutive model for 2D NLFEA model: sensitivity to modulus of elasticity (E_c)

5.4.2 Sensitivity to reduction of concrete strength due to cracking (c_f)

The compressive strength of concrete in the 2D model is reduced when cracking occurs in the perpendicular direction. In SBETA, the maximum reduction in strength is limited by a user defined multiple c_f with a default value of 0.8 which can be freely chosen between zero and one. A sensitivity analysis was carried out to study the influence of c_f. The parameter has relatively little effect on peak load as shown in Figure 5-29. Based on the results shown in Figure 5-29, c_f was chosen to be 0.2 since this choice reduced the predicted failure load closest to the measured failure load of specimen BCJ 11 from this program. Further reduction in failure load is required and this can be reached by changing other parameters like tension stiffening (σ_{st}) which is described in the following sections.

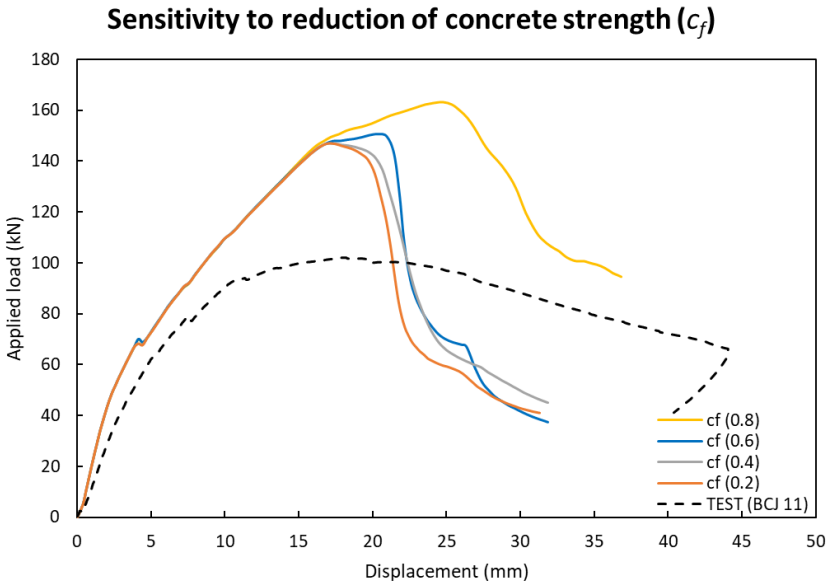

Figure 5-29 Material constitutive model for 2D NLFEA model: sensitivity to reduction of concrete strength due to cracking (c_f)

5.4.3 Sensitivity to concrete tensile strength (f_t)

The influence of varying the concrete tensile strength was studied in the 2D model. Reduction factors of 75%, 50% and 25% were applied to the default tensile strength of 3.61 MPa adopted in ATENA. This strength is calculated from the compressive strength using the formula given in Table 5-2. The default tensile strength adopted in ATENA is significantly less than the measured tensile strength of 5.5 MPa. The predicted failure load is sensitive to the choice of tensile strength with the best predictions of failure load obtained with low values of concrete tensile strength as illustrated in Figure 5-30. It was decided to use a reduction factor of 0.5 on tensile strength in the 2D model. Further reduction in failure load is required and this can be achieved by studying the tension stiffening, which is explained in the next section.

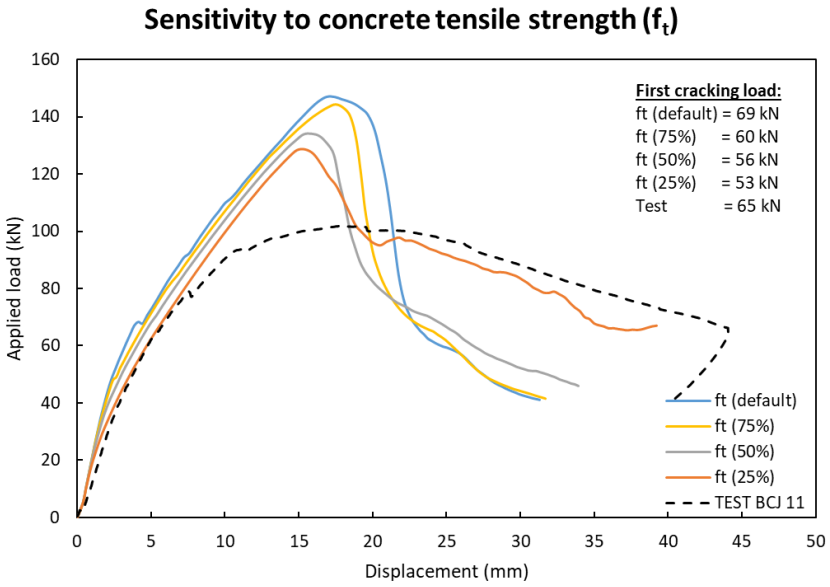

Figure 5-30 Material constitutive model for 2D NLFEA model using BCJ 11: sensitivity to concrete tensile strength (F_t)

5.4.4 Sensitivity to tension stiffening stress (σ_{st})

The mean tensile strain in the reinforcement is reduced by the development of tension in the concrete between cracks. This phenomenon is known as tension stiffening. In SBETA, tension stiffening is modelled by limiting the minimum tensile stress in the concrete after cracking to a proportion of the concrete tensile strength. The default value of this multiplier in ATENA is zero. As shown in Figure 5-31, a range of tension stiffening values (0.2 to 1.0) was studied. The results show that a tension stiffening value of 0.6 nearly captures the change in slope after cracking of the load-deflection graph of specimen BCJ 11. Further investigations were carried out by varying σ_{st} between 0.5 to 0.6 after calibrating this model with the rest of tested BCJ specimens. Based on these results σ_{st} was taken as 0.58 in the 2D model. Somewhat surprisingly, the introduction of tension stiffening reduced the failure load. This appears to be due to a reduction of compressive strength of the concrete under biaxial tension and compression.

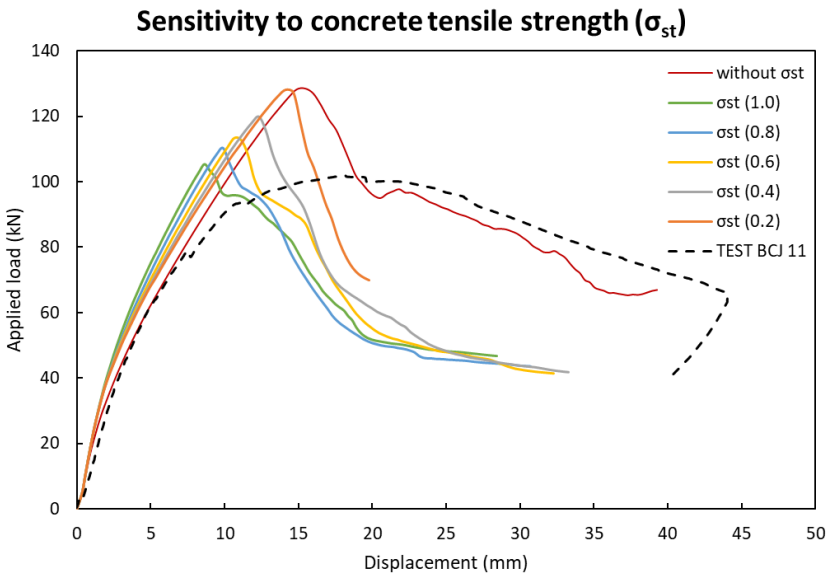

Figure 5-31 Material constitutive model for 2D NLFEA model: sensitivity to tenson stiffening (σ_{st}).

5.4.5 Sensitivity to critical compressive displacement (w_d)

The influence of varying the compressive displacement w_d at complete loss of compressive resistance was investigated. As shown in Figure 5-32, four values of critical compressive displacement (0.5 mm to 2.0 mm) were studied. The plot shows that the best estimate of peak load is obtained with w_d = 1.0 mm but the post-peak response is marginally better predicted with w_d = 2.0 mm. It was decided to use a critical compressive displacement value of 2.0 mm because the difference between the predicted failure load for compressive displacements of w_d = 1.0 mm and w_d = 2.0 mm is small.

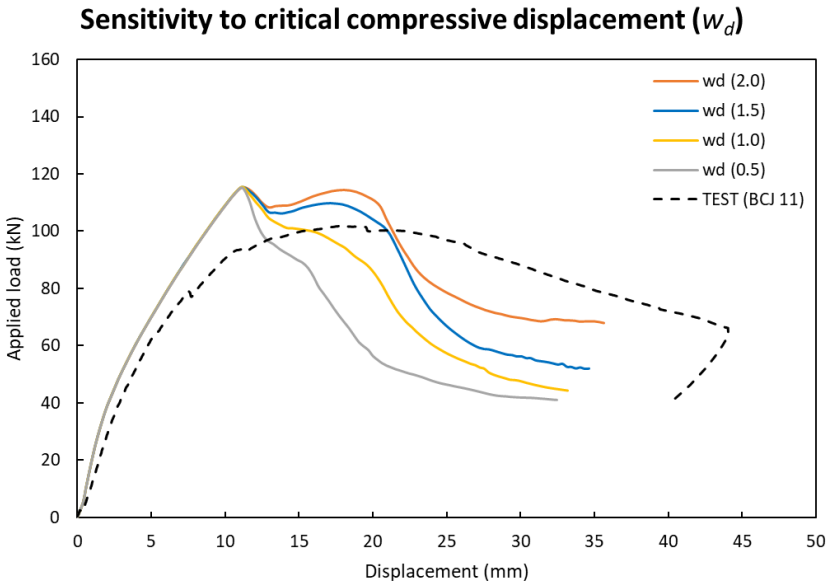

Figure 5-32 Material constitutive model for 2D NLFEA model using BCJ 11: sensitivity to critical compressive displacement (w_d).

5.4.6 Sensitivity to fixed vs rotated crack model

Due its simplicity a rotated crack model was initially considered. As shown in Figure 5-33, varying the shear factor in the fixed crack model can give equally good or better predictions of failure load. Th rotated crack model was finally adopted in this research because it is more objective than the fixed crack model which requires the user to define a value for the shear factor.

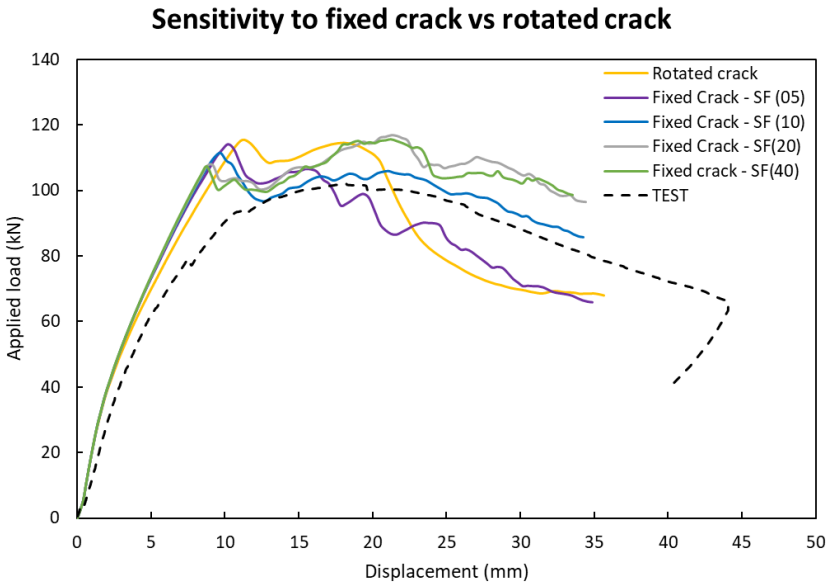

Figure 5-33 Material constitutive model for 2D NLFEA model: sensitivity to fixed vs rotated crack model

5.4.7 Sensitivity to bond-slip model

The influence of bond-slip was investigated to study its effect. The Bigaj model [71] with bond quality equal to excellent was used for simulating the bond-slip effect acting between concrete and steel reinforcement. The choice of excellent bond quality shows less influence on peak load compared to other choices discussed in section 5.2.2, where the failure load reduced rapidly. The bond-slip model was applied to the reinforcement bars inside the joint. As shown in Figure 5-34, bond-slip was activated inside the joint (including beam anchorage reinforcement located inside joint, column bars crossing the joint and stirrups located inside the joint). Both anchorage type including L-anchorage reinforcement and U-anchorage reinforcement was simulated with bond-slip model. The influence of introducing bond-slip on the load-displacement of the specimen is presented in Figure 5-35 which shows that a small reduction in failure load occurred when the bond-slip model was used.

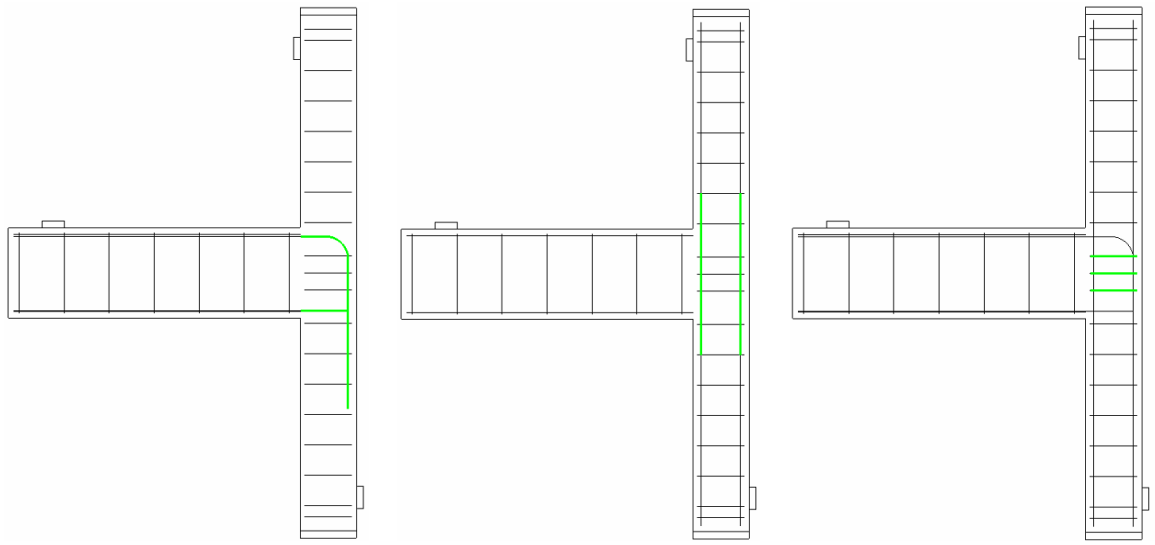

a) Specimens with L-anchorage beam reinforcement

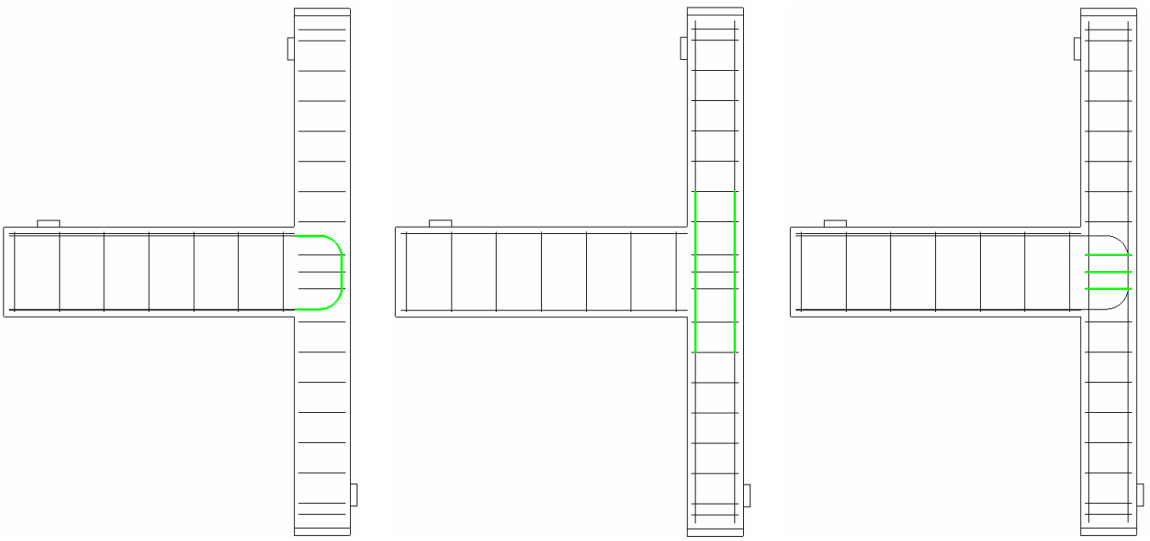

b) Specimens with U-anchorage beam reinforcement

Figure 5-34 Material constitutive model for 2D NLFEA model: sensitivity bond-slip model

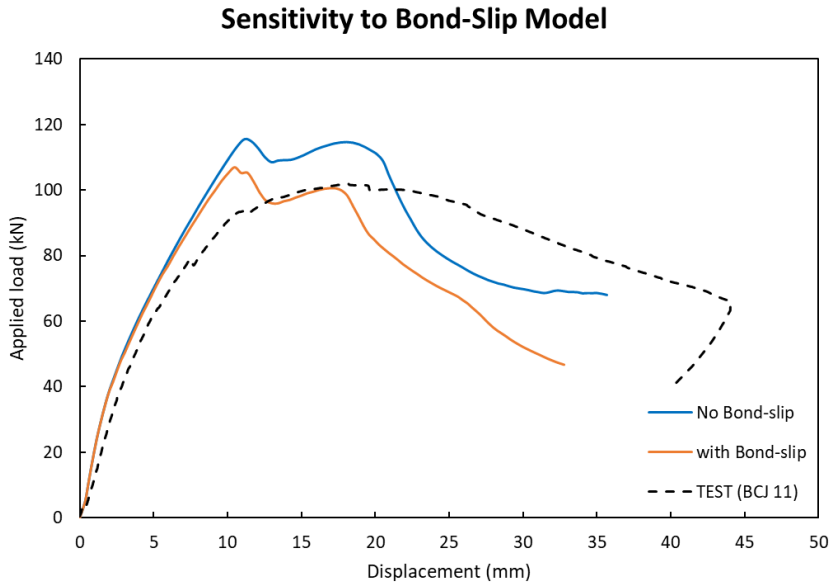

Figure 5-35 Material constitutive model for 3D NLFEA model: sensitivity to bond-slip model

5.4.8 Summary of adopted 2D modelling parameters

The material properties selected in the sensitivity study are summarised in Table 5-5. The remaining parameters are kept at the default values as shown in Table 5-2.

Table 5-5 2D chosen parameters input for 2D model

Parameter	Function/reference
Concrete constitutive model	
Concrete cylinder strength	f_c' = -0.85 f_{cu} f_{cu} = defined by the user
Concrete elastic modulus (E_c)	$E = (6000 - 15.5 f_{cu})\sqrt{f_{cu}}$ **Taken as 75% of default value**
Concrete Tensile strength (f_t)	$f_t = 0.24\ fcu^{2/3}$ **Taken as 50% of default value**
Concrete fracture energy factor (G_f)	$G_f = 0.000025\ f_t$
Concrete ductility (w_d)	Default value = -0.5 mm **Taken as -2.0 mm**
reduction of concrete strength due to cracking (c_f)	0.8 f_c' **Taken as 0.2**
Poisson's ratio (ν)	0.2
Tension stiffening stress (σ_{st})	σ_{st} = 0 **Taken as 0.58**
Maximum aggregate size	d_{agg} = specified by user
Crack model	**Rotated crack = 0**
Reinforcement bar model	
Stress-strain relationship	Bilinear
Bond-slip model	**Bigaj model with excellent bond quality inside joint region; and perfect bond with the remainders.**
Loading procedure and convergence	
Loading procedure	Force controlled
Iteration method	Arc-length method

5.5 Use of 2D model to investigate parameters varied in current test program

This section investigates the ability of the adopted modelling parameters to simulate the response of the author's test specimens. The final parameters chosen from the sensitivity analysis presented in section 5.4.8 are used in this validation. The test results are presented in Chapter 4 (see sections 4.2.2, 4.3.2 and 4.4.2).

5.5.1 Effect of beam bar detailing

As shown in Figure 5-36, the 2D model correctly predicts the influence of varying the type of beam anchorage bar detailing (L-anchorage bar and U-anchorage bar) and bend radius on joint shear strength. However, the predicted response is more brittle than observed. The standard bend radius is the minimum allowed by EC2 while the large bend radius is double the standard radius as described in Chapter 3.

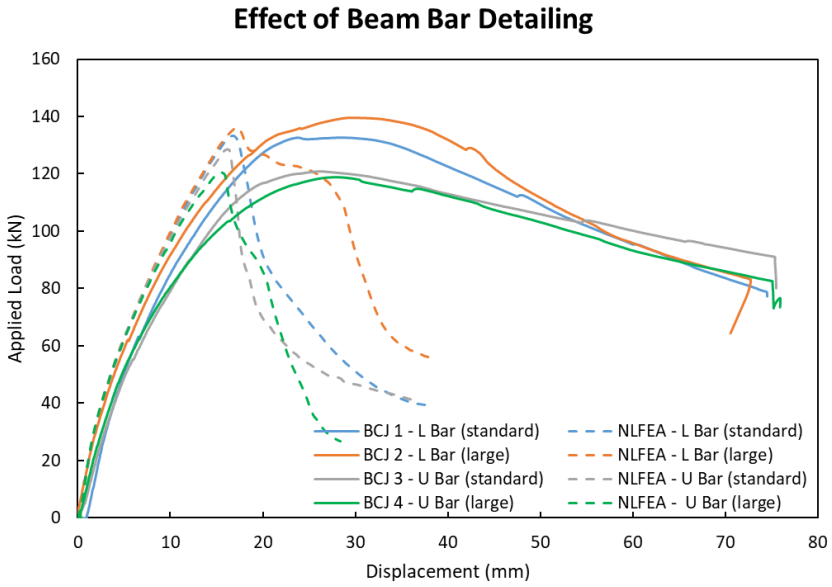

Figure 5-36 Validation of 2D model to experimental test parameters: effect of beam bar detailing.

5.5.2 Effect of joint stirrups

The tests examined the influence on joint strength of joint stirrups in specimens with L-anchorage type and U-anchorage type. Figure 5-37 and Figure 5-38 show that the predicted joint capacity increased significantly when joint stirrups were included as observed experimentally.

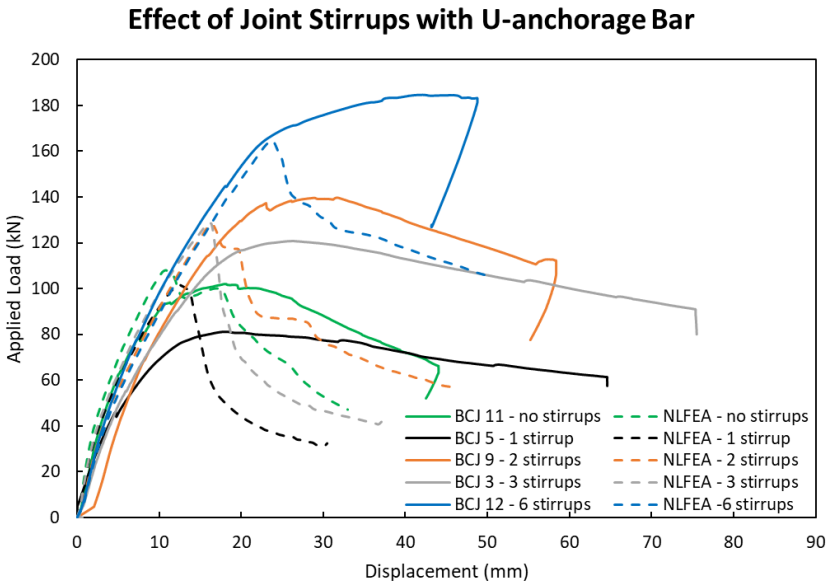

Figure 5-37 Validation of 2D model to experimental test parameters: effect of joint stirrups with U-anchorage bar.

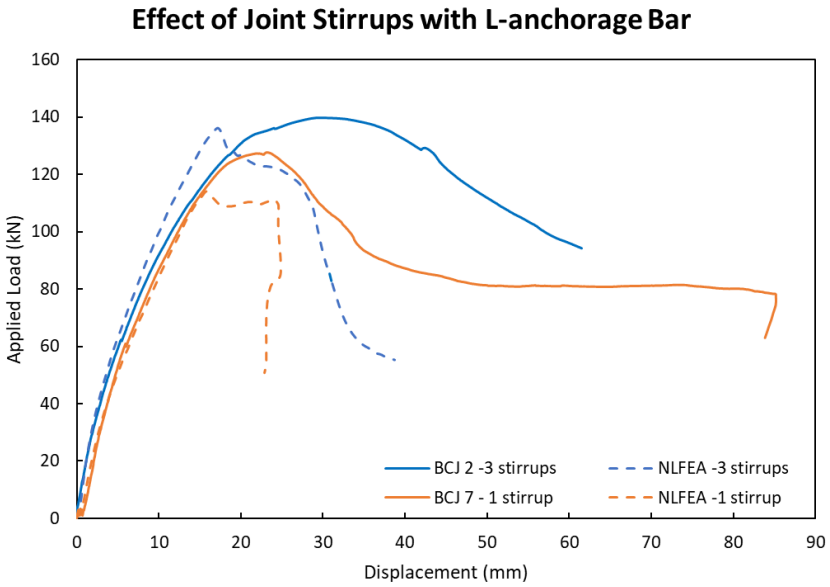

Figure 5-38 Validation of 2D model to experimental test parameters: effect of joint stirrups with L-anchorage bar.

5.5.3 Effect of column bars

It was observed joint strength was increased by the provision of column intermediate bar in the author's laboratory tests. As show in Figure 5-39, the predicted failure load also increased when column intermediate bars were provided. This increase in failure load was about 23% in test results and 11% in 2D model. However, the response of the 2D model was more brittle than experimentally observed.

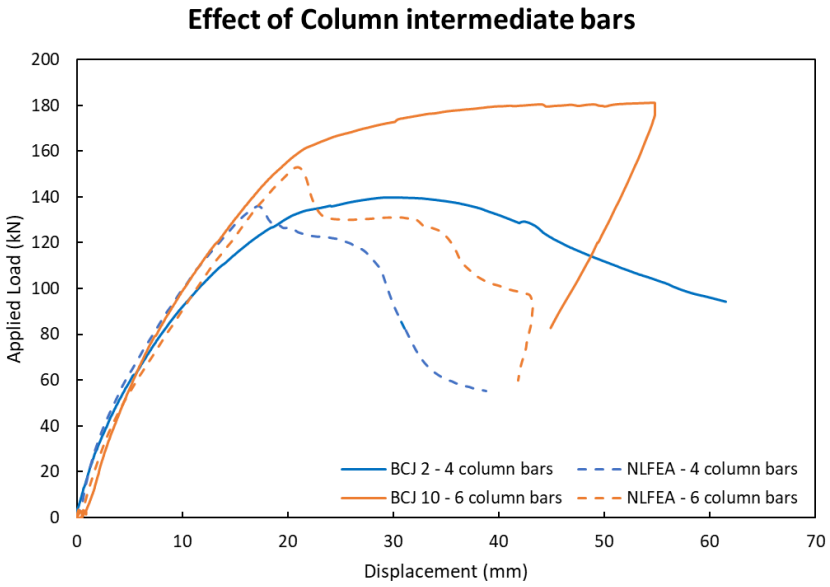

Figure 5-39 Validation of 2DD model to experimental test parameters: effect of column intermediate bar.

5.5.4 Effect of column axial load

The influence of column axial load was studied in the 2D model. The predicted failure load reduced when the column axial load was increased from 300 to 600 kN but remained almost constant when the column load was increased from 600 kN to 900 kN as presented in Figure 5-40. The test results similarly showed a reduction in failure load when the column axial load increased from 300 kN to 600 kN and little further change when the column load was increased to 900 kN. It should however be noted that the concrete strength was 33.2 MPa for BCJ3 but 26.9 MPa and 26.8 MPa for BCJ6 and BCJ8.

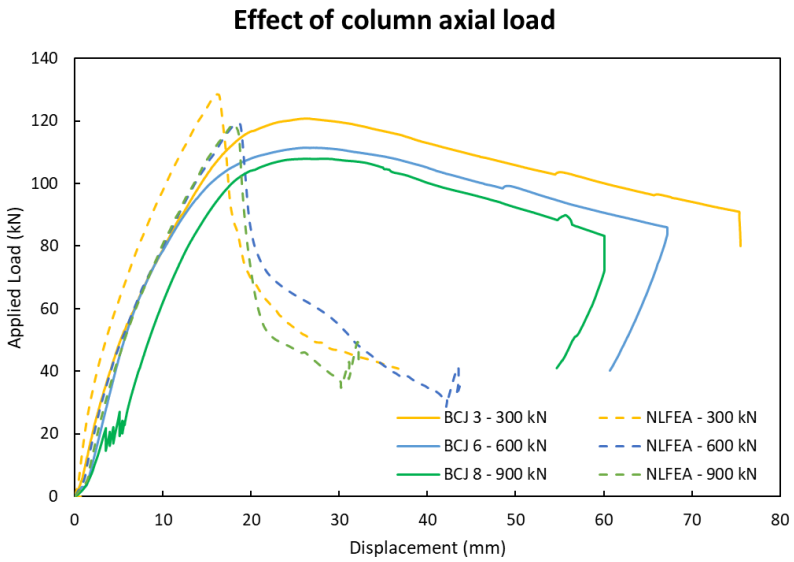

Figure 5-40 Validation of 2D model to experimental test parameters: effect of column axial load.

5.5.5 Effect of concrete strength

The influence of concrete strength was investigated for specimens with and without joint stirrups although the effect of concrete strength was not investigated for similar specimens in this research. Thus, a comparison was carried out based on the 2D model response to study its sensitivity to concrete strength using models with and without joint stirrups. As shown in Figure 5-41, the 2D model predicted the joint strength to increase with concrete compressive strength as expected. This influence can be noticed in all concrete compressive strength (20 MPa to 60 MPa) with and without joint stirrups.

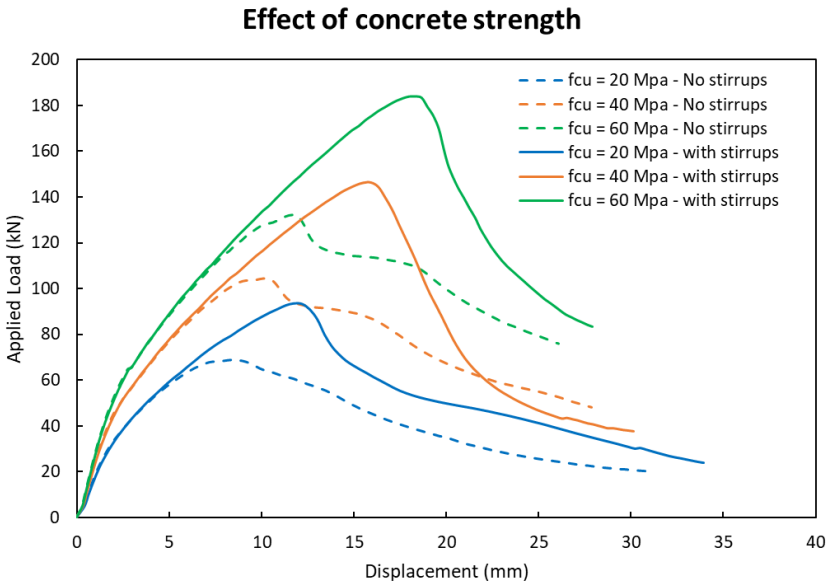

Figure 5-41 Validation of 2D model to experimental test parameters: effect of concrete strength.

5.6 Validation of 2D NLFEA model with test results of the author and others

Figure 5-42 compares the measured and predicted 2D NLFEA load displacement response for all the authors test results. The results of 2D model showed a good agreement with author's test results in terms of initial stiffness of load-displacement curve and failure load but not the post peak response which is predicted to be more brittle than observed experimentally. The results are summarised in Table 5-6.

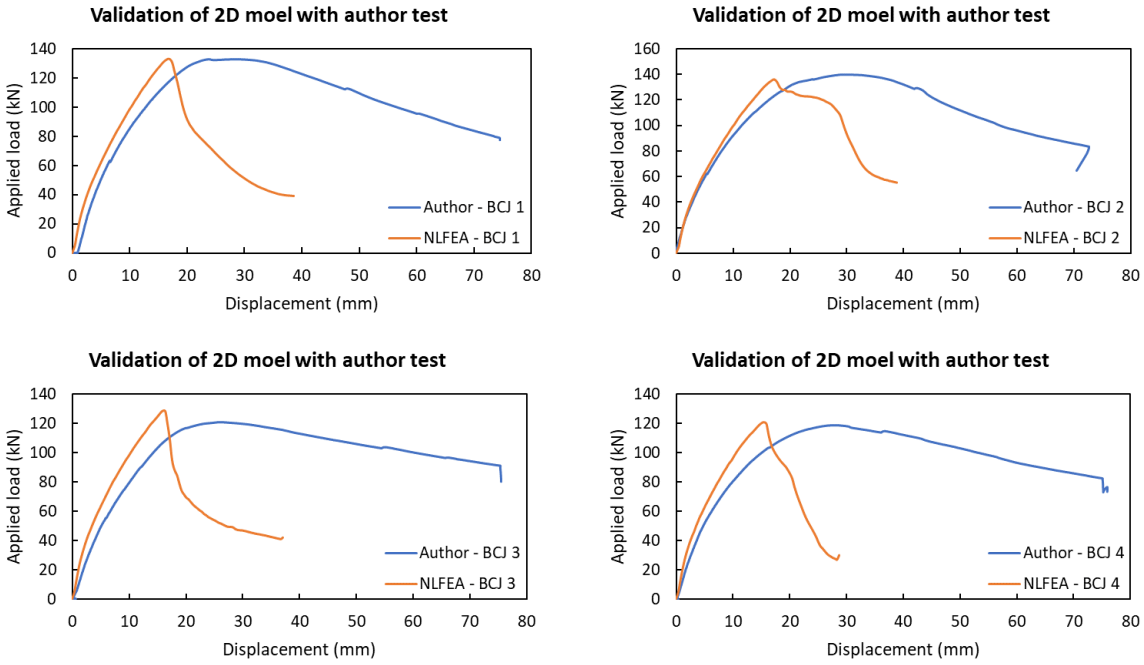

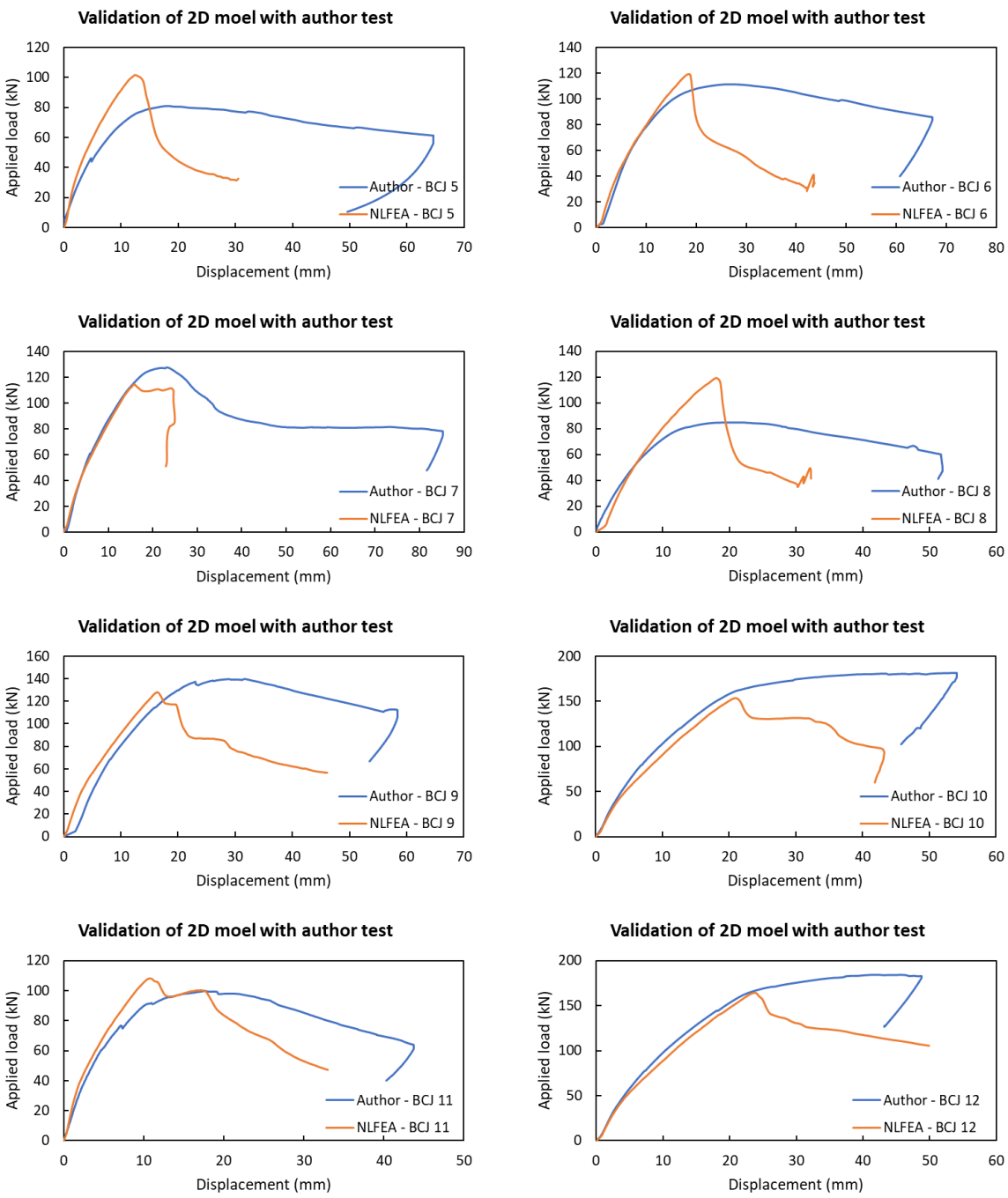

Figure 5-42 Validation of 2D model with Author's tests.

Table 5-6 Summary of validation of 2D model with Author tests: measured/predicted failure load from ATENA.

Test	Specimens	Measured failure load (kN)	Predicted failure load (kN)	Measured/Predicted
Author test	BCJ 1	132.8	133.3	1.00
	BCJ 2	139.7	136.2	1.03
	BCJ 3	120.8	128.2	0.94
	BCJ 4	118.8	120.7	0.98
	BCJ 5	81.1	101.6	0.80
	BCJ 6	111.5	119.1	0.94
	BCJ 7	127.6	114.2	1.12
	BCJ 8	107.9	119.0	0.91
	BCJ 9	139.7	128.1	1.09
	BCJ 10	181.2	152.9	1.18
	BCJ 11	101.9	107.9	0.95
	BCJ 12	184.6	164.4	1.12
			Mean	1.00
			Standard deviation	0.11

The general applicability of the proposed input material properties was investigated further by modelling seven beam-column joint specimens tested by Ortiz [12] for which only failure loads are available which is explained in section 2.2.5. The results of validation of 2D model with Ortiz tests are presented in Figure 5-43 and Table 5-7. The predicted failure load to measured failure load are presented in Table 5-8 for validating the 2D model with both Ortiz and the author's tests. The predicted failure load to measured failure load is plotted in Figure 5-44 for both experimental tests. In general, the 2D model results provided a mean value of 1.12 and a standard deviation of 0.20.

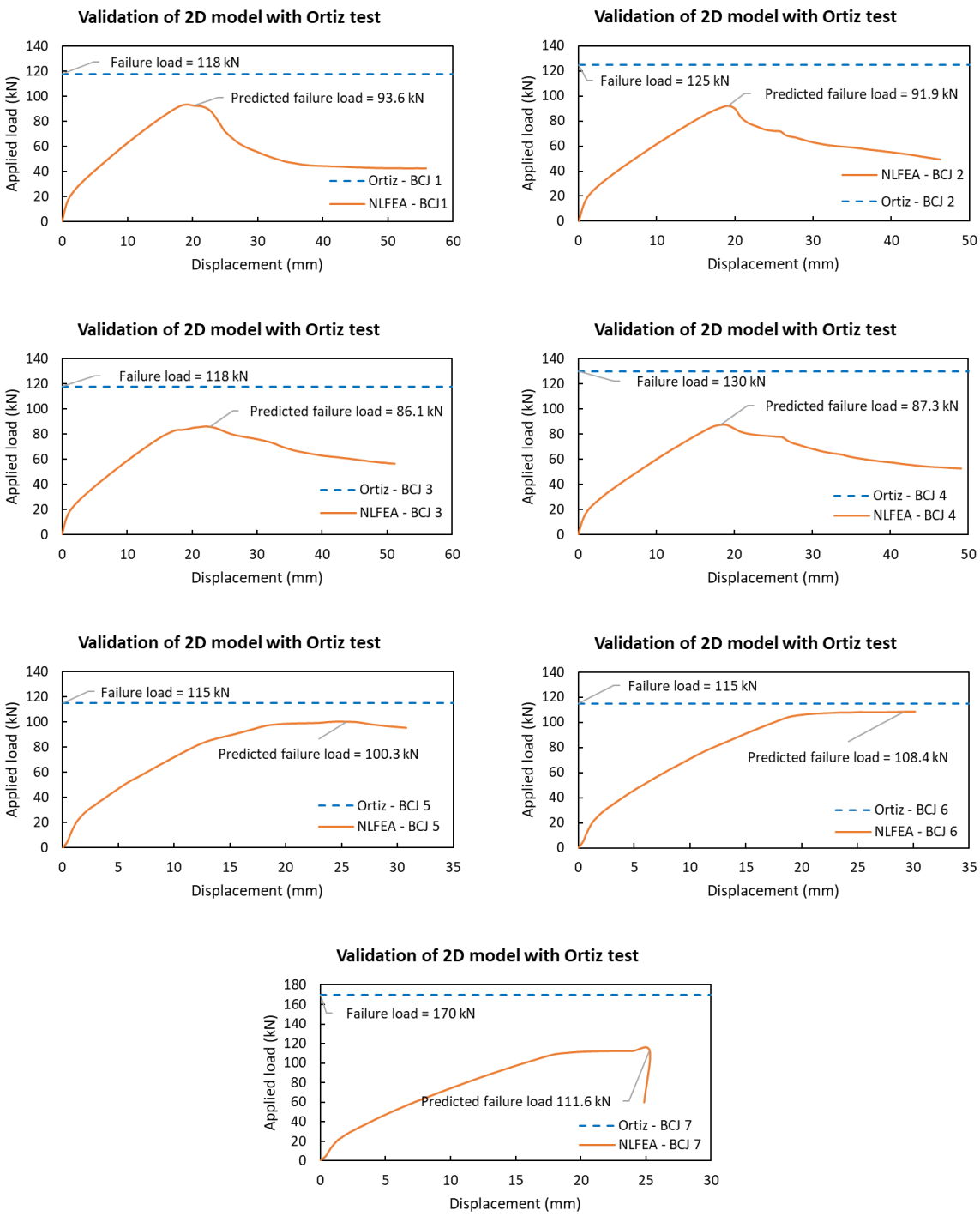

Figure 5-43 Validation of 2D model with Ortiz tests

Table 5-7 Summary of validation of 2D model with Ortiz tests: measured/predicted failure load from ATENA.

Test	Specimens	Measured failure load (kN)	Predicted failure load (kN)	Measured/Predicted
Ortiz test	BCJ 1	118.0	93.6	1.26
	BCJ 2	125.0	91.9	1.36
	BCJ 3	118.0	86.1	1.37
	BCJ 4	130.0	87.3	1.49
	BCJ 5	115.0	100.3	1.15
	BCJ 6	115.0	108.4	1.06
	BCJ 7	170.0	111.6	1.52
			Mean	1.32
			Standard deviation	0.17

Table 5-8 Summary of 2D model measured/predicted failure load from ATENA.

Test	Specimens	Measured failure load (kN)	Predicted failure load (kN)	Measured/Predicted
Ortiz test	BCJ 1	118	93.6	1.26
	BCJ 2	125	91.9	1.36
	BCJ 3	118	86.1	1.37
	BCJ 4	130	87.3	1.49
	BCJ 5	115	100.3	1.15
	BCJ 6	115	108.4	1.06
	BCJ 7	170	111.6	1.52
Author test	BCJ 1	132.8	133.3	1.00
	BCJ 2	139.7	136.2	1.03
	BCJ 3	120.8	128.2	0.94
	BCJ 4	118.8	120.7	0.98
	BCJ 5	81.1	101.6	0.80
	BCJ 6	111.5	119.1	0.94
	BCJ 7	127.6	114.2	1.12
	BCJ 8	107.8	119.0	0.91
	BCJ 9	140	128.1	1.09
	BCJ 10	181.2	152.9	1.18
	BCJ 11	102	107.9	0.95
	BCJ 12	184.6	164.4	1.12
			Mean	1.12
			Standard deviation	0.20

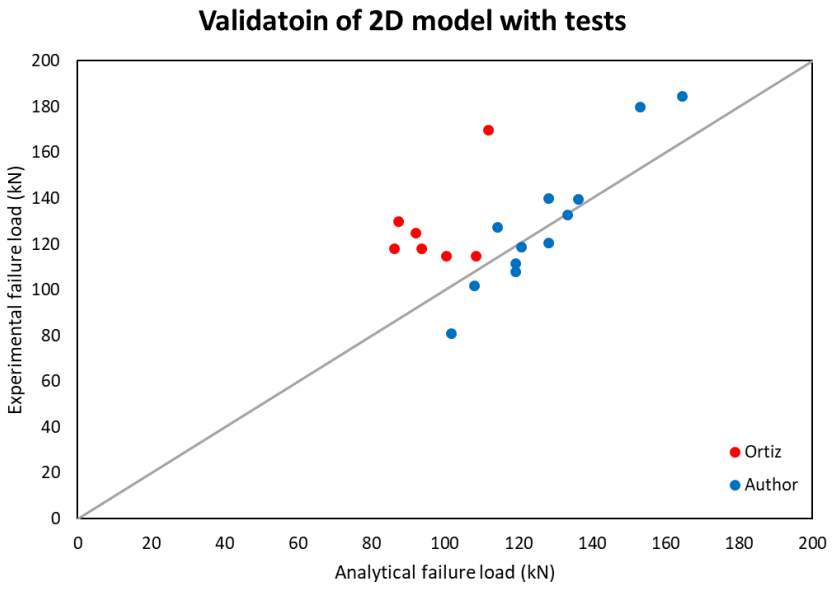

Figure 5-44 Validation of 2D model with Ortiz and Author tests.

5.7 Material modelling for 3D NLFEA model

This section describes the calibration of the concrete material model for 3D solid elements. The procedure followed was similar to that for 2D elements. The parameters investigated in ATENA were concrete elastic modulus (E_c), reduction of concrete strength due to cracking (c_f reduction), critical compressive displacement (w_d), tensile fracture energy (G_f), concrete tensile strength (f_t), fixed vs rotated crack model and bond-slip model. Default values were adopted for the remaining parameters. The mesh used in this analysis is C40/D20 for brick elements as shown in Table 5-4. Steel plates were meshed with 25 mm^3 tetrahedral elements. Reinforcement was modelled with embedded truss elements. The baseline material input parameters used in the 3D model are shown in Table 5-2. These parameters were calibrated using the test results of specimen BCJ 11 from the author's experimental program. If these parameters were applied in different experimental tests (rather than the author and Ortiz tested specimens), this might give different results when compared with the results obtained in this research.

5.7.1 Sensitivity to the concrete elastic modulus E_c

The effect of reducing the default concrete elastic modulus by reduction factors of 75%, 50% and 25% of default value was investigated. As shown in Figure 5-45, using a 50% of the default value of modulus of elasticity showed better results in terms of the slope of load-

displacement response. Thus, it was decided to use this reduction factor (50% E_c) as the default value of material parameter.

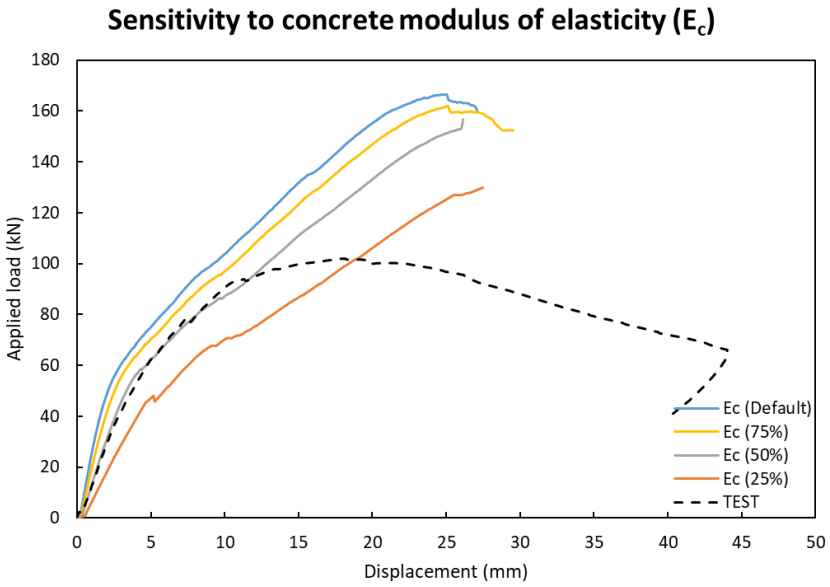

Figure 5-45 Material constitutive model for 3D NLFEA model: sensitivity to modulus of elasticity (E_c)

5.7.2 Sensitivity to reduction of concrete strength due to cracking (c_f)

A reduction of compressive strength occurs after cracking in the direction parallel to the compressive stress. The concept of this parameter was first introduced by Vecchio and Collins [63] and formulated in the Compression Field Theory. ATENA utilises a similar approach to Vecchio and Collins but with different function which has a form of the Gauss's function to allow the users to adjust this parameter within a limit. This parameter has a limit to the reduction of compressive strength factor ranging from zero to one. Kollegger and Mehlhorn [74] chose a value of 0.45 for this parameter based on their experiments whereas Dyngeland [75] recommended the reductions should not be taken as less than 0.8. The default value of this parameter in ATENA is 0.8. In this research, a reduction factor of 0.2 was found to provide better results in terms of failure load as shown in Figure 5-46.

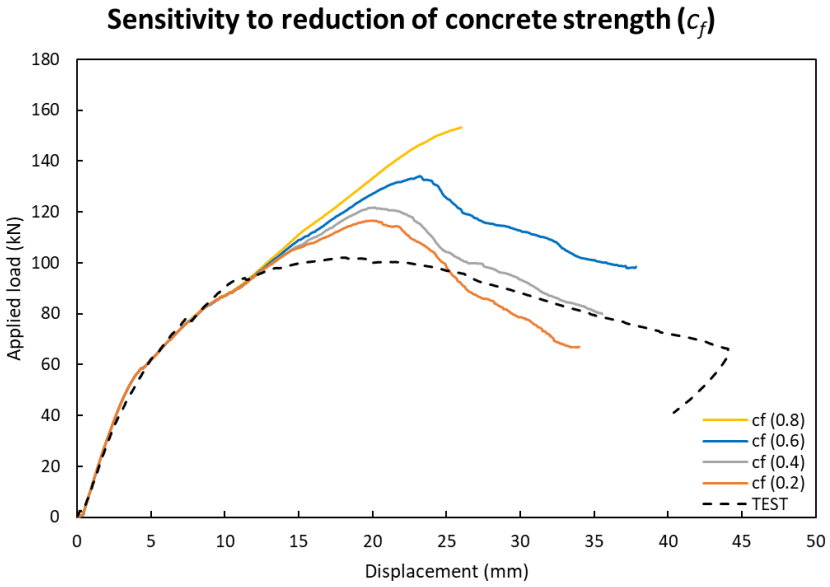

Figure 5-46 Material constitutive model for 3D NLFEA model: sensitivity to reduction of concrete strength due to cracking (c_f)

5.7.3 Sensitivity to tensile fracture energy (G_f)

As shown in Figure 5-47, the initial post cracking stiffness of the load-displacement response as well as the failure load were found to reduce when the fracture energy was reduced. A reduction factor of 0.8 (G_f = 0.8) was adopted but a value of 1.0 could also have been chosen without significantly affecting the predicted response.

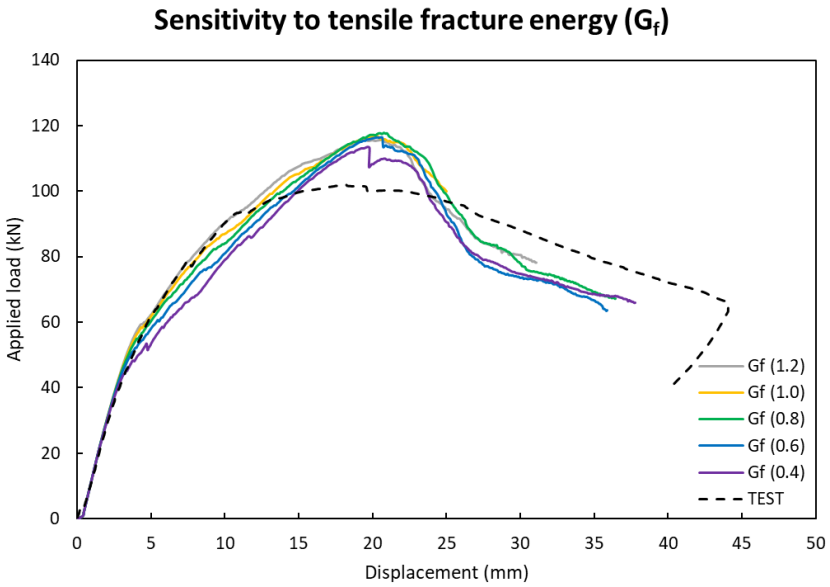

Figure 5-47 Material constitutive model for 3D NLFEA model: sensitivity to tensile fracture energy (G_f)

5.7.4 Sensitivity to concrete tensile strength (f_t)

The influence of reducing the concrete tensile to 25%, 50% and 75% of its default value (see Table 5-2) was investigated for the author's specimens BCJ5 and BCJ 11. Reducing the tensile strength caused a reduction in failure load and the stiffness of load-displacement response as shown in Figure 5-48 and Figure 5-49. Based on these figures a 50% reduction in the default tensile strength was adopted.

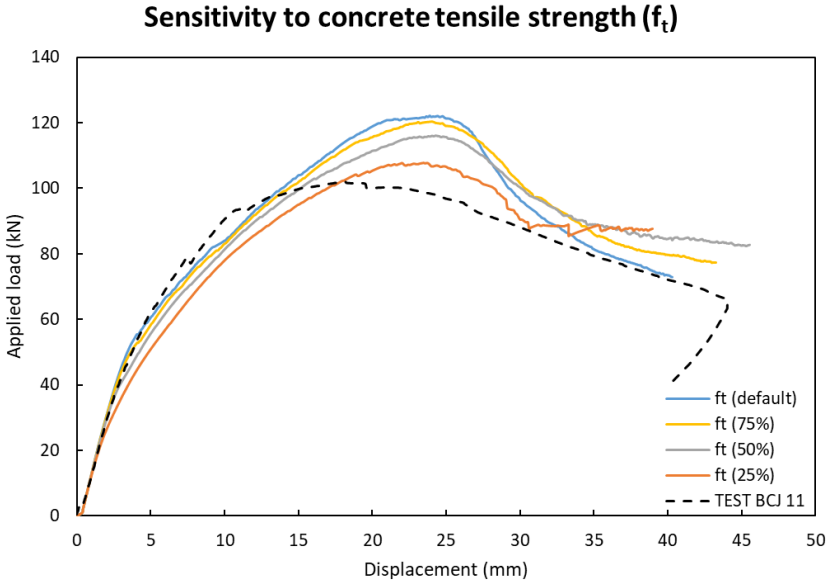

Figure 5-48 Material constitutive model for 3D NLFEA model using BCJ 11: sensitivity to concrete tensile strength (f_t)

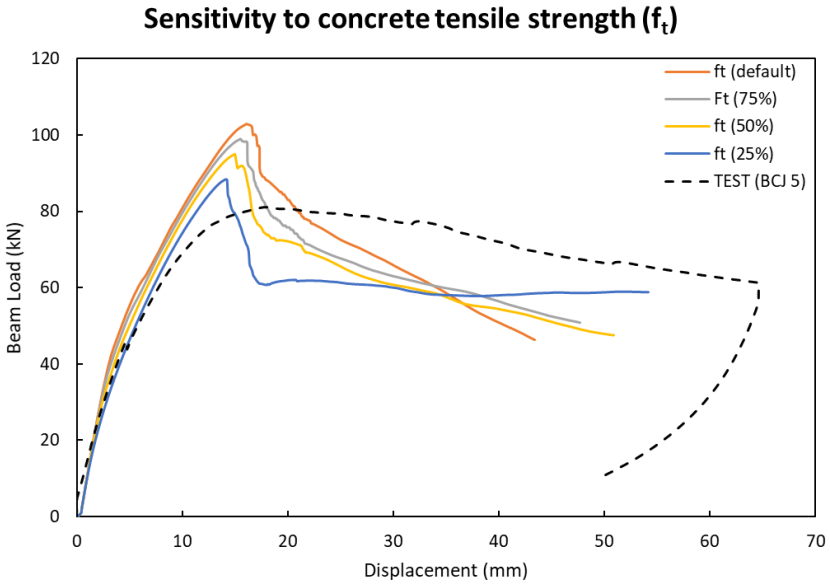

Figure 5-49 Material constitutive model for 3D NLFEA model using BCJ 5: sensitivity to concrete tensile strength (ft)

5.7.5 Sensitivity to critical compressive displacement (w_d)

The post-peak compressive displacement (softening branch) is modelled linearly in ATENA. The end of the softening curve is defined by a plastic displacement (w_d) which has a default value in ATENA of 0.5 mm. A sensitivity analysis was also carried out on both specimens BCJ 5 and BCJ 11 to determine a preferred value for w_d. Based on Figure 5-50 and Figure 5-51, a compressive displacement value of 0.9 mm is considered a good choice for simulating the tested specimens BCJ 5 and BCJ 11.

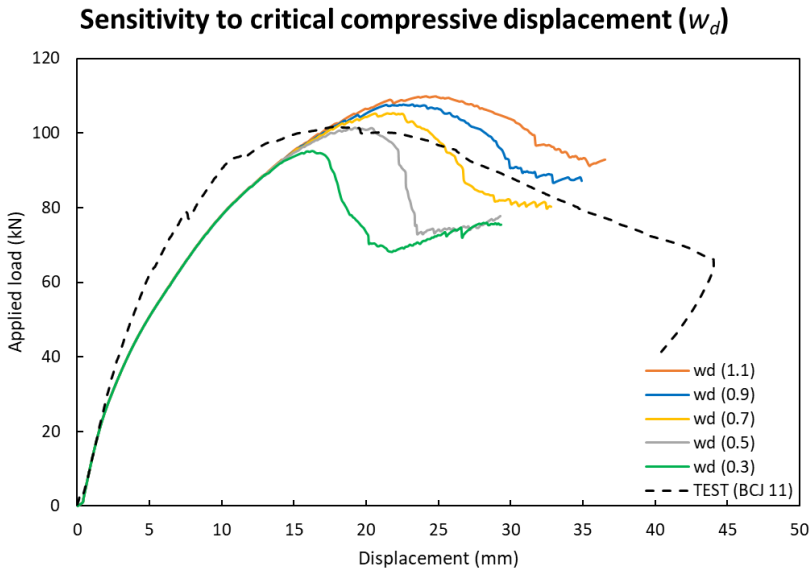

Figure 5-50 Material constitutive model for 3D NLFEA model using BCJ 11: sensitivity to critical compressive displacement (w_d)

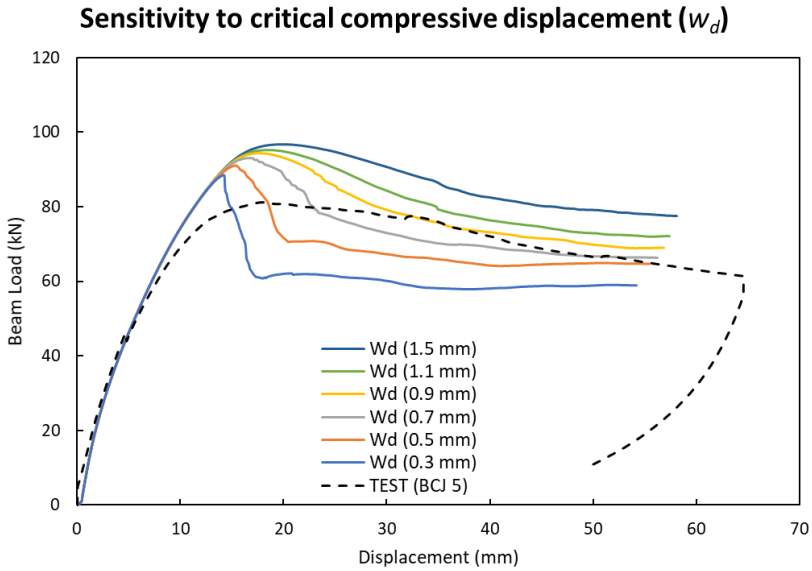

Figure 5-51 Material constitutive model for 3D NLFEA model using BCJ 5: sensitivity to critical compressive displacement (wd)

5.7.6 Sensitivity to fixed vs rotated crack model

The fixed crack model requires a shear factor (SF) to be input by the user, with a default value of 20. A study was carried out to determine the influence of the shear factor on the predicted response of BCJ11. Shear factors of 5, 10, 20 and 40 were investigated as shown in Figure 5-52. With all the considered shear factors the fixed crack model was found to underestimate joint shear strength. Consequently, the rotated crack model was used in this research.

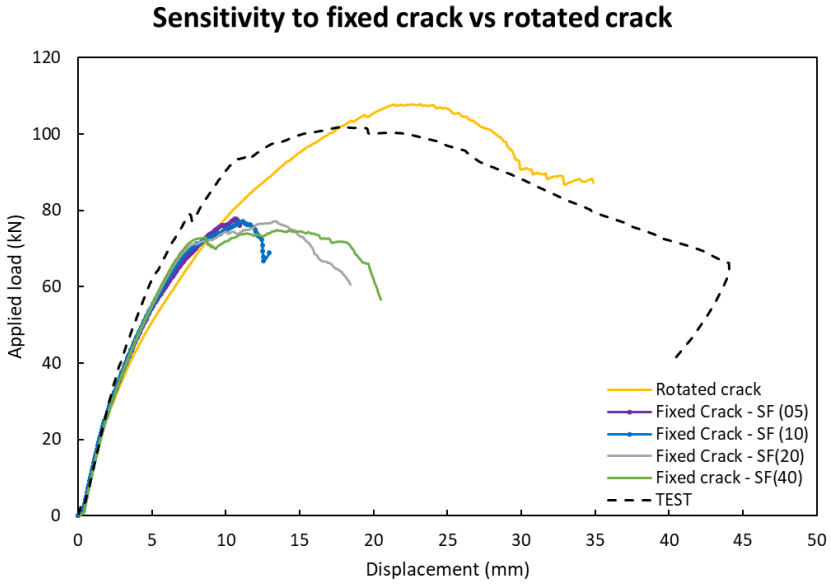

Figure 5-52 Material constitutive model for 3D NLFEA model: sensitivity to fixed vs rotated crack model

5.7.7 Sensitivity to bond-slip model

The influence of bond-slip model was investigated in the 3D model. ATENA provides three bond-slip models: Bigaj model [71], CEB-FIB model code [35] and a user defined bond-slip law. This research used Bigaj model for predicting the bond-slip occurred between concrete and steel reinforcement, with bond quality equal to excellent. The bond-slip model was applied to different parts of beam-column joint (the entire length of beam anchorage bars, the straight beam anchorage bars with only the bend bar portion and all the steel reinforcements inside the joint). Applying the bond-slip model just to the bars inside the joint was found to result in reasonable predictions. As shown in Figure 5-53, the bond-slip model was applied on beam anchorage reinforcement located inside joint, column bars crossing the joint and stirrups located inside the joint. This method was applied on both anchorage bar detailing for specimens having L-anchorage reinforcement and U-anchorage reinforcement. This technique also helps in determining the shear resisting mechanism of the concrete in the joint

core and the truss mechanism of the joint core (bond behaviour between concrete and steel reinforcement) acting inside the joint.

The crack width and principal strains are presented at peak load in Figure 5-54 and Figure 5-55. It can be seen the bond-slip model influenced the crack width compared with the 3D model with perfect bond. The principal strain was also monitored in both 3D models and it was found the maximum value of principal strain in steel reinforcement became smaller when bond-slip model was used. Figure 5-54 shows small differences in crack width and principal maximum strain while this difference became larger when joint stirrups are present as shown in Figure 5-55. Additionally, the results of the response of load-displacement curve are presented in Figure 5-56. The influence of the bond-slip model can be seen clearly in the failure which reduced when bond-slip was activated.

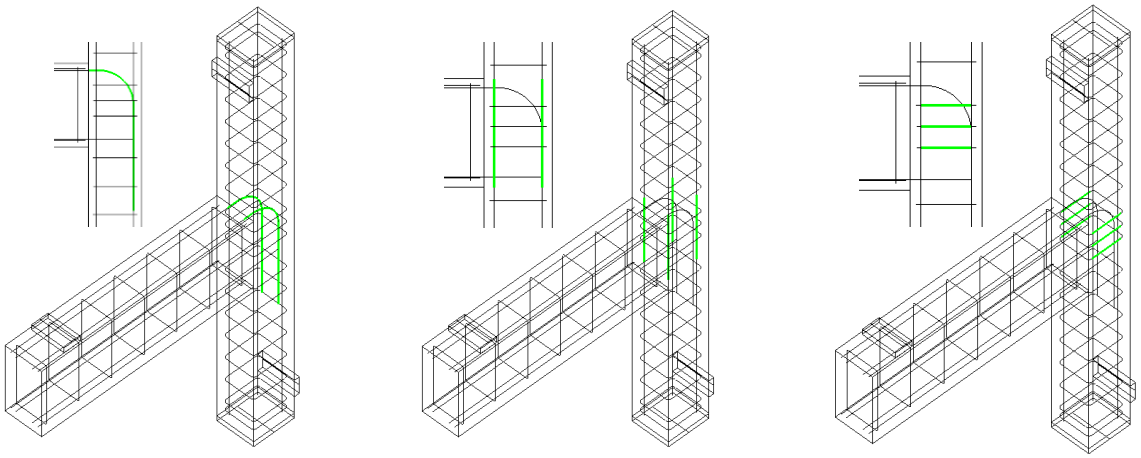

a) Specimens with L-anchorage beam bar reinforcement

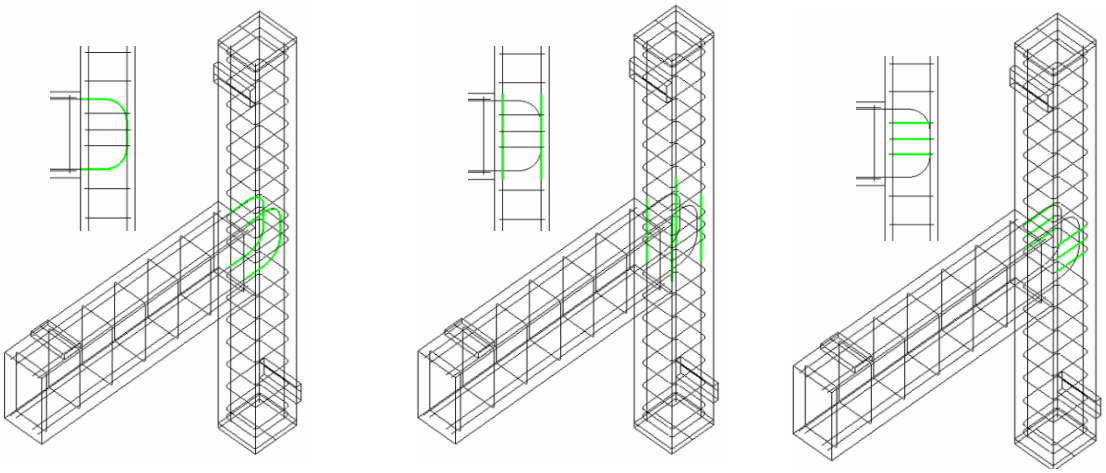

b) Specimens with U-anchorage beam bar reinforcement

Figure 5-53 Application of bond-slip model on steel reinforcements

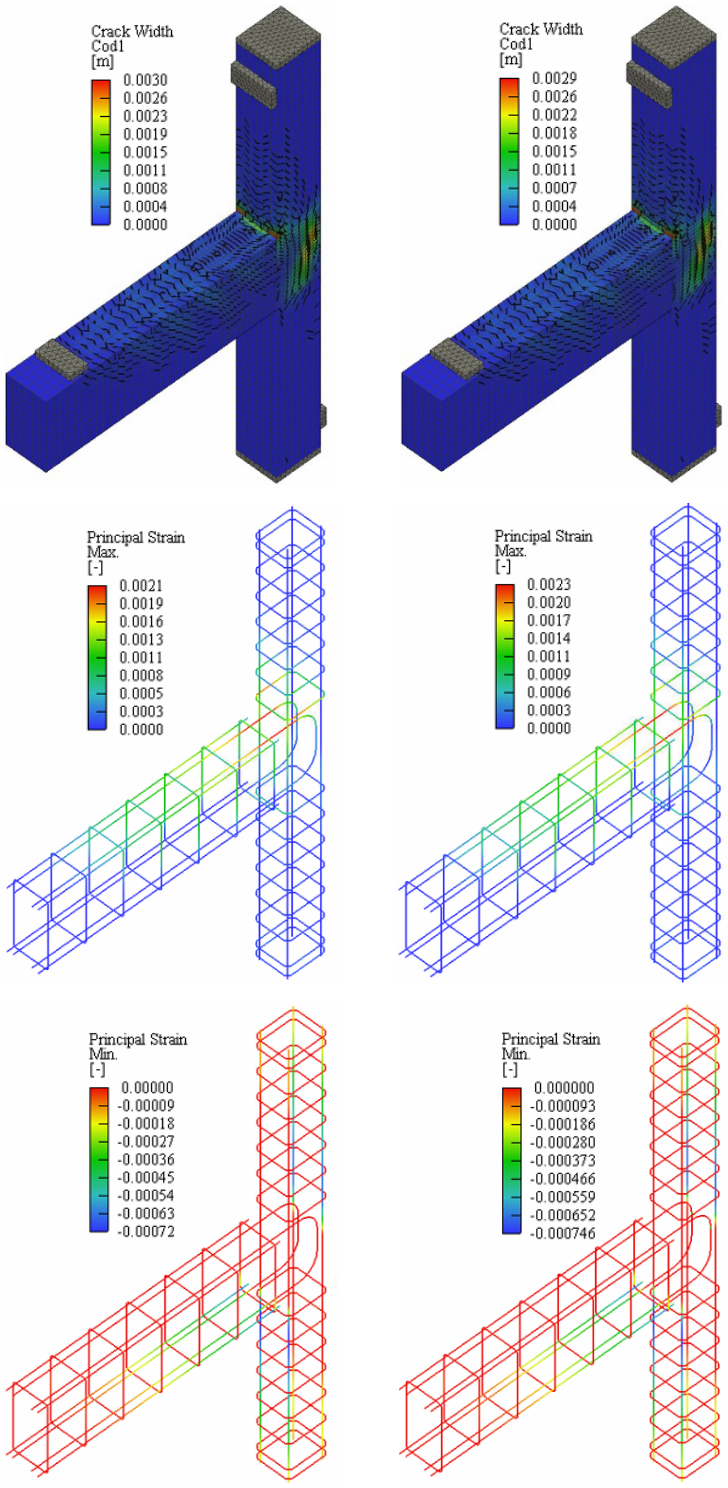

a) With bond-slip model b) Perfect bond model

Figure 5-54 Crack width and principal strain of 3D model using specimen BCJ 11.

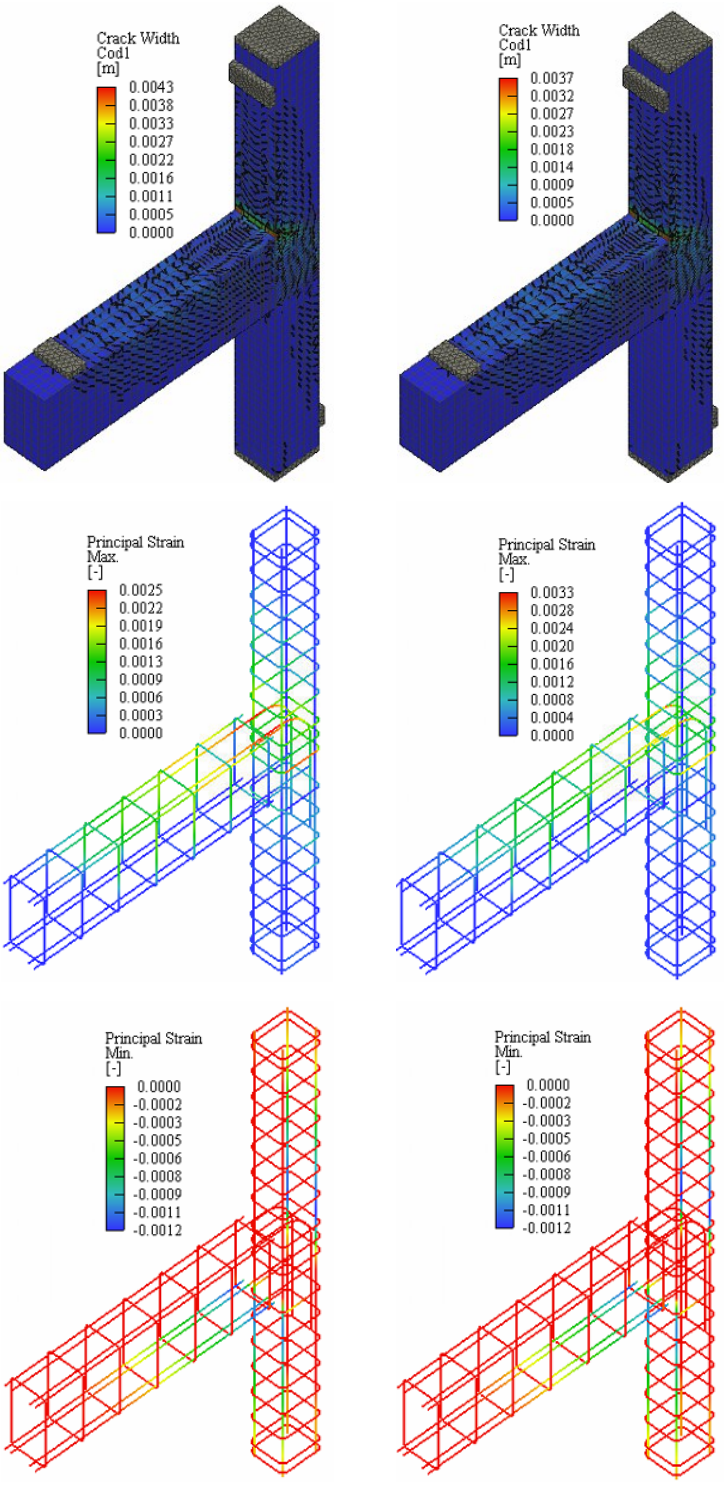

a) With bond-slip model b) Perfect bond model

Figure 5-55 Crack width and principal strain of 3D model using specimen BCJ 2.

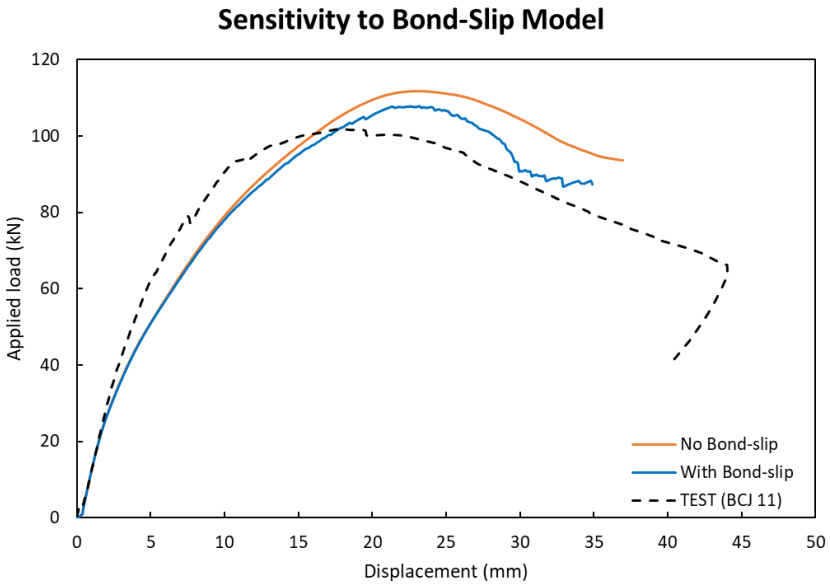

Figure 5-56 Material constitutive model for 3D NLFEA model: sensitivity bond-slip model

5.7.8 Summary of adopted 3D modelling parameters

The final parameters adopted in the 3D model are presented in Table 5-9. The remaining material constitutive parameters were kept as default value as shown in Table 5-2.

Table 5-9 Chosen parameters input for 3D model.

Parameter	Function/reference
Concrete constitutive model	
Concrete cylinder strength	f_c' = -0.85 f_{cu} f_{cu} = defined by the user
Concrete elastic modulus (E_c)	$E = (6000 - 15.5 f_{cu})\sqrt{f_{cu}}$ **Taken as 50% of default value**
Concrete Tensile strength (f_t)	$f_t = 0.24\ fcu^{2/3}$ **Taken as 25% of default value**
Concrete fracture energy factor (G_f)	$G_f = 0.000025\ f_t$ **Taken as 80% of default value**
Concrete ductility (w_d)	Default value = -0.5 mm **Taken as -0.9 mm**
reduction of concrete strength due to cracking (c_f)	0.8 f_c' **Taken as 0.2**
Poisson's ratio (ν)	0.2
Tension stiffening stress (σ_{st})	σ_{st} = 0
Maximum aggregate size	d_{agg} = specified by user
Crack model	**Rotated crack = 0**
Reinforcement bar model	
Stress-strain relationship	Bilinear
Bond-slip model	**Bigaj model with excellent bond quality inside joint region; and perfect bond with the remainders.**
Loading procedure and convergence	
Loading procedure	Force controlled
Iteration method	Arc-length method

5.8 Use of 3D model to investigate parameters varied in current test program

The ability of the NLFEA to simulate the parameters varied in the author's tests was investigated using the final chosen parameters from Table 5-9. These parameters include column axial load, beam bar detailing, joint stirrups and column intermediate bars. The following sections describe the effect of each parameter on the 3D model.

5.8.1 Effect of column axial load

The ability of the NLFEA to simulate the influence of column axial load was investigated by modelling the author's specimens BCJ 3, BCJ 6 and BCJ 8 with axial loads of 300 kN for BCJ 3, 600 kN for BCJ 6 and 900 kN for BCJ 8. The 3D models slightly overestimated the measured failure loads as shown in Figure 5-57. The predicted failure load reduced slightly when the column axial load was increased from 300 kN to 600 kN as observed. However, increasing the column load to 900 kN made virtually no change to the predicted failure load unlike the measured failure load which reduced.

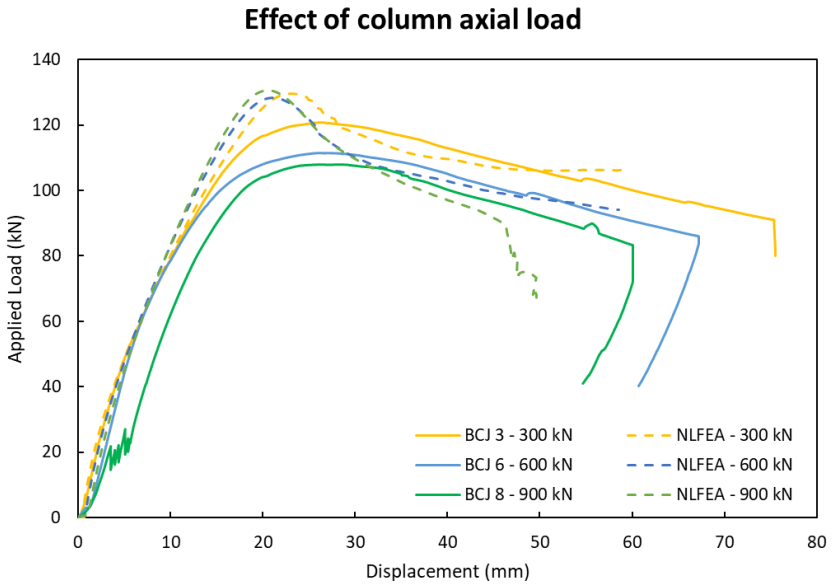

Figure 5-57 Validation of 3D model to experimental test parameters: effect of column axial load.

5.8.2 Effect of beam bar detailing

The ability of the 3D model to simulate the influence of beam bar detailing was investigated as shown in Figure 5-58. The simulation of beam bar detailing using L-anchorage bar showed good agreement with tested specimens BCJ 1 and BCJ 2 but the failure load of specimens BCJ

3 and BCJ 4 with U-anchorage bar was overestimated. Changing the size of the bend radius had a relatively small effect on the predicted failure load as experimentally observed.

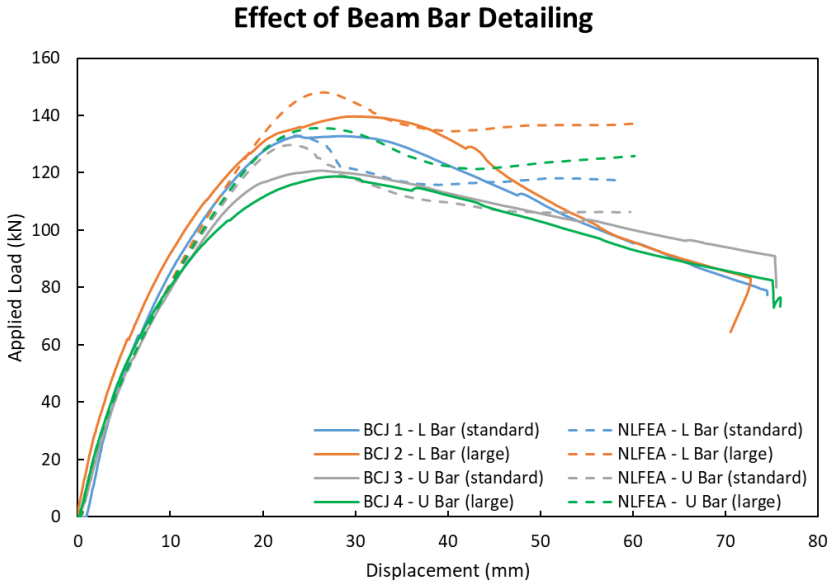

Figure 5-58 Validation of 3D model to experimental test parameters: effect of beam bar detailing.

5.8.3 Effect of joint stirrups

The influence of joint stirrups was investigated for both L-bars and U-bars. The results are presented in Figure 5-59 and Figure 5-60 which show that the NLFEA predicted the experimentally observed influence of joint stirrups well for both L-bars and U-bars.

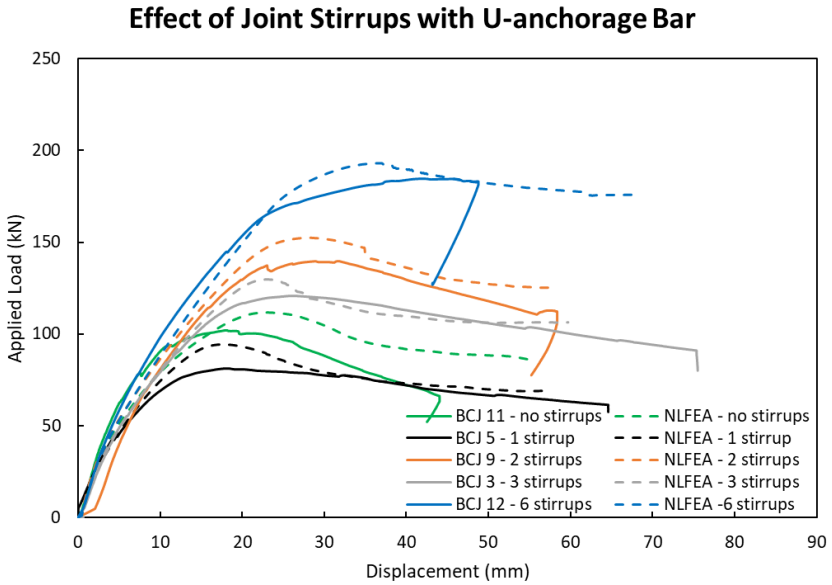

Figure 5-59 Validation of 3D model to experimental test parameters: effect of joint stirrups with U-anchorage bar.

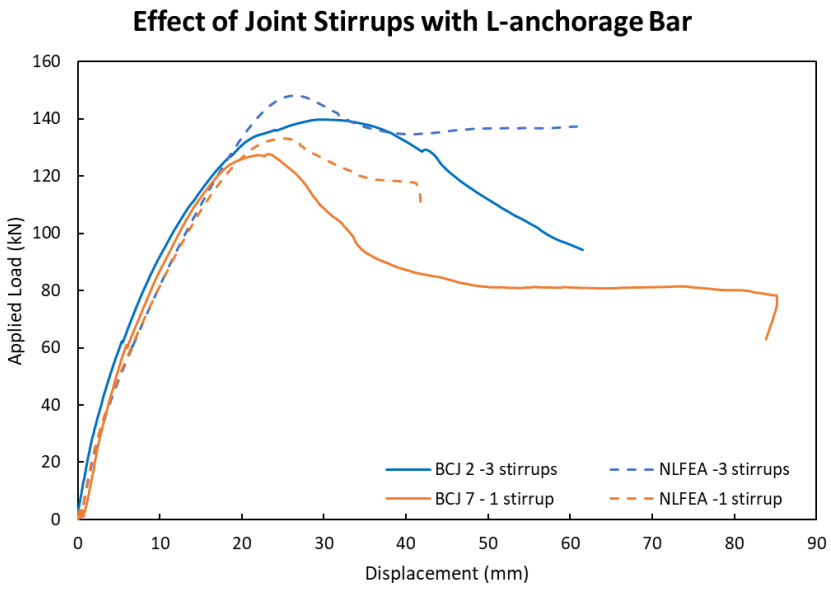

Figure 5-60 Validation of 3D model to experimental test parameters: effect of joint stirrups with L-anchorage bar.

5.8.4 Effect of column bars

The influence of adding intermediate bars in BCJ 10 was investigated numerically. As shown in Figure 5-61, the increase in strength of BCJ 10, with intermediate column bars, relative to BCJ 2 without intermediate column bars was well predicted.

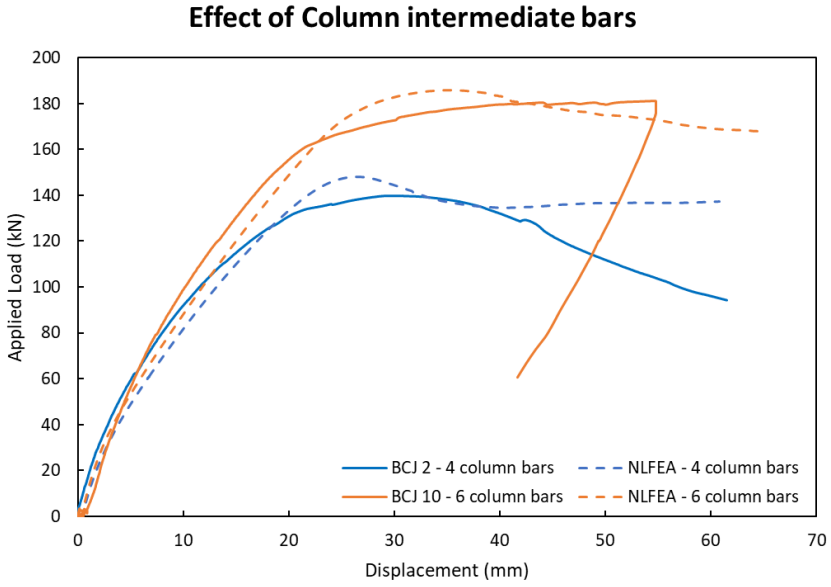

Figure 5-61 Validation of 3D model to experimental test parameters: effect of joint stirrups with U-anchorage bar.

5.9 Validation of 3D NLFEA model with test results

Figure 5-62 compares the measured and predicted load displacement responses for all the authors specimens. The measured and predicted responses are seen to compare well as also shown in Table 5-10 which lists the measured and predicted failure loads. The mean and standard deviation of P_{test}/P_{NLFEA} are 0.93 and 0.05 respectively.

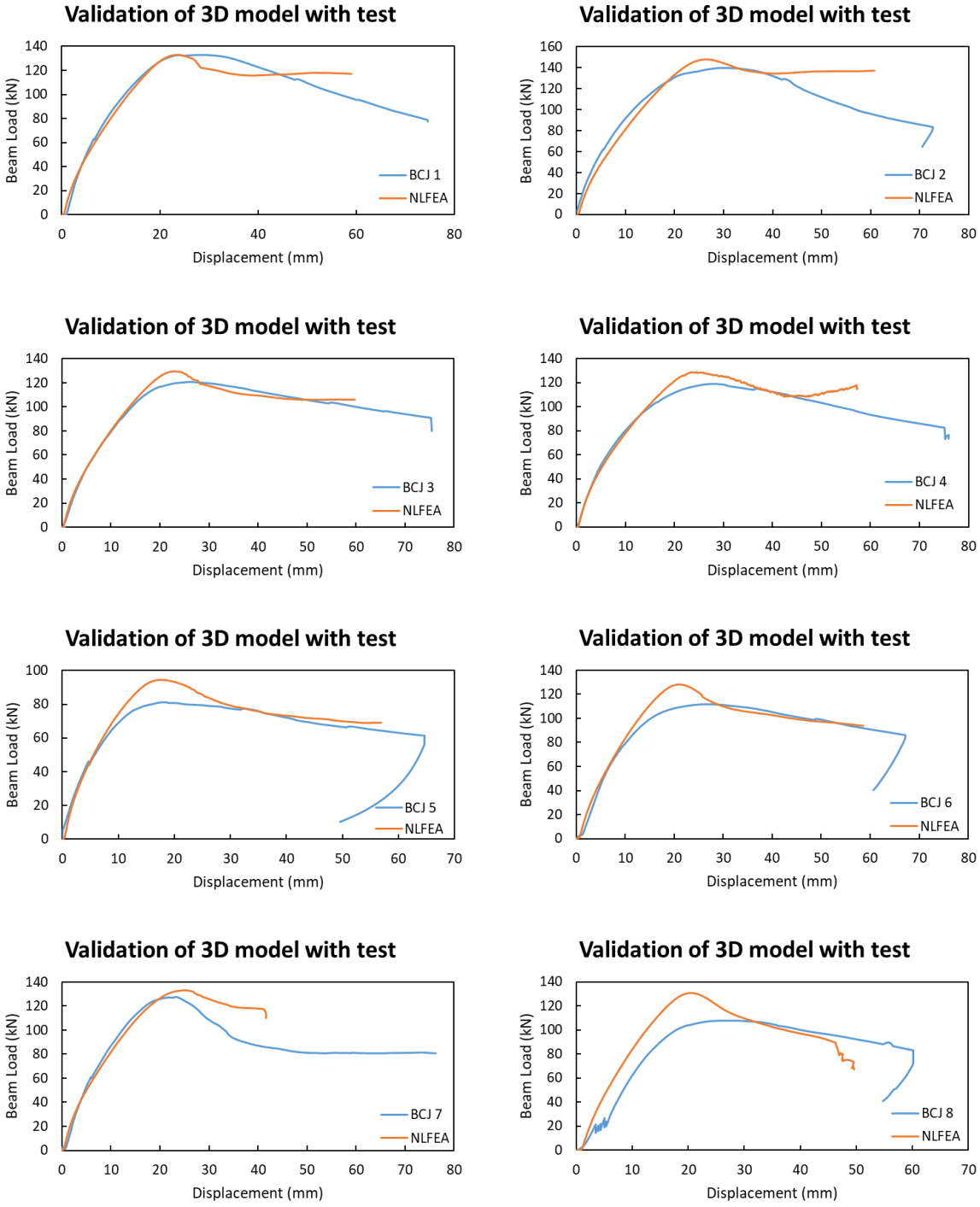

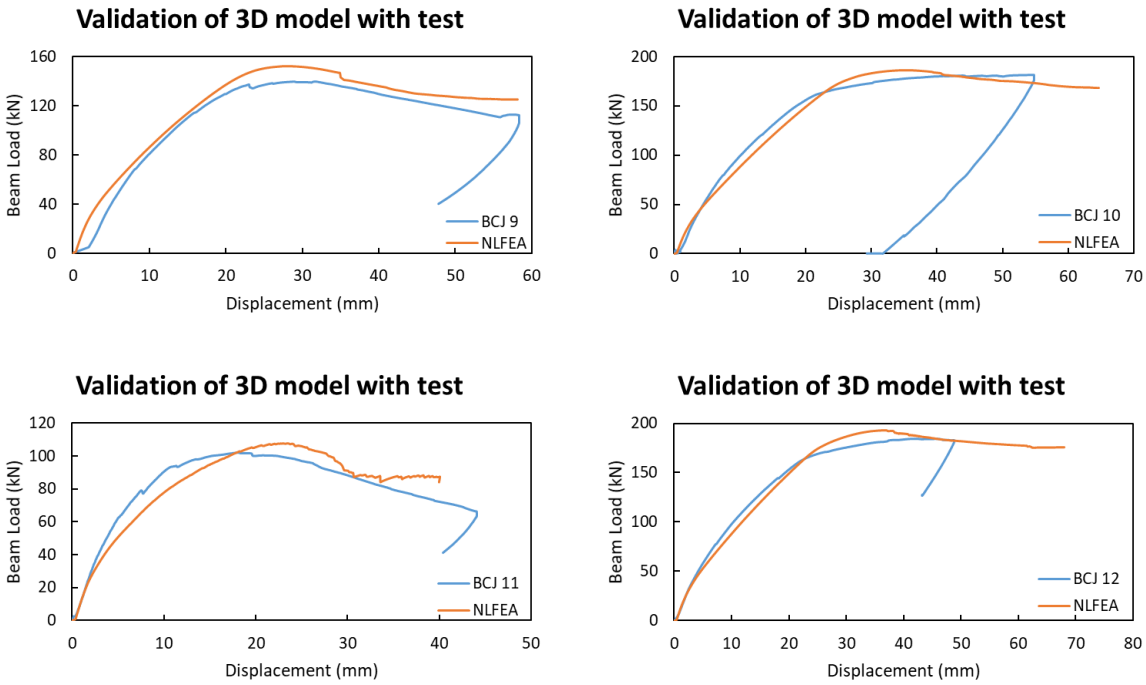

Figure 5-62 Validation of 3D model with Author tests

Table 5-10 Summary of validation of 3D model with Author tests: measured/predicted failure load from ATENA.

Test	Specimens	Measured failure load (kN)	Predicted failure load (kN)	Measured/Predicted
Author test	BCJ 1	132.8	134.8	0.99
	BCJ 2	139.7	148.5	0.94
	BCJ 3	120.8	128.8	0.94
	BCJ 4	118.8	128.9	0.92
	BCJ 5	81.1	92.7	0.88
	BCJ 6	111.5	129.0	0.86
	BCJ 7	127.6	129.1	0.99
	BCJ 8	107.9	131.5	0.82
	BCJ 9	139.7	150.1	0.93
	BCJ 10	181.2	190.3	0.95
	BCJ 11	101.9	107.9	0.95
	BCJ 12	184.6	196.3	0.94
			Mean	0.93
			Standard deviation	0.05

The calibrated 3D model was also used to simulate seven beam-column joint specimens tested by Ortiz [12] for which only the failure load is available and not the load-displacement response. Thus, the 3D model was assessed with only the failure load as shown in Figure 5-63. Overall, the comparison between measured and predicted failure loads is good as shown in Table 5-11 and Figure 5-64.

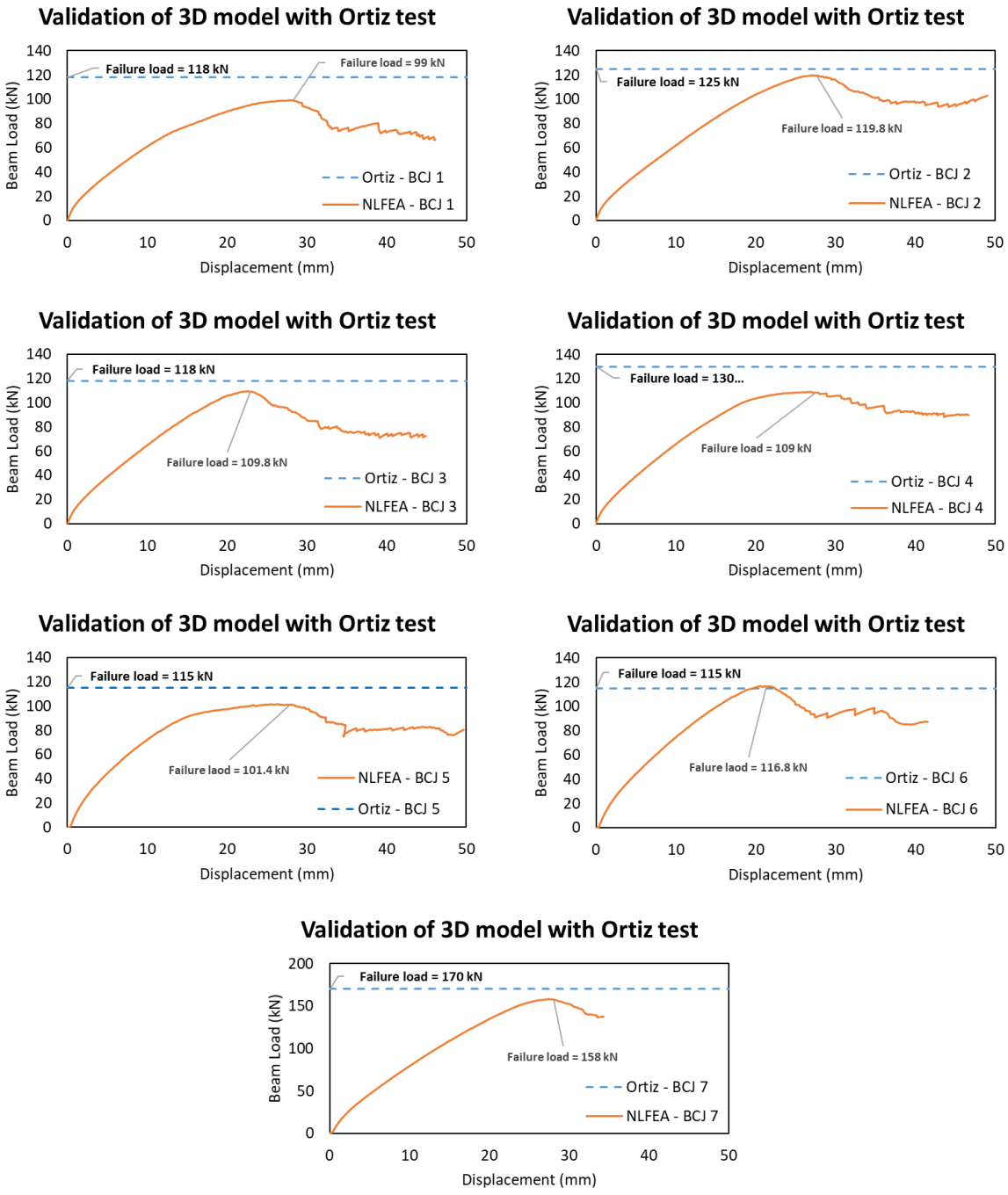

Figure 5-63 Validation of 3D model with Ortiz tests

Table 5-11 Summary of validation of 3D model with Ortiz tests: measured/predicted failure load from ATENA.

Test	Specimens	Measured failure load (kN)	Predicted failure load (kN)	Measured/Predicted
Ortiz test	BCJ 1	118.0	99.0	1.19
	BCJ 2	125.0	119.8	1.04
	BCJ 3	118.0	109.8	1.07
	BCJ 4	130.0	109.0	1.19
	BCJ 5	115.0	101.4	1.13
	BCJ 6	115.0	116.8	0.98
	BCJ 7	170.0	158.0	1.08
			Mean	1.10
			Standard deviation	0.08

Measured and predicted results are compared for the tests of both the author and Ortiz in Table 5-12 and Figure 5-64. Overall, the 3D model gives excellent predictions with a mean value of 0.99 and a standard deviation of 0.10 for P_{test}/P_{NLFEA}.

Table 5-12 Summary of 3D model measured/predicted failure load from ATENA.

Test	Specimens	Measured failure load (kN)	Predicted failure load (kN)	Measured/Predicted
Ortiz test	BCJ 1	118.0	99.0	1.19
	BCJ 2	125.0	119.8	1.04
	BCJ 3	118.0	109.8	1.07
	BCJ 4	130.0	109.0	1.19
	BCJ 5	115.0	101.4	1.13
	BCJ 6	115.0	116.8	0.98
	BCJ 7	170.0	158.0	1.08
Author test	BCJ 1	132.8	134.8	0.99
	BCJ 2	139.7	148.5	0.94
	BCJ 3	120.8	128.8	0.94
	BCJ 4	118.8	128.9	0.92
	BCJ 5	81.1	92.7	0.88
	BCJ 6	111.5	129.0	0.86
	BCJ 7	127.6	129.1	0.99
	BCJ 8	107.9	131.5	0.82
	BCJ 9	139.7	150.1	0.93
	BCJ 10	181.2	190.3	0.95
	BCJ 11	101.9	107.9	0.95
	BCJ 12	184.6	196.3	0.94
			Mean	0.99
			Standard deviation	0.10

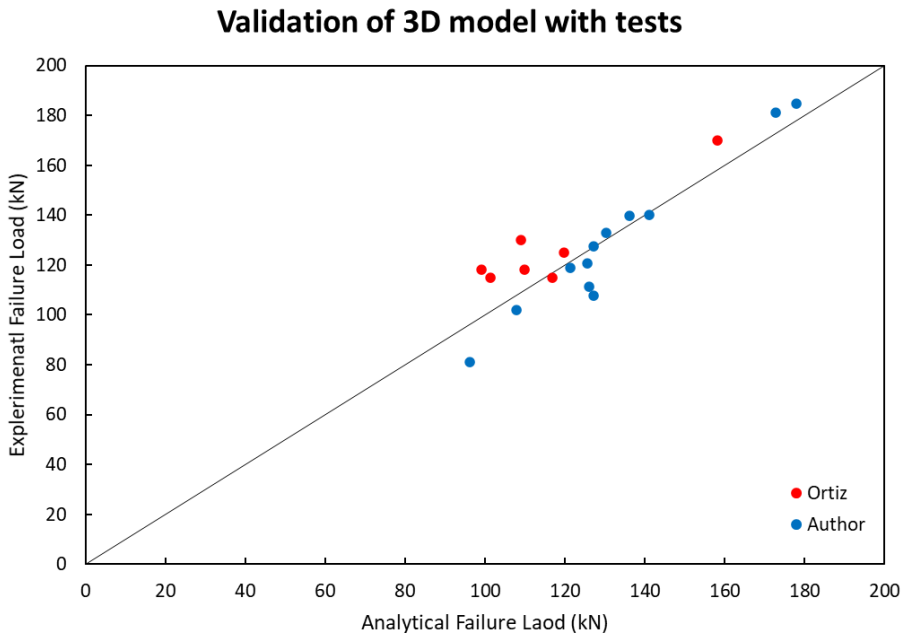

Figure 5-64 Validation of 3D model with Ortiz and Author tests

5.10 Reviewing 2D and 3D models

This section addresses the differences between the predictions of the results obtained with 2D and 3D models. Overall, significantly better predictions of failure load and load-displacement response were obtained with the 3D than 2D models. The 3D model was able to capture not only the failure load of the authors specimens but also the shape of the load-displacement curve unlike the 2D model where the post peak response was overly brittle. This may be due to the ability of 3D model to simulate the response of the joint in the transverse direction (stresses through the column width), the effect of stirrup confinement in the joint core and spalling of the concrete at the back of joint. Both the 2D and 3D models gave better predictions for the failure loads of the author's specimens than Ortiz's. This is unsurprising since the NLFEA was calibrated using specimen BCJ 11 from this program. The load-displacement curve is not generally reported in previous tests of monotonically loaded beam-column joints. This precludes rigorous validation of NLFEA modelling procedures with data from most previous test campaigns on monotonically loaded external beam-column joints. Further test data, with load-displacement curves, are required to properly assess the generality of the proposed 2D and 3D NLFEA modelling procedures. The 2D NLFEA model utilized a plane-stress model which did not take into account the effect of out-of-plane behaviour.

5.11 Summary

The chapter describes the background to the NLFEA carried out in this project using ATENA. The theoretical background to the constitutive material models adopted for 2D and 3D models is presented. The constitutive concrete model used for 2D analysis is depicted "SBETA" while that used for 3D analysis is depicted "CC3D Nonlinear Cementitious2". As described, some of the theoretical background is common to both the 2D and 3D models. A bilinear model is adopted for reinforcement in both the 2D and 3D models. Some background is given on iterative solution methods including full Newton-Raphson, modified Newton-Raphson and the arc-length method which is used in this research.

The chapter goes on to describe the development of the 2D and 3D NLFEA modelling procedures used to simulate external beam-column joints. The validation of the NLFEA models with experimental results is described. Both mesh and material model input parameter sensitivity studies were carried out for both the 2D and 3D models. The parameters studied include elastic modulus of elasticity, reduction of concrete strength factor, concrete tensile strength, tension stiffening, critical compressive displacement, fixed crack and rotated crack models and bond-slip.

The proposed 2D and 3D modelling procedures are assessed by modelling the BCJ specimens tested by the author and Ortiz [12]. Both models are shown to give reasonable predictions of failure load but overall the behaviour of the analysed beam-column joints is significantly better simulated with the 3D than 2D models.

Chapter 6 Crack kinematics and Shear Transfer Actions

This chapter describes the crack kinematics and calculation of shear transfer actions for each test. Shear transfer actions are evaluated by studying the relative contributions of shear reinforcement, concrete compression zone, bend in beam anchorage bar and aggregate interlock to joint shear strength.

6.1 Analysis of shear transfer actions in beam-column joint

The shear transfer actions were determined from consideration of the forces acting on a free body defined by the joint boundaries and the dominant shear crack at failure. The forces acting on the free body include those in the reinforcement and concrete at the joint boundaries with the beam and column as well as the forces acting on the dominant shear crack. The latter include aggregate interlock and tensile forces in the stirrups and beam flexural reinforcement.

Horizontal equilibrium of free body (B):

The considered free body diagram (B) and the forces acting on it are shown in Figure 6-1. The horizontal forces acting on free body A are shown in red. Forces acting on the joint boundaries with the beam and column are depicted external. These include the compressive and tensile flexural forces coming from beam and the column shear forces acting on the joint boundaries (V_{col}). Forces acting on the diagonal shear crack are depicted internal. These include aggregate interlock, tension in the shear and beam reinforcement crossing the shear crack and below the crack a component of flexural compression from the beam. The following expression describes the horizontal equilibrium of the free body diagram (B).

$$V_{agg,hor} + \sum T_{stirrup} + T_{b,hor} + C_b - C_{comp} = T_b - V_{col} = V_j \quad (6\text{-}1)$$

In which $V_{agg,hor}$ is the horizontal force of aggregate interlock and $T_{b,hor}$ is the horizontal force in the bend anchorage bar crossing the critical crack. $\sum T_{stirrup}$ is the total force resisted by shear reinforcement, C_b is the beam flexural compressive force and C_{comp} is the component of flexural compressive force in the beam resisted by free body A. These forces are equilibrated by the joint shear force ($T_b - V_{col} = V_j$), where T_b and V_{col} represent tensile force in beam anchorage bar and shear force in column respectively. The contribution of shear reinforcement $\sum T_{stirrup}$ is omitted if the beam-column joint has no joint stirrups.

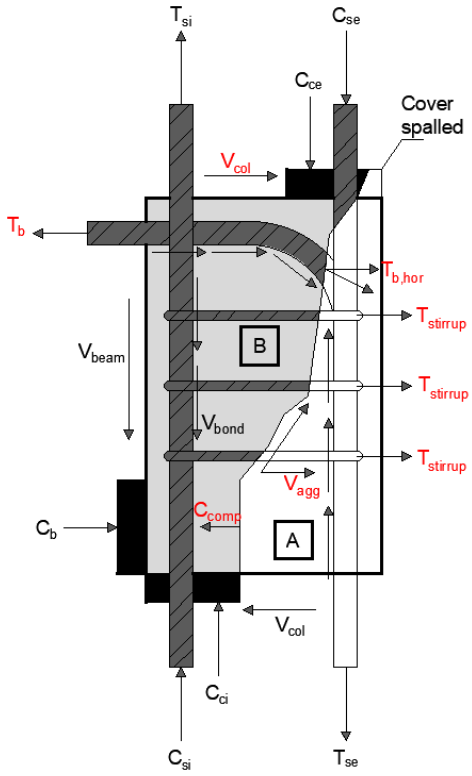

Figure 6-1 Horizontal equilibrium of shear transfer actions in a free body diagram of a beam-column joint.

Vertical equilibrium of free body (B):

The considered free body diagram (B) is shown in Figure 6-2 with vertical components of force marked in red. The vertical components of the external forces applied at the joint boundaries comprise the column axial load (N_{col}), beam shear force (V_{beam}) and flexural forces from the column. The vertical forces acting on the shear crack comprise components from aggregate interlock and the bend of the beam reinforcement. Vertical equilibrium of the free body diagram (B) is defined using the following formula:

$$V_{beam} + N_{col} - C_{se} + T_{b,ver} = V_{agg,vert} + C_{si} + V_{comp,A} \quad (6\text{-}2)$$

The force $V_{agg,vert}$ is the vertical component of aggregate interlock, $V_{comp,A}$ is the resultant vertical compressive force acting on free body A at the boundary with the lower column. This force is indeterminate due to the presence of the indeterminate vertical shear force V_{comp} acting on free body A at the base of the diagonal shear crack. These upward forces are balanced by the upper column axial force (N_{col}) less the upper column bar flexural compressive force (C_{se}), the beam shear force (V_{beam}) and the beam bend bar force ($T_{b,ver}$).

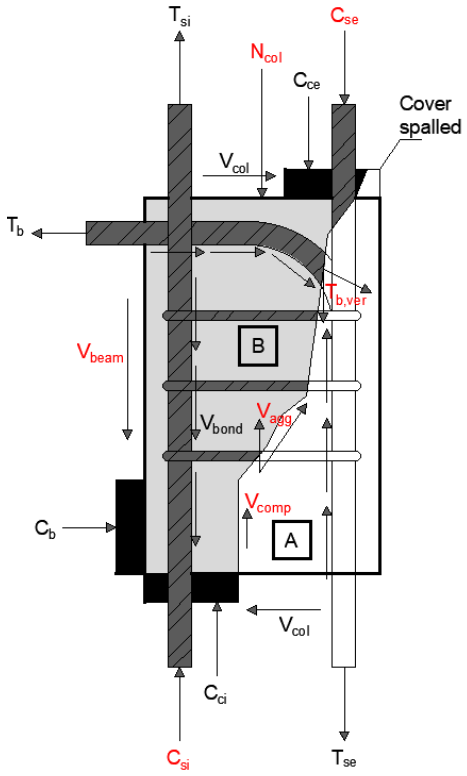

Figure 6-2 Vertical equilibrium of shear transfer actions in a free body diagram of a beam-column joint.

As explained in the literature review, the truss mechanism is responsible for resisting the horizontal and vertical forces acting on joint stirrups and column intermediate bars. This research focuses on the horizontal shear transfer mechanism since this directly controls the joint shear resistance. Additionally, the influence of dowel action is omitted because it is considered to only make a significant contribution to shear resistance in specimens with intermediate column bars of which only one was tested in this research. The effect of residual tensile stress was also not considered within the shear transfer actions since the forces in joint are indeterminate and adding this action to the calculation made it more complex.

6.2 Free body diagram of each tested BCJ specimen

A free body diagram was produced for each BCJ specimen to obtain the shear transfer mechanism in the horizontal direction. This process assessed the horizontal forces resisting shear force in the joint which comprise the shear reinforcement force, aggregate interlock force, bend force in beam anchorage bar, concrete compression zone and external forces at joint boundaries. The following sections describe the analysis of the free body diagram for each BCJ specimen in the three series. In all specimens, the forces acting along the crack due to aggregate interlock and tension in the stirrups were calculated in terms of the crack

displacements while the force in the bend of the beam reinforcement was estimated from both strain gauge measurements and the observed crack width. The resultant horizontal concrete compressive force (C_{comp}) was calculated from equilibrium using equation (6-1).

6.2.1 BCJ series 1

The variables in this series were the beam reinforcement anchorage type and the beam bar bend radius. The joint shear reinforcement consisted of three stirrups and the upper column load was 300 kN. The anchorage type was L-bar and U-bar with either a standard or large bend radius, as described in chapters 3 and 4.

6.2.1.1 Specimen BCJ 1

The critical crack appeared at the centre of joint and propagated continuously towards the top right corner of the joint. The critical shear crack crossed all three joint stirrups, the bend of the beam anchorage bar and the back column bars. At peak load, the concrete cover spalled off near the back of top column as shown in Figure 6-3(a).

6.2.1.2 Specimen BCJ 2

The tip of the critical shear crack ended just below the top right corner of the joint. The crack passed through the bend of the beam bars, joint stirrups and the back column bars but did not cause spalling of the concrete cover. The horizontal forces acting on the considered free body are shown in Figure 6-3(b).

6.2.1.3 Specimen BCJ 3

Similar to specimens BCJ 1 and 2, the critical shear crack ran from the compression zone at which the beam and column compression flexural forces meet to the top right hand corner of the joint. The crack passed through all the three joint stirrups, the bend of anchorage bar and back column bars. The horizontal forces acting on the considered free body are shown in Figure 6-3(c). No spalling of the concrete cover occurred in the top column.

6.2.1.4 Specimen BCJ 4

The development of the critical crack in this specimen differed from the other specimens since the critical shear crack intersected both the bottom and top bends of the U-bar. The diagonal crack also passed through the joint stirrups and back column bars. The horizontal forces acting on the joint are shown in Figure 6-3(d). The diagonal crack propagated towards the top column at peak load but did not cause spalling of the concrete cover.

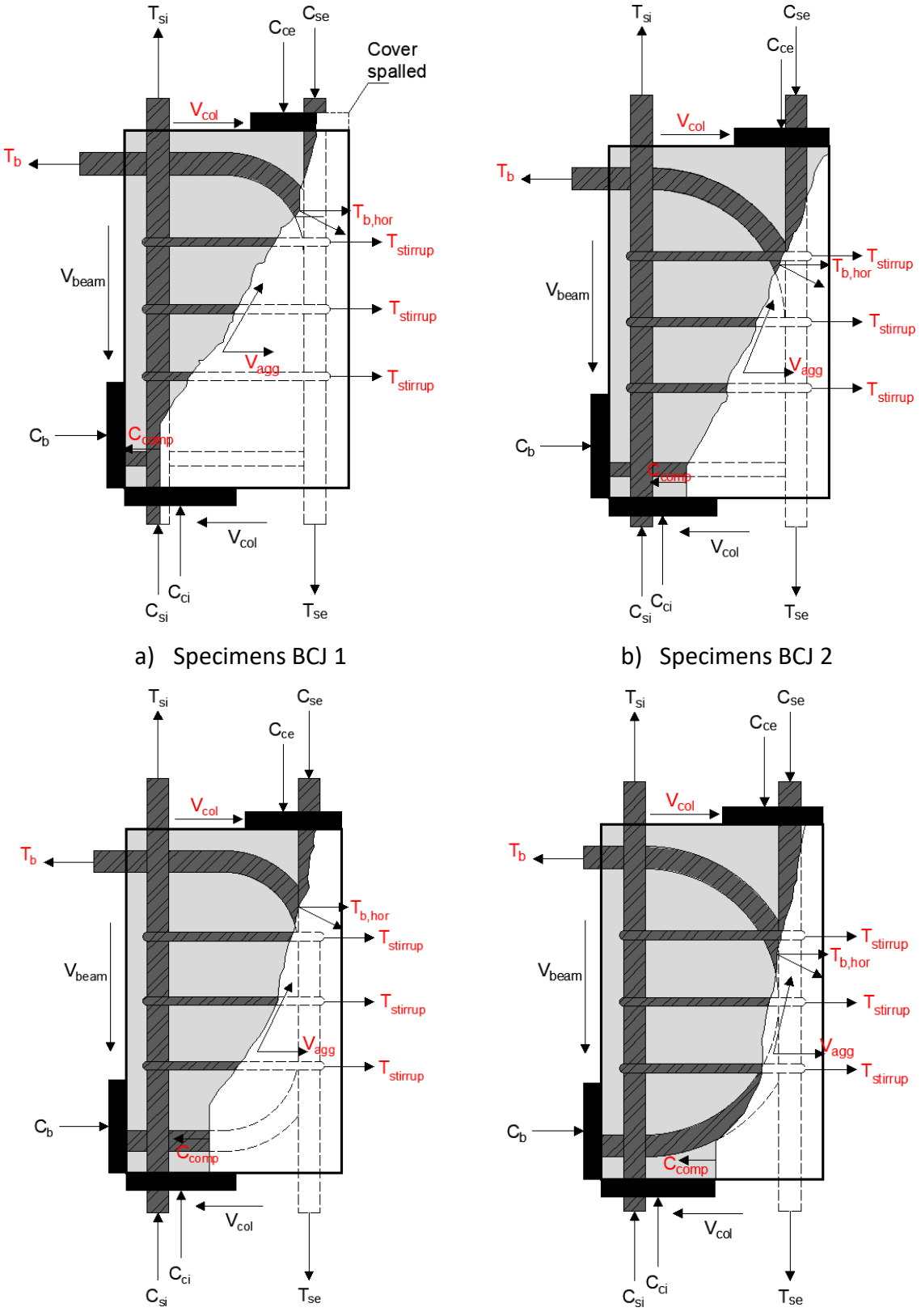

Figure 6-3 Horizontal equilibrium of shear transfer actions of series 1.

6.2.2 BCJ series 2

This series investigated the influence of increasing the column axial load as well as varying the number of joint stirrups. The joint shear reinforcement consisted of either one stirrup (BCJ 5 and BCJ 7) with low column load of 300 kN or three stirrups (BCJ 6 and BCJ 8) with higher column loads of 600 and 900 kN respectively. The anchorage type used in this series was U-bar except for BCJ 7 having L-bar with large bend radius of 150 mm, as described in chapters 3 and 4.

6.2.2.1 Specimen BCJ 5

The diagonal crack in this specimen initiated at the centre of joint and propagated towards the top right corner of joint running vertically before extending along the back column bars. The crack passed through the shear reinforcement and the bend of the beam anchorage bar. The horizontal forces acting on the considered free body are shown in Figure 6-4(a).

6.2.2.2 Specimen BCJ 6

The critical shear crack propagated diagonally from the compression zone at the bottom corner of the joint to the diagonally opposite corner at the top of the joint. The diagonal crack crossed all the three joint stirrups, the top bend of the beam anchorage bars and a portion of the back column bars. The horizontal forces acting on the considered free body are shown in Figure 6-4(b). This specimen had a high column axial load of 600 kN.

6.2.2.3 Specimen BCJ 7

The critical shear crack in this specimen propagated from the compression zone at the left bottom corner of joint to the diagonally opposite corner at the top of joint. The joint stirrup and the bend of beam tension bar were crossed by the critical crack. These horizontal forces acting on the considered free body are shown in Figure 6-4(c).

6.2.2.4 Specimen BCJ 8

The critical shear crack in this specimen formed near the back of the column bars. This crack intersected all three stirrups, the bend of beam tension bars and the back column bars. The horizontal equilibrium forces are presented in Figure 6-4(d). This specimen had the highest column axial load of 900 kN.

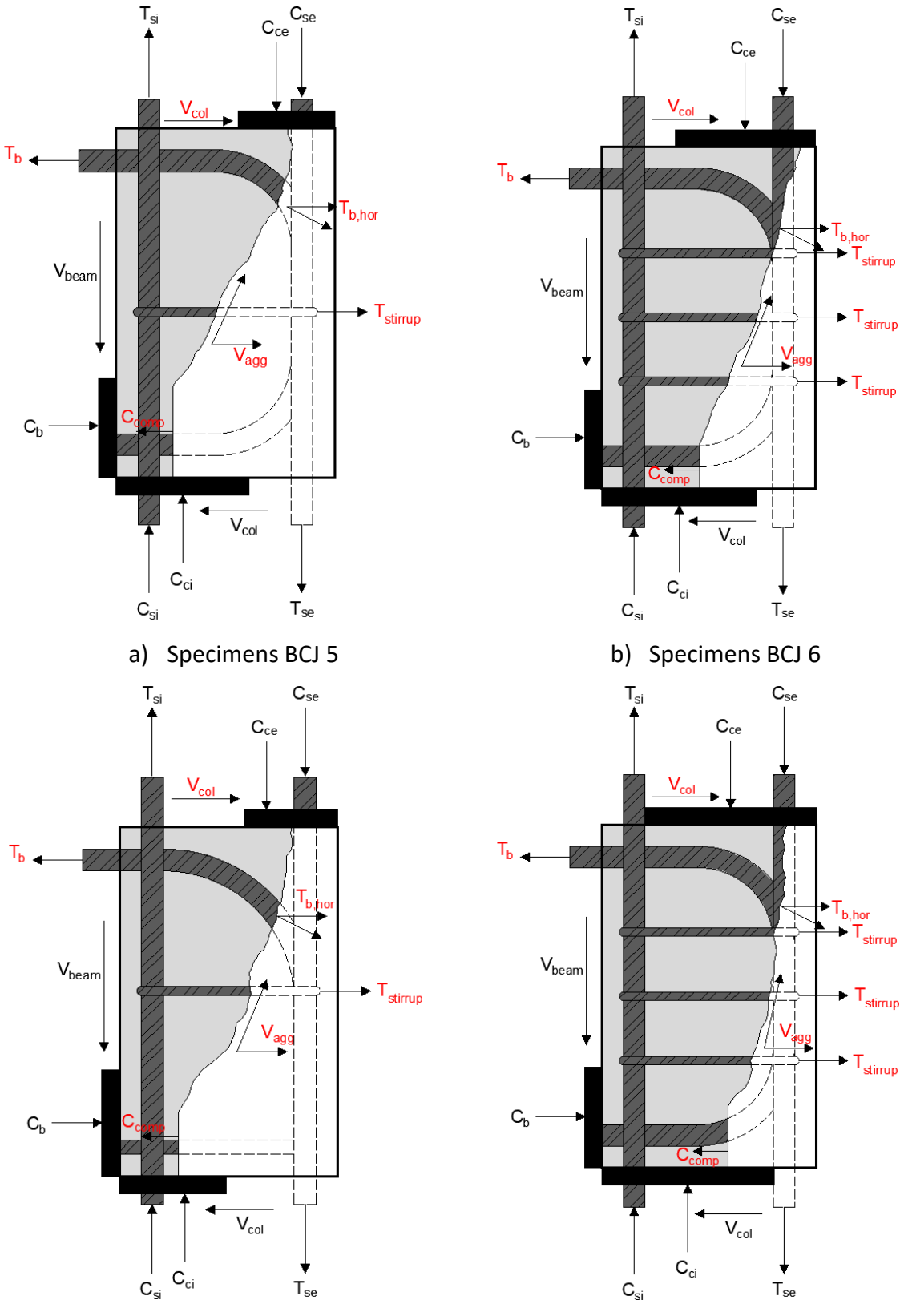

a) Specimens BCJ 5

b) Specimens BCJ 6

c) Specimens BCJ 7

d) Specimens BCJ 8

Figure 6-4 Horizontal equilibrium of shear transfer actions of series 2.

6.2.3 BCJ series 3

The influences of joint stirrups and intermediate column bars were investigated in this series. The number of joint stirrups was varied between two and six in specimens BCJ 9, BCJ 10 and BCJ 12. No joint stirrups were provided in specimen BCJ 11. Intermediate column bars were added in specimen BCJ 10 at the centre of column cross-section. Further details about this series are provided in chapters 3 and 4.

6.2.3.1 Specimen BCJ 9

The critical shear crack formed at the centre of joint and extended almost vertically along the back column bars towards the top right corner of the joint after crossing the central joint stirrup. The horizontal forces acting on the considered free body are shown in Figure 6-5(a).

6.2.3.2 Specimen BCJ 10

The critical diagonal crack formed near the compression zone in the beam and lower column. The crack extended to the opposite corner at the top of the joint. The crack became steep near the back column bars and extended vertically parallel with the back column bars. The crack passed through the intermediate column bars, all three joint stirrups and the bend in the beam anchorage bars. The horizontal forces acting on the considered free body diagram are shown in Figure 6-5(b).

6.2.3.3 Specimen BCJ 11

A steep crack formed in joint and extended vertically from above the second bend (bottom bend) to the top of joint, running parallel with the back column bars. The crack passed through the top bend in the beam anchorage bars. The horizontal equilibrium forces are shown in Figure 6-5(c).

6.2.3.4 Specimen BCJ 12

The critical crack in this specimen intersected the joint stirrups, the bend in the beam tension bars and part of back column bars. The horizontal equilibrium forces resisted the joint shear force are presented in Figure 6-5(d).

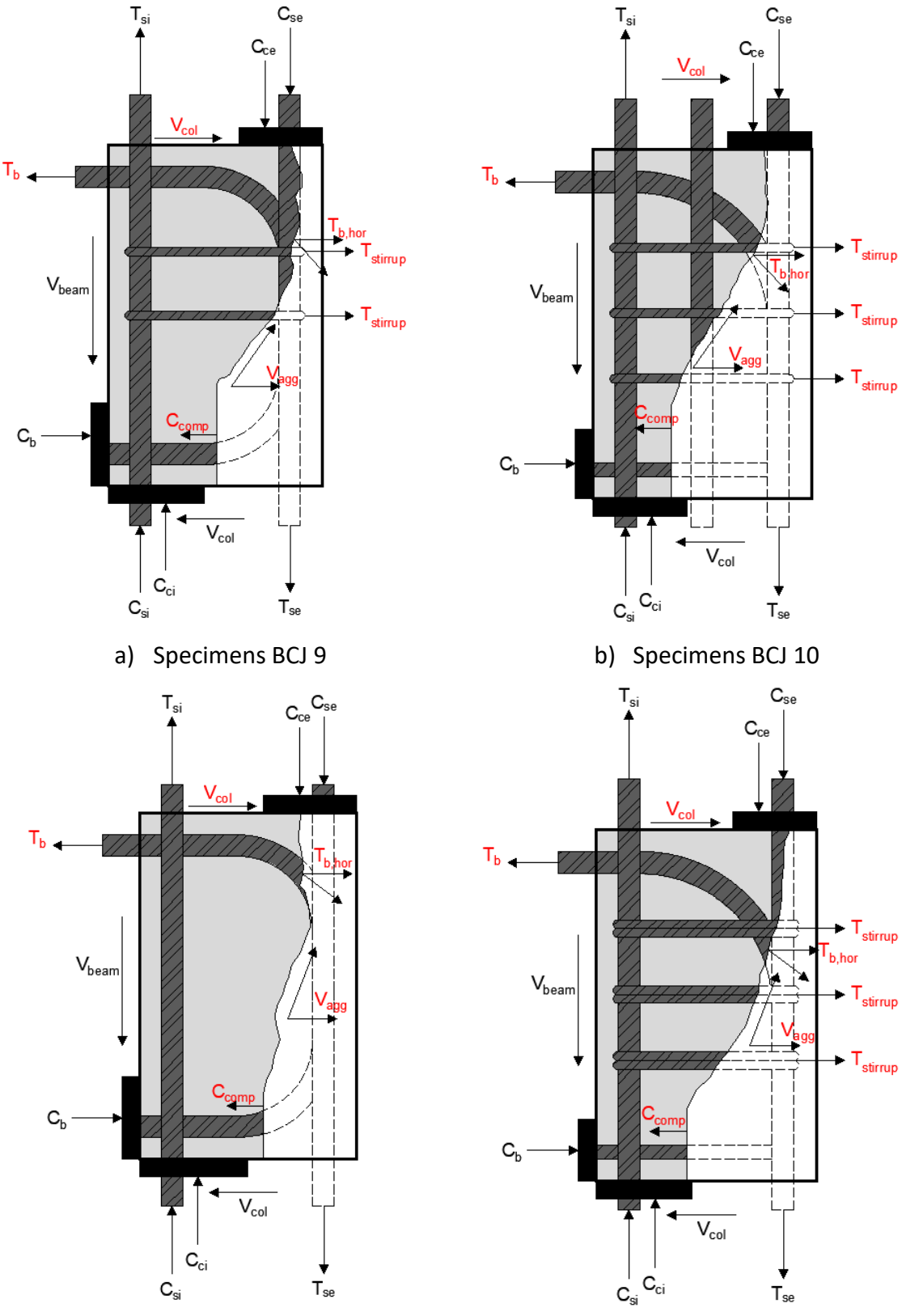

Figure 6-5 Horizontal equilibrium of shear transfer actions of series 3.

6.3 Total resultant force of aggregate interlock

The shear force transferred through the critical crack by aggregate interlock was assessed using the two-phase model of Walraven [41], Hamadi and Regan [44], the rough crack model (Bazant and Gambarova [45] & Gambarova and Karakoc [46]) and the simplified contact density method of Li et al. [42]. The rough crack model and the Hamadi and Regan method were derived from regression analysis of experimental results. The remaining two methods were developed theoretically. The contribution of aggregate interlock was calculated in terms of the crack opening and sliding displacements obtained with DIC. The results of the contribution of aggregate interlock for each beam-column joint specimen are shown in Figure 6-6.

The contribution of aggregate interlock to joint shear resistance was influenced by the parameters varied in the tests. The beam bar anchorage type affected the contribution of aggregate interlock in series 1, especially near the failure load. Specimens with L-anchorage detailing showed higher aggregate interlock forces compared with specimens with U-anchorage type. The bend bar size also influenced the response of joint in terms of aggregate interlock. Column axial load was a significant parameter in aggregate interlock, where increasing the column load led to an increase in aggregate interlock. This can be seen in specimen BCJ 6 and BCJ 8 with column load of 600 kN and 900 kN respectively. The absence and presence of joint stirrups affected the aggregate interlock. The aggregate interlock in specimen BCJ 11 with no joint shear reinforcement increased suddenly near the failure load while gradual increase of aggregate interlock at early stage of loading was observed in specimens with joint stirrups. The provision of column intermediate bars affected the aggregate interlock as well. It can be seen in specimen BCJ 10 the influence of this parameter reduced the aggregate interlock when compared with BCJ 2.

Aggregate interlock contribution - specimen BCJ 1

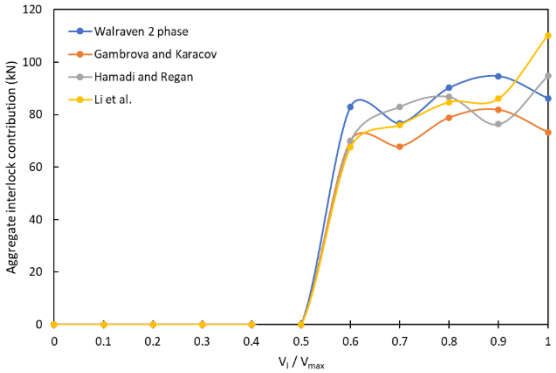

Aggregate interlock contribution - specimen BCJ 2

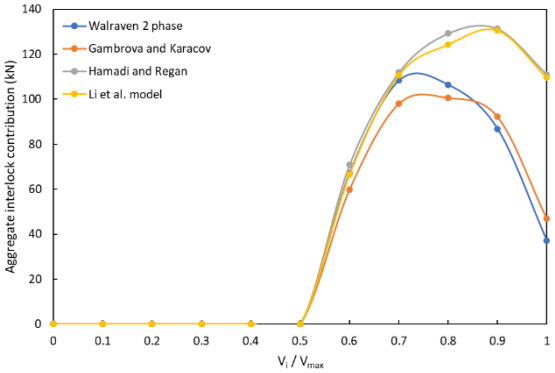

Aggregate interlock contribution - specimen BCJ 3

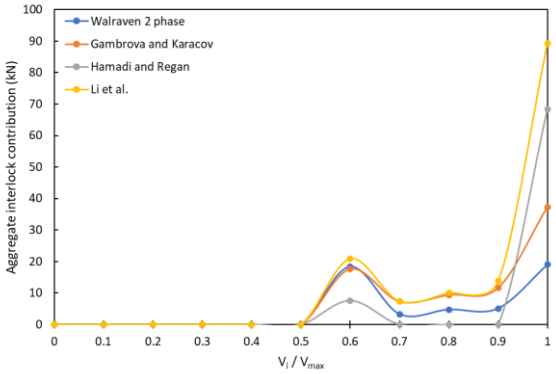

Aggregate interlock contribution - specimen BCJ 4

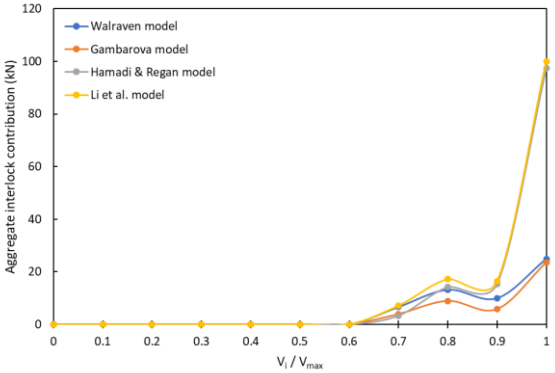

Aggregate Interlock Contribution - Specimen BCJ 5

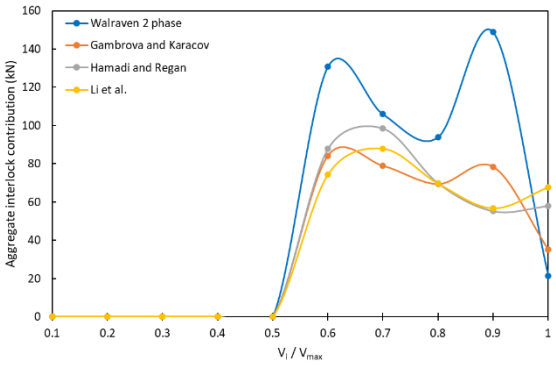

Aggregate Interlock Contribution - Specimen BCJ 6

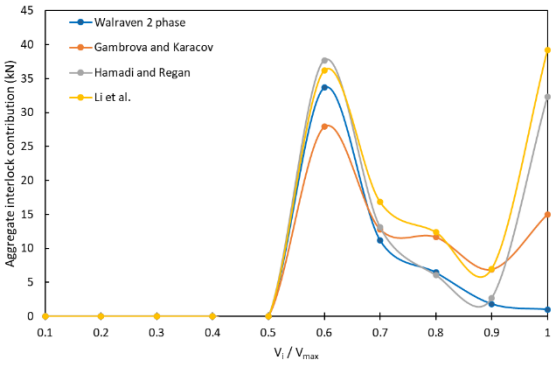

Aggregate Interlock Contribution - Specimen BCJ 7

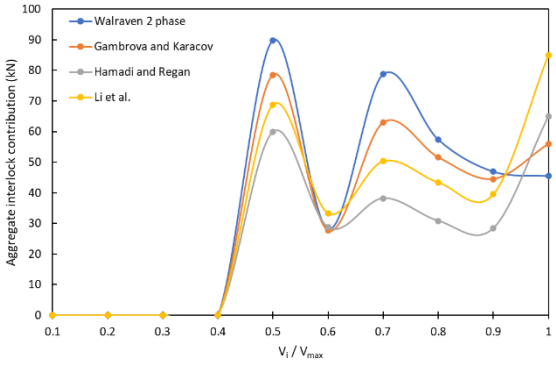

Aggregate Interlock Contribution - Specimen BCJ 8

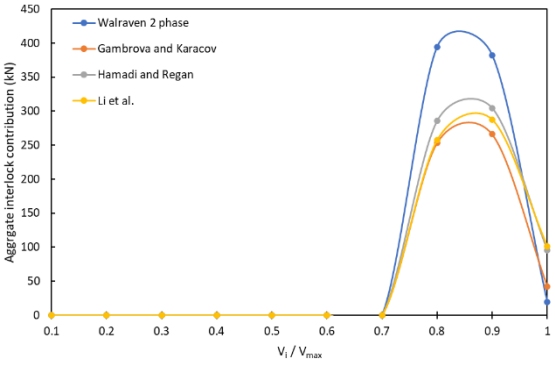

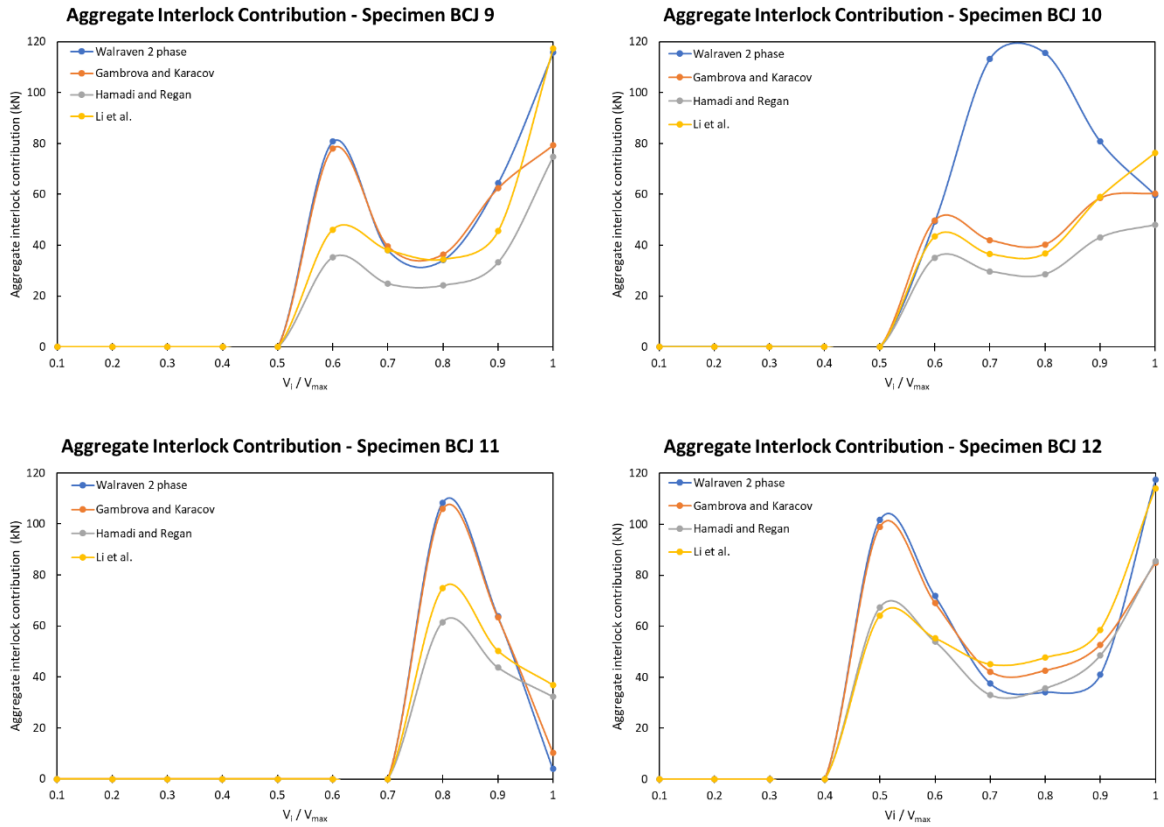

Figure 6-6 Resultant force of aggregate interlock.

6.4 Evaluation of section forces on joint boundaries using stress-block factors

To determine concrete and steel reinforcement forces acting on joint boundaries, the stress-block factors proposed by Collins and Mitchell [33] were used. This method uses equivalent uniform stress distributions for concrete to model the actual non-linear stress distribution as shown in Figure 6-7. The resultant force of the equivalent uniform stress distribution is determined using the stress-block factors α_1 and β_1 which represent the actual stress distribution. Equation (6-3) is used to obtain the resultant force. For a constant width of cross-section, the stress-block factors α_1 and β_1 are determined using equations (6-4) and (6-5). The location of the resultant force is calculated using equation (6-6).

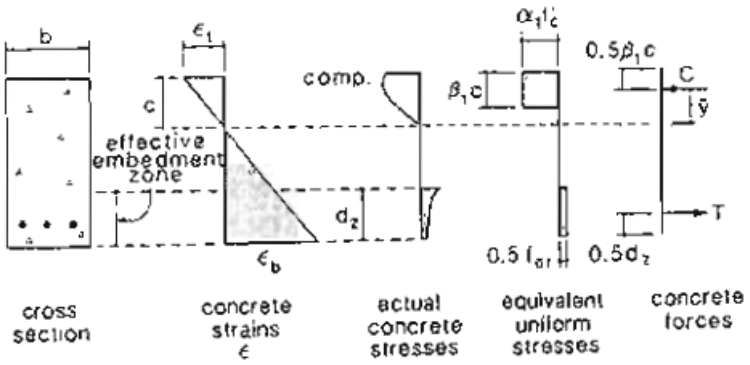

Figure 6-7 Stress-block factors; reproduced from [33].

$$\int_0^c f_c \, b \, dy = \alpha_1 \, f'_c \, \beta_1 \, c \, b \tag{6-3}$$

$$\alpha_1 \, \beta_1 = \frac{\epsilon_t}{\epsilon'_c} - \frac{1}{3}\left(\frac{\epsilon_t}{\epsilon'_c}\right)^2 \tag{6-4}$$

$$\beta_1 = \frac{4 - \frac{\epsilon_t}{\epsilon'_c}}{6 - 2\left(\frac{\epsilon_t}{\epsilon'_c}\right)} \tag{6-5}$$

$$\bar{y} = \frac{\int_0^c f_c \, by \, dy}{\int_0^c f_c \, b \, dy} = c - 0.5 \, \beta_1 \, c \tag{6-6}$$

Where ϵ_t is the extreme compressive fibre strain, c is compressive fiber depth, b is the cross-section width, f'_c is the maximum concrete stress and ϵ'_c is the concrete strain at maximum stress. The concrete strength (f'_c) obtained in chapter 4 was used in the section analysis for all BCJ specimens. For steel reinforcement, a bilinear stress strain relationship was assumed as shown in Figure 6-8. Equation (6-7) was used to obtain the stress and strain of steel reinforcement.

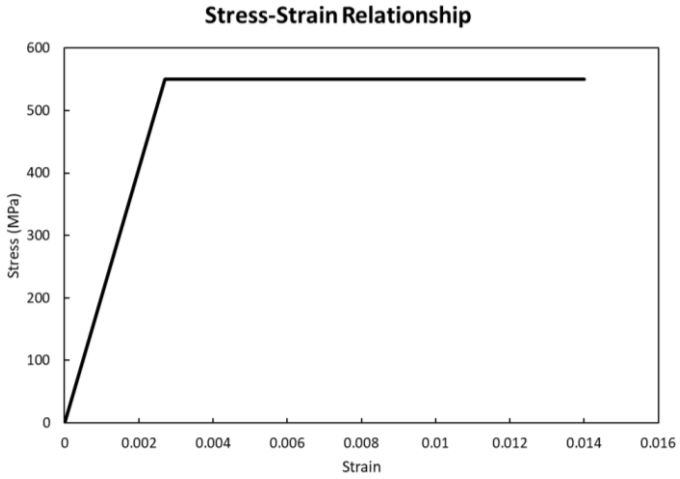

Figure 6-8 Stress-strain relationship used in the section analysis

$$f_s = E_s \varepsilon_s < f_y$$
$$f_s = f_y \ (if, E_s \varepsilon_s \geq f_y) \quad (6\text{-}7)$$

Where f_s is the stress of steel reinforcement, ε_s is the strain in steel reinforcement and E_s is the modulus of elasticity for steel reinforcement (200 x10^3 MPa). This relationship was used for reinforcement in both tension and compression. The tension stiffening effect of concrete between cracks evident in Figure 6-7 was neglected. Collins and Mitchell obtained good correspondence and good agreement between the predicted and measured moment-curvature response using these stress-block factors as shown in Figure 6-9.

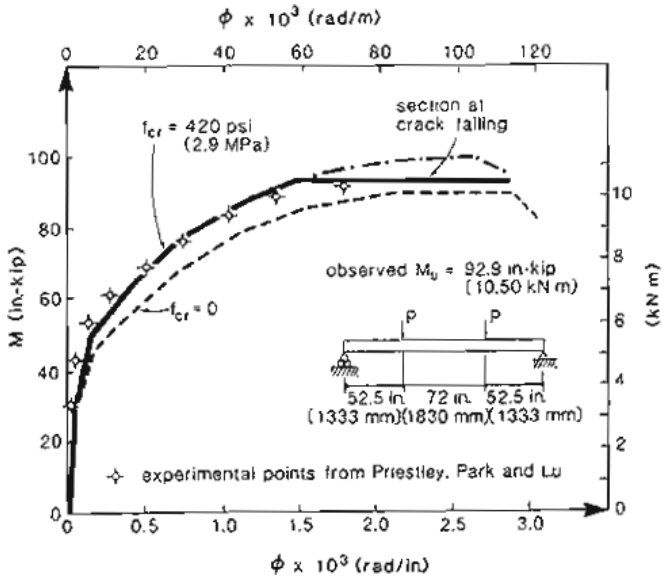

Figure 6-9 Comparison of predicted and measured moment-curvature responses; reproduced from [33].

The following sections describe the section analysis carried out to determine the compressive and tensile forces acting on the three sides of the joint including beam-column interface, top column and bottom column.

6.4.1 Section analysis at beam-column interface

The flexural compressive and tensile forces acting on the beam-column interface was calculated using the stress-block factors as shown in Figure 6-10. The tension and compression reinforcement in beams with U-bars was two 25 mm bars. In beams with L-bars the tension reinforcement was two 25 mm bars and the compression reinforcement two 16 mm bars. Measured strains were compared with strains obtained from the section analysis as shown in Figure 6-11 which shows reasonable comparison of strains up to peak load.

Specimens with L-anchorage bars had no strain gauges on the compression bars as shown in Figure 6-11 where only predicted compressive strains are given. These specimens include BCJ 1, BCJ 2, BCJ 7, BCJ 10 and BCJ 12. In specimen BCJ 11, the strain gauges on the tension side became compressive for loads exceeding 60 kN. This specimen had a pair of strain gauges attached to the beam anchorage bar and unfortunately one of these gauges broke during the test, which is discussed in chapter 4. The compressive strain reading is attributed to a faulty gauge.

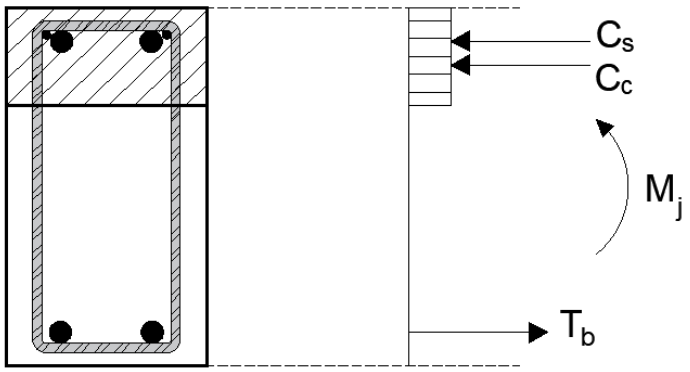

Figure 6-10 Concrete and steel forces acting on beam-column interface.

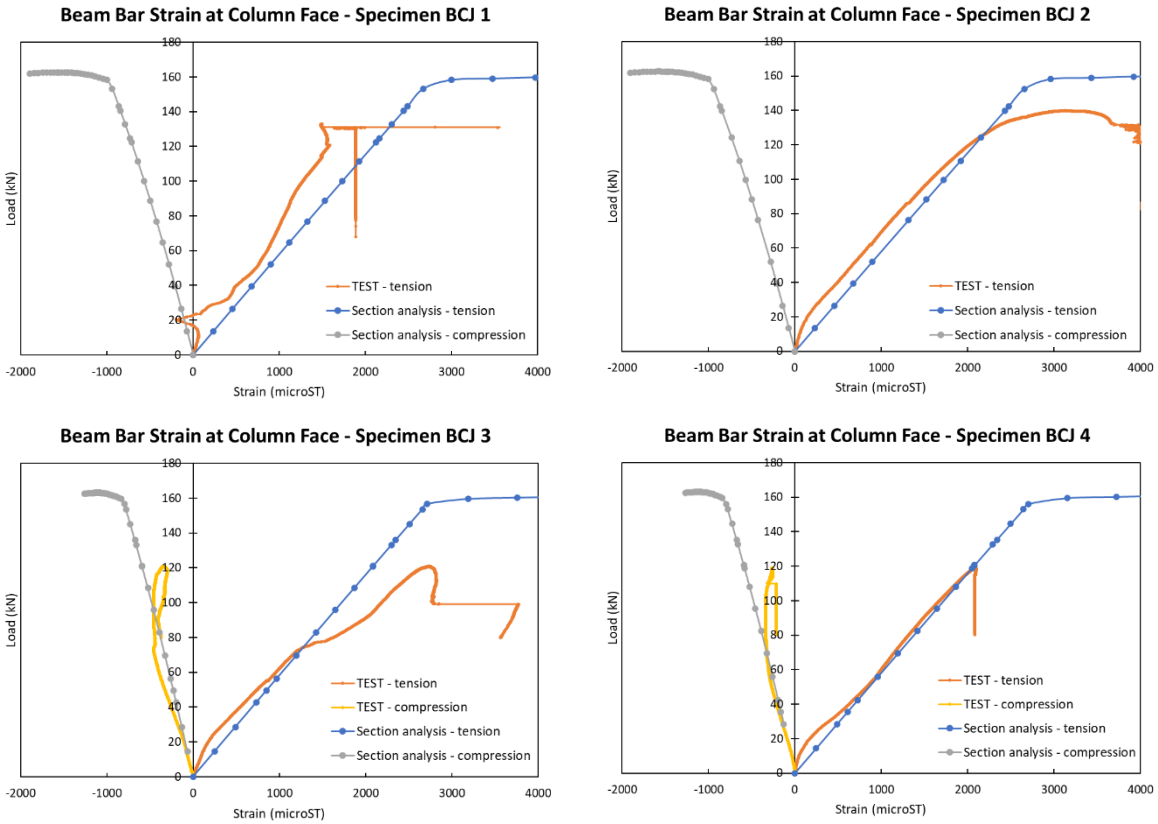

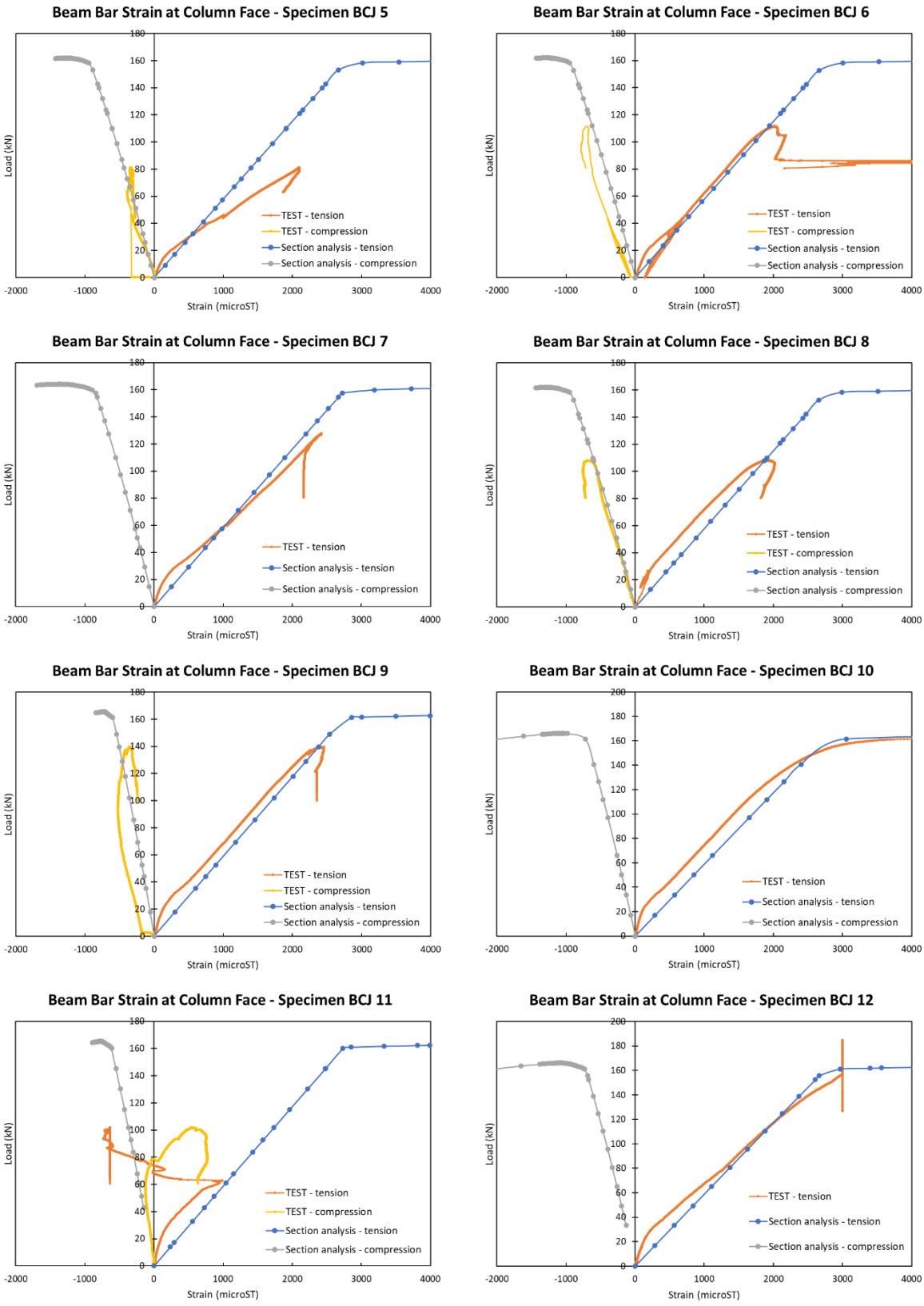

Figure 6-11 Predicted and measured strains in steel reinforcement at beam-column interface.

6.4.2 Section analysis at top column

Section analysis was carried out to determine the flexural concrete and steel reinforcement forces acting in the column at the top of the joint as shown in Figure 6-12. The measured and calculated strains in the column bars at the top of the joint are shown in Figure 6-13. The load shown on the vertical axis of Figure 6-13 is the beam load. The predicted strains are shown up to flexural failure of the column. All the specimens had an upper column axial load of 300 kN, apart from specimens BCJ 6 and BCJ 8 which had upper column loads of 600 kN 900 kN respectively. The column was reinforced with four 25 mm diameter bars in all specimens, except for specimen BCJ 10 where an extra couple of 25 mm diameter intermediate bars were provided. In the test, the column axial load was applied first up to the required column load (300 kN, 600 kN or 900 kN) and then the beam load was applied gradually up to failure while holding the column axial load constant throughout the test. The same loading history was adopted in the section analysis as in the experimental tests.

There are some differences between the measured and calculated reinforcement strains. The predicted strains in the compression bars were typically less than the measured strains. This may be a consequence of the loss of cover near the back of column face. Additionally, the measured tension strains were less than calculated strains in some specimens possibly due to tension stiffening in the concrete at the gauge location.

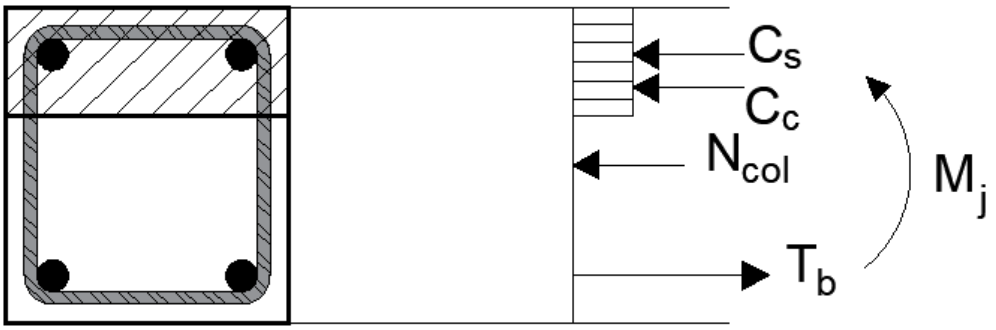

Figure 6-12 Concrete and steel forces acting at top column.

Column Bar Strain at Top Joint - Specimen BCJ 1

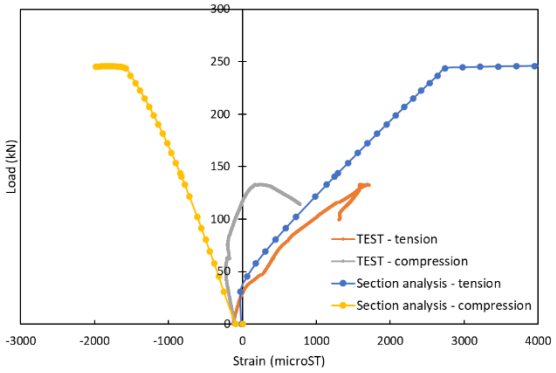

Column Bar Strain at Top Joint - Specimen BCJ 2

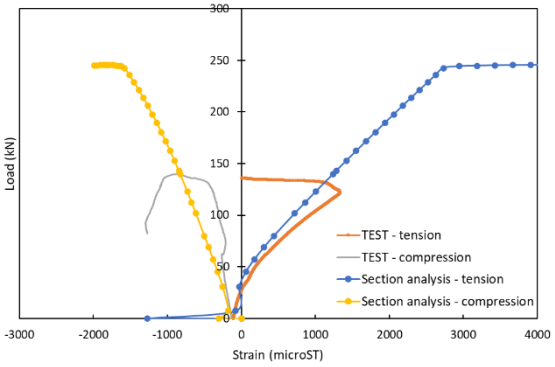

Column Bar Strain at Top Joint - Specimen BCJ 3

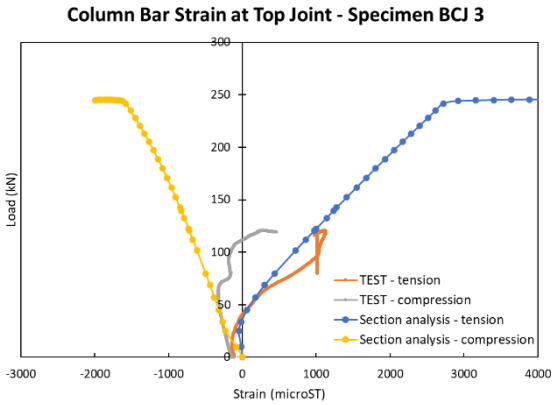

Column Bar Strain at Top Joint - Specimen BCJ 4

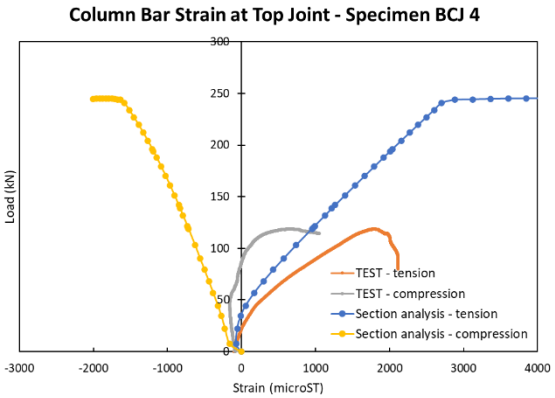

Column Bar Strain at Top Joint - Specimen BCJ 5

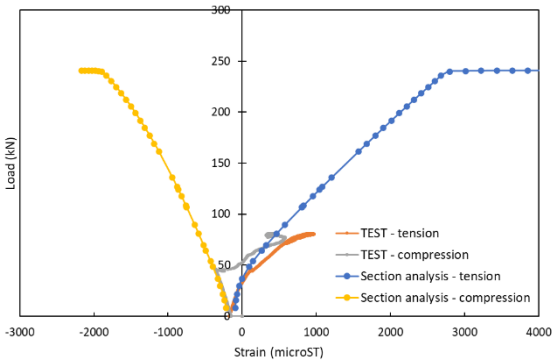

Column Bar Strain at Top Joint - Specimen BCJ 6

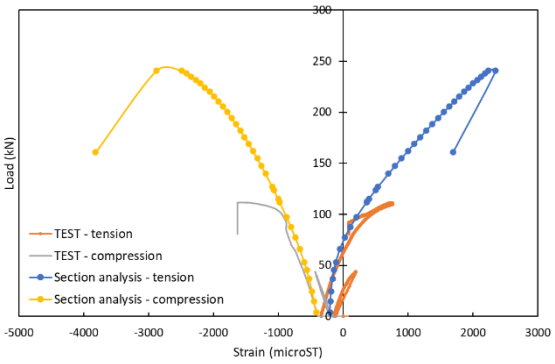

Column Bar Strain at Top Joint - Specimen BCJ 7

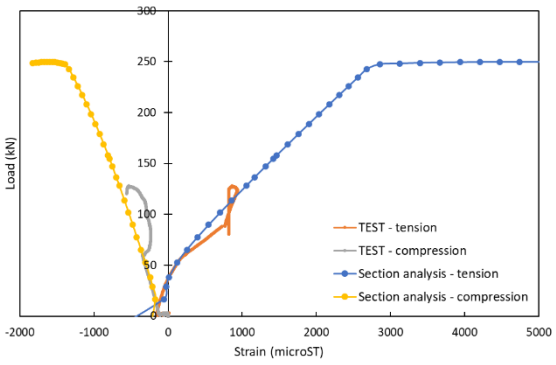

Column Bar Strain at Top Joint - Specimen BCJ 8

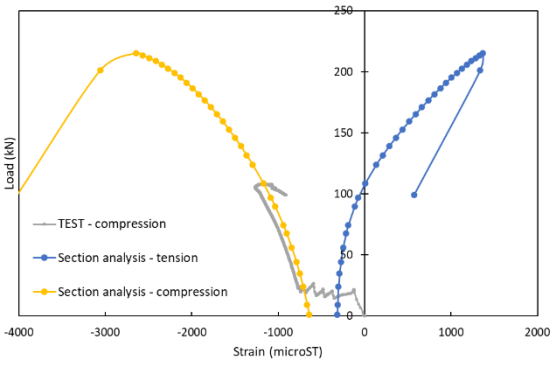

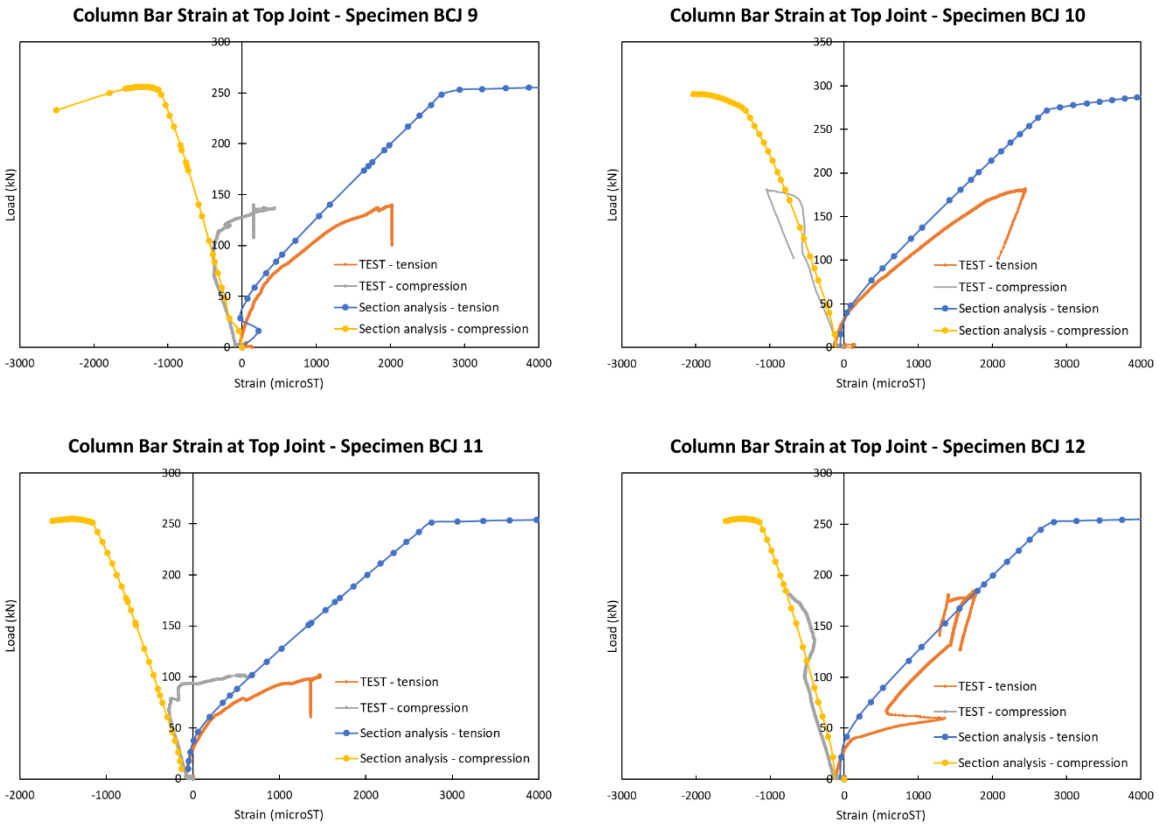

Figure 6-13 Predicted and measured strains in steel reinforcement at top column.

6.4.3 Section analysis at bottom of joint

The flexural forces in concrete and reinforcement at the bottom of the joint were estimated using section analysis. The column cross-section was subjected to the upper column axial load as well as the beam load as shown in Figure 6-14. The column was reinforced with four 25 mm diameter bars in all the tested specimens apart from BCJ 10 which had an additional two extra 25 mm diameter bars at the centre of the cross-section. The measured and calculated column bar strains at the bottom of the joint are compared and given in Figure 6-15. The load shown on the vertical axis of Figure 6-15 is the beam load. The predicted strains are shown up to flexural failure of the column. The loading history applied in the section analysis was similar to the experimental test. Firstly, the column axial load was applied to the cross-section after which the bending moment was applied gradually. The upper column component of the axial load was held constant after applying the bending moment while the beam load was increased gradually along with the bending moment.

Some specimens showed a change of strain measurements from tension to compression or vice versa. This may be due to the positioning of strain gauge locating at the compression or

tension side of steel reinforcement. In some cases, the strain readings may also have been affected towards failure by spalling of concrete at the bottom left hand corner of joint where the beam meets the column. This concrete spalling led to concrete crushing in the post-peak response as shown in the discussion of failure modes and crack patterns in chapter 4.

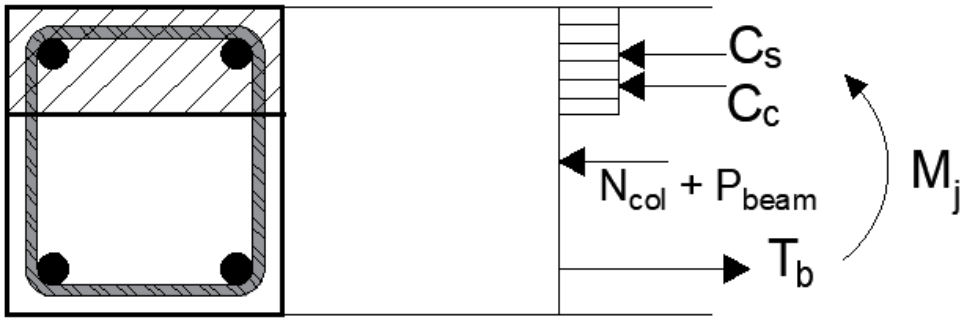

Figure 6-14 Concrete and steel forces acting at bottom column.

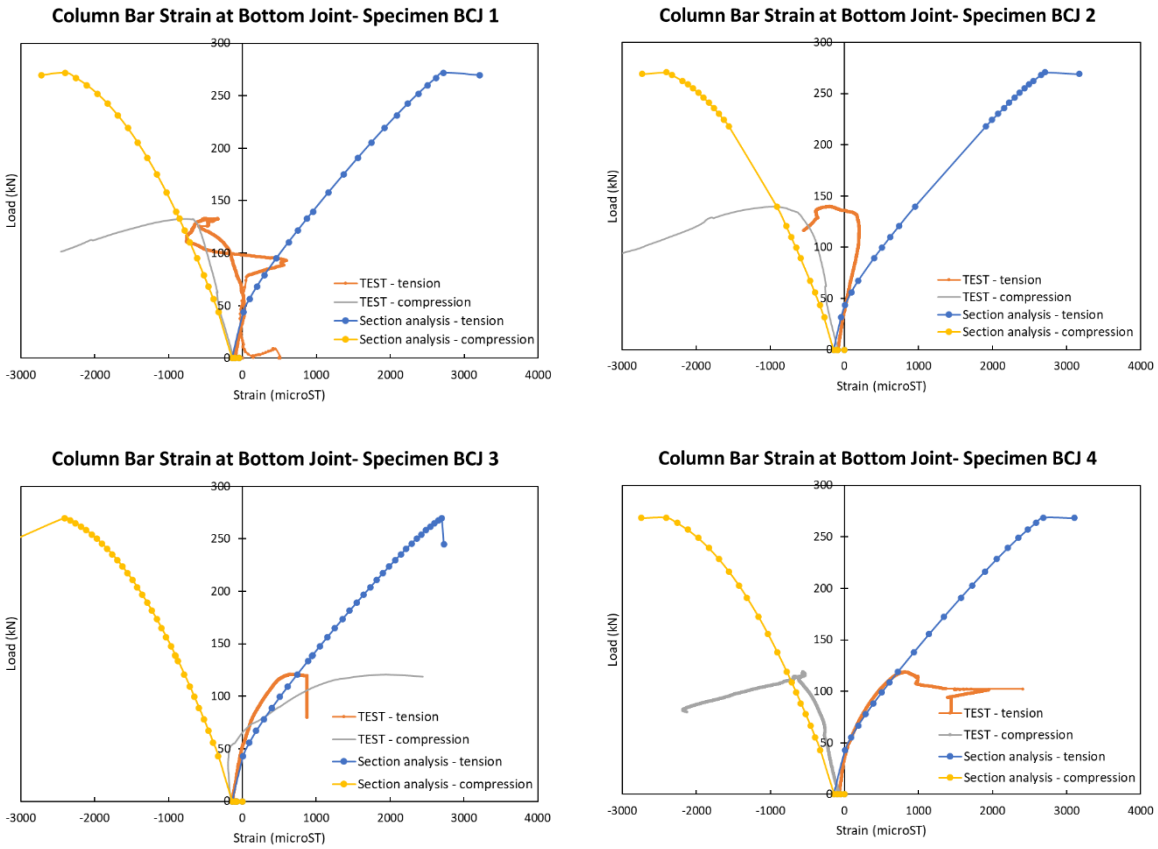

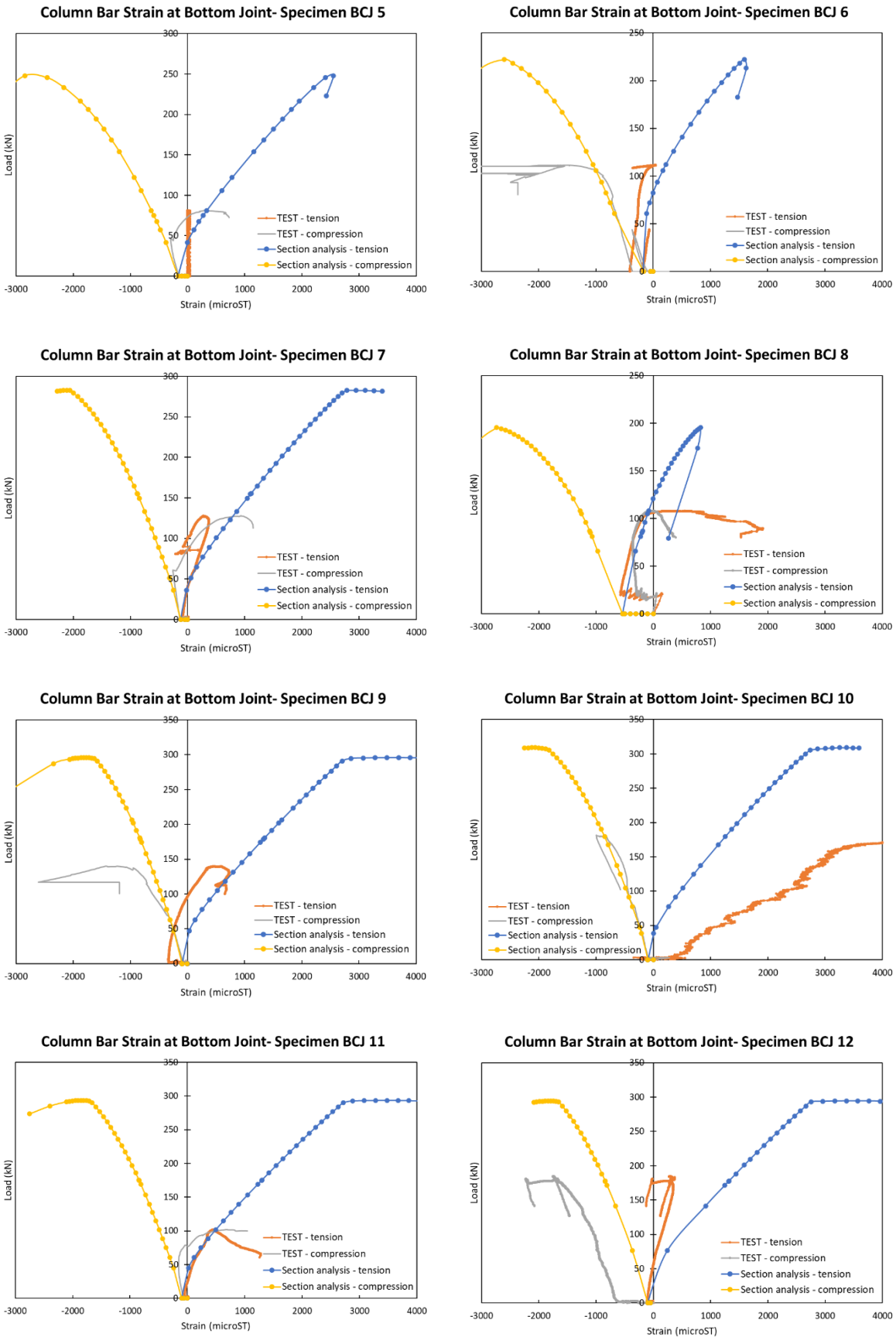

Figure 6-15 Predicted and measured strains in steel reinforcement at bottom column.

6.5 Contribution of horizontal equilibrium of shear transfer mechanism

6.5.1 Contribution of aggregate interlock

The contribution of aggregate interlock to the resultant forces in the horizontal direction ($V_{agg,hor}$) was calculated using the four aggregate interlock models discussed earlier in section 6.3. The results of the contribution of aggregate interlock in horizontal direction for each series used in the experimental tests are described in the following sections.

6.5.1.1 Aggregate interlock for series 1

Throughout loading process up to failure load, the contribution of aggregate interlock in this series showed minor differences between the four models. Aggregate interlock was mobilised at around 60% of the failure load as shown in Figure 6-16. With the exception of BCJ 1, the methods of Hamadi and Regan and Li et al. predicted the greatest shear contributions from aggregate interlock at failure. In all cases the contribution of aggregate interlock to joint shear resistance was relatively low compared with the joint shear force. The shear force resisted by aggregate interlock was slightly greater in BCJ 1 and BCJ 2 with L-bar anchorage type than BCJ 3 and BCJ 4 with U-bars.

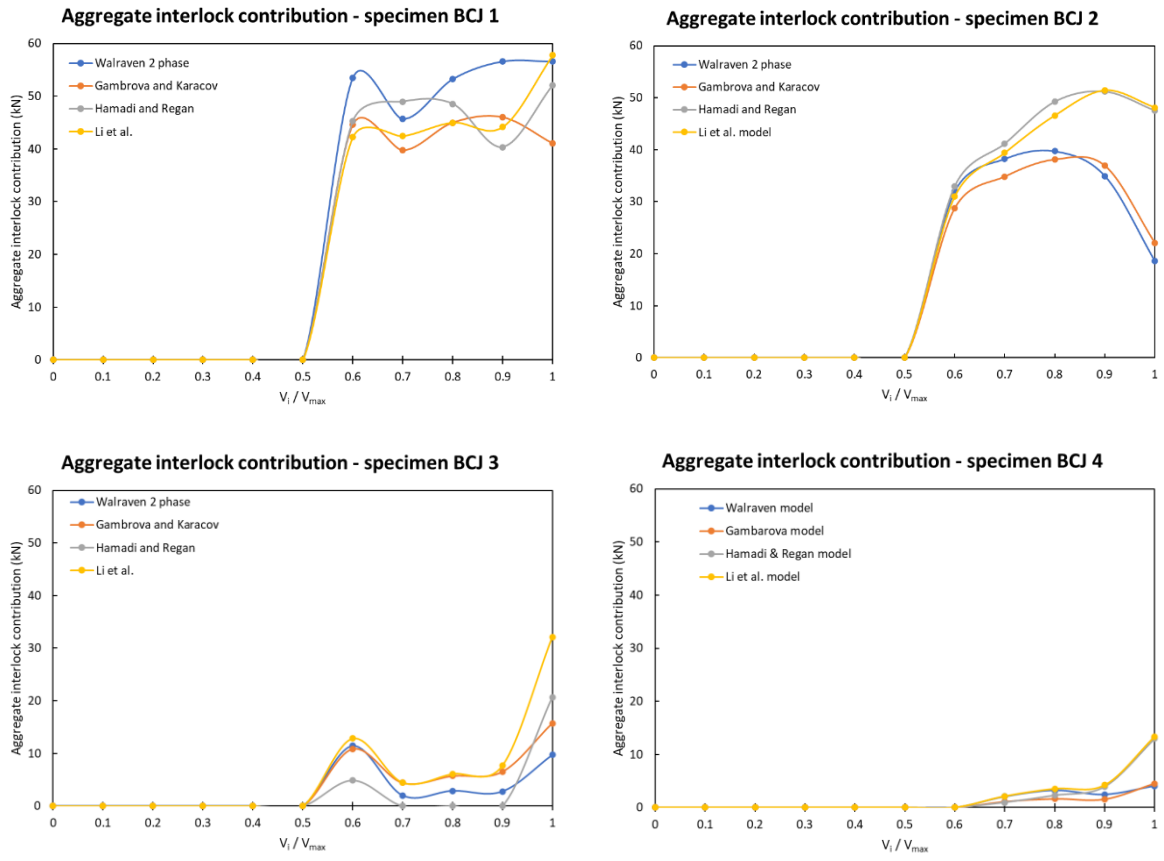

Figure 6-16 Results of aggregate interlock in horizontal direction for series 1.

6.5.1.2 Aggregate interlock for series 2

The joint shear forces resisted by each aggregate interlock model at peak load are fairly similar for series 2 as shown in shown Figure 6-17 although prior to failure the Walraven 2 phase model gives relatively high aggregate interlock contributions for specimens BCJ 5 and BCJ 8 compared to the other models. The joint shear force resisted by aggregate interlock was greatest in BCJ 8 with greatest column axial load of 900 kN. Despite this, the influence of column axial load on aggregate interlock is unclear since the shear force resisted by aggregate interlock was least for BCJ 6, with column axial load of 600 kN. At failure, the shear force resisted by aggregate interlock was low in all specimens.

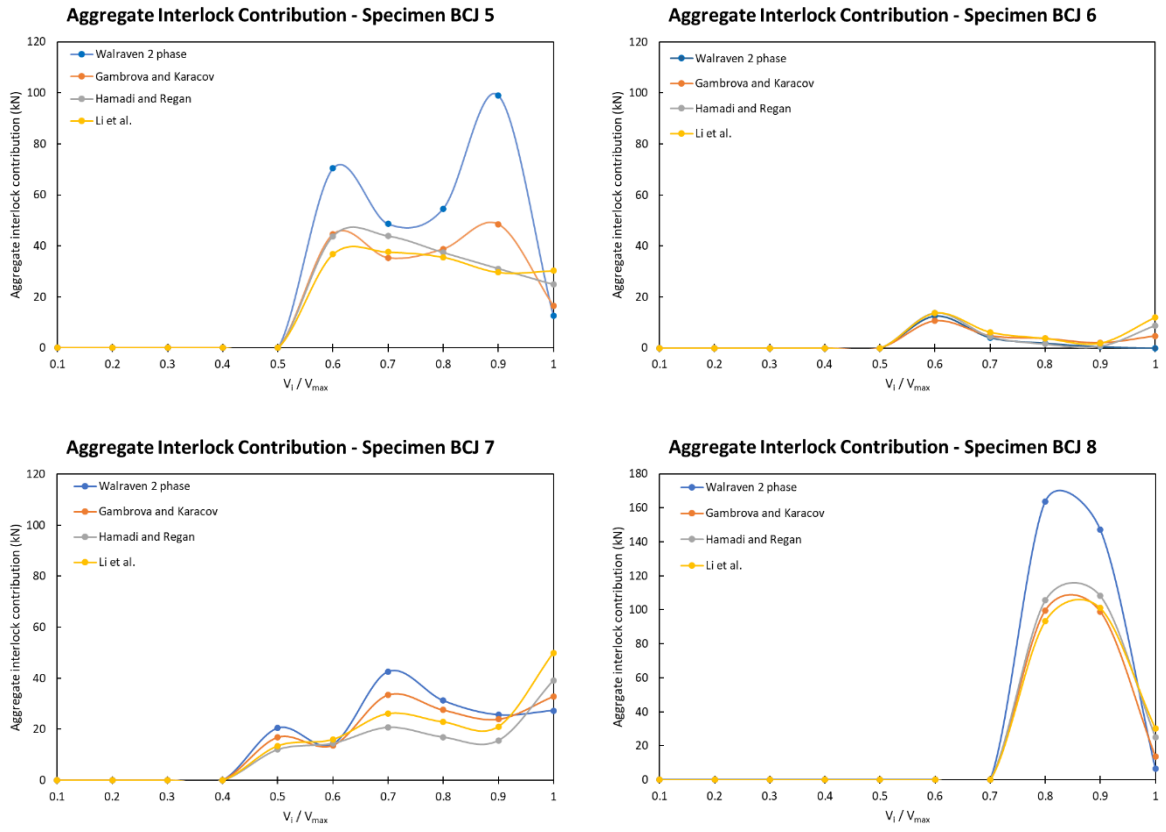

Figure 6-17 Results of aggregate interlock in horizontal direction for series 2.

6.5.1.3 Aggregate interlock for series 3

As shown in Figure 6-18, the Walraven 2 phase and Gambrova and Karacov models predicted slightly larger shear forces than the other two models but in all cases the contribution of aggregate interlock to the joint shear force was relatively small. The absence of joint stirrups in specimen BCJ 11 led to mobilisation of aggregate interlock at 80% of the failure load compared with around 60% in the other specimens with joint stirrups. This is due to the

smaller difference between cracking load and failure load in specimen BCJ 11 compared with the other specimens. The provision of intermediate column bars in specimen BCJ 10 increased the shear force resisted by aggregate interlock relative to BCJ 2 which was otherwise similarly reinforced. This appears to be a result of the crack opening and sliding displacements in BCJ 10 being controlled by the intermediate column bars as discussed in chapter 4. However, the concrete strength was 51 MPa for BCJ 10 compared with 33 MPa for BCJ 2 ruling out direct comparison of results. When compared with specimen BCJ 2, doubling of the joint stirrups in specimen BCJ 12 had little effect on the shear force resisted by aggregate interlock.

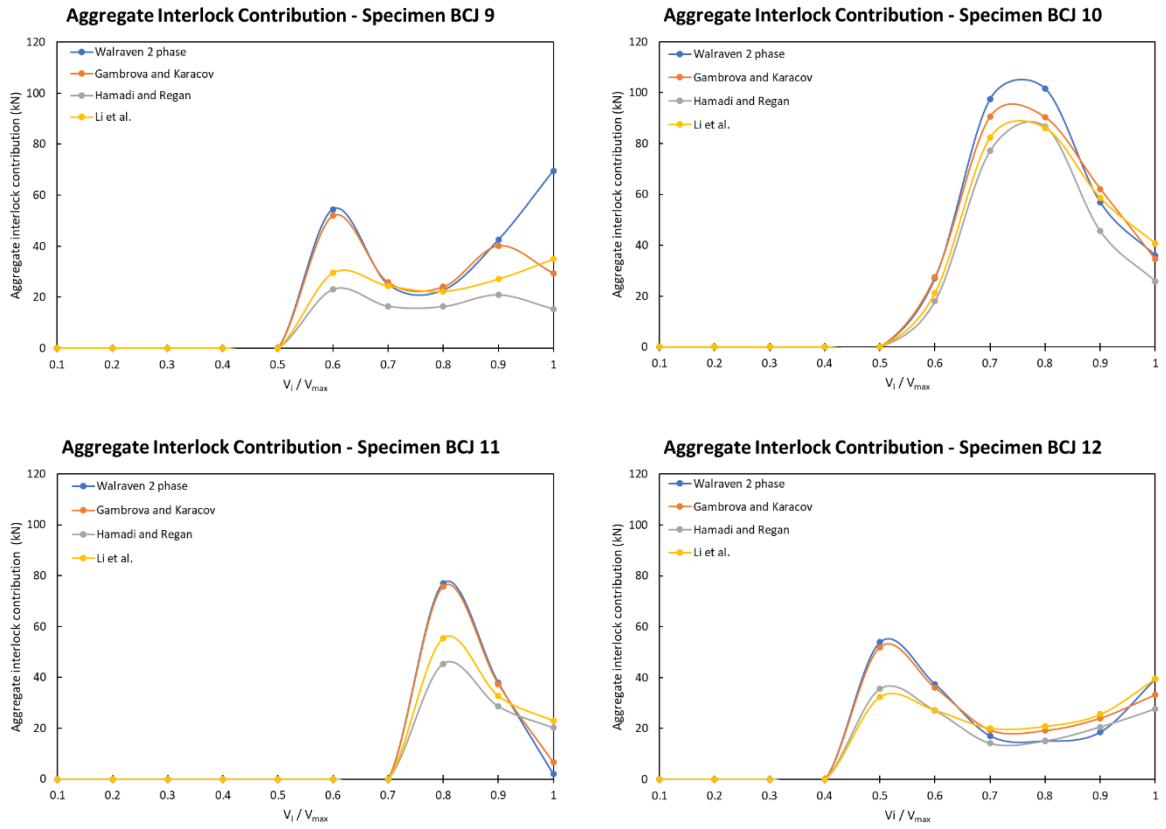

Figure 6-18 Results of aggregate interlock in horizontal direction for series 3.

6.5.2 Contribution of joint stirrups

All the beam-column joint specimens were reinforced with joint stirrups, except for specimen BCJ 11 which had no joint stirrups. The tensile force in the joint stirrups ($\sum T_{stirrup}$) at the critical crack was calculated using the Sigrist [49] two-step bond model discussed in the literature review. The stirrup stress was calculated in terms of the crack width, at the intersection with the stirrup, which was obtained using DIC. The predicted stresses were compared with those derived from the strain gauges.

6.5.2.1 Results of joint stirrups action for series 1

The estimated total force resisted by the joint stirrups is shown in Figure 6-19 for both the Sigrist model and the measured strains. With the exception of BCJ 1, the forces predicted by each method, and the shape of the response, are similar particularly near failure. The reduction in measured strain joint stirrup force near failure in BCJ 1 is associated with the development of compressive strain in the bottom stirrup as described in chapter 4. The relatively minor differences between the forces predicted by each method are related to the assumptions made in the Sigrist model and differences in location between the strain gauge (located at the centre of stirrup) and the intersection point of the crack and stirrup.

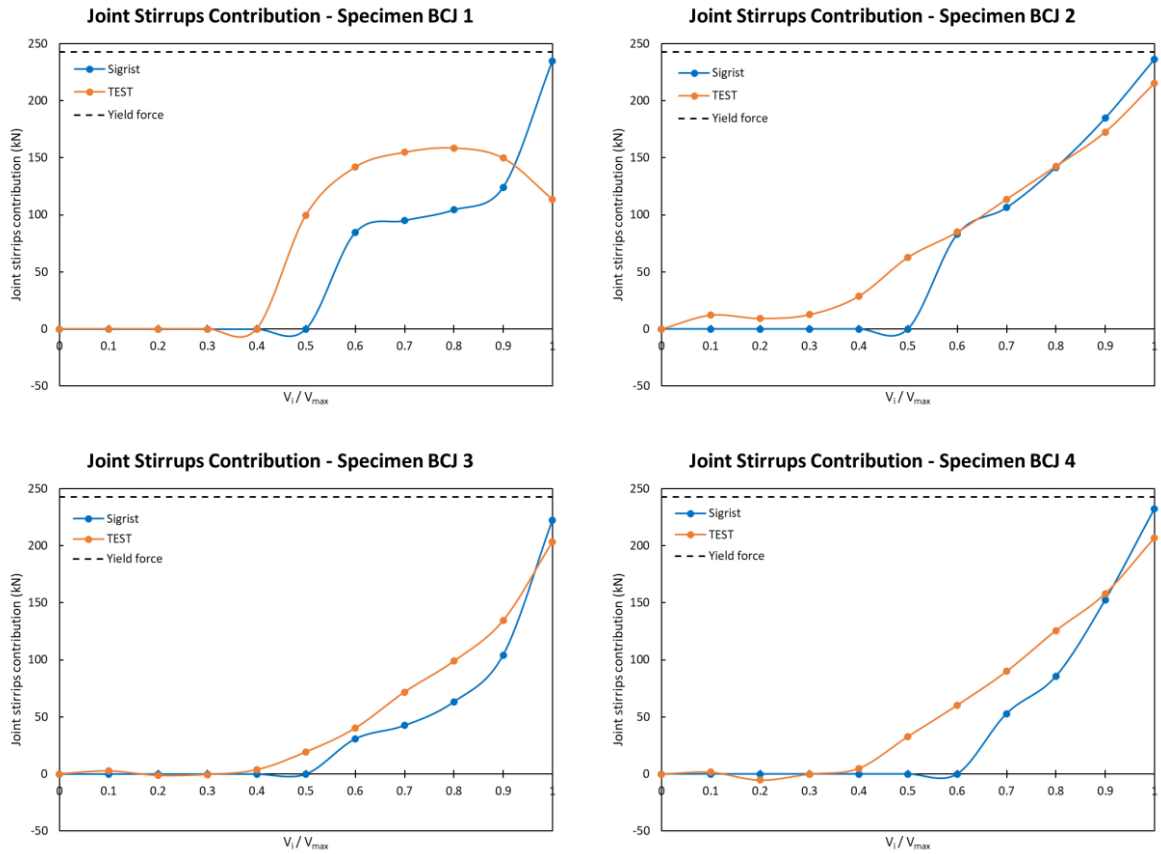

Figure 6-19 Joint stirrups contribution results for series 1.

6.5.2.2 Results of joint stirrups action for series 2

The total joint stirrup forces for this series are shown in Figure 6-20. No strain gauge results are presented for BCJ 5 and BCJ 7 since the strain gauges malfunctioned. The difference between the joint stirrups forces derived for BCJ 6 are primarily due to a gauge failing on the bottom stirrup. In both BCJ 6 and BCJ 8, the joint stirrup force increased significantly between 90 % of the failure load and failure. Specimen BCJ 3 showed a similar rapid increase in joint

stirrup force near failure load. At failure, the joint stirrup force predicted with the Sigrist method was at or close to the yield capacity of the stirrups for all the specimens in this series.

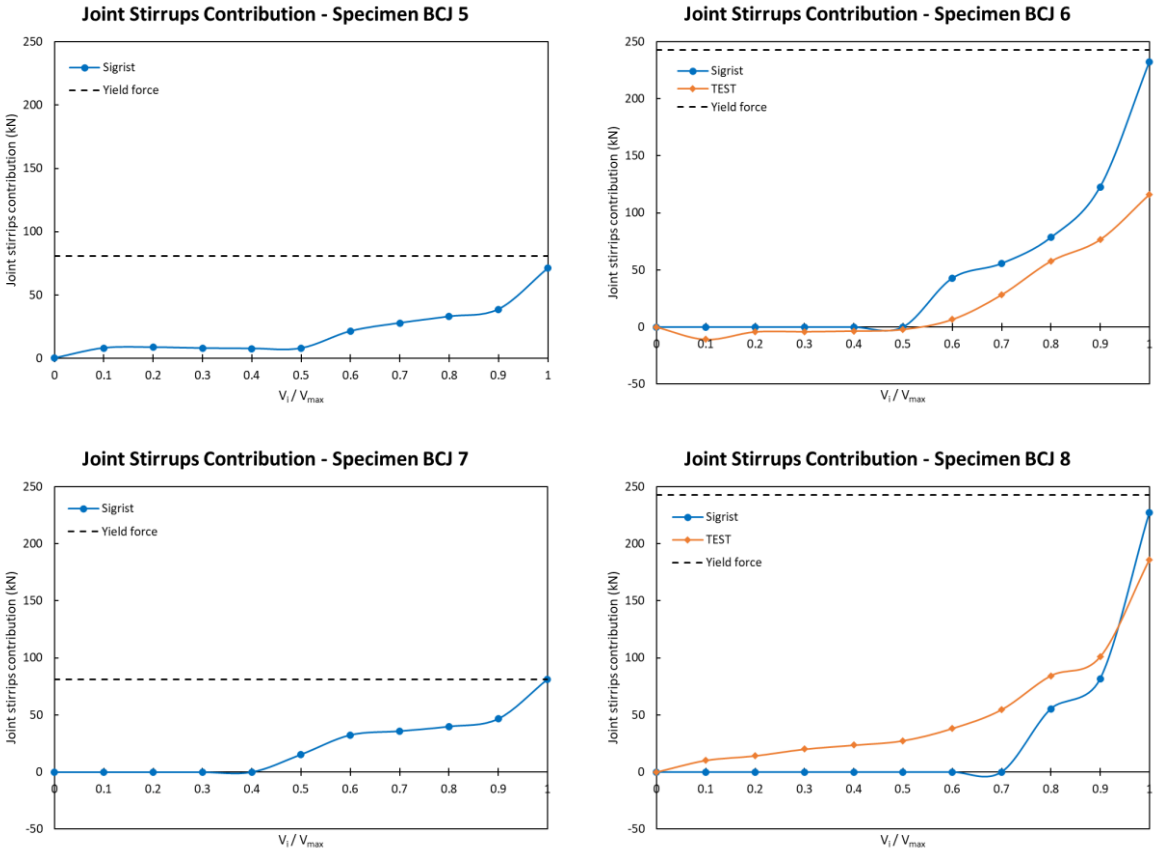

Figure 6-20 Joint stirrups contribution results for series 2.

6.5.2.3 Results of joint stirrups action for series 3

The joint stirrup forces for the third series are shown in Figure 6-21. There are some significant differences between the forces derived using the strain gauge readings and Sigrist for this series. The reasons for the differences are uncertain. However, the maximum stirrup force is estimated to be close to the yield capacity of the sirups for both methods where results are available. Due to the absence of joint stirrups, specimen BCJ 11 is not included in Figure 6-21.

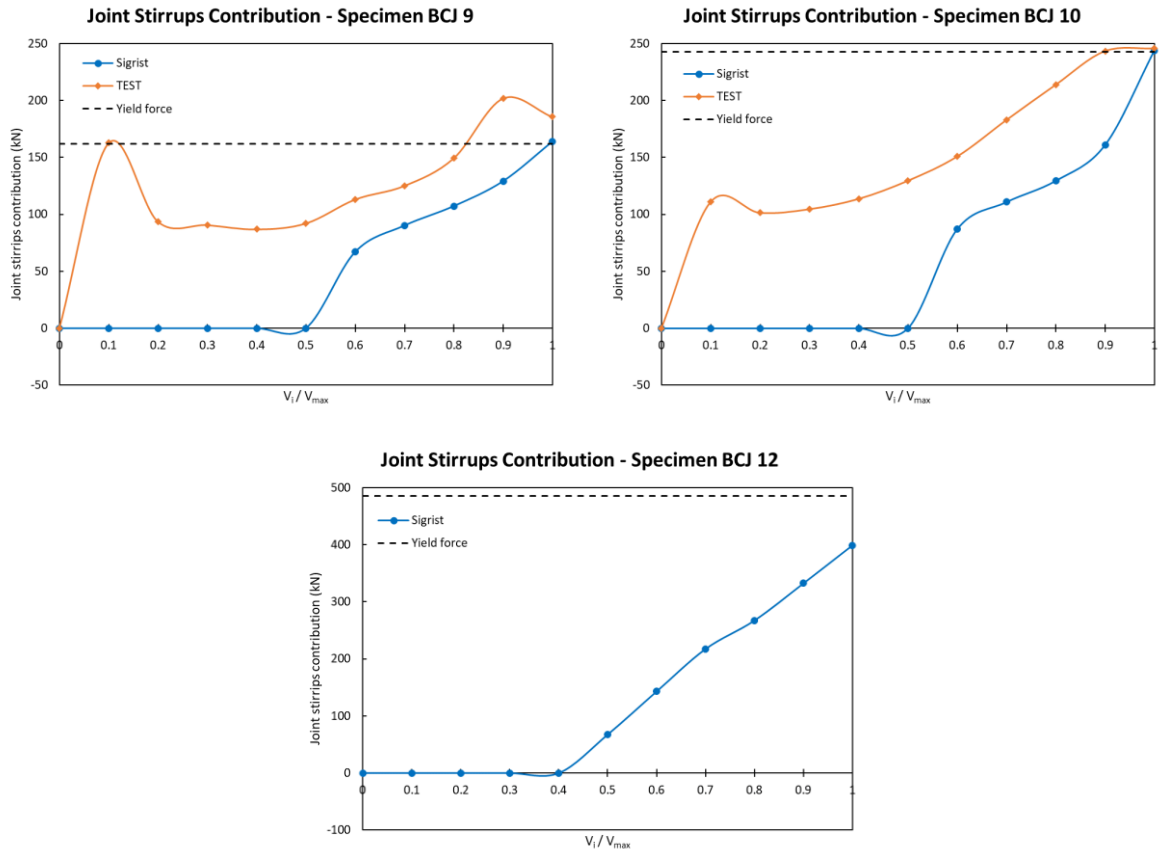

Figure 6-21 Joint stirrups contribution results for series 3.

6.5.3 Contribution of beam bend bar

The horizontal component of force in the bend of beam bar at the intersection with the diagonal crack ($T_{b,hor}$) was derived from the strain gauges located at the beginning and end of the bend for specimens with standard bend radius or positioned at midway around the bend and at the end of the bend in specimens with large bend radius. This method was used because the critical crack in all specimens crossed the top bend of beam L- and U-anchorage bar at a location between the strain gauges positioned at the beginning and end of the bend. Thus, the average of these measured strains was considered in the calculations to represent the resultant contribution beam bend bar. The horizontal component of force ($T_{b,hor}$) was obtained from the angle of the bar at the intersection with the critical crack. This assumes that the shape of the bar is not distorted in the radius of the bend during loading.

6.5.3.1 Results of beam bend bar action for series 1

The horizontal component of the beam bar force at the intersection with the critical shear crack is shown for each specimen of series 1 in Figure 6-22. There are significant differences in the forces derived for specimens BCJ 1 and BCJ 2 with L-bars and BCJ 3 and BCJ 4 with U-

bars. As the load was increased, specimens with L-anchorage type (BCJ 1 and BCJ 2) showed noticeable increases in the contribution of the beam bend bar, while a much lower increase was observed for specimens with U-anchorage type (BCJ 3 and BCJ 4). For L-anchorage bar, specimen BCJ 1 had larger value of beam bend bar contribution than specimen BCJ 2 near failure load. This may be due to the difference between the bend radius used in both specimens including 87.5 mm for BCJ 1 and 150 mm for BCJ 2. For U-anchorage bar, the horizontal tensile force in the bend of beam bar was lower than specimens with L-anchorage type. The behaviour of specimens BCJ 3 and BCJ 4 was very similar apart from at the failure load where BCJ 3 showed a slight reduction of the contribution of beam bend bar. The bend radius did not influence the behaviour of these specimens with U-anchorage bar.

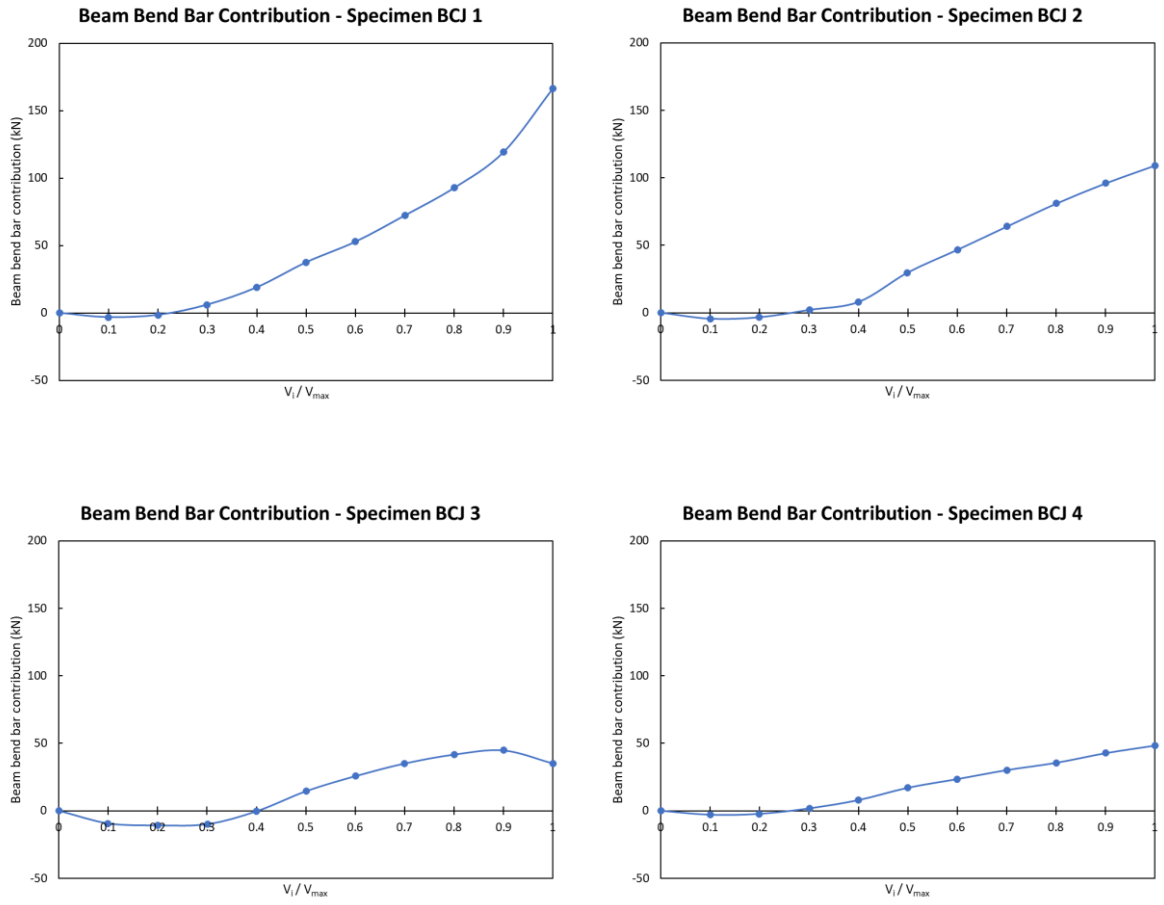

Figure 6-22 Contribution of beam bend bar for series 1.

6.5.3.2 Results of beam bend bar action for series 2

The beam bend bar horizontal forces are shown in Figure 6-23 for series 2. The results show that the contribution of the beam bend bar increased gradually with load except for specimen BCJ 8. The greatest contribution of the beam bend bar to joint shear occurred in specimen

BCJ 7 which failed at the highest beam load. The contribution of the horizontal force in the beam bar bend was very low in specimen BCJ 8 possibly due to its high axial column load of 900 kN. The rate of increase in beam bend bar force was steeper in specimen BCJ 7 than specimens BCJ 5 and BCJ 6. This was probably related to the use of L-bars in specimen BCJ 7 and U-bars in the other specimens.

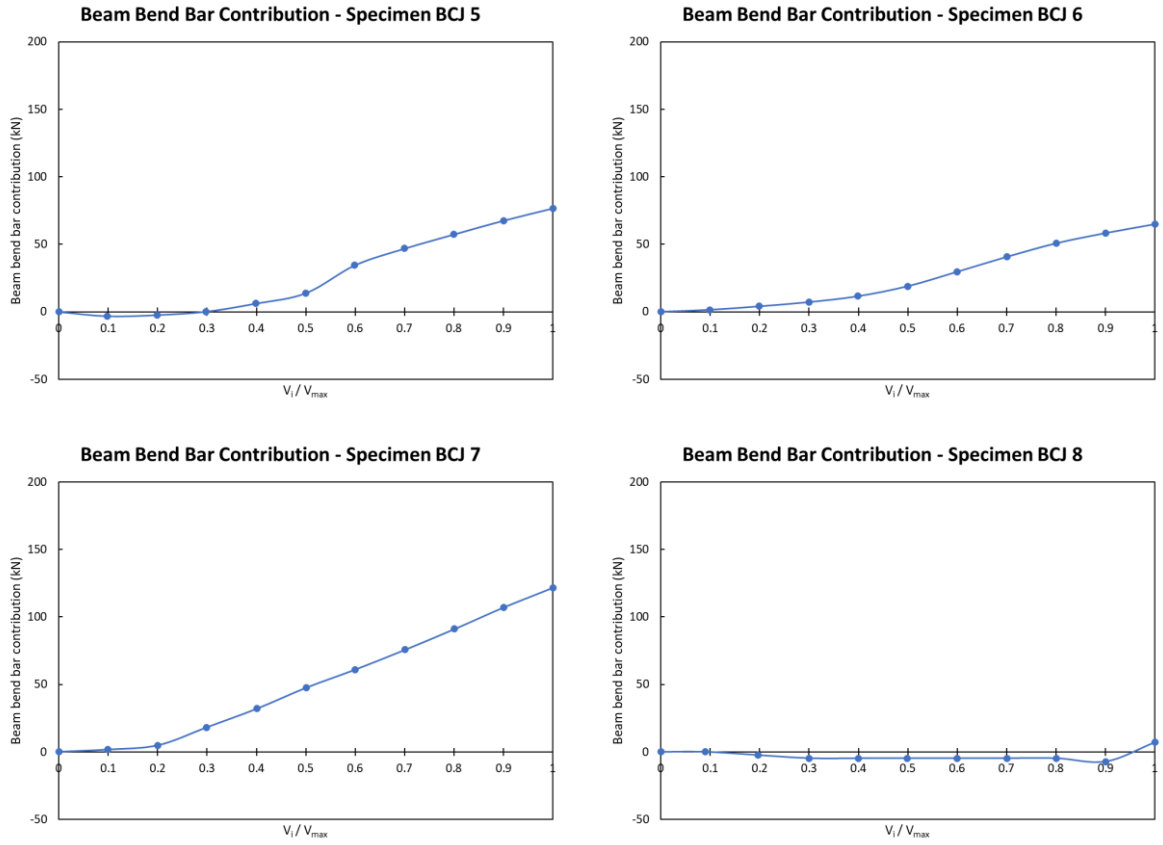

Figure 6-23 Contribution of beam bend bar for series 2.

6.5.3.3 Results of beam bend bar action for series 3

The beam bend bar forces are shown for series 3 in Figure 6-24. Specimens with L-bars (BCJ 10 and BCJ 12) had greater beam bend bar forces than specimens with U-bars (BCJ 9 and BCJ 11). The beam bend bar force is slightly larger for BCJ 10, with intermediate column bars, than specimen BCJ 12, with six joint stirrups, despite the specimens having very similar failure loads but no great significance is attributed to this.

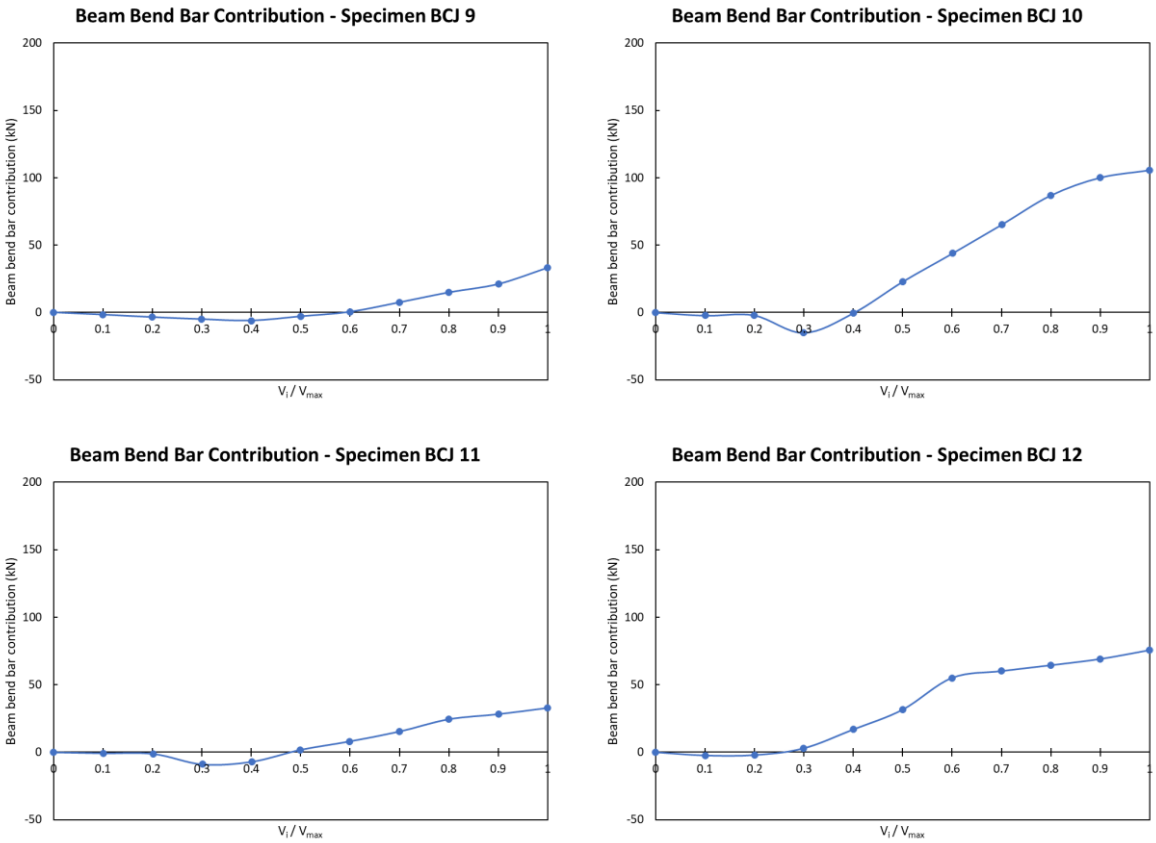

Figure 6-24 Contribution of beam bend bar for series 3.

6.5.4 Contribution of concrete compression zone

The contribution of the concrete compression zone (C_b-C_{comp}) in the horizontal direction was determined from equilibrium using equation (6-1). Consequently, the force C_{comp} can also be described as strength not explained by the previous mechanisms. Prior to diagonal joint cracking $C_{comp} \sim V_{col}$ since contributions from aggregate interlock, joint stirrups and beam bar bend are near zero. Prior to diagonal joint cracking, there is a contribution to horizontal equilibrium along the diagonal boundary of free body B from tension in the concrete but this is not considered in the analysis. This section presents the concrete compression zone contribution for each series of specimens.

6.5.4.1 Results of concrete compression zone for series 1

The concrete compression zone forces (C_b-C_{comp}) are shown for series 1 in Figure 6-25. Forces are presented for all four of the models used for aggregate interlock. In all cases, the compressive force increased almost linearly to a maximum at around 50% of the failure load before reducing significantly with increasing load to near zero at failure. The maximum concrete compression zone force was similar in all specimens and occurred just before joint

cracking when the other considered internal forces were near zero. The drop in force after joint cracking was more sudden in specimens BCJ 1 and BCJ 2 with L-bars than BCJ-3 and BCJ-4 with U-bars. The four models used in aggregate interlock contribution showed similar trends in all specimens of this series.

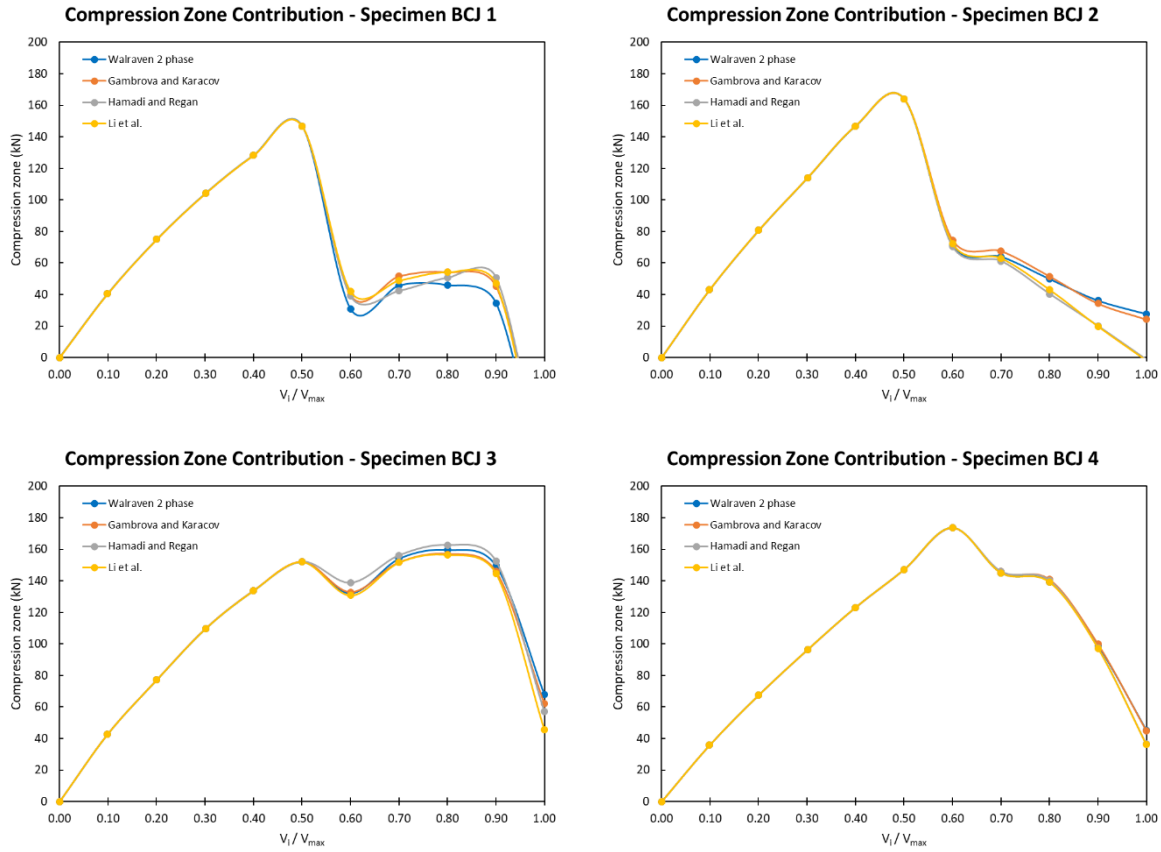

Figure 6-25 Contribution of concrete compression zone for series 1.

6.5.4.2 Results of concrete compression zone for series 2

The concrete compression zone forces (C_b-C_{comp}) are shown for series 2 in in Figure 6-26. Results are presented for all four models used to determine the contribution of aggregate interlock. All specimens exhibited a reduction of concrete compression zone contribution following diagonal joint cracking due to the activation of aggregate interlock, joint stirrups and beam bar bend. The sudden drop in force in specimen BCJ 6 resulted from an increase in the joint stirrup force near failure. The force (C_b-C_{comp}) is greatest for specimen BCJ 8 since diagonal joint cracking was delayed by the high column load of 900 kN. The four models utilized in obtaining aggregate interlock gave similar results for all specimens.

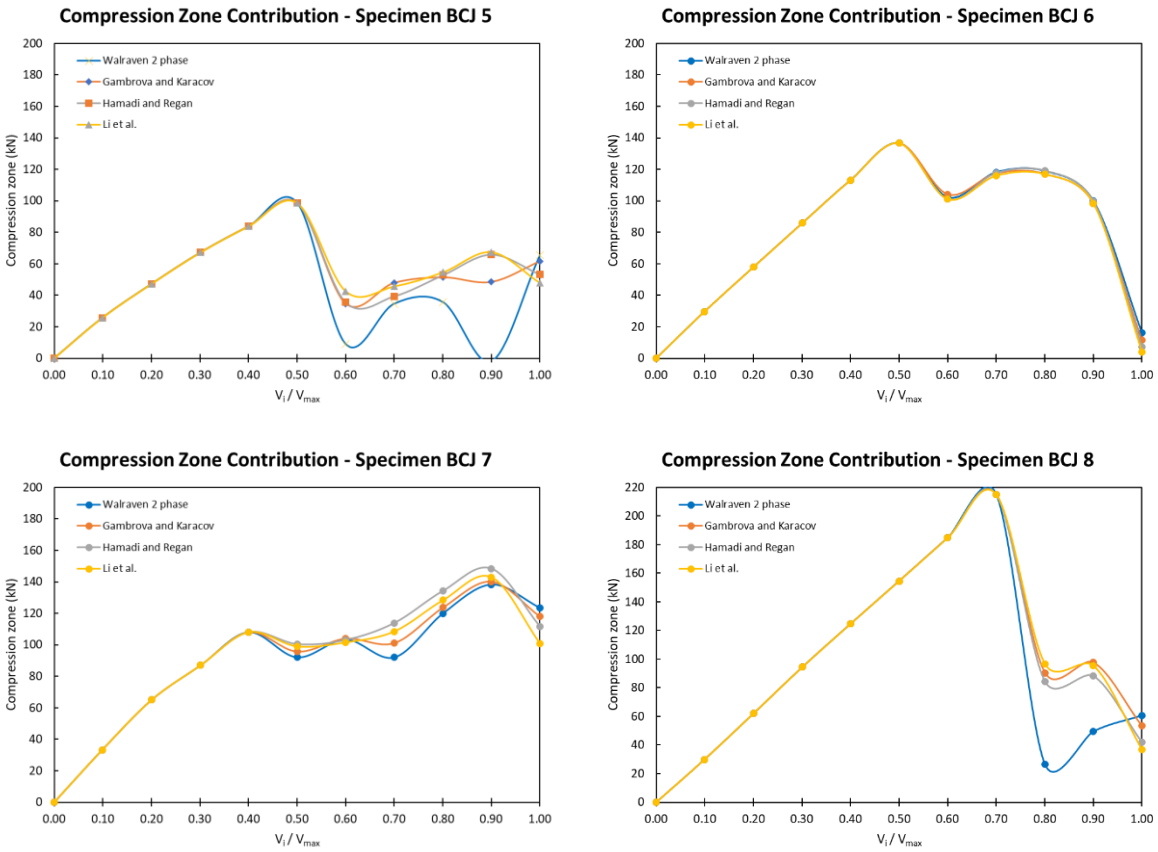

Figure 6-26 Contribution of concrete compression zone for series 2.

6.5.4.3 Results of concrete compression zone for series 3

The compression zone forces (C_b-C_{comp}) for series 3 are shown in Figure 6-27. Results are shown for all four models used to obtain the contribution of aggregate interlock. Both specimens BCJ 10 and BCJ 12 exhibited a rapid reduction of concrete compression zone contribution after joint cracking. This was due to the increase of the contribution of aggregate interlock in specimen BCJ 10 and the contribution of joint stirrups in specimen BCJ 12. The response of specimen BCJ 11, without joint stirrups, was different from the other specimens since (C_b-C_{comp}) increased up to failure with a slight dip after joint cracking. The four models utilized in obtaining aggregate interlock gave similar results for all specimens.

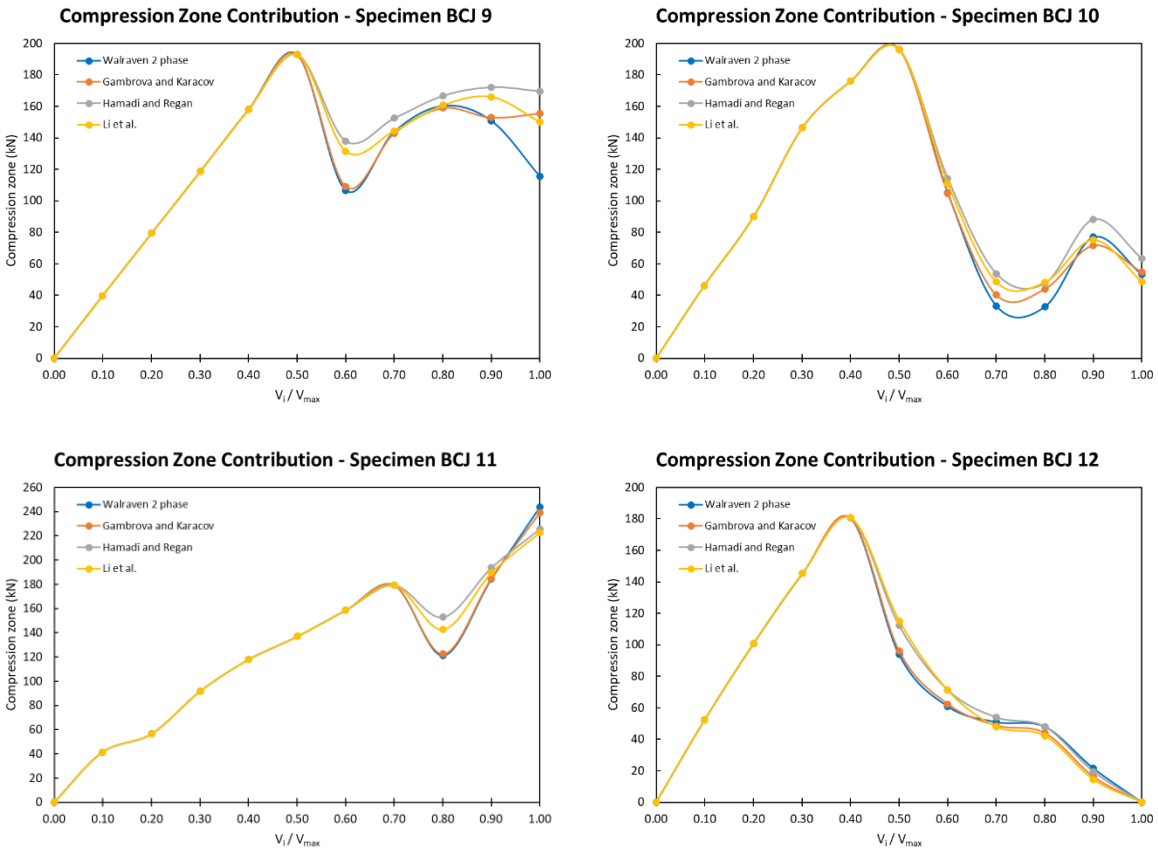

Figure 6-27 Contribution of concrete compression zone for series 3.

6.5.5 Relative contribution of each shear action in horizontal equilibrium

The relative contributions of each shear action are plotted in Figure 6-28 against the proportion of joint shear force applied for each test. The graphs show the variation with load of the relative contribution of each considered shear resisting mechanism and the load at which it became active. The graphs show that the contribution of aggregate interlock was minimal at joint shear failure. Significant contributions to horizontal equilibrium were made by the beam bend bar force in several specimens. Joint stirrups also made a significant contribution to joint shear strength. The compression zone contribution (C_b-C_{comp}) varied significantly between specimens dependent on their detailing. In general, the relative contribution of (C_b-C_{comp}) was reduced by use of L-bars (BCJ 1, BCJ 2, BCJ 7, BCJ 10 and BCJ 12) and increasing the number of joint stirrups (typically 3 stirrups apart from BCJ 11; no stirrups, BCJ 5 and BCJ 7; 2 stirrups, BCJ 12: 6 stirrups). The relative contribution of (C_b-C_{comp}) represents the grey region in Figure 6-28 and its contribution was effective at early stages (before initial crack); however, after cracking the grey region represents the contribution to shear resistance by actions other than aggregate interlock and joint stirrups. The contribution

of aggregate interlock used in this analysis was from the results of Gambarova and Karakoc model.

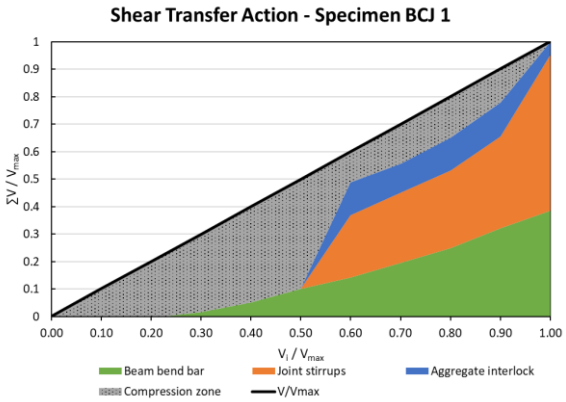

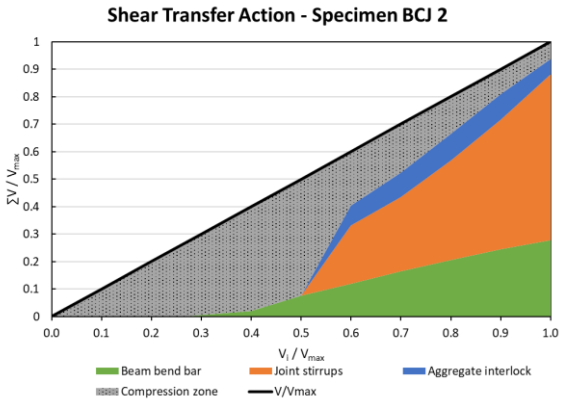

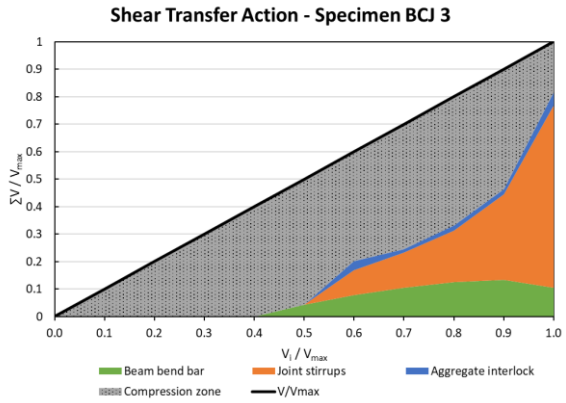

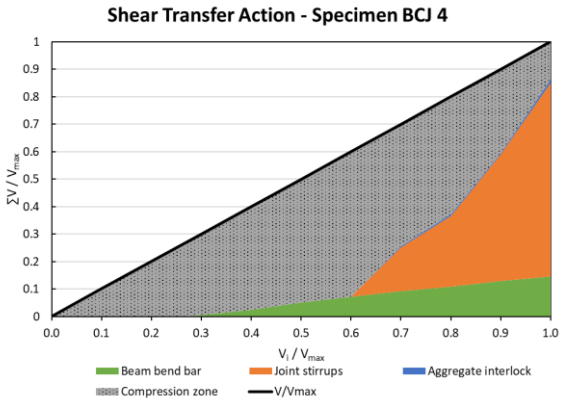

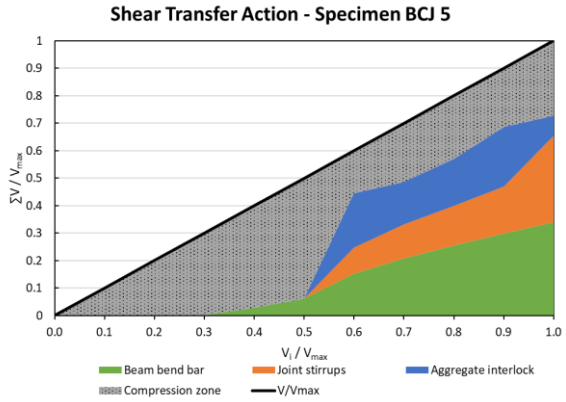

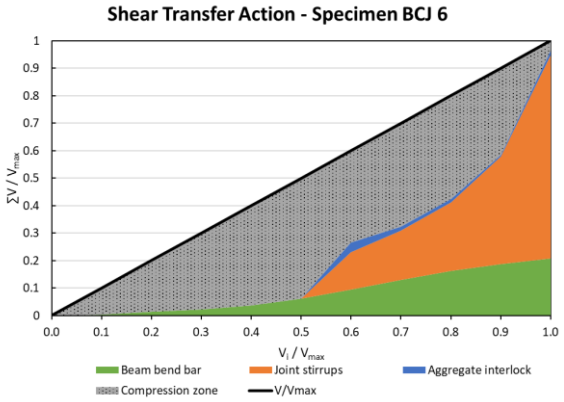

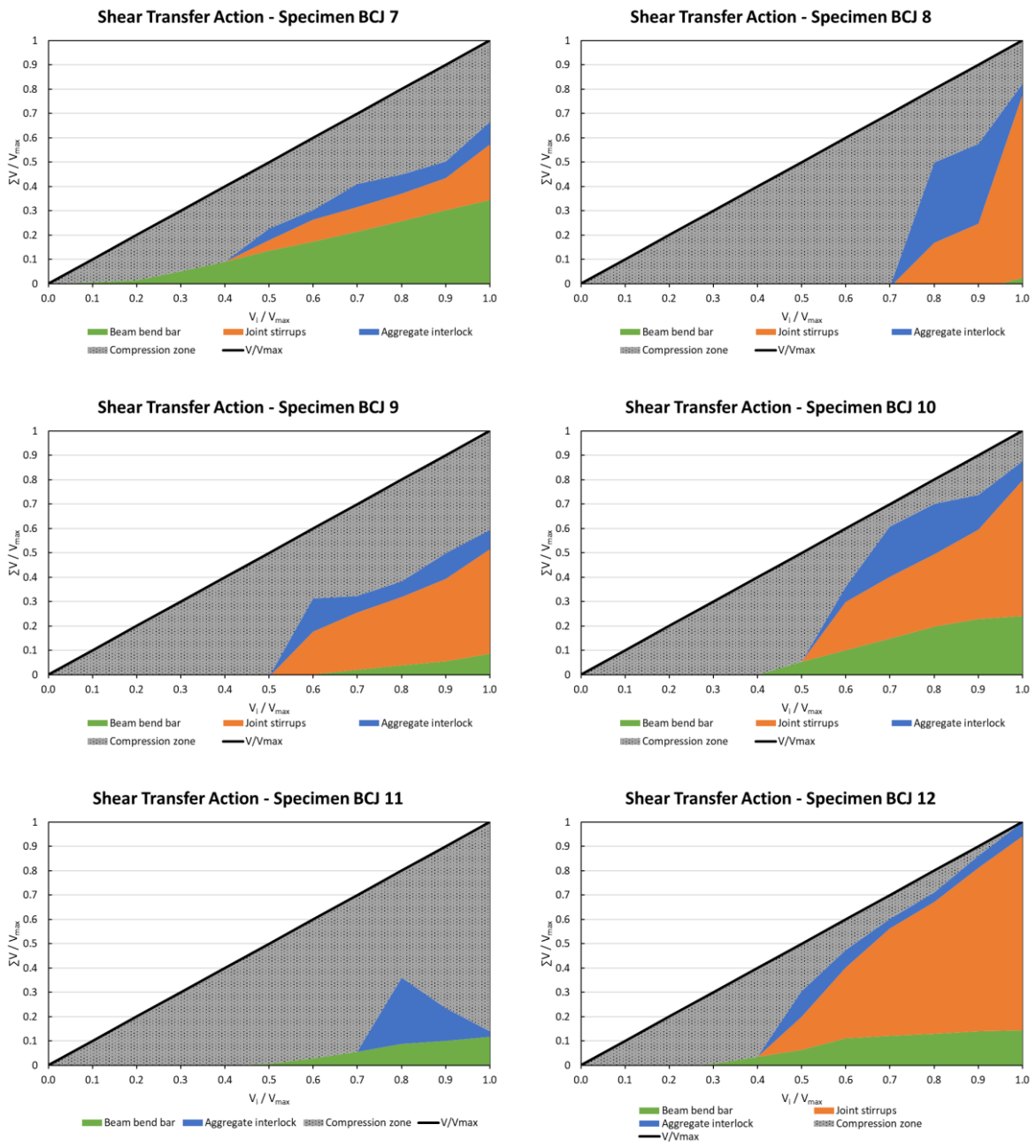

Figure 6-28 Shear transfer mechanism in horizontal direction.

6.6 Summary

Shear transfer mechanisms within the joint were studied for each specimen. The contributions of aggregate interlock and joint stirrups were determined in terms of the opening and sliding displacements in the critical shear crack which were determined using DIC. The influence of the parameters varied in the experimental tests on crack kinematics and shear transfer actions was investigated for each specimen. These parameters include anchorage type and bend radius, joint shear reinforcement, column axial load and column

intermediate bars. The investigation showed that the crack opening and sliding was influenced significantly by these parameters.

Free body diagrams were produced for each specimen to identify the horizontal forces acting on the critical diagonal shear crack. In some specimens, the cover spalled above the joint along the back column bars as shown in the free body diagrams. The free body diagrams indicate the internal forces (total joint stirrups force, horizontal aggregate interlock resultant force and beam bend bar resultant force in horizontal direction) and external forces (column shear force and beam anchorage bar tensile force) acting on the joint.

The contribution of aggregate interlock was calculated using the Walraven two-phase model [41], the Hamadi and Regan method [44], the rough crack model (Bazant and Gambarova [45] & Gambarova and Karakoc [46]) and the simplified contact density method of Li et al. [42]. The rough crack model and the Hamadi and Regan method were derived from regression analysis of experimental results. The remaining two methods were developed theoretically. The contribution of aggregate interlock varied between models but was small in all cases relative to the joint shear force particularly at failure. The Gambarova and Karakoc model was used for determining the relative contributions of each shear transfer action.

Flexural forces at the joint boundaries were determined from section analysis carried out using the stress-block factors proposed by Collins and Mitchell [33]. The section analysis was carried out at the beam-column interface and in the column at the top and bottom of the joint. The calculated strains were compared with the strain gauges measurements. Where available, the calculated strains showed a good agreement with the measured strains in tested specimens.

The contribution of joint stirrups was determined using the Sigrist two-step bond model [49] as well as strain measurements in the stirrups. This method calculates the stress in stirrups in terms of the crack width at the intersection of the stirrup and shear crack which was determined using DIC. The contribution of joint stirrups was determined as the total force of the total number of stirrups in the joint ($\sum \mathrm{T}_{\mathrm{stirrup}}$).

The horizontal force ($T_{b,hor}$) applied to the considered free body at the bend in the beam tension bar was determined from the strain gauges placed around the bend. The gauges were located at the beginning and end of the bend in specimens with standard bend radius and

mid-way along and at the end of the bend in specimens with large bend radius. Since the critical crack crossed the bend between these strain gauges, this method was used to obtain the resultant force of beam bend bar in horizontal direction.

The contribution of concrete compression zone (C_b-C_{comp}) was from horizontal equilibrium using equation (6-1). Consequently, the force C_{comp} can also be described as strength not explained by the other considered mechanisms.

Chapter 7 Analysis of the Experimental Results and Design Recommendations

Comparisons are made between the measured reinforcement and concrete surface strains and those predicted in the NLFEA. Various previously published empirical and mechanically based design models for external beam-column connections are assessed using a large database of experimental results including those from this campaign. Design recommendations are made for external beam-column joints.

7.1 Introduction

The chapter starts by comparing the experimentally determined reinforcement and concrete surface strains with those determined using NLFEA. The aim of this exercise is to assess the realism of the NLFEA. Subsequently, various previously proposed design methods for external beam-column joints are assessed using a large experimental database. These proposed methods are evaluated for the purpose of designing external beam-column joints. A technique is used to assess these methods based on the demerit point classification system proposed by Collins [76]. The chapter provides the strut geometry of the twelve specimens studied in this research using the findings of joint surface strain from DIC, 2D NLFEA and section analysis using stress-block factors as well as the results of proposed STM.

7.2 Assessment of NLFEA

This section compares the reinforcement and concrete surface strains obtained using NLFEA with those measured in the author's experimental campaign. For each series of tests, reinforcement strains obtained with 2D and 3D NLFEA are compared with strains measured in the beam reinforcement, front column bars and back column bars. Comparisons with surface strains are only made for the 2D NLFEA.

7.2.1 Strain measurements in beam anchorage bars

The following sub-sections compare the predicted and measured strains in the beam anchorage bars. Results are presented for each series sequentially.

7.2.1.1 Results of BCJ series 1

This section compares measured and predicted strains in the beam anchorage bars of the BCJ specimens in series 1. The positions of the strain gauges are indicated in Figures 3-17 to 3-20

of chapter 3. The results are shown in Figure 7-1, in which predicted strains from the 2D and 3D analyses are shown on the left and right hand sides respectively. Strain gauges (SG17) in specimen BCJ 2 and (SG13 and SG16) in specimen BCJ 3 were broken. The measured and predicted strains in specimens BCJ 1 and BCJ 2 with L-anchorage bars compare favourably for both 2D and 3D models. Measured and predicted tensile strains compare reasonably for specimens BCJ 3 and BCJ 4 with U-bars but the comparison is poor where the measured strains are compressive.

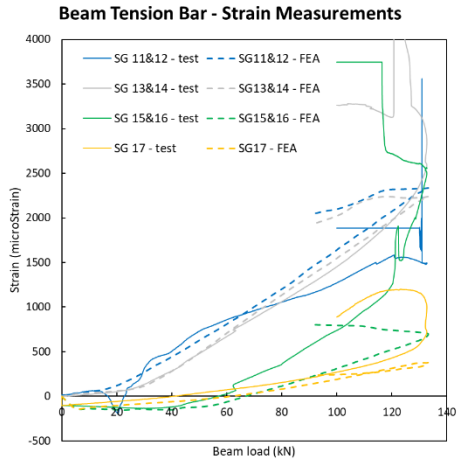

a) Specimen BCJ 1 (2D NLFEA)

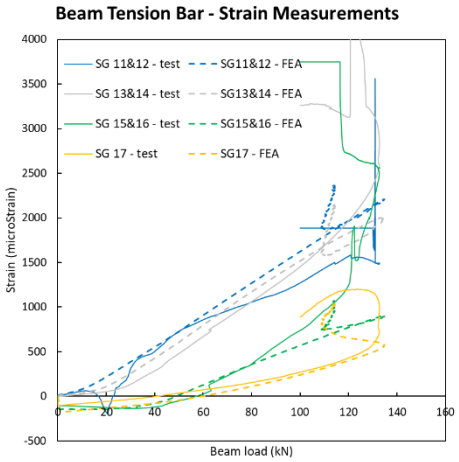

b) Specimen BCJ 1 (3D NLFEA)

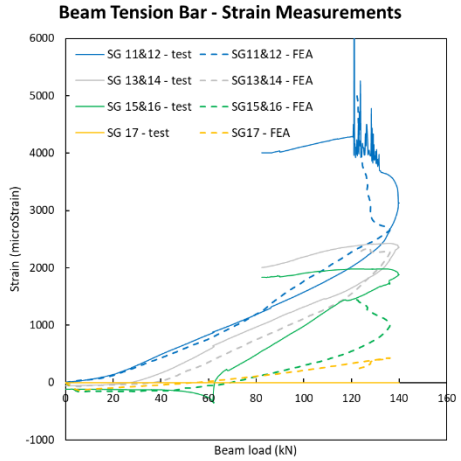

c) Specimen BCJ 2 (2D NLFEA)

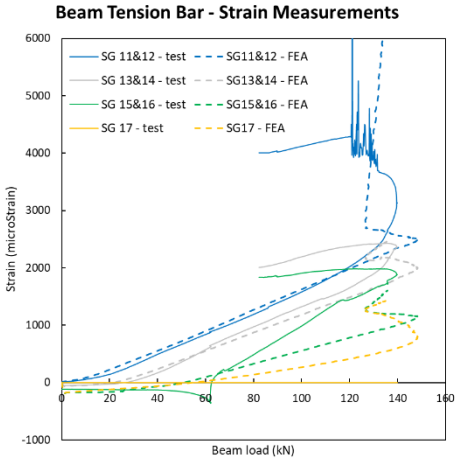

d) Specimen BCJ 2 (3D NLFEA)

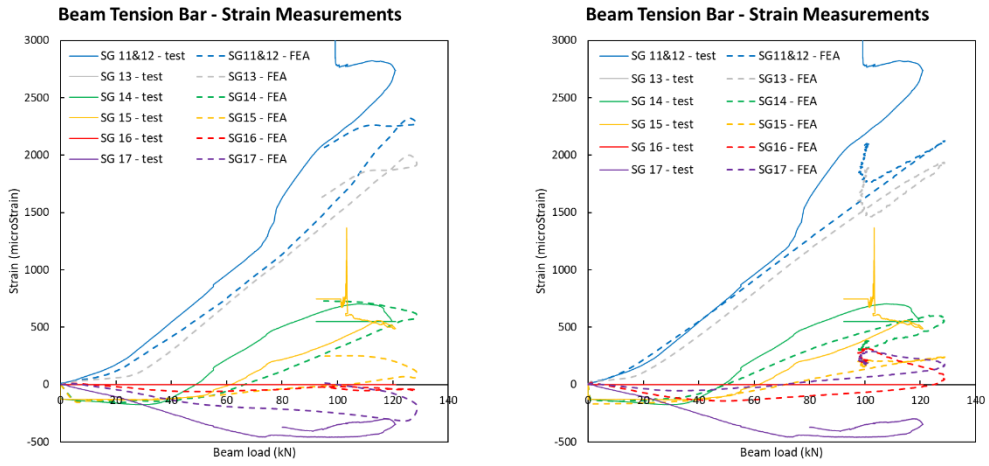

a) Specimen BCJ 3 (2D NLFEA) b) Specimen BCJ 3 (3D NLFEA)

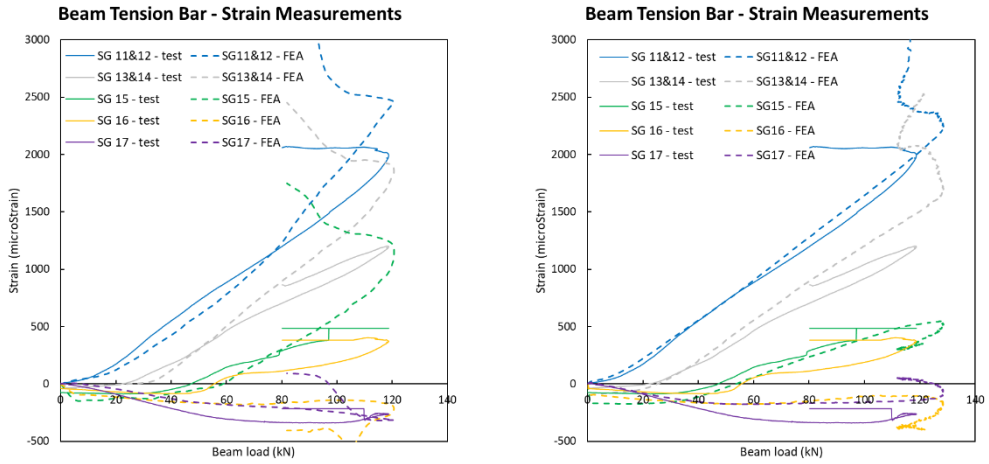

c) Specimen BCJ 4 (2D NLFEA) d) Specimen BCJ 4 (3D NLFEA)

Figure 7-1 Measured and predicted strains of series 1; beam anchorage bar.

7.2.1.2 Results of BCJ series 2

The measured and predicted strains in the beam anchorage bars of series 2 are shown in Figure 7-2 for 2D and 3D models. Strains are compared on the left side for the 2D models and on the right side for the 3D models. The positions of the strain gauges where strains are shown are indicated in Figures 3-17 and 3-20 of chapter 3. Strain gauges (SG 17&18) and (SG 19) were broken in specimen BCJ 7. Strain gauges (SG 13) and (SG 15) were also broken in specimen BCJ 8. Overall, the comparison is reasonable but there are some significant differences in measured and predicted strains. For example, a much larger tensile strain was measured at SG17 in BCJ5, positioned on the vertical leg of the U-bar, than predicted. The 3D model predictions are slightly better than the 2D predictions.

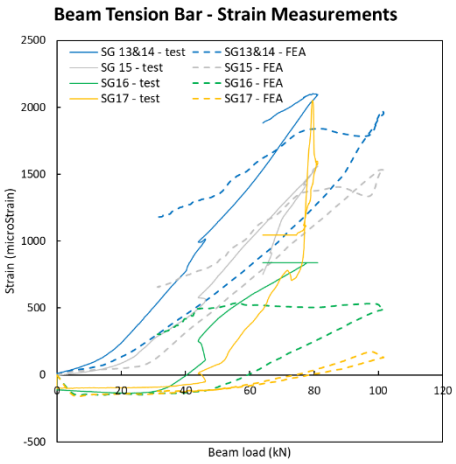

a) Specimen BCJ 5 (2D NLFEA)

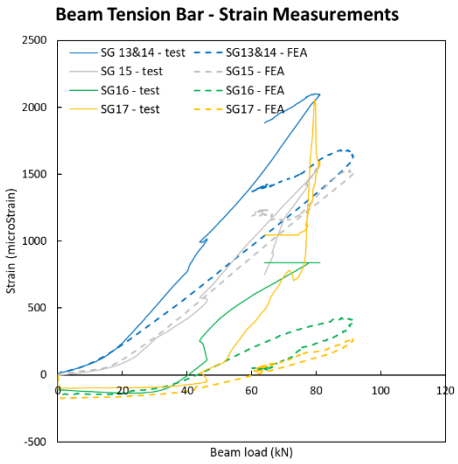

b) Specimen BCJ 5 (3D NLFEA)

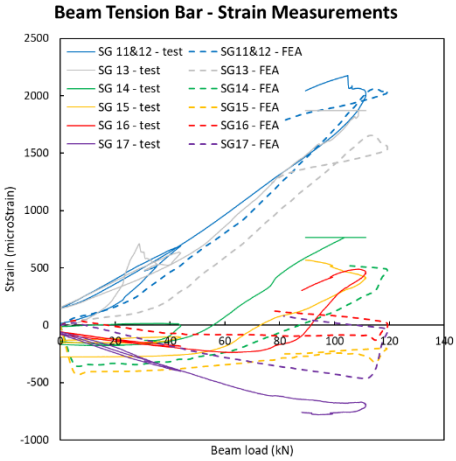

c) Specimen BCJ 6 (2D NLFEA)

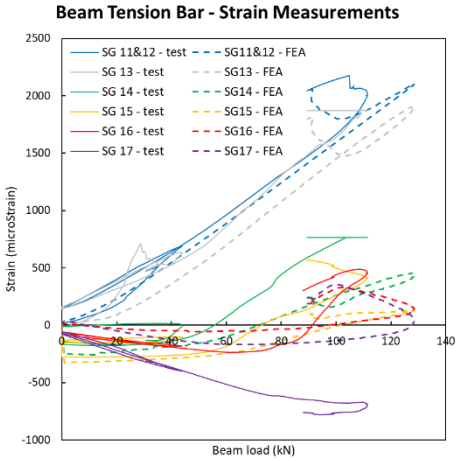

d) Specimen BCJ 6 (3D NLFEA)

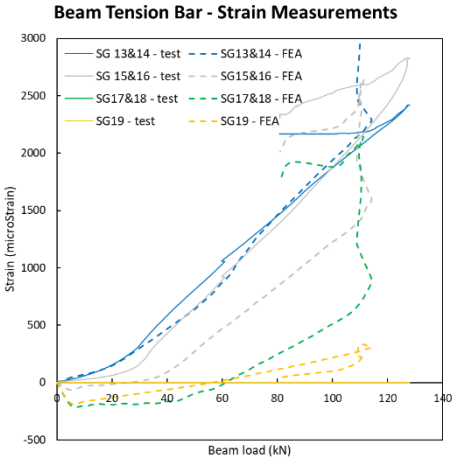

e) Specimen BCJ 7 (2D NLFEA)

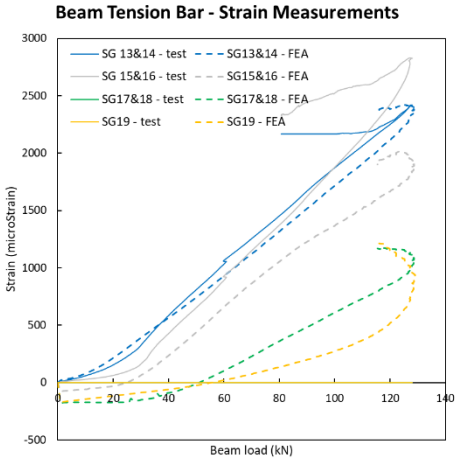

f) Specimen BCJ 7 (3D NLFEA)

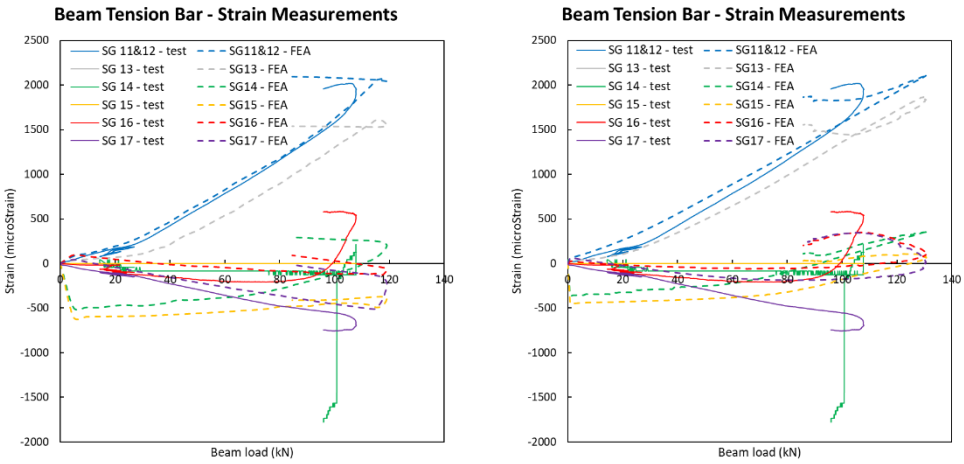

g) Specimen BCJ 8 (2D NLFEA) h) Specimen BCJ 8 (3D NLFEA)

Figure 7-2 Measured and predicted strains of series 2; beam anchorage bar.

7.2.1.3 Results of BCJ series 3

The measured and predicted strains in the beam anchorage bars of series 3 are shown in Figure 7-3. Strains are compared on the left side for the 2D models and on the right side for the 3D models. The positions of the strain gauges where strains are shown are indicated in Figures 3-17 and 3-20 of chapter 3. Strain gauges SG 13, SG 14 and SG 15 were broken in specimen BCJ 9. The comparison between the predicted and measured strains is acceptable for most strain gauges. Some of the measured strains showed odd readings such as (SG 13&14) in specimen BCJ 11 after a load of 60 kN and (SG 13&14) in specimen BCJ 12 after a load of 120 kN. In general, strains from both 2D and 3D models compared favourably with measured strains.

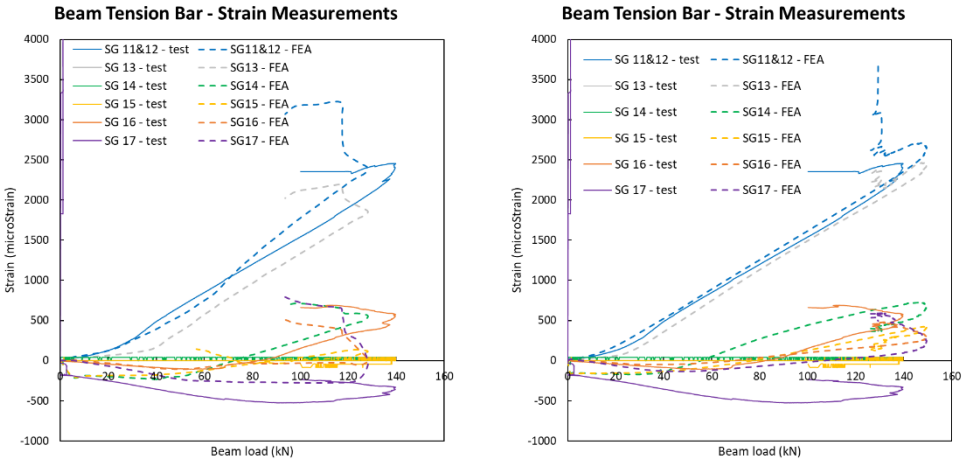

a) Specimen BCJ 9 (2D NLFEA) b) Specimen BCJ 9 (3D NLFEA)

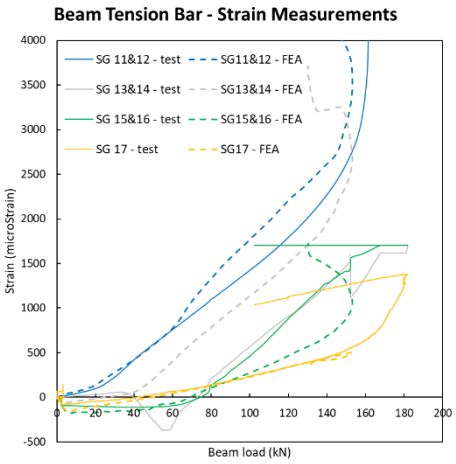

c) Specimen BCJ 10 (2D NLFEA)

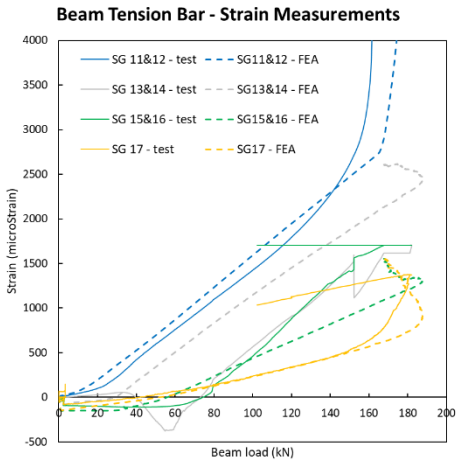

d) Specimen BCJ 10 (3D NLFEA)

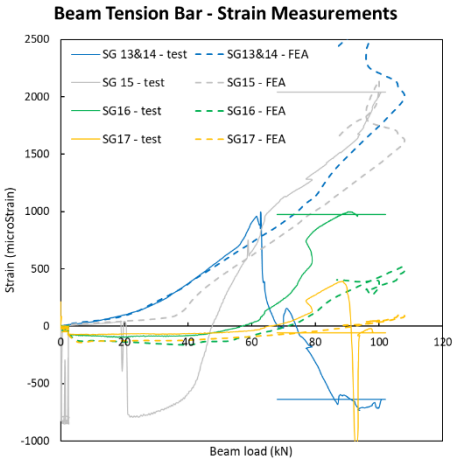

e) Specimen BCJ 11 (2D NLFEA)

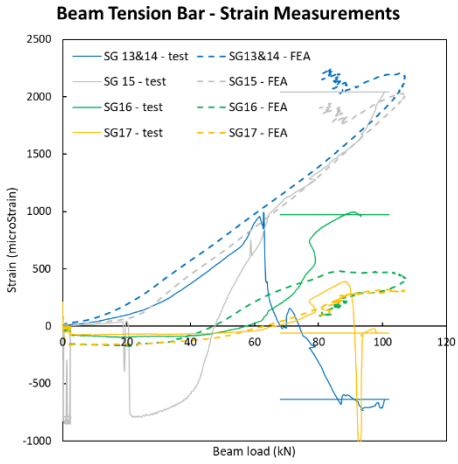

f) Specimen BCJ 11 (3D NLFEA)

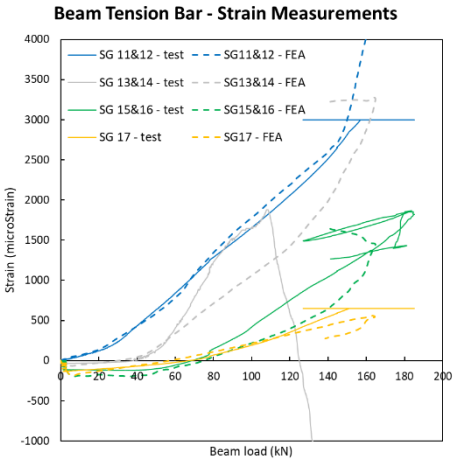

g) Specimen BCJ 12 (2D NLFEA)

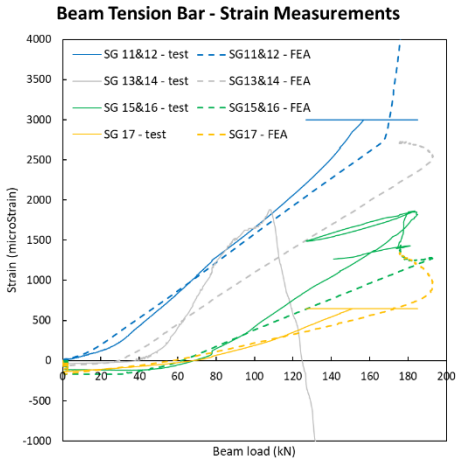

h) Specimen BCJ 12 (3D NLFEA)

Figure 7-3 Measured and predicted strains of series 3; beam anchorage bar.

7.2.2 Strain measurements in column bars

This section compares the measured front and back column bar strains with the NLFEA strains for both 2D and 3D models.

7.2.2.1 Strains in front column bars

7.2.2.1.1 Results of BCJ series 1

Measured and predicted strains in the front column bars of series 1 are shown in Figure 7-4. Positions of the strain gauges are shown in Figure 3-15 of chapter 3. Strains are compared on the left side for the 2D models and on the right side for the 3D models. The predicted 2D and 3D strains match the measured strains from early stage of loading up to near failure load in specimens with L-anchorage bars. The predicted strains in specimens with U-anchorage bars (BCJ 3 and BCJ 4) showed different trends than the companion specimens. For example, the strain in gauge (SG 5) of specimen BCJ 3, just below the beam, switched sign and became tensile at a load of 60 kN. This switch in sign of the strain in gauge SG 5, which seems physically unlikely, was not predicted by the NLFEA and did not occur in any of the other tests.

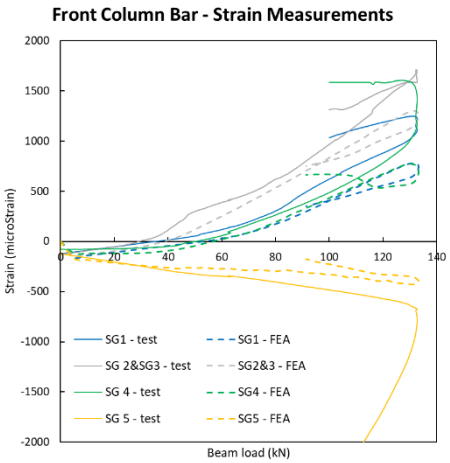

a) Specimen BCJ 1 (2D NLFEA)

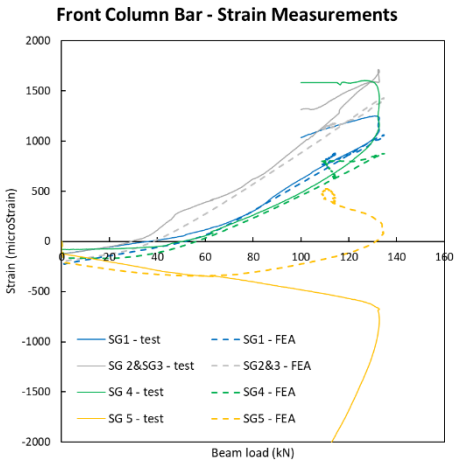

b) Specimen BCJ 1 (3D NLFEA)

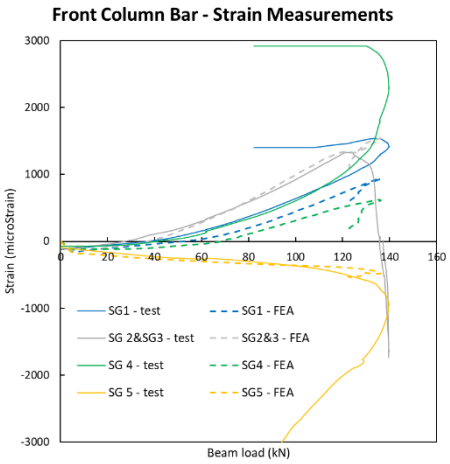

c) Specimen BCJ 2 (2D NLFEA)

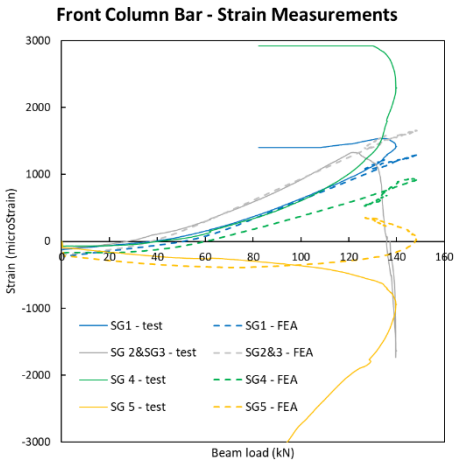

d) Specimen BCJ 2 (3D NLFEA)

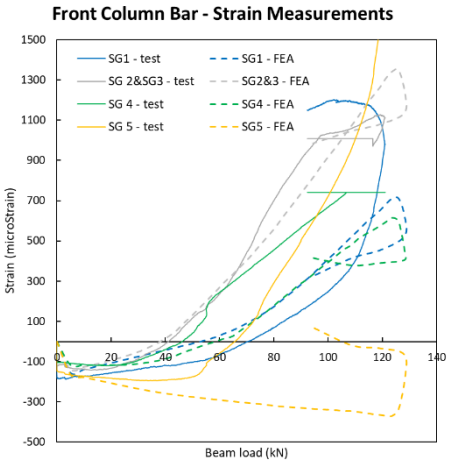

e) Specimen BCJ 3 (2D NLFEA)

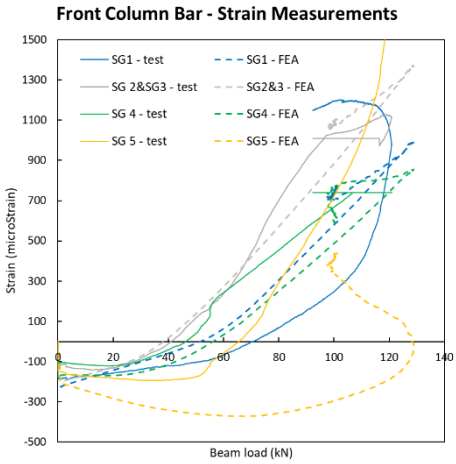

f) Specimen BCJ 3 (3D NLFEA)

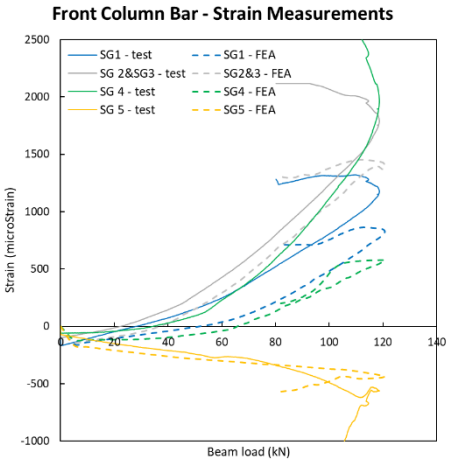

g) Specimen BCJ 4 (2D NLFEA)

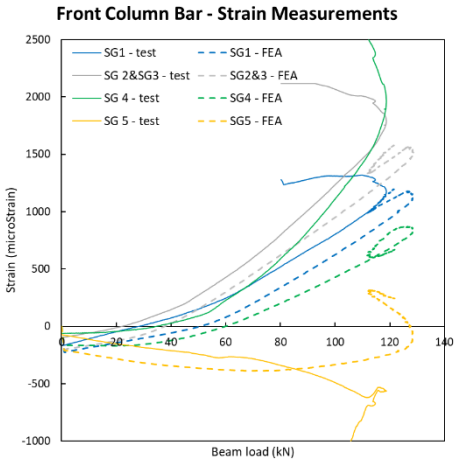

h) Specimen BCJ 4 (3D NLFEA)

Figure 7-4 Measured and predicted strains of series 1; front column bars.

7.2.2.1.2 Results of BCJ series 2

The predicted and measured strains in the front column bars are shown in Figure 7-5. Strains are compared on the left side for the 2D models and on the right side for the 3D models. The positions of the strain gauges where strains are shown are indicated in Figures 3-15 and 3-16 of chapter 3. Strain gauge (SG 1) in specimen BCJ 1 and (SG 2&3) in specimen BCJ 8 were broken. The predicted strains in all specimens in this series were acceptable for both 2D and 3D models when compared with measured strains from tested specimens. The influence of applying a high column axial load can be seen in the mainly compressive predicted and measured strains in specimen BCJ 8.

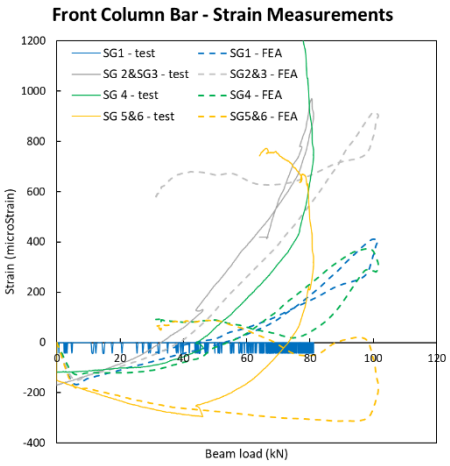

a) Specimen BCJ 5 (2D NLFEA)

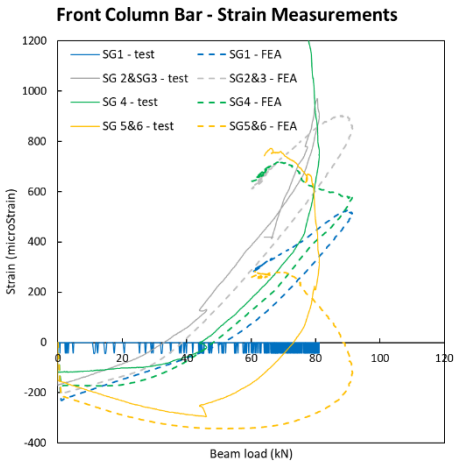

b) Specimen BCJ 5 (3D NLFEA)

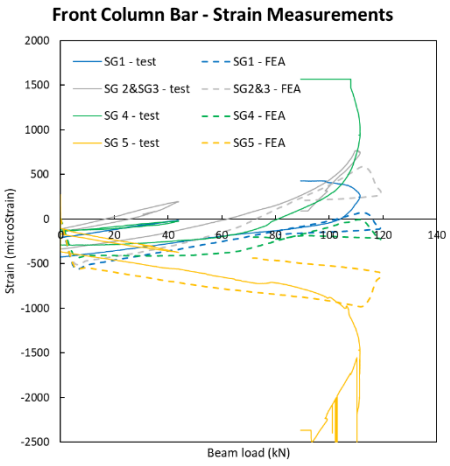

c) Specimen BCJ 6 (2D NLFEA)

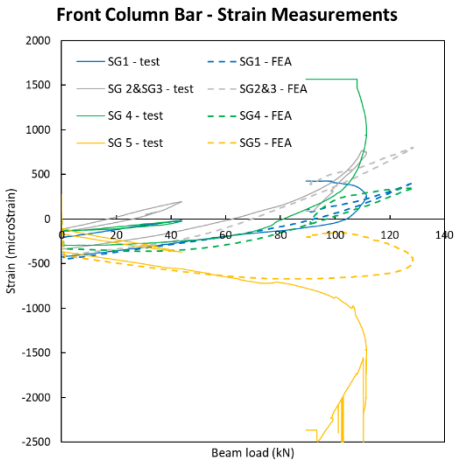

d) Specimen BCJ 6 (3D NLFEA)

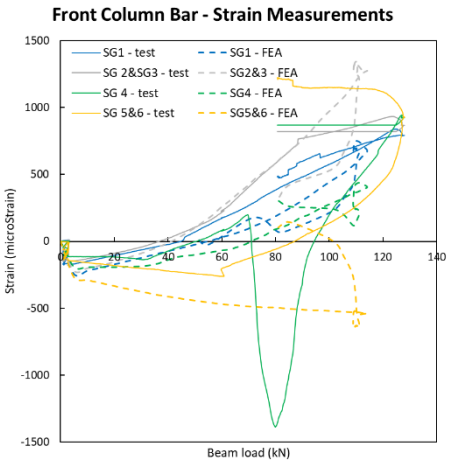

e) Specimen BCJ 7 (2D NLFEA)

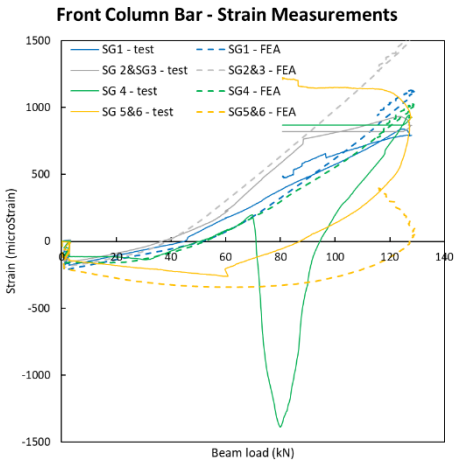

f) Specimen BCJ 7 (3D NLFEA)

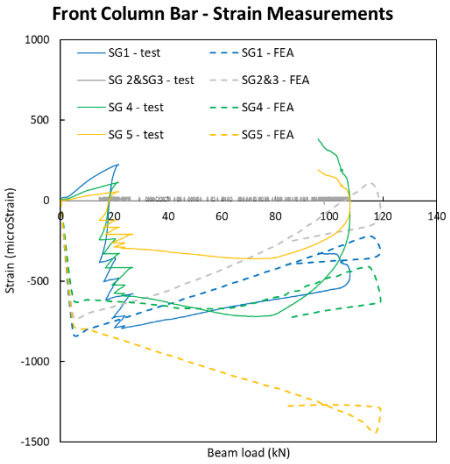

g) Specimen BCJ 8 (2D NLFEA)

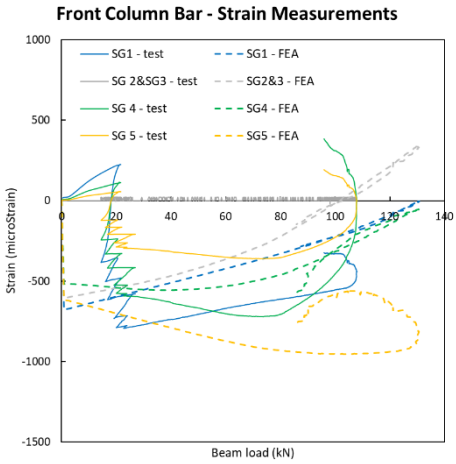

h) Specimen BCJ 8 (3D NLFEA)

Figure 7-5 Measured and predicted strains of series 2; front column bars.

7.2.2.1.3 Results of BCJ series 3

The measured and predicted strains in front column bars are shown in Figure 7-6 for series 3. Strains are compared on the left side for the 2D models and on the right side for the 3D models. The positions of the strain gauges where strains are shown are indicated in Figures 3-15 and 3-16 of chapter 3. The measured and predicted strains compare well for bars in tension for both 2D and 3D models. Clear differences can be seen where measured strains are compressive particularly in specimens BCJ 9, BCJ 10 and BCJ 12. Some of the predicted strains in 3D models changed from compression to tension near failure but this was not observed experimentally (observed in SG 5 for specimens BCJ 9, BCJ 10 and BCJ 12).

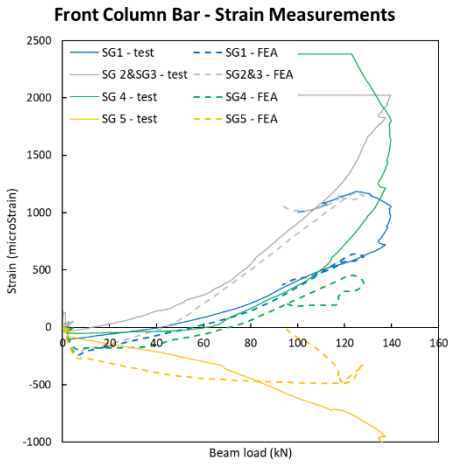

a) Specimen BCJ 9 (2D NLFEA)

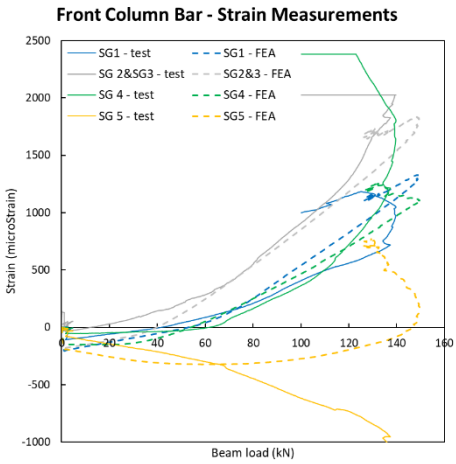

b) Specimen BCJ 9 (3D NLFEA)

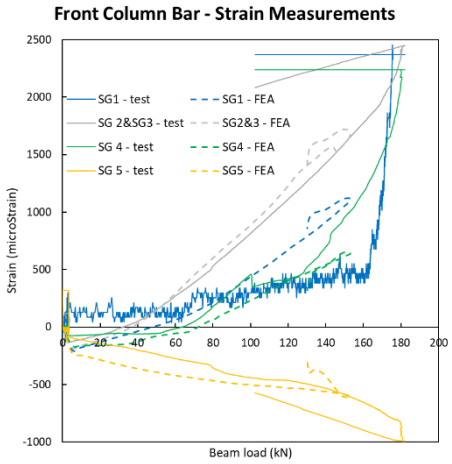

c) Specimen BCJ 10 (2D NLFEA)

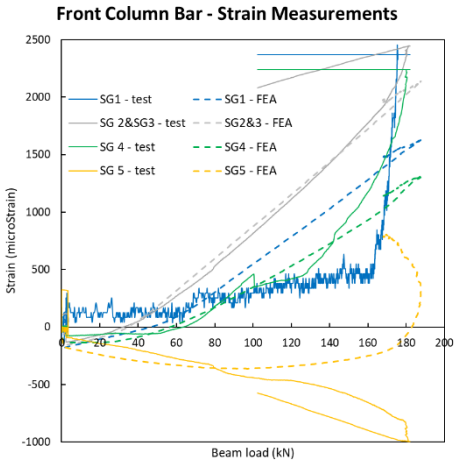

d) Specimen BCJ 10 (3D NLFEA)

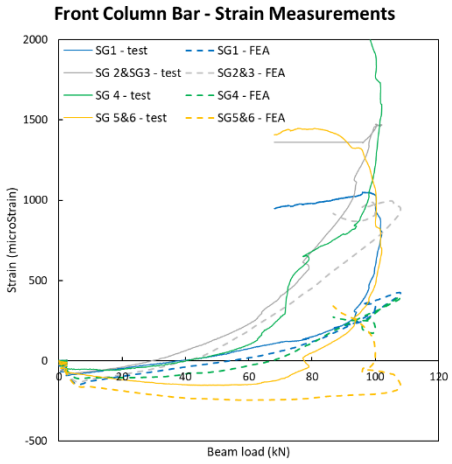

e) Specimen BCJ 11 (2D NLFEA)

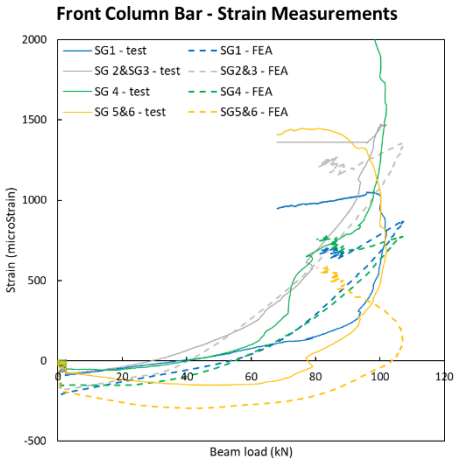

f) Specimen BCJ 11 (3D NLFEA)

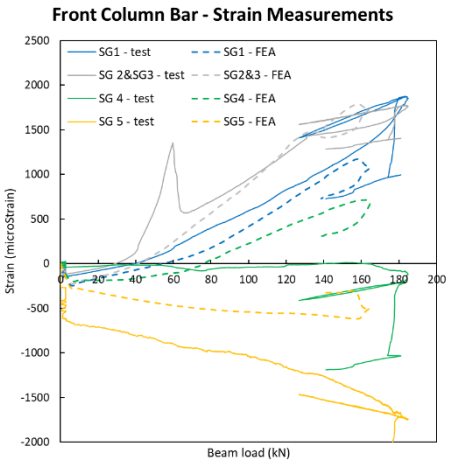

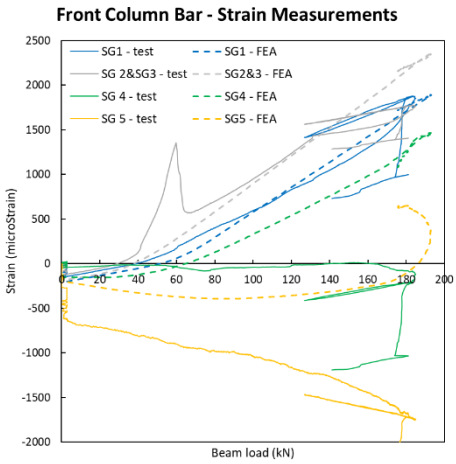

g) Specimen BCJ 12 (2D NLFEA) h) Specimen BCJ 12 (3D NLFEA)

Figure 7-6 Measured and predicted strains of series 3; front column bars.

7.2.2.2 Strains in back column bars

7.2.2.2.1 Results of BCJ series 1

The measured and predicted strains in the back column bars are compared for series 1 in Figure 7-7. Strains are compared on the left side for the 2D models and on the right side for the 3D models. The positions of the strain gauges where strains are shown are indicated in Figure 3-15 of chapter 3. Strain gauge (SG 7) in specimen BCJ 2 was broken. Strains were predicted to be compressive by both 2D and 3D models at gauge SG 6, whereas the measured strain was tensile near failure in specimens BCJ 1, BCJ 3 and BCJ 4. At other gauges, measured and predicted strains compare favourably for 2D and 3D models.

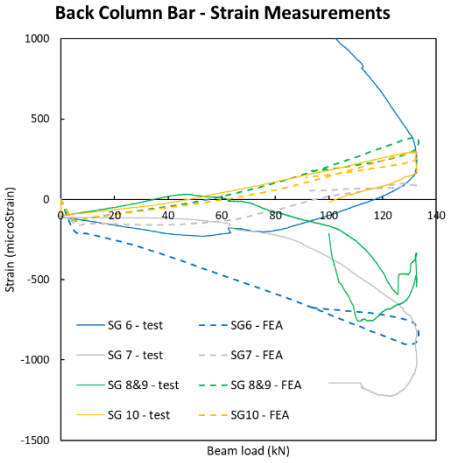

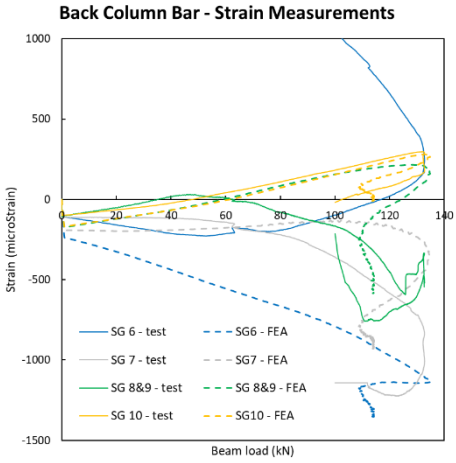

a) Specimen BCJ 1 (2D NLFEA) b) Specimen BCJ 1 (3D NLFEA)

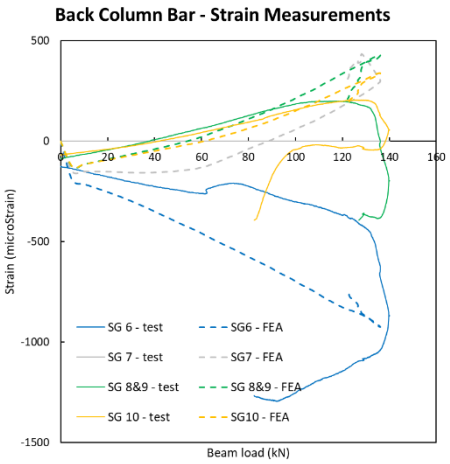

c) Specimen BCJ 2 (2D NLFEA)

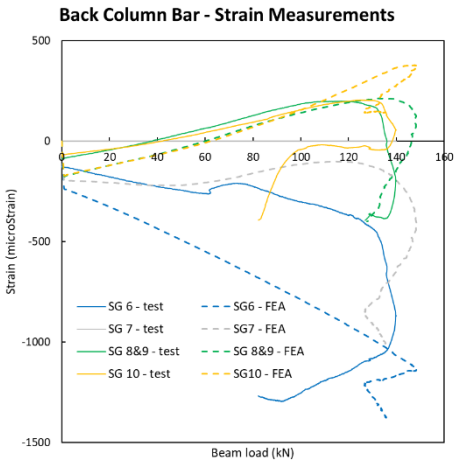

d) Specimen BCJ 2 (3D NLFEA)

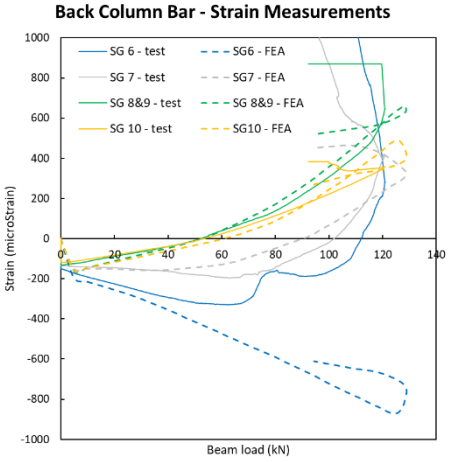

e) Specimen BCJ 3 (2D NLFEA)

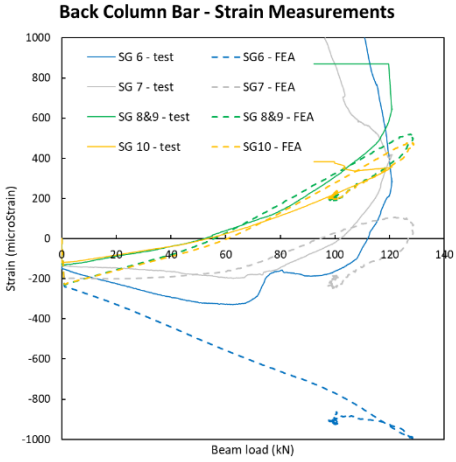

f) Specimen BCJ 3 (3D NLFEA)

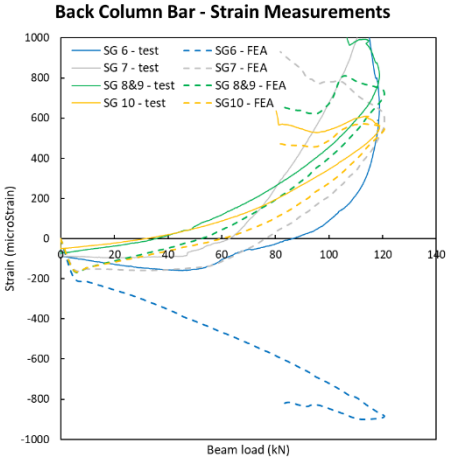

g) Specimen BCJ 4 (2D NLFEA)

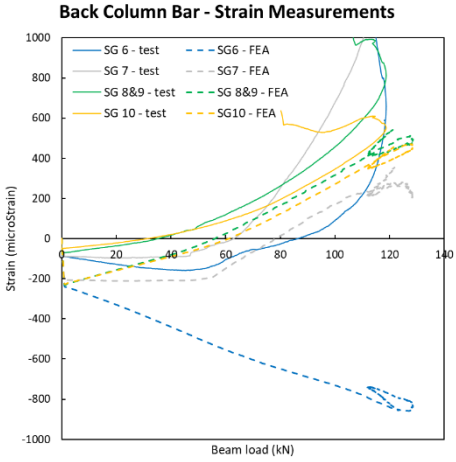

h) Specimen BCJ 4 (3D NLFEA)

Figure 7-7 Measured and predicted strains of series 1; back column bars.

7.2.2.2.2 Results of BCJ series 2

The measured and predicted strains in the back column bars are compared in Figure 7-8. Strains are compared on the left side for the 2D models and on the right side for the 3D

models. The positions of the strain gauges where strains are shown are indicated in Figures 3-15 and 3-16 of chapter 3. Strain gauges (SG 10&11) in specimen BCJ 5 and (SG 10) in specimen BCJ 6 were broken. The predicted strains follow similar trends to the measured tension and compression strains. Small gaps can be seen between the predicted and measured strains in both 2D and 3D models. The effect of applying high column axial load can also be observed in the predicted and measured strains. The 2D and 3D models showed compression strains at early stage of loading which are comparable with the measured strains for (SG 7&8).

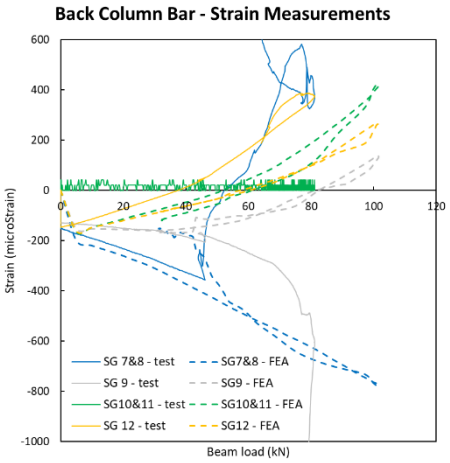

a) Specimen BCJ 5 (2D NLFEA)

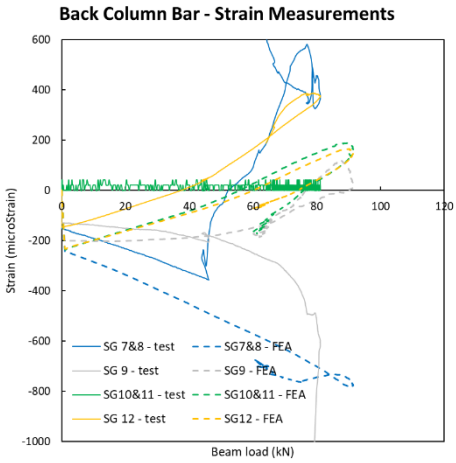

b) Specimen BCJ 5 (3D NLFEA)

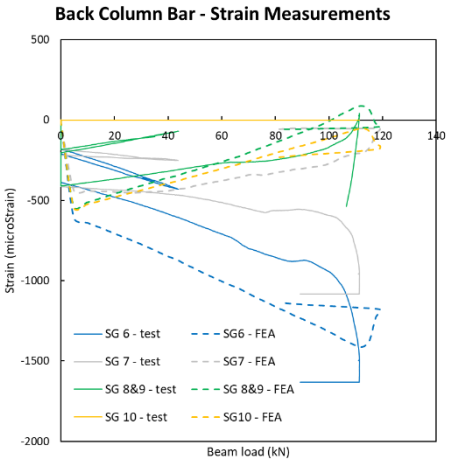

c) Specimen BCJ 6 (2D NLFEA)

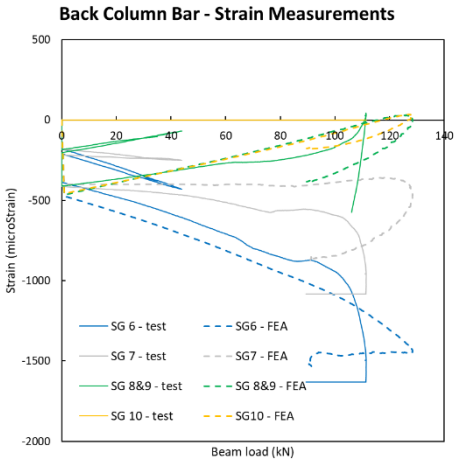

d) Specimen BCJ 6 (3D NLFEA)

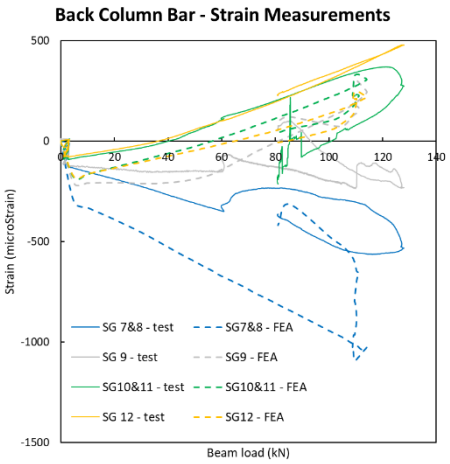

e) Specimen BCJ 7 (2D NLFEA)

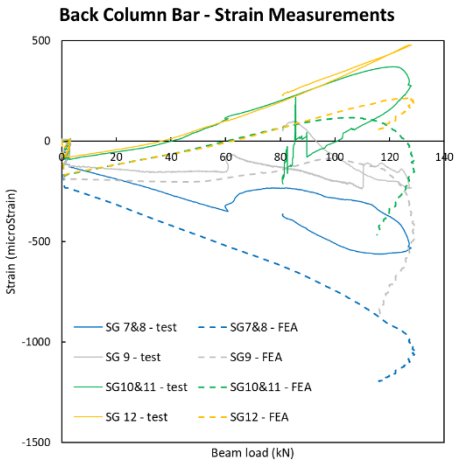

f) Specimen BCJ 7 (3D NLFEA)

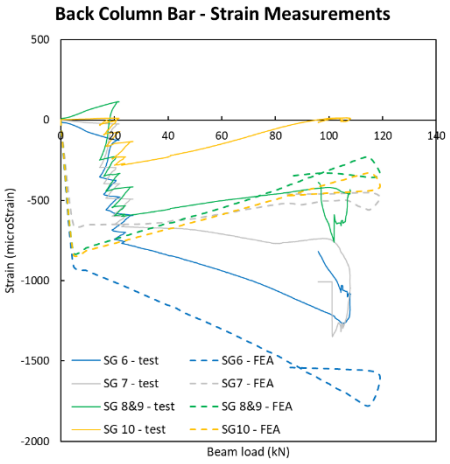

g) Specimen BCJ 8 (2D NLFEA)

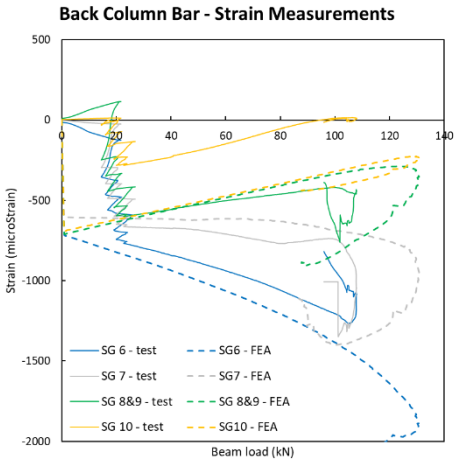

h) Specimen BCJ 8 (3D NLFEA)

Figure 7-8 Measured and predicted strains of series 2; back column bars.

7.2.2.2.3 Results of BCJ series 3

The measured and predicted strains in the back column bars are compared in Figure 7-9. Strains are compared on the left side for the 2D models and on the right side for the 3D models. The positions of the strain gauges where strains are shown are indicated in Figures 3-15 and 3-16 of chapter 3. Specimen BCJ 9 had broken strain gauges (SG 7 and SG 10). Measured strains at gauge (SG 6) were compressive in specimens BCJ 10 and BCJ 12 as predicted by the 2D and 3D models. However, in specimens BCJ 9 and BCJ 11 strains in SG 6 switched from compression to tension near failure load which was not predicted. Strains at gauge (SG 7) were well predicted by both 2D and 3D models in all specimens, except BCJ 11 where tension was measured but compression predicted by 2D and 3D models.

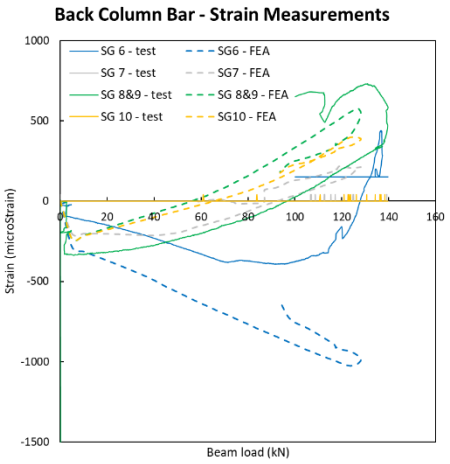

a) Specimen BCJ 9 (2D NLFEA)

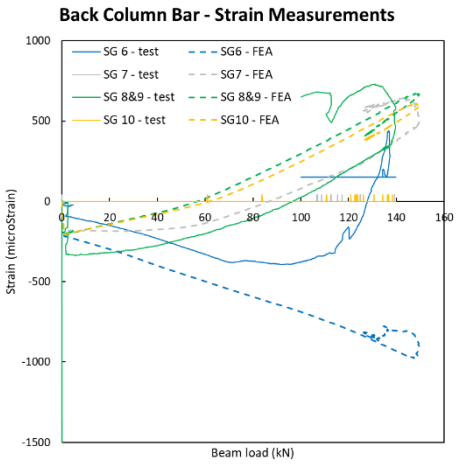

b) Specimen BCJ 9 (3D NLFEA)

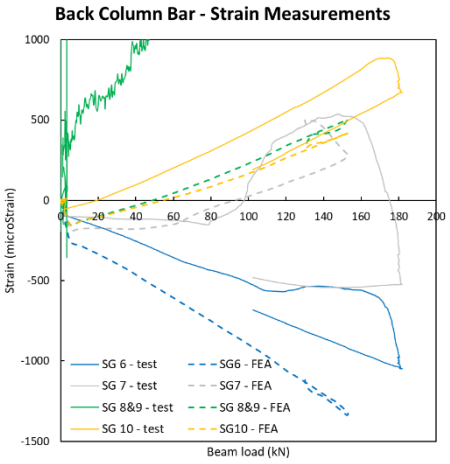

c) Specimen BCJ 10 (2D NLFEA)

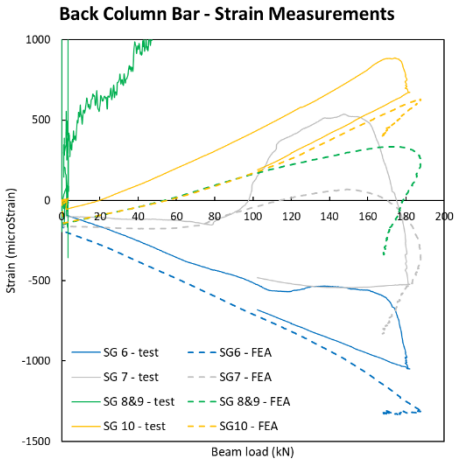

d) Specimen BCJ 10 (3D NLFEA)

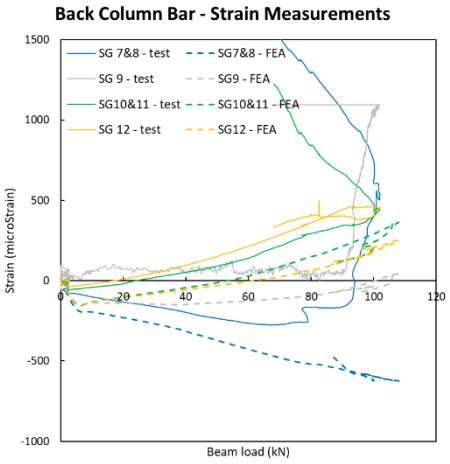

e) Specimen BCJ 11 (2D NLFEA)

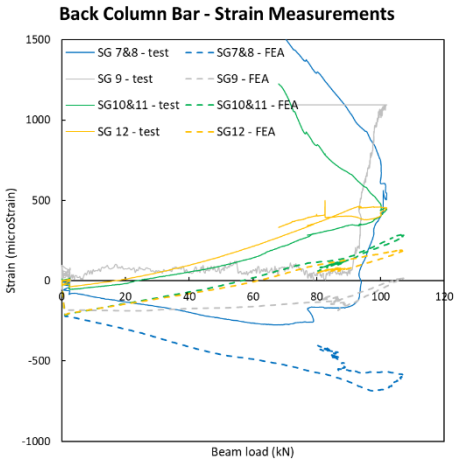

f) Specimen BCJ 11 (3D NLFEA)

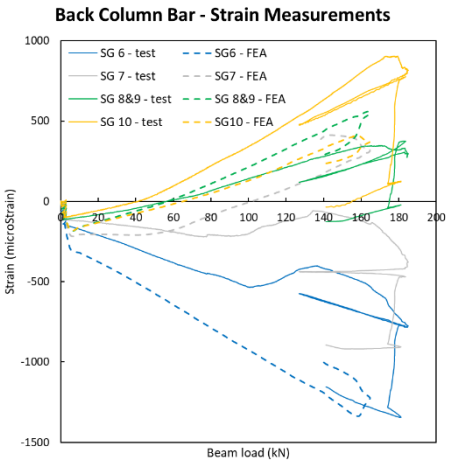

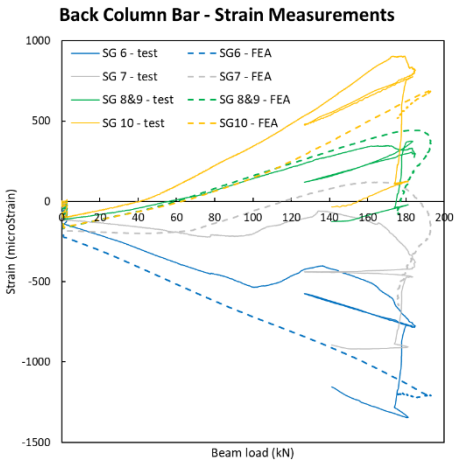

g) Specimen BCJ 12 (2D NLFEA) h) Specimen BCJ 12 (3D NLFEA)

Figure 7-9 Measured and predicted strains of series 3; back column bars.

7.2.3 Strain measurements in joint stirrups

The measured and predicted strains in the joint stirrups are compared in this section.

7.2.3.1 Results of BCJ series 1

The measured and predicted strains in the joint stirrups of series 1 are shown in Figure 7-10. The positions of the strain gauges where strains are shown are indicated in Figure 3-22 of chapter 3. The results presented in the left side are for 2D models while in the right side are for 3D models. Overall, the measured and predicted strains compare reasonably well up to near failure. The exception is strains at gauges SG 18 and SG 19 in specimen BCJ 1 where strains diverge at 60 kN.

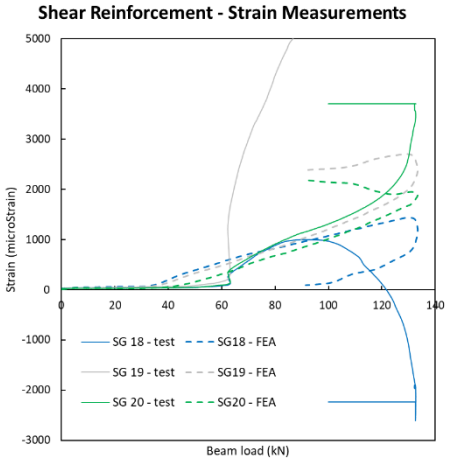

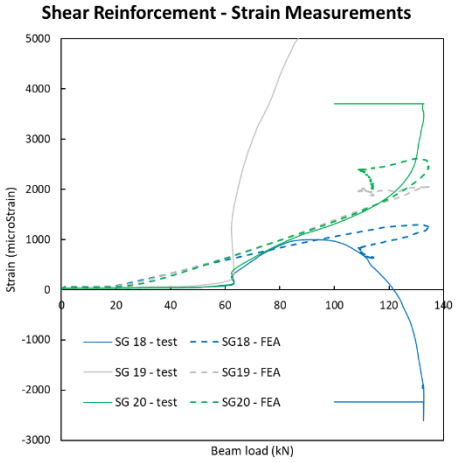

a) Specimen BCJ 1 (2D NLFEA) b) Specimen BCJ 1 (3D NLFEA)

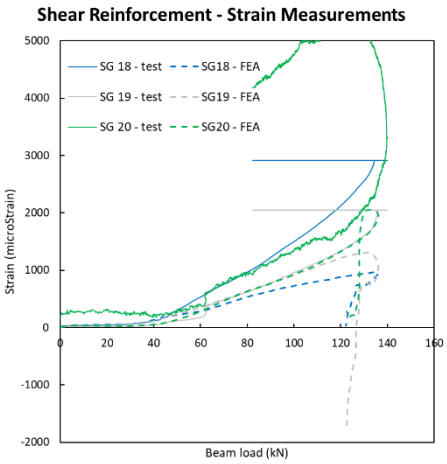

c) Specimen BCJ 2 (2D NLFEA)

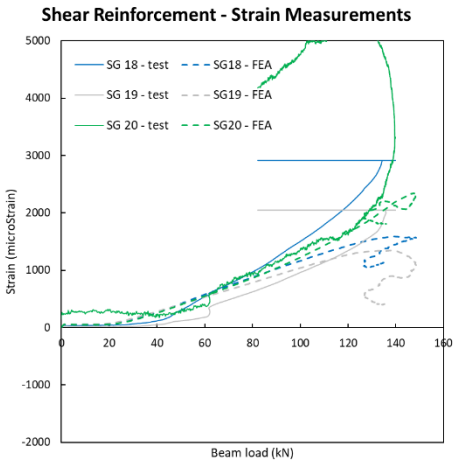

d) Specimen BCJ 2 (3D NLFEA)

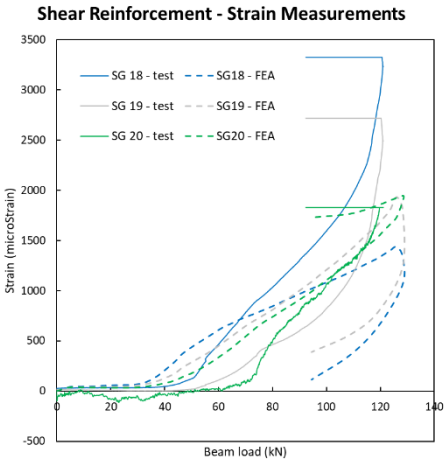

e) Specimen BCJ 3 (2D NLFEA)

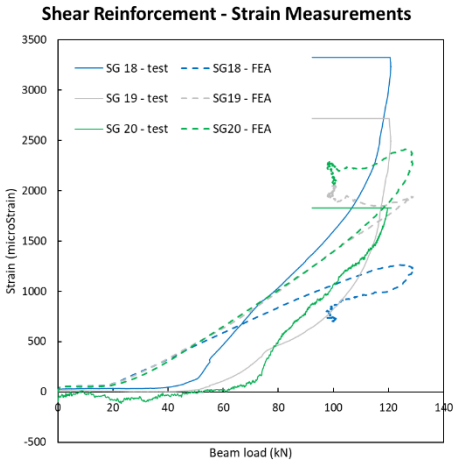

f) Specimen BCJ 3 (3D NLFEA)

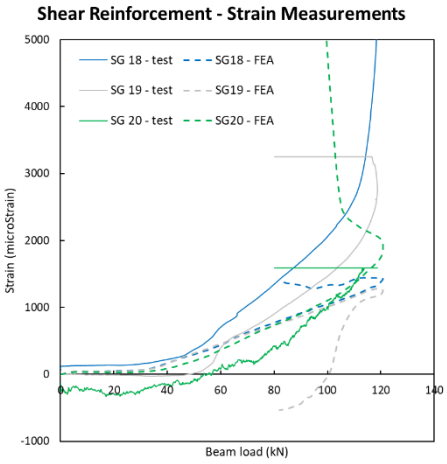

g) Specimen BCJ 4 (2D NLFEA)

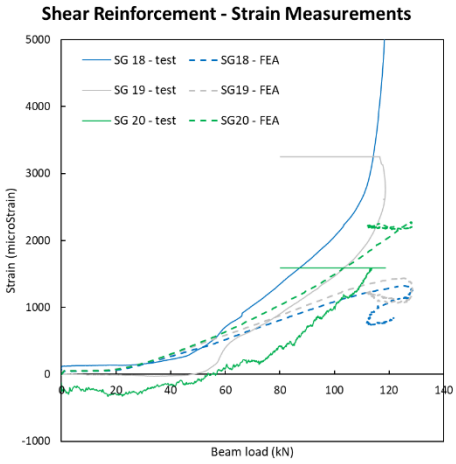

h) Specimen BCJ 4 (3D NLFEA)

Figure 7-10 Measured and predicted strains of series 1; joint stirrups.

7.2.3.2 Results of BCJ series 2

The measured and predicted strains in the joint stirrups of series 2 are shown in Figure 7-11. The positions of the strain gauges where strains are shown are indicated in Figures 3-21 and 3-22 of chapter 3. Strains are compared on the left side for the 2D models and on the right side for the 3D models. Strain gauges (SG 20) in specimen BCJ 5 and BCJ 6 were faulty while strain gauge (SG 20) in specimens BCJ 7 was broken. Both 2D and 3D models showed some gaps between the predicted and measured strains curves. This gap was larger in specimen BCJ 6 in comparison with specimen BCJ 8.

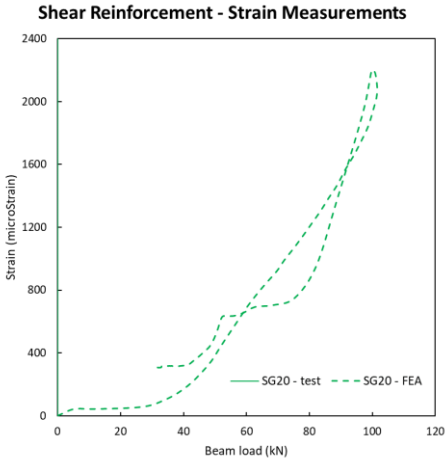

a) Specimen BCJ 5 (2D NLFEA)

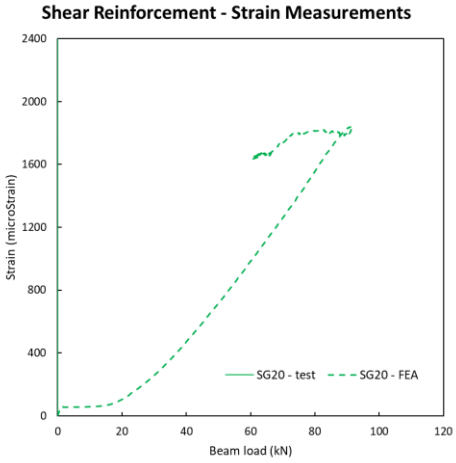

b) Specimen BCJ 5 (3D NLFEA)

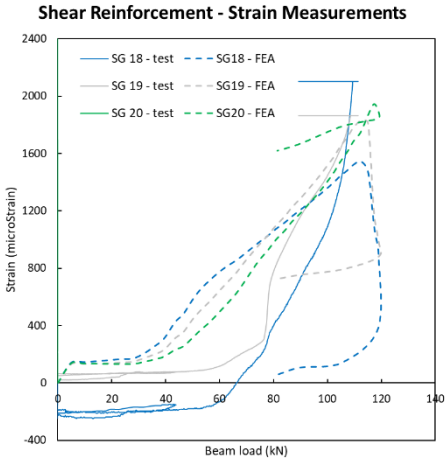

c) Specimen BCJ 6 (2D NLFEA)

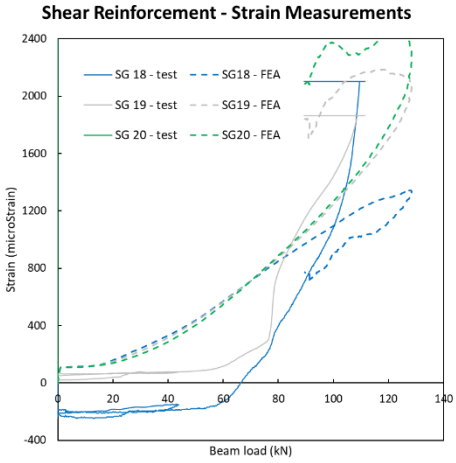

d) Specimen BCJ 6 (3D NLFEA)

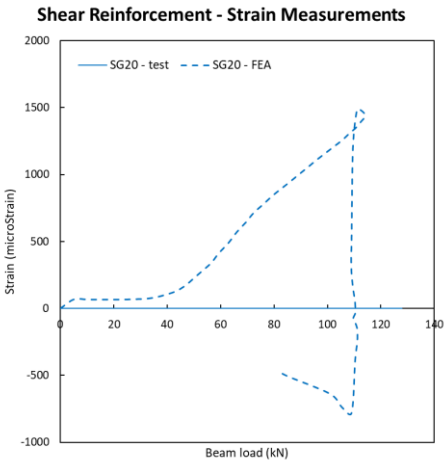

e) Specimen BCJ 7 (2D NLFEA)

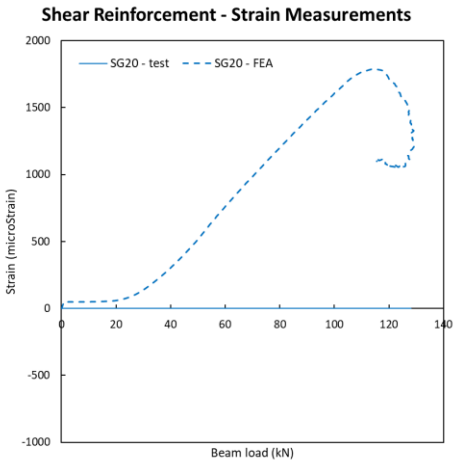

f) Specimen BCJ 7 (3D NLFEA)

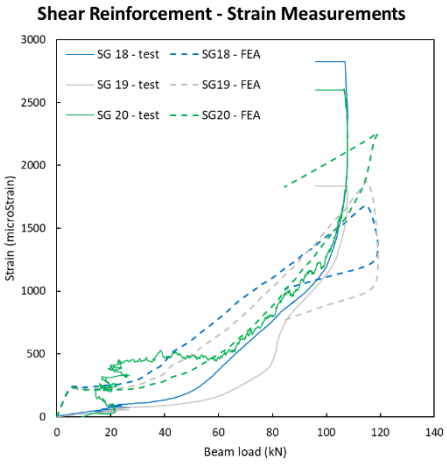

g) Specimen BCJ 8 (2D NLFEA)

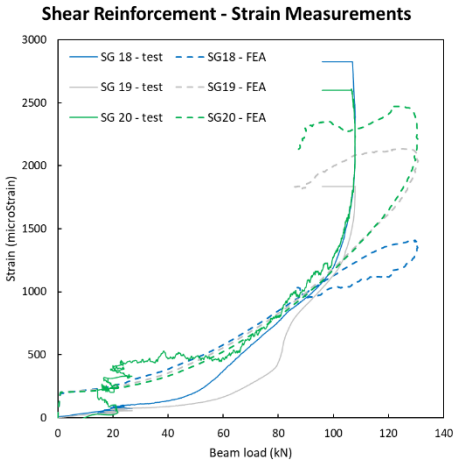

h) Specimen BCJ 8 (3D NLFEA)

Figure 7-11 Measured and predicted strains of series 2; joint stirrups.

7.2.3.3 Results of BCJ series 3

The measured and predicted strains in joint stirrups for 2D and 3D models are shown in Figure 7-12. The positions of the strain gauges where strains are shown are indicated in Figures 3-21 and 3-22 of chapter 3. Strains are compared on the left side for the 2D models and on the right side for the 3D models. Specimen BCJ 11 is not included as it had no joint stirrup. Strain gauge SG 19 in specimen BCJ 12 was broken while faulty strain gauges were observed in specimen BCJ 10 (SG 20) and specimen 12 (SG 12 and SG 20). Due to some broken and faulty strain measurements, the comparison between predicted and measured strains could not be assessed in specimens BCJ 10 and BCJ 12. The predicted strains in 3D models were larger than the strains in 2D model. The functioning strain gauges in specimen BCJ 10 showed acceptable comparison between the predicted and measured strains. Large gaps between the predicted and measured strains were observed in specimen BCJ 9.

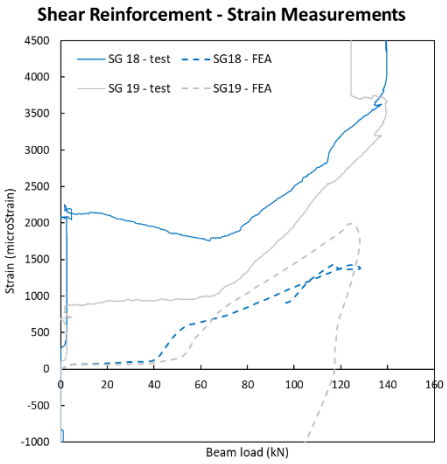

a) Specimen BCJ 9 (2D NLFEA)

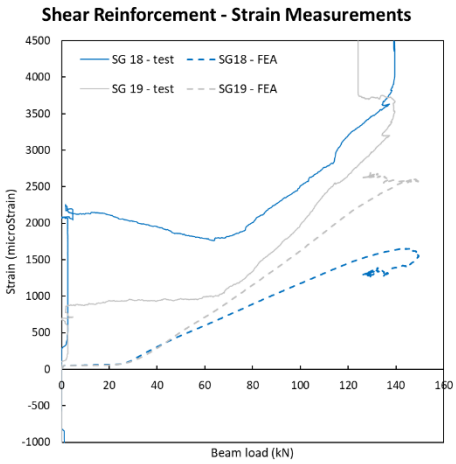

b) Specimen BCJ 9 (3D NLFEA)

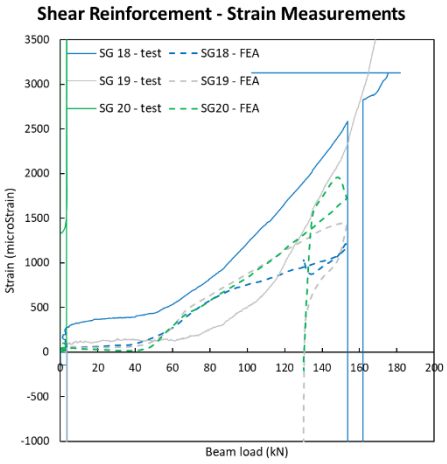

c) Specimen BCJ 10 (2D NLFEA)

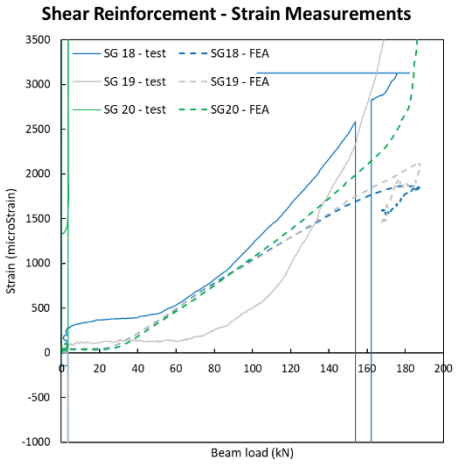

d) Specimen BCJ 10 (3D NLFEA)

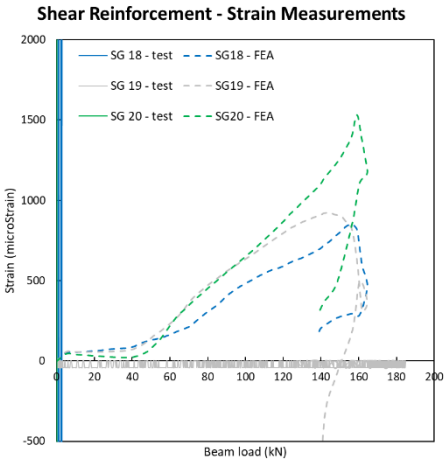

e) Specimen BCJ 12 (2D NLFEA)

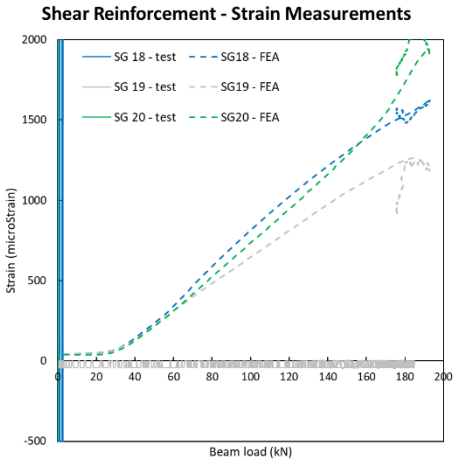

f) Specimen BCJ 12 (3D NLFEA)

Figure 7-12 Measured and predicted strains of series 3; joint stirrups.

7.2.4 Summary of predicted strains with measured strains:

This section provides a brief overview of the comparison of measured and predicted reinforcement strains. The comparison of strains was done for the beam anchorage bars, front/back column bars and joint stirrups. The following conclusions are drawn from the comparison:

- In series 1, measured and predicted strains compared well in beam anchorage bars and front column bars of specimens with L-anchorage bars but less well for specimens with U-anchorage bars. This was the case for both 2D and 3D models. In back column bars, the 2D and 3D models showed compression strains response throughout the entire loading history while the measured strains switched from compression at early stage of loading to tension near failure. All BCJ specimens showed acceptable predicted strains in joint stirrups when compared with measured strains.
- For series 2, with U-bars in BCJ 5, BCJ 7 and BCJ 8, the measured and predicted strains were mainly similar in beam bars. For front/back column bars, the measured and predicted strains compared well in all specimens. Both the 2D and 3D models were capable of simulating the experimentally observed influence of applying high column axial load in BCJ 8. Specimens BCJ 6 and BCJ 8 had functional strain gauges in joint stirrups and the results of predicted and measured strains showed some gaps throughout the loading history of NLFEA and tested specimens. In general, the results of predicted and measured strains in joint stirrups were acceptable.
- In BCJ series 3, the measured and predicted strains compared reasonably well for beam anchorage bars, particularly for gauges in tension. Strain gauges under compression had different curve response in front/back column bars where the switch from compression to tension was not predicted by either the 2D or 3D models. Several strain gauges in joint stirrups were either broken or gave faulty readings in tested specimens making the comparison between the predicted and measured strains incomplete.

7.2.5 Surface strain measurements at joint boundaries and strut

This section describes the comparison of measured and predicted surface strains at joint boundaries and along the diagonal strut. The measured strains were derived from the DIC measurements while the predicted strains were derived from displacements obtained with the 2D NLFEA model. As shown in Figure 7-13, virtual DEMEC vertical gauges were placed above and below joint while horizontal virtual DEMEC gauges were placed over the height of beam-column interface to determine the compression and tension strains in the concrete surface. Six gauges were used above and below the joint and nine gauges were distributed over the beam-column interface. The spacing between gauges was 50 mm for DIC and NLFEA analysis. The spacings between the DEMEC gauges are given in Table 7-1 and Table 7-2. Additionally, diagonal virtual DEMEC gauges were placed inside the joint to calculate the strain in the strut. Two rows of gauges were distributed diagonally along the joint width at an angle oriented parallel to the vectors of minimum principal strain in the joint which were determined using DIC. The angles of the diagonal gauges for all specimens are given in Table 7-3. The first row contains four gauges and the second row consists of five gauges. The positions of these gauges are show in Figure 7-13. A sensitivity analysis was carried out to obtain a suitable gauge length for measuring the strains in the joint. Gauge lengths of 50, 75, and 100 mm were investigated. The results show that the difference between the strains reduces with increasing gauge length. Based on the results, it was decided to use a gauge length of 100 mm. If the gauge crosses a crack, the gauge length was reduced or shifted slightly from its position to avoid the crack as much as possible. The 2D NLFEA used similar scale of gauge length 50, 75 and 100 mm. It was decided to use a gauge length of 100 mm similar to gauge length used in the DIC. An example is shown in Figure 7-14 of the sensitivity analysis carried out for gauge number 4 positioned below joint (at a distance of 150 mm away from beam) using specimen BCJ 1. It can be seen as gauge length increases the measured strains in DIC decreased up to a small difference observed between strains in different gauge lengths, especially near failure load.

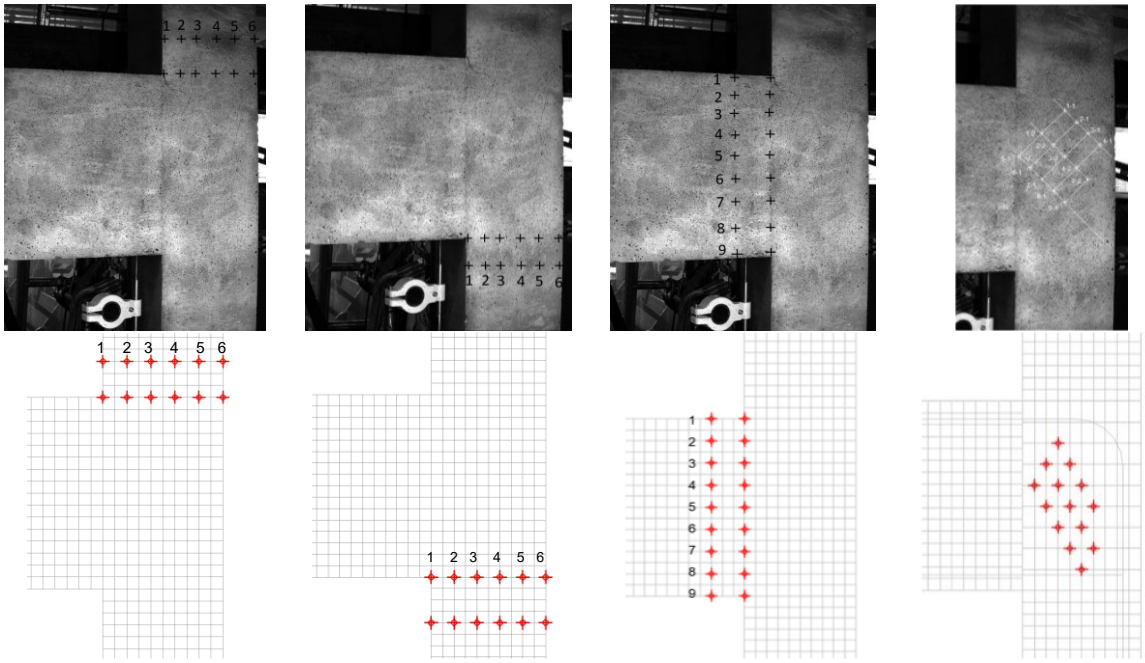

a) Vertical gauges above joint b) Vertical gauges below joint c) Horizontal gauges at beam d) Diagonal gauges inside joint (strut)

Figure 7-13 Virtual DEMC gauges at joint boundaries and in the strut; DIC vs 2D NLFEA.

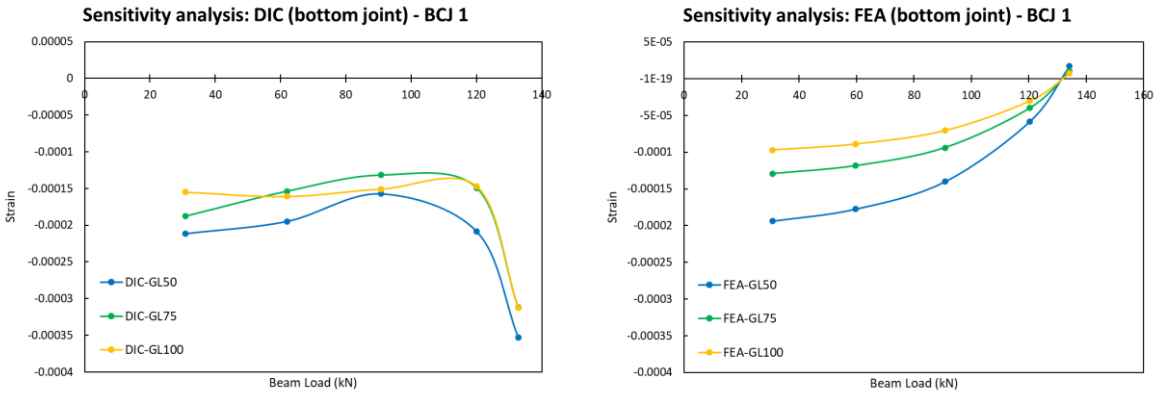

a) Measured strains from DIC b) Predicted strains from NLFEA

Figure 7-14 Sensitivity analysis at gauge 4 for gauge length of 50, 75 and 100 mm; DIC vs 2D NLFEA.

Table 7-1 Spacing between DEMEC gauges above and below the joint; DIC and 2D NLFEA.

	Distance from front column face (mm)					
	G1	**G2**	**G3**	**G4**	**G5**	**G6**
Top joint	0	50	100	150	200	250
Bottom joint	0	50	100	150	200	250

Table 7-2 Spacing between DEMEC gauges at beam-column interface; DIC and 2D NLFEA.

	Distance from bottom joint (mm)								
	G1	**G2**	**G3**	**G4**	**G5**	**G6**	**G7**	**G8**	**G9**
Beam-column interface	0	50	100	150	200	250	300	350	400

Table 7-3 Angle of diagonal gauges; DIC and 2D NLFEA.

Specimen	Gauge angle
BCJ 1	62
BCJ 2	60
BCJ 3	60
BCJ 4	60
BCJ 5	60
BCJ 6	65
BCJ 7	61
BCJ 8	60
BCJ 9	60
BCJ 10	60
BCJ 11	60
BCJ 12	55

7.2.5.1 Results of strains measured at top joint in all BCJ specimens

The strains above the joint were measured using DIC and 2D NLFEA in all specimens. An analysis was carried out to validate the performance of 2D NLFEA compared with DIC results. The results of this comparison are shown in Figure 7-15, Figure 7-16 and Figure 7-17. The front column face begins at 0 mm and back column face ends at 250 mm as shown in the figures. The 2D NLFEA showed almost similar trends in compression and tension strains when compared with the results of DIC. The strains in DIC results near failure load were not shown in gauge number one (located at front column face, 0 mm) for all specimens in series 1 and BCJ 12 due to large values of strains. This may be related to the presence of cracks crossed or close to the gauge. The difference between the location of neutral axis in some specimens was large when compared 2D NLFEA results with DIC results.

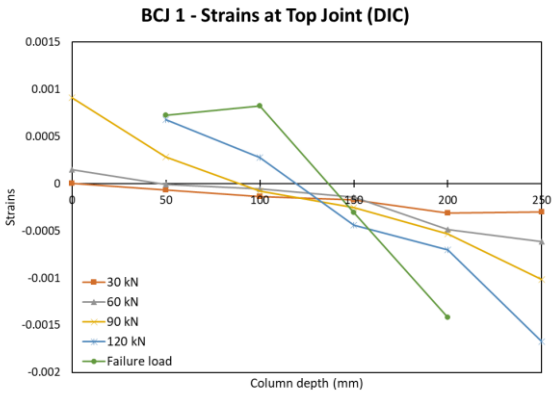

a) Specimen BCJ 1 (DIC)

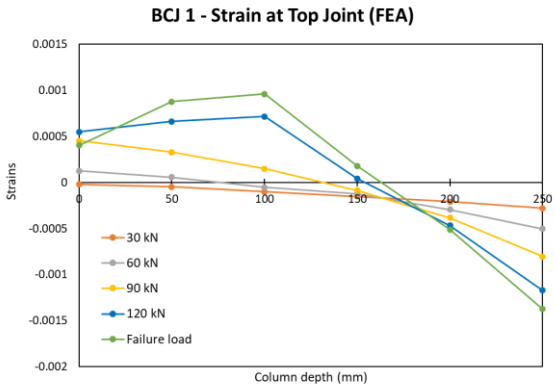

b) Specimen BCJ 1 (2D NLFEA)

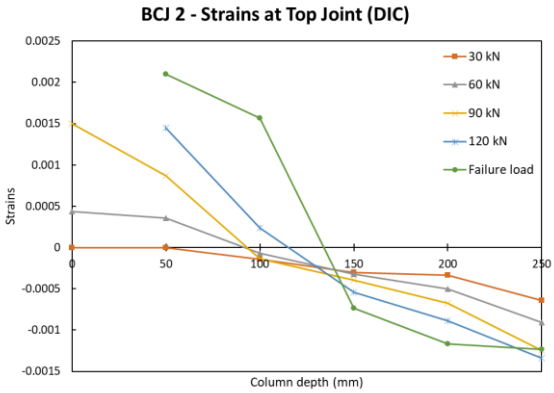

c) Specimen BCJ 2 (DIC)

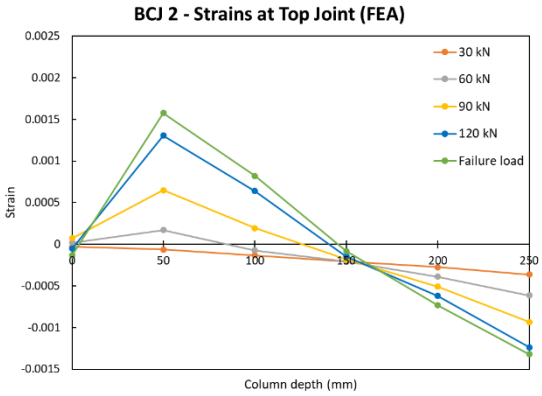

d) Specimen BCJ 2 (2D NLFEA)

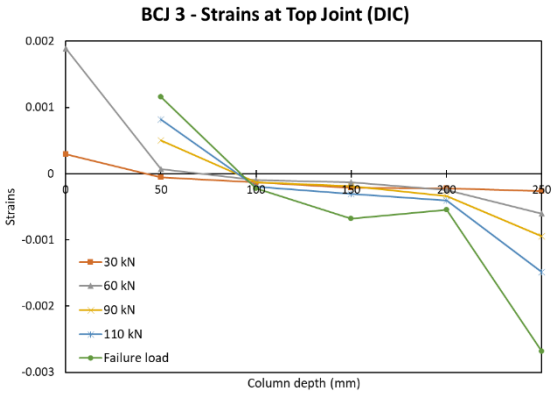

e) Specimen BCJ 3 (DIC)

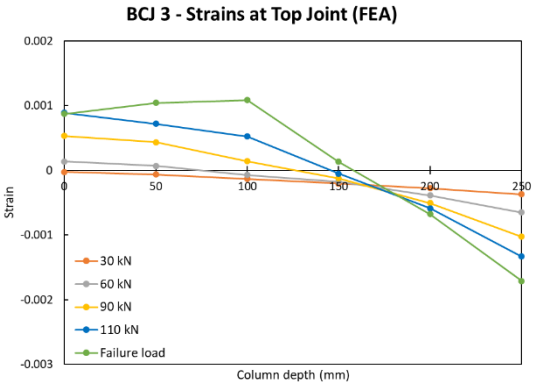

f) Specimen BCJ 3 (2D NLFEA)

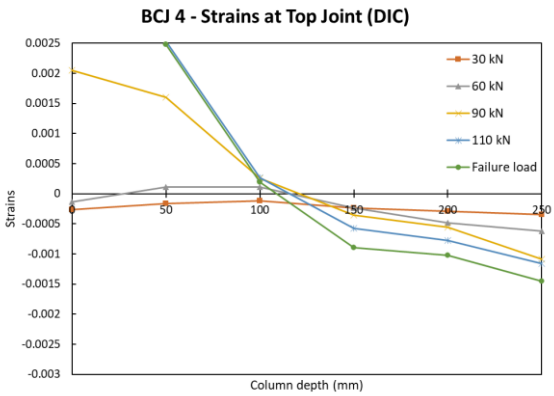

g) Specimen BCJ 4 (DIC)

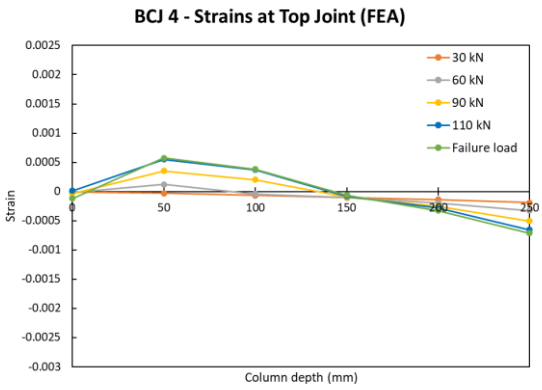

h) Specimen BCJ 4 (2D NLFEA)

Figure 7-15 Strains at top joint for BCJ series 1; DIC vs 2D NLFEA.

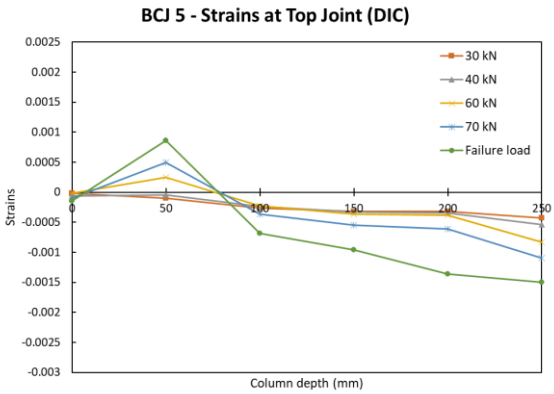

a) Specimen BCJ 5 (DIC)

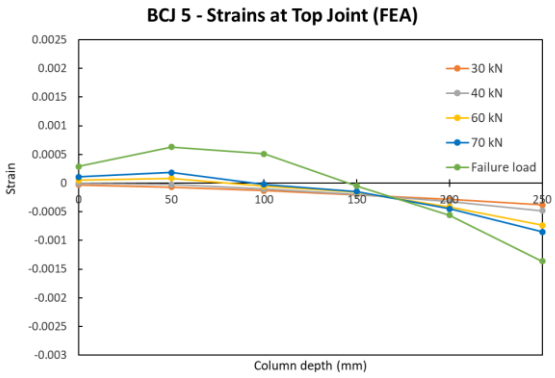

b) Specimen BCJ 5 (2D NLFEA)

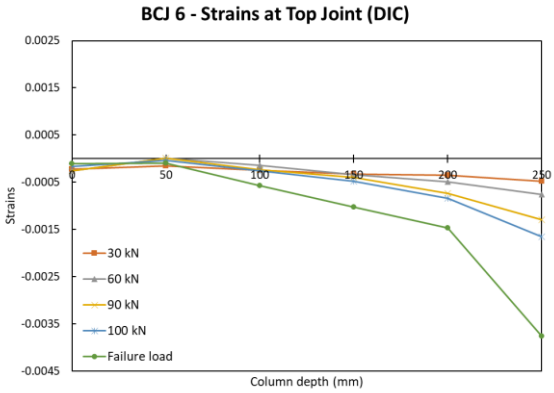

c) Specimen BCJ 6 (DIC)

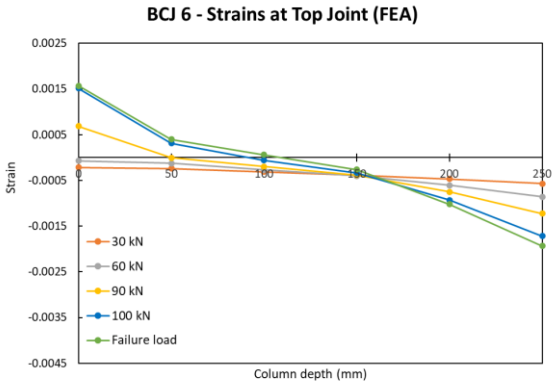

d) Specimen BCJ 6 (2D NLFEA)

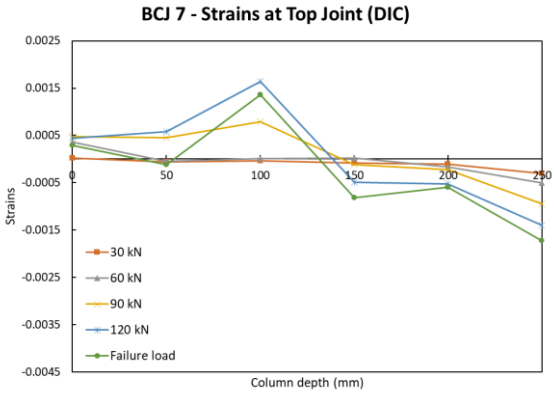

e) Specimen BCJ 7 (DIC)

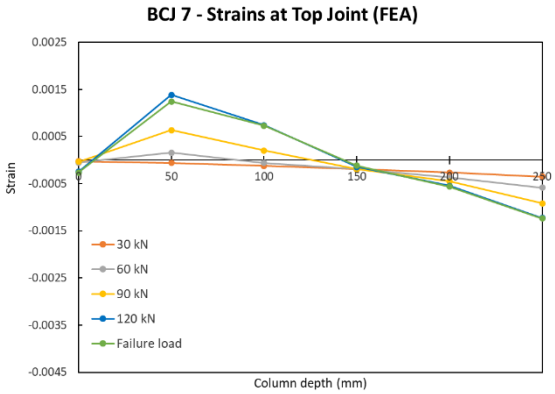

f) Specimen BCJ 7 (2D NLFEA)

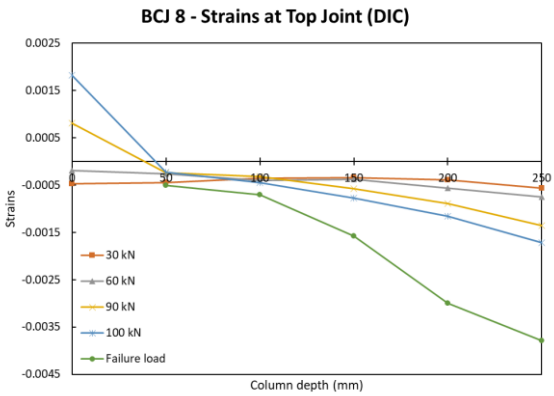

g) Specimen BCJ 8 (DIC)

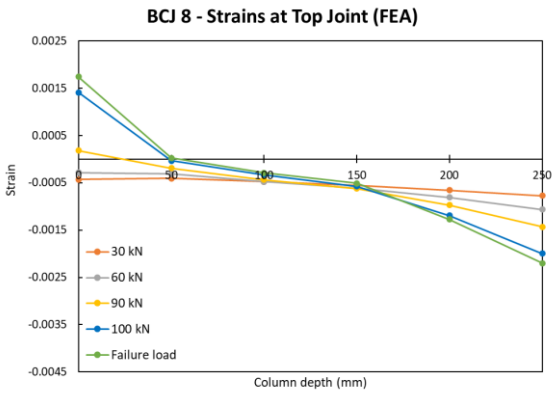

h) Specimen BCJ 8 (2D NLFEA)

Figure 7-16 Strains at top joint for BCJ series 2; DIC vs 2D NLFEA.

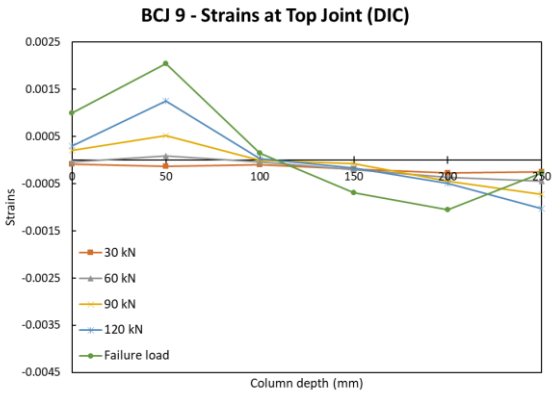

a) Specimen BCJ 9 (DIC)

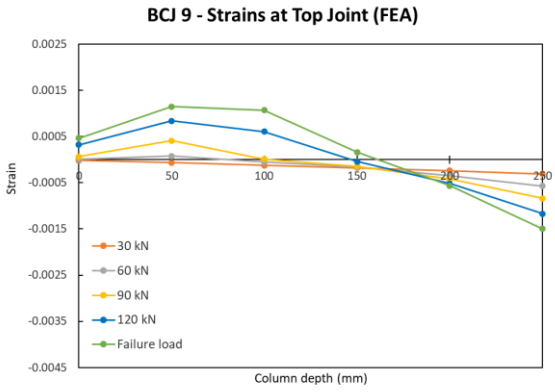

b) Specimen BCJ9 (2D NLFEA)

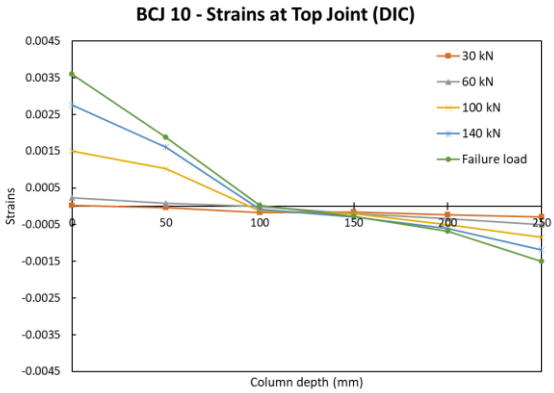

c) Specimen BCJ 10 (DIC)

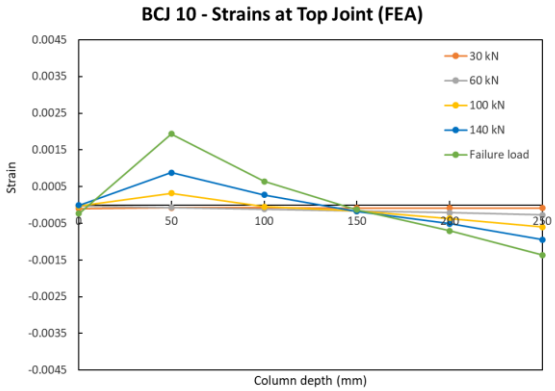

d) Specimen BCJ 10 (2D NLFEA)

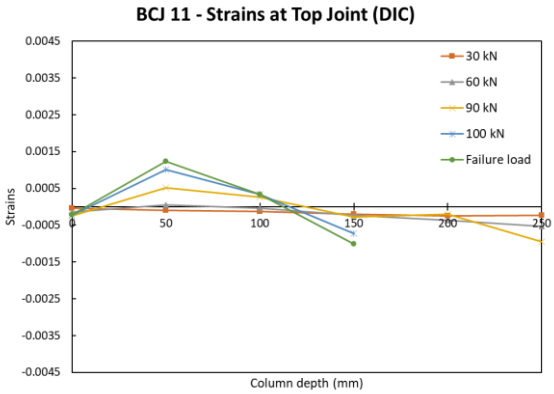

e) Specimen BCJ 11 (DIC)

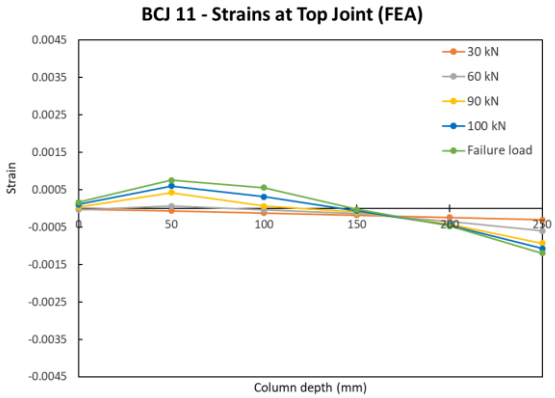

f) Specimen BCJ 11 (2D NLFEA)

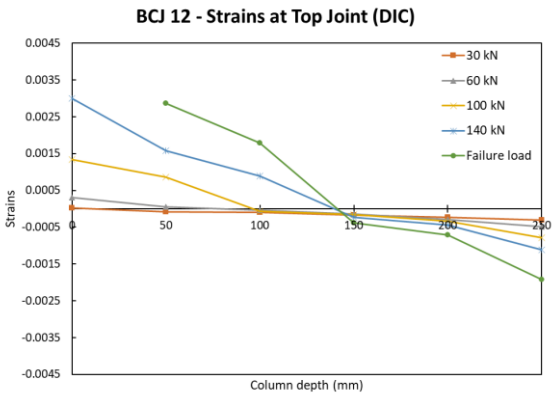

g) Specimen BCJ 12 (DIC)

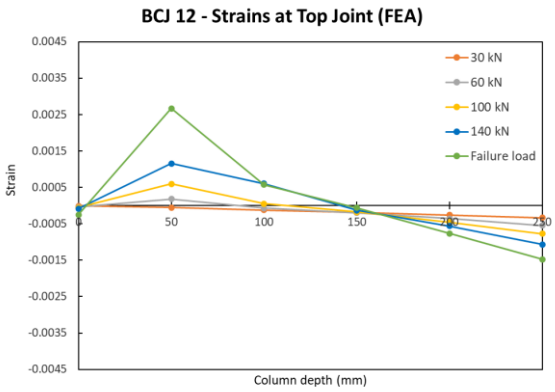

h) Specimen BCJ 12 (2D NLFEA)

Figure 7-17 Strains at top joint for BCJ series 3; DIC vs 2D NLFEA.

7.2.5.2 Results of strains measured at bottom joint in all BCJ specimens

The strains in the column below the joint were obtained with DIC and 2D NLFEA in all specimens. The predicted and measured strains are shown in Figure 7-18, Figure 7-19 and Figure 7-20. The front column face begins at 0 mm and back column face ends at 250 mm as shown in the figures. The predicted results show a curved response very similar to the measured strain response. The accuracy of the predicted strains is better at the bottom than top of the joint in terms of overall curve shape and location of neutral axis. Strains are omitted from the DIC results where very large.

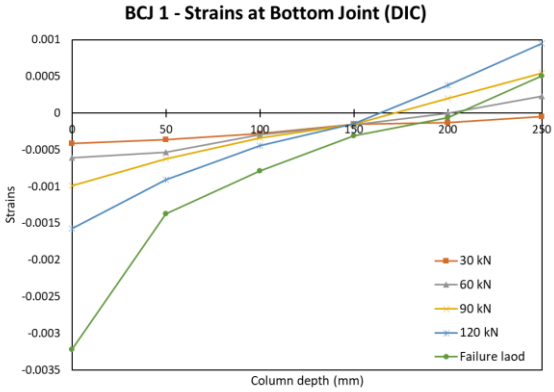

a) Specimen BCJ 1 (DIC)

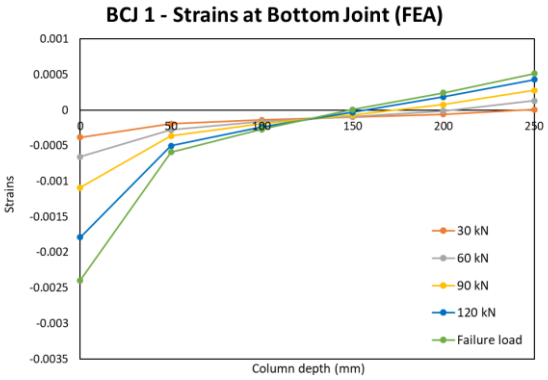

b) Specimen BCJ 1 (2D NLFEA)

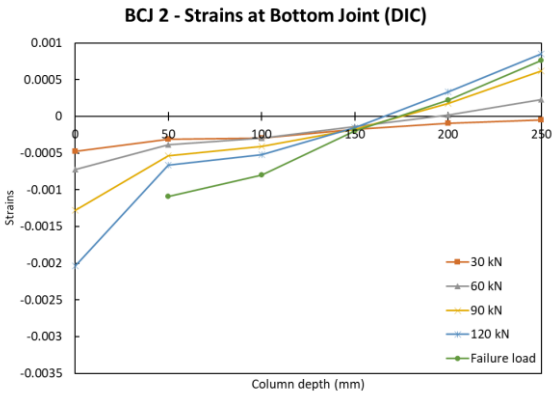

c) Specimen BCJ 2 (DIC)

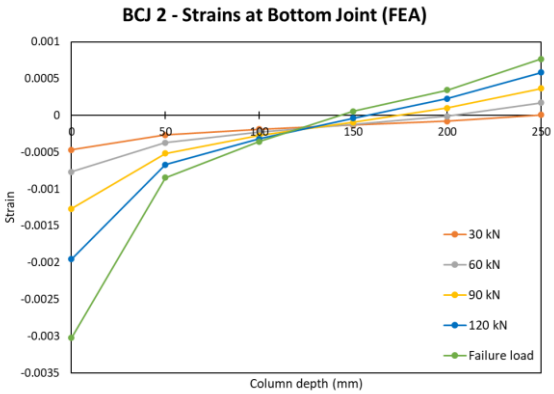

d) Specimen BCJ 2 (2D NLFEA)

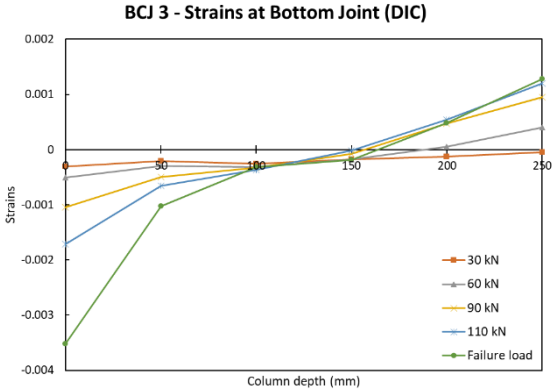

e) Specimen BCJ 3 (DIC)

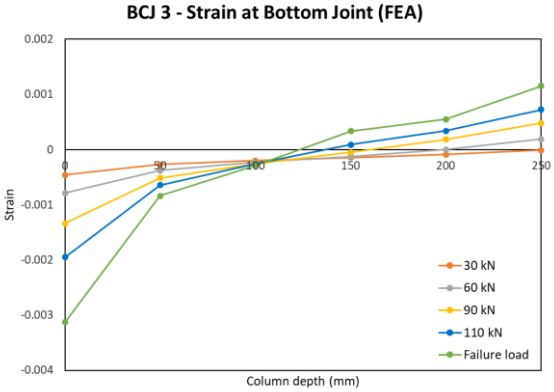

f) Specimen BCJ 3 (2D NLFEA)

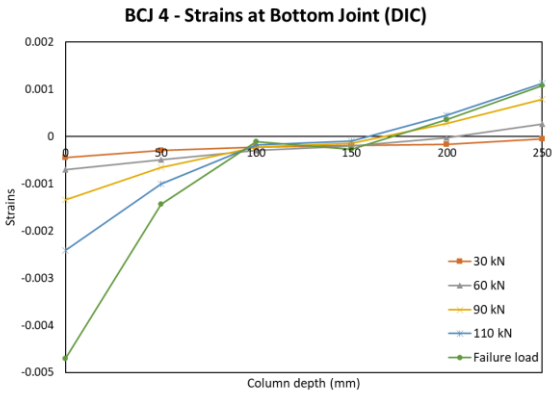

g) Specimen BCJ 4 (DIC)

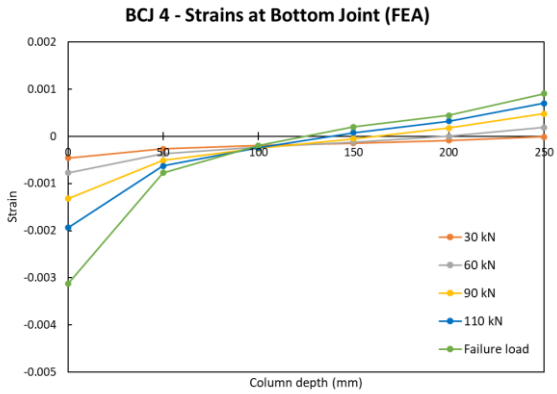

h) Specimen BCJ 4 (2D NLFEA)

Figure 7-18 Strains at bottom joint for BCJ series 1; DIC vs 2D NLFEA.

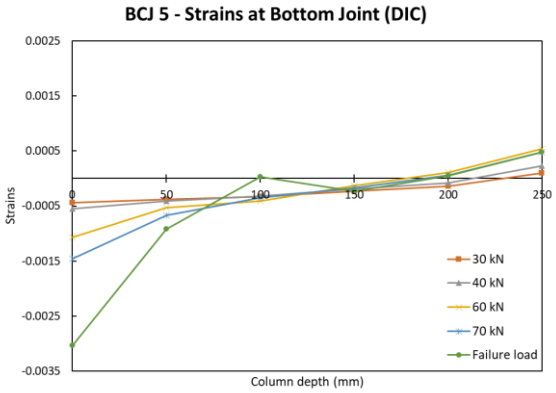

a) Specimen BCJ 5 (DIC)

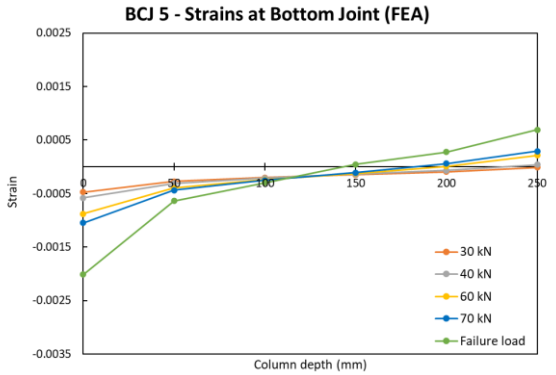

b) Specimen BCJ 5 (2D NLFEA)

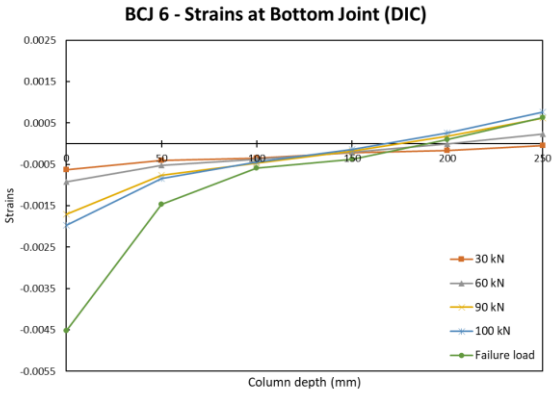

c) Specimen BCJ 6 (DIC)

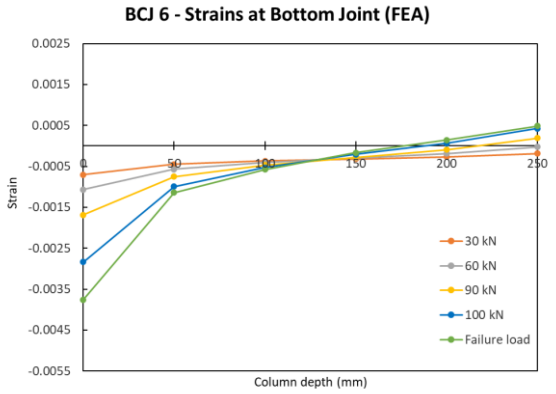

d) Specimen BCJ 6 (2D NLFEA)

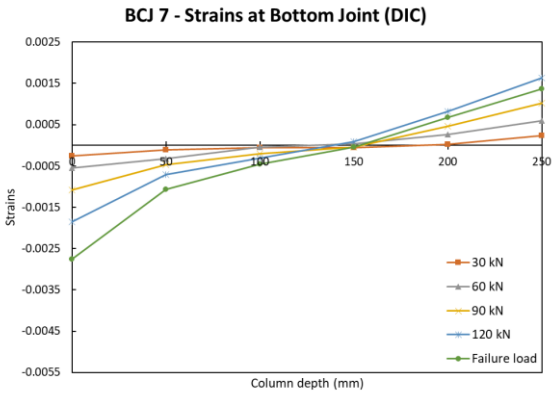

e) Specimen BCJ 7 (DIC)

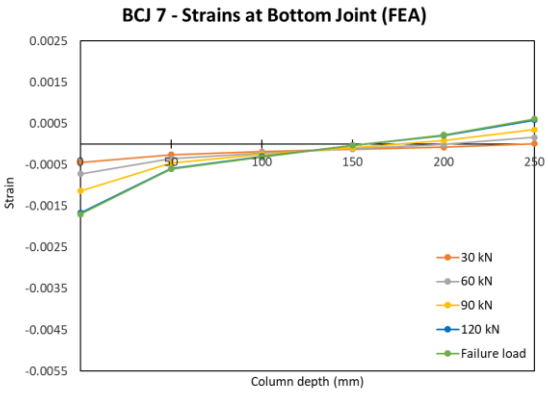

f) Specimen BCJ 7 (2D NLFEA)

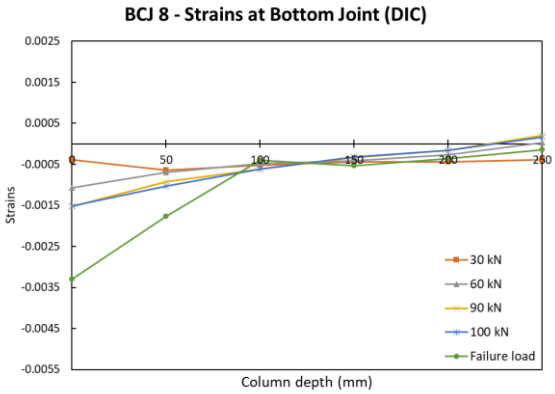

g) Specimen BCJ 8 (DIC)

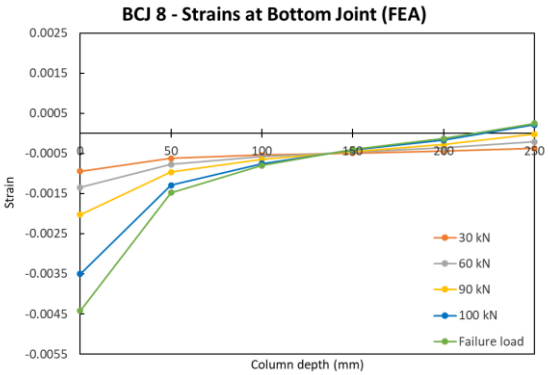

h) Specimen BCJ 8 (2D NLFEA)

Figure 7-19 Strains at bottom joint for BCJ series 2; DIC vs 2D NLFEA.

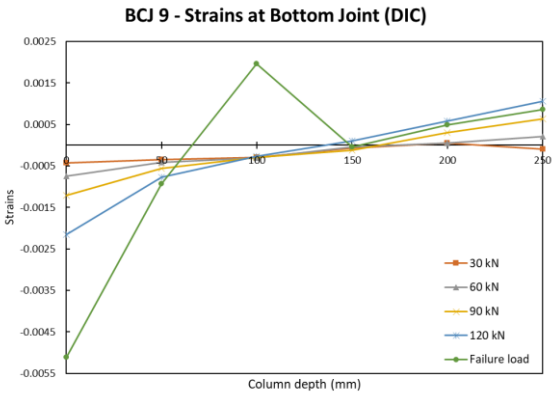

a) Specimen BCJ 9 (DIC)

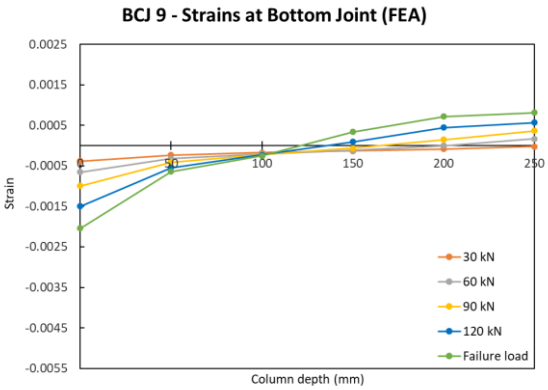

b) Specimen BCJ9 (2D NLFEA)

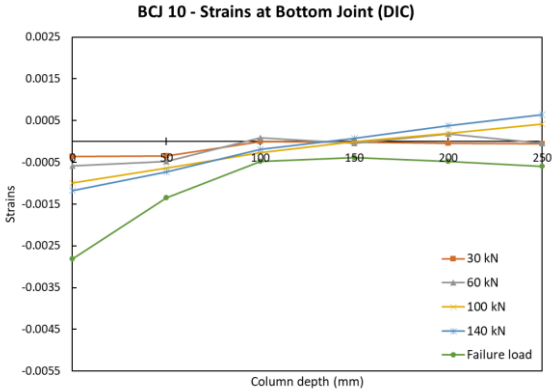

c) Specimen BCJ 10 (DIC)

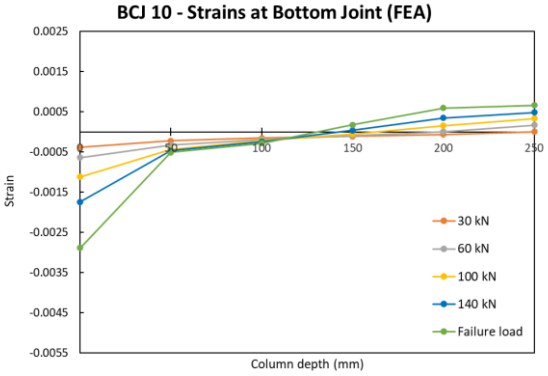

d) Specimen BCJ 10 (2D NLFEA)

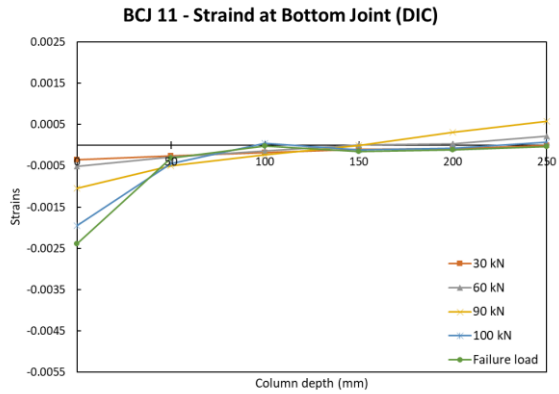

e) Specimen BCJ 11 (DIC)

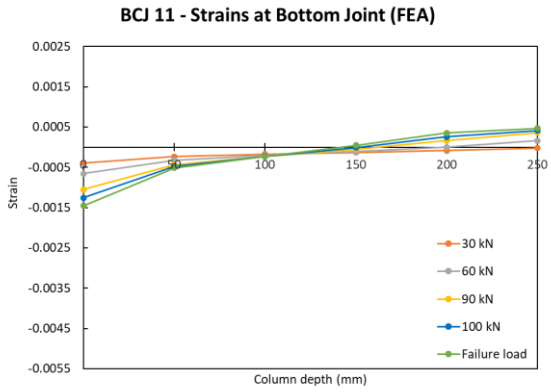

f) Specimen BCJ 11 (2D NLFEA)

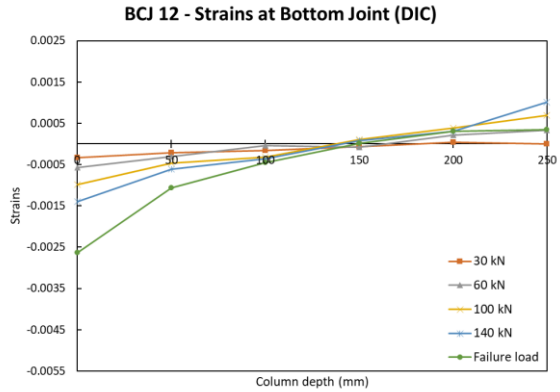

g) Specimen BCJ 12 (DIC)

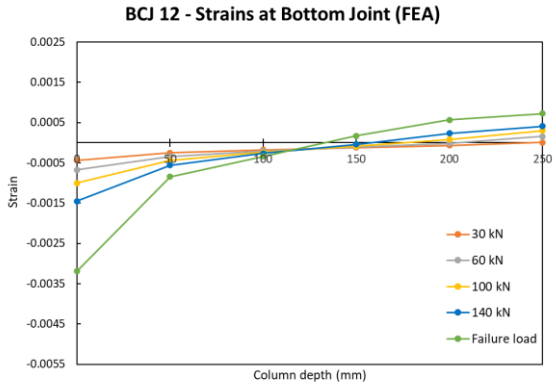

h) Specimen BCJ 12 (2D NLFEA)

Figure 7-20 Strains at bottom joint for BCJ series 3; DIC vs 2D NLFEA.

7.2.5.3 Results of strains measured at beam-column interface in all BCJ specimens

The DIC and 2D NLFEA strains were compared at the beam-column interface in all specimens. The results of this comparison are shown in Figure 7-21, Figure 7-22 and Figure 7-23. In the figures, the beam depth extends from 0 mm (bottom of joint) to 400 mm (top of joint). The DIC strains in the tension zone are smaller than expected from the assumption that plane sections remain plane. This is a consequence of cracking outside the gauge length within the joint adjacent to the beam-column interface. The predicted neutral axis position compares well with the experimentally derived position.

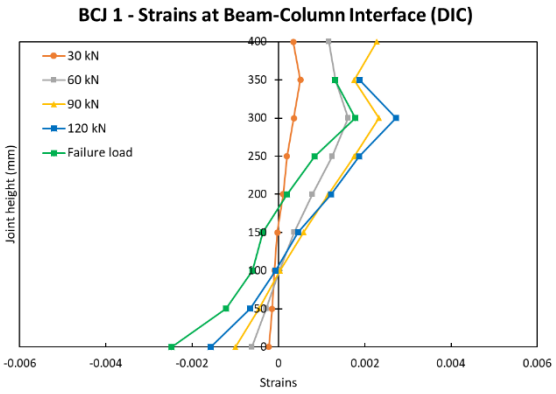

a) Specimen BCJ 1 (DIC)

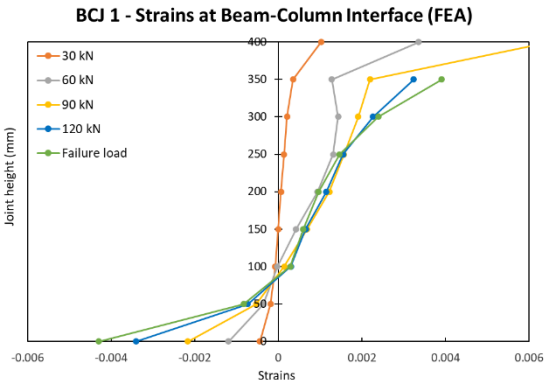

b) Specimen BCJ 1 (2D NLFEA)

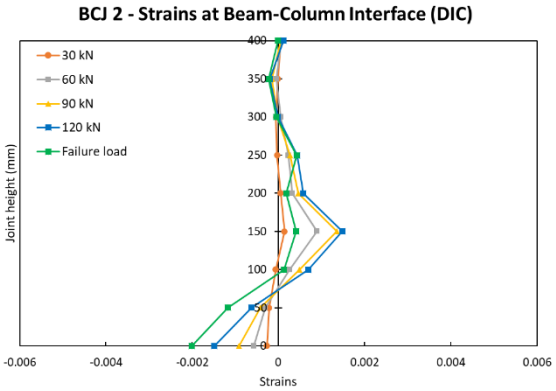

c) Specimen BCJ 2 (DIC)

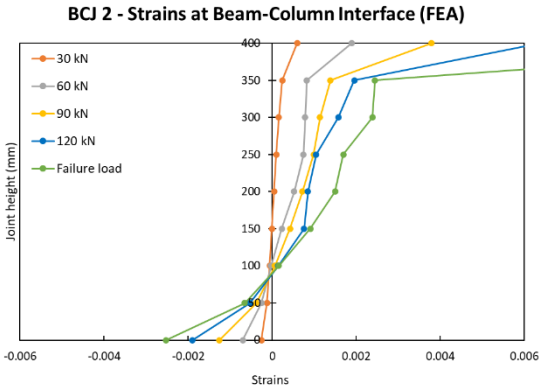

d) Specimen BCJ 2 (2D NLFEA)

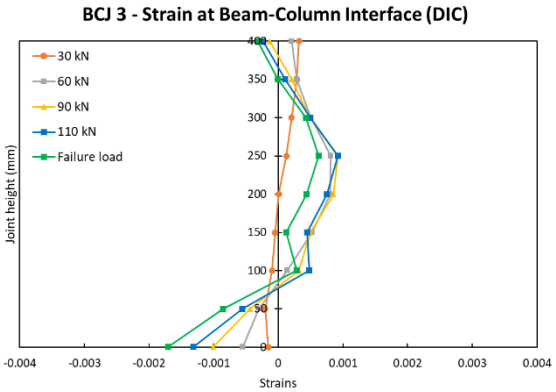

e) Specimen BCJ 3 (DIC)

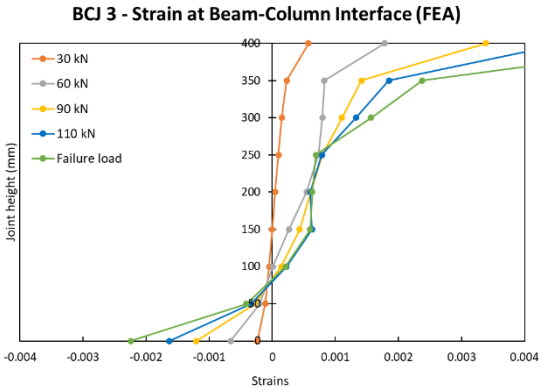

f) Specimen BCJ 3 (2D NLFEA)

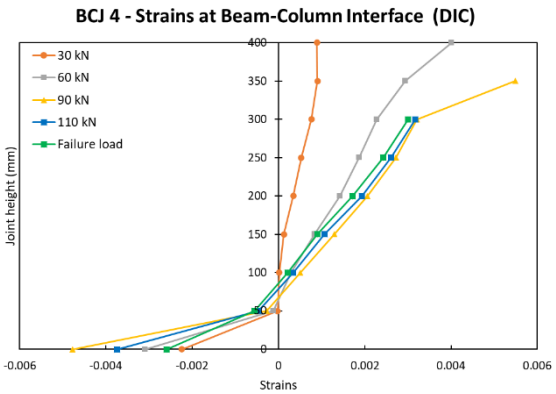

g) Specimen BCJ 4 (DIC)

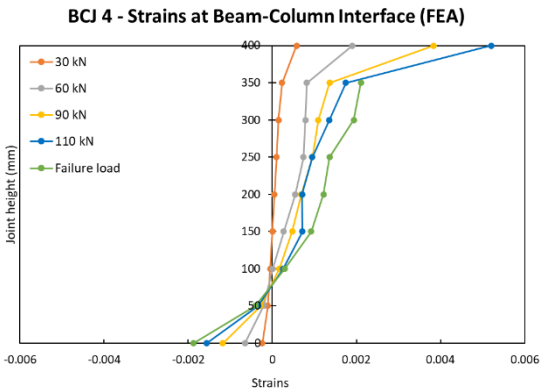

h) Specimen BCJ 4 (2D NLFEA)

Figure 7-21 Strains at beam-column interface for BCJ series 1; DIC vs 2D NLFEA.

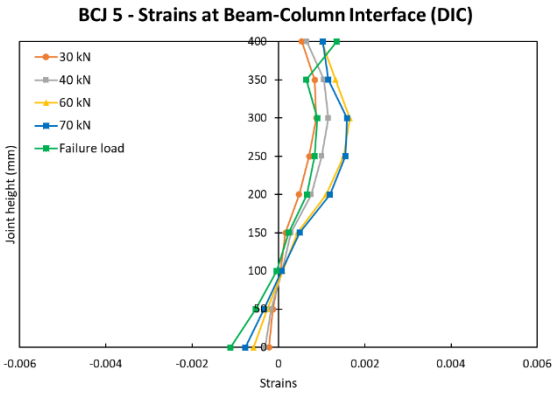

a) Specimen BCJ 5 (DIC)

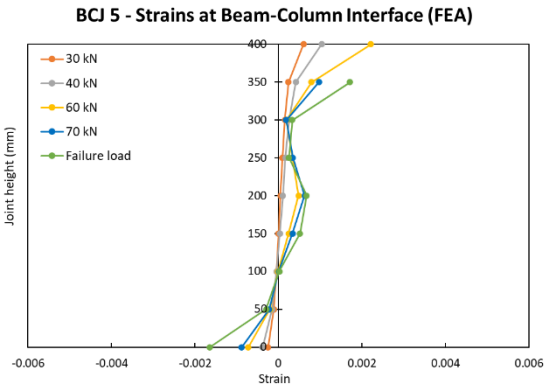

b) Specimen BCJ 5 (2D NLFEA)

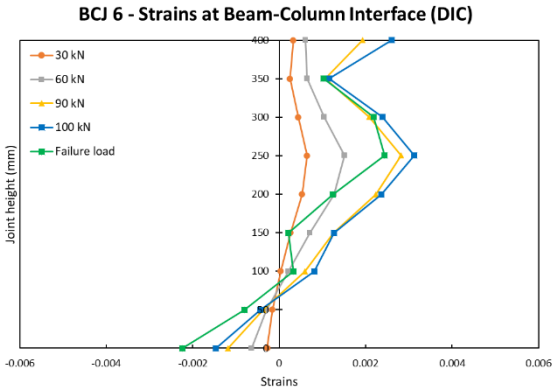

c) Specimen BCJ 6 (DIC)

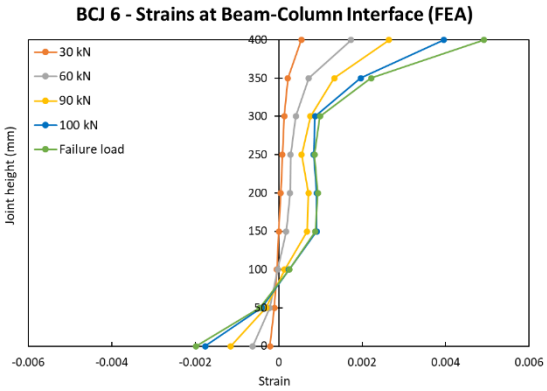

d) Specimen BCJ 6 (2D NLFEA)

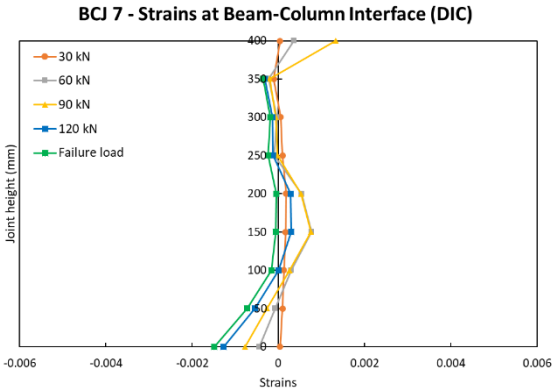

e) Specimen BCJ 7 (DIC)

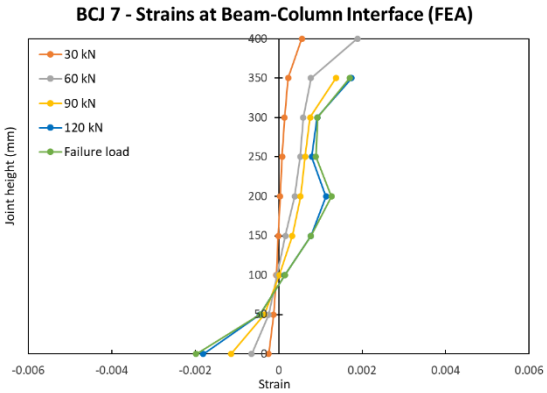

f) Specimen BCJ 7 (2D NLFEA)

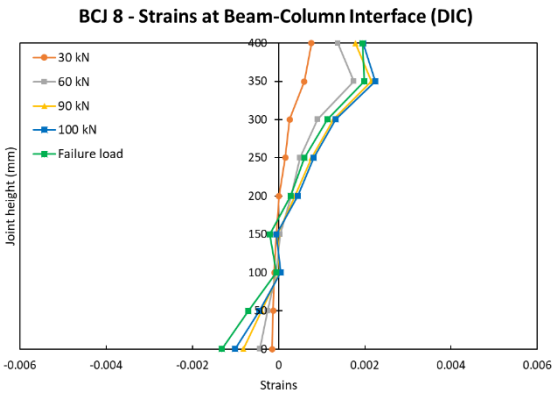

g) Specimen BCJ 8 (DIC)

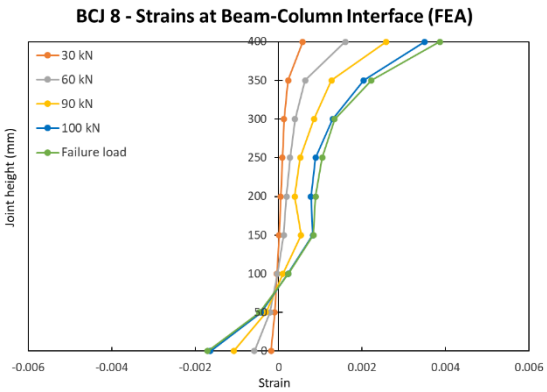

h) Specimen BCJ 8 (2D NLFEA)

Figure 7-22 Strains at beam-column interface for BCJ series 2; DIC vs 2D NLFEA.

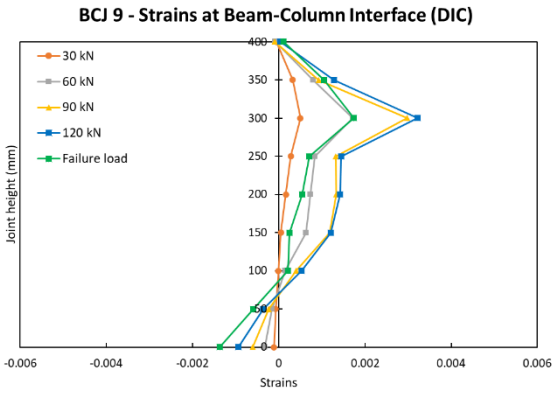

a) Specimen BCJ 9 (DIC)

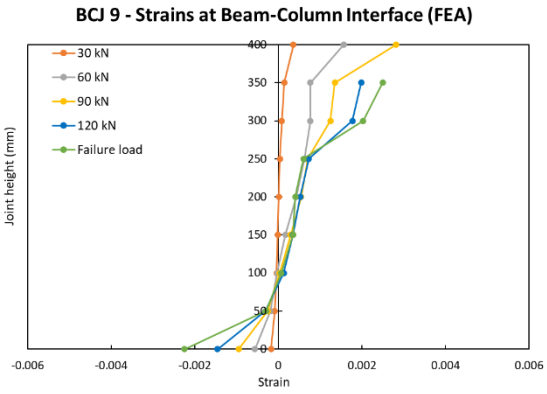

b) Specimen BCJ9 (2D NLFEA)

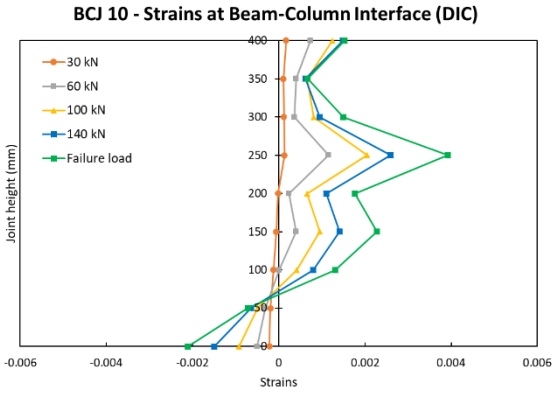

c) Specimen BCJ 10 (DIC)

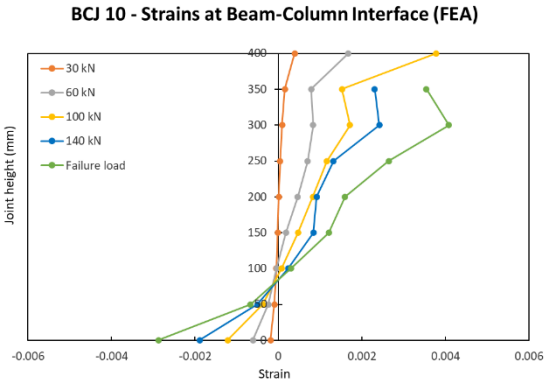

d) Specimen BCJ 10 (2D NLFEA)

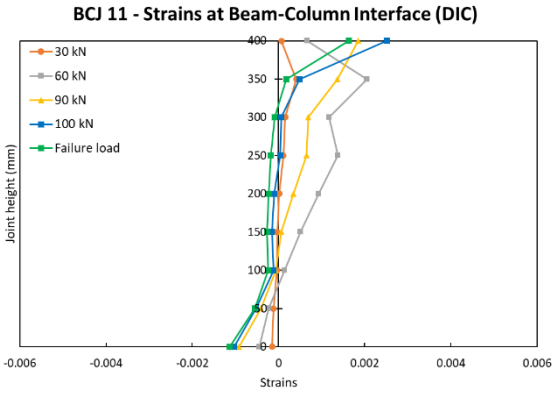

e) Specimen BCJ 11 (DIC)

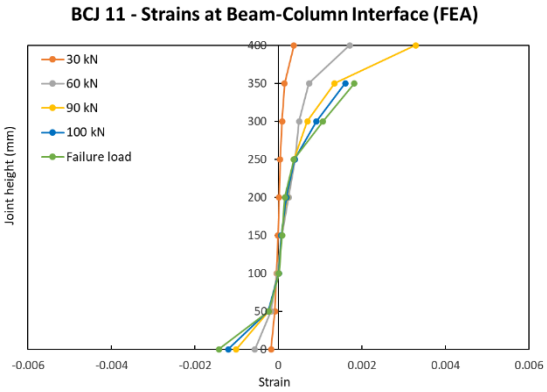

f) Specimen BCJ 11 (2D NLFEA)

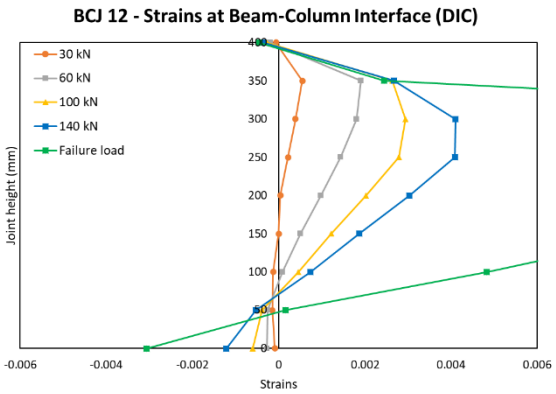

g) Specimen BCJ 12 (DIC)

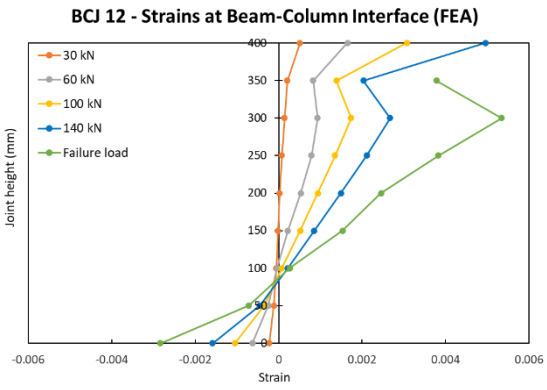

h) Specimen BCJ 12 (2D NLFEA)

Figure 7-23 Strains at beam-column interface for BCJ series 3; DIC vs 2D NLFEA.

7.2.5.4 Results of strains measured in joint strut

Axial strains in the diagonal strut were studied between two parallel two rows of DEMEC gauges positioned inside the joint. Strains obtained using DIC and 2D NLFEA were compared. The DEMEC gauges were positioned between the bend in the beam tension bars and the beam compression bars. The top and bottom rows of gauges are depicted first and second in the figures below as shown in Figure 7-24. The first row consists of four gauges while the second row had five gauges. The results of this investigation are presented below.

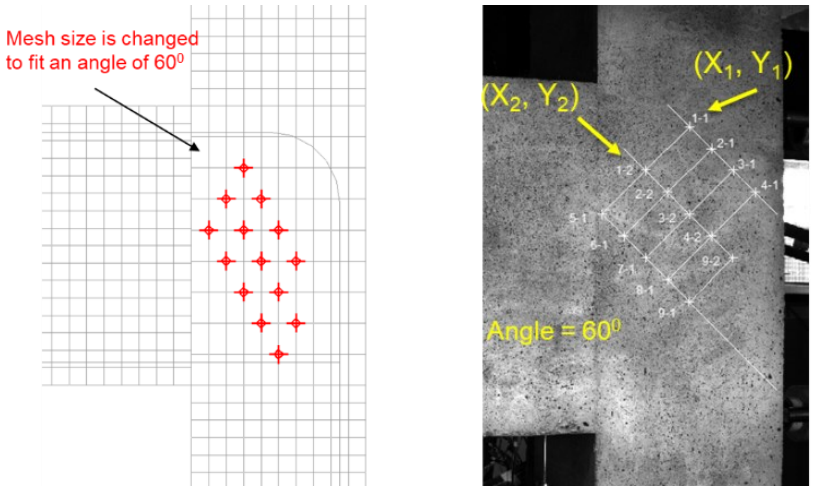

a) Diagonal gauges for NLFEA b) Diagonal gauges for DIC

Figure 7-24 Diagonal gauges position in joint; DIC and 2D NLFEA.

7.2.5.4.1 Strains in the strut for first row

Strains in the first row of diagonal gauges are shown in Figure 7-25, Figure 7-26 and Figure 7-27. Overall, the comparison of strains is good apart from at the extreme left point (point: 1-2) in Figure 7-24 where tensile strains were measured in most specimens but compression is predicted. The tensile strain may be due to positioning the DEMEC gauge near to the beam tension bar or the presence of a crack passing through the gauge. The tested specimens showed many diagonal cracks in joint as described in chapter 4. The predicted strains resulted in maximum compression strain value almost similar to the measured strains in most specimens.

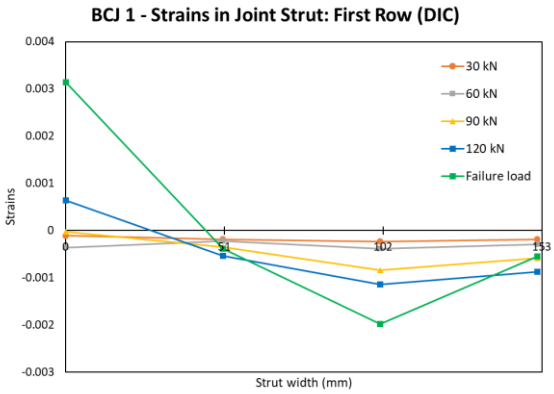

a) Specimen BCJ 1 (DIC)

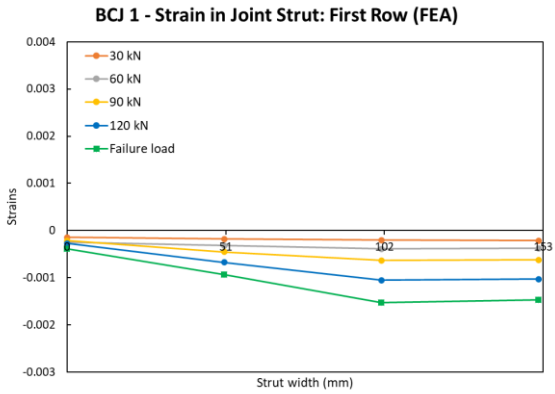

b) Specimen BCJ 1 (2D NLFEA)

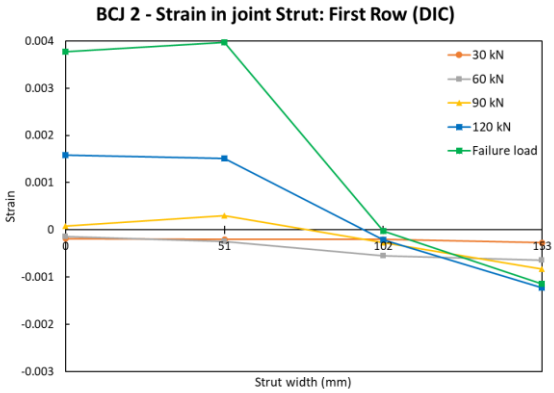

c) Specimen BCJ 2 (DIC)

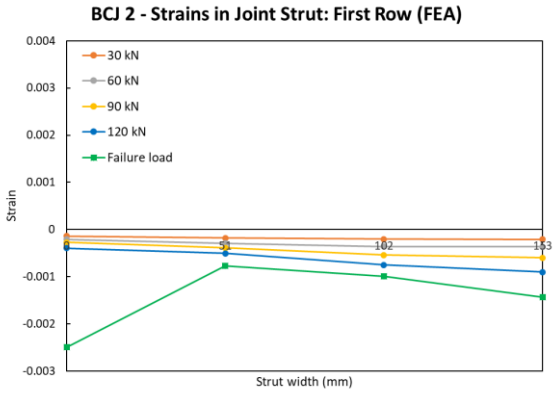

d) Specimen BCJ 2 (2D NLFEA)

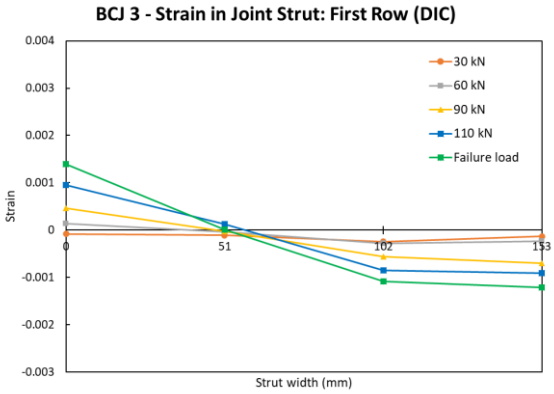

e) Specimen BCJ 3 (DIC)

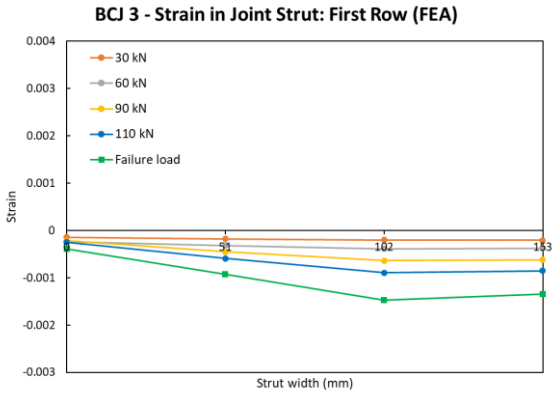

f) Specimen BCJ 3 (2D NLFEA)

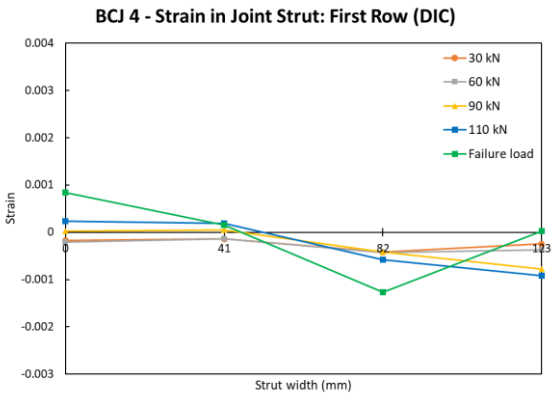

g) Specimen BCJ 4 (DIC)

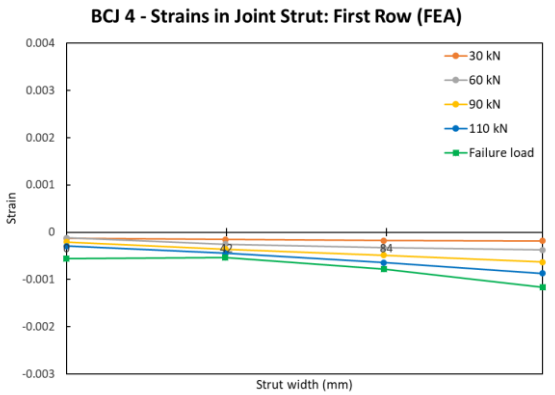

h) Specimen BCJ 4 (2D NLFEA)

Figure 7-25 Strains in first row of diagonal gauges for BCJ series 1; DIC vs 2D NLFEA.

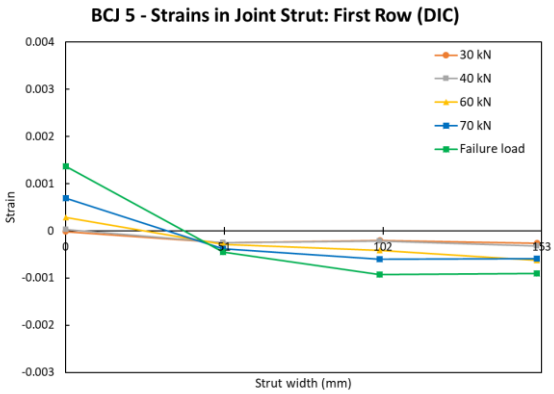

a) Specimen BCJ 5 (DIC)

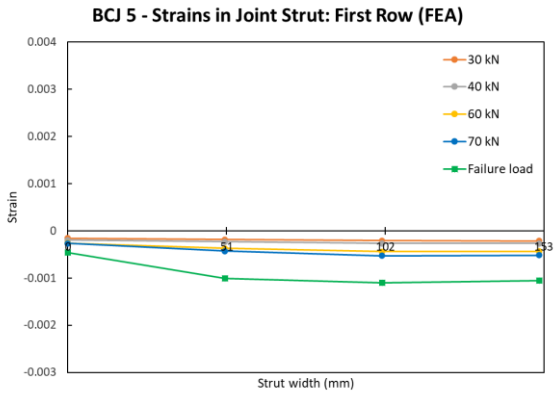

b) Specimen BCJ 5 (2D NLFEA)

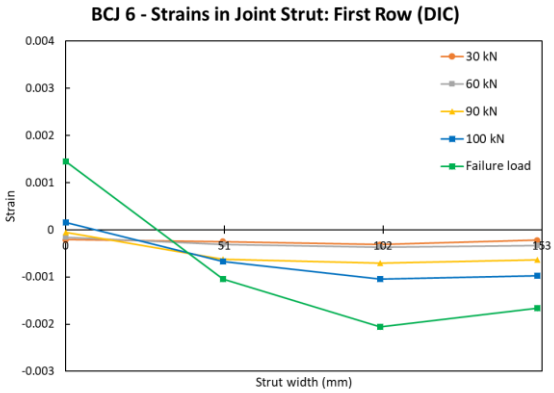

c) Specimen BCJ 6 (DIC)

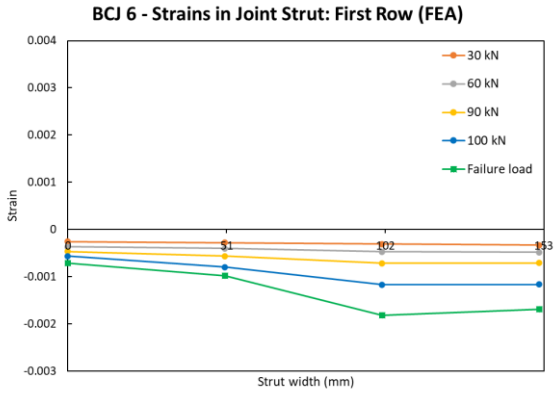

d) Specimen BCJ 6 (2D NLFEA)

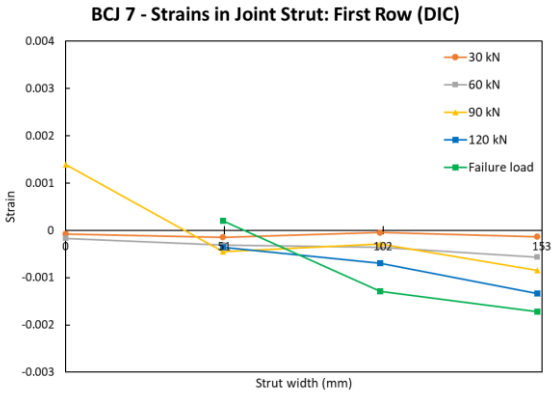

e) Specimen BCJ 7 (DIC)

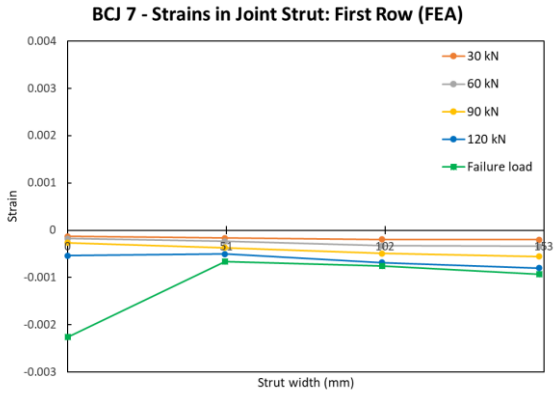

f) Specimen BCJ 7 (2D NLFEA)

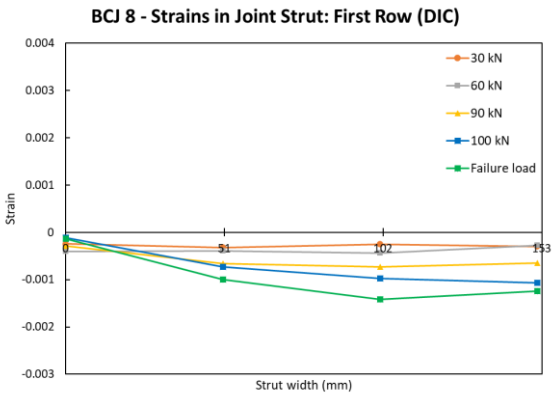

g) Specimen BCJ 8 (DIC)

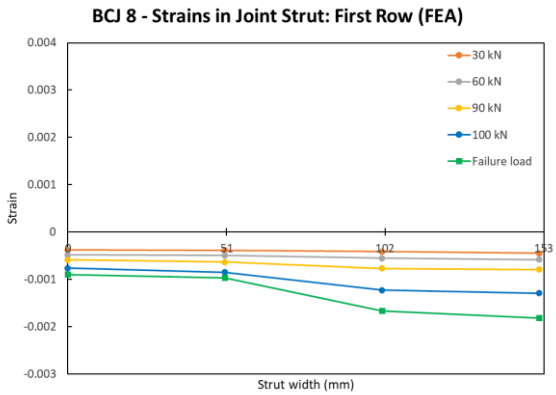

h) Specimen BCJ 8 (2D NLFEA)

Figure 7-26 Strains in first row of diagonal gauges for BCJ series 2; DIC vs 2D NLFEA.

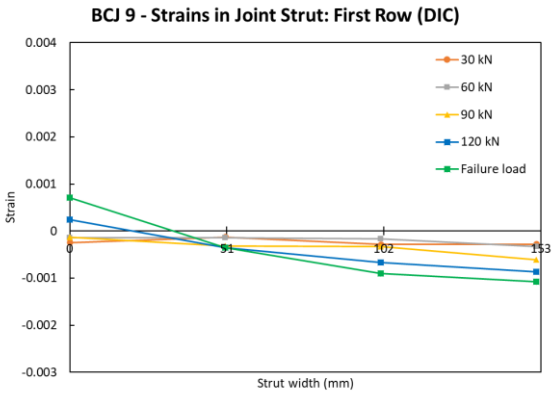

a) Specimen BCJ 9 (DIC)

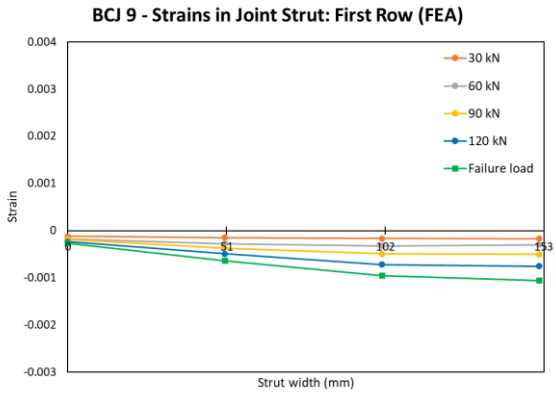

b) Specimen BCJ9 (2D NLFEA)

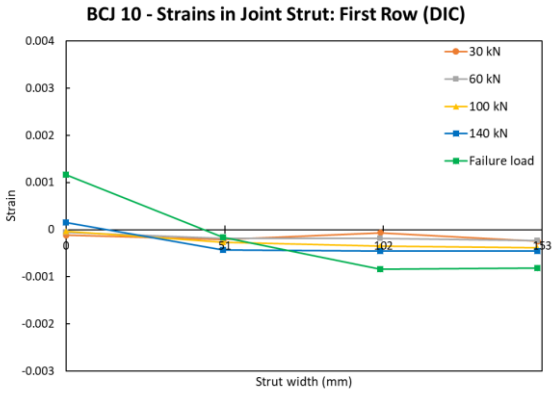

c) Specimen BCJ 10 (DIC)

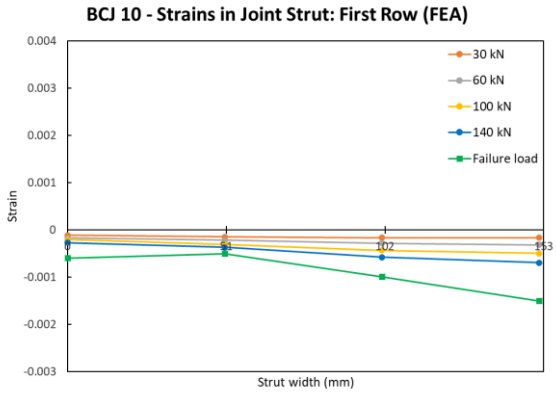

d) Specimen BCJ 10 (2D NLFEA)

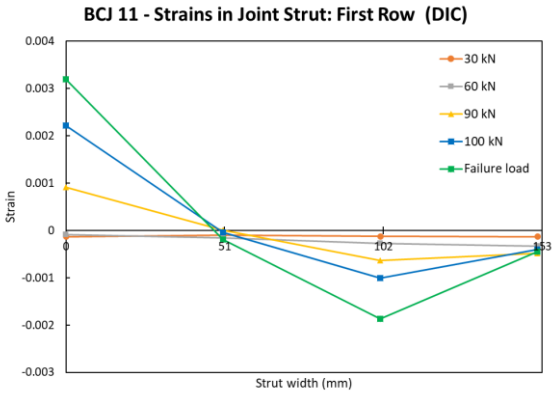

e) Specimen BCJ 11 (DIC)

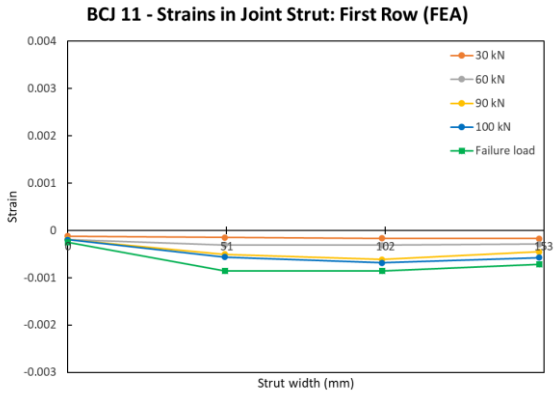

f) Specimen BCJ 11 (2D NLFEA)

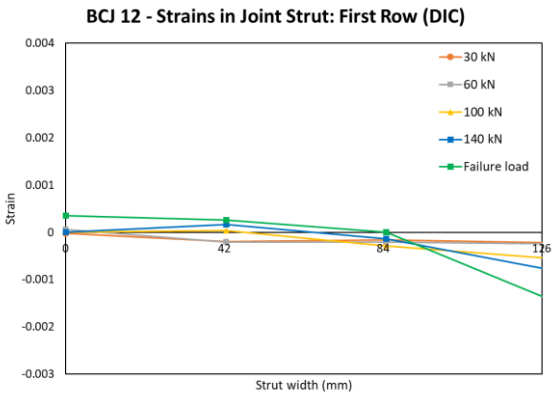

g) Specimen BCJ 12 (DIC)

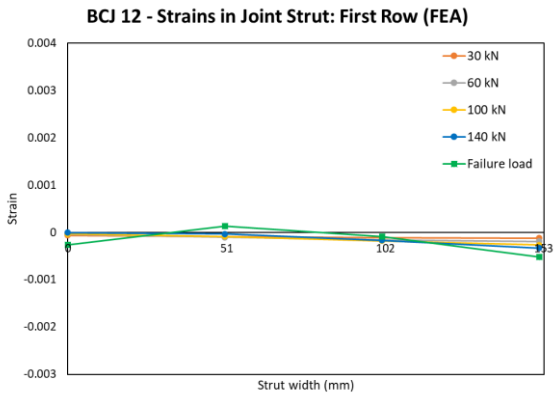

h) Specimen BCJ 12 (2D NLFEA)

Figure 7-27 Strains in first row of diagonal gauges for BCJ series 3; DIC vs 2D NLFEA.

7.2.5.4.2 Strains in the strut for second row

The strains in the second row of diagonal gauges are shown in Figure 7-28, Figure 7-29 and Figure 7-30. Both the predicted and measured strains are larger than in the first row. The DIC strains are tensile at the extreme left gauge (point: 1-2 in Figure 7-24) in seven of the twelve specimens while the corresponding measured strains are compressive. The measured tensile strains appear to have arisen due to diagonal cracks crossing the gauge. The maximum measured and predicted compressive strains are similar as for the first row.

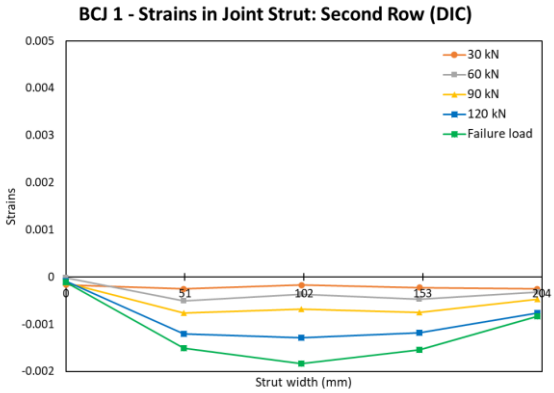

a) Specimen BCJ 1 (DIC)

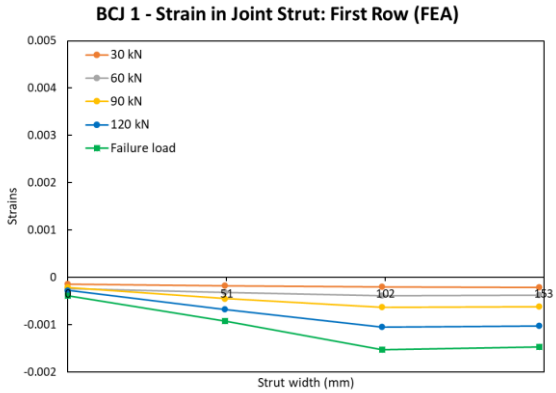

b) Specimen BCJ 1 (2D NLFEA)

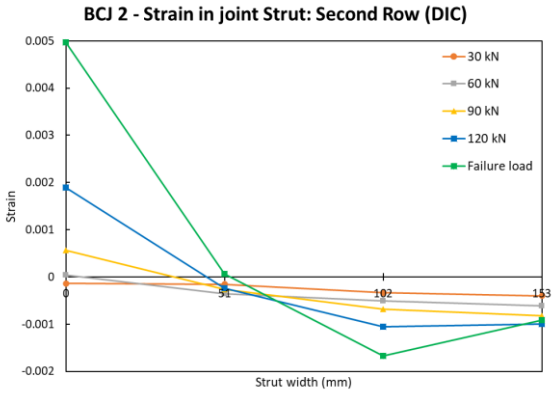

c) Specimen BCJ 2 (DIC)

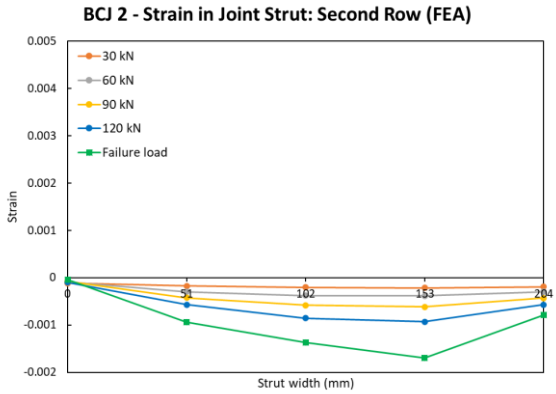

d) Specimen BCJ 2 (2D NLFEA)

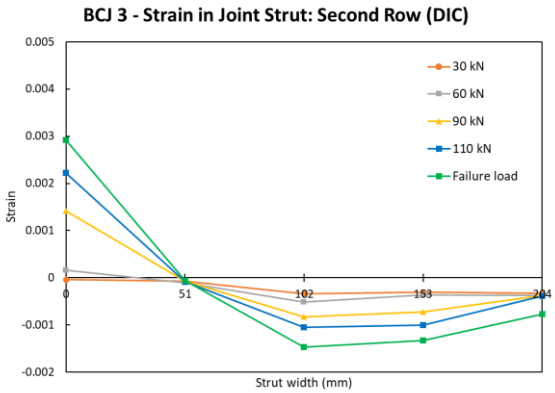

e) Specimen BCJ 3 (DIC)

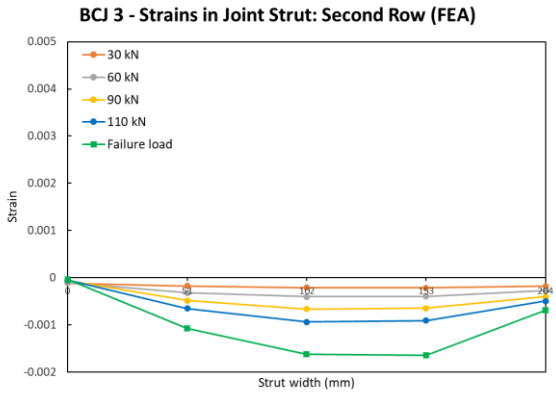

f) Specimen BCJ 3 (2D NLFEA)

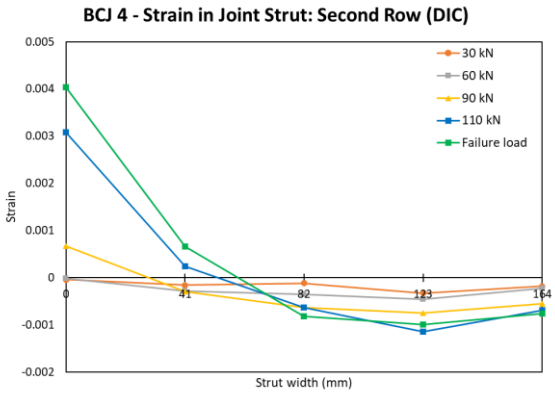

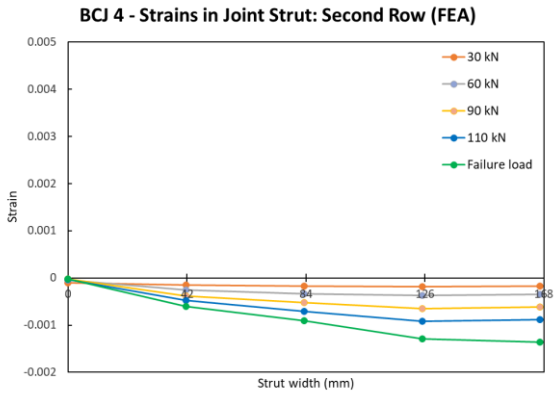

g) Specimen BCJ 4 (DIC) h) Specimen BCJ 4 (2D NLFEA)

Figure 7-28 Strains in second row of diagonal gauges for BCJ series 1; DIC vs 2D NLFEA.

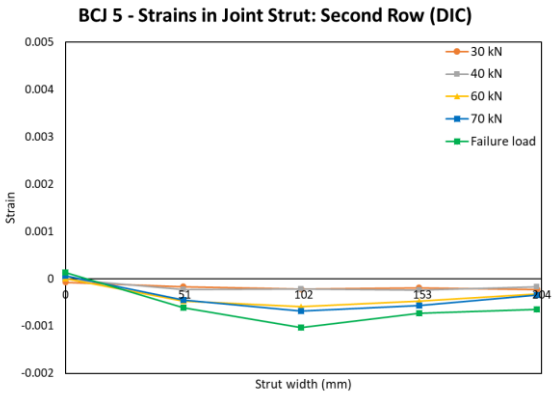

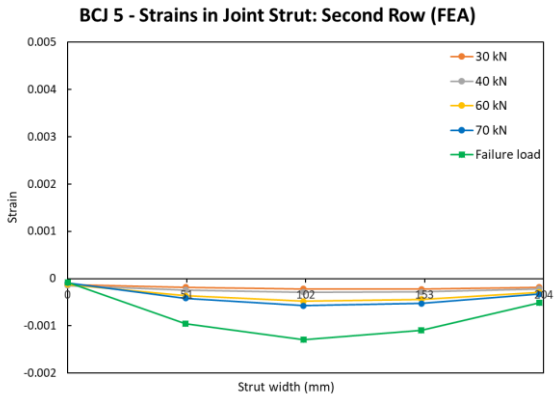

a) Specimen BCJ 5 (DIC) b) Specimen BCJ 5 (2D NLFEA)

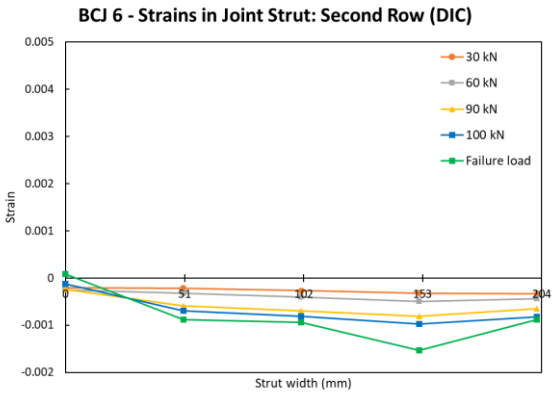

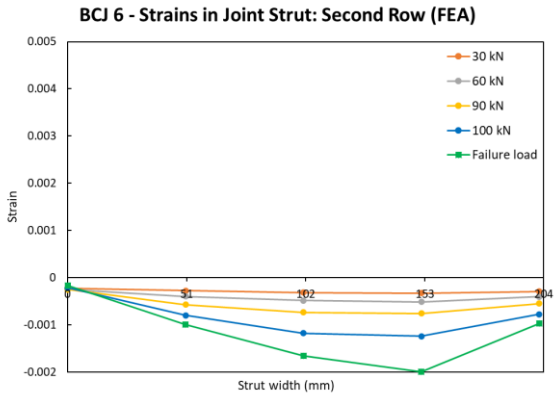

c) Specimen BCJ 6 (DIC) d) Specimen BCJ 6 (2D NLFEA)

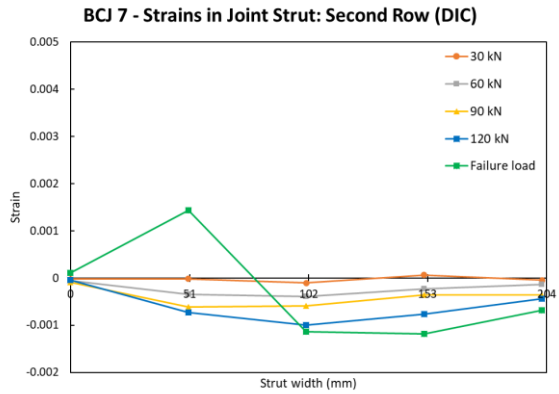

e) Specimen BCJ 7 (DIC)

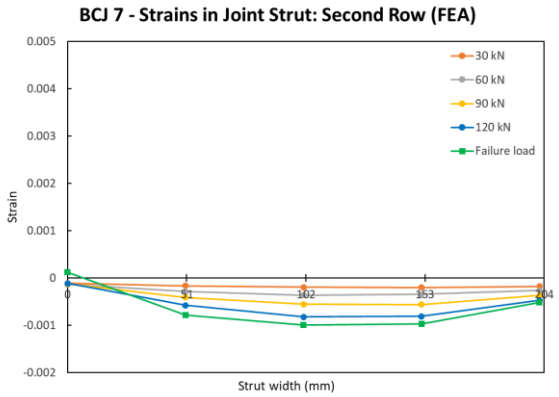

f) Specimen BCJ 7 (2D NLFEA)

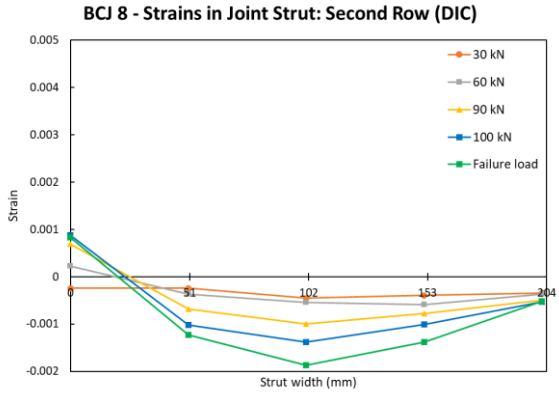

g) Specimen BCJ 8 (DIC)

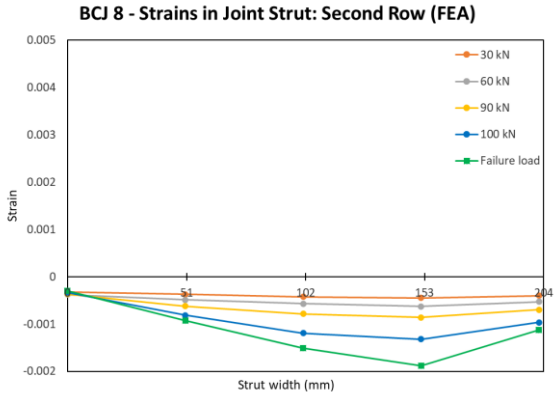

h) Specimen BCJ 8 (2D NLFEA)

Figure 7-29 Strains in second row of diagonal gauges for BCJ series 2; DIC vs 2D NLFEA.

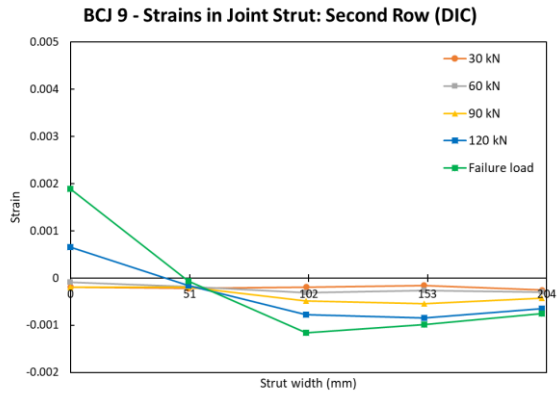

a) Specimen BCJ 9 (DIC)

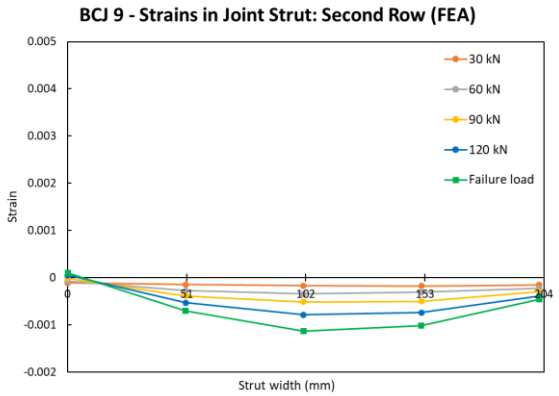

b) Specimen BCJ9 (2D NLFEA)

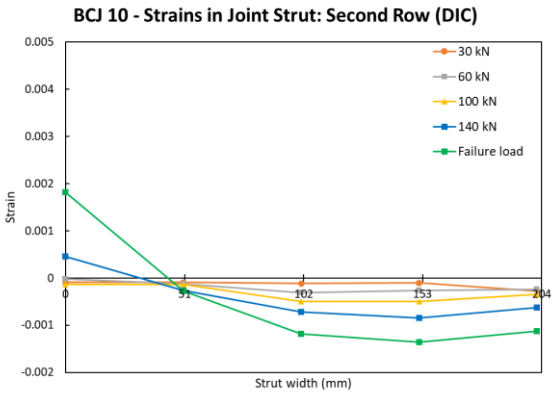

c) Specimen BCJ 10 (DIC)

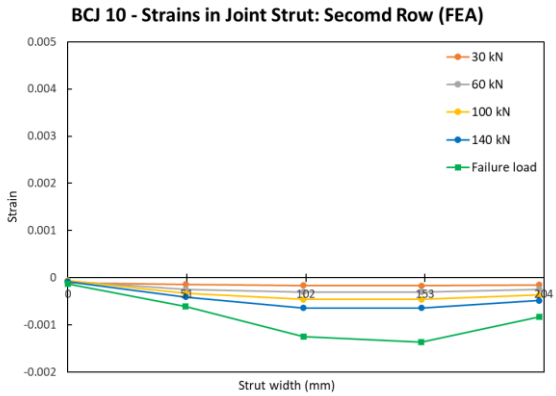

d) Specimen BCJ 10 (2D NLFEA)

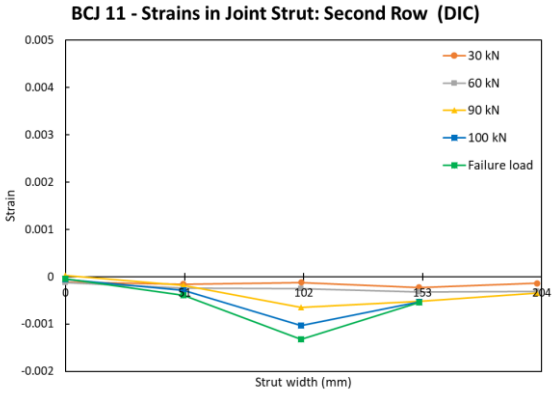

e) Specimen BCJ 11 (DIC)

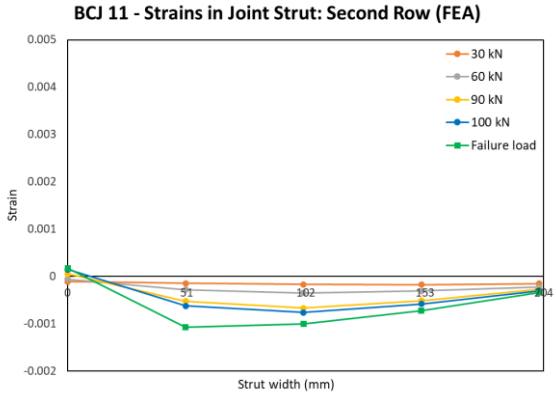

f) Specimen BCJ 11 (2D NLFEA)

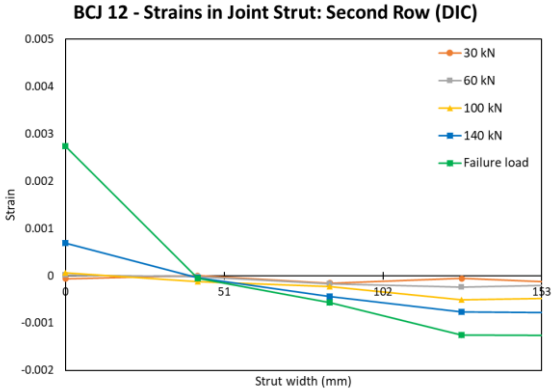

g) Specimen BCJ 12 (DIC)

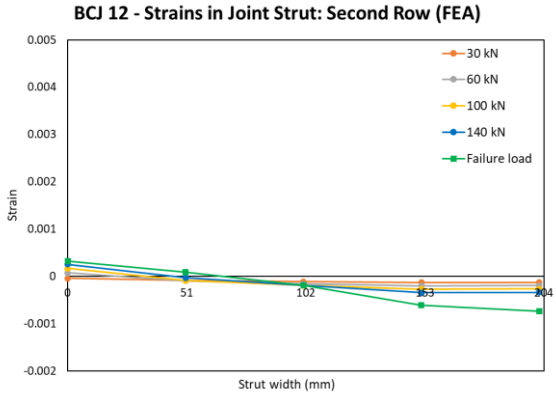

h) Specimen BCJ 12 (2D NLFEA)

Figure 7-30 Strains in second row of diagonal gauges for BCJ series 3; DIC vs 2D NLFEA.

7.3 Effect of parametric studies on strains measured around and within joint

This investigates the influence of key parameters influencing joint behaviour on the strains measured and predicted within the joint and at the joint boundaries. The parameters considered in this study are beam bar anchorage type and bend radius, column axial load, number of joint stirrups, absence of joint stirrups and intermediate column bars. The following sections describe the influence of each parameter.

7.3.1 Effect of column axial load

This section investigates the influence of column axial load on the strains measured at the joint boundaries and along the diagonal strut inside the joint. Strains were compared in specimens BCJ 3, BCJ 6 and BCJ 8 at the failure load (test: 120.8, 111.5 and 107.9 kN respectively; NLFEA: 128.2, 119.1 and 119 kN respectively) as shown in Figure 7-31. The 2D NLFEA is shown to predict the influence of column axial load on strain in the column and diagonal strut reasonably well despite not capturing the influence of axial load on joint strength.

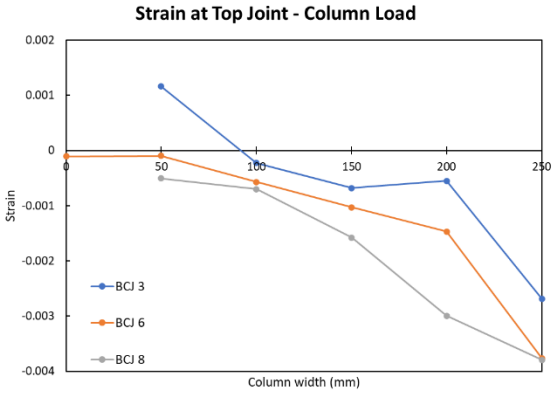

a) Results of DIC

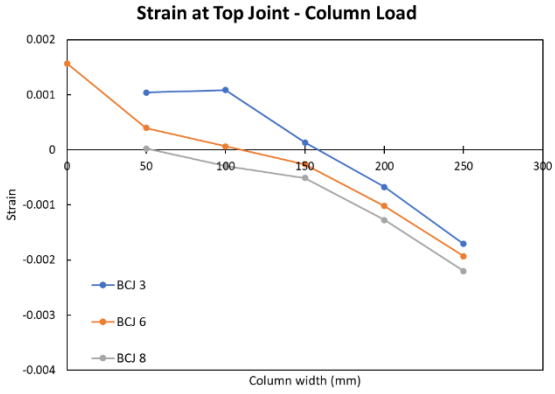

b) Results of 2D NLFEA

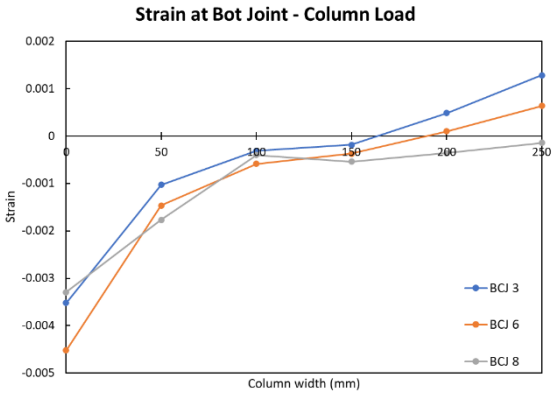

c) Results of DIC

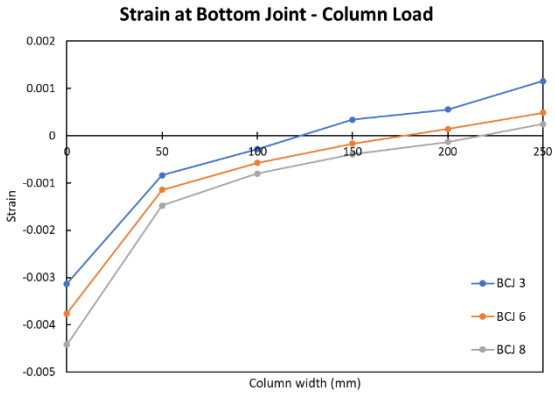

d) Results of 2D NLFEA

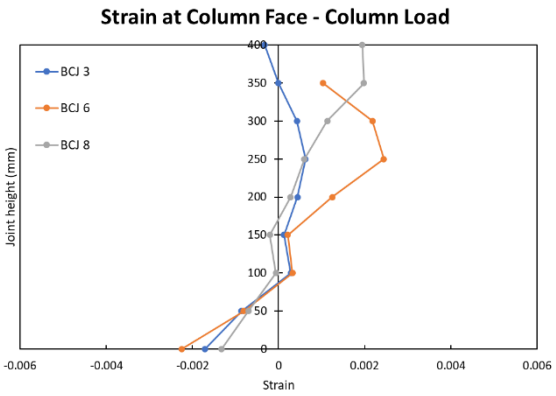

e) Results of DIC

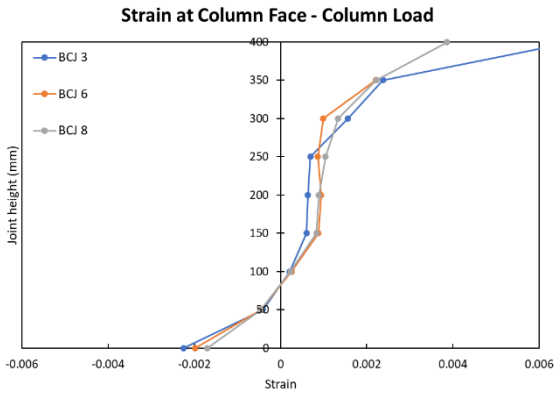

f) Results of 2D NLFEA

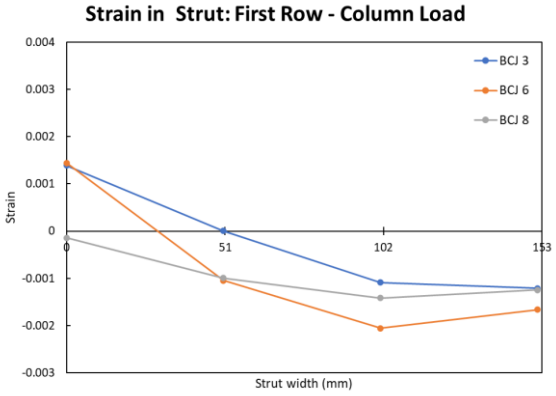

g) Results of DIC

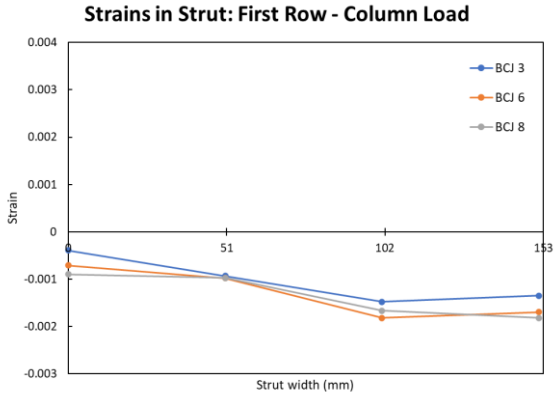

h) Results of 2D NLFEA

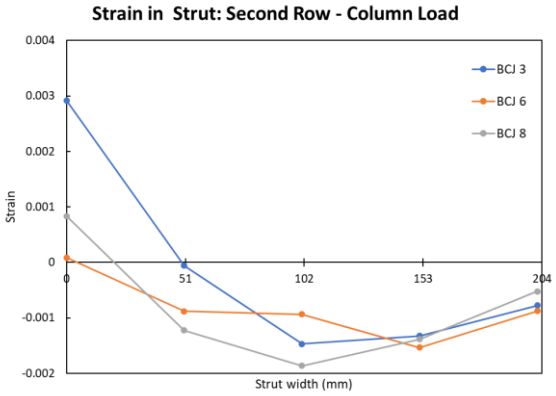

i) Results of DIC

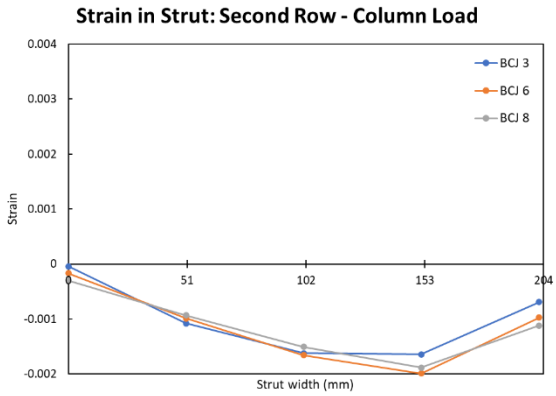

j) Results of 2D NLFEA

Figure 7-31 Effect of column load; DIC vs 2D NLFEA.

7.3.2 Effect of beam bar detailing

The influence of beam bar detailing on the strains measured on surface of joint was investigated for specimens BCJ 1, BCJ 2, BCJ 3 and BCJ 4. Predicted strains were compared with the measured strains at the respective failure loads. The tested specimens had failure loads of 132.8, 139.7, 120.8 and 118.8 kN respectively while the failure load of NLFEA was 133.3, 136.2, 128.2 and 120.7 kN respectively. The results of the effect of beam bar detailing

are shown in Figure 7-32. Overall, the comparison of strains is reasonable but there are a few significant differences which may be due to the DIC results being influenced by localised cracking.

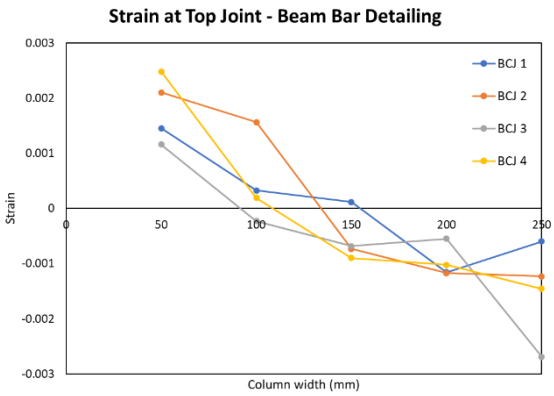

a) Results of DIC

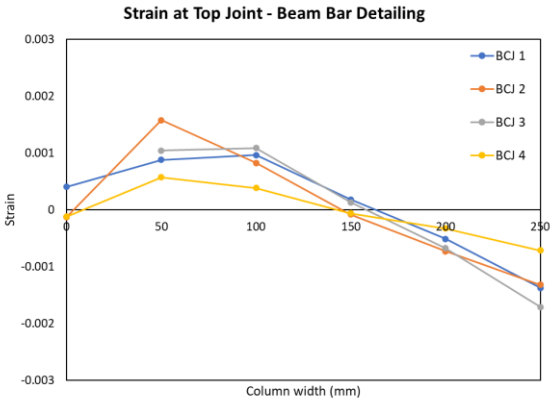

b) Results of 2D NLFEA

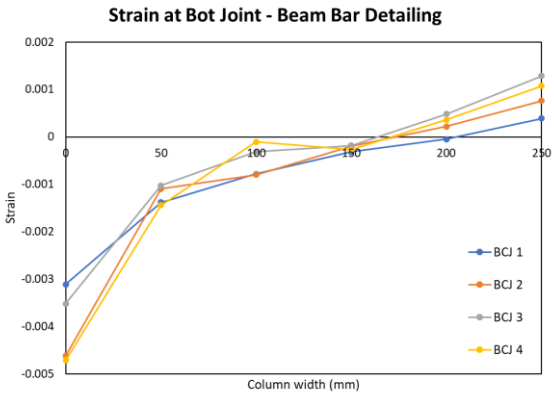

c) Results of DIC

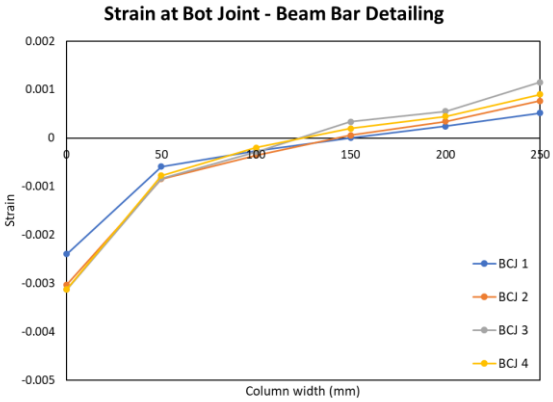

d) Results of 2D NLFEA

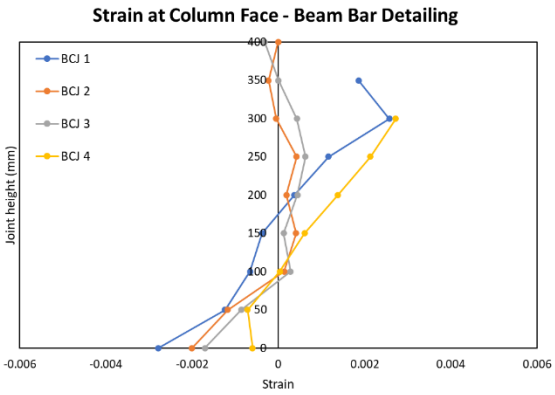

e) Results of DIC

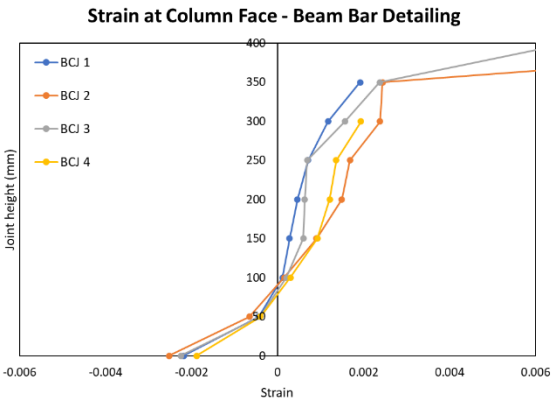

f) Results of 2D NLFEA

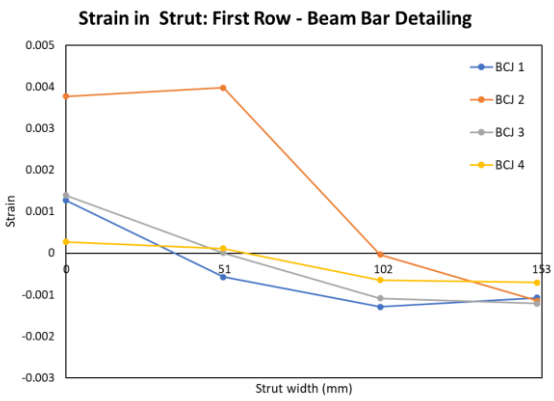

g) Results of DIC

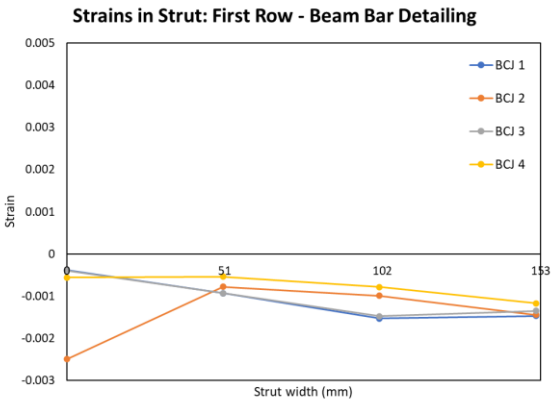

h) Results of 2D NLFEA

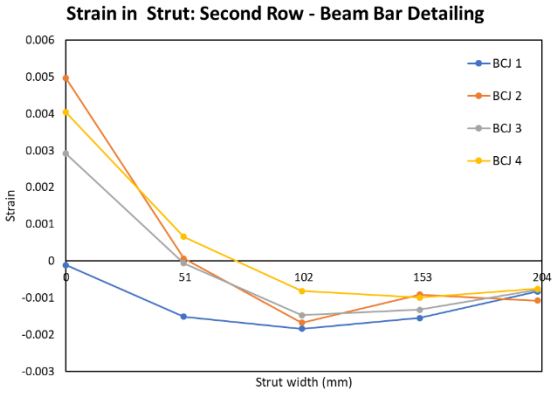

i) Results of DIC

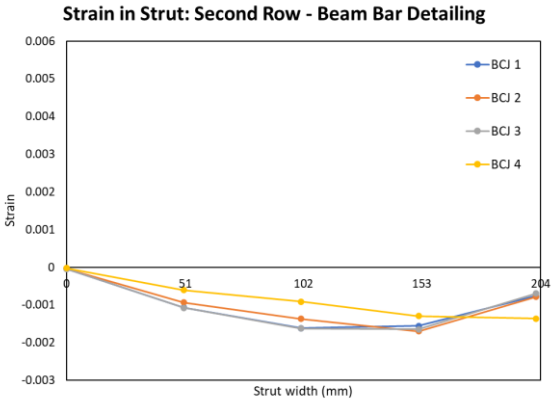

j) Results of 2D NLFEA

Figure 7-32 Effect of beam bar detailing; DIC vs 2D NLFEA.

7.3.3 Effect of shear reinforcement (specimens with U-anchorage bar)

An analysis was carried out to determine the effect of joint stirrups in specimens with U-anchorage bar. The study showed similar trends for both the predicted and measured strains in specimens with two or more joint stirrups. The measured and predicted responses differed for specimens with one or no joint stirrups. The specimens investigated in this section were BCJ 3 with 3 stirrups, BCJ 5 with 1 stirrup, BCJ 9 with 2 stirrups and BCJ 11 with no stirrups. The failure load of NLFEA and DIC was 120.8 kN vs 128.2 kN for BCJ 3, 81.1 kN vs 101.6 kN for BCJ 5, 139.7 kN vs 128.1 kN for BCJ 9 and 101.9 kN vs 107.9 kN for BCJ 11. The results of the effect of shear reinforcement are shown in Figure 7-33.

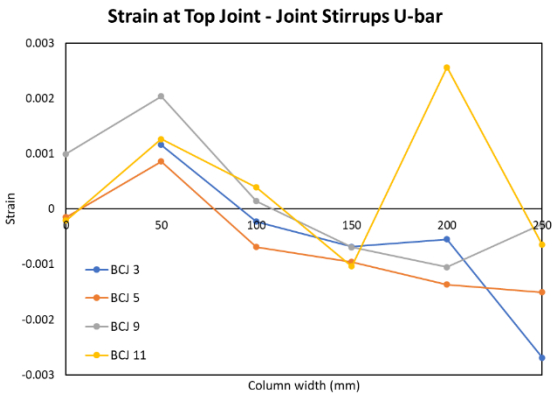

a) Results of DIC

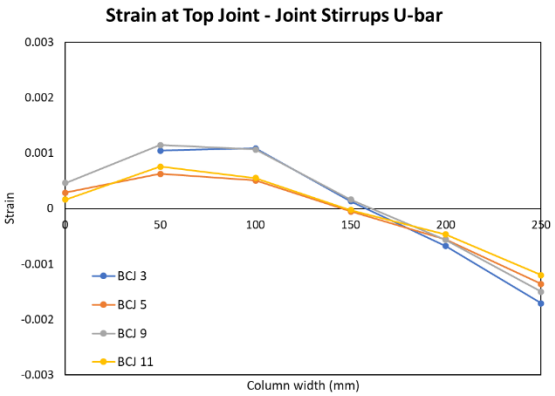

b) Results of 2D NLFEA

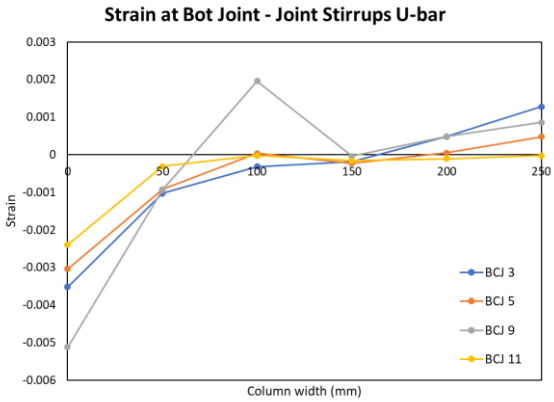

c) Results of DIC

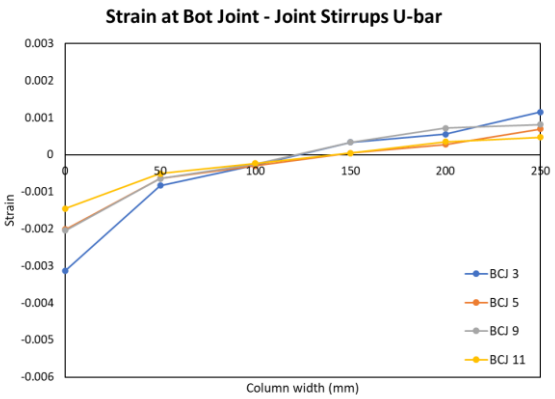

d) Results of 2D NLFEA

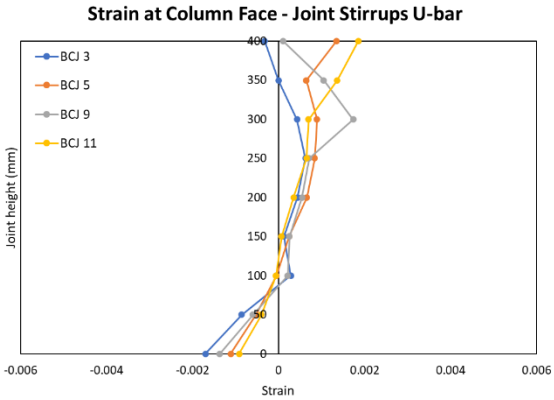

e) Results of DIC

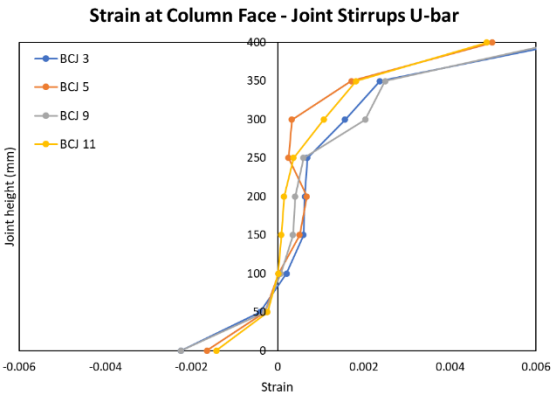

f) Results of 2D NLFEA

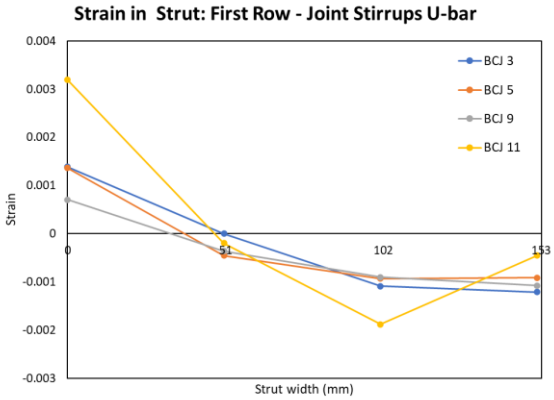

g) Results of DIC

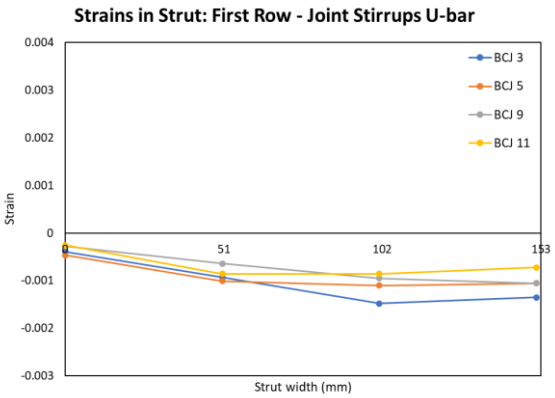

h) Results of 2D NLFEA

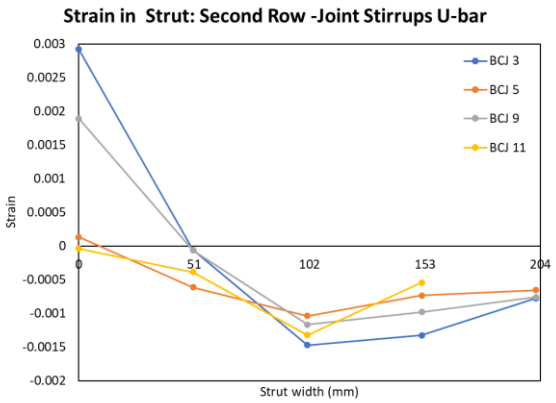

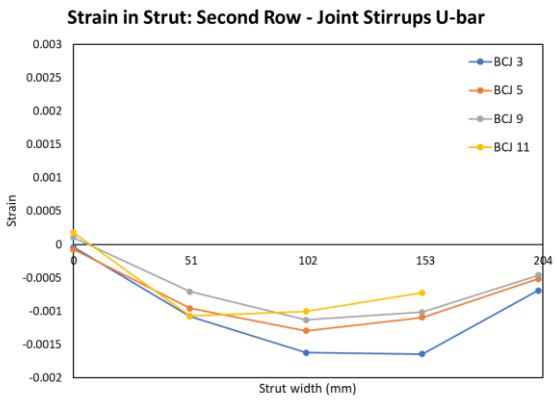

i) Results of DIC j) Results of 2D NLFEA

Figure 7-33 Effect of shear reinforcement for specimens with U-anchorage type; DIC vs 2D NLFEA.

7.3.4 Effect of shear reinforcement (specimens with L-anchorage bar)

Same analysis procedure applied in the previous section was applied on this section but with different specimens with L-anchorage bar. The specimens studied in this section were BCJ 2 (having 3 stirrups), BCJ 7 (having 1 stirrup) and BCJ 12 (having 3 doubled stirrups). The specimens had a failure load of 139.7 kN for test and 136.2 for NLFEA, 127.6 kN for test and 114.2 kN for NLFEA and 184.6 kN for test and 164.4 kN for NLFEA respectively. The results of the effect of shear reinforcement in specimens with L-anchorage bar are shown in Figure 7-34. The 2D NLFEA showed the ability of predicting the effect of shear reinforcement in specimens with L-anchorage bar when compared the measured strains.

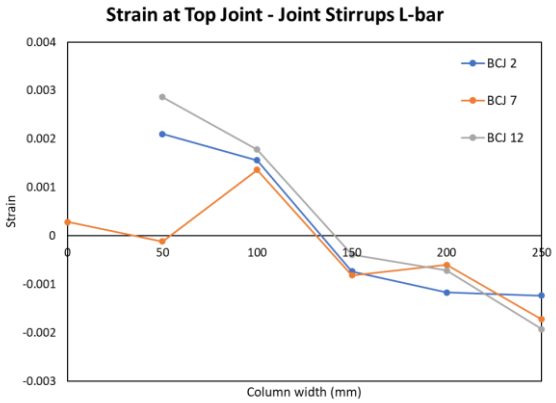

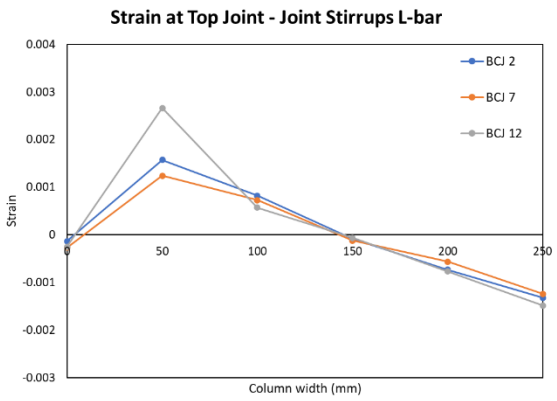

a) Results of DIC b) Results of 2D NLFEA

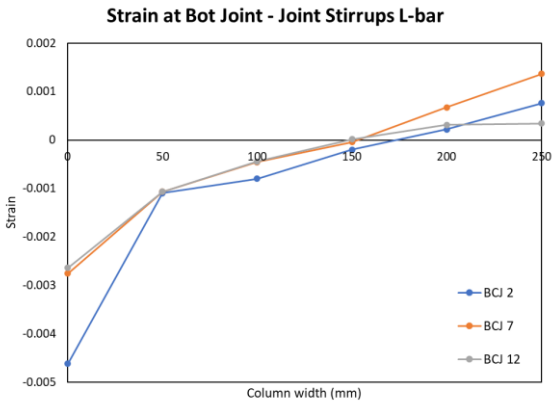

c) Results of DIC

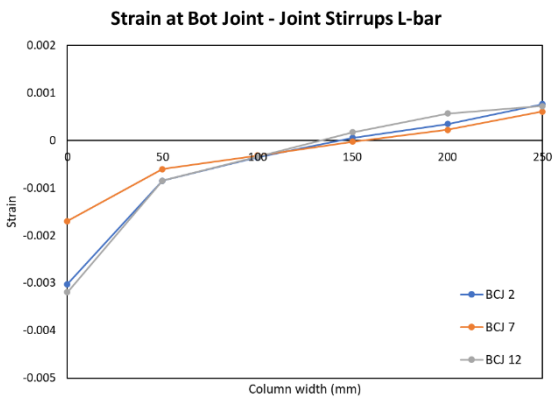

d) Results of 2D NLFEA

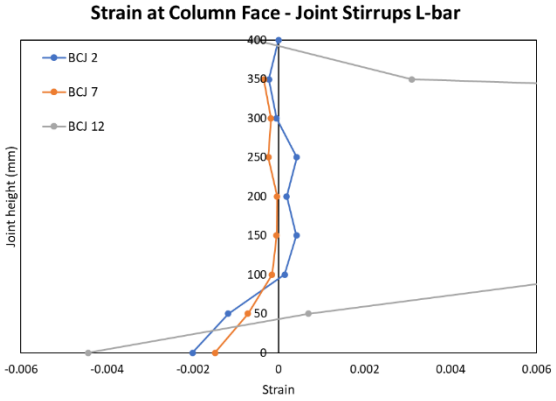

e) Results of DIC

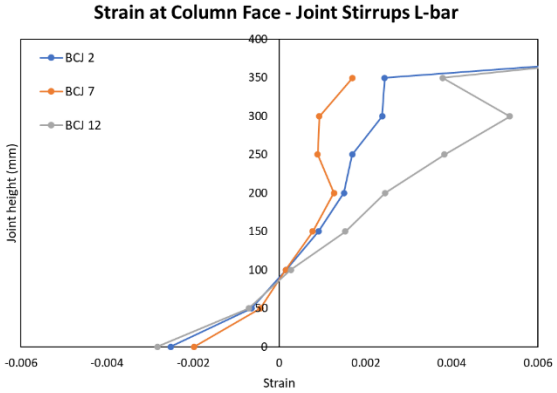

f) Results of 2D NLFEA

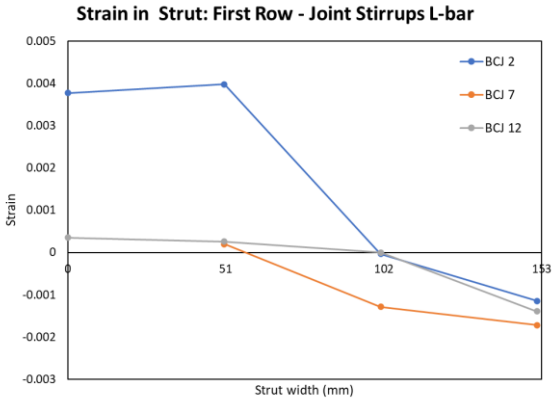

g) Results of DIC

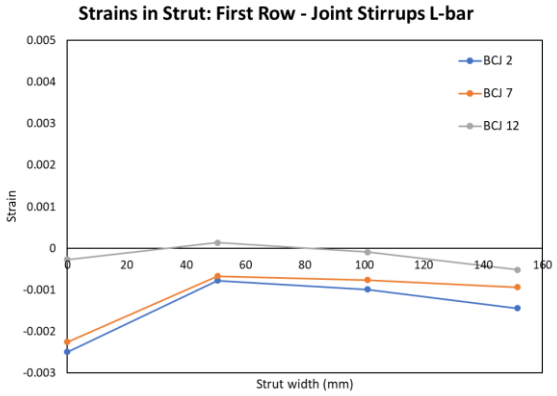

h) Results of 2D NLFEA

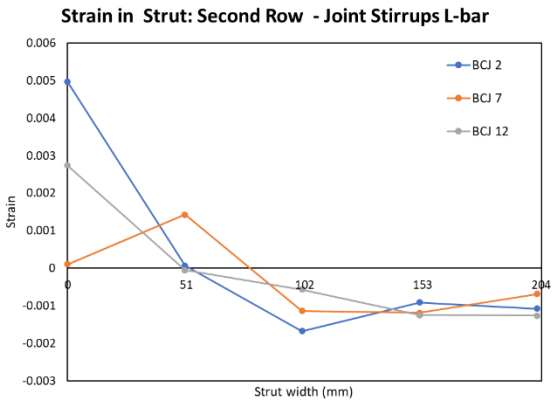

i) Results of DIC

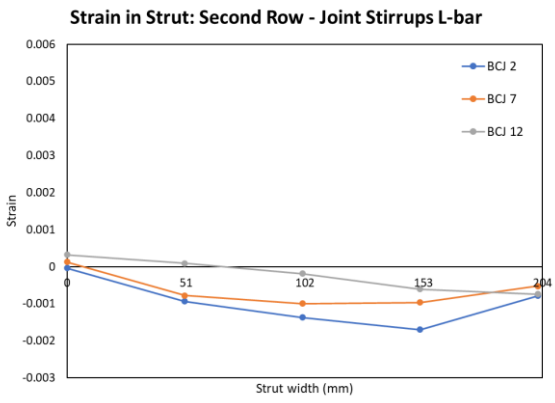

j) Results of 2D NLFEA

Figure 7-34 Effect of shear reinforcement for specimens with L-anchorage type; DIC vs 2D NLFEA.

7.3.5 Effect of intermediate column bars

The influence of providing intermediate column bars on the joint surface strains was studied using specimens BCJ 2 (without intermediate column bars) and BCJ 10 (with intermediate column bars). The results of the effect of beam bar detailing are shown in Figure 7-35. The failure load was 132.8 kN for test and 139.7 kN for NLFEA in BCJ 2 while BCJ 10 had a failure load of 181.2 kN for test and 152.9 kN for 2D NLFEA. The influence of the intermediate column bars on the measured strain distribution is not very clear and is not captured by the 2D NLFEA.

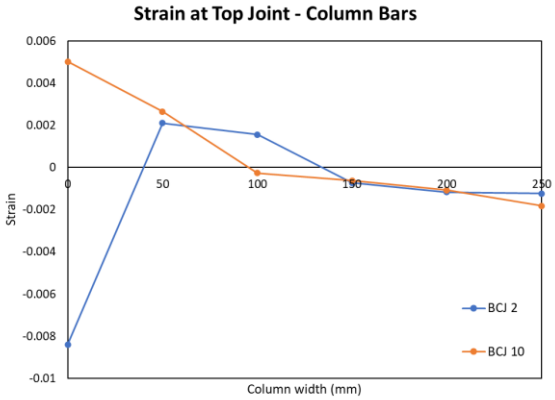

a) Results of DIC

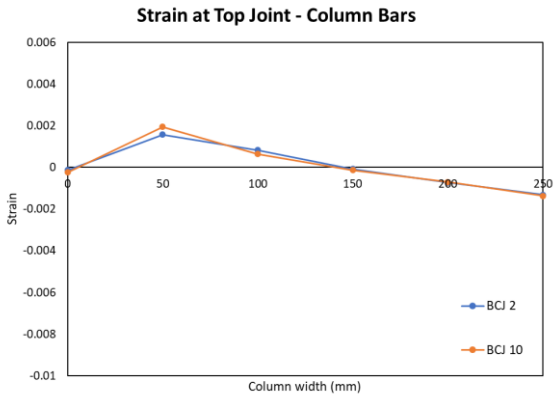

b) Results of 2D NLFEA

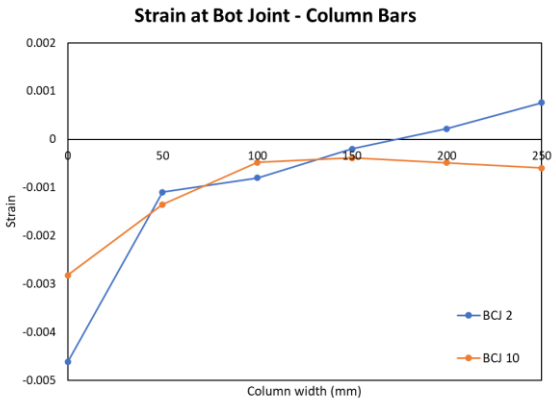

c) Results of DIC

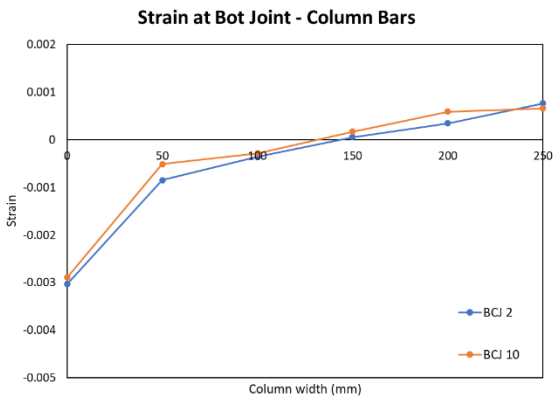

d) Results of 2D NLFEA

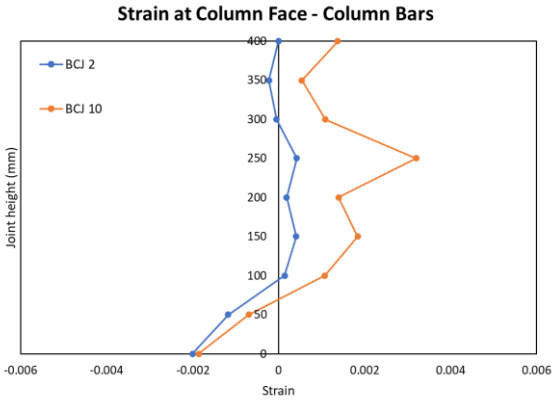

e) Results of DIC

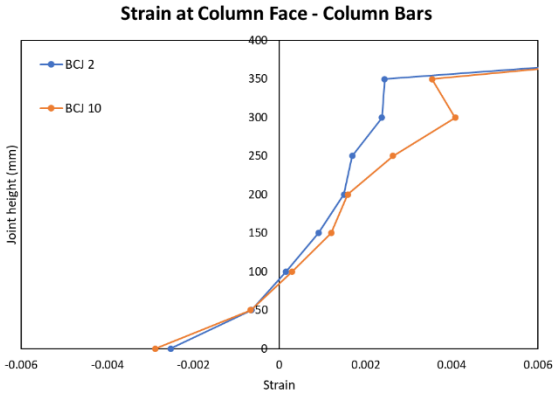

f) Results of 2D NLFEA

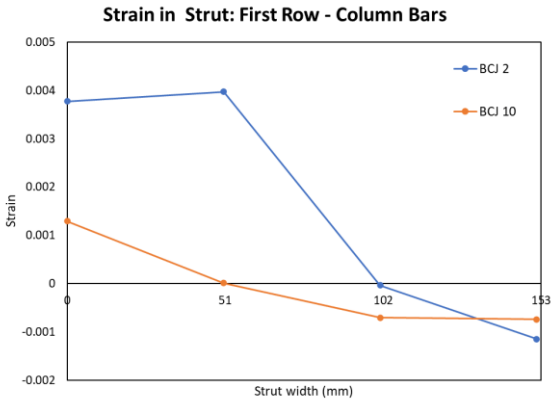

g) Results of DIC

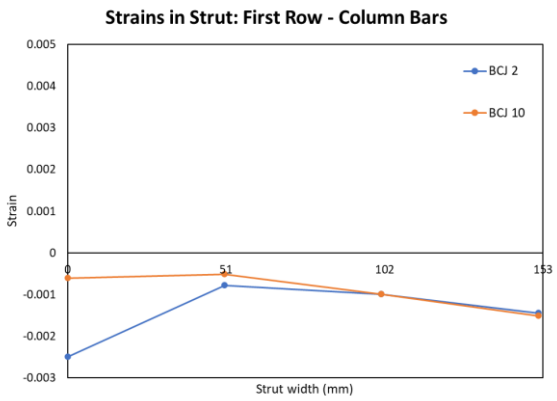

h) Results of 2D NLFEA

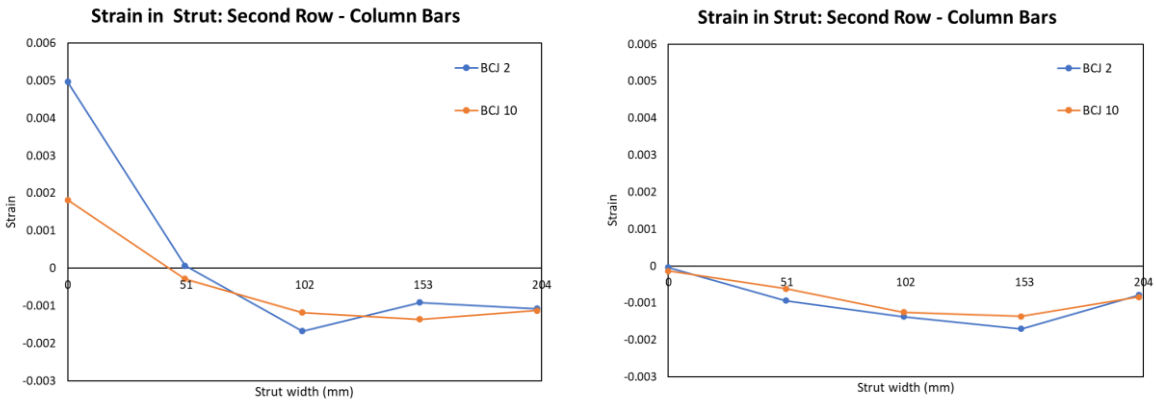

i) Results of DIC j) Results of 2D NLFEA

Figure 7-35 Effect of intermediate column bars; DIC vs 2D NLFEA.

7.4 Evaluation of existing proposed methods for designing beam-column joint

This section uses a database collated by the author to evaluate various methods proposed by previous researchers for designing monotonically loaded external beam-column joints. The database includes 81 specimens of which 13 specimens failed in flexure. The database is given in Table 7-4, Table 7-5, Table 7-6, Table 7-7 and Table 7-8. A number of 68 specimens was included. The letters “J” and “B” in the database depicted flexural failure and joint failure mode respectively. The anchorage type on the database is denoted as “L” for L-anchorage bar, “U” for U-anchorage bar and “H” for headed anchorage bar. The column “Axial Stress” in the database depicts the axial stress applied in the upper column. The analysis investigates the ability of the investigated design methods to capture the influence on joint strength of the parameters varied in this thesis (anchorage type, axial column load, joint stirrup ratio and index, concrete strength and column intermediate bar). Four empirical equations and three STMs are considered in this analysis. The investigated empirical design methods are those of: Hegger et al. [15], Vollum and Newman [24], Bakir and Boduroğlu [25] and Hassan and Moehle [26]. The investigated STMs are those of Hassan and Moehle [26], Hwang et al. [38] and Vollum & Parker [39]. All these methods are described in detail in the literature review of chapter 2, except for the STM proposed by Hassan & Moehle [26] which is described in section 7.4.2.1. The results of the assessments of the considered design methods are presented in the following sections.

Table 7-4 Experimental database of external beam-column joints (1/5).

	Specimen	Concrete (MPa)		Column Reinf.	Beam Reinforcement Top	Beam reinforcement Bottom	Bar type	Bend radius (mm)	Joint links	column load (kN)	Failure Load (kN)	Failure mode	Axial Stress (MPa)
		f_{cu}	f'_c										
Author	BCJ 1	38.3	33.7	4B25	2B25	2B16	L	87.5	3B10	300	133	J	5.3
	BCJ 2	38.8	33.4	4B25	2B25	2B16	L	150	3B10	300	140	J	5.3
	BCJ 3	38.0	33.2	4B25	2B25	2B25	U	87.5	3B10	300	121	J	5.3
	BCJ 4	-	32.9	4B25	2B25	2B25	U	150	3B10	300	119	J	5.3
	BCJ5	34.1	27	4B25	2B25	2B25	U	87.5	1B10	300	81	J	5.3
	BCJ6	34.8	26.9	4B25	2B25	2B25	U	87.5	3B10	600	112	J	10.7
	BCJ 7	46.7	39.9	4B25	2B25	2B16	L	150	1B10	300	128	J	5.3
	BCJ8	33.6	26.80	4B25	2B25	2B25	U	87.5	3B10	900	108	J	16.0
	BCJ 9	60.2	51.3	4B25	2B25	2B25	U	87.5	2B10	300	140	J	5.3
	BCJ 10	58.4	51.1	6B25	2B25	2B16	L	150	3B10	300	181	B	5.3
	BCJ 11	57.2	48.9	4B25	2B25	2B25	U	87.5	NO	300	102	J	5.3
	BCJ 12	54.0	49.9	4B25	2B25	2B16	L	150	6B10	300	185	B	5.3
Ortiz [12]	BCJ 1	42.3	34	6B16	4B16	2B8	L	65	NO	-	118	J	-
	BCJ 2	47.2	38	6B16	4B16	2B8	L	65	1B8	-	125	J	-
	BCJ 3	41.3	33	8B16	4B16	2B8	L	130	NO	-	118	J	-
	BCJ 4	42	34	10B16	4B16	2B8	L	65	2B8	-	130	J	-
	BCJ5	47.4	38	10B16	4B16	2B8	L	65	NO	300	115	J	5
	BCJ6	43.7	35	10B16	4B16	2B8	L	130	NO	300	115	J	5
	BCJ 7	44	35	10B16	4B16	2B8	L	130	3B10	300	170	B	5

Table 7-5 Experimental database of external beam-column joints (2/5).

	Specimen	Concrete (MPa)		Column Reinf.	Beam Reinforcement Top	Beam reinforcement Bottom	Bar type	Bend radius (mm)	Joint links	column load (kN)	Failure Load (kN)	Failure mode	Axial Stress (MPa)
		f_{cu}	f'_c										
Taylor [5]	P1/41/24	-	33	4Y16	2Y16	2Y6	L	48	1Y6	240	35	J	12.2
	P2/41/24	-	29	4Y16	2Y16	2Y6	L	48	1Y6	240	35	J	12.2
	P2/41/24A	-	46.5	4Y16	2Y16	2Y6	L	48	1Y6	240	47	J	12.2
	A3/41/24	-	27	4Y16	2Y16	2Y6	L	48	1Y6	240	35	J	12.2
	D3/41/24	-	53	4Y16	2Y16	2Y6	L	48	1Y6	60	50	J	3.1
	B3/41/24	-	22	4Y16	2Y16	2Y6	L	48	2Y6	240	30	J	12.2
	C3/41/24BY	-	31.7	4Y16	2Y16	2Y16	U	48	1Y6	240	29	J	12.2
	C3/41/13Y	-	28.2	4Y16	3Y10	3Y10	U	30	1Y6	240	27	J	12.2
	C3/41/24Y	-	59.5	4Y16	2Y16	2Y16	U	48	1Y6	240	45	J	12.2
Kordina [8]	RE2	32	25	4T16	2T20	2T20	L	100	NO	240	67	-	6.0
	RE3	51	40	4T16	2T20 + 4T10	2T20	L	100	1T10	400	80	-	10
	RE4	40	32	4T16	2T20	2T20	L	100	1T8	51	51	-	1.3
	RE6	40	32	4T16	2T20	2T20	H	NO	2T8	213	66	-	5.3
	RE7	32	26	4T16	3T20	2T20	L	100	3T8	650	117	-	16.3
	RE8	35	28	4T16	3T20	3T20	U	100	3T8	525	105	-	13.1
	RE9	36	28	4T16	3T20	3T20	U	100	3T8	770	110	-	19.3
	RE10	30	24	4T16	3T20	3T20	U	160	3T8	551	100	-	13.775

Table 7-6 Experimental database of external beam-column joints (3/5).

	Specimen	Concrete (MPa) f_{cu}	Concrete (MPa) f'_c	Column Reinf.	Beam Reinforcement Top	Beam reinforcement Bottom	Bar type	Bend radius (mm)	Joint links	column load (kN)	Failure Load (kN)	Failure mode	Axial Stress (MPa)
Scott [11]	ClAL	41.7	33	4T16	2T12	2T12	L	36	1T6	50	22	J	2.2
	C3L	44.4	35	4T16	2T12	2T12	U	36	1T6	50	22	J	2.2
	C4	51.8	41	4T16	2T16	2T12	L	48	1T6	275	30	J	12.2
	C4A	55.4	44	4T16	2T16	2T12	L	48	1T6	275	32	J	12.2
	C4AL	44.7	36	4T16	2T16	2T12	L	48	1T6	50	28	J	2.2
	C6	49.8	40	4T16	2T16	2T16	U	48	1T6	275	22	J	12.2
	C6L	57.3	46	4T16	2T16	2T16	U	48	1T6	50	26	J	2.2
	C7	44	35	4T16	2T16	2T12	L	48	1T6	275	32	J	12.2
	C9	44.9	36	4T16	2T16	2T16	U	48	1T6	275	28	J	12.2
Parker & Bullman [13]	4a	49	39	4T16	2T25	2T16	L	75	NO	0	118	B	0
	4b	49	39	4T16	2T25	2T16	L	75	NO	300	138	J	3.3
	4c	46	37	4T16	2T25	2T16	L	75	NO	570	170	J	6.3
	4d	49	39	4T16	2T25	2T16	L	75	NO	0	150	J	0
	4e	50	40	4T16	2T25	2T16	L	75	NO	300	160	J	3.3
	4f	47	38	4T16	2T25	2T16	L	75	NO	600	183	J	6.7
	5a	53	42	4T16	2T25	2T16	L	75	3T12	0	213	B	0
	5b	54	43	4T16	2T25	2T16	L	75	2T12	300	236	J	3.3
	5d	54	43	4T16	2T32	2T16	L	75	5T12	0	226	B	0
	5e	56	45	4T16	2T32	2T16	L	75	5T12	300	295	B	3.3
	5f	54	43	4T16	2T32	2T16	L	75	3T12	600	322	J	6.7

Table 7-7 Experimental database of external beam-column joints (4/5).

	Specimen	Concrete (MPa)		Column Reinfor.	Beam Reinforcement Top	Beam Reinforcemen Bottom	Bar type	Bend radius (mm)	Joint links	colum n load (kN)	Failure Load (kN)	Failure mode	Axial Stress (MPa)
		f_{cu}	f'_c										
Hamil [14]	C4ALNO	53	42	4T16	2T16	2T12	L	48	NO	50	27	B	2.2
	C4ALN 1	57	46	4T16	2T16	2T12	L	48	1T6	50	34	J	2.2
	C4ALN3	52	42	4T16	2T16	2T12	L	48	2T6	50	35	J	2.2
	C4ALN5	63	50	4T16	2T16	2T12	L	48	4T6	50	40	J	2.2
	C4ALHO	130	104	4T16	2T16	2T12	L	48	NO	100	43	B	4.4
	C6LNO	64	51	4T16	2T16	2T16	U	48	NO	50	24	J	2.2
	C6LNI	64	51	4T16	2T16	2T16	U	48	1T6	50	25	J	2.2
	C6LN3	61	49	4T16	2T16	2T16	U	48	2T6	50	29	J	2.2
	C6LN5	46	37	4T16	2T16	2T16	U	48	4T6	50	34	J	2.2
	C6LHO	126	101	4T16	2T16	2T16	U	48	NO	100	36	J	4.4
	C6LHI	127	102	4T16	2T16	2T16	U	48	1T6	100	37	J	4.4
	C6LH3	121	97	4T16	2T16	2T16	U	48	2T6	100	41	J	4.4

Table 7-8 Experimental database of external beam-column joints (5/5).

	Specimen	Concrete (MPa)		Column Reinfor.	Beam Reinforcement Top	Beam Reinforceme Bottom	Bar type	Bend radius (mm)	Joint links	column load (kN)	Shear failure V_j (kN)	Failure mode	Axial Stress (MPa)
		f_{cu}	f'_c										
Sarsam and Phipps [10]	EX1	69	55.2	4Y16	2Y16	2Y12	L	48	3Y8	298.4	181	B	9.39
	EX2	66	52.8	4Y16	2Y16	2Y12	L	48	NO	304.9	164.3	J	9.52
	EX3	53	42.4	4Y17	2Y17	2Y12	L	48	3Y8	303.3	161	B	9.47
	EX4	66	52.8	4Y18	2Y18	2Y12	L	48	3Y9	311.3	173	B	9.72
Hegger et al [15]	RK1	-	57.9	4ϕ16	2ϕ20	2ϕ20	U	115	4ϕ10	500	374	B	13.9
	RK2	-	57.4	2ϕ16+2ϕ20	2ϕ20+Diagonalϕ20	2ϕ20	U	115	4ϕ8	500	417	B	13.9
	RK3	-	57.2	4ϕ16	2ϕ20	-	H	-	4ϕ10	500	402	B	13.9
	RK4	-	51.7	4ϕ16	2ϕ20	2ϕ20	U	115	3ϕ10	500	357	J	16.7
	RK5	-	54.9	4ϕ16	2ϕ25	-	H	-	3ϕ10	500	423	J	16.7
	RK6	-	86.5	4ϕ16	2ϕ25	-	H	-	3ϕ10	500	556	J	16.7
	RK7	-	54.7	4ϕ16	2ϕ20	2ϕ20	U	165	3ϕ10	500	277	J	16.7
	RK8	-	38.6	4ϕ16	2ϕ20	2ϕ20	U	115	3ϕ10	500	273	J	16.7

7.4.1 Evaluation of beam-column joint using empirical equations

This section presents the results of the assessment of the four empirically based design equations discussed earlier. Details of the considered design methods are presented in the literature review of chapter 2. Each method was used to assess the failure load of the specimens listed in Table 7-9. The presented results depict the influences on the accuracy of the strength predictions of concrete strength, anchorage type, axial column load, joint stirrup ratio and index and column intermediate bar. The results of the assessment of each method are presented below.

Table 7-9 The parameters used in the proposed design methods.

Method	Joint aspect ratio	Column load	Joint shear reinforcement	Beam anchorage detail	Concrete strength	Column reinforcement ratio
Hegger et al. [15]	yes	no	yes	yes	yes	yes
Vollum & Newman [24]	yes	no	yes	yes	yes	no
Bakir & Boduroğlu [25]	yes	yes	yes	yes	yes	yes
Hassan & Mohele [26]	yes	yes	no	no	yes	no
Hwang et al [38]	no	yes	yes	no	yes	yes
Vollum & Parker [39]	yes	no	yes	no	yes	no

7.4.1.1 Hegger et al. [15]

Details of the design method of Hegger et al. [15] are given in section 2.3.3.3 of chapter 2. The method accounts for the influences of joint aspect ratio, joint stirrups, detail of anchorage bar, concrete strength and column reinforcement ratio. The ratio $P_{predicted}$ / $P_{measured}$ is plotted against an index representing the considered variable in Figure 7-36. The figures indicate the influence on $P_{predicted}$ / $P_{measured}$ of concrete strength, axial column load, joint stirrup ratio and index, anchorage reinforcement type and column reinforcement ratio. The stirrup index is defined as A_{sje} f_y/b_e h_c $f_c^{0.5}$, in which A_{sje} is the effective area of joint stirrups (five-eighth of beam depth below anchorage bar), b_e and h_c are effective joint width and column depth respectively and f_y and f_c are steel yield and concrete strength. The results showed an increase of $P_{predicted}$ / $P_{measured}$ as the influences of concrete strength, column reinforcement ratio and anchorage type increase. The effect of joint stirrups ratio & index and column axial load showed a reduction of the trend as these parameters increase. The mean and standard deviation of $P_{predicted}$ / $P_{measured}$ are 1.16 and 0.21 respectively as given in Table 7-10 and Table 7-11. The measured failure load is plotted against the predicted failure load in Figure 7-37. The trend lines shown in Figure 7-36 should be treated with caution since the number of specimens in the database having any particular attribute varies widely. For example, there are only four specimens from Hamil [14] with high strength concrete. Consequently, it is unclear whether the apparent increased conservatism of the design method of Hegger et al. [15] with increasing concrete strength is real in general or particular to the specimens of Hamil. Similarly, there are relatively few specimens in the database having headed bar anchorage of beam flexural reinforcement or specimens with the maximum considered joint aspect ratio of 2. Additionally, since the joint shear strength depends on many variables, the source of scatter evident in each sub-figure of Figure 7-37 is unclear. Similar observations can be made about the trend lines in the following sections which should also be considered as indicative.

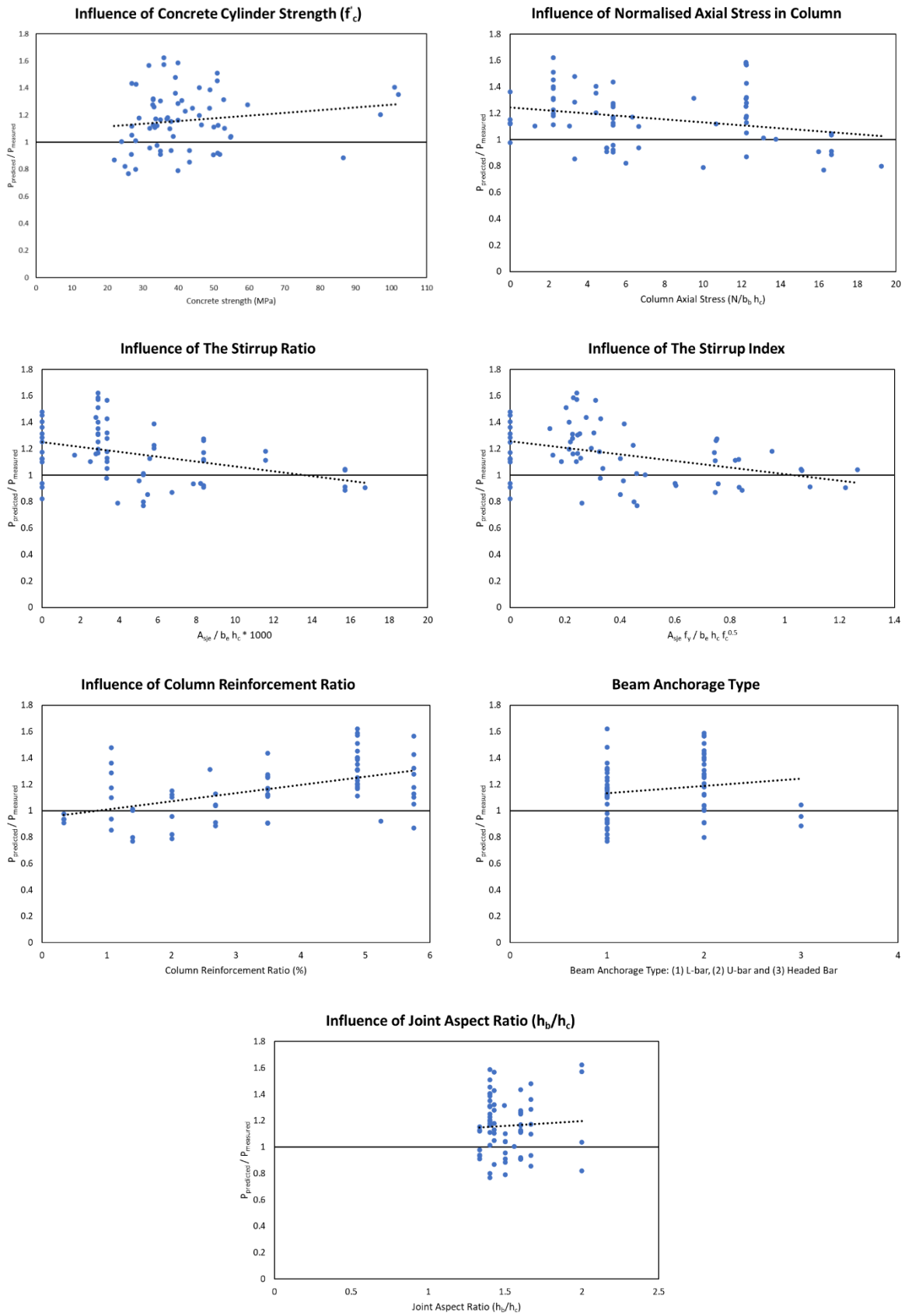

Figure 7-36 Results of empirical equation proposed by Hegger et al. [15].

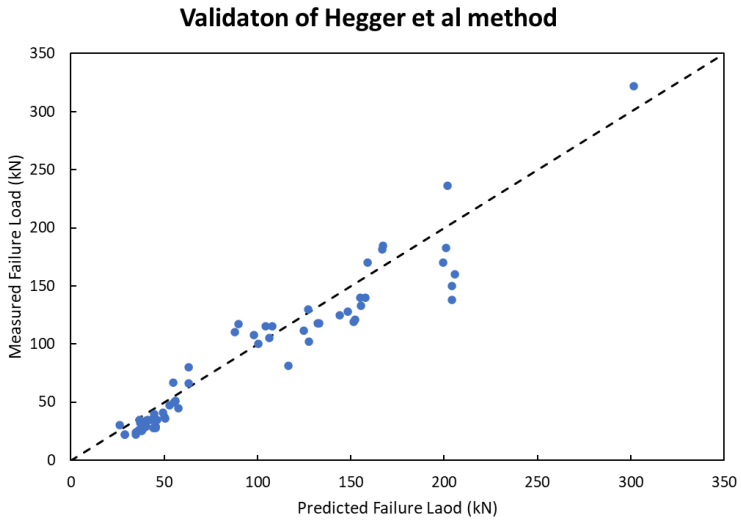

Figure 7-37 Results of measured to predicted failure load for Hegger et al [15] empirical method.

7.4.1.2 Vollum and Newman [24]

Details of this method are given in Section 2.3.3.1 of chapter 2. The ability of the method to capture the influence of the parameters influencing joint strength is shown in Figure 7-38. The results show good agreement on average between the measured and predicted joint strengths. The trendline in some figures almost matched the solid line (at $P_{predicted}$ / $P_{measured}$ = 1.0), which indicates the sufficiency of this method in predicting joint strength. The mean and standard deviation of $P_{predicted}$ / $P_{measured}$ are 0.99 and 0.17 respectively as shown in Table 7-10 and Table 7-11. The measured failure load is plotted against predicted failure load in Figure 7-39.

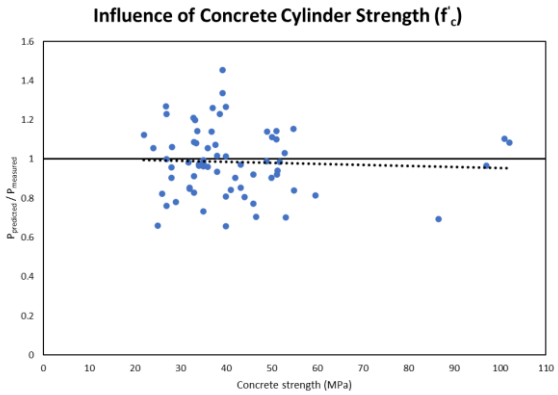

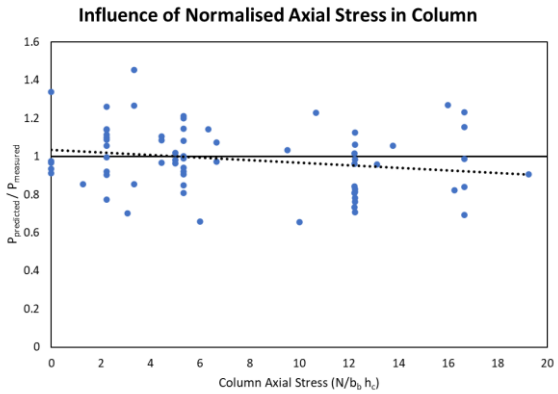

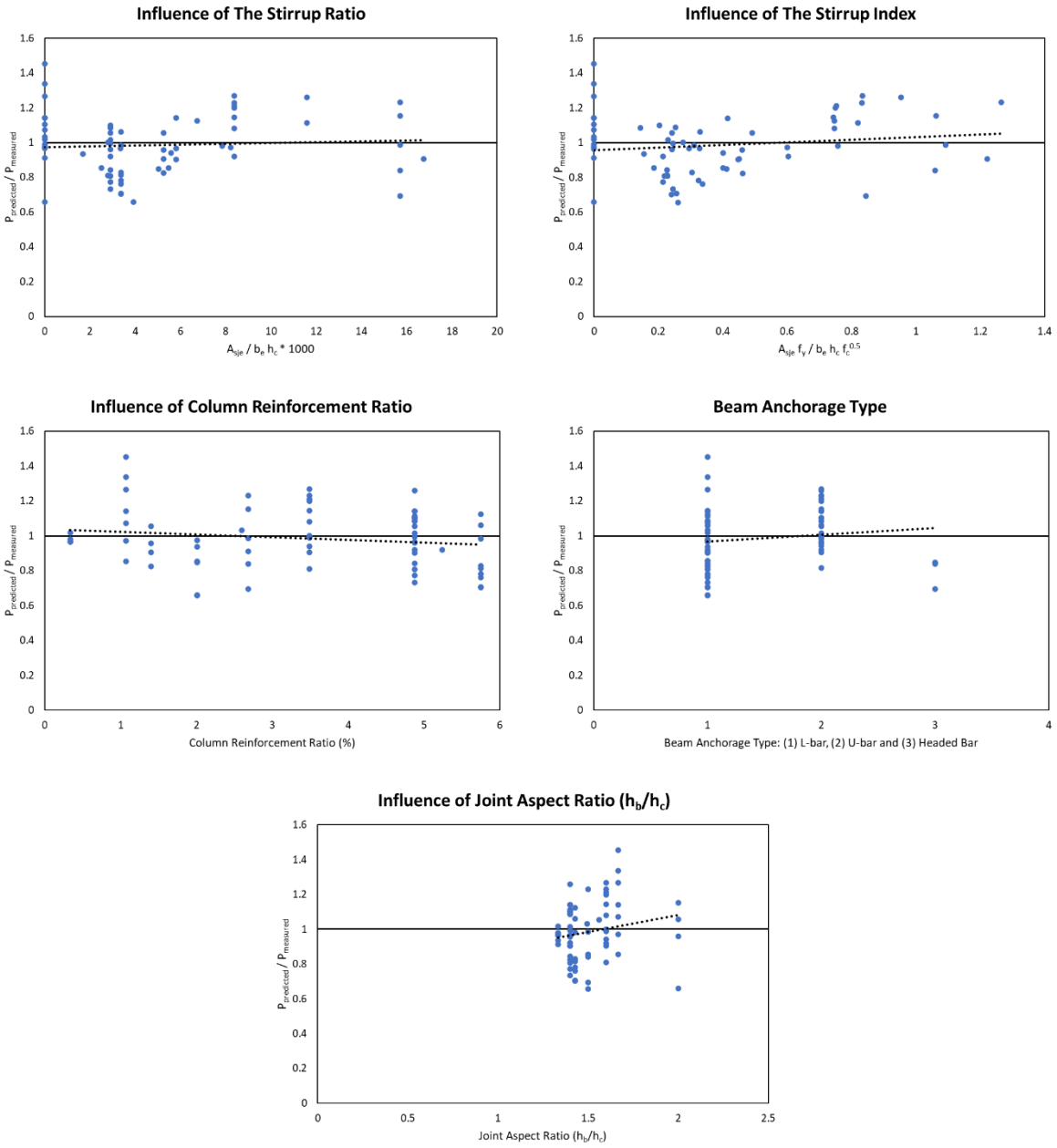

Figure 7-38 Results of empirical equation proposed by Vollum & Newman [24].

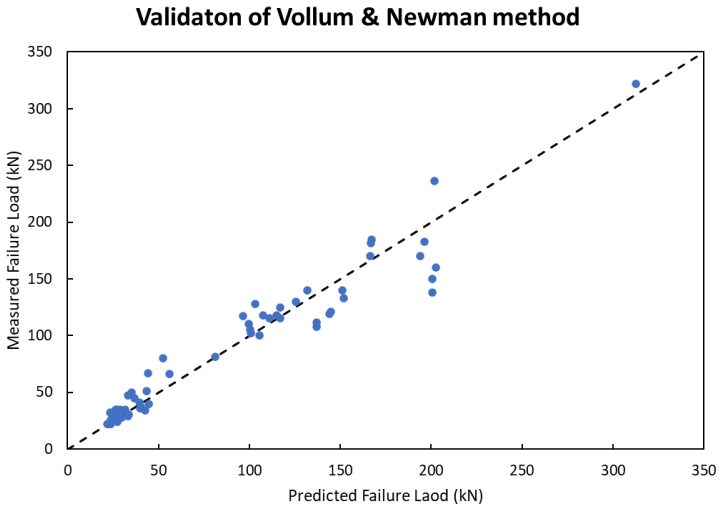

Figure 7-39 Results of measured to predicted failure load for Vollum & Newman [24] empirical method.

7.4.1.3 Bakir and Boduroğlu [25]

The influences of the parameters studied in this thesis on joint strength were analysed using the empirical equation proposed by Bakir and Boduroğlu [25]. Details of this method are given in Section 2.3.3.2 of chapter 2. The results of this analysis are shown in Figure 7-40. The method captures the influences of column reinforcement ratio and concrete strength by showing an increase of the trendline as these parameters increase while a decrease of trendline can be seen in the influence of column axial load. The remaining parameters showed a small influence in joint strength. The method gives a mean of $P_{predicted}$ / $P_{measured}$ of 0.80 and a standard deviation of 0.12 as shown in Table 7-10 and Table 7-11. The measured failure load is plotted against the predicted failure load in Figure 7-41.

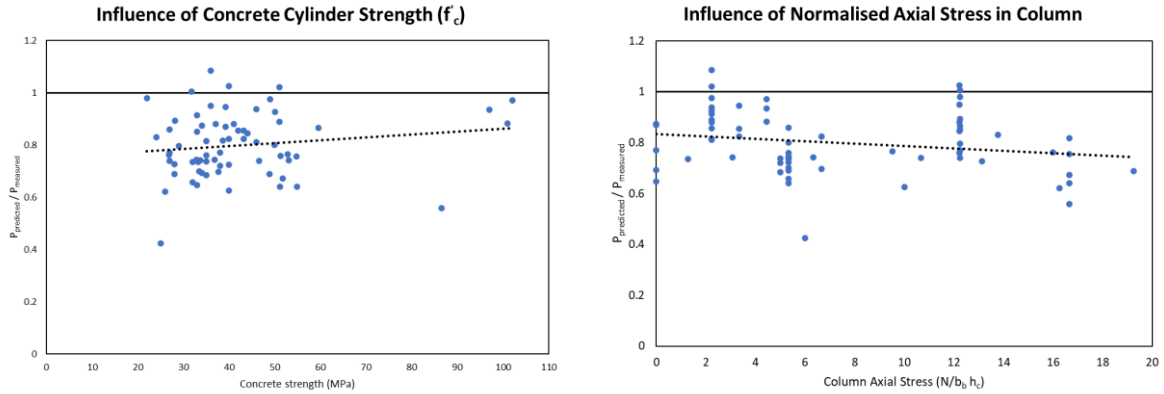

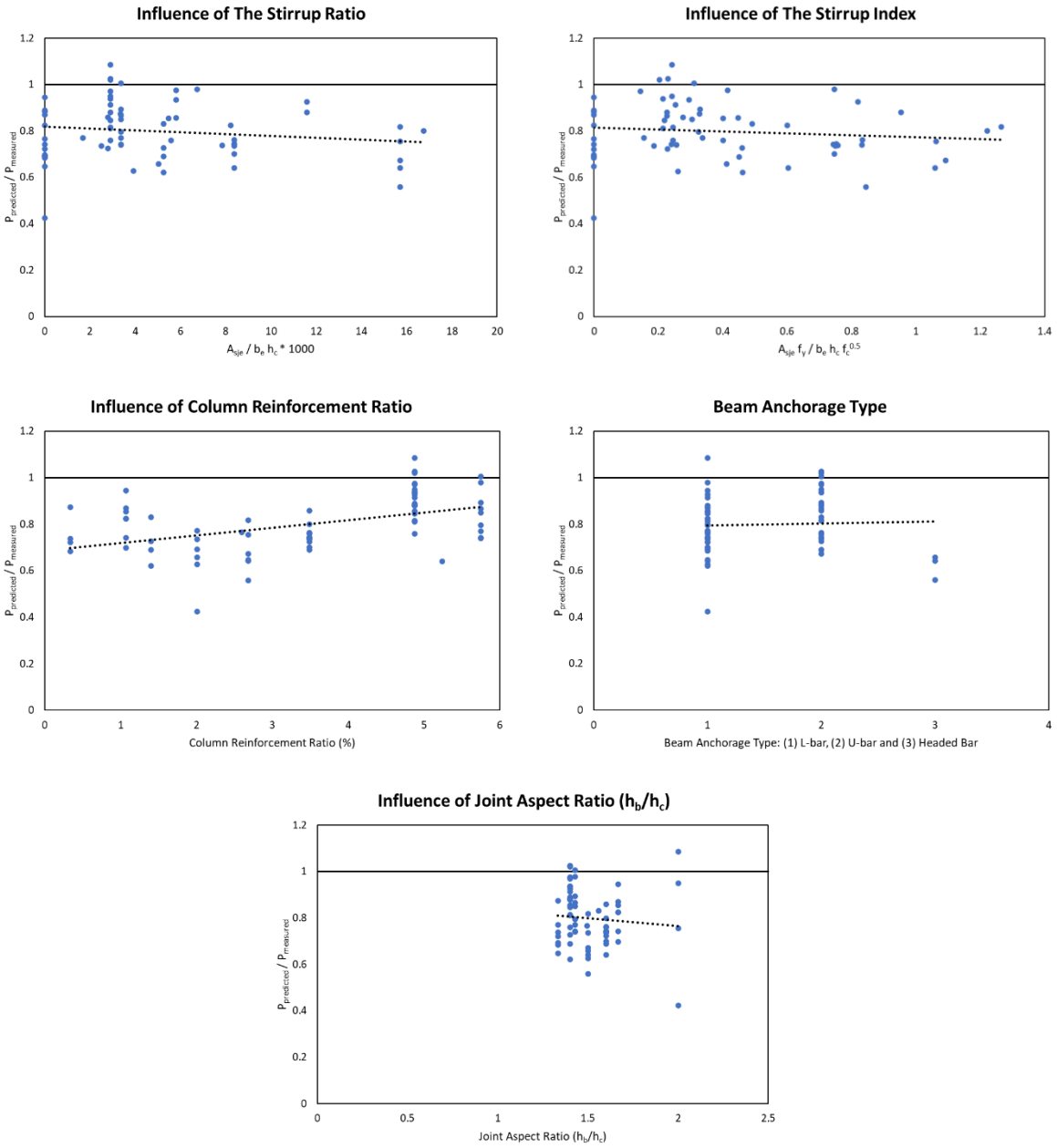

Figure 7-40 Results of empirical equation proposed by Bakir and Boduroğlu [25].

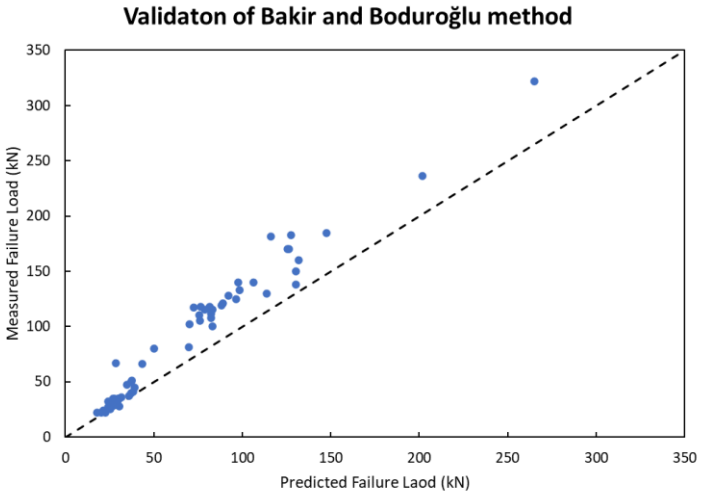

Figure 7-41 Results of measured to predicted failure load for Bakir and Boduroğlu [25] empirical method.

7.4.1.4 Hassan and Mohele [26]

As discussed in the literature review, this method considers the joint strength of external and corner beam-column connections without joint stirrups. Thus, only 14 specimens without joint stirrups were used from the database to predict the joint strength. The results of the analysis are shown in Figure 7-42. The results showed acceptable predictions of predicted failure load when compared with measured failure load. The influences of column axial load and reinforcement ratio showed a reduction in trendline of $P_{predicted}$ / $P_{measured}$ while an increase was observed in the influences of the remaining parameters. The method gives a mean of 0.96 and a standard deviation of 0.16. The measured failure load is plotted against the predicted failure load in Figure 7-43.

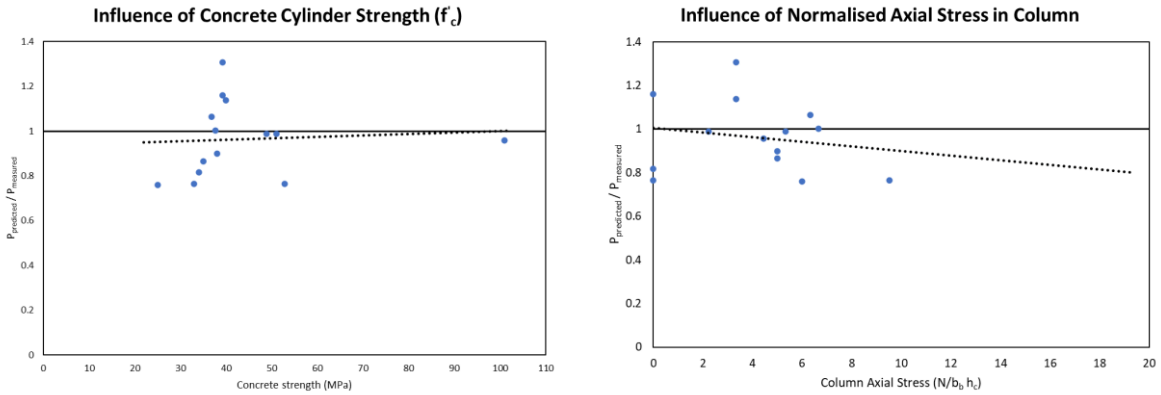

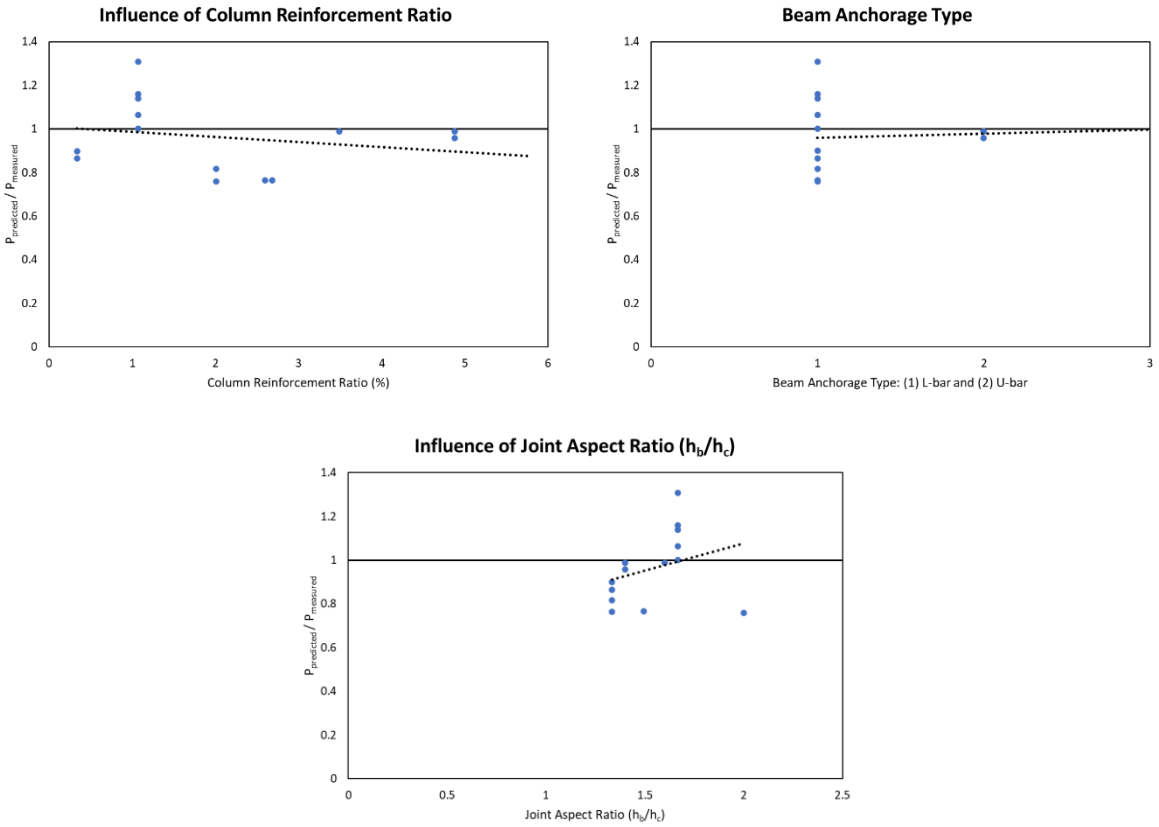

Figure 7-42 Results of empirical equation proposed by Hassan and Mohele [26].

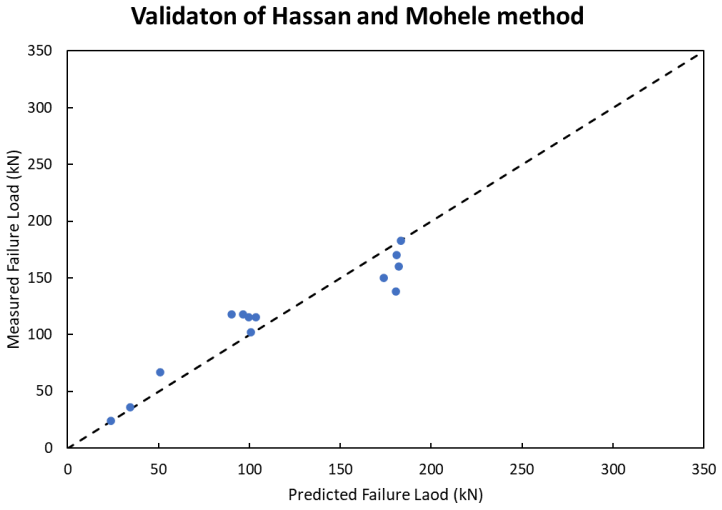

Figure 7-43 Results of measured to predicted failure load for Hassan and Mohele [26] empirical method.

Table 7-10 Results of proposed empirical equations (1/2).

	Specimen	$P_{predict}$ / $P_{measured}$			
		Hegger et al. [15]	Vollum&Newman [24]	Bakir and Boduroğlu[25]	Hassan & Mohele [26]
Author	BCJ 1	1.17	1.14	0.74	-
	BCJ 2	1.11	1.08	0.70	-
	BCJ 3	1.26	1.20	0.74	-
	BCJ 4	1.28	1.21	0.74	-
	BCJ5	1.44	1.00	0.86	-
	BCJ6	1.12	1.23	0.74	-
	BCJ 7	1.16	0.81	0.72	-
	BCJ8	0.91	1.27	0.76	-
	BCJ 9	1.13	0.94	0.76	-
	BCJ 10	0.92	0.92	0.64	-
	BCJ 11	1.25	0.99	0.69	0.99
	BCJ 12	0.91	0.91	0.80	-
Ortiz [12]	BCJ 1	1.12	0.97	0.69	0.82
	BCJ 2	1.15	0.94	0.77	-
	BCJ 3	1.13	0.91	0.65	0.76
	BCJ 4	0.98	0.97	0.87	-
	BCJ5	0.94	1.02	0.72	0.90
	BCJ6	0.91	0.96	0.68	0.87
	BCJ 7	0.93	0.98	0.74	-
Taylor [5]	P1/41/24	1.32	0.83	0.85	-
	P2/41/24	1.18	0.78	0.80	-
	P2/41/24A	1.13	0.71	0.74	-
	A3/41/24	1.05	0.76	0.77	-
	D3/41/24	1.10	0.70	0.74	-
	B3/41/24	0.87	1.12	0.98	-
	C3/41/24BY	1.57	0.98	1.01	-
	C3/41/13Y	1.43	1.06	0.89	-
	C3/41/24Y	1.28	0.81	0.87	-
Kordina [8]	RE2	0.82	0.66	0.42	0.76
	RE3	0.79	0.66	0.63	-
	RE4	1.10	0.85	0.74	-
	RE6	0.96	0.85	0.66	-
	RE7	0.77	0.82	0.62	-
	RE8	1.01	0.96	0.73	-
	RE9	0.80	0.91	0.69	-
	RE10	1.00	1.05	0.83	-

Table 7-11 Results of proposed empirical equations (2/2).

	Specimen	$P_{predict}$ / $P_{measured}$			
		Hegger et al. [15]	Vollum&Newman [24]	Bakir and Boduroğlu[25]	Hassan & Mohele [26]
Scott [11]	ClAL	1.31	1.09	0.91	-
	C3L	1.31	0.99	0.81	-
	c4	1.31	0.84	0.88	-
	C4A	1.25	0.81	0.85	-
	C4AL	1.62	1.06	1.09	-
	C6	1.59	1.01	1.03	-
	C6L	1.40	0.92	0.94	-
	c7	1.17	0.73	0.76	-
	c9	1.57	0.96	0.95	-
Parker & Bullman [13]	4b	1.48	1.45	0.95	1.31
	4c	1.17	1.14	0.74	1.06
	4d	1.36	1.34	0.87	1.16
	4e	1.29	1.27	0.82	1.14
	4f	1.10	1.07	0.70	1.00
	5b	0.85	0.85	0.85	-
	5f	0.94	0.97	0.82	-
Hamil [14]	C4ALN 1	1.20	0.77	0.81	-
	C4ALN3	1.23	0.90	0.86	-
	C4ALN5	1.11	1.11	0.93	-
	C6LNO	1.45	1.14	0.89	0.99
	C6LNI	1.51	1.10	1.02	-
	C6LN3	1.39	1.14	0.97	-
	C6LN5	1.18	1.26	0.88	-
	C6LHO	1.40	1.10	0.88	0.96
	C6LHI	1.35	1.08	0.97	-
	C6LH3	1.20	0.97	0.94	-
Hegger et al [15]	RK4	0.91	0.99	0.67	-
	RK5	1.04	0.84	0.64	-
	RK6	0.89	0.69	0.56	-
	RK7	1.04	1.15	0.76	-
	RK8	1.04	1.23	0.82	-
Sarsam and Phipps [10]	EX2	1.31	1.03	0.77	0.77
Mean		1.16	0.99	0.80	0.96
Standard deviation		0.21	0.17	0.12	0.16

7.4.2 Evaluation of beam-column joint using strut and tie method (STM)

This section assesses the STMs proposed by other researchers and compares the predictions of these models with the experimental results in the author's database. Three strut-and-tie methods were considered in this analysis. These models are explained in the following sections.

7.4.2.1 Hassan and Mohele [26]

This strut-and-tie method was proposed in the same study [26] as the empirical design equation described section 2.3.3.4. The strut geometry depends on the depth of the flexural compression zones in the beam and column which are depicted as " a_b" and " a_c" respectively. The flexural compression depth in the beam and column is calculated using equation (7-1). The coefficient κ in a_b is based on elastic beam sections analysis and its value can be estimated by using equation (7-2).

$$a_b = k\, d_b \text{ and } a_c = \left(0.25 + 0.85\frac{P}{f_c' A_g}\right) h_c \leq 0.4\, h_c \quad (7\text{-}1)$$

$$\kappa = \left[(\rho + \rho')^2 n^2 + 2\left(\rho + \rho'\frac{d_b'}{d_b}\right)n\right]^{1/2} - (\rho + \rho')\, n \quad (7\text{-}2)$$

In which ρ and ρ' represent the ratios of tension and compression steel reinforcement. The depth from centroid of tension and compression steel reinforcement to extreme compression fiber in beam are depicted as d_b and d_b' respectively. The coefficient n is modular ratio. The angle of strut is estimated as follows:

$$\theta = \tan^{-1}\left(\frac{d_b - d_b'}{d_c - d_c'}\right) \quad (7\text{-}3)$$

In which d_c and d_c' are the depths from centroid of tension and compression steel reinforcement to the extreme compression fibre in the column. The strut width is calculated as follows:

$$a_s = a_b cos\theta + a_c sin\theta \quad (7\text{-}4a)$$

$$a_s = \sqrt{a_b^2 + a_b^2} \quad (7\text{-}4b)$$

For simplicity, equation (7-4b) can be used as a close approximation of equation (7-4a). The joint shear strength in horizontal direction then can be calculated from the following expressions:

$$V_j = f_{cu}\, a_s\, b_j\, cos\theta \quad (7\text{-}5)$$

$$f_{cu} = 0.85\beta f_c' \quad (7\text{-}6)$$

As discussed earlier, this method predicts the joint strength of beam-column joints without stirrups. Similarly to the empirical equation discussed in section 7.4.1.4, the method was assessed using the 14 specimens without joint stirrups in the database. The influence of the parameters assessed using this method are shown in Figure 7-44. The predicted failure loads tend to overestimate the measured failure load and the scatter is relatively high. The mean and standard deviation of $P_{predicted}$ / $P_{measured}$ are 1.14 and 0.21 respectively as given in Table 7-12 and Table 7-13. The measured failure load is plotted against the predicted failure load in Figure 7-45.

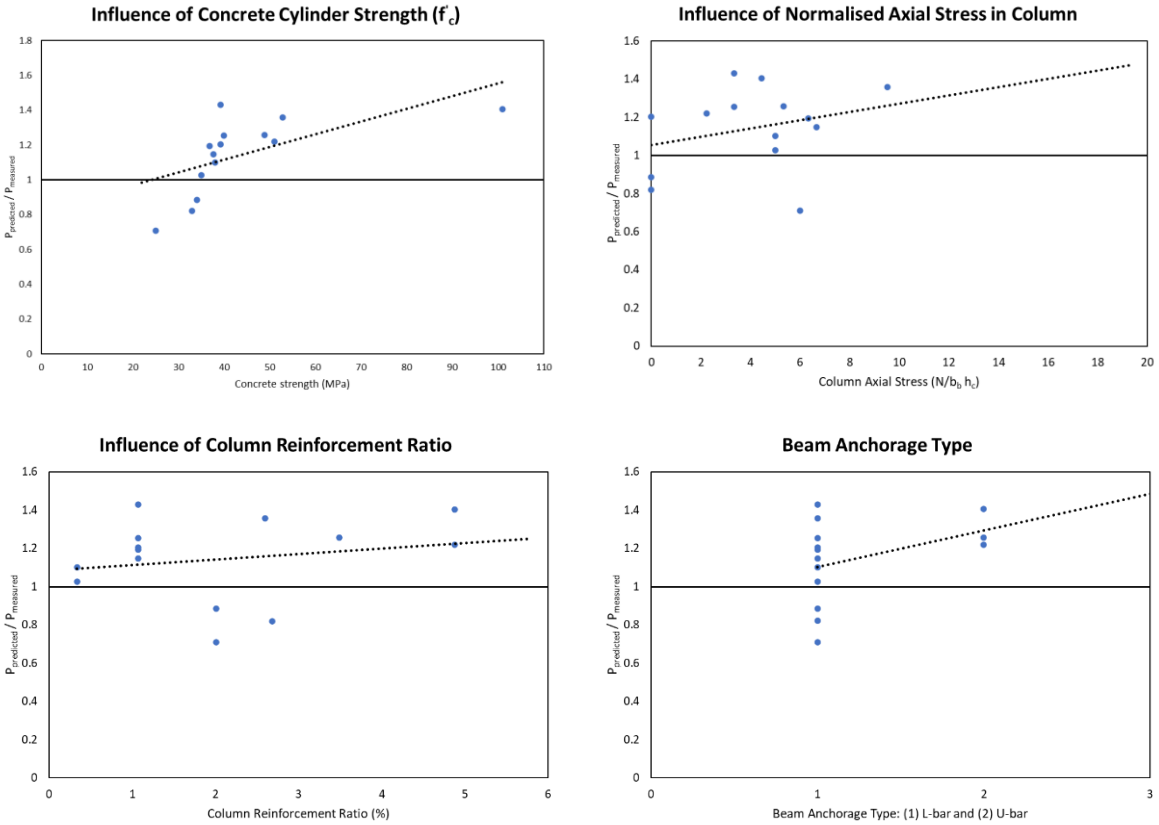

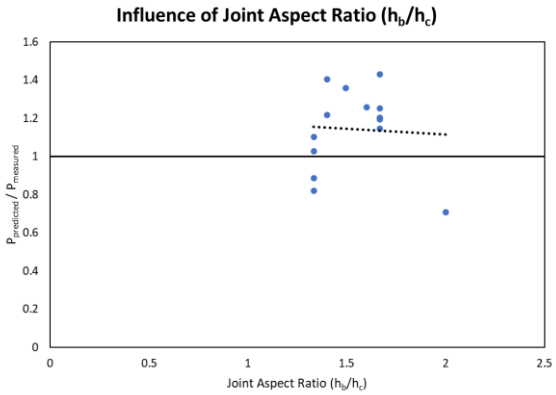

Figure 7-44 Results of STM proposed by Hassan and Mohele [26].

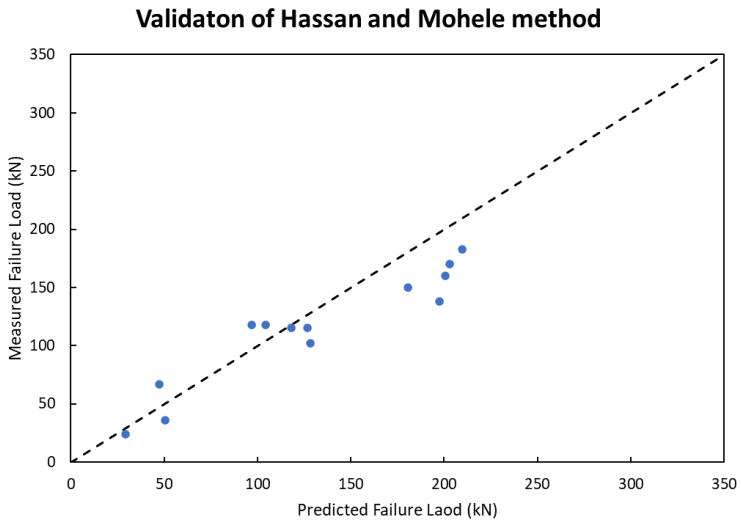

Figure 7-45 Results of measured to predicted failure load of STM for Hassan and Mohele [26].

7.4.2.2 Hwang et al. [38]

Hwang et al. proposed a STM for the design of external beam-column joints which is described in Section 2.4.4.3 of chapter 2. The assessment of the parameters influencing joint strength for this method is shown in Figure 7-46. It can be seen from the results that this method tends to underestimate the joint strength on average. The scatter in the results is also high. The method gives a mean of $P_{predicted}$ / $P_{measured}$ of 0.84 and a standard deviation of 0.25 as presented in Table 7-13 and Table 7-13. The measured failure load is plotted against the predicted failure load in Figure 7-47.

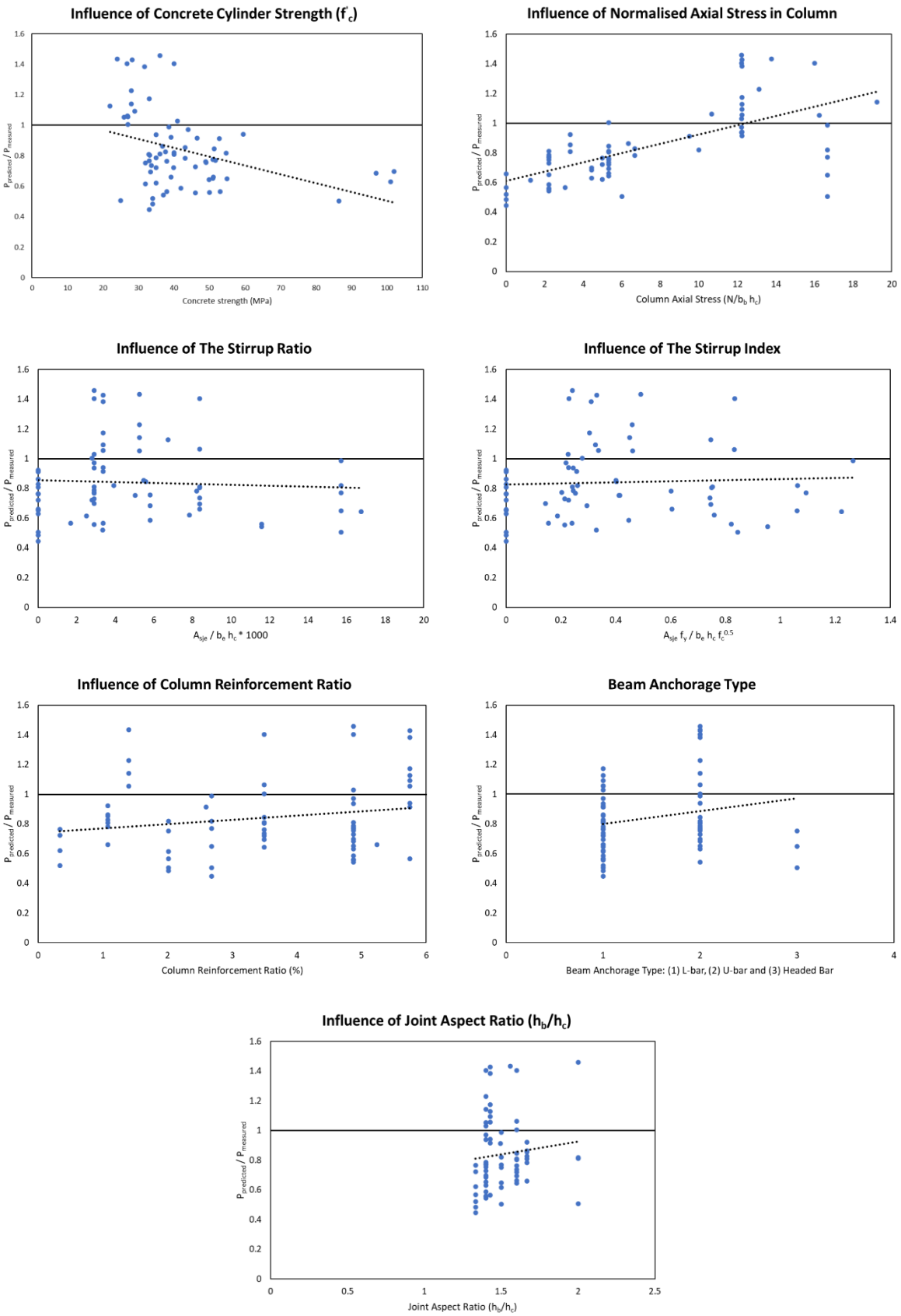

Figure 7-46 Results of STM proposed by Hwang et al [38].

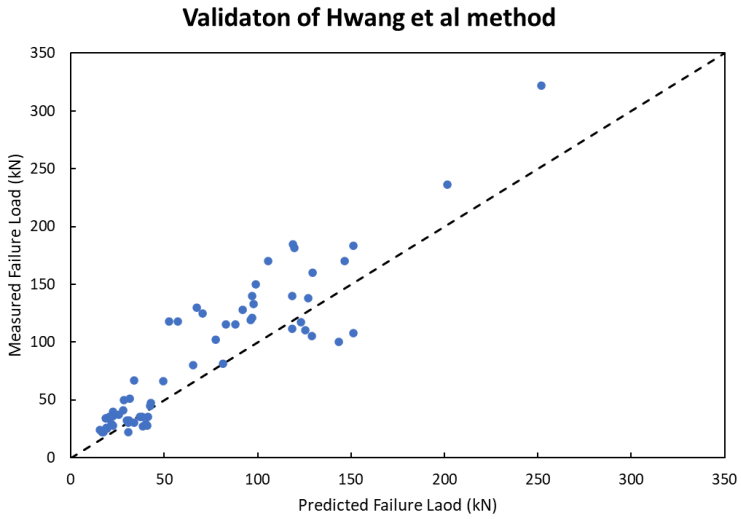

Figure 7-47 Results of measured to predicted failure load of STM for Hwang et al [38].

7.4.2.3 Vollum and Parker [39]

This method, which is described in section 2.4.4.4 from chapter 2, is applicable to joints anchored with L-anchorage bars. Specimens with different anchorage type were excluded from the database and leaving a total of 38 specimens which were used to assess the method. The results of the analysis for this proposed method are shown in Figure 7-48. The method is reasonably accurate with a mean of $P_{predicted}$ / $P_{measured}$ 0.96 and a standard deviation of 0.14 as shown in Table 7-12 and Table 7-13. The measured failure loads are plotted against the predicted failure loads in Figure 7-49.

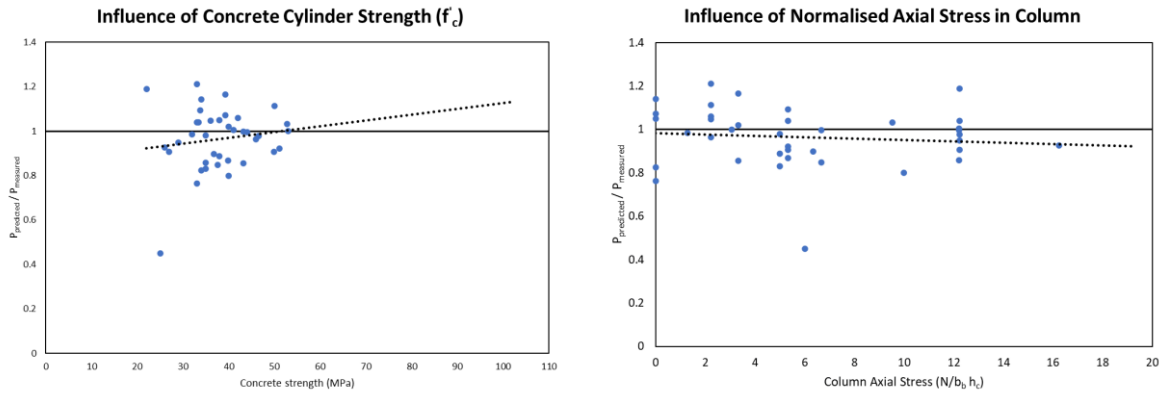

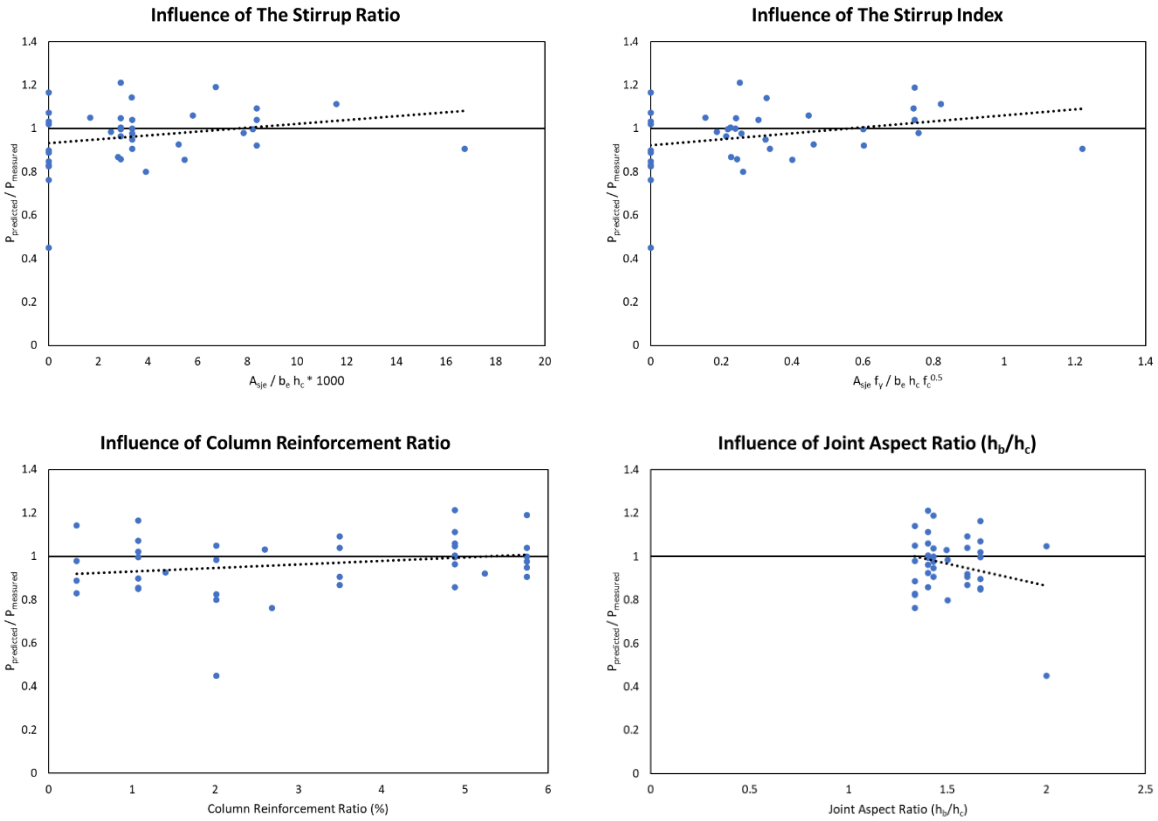

Figure 7-48 Results of STM proposed by Vollum and Parker [39].

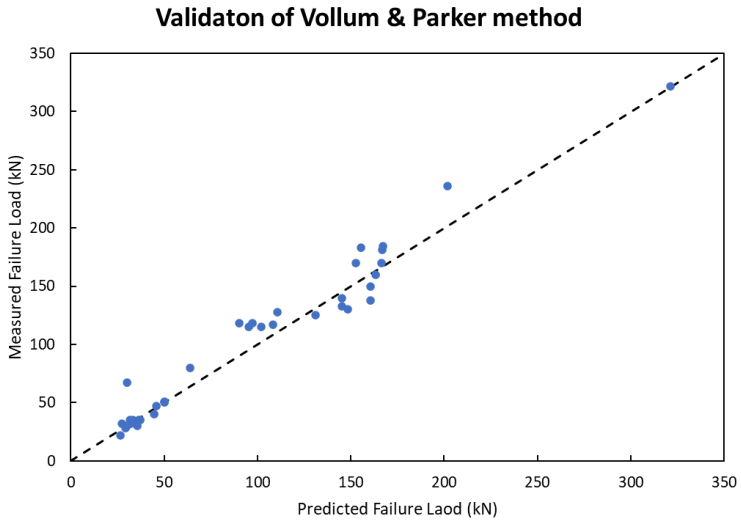

Figure 7-49 Results of measured to predicted failure load of STM for Vollum and Parker [39].

Table 7-12 Results of proposed STMs (1/2).

	Specimen	$P_{predict}$ / $P_{measured}$		
		Hassan & Mohelle [26]	Hwang et al. [38]	Vollum&Parker [39]
Author	BCJ 1	-	0.74	1.09
	BCJ 2	-	0.69	1.04
	BCJ 3	-	0.80	-
	BCJ 4	-	0.81	-
	BCJ5	-	1.00	-
	BCJ6	-	1.06	-
	BCJ 7	-	0.72	0.87
	BCJ8	-	1.40	-
	BCJ 9	-	0.85	-
	BCJ 10	-	0.66	0.92
	BCJ 11	1.26	0.76	-
	BCJ 12	-	0.64	0.91
Ortiz [12]	BCJ 1	0.89	0.48	0.82
	BCJ 2	-	0.57	1.05
	BCJ 3	0.82	0.45	0.76
	BCJ 4	-	0.52	1.14
	BCJ5	1.10	0.76	0.89
	BCJ6	1.03	0.72	0.83
	BCJ 7	-	0.62	0.98
Taylor [5]	P1/41/24	-	1.17	1.04
	P2/41/24	-	1.09	0.95
	P2/41/24A	-	0.91	0.98
	A3/41/24	-	1.06	0.91
	D3/41/24	-	0.56	1.00
	B3/41/24	-	1.13	1.19
	C3/41/24BY	-	1.38	-
	C3/41/13Y	-	1.43	-
	C3/41/24Y	-	0.94	-
Kordina [8]	RE2	0.71	0.50	0.45
	RE3	-	0.82	0.80
	RE4	-	0.61	0.98
	RE6	-	0.75	-
	RE7	-	1.05	0.93
	RE8	-	1.23	-
	RE9	-	1.14	-
	RE10	-	1.43	-

Table 7-13 Results of proposed STMs (2/2).

	Specimen	$P_{predict}$ / $P_{measured}$		
		Hassan & Mohelle [26]	**Hwang et al. [38]**	**Vollum&Parker [39]**
Scott [11]	ClAL	-	0.77	1.21
	C3L	-	0.79	-
	c4	-	1.03	1.00
	C4A	-	0.97	1.00
	C4AL	-	0.81	1.05
	C6	-	1.40	-
	C6L	-	0.73	-
	c7	-	0.94	0.86
	c9	-	1.46	-
Parker & Bullman [13]	4b	1.43	0.92	1.16
	4c	1.19	0.86	0.90
	4d	1.20	0.66	1.07
	4e	1.25	0.81	1.02
	4f	1.15	0.83	0.85
	5b	-	0.85	0.85
	5f	-	0.78	1.00
Hamil [14]	C4ALN 1	-	0.56	0.96
	C4ALN3	-	0.59	1.06
	C4ALN5	-	0.56	1.11
	C6LNO	1.22	0.65	-
	C6LNI	-	0.77	-
	C6LN3	-	0.75	-
	C6LN5	-	0.54	-
	C6LHO	1.40	0.63	-
	C6LHI	-	0.70	-
	C6LH3	-	0.68	-
Hegger et al [15]	RK4	-	0.77	-
	RK5	-	0.65	-
	RK6	-	0.50	-
	RK7	-	0.82	-
	RK8	-	0.99	-
Sarsam and Phipps [10]	EX2	1.36	0.91	1.03
Mean		1.14	0.84	0.96
Standard deviation		0.21	0.25	0.14

7.5 Strut geometry of findings of DIC, 2D-NLFEA, section analysis and STM

The strut geometry was determined based on the findings of joint surface strain from DIC, 2D NLFEA and section analysis using stress-block factors as well as the results of proposed STM. The findings of DIC, 2D NLFEA and section analysis for producing the strut dimensions are described in one section while the strut geometry produced from the proposed STM is presented in another section.

7.5.1 Strut geometry from the findings of DIC, 2D NLFEA and section analysis

The twelve specimens tested in this research were used to obtain the strut geometry using the measured surface strain from DIC and 2D NLFEA as well as the section analysis carried out in chapter 6. The strut geometry was assumed to be defined by the width of the flexural compressive zones in the beam and columns. The results of this analysis are shown in Figure 7-50, Figure 7-51 and Figure 7-52. The diagonal lines at angle (θ) in these figures are included to show the strut angle. The lower of the two diagonal lines is not intended to define the geometry of the top node. The strut width from DIC was larger than the other two methods. All methods showed an increase of strut angle and flexural compression depth around joint boundaries when column axial load increased as in specimens BCJ 6 and BCJ 8. Overall, the difference of strut angle was small when all methods compared with each other in specimens with column load of 300 kN. The DIC gave a much greater beam flexural compression zone depth for BCJ 11 than obtained with the other methods. This may be due the formation of a vertical crack in the joint as discussed in chapter 4.

7.5.2 Strut geometry from proposed strut-and-tie methods

The strut dimensions were determined based on the proposed existing STM discussed in section 7.4.2. The twelve specimens tested in this thesis were used to produce the strut geometry. Due to the limitation of Vollum & Parker [39] and Hassan & Moehle [26], a few specimens were used for obtaining the strut geometry including BCJ 1, BCJ 2, BCJ 7, BCJ 10 and BCJ 12 for Parker & Vollum method while only BCJ 11 was used in Hassan & Moehle method. The results of this analysis are shown in Figure 7-53, Figure 7-54 and Figure 7-55. The angle (θ) of the strut geometry was added in the figures to show the strut angle as indicated above. The Vollum and Parker method assumes a uniform width of half the column depth for the flexural compressive zone in the upper and lower column. This is done to make the failure load independent of column load. The method also reduces the width of the direct strut as

the joint shear reinforcement is increased. This refinement is not accounted for in the figures next pages. The strut width was smaller in Hwang et al [38] method when compared with other two methods and that due to small flexural compression depth around the joints.

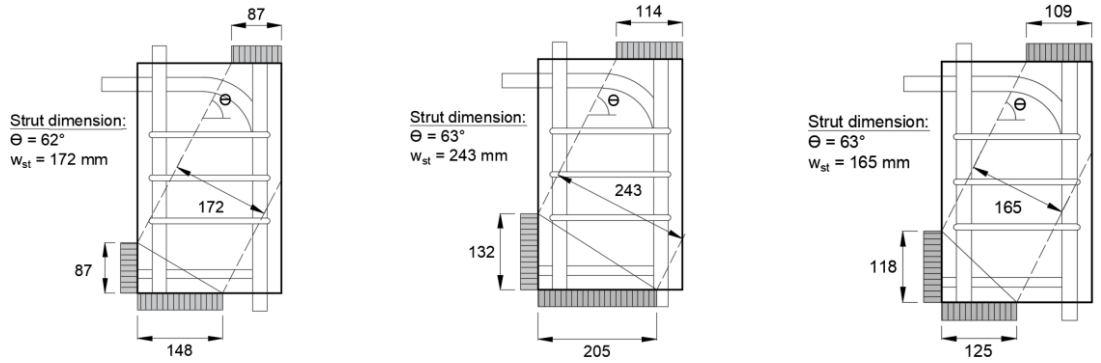

2D-NLFEA DIC Section analysis

a) Strut geometry for specimen BCJ 1

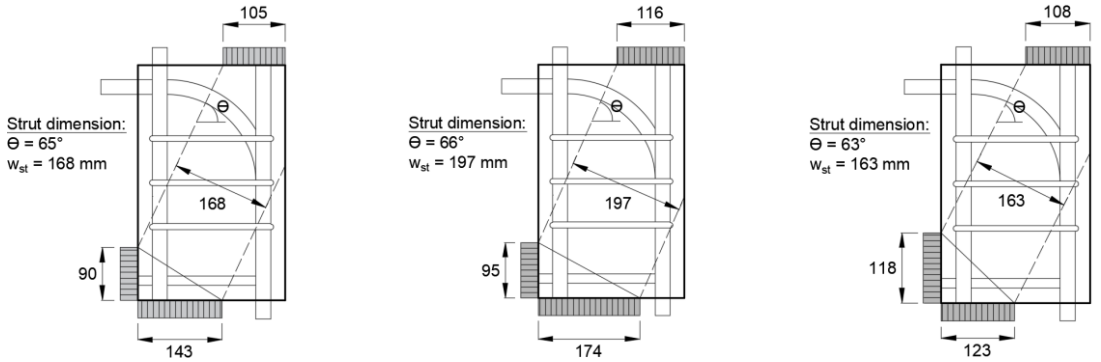

2D-NLFEA DIC Section analysis

b) Strut geometry for specimen BCJ 2

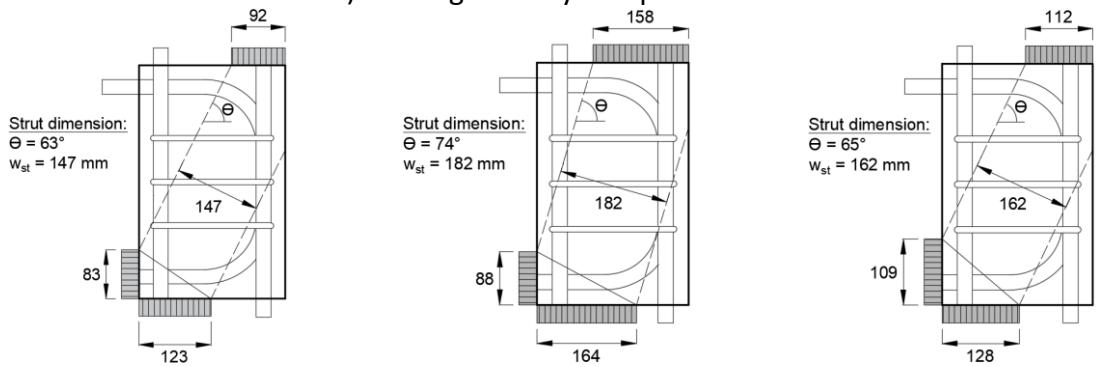

2D-NLFEA DIC Section analysis

c) Strut geometry for specimen BCJ 3

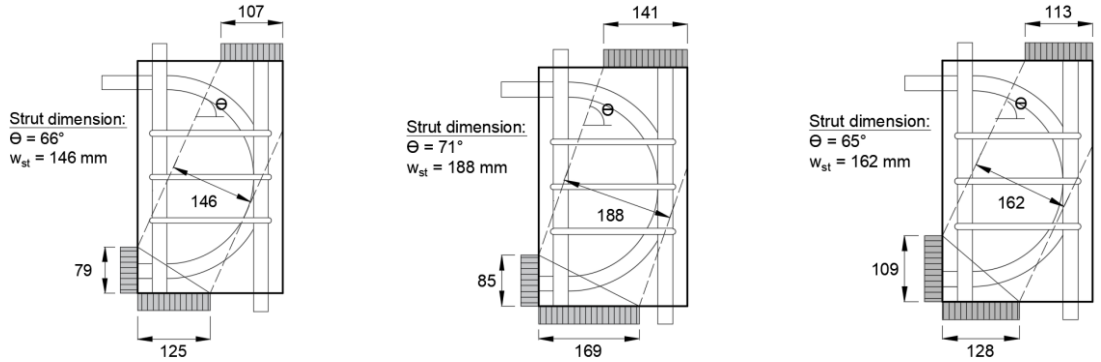

2D-NLFEA DIC Section analysis

d) Strut geometry for specimen BCJ 4

Figure 7-50 Strut geometry from the findings of DIC, 2D NLFEA and section analysis; specimens in series 1.

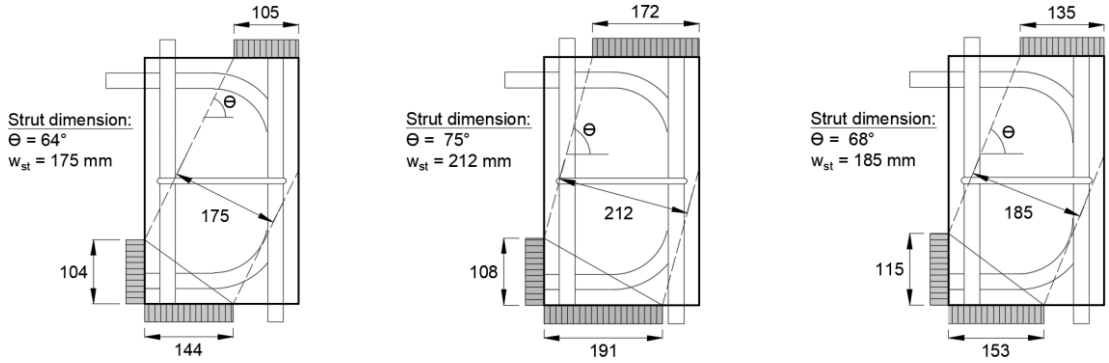

2D-NLFEA DIC Section analysis

a) Strut geometry for specimen BCJ 5

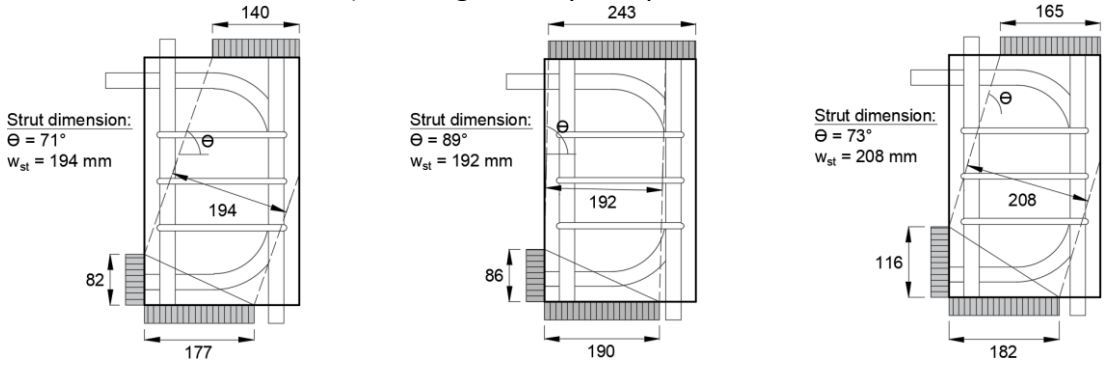

2D-NLFEA DIC Section analysis

b) Strut geometry for specimen BCJ 6

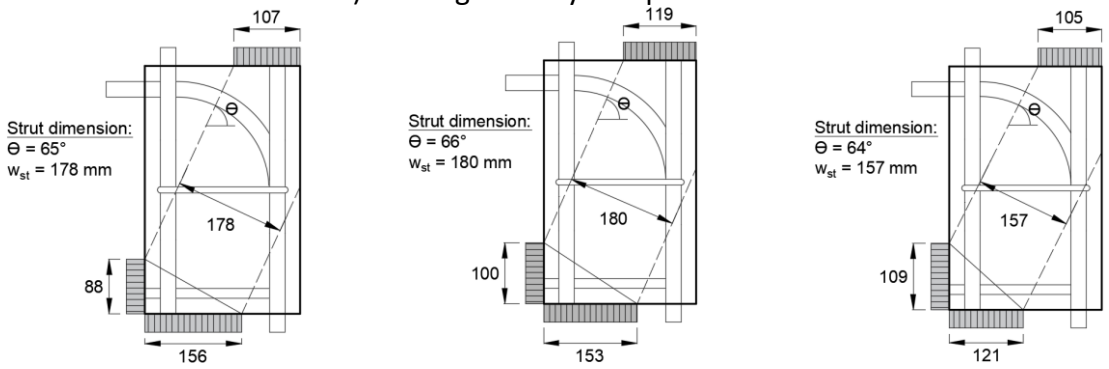

2D-NLFEA DIC Section analysis

c) Strut geometry for specimen BCJ 7

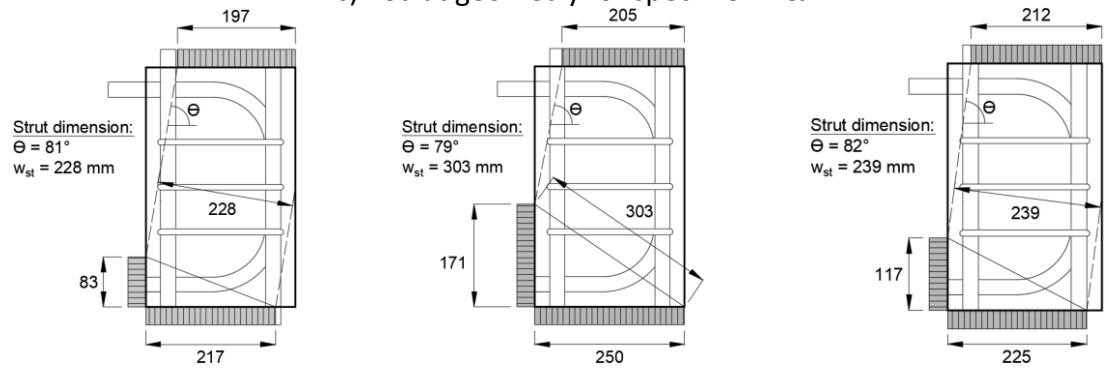

2D-NLFEA DIC Section analysis

d) Strut geometry for specimen BCJ 8

Figure 7-51 Strut geometry from the findings of DIC, 2D NLFEA and section analysis; specimens in series 2.

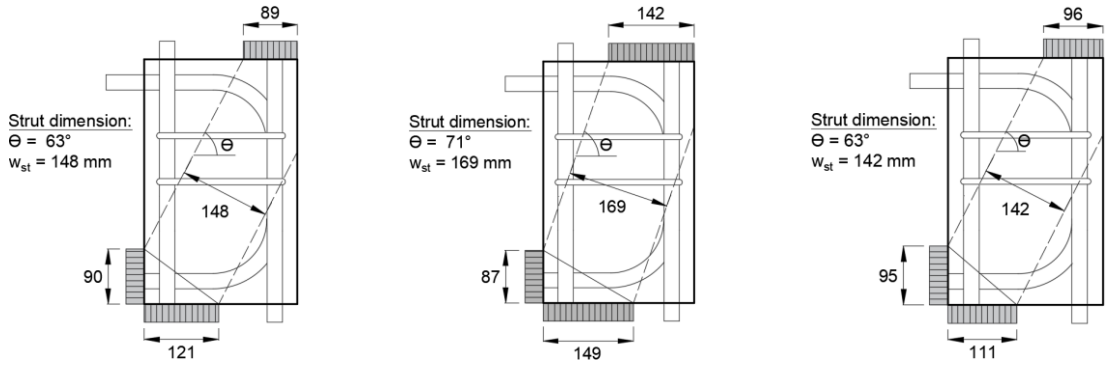

2D-NLFEA DIC Section analysis

a) Strut geometry for specimen BCJ 9

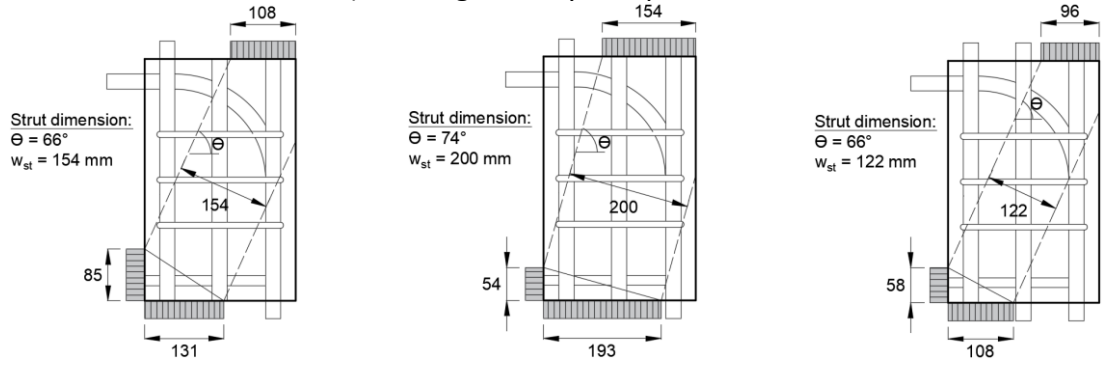

2D-NLFEA DIC Section analysis

b) Strut geometry for specimen BCJ 10

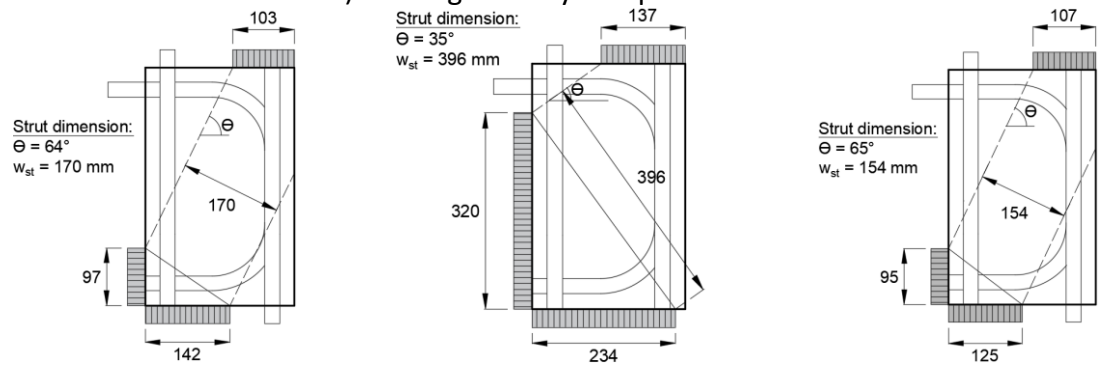

2D-NLFEA DIC Section analysis

c) Strut geometry for specimen BCJ 11

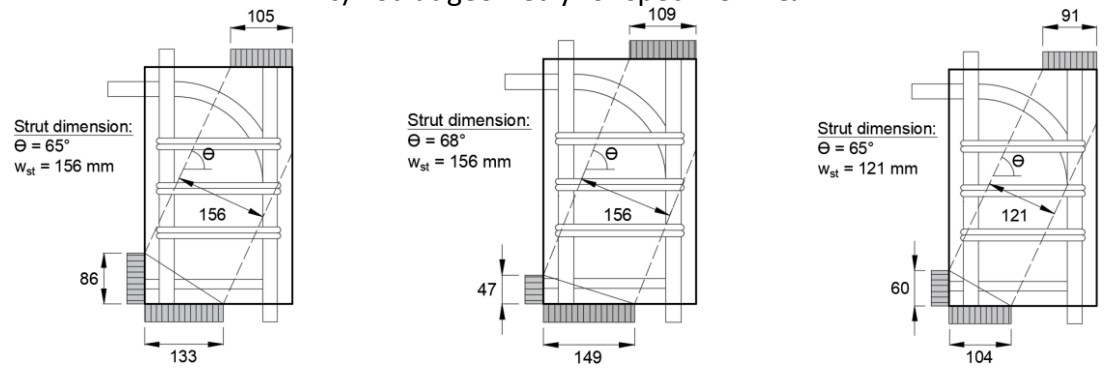

2D-NLFEA DIC Section analysis

d) Strut geometry for specimen BCJ 12

Figure 7-52 Strut geometry from the findings of DIC, 2D NLFEA and section analysis; specimens in series 3.

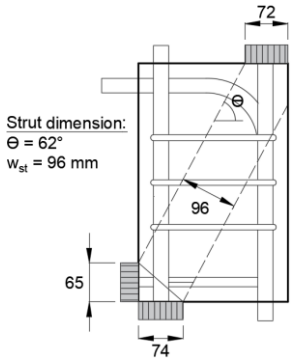

Hwang et al. method

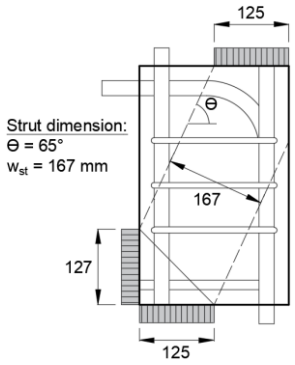

Vollum & Parker method

a) Strut geometry for specimen BCJ 1

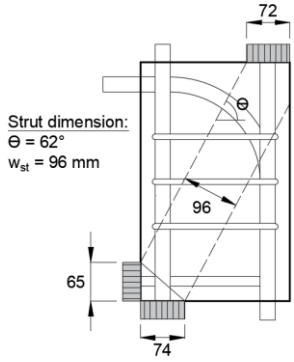

Hwang et al. method

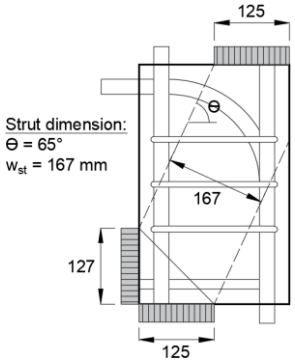

Vollum & Parker method

b) Strut geometry for specimen BCJ 2

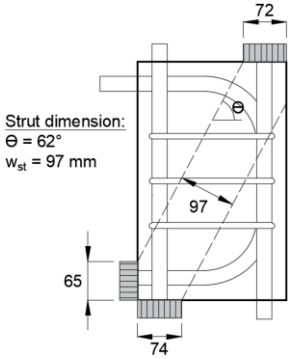

Hwang et al. method

c) Strut geometry for specimen BCJ 3

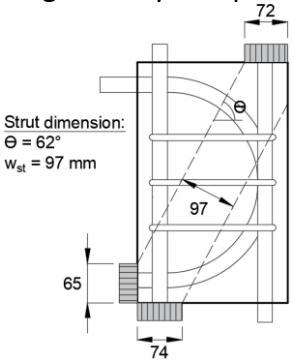

Hwang et al. method

d) Strut geometry for specimen BCJ 4

Figure 7-53 Strut geometry from the findings of STM; specimens in series 1.

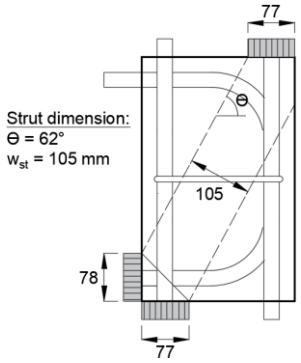

Hwang et al. method

a) Strut geometry for specimen BCJ 5

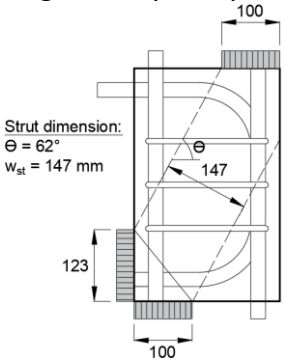

Hwang et al. method

b) Strut geometry for specimen BCJ 6

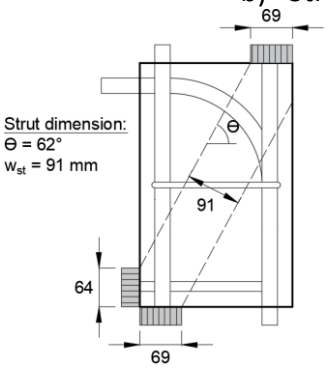

Hwang et al. method

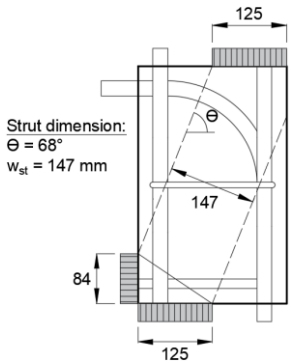

Vollum & Parker method

c) Strut geometry for specimen BCJ 7

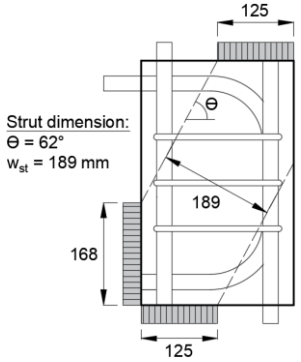

Hwang et al. method

d) Strut geometry for specimen BCJ 8

Figure 7-54 Strut geometry from the findings of STM; specimens in series 2.

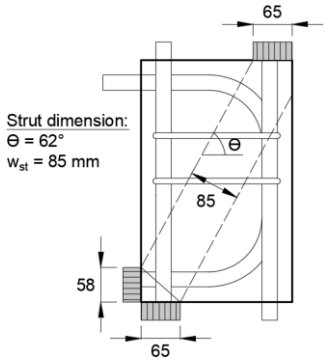

Hwang et al. method

a) Strut geometry for specimen BCJ 9

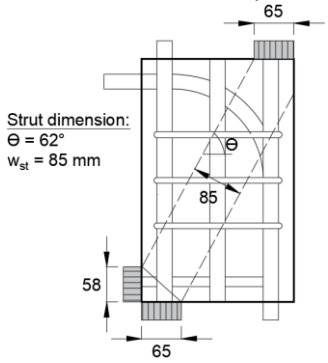

Hwang et al. method

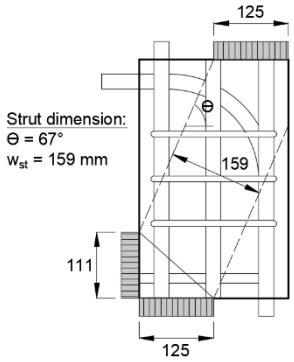

Vollum & Parker method

b) Strut geometry for specimen BCJ 10

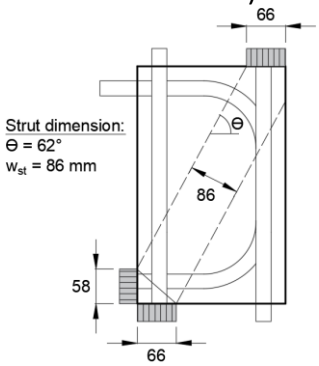

Hwang et al. method

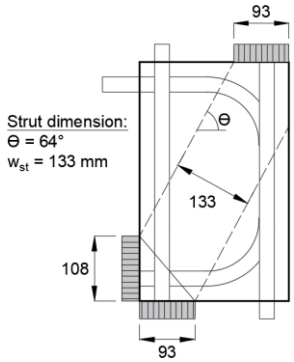

Hassan & Moehle method

c) Strut geometry for specimen BCJ 11

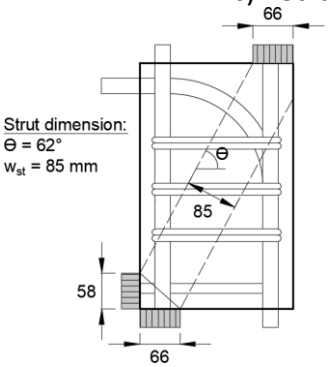

Hwang et al. method

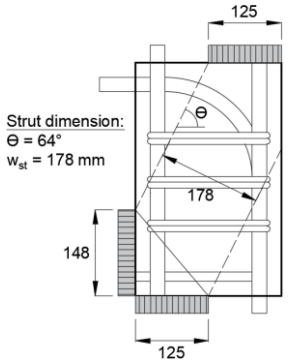

Vollum & Parker method

d) Strut geometry for specimen BCJ 12

Figure 7-55 Strut geometry from the findings of STM; specimens in series 3.

7.6 Evaluation of the considered empirical equations and STMs

The results of the considered existing empirical design equations and STM are evaluated in this section. The Vollum and Newman [24] empirical equation gave better predictions of joint strength than the other methods. The method was able to capture the influences of concrete strength, joint stirrup ratio and index, anchorage reinforcement type and column reinforcement ratio. For proposed STM, the results of Hassan & Mohele [26] and Vollum & Parker [39] methods showed good agreement with $P_{measured}/P_{predicted}$. However, these methods need to be re-evaluated for purposes of design. To assess the results of proposed methods, the demerit point classification system proposed by Collins [76] was used to validate each method in regard for designing external beam-column joints. This approach is used to assign marks (DP: Demerit Point) to each range of P_{test}/P_{pred} to penalize the proposed existing methods. After that, the number of specimens within a specific range are summed for each proposed method to calculate the total demerit point that is determined by summing the products of the percentage of specimens within each range of P_{test}/P_{pred} by the demerit point (DP) assigned for that specific range. This process was applied on the proposed existing methods for both empirical equations and STM as presented in Table 7-14. The range of 0.85-1.30 is considered appropriate and had demerit point of zero. Specimens outside that range were penalized with different demerit points as given in Table 7-14. The total demerit point of each proposed method is also shown in Figure 7-46. The low score of total demerit point indicates better methods for design. It can be seen from this analysis that Vollum & Newman [24] had lower score of total demerit point than Bakir and Boduroğlu [25] method and Hegger et al. [15] method. The empirical equation proposed by Hassan & Mohele [26] has also lower total demerit point than the other models but this method accounts for only specimens without shear reinforcement. For STM, the methods of Hassan & Mohele [26] and Vollum & Parker [39] showed lower total demerit point when compared with the remaining method but these methods are limited for specimens without joint stirrups and L-anchorage bar respectively. Additionally, Hwang et al [38] method had large number of specimens within a range of 0.85 to 2.0 showing appropriate to extremely conservative results but large score of total demerit point was observed indicating the unsuitability of the method for design.

Table 7-14 Demerit point classification of proposed methods

			Empirical equations				STM		
P_{test}/P_{pred}	Joint aspect ratio (1.3-2.0)	DP	Hegger et al. [15]	Vollum & Newma-n [24]	Bakir & Bodur-oğlu [25]	Hassan & Mohel-e [26]	Vollum & Parker [39]	Hwang et al. [38]	Hassan & Mohel-e [26]
<0.5	Extremely dangerous	10	0	0	0	0	0	0	0
0.5-0.65	Dangerous	5	4	0	0	0	0	0	0
0.65-0.85	Low safety	2	26	9	0	1	2	7	7
0.85-1.30	Appropriate safety	0	37	52	36	10	34	30	5
1.30-2.00	Conservative	1	1	7	31	3	1	29	1
>2.00	Extremely conservative	2	0	0	1	0	1	2	0
TOTAL DP			73	25	33	5	7	47	15

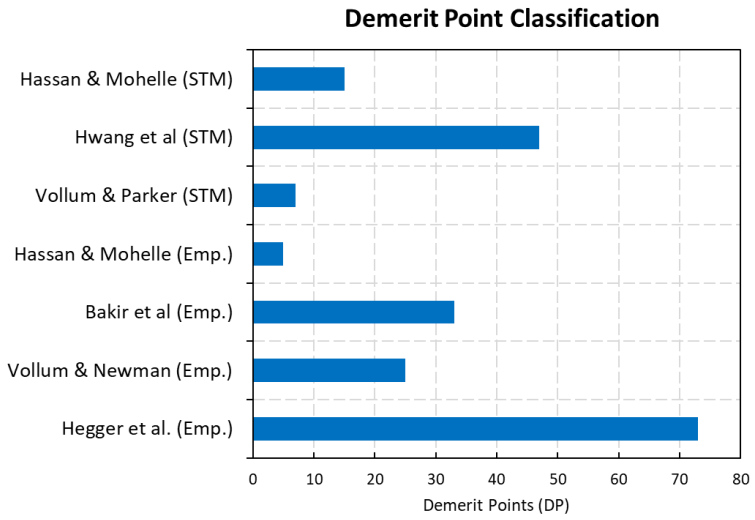

Figure 7-56 Demerit point classification of external beam-column joints for different design methods.

7.7 Summary

This chapter assesses the ability of the proposed 2D and 3D NLFEA modelling procedures to simulate reinforcement and concrete surface strains measured in the author's tested specimens. Measured and predicted reinforcement strains are compared in the joint and at the joint boundaries for both the 2D and 3D NLFEA models. Comparisons are also made between measured and 2D NLFEA concrete surface strains normal to the joint boundaries and along the diagonal strut. A study is made of the influences on these strains of detailing of beam reinforcement, column axial load and number of joint stirrups.

The chapter also assesses the accuracy of various previously developed empirical and STM design models for external beam-column joints using a database of 68 test results. Comparisons are made between the diagonal strut geometry of each specimen tested in this campaign obtained with DIC, 2D NLFEA, section analysis and STM. Finally, the strength predictions from the considered design models are evaluated using the demerit point classification system of Collins [76]. The key conclusions and observations from this chapter are as follows:

- The predicted 2D and 3D NLFEA strains in the beam anchorage bar, column bars and joint stirrups were compared with the measured strains. Typically, the measured and predicted strains from both 2D and 3D models compare well for the beam anchorage bars with predictions best for series 1 and 3. The measured and predicted column bar strains also compare well for both the 2D and 3D models. The measured and predicted joint stirrups strains are comparable for series 1 but the comparison is less good for series 2 and 3 where a significant number of gauges failed. Overall, the results show that both the 2D and 3D NLFEA were able to broadly capture the strain distribution in the reinforcement.
- The surface strain was obtained at the joint boundaries and parallel to the diagonal strut using DIC and 2D-NLFEA. Good agreement was obtained between measured and predicted strains particularly at the bottom of the joint. A good match was also obtained between the neutral axis depths obtained with DIC and 2D NLFEA. The strain in the diagonal strut was studied using two rows of virtual gauges centred on the strut. The magnitude of measured and predicted peak strains compared favourably in the top row of virtual DEMECS, closest to the bend in the beam reinforcement, but the measured shape of the strain distribution was not always well captured. Better comparison of measured and predicted strains was obtained in the second row of gauges. Overall, the 2D NLFEA was able to reasonably capture the strain distributions measured in the reinforcement and the concrete even though the strength predictions were less good than for the 3D NLFEA.
- A study was made of the influence of the parameters studied in this research on the surface distribution. The results show that the 2D NLFEA is broadly able to capture the

influence of column axial load on strain and strain distributions in specimens with varying number of joint stirrups for both L-bar and U-bar beam anchorage detail.

- Various existing empirical design equations and STM were evaluated using a database of 68 specimens made up of 56 previously tested specimens and 12 of the author. The considered empirical design methods were those of Vollum & Newman [24], Bakir and Boduroğlu [25], Hassan & Moehle [26] and Hegger et al. [15]. The Vollum & Newman [24] method was found to be the best of these methods. The strut and tie methods of Hassan & Moehle [26], Vollum and Parker [39]and Hwang et al. [38] were considered. Of these, Vollum & Parker [39] performed best but is limited to joints with L-anchorage bars.
- The strut geometry was estimated in terms of the depths of the flexural compressive stress blocks in the beam and column determined with DIC, 2D NLFEA and section analysis. These widths were compared with each other as well as the widths adopted in the considered STM. The resulting strut width obtained with DIC was larger than obtained with 2D NLFEA and section analysis.
- The accuracy of the considered design methods was evaluated using the demerit point classification system proposed by Collins [76]. In this assessment method, points are allocated according to the level of safety of the strength prediction with the best method being that with the lowest total demerit point score. The method of Hassan & Moehle [26] is of limited application since it does not consider the effect of joint stirrups. Of the methods that include joint stirrups, the lowest demerit score was 25 for the Vollum and Newman method. The largest total demerit point score of 73 was obtained for Hegger et al. [15]. Of the STM methods, Vollum and Parker had the lowest demerit score of 7 but this only includes the 38 specimens with L-bars. Overall, the empirical methods are easiest to apply and seem most practical for design even though not based on mechanical models. The Vollum and Newman method is recommended for practical design based on it having the lowest demerit score of the considered empirical design methods. However, the proposed NLFEA modelling procedures give useful insights into the influence of key variables on joint shear strength.

Chapter 8: Conclusions and future work

This chapter provides a summary of the research, highlights key conclusions and provides recommendations for further work.

8.1 Introduction

This thesis is concerned with the design and behaviour of external beam-column joints subjected to monotonic loading. Transfer of the beam end moment into the upper and lower columns causes shear force to develop in the joint. The joint shear force is given by the difference between the tensile force in the beam flexural reinforcement and the shear force in the upper column. The joint shear force is very high compared with that in the columns and can be sufficient to cause diagonal joint cracking and even joint failure. The joint shear strength is enhanced by the provision of horizontal links and vertical reinforcement bars within the joint. Considerable research has been carried out into seismically loaded beam-column connections but experimental studies into the behaviour of monotonically loaded beam-column joints are much fewer. Previous studies of beam-column joints tend to focus on joint strength with little or no information reported on specimen deformation which is required for the validation of nonlinear finite element models. Information on joint stiffness is also needed for assessment of moment redistribution from the column into the span following joint cracking. Furthermore, little attention has been given to the study of shear transfer mechanisms in cracked beam-column joints. The research methodology involves assessment of existing test data, nonlinear finite element modelling, laboratory testing and assessment of various existing design methods for determining joint shear strength. The main parameters investigated in this work are the column load, beam bend radius and anchorage type, joint shear reinforcement and intermediate column bars to study the effect on joint strength. This chapter summarises this research by providing key conclusions, design recommendations and suggested further work.

8.2 Background Overview

Shear in monotonically loaded beam-column connections has been studied for many years but very limited attention has been given to joint deformation and its influence on frame behaviour. The literature review in Chapter 2 provides key conclusions and observations

relevant to this thesis and describes the gaps in the literature, which are summarised as follows:

- The literature reports two main mechanisms for transferring shear force through joints. In the absence of joint shear reinforcement, shear is resisted by an inclined compressive strut. In the presence of shear reinforcement, a secondary truss mechanism also develops in which an inclined compressive stress field is equilibrated by horizontal joint stirrups and if present intermediate column bars.
- Joint shear strength is enhanced by the provision of horizontal and vertical joint reinforcement (stirrups and intermediate column bars). The joint shear strength increases in proportion with the shear reinforcement ratio up to a limiting strength which depends on the joint geometry and concrete strength.
- The application of high column axial load plays a crucial role in improving joint behaviour and can change the failure mode from beam and upper column flexure to joint shear failure. However, the influence of column load on joint strength is less clear with some studies finding joint shear strength to increase and others to reduce with increasing column axial load.
- The bend radius influences the bearing stresses inside the bend of the beam reinforcement, by reducing the bearing stresses when bend radius is increased. The influence of bend radius on joint shear strength is unclear and is investigated further in this thesis.
- Various models for calculating shear force transferred through aggregate interlock are reviewed. Of these, the physically based models of Walraven [41] and Li et al. [42] are derived from considerations of contact area during shear displacement. The other considered models are the empirically based models of Hamadi and Regan [44], Bazant and Gambarova [45] and Gambarova and Karakoc [46].
- The Sigrist model [49] for determining reinforcement stress in terms of crack width is summarised in detail along with the formulae used in this model.
- Design standards like ACI 318 and EC2 do not give comprehensive design methods for beam-column joints under monotonic loading. ACI 318 gives guidance on designing beam-column joints but the influence of key variables influencing joint behaviour is

neglected. EC2 gives no guidance apart from the very diagrammatic strut and tie models presented in Annex J which is informative and not adopted in the UK.

- The maximum tensile force that can be developed in the beam bar anchorage tends to be underestimated by code provisions for anchorage unless the anchorage is designed for bar yield. In framed structures, this can result in the maximum joint shear stress being underestimated if limited by beam bar anchorage.
- The lack of reporting load-displacement curves for previous tests on beam-column joints prevents accurate assessment of NLFEA models.
- The literature review describes the procedure adopted for using Digital Image Correlation (DIC) to estimate the crack displacements within the joint. Further details are given in Chapter 3.
- Previous experimental investigations into the behaviour of monotonically loaded external beam-column joints provide no detailed information about shear transfer through aggregate interlock in beam-column joints.

8.3 Description of the Experimental Program and Summary of the Test Results

Twelve geometrically identical beam-column joint specimens were tested in the Heavy Structures Laboratory at Imperial College London. The column of each specimen measured 2300 mm long by 250 mm deep by 225 mm wide. The beam measured 1300 mm long by 400 mm deep by 225 mm wide. The beam-column joint specimens were tested in three groups of four. Series 1 was designed to study the influence of the beam anchorage type and bend radius in the joint. Series 2 studies the effect of varying the column axial load on the joint failure mode and strength. Series 3 investigates the influence of joint shear reinforcement and intermediate column bars.

The beams were cast in three batches of four using ready-mixed concrete with strength C30/37 and maximum coarse aggregate size of 10 mm. Specimen BCJ 7 of series 2 was cast from laboratory batched concrete having a nominal strength of C40/50 subsequent to casting series 3. This specimen was a replacement of a specimen failed during application of the upper column load due to a testing rig malfunction. Forty-two control specimens, comprising cubes and cylinders, were cast to obtain the compressive and tensile strength of concrete in each series. Eighteen cubes (100 x 100 x 100 mm), twelve cylinders (100 x 150 mm) and twelve

cylinders (150 x 300 mm) were cast with each batch. Half the specimens were cured in water and the rest were cured in air.

The experimental results of the tested specimens are presented in terms of failure modes and crack patterns, load-deflection response, joint and beam rotation, crack kinematics and reinforcement strain. The tested specimens were loaded in displacement control to capture the post-failure response. Detailed measurements of displacements and crack kinematics were determined by means of Digital Image Correlation (DIC). To measure the horizontal and vertical displacements, transducers and LVDTs are used in the experimental program. Reinforcement strains were measured using 20 strain gauges at selected locations on the beam anchorage bars, column bars and joint stirrups.

BCJ series 1 provides information on the influence of beam anchorage type and bend radius on joint behaviour. The beam tension bars were anchored into the column with L-anchorage or U-anchorage bars. The bend radius used in tests was either standard (3.5ϕ) or large (6ϕ) according to EC2 [23]. The experimental results show that L-anchorage type enhanced the joint shear strength considerably when compared to U-anchorage type. Use of a large radius bend increased the joint strength of specimens with L-bars but not U-bars where the best results were obtained with standard bend radius.

BCJ series 2 investigates the influence of column axial load and joint stirrup on joint strength. Upper column loads of 300 kN, 600 kN and 900 kN were considered. These loads were applied at the beginning of the test and maintained constant during the test. The results of this series show that increasing the column load from 300 kN to 900 kN increased the load at first diagonal cracking but had minimal influence on joint shear strength in specimens with both one and three joint stirrups. As expected, increasing the number of joint stirrups increased joint shear strength.

BCJ series 3 studies the effect of intermediate column bars and increasing the number of joint stirrups. The experimental results of this series showed that the provision of intermediate column bars significantly increased joint shear strength and changed the failure mode from joint shear to beam flexure. Doubling the joint shear reinforcement from three to six joint stirrups, without intermediate column bars, significantly improved the joint response and

changed the failure mode from joint shear to flexure. Furthermore, the absence of joint shear reinforcement reduced the first diagonal cracking load and failure load.

8.4 Analysis of the Results and Shear Transfer Actions

This thesis carried out a detailed analysis of shear transfer actions within external beam-column joints for the first time. The study determined the forces acting on a free body defined by the joint boundaries and the dominant shear crack at failure. The considered forces are those in the reinforcement and concrete at the joint boundaries with the beam and column as well as the forces acting on the dominant shear crack. The latter include aggregate interlock and tensile forces in the stirrups and beam flexural reinforcement. This study focussed on the horizontal shear transfer mechanism since this directly controls the joint shear resistance.

A free body diagram was produced for each specimen to investigate shear transfer mechanisms within the joint. DIC was used to obtain the contributions of aggregate interlock and joint stirrups in terms of the opening and sliding displacements of the critical shear crack. An investigation was carried out to study the influence of the parameters varied in the experimental tests on crack kinematics and shear transfer actions for each specimen. These parameters include anchorage type and bend radius, joint shear reinforcement, column axial load and column intermediate bars. The investigation showed that the crack opening and sliding was influenced significantly by these parameters.

The free body diagrams produced for each specimen identified the horizontal forces acting on the critical diagonal shear crack. The free body diagrams indicate the internal forces (total joint stirrups force, horizontal aggregate interlock resultant force and beam bend bar resultant force in horizontal direction) and external forces (column shear force and beam anchorage bar tensile force) acting on the joint.

The contribution of aggregate interlock was obtained using the four models described in the literature review. These models are two-phase model of Walraven [41], the Hamadi and Regan method [44], the rough crack model (Bazant and Gambarova [45] & Gambarova and Karakoc [46]) and the simplified contact density method of Li et al. [42]. The contribution of aggregate interlock varied between models but was small in all cases relative to the joint shear force particularly at failure. The Gambarova and Karakoc model was used for determining the relative contributions of each shear transfer action.

Section analysis using the stress-block factors proposed by Collins and Mitchell [33] was carried out to determine the flexural forces at the joint boundaries. The calculated reinforcement strains typically compared well with the strain gauges measurements. However, in a few cases the signs of the measured and predicted strains were switched. Examples of this are the external column bars of BCJ 5 and BCJ 11 where the measured strains at the top of the joint were tensile but predicted to be compressive. The unexpected tensile strain appears to have occurred due to loss of bond resulting from spalling of cover at the back face of the column.

The Sigrist two-step bond model [49] was used to calculate the strain, and hence the force, in the stirrups at the intersection with the critical shear crack. In this method, the reinforcement strain is calculated in terms of the crack width which was determined using DIC. The resultant contribution of the joint stirrups was obtained by summing the contributions of all the stirrups in the joint ($\sum \mathrm{T_{stirrup}}$).

The force in the bend of the beam tension bar at the intersection with the critical shear crack was determined from strains measured at the gauges placed around the bend. The horizontal component of force in the beam bar at the intersection with the shear crack ($T_{b,hor}$) was obtained by resolution of forces assuming no change in geometry of the bend. The resultant horizontal contribution of the concrete compression zone (C_b-C_{comp}) was calculated from equilibrium. This component represents the total horizontal force required for equilibrium that is not accounted for by tension in the stirrups, tension in the beam bar and aggregate interlock.

The relative contributions of each shear action were plotted against the proportion of joint shear force applied for each test. The graphs show that the contribution of aggregate interlock was minimal at joint shear failure. Significant contributions to horizontal equilibrium were made by the beam bend bar force in several specimens. Joint stirrups also made a significant contribution to joint shear strength. The compression zone contribution (C_b-C_{comp}) varied significantly between specimens dependent on their detailing. The relative contribution of (C_b-C_{comp}) was reduced by use of L-bars (BCJ 1, BCJ 2, BCJ 7, BCJ 10 and BCJ 12) and increasing the number of joint stirrups (typically 3 stirrups apart from BCJ 11; no stirrups, BCJ 5 and BCJ 7; 2 stirrups, BCJ 12: 6 stirrups).

8.5 Design Observations and Recommendations

Chapter 7 compares the experimentally determined reinforcement and concrete surface strains with those determined using NLFEA. The reinforcement strains are compared in the joint and at the joint boundaries for both the 2D and 3D NLFEA models following the strain gauges positions in tested specimens as discussed in chapter 3. The concrete surface strains were studied at positions normal to the joint boundaries and along the diagonal strut where comparisons were made between measured and 2D NLFEA. Additionally, a study is made of the influences on these strains of detailing of beam reinforcement, column axial load, number of joint stirrups and intermediate column bars.

The strains in the beam anchorage bar, column bars and joint stirrups were compared between the measured strains and predicted 2D and 3D NLFEA strains. The measured and predicted reinforcement strains from both 2D and 3D models compare well for the beam anchorage bars with predictions best for series 1 and 3. The measured and predicted column bar strains also compare well for both the 2D and 3D models. The measured and predicted joint stirrups strains are comparable for series 1 but the comparison is less good for series 2 and 3 where a significant number of gauges failed. In general, the results show that both the 2D and 3D NLFEA were able to broadly capture the strain distribution in the reinforcement.

The concrete surface strain was investigated at the joint boundaries and parallel to the diagonal strut using DIC and 2D NLFEA. The results showed good agreement between measured and predicted strains particularly at the bottom of the joint. A good match was also obtained between the neutral axis depths obtained with DIC and 2D NLFEA. Two rows of virtual gauges centred on the strut were used to study the strain in the diagonal strut. The top row of virtual DEMECS compared favourably when compared measured with predicted peak strains, closest to the bend in the beam reinforcement, but the measured shape of the strain distribution was not always well captured. The second row of gauges showed better comparison of measured and predicted strains. Overall, the 2D NLFEA was able to reasonably capture the strain distributions measured in the reinforcement and the concrete even though the strength predictions were less good than for the 3D NLFEA.

The study made of the influence of the parameters studied in this research on the surface distribution showed comparable results. The 2D NLFEA is broadly able to capture the

influence of column axial load on strain and strain distributions in specimens with varying number of joint stirrups for both L-bar and U-bar beam anchorage detail.

The chapter finally evaluates the accuracy of various previously developed empirical and STM design models for external beam-column joints using a database of 68 test results. Comparisons are made between the diagonal strut geometry of each specimen tested in this campaign obtained with DIC, 2D NLFEA, section analysis and STM. The strength predictions from the considered design models are evaluated using the demerit point classification system of Collins [76].

A database comprising 68 specimens made up of 56 previously tested specimens and 12 from this study were used to assess various existing empirical design methods and STM. The considered empirical design methods were those of Vollum & Newman [24], Bakir and Boduroğlu [25], Hassan & Moehle [26] and Hegger et al. [15]. Of these, Vollum & Newman [24] method was found to be the best of these methods. The strut and tie methods of Hassan & Moehle [26], Vollum and Parker [39] and Hwang et al. [38] were considered. The Vollum & Parker [39] performed best but is limited to joints with L-anchorage bars.

The demerit point classification system proposed by Collins [76] was used to evaluate the accuracy of the considered design methods. In this assessment method, points are allocated according to the level of safety of the strength prediction with the best method being that with the lowest total demerit point score. The method of Hassan & Moehle [26] is of limited application since it does not consider the effect of joint stirrups. Of the methods that include joint stirrups, the lowest demerit score was 25 for the Vollum and Newman method. The largest total demerit point score of 73 was obtained for Hegger et al. [15]. Of the STM methods, Vollum and Parker had the lowest demerit score of 7 but this only includes the 38 specimens with L-bars.

The key conclusions of this study are:

- It is important to account for the detailing of beam flexural reinforcement in the calculation of joint shear strength. In cases where the joint shear strength is critical, L-bars, with the vertical leg bent down into the column, are recommended for anchorage of beam reinforcement. The strength of joints with L-bars in series 1 was slightly increased (5%) by the use of large radius bends. In the case of U-bars, no

significant change in strength was observed when a large diameter radius was used. Use of U-bars reduced the joint shear strength of specimens in series 1 compared with similar specimens with L-bars by 11% for standard radius bends and 15% for large radius bends.

- Joint shear reinforcement is a significant parameter that should be considered in the calculation of joint shear strength. Increasing the number of joint stirrups improved the joint strength of the tested specimens due to increased confinement provided to the joint core. For instance, the failure load increased from 81 kN for BCJ 5 (with one joint stirrup) to 139.7 kN for BCJ 3 (with three joint stirrups) resulting in an increase of failure load of more than 70%, despite the differences in concrete compressive strength between the two specimens. However, doubling the joint shear reinforcement from three to six joint stirrups significantly changed the failure mode from joint shear to flexure. Additionally, the load at first diagonal cracking increased when joint shear reinforcement was provided.
- Increasing the upper column load increases the load at first joint cracking but has relatively little effect on joint shear strength. This can be seen by comparing the normalised joint shear strengths of the author's specimens BCJ 3 (f_c = 33.2 MPa), BCJ 6 (f_c = 26.9 MPa) and BCJ 8 (f_c = 26.8 MPa) with column axial loads of 300 kN, 600 kN and 900 kN. The corresponding normalised column stresses (N/f_cA_c) are 0.16, 0.40 and 0.60. All three specimens were reinforced with standard radius U-bars and three 10 mm diameter joint stirrups. The failure loads of these specimens were 121 kN, 112 kN and 108 kN. The influence of the higher concrete strength of BCJ 3 is difficult to isolate. However, one way of doing this is to compare the strength predictions obtained with Vollum and Newman which assumes joint strength to be independent of column load. For these specimens the method overestimates joint strength giving $V_{test}/V_{predicted}$ equal to 1.20, 1.23 and 1.27 for BCJ 3, BCJ 6 and BCJ 8 respectively. The normalised ratios are 1.00: 1.03 and 1.06 suggesting that the reduction in joint strength due to increasing the column load from 300 kN to 600 kN is around 6% which is insignificant compared with the greater influence of concrete strength.
- Overall, empirical design methods are easier to apply than STM and seem better suited to practical design even though not mechanically based. The Vollum and Newman method is recommended for practical design based on it having the lowest

demerit score of the considered empirical design methods. However, the proposed NLFEA modelling procedures give useful insights into the influence of key variables on joint shear strength.

8.6 Suggestions for Further Work

This research addresses the lack of data on beam displacement and crack kinematics in existing studies of monotonically loaded external beam-column connections. Some recommendations for further work are as follows:

- The present research provides information on joint stiffness which can be used by others to calibrate numerical models of external beam-column joints. Additionally, the influence of joint shear cracking on moment redistribution from the support to the span needs to be investigated in statically indeterminate beam-column subassemblies.
- Research is needed to investigate the influence of perimeter beams on the strength and stiffness of external beam-column connections.
- This thesis examines the effect of beam anchorage type and bend radius on the joint response. Large bend radius increased joint strength when L-anchorage bar was used but reduced joint strength for U-anchorage bar. The generality of this finding requires further investigation for other joint geometries than tested.
- In this campaign, a small reduction in joint strength was observed in specimens with U-bars when the column load was increased. Research is required to investigate the influence of column axial load in specimens with L-bars for both standard and large radius bends.
- Further, research is required to investigate the effect of intermediate column bars on joint shear strength and shear transfer mechanisms.
- Further information on the of load-displacement response of monotonically loaded joints is needed for validation of NLFEA modelling procedures.

References

1. Paulay T.: "Equilibrium criteria for reinforced concrete beam-column joints", ACI Structural Journal, Vol. 86, No. 6, Nov. 1989, pp. 635-643.

2. Park R. and Paulay, T.: "Reinforced Concrete Structures", John Wiley, 1975, pp 736-758.

3. Gao X, Xiang D, He Y, Li J.: “shear deformation and force transfer of exterior beam-column joints”, ACI Structural Journal, Volume 117, No. 6, 2020, pp.253-67.

4. Uma SR, Prasad AM.: “seismic behavior of beam column joints in reinforced concrete moment resisting frames”, Document No, IITK-GSDMA-EQ32-V1. 0, Final Report: A-Earthquake Codes, IITK-GSDMA Project on Building Codes, 2015.

5. Taylor H. P. J.: "The behaviour of insitu concrete beam-column joints", Cement and Concrete Association, Technical Report 42.492, May 1974.

6. BSI: "CP 110: 1972 The structural use of concrete. Part 1: Design, materials and workmanship", British Standards Institution, London.

7. BS 8110 “Structural Use of Concrete BS 8110: Part 1,” British Standards Institution, London, UK, 1997.

8. Kordina, K.: "Bewehrungsfuhrung in Ecken und Rahmenendknoten, Deutscher Ausschuss fur Stahlbeton", Heft 354, 1984, pp. 93.

9. Vollum R.L. : “Design and analysis of reinforced concrete beam-column joints”, PhD thesis, Imperial College, London, 1998.

10. Sarsam, K.F., Phipps, M.E.: "The shear design of insitu reinforced beam-column joints subjected to monotonic loading", Magazine of Concrete Research Vol 37, No130, March 1985, pp16-28.

11. Scott, R. H.: "The effects of detailing on RC beam/column connection behaviour", The Structural Engineer, Volume 70, No. 18, 1992, pp.318-324.

12. Reys de Ortiz I.: “Strut and Tie Modelling of Reinforced Concrete Short Beams and Beam–column Joints”. PhD Thesis, University of Westminster, 1993.

13. Parker, D.E. and Bullman, P.J.M.: “Shear strength within reinforced concrete beam-column joints”. The Structural engineer, Vol 75, No. 4. 1997.

14. Hamil, Stephen J.: “Reinforced concrete beam-column connection behaviour”, Doctoral thesis, Durham University, 2000.

15. Hegger J, Sherif A, Roeser W.: “Nonseismic design of beam-column joints”, ACI Structural Journal, Volume 100, No. 5, 2003, pp.654-64.

16. ACI-ASCE Committee 352: "Recommendations for the design of beam-column joints in monolithic reinforced concrete structures", ACI Journal, Proceedings V.82, No. 3, May-June 1985, pp. 266-283.

17. ACI-ASCE Committee 352R-02: “Recommendations for the Design of Beam–column Joints in Monolithic Reinforced Concrete Structures”. American Concrete Institute, Detroit, ACI Manual of Concrete Practice, Technical Documents, 2002, pp.38.

18. Sperry J, Darwin D, O’Reilly M, Lequesne RD, Yasso S, Feldman L, Lepage A.: “Conventional and High-Strength Hooked Bars—Part: 1 Anchorage Tests”, American Concrete Institute, 2017.

19. Sperry J, Darwin D, O’Reilly M, Lequesne RD, Yasso S, Feldman L, Lepage A.: “Conventional and High-Strength Hooked Bars—Part 2: Data Analysis”, American Concrete Institute, 2017.

20. ACI Committee 318: “Building Code Requirements for Structural Concrete (ACI 318-14) and Commentary (ACI 318R-14)”, American Concrete Institute, Farmington Hills, MI, 2014, pp. 519.

21. ACI Committee 318: “Building code requirements for structural concrete:(ACI 318-02) and commentary (ACI 318R-02)”, American Concrete Institute, 2002.

22. Eurocode 8: “Design provisions for earthquake resistance of structures”, London, British Standards Institution, 1995.

23. EN 1992-1-1, “Eurocode 2: Design of Concrete Structures-Part 1-1: General Rules and Rules for Buildings,” CEN, Brussels, Belgium, 2004.

24. Vollum R.L. and Newman J.B.: “The design of external, reinforced concrete beam-column joints”, The Structural Engineer, Volume 77, Numbers 23 & 24, 7 December 1999, pages 21-27.

25. Bakir, P. G., and Boduroğlu, H. M.: “A new design equation for predicting the joint shear strength of monotonically loaded exterior beam-column joints”, Engineering Structures, Volume 24, No. 8, 2002, pp. 1105-1117.

26. Hassan, W.M. and Moehle, J.P.: “shear strength of exterior and corner beam column joints without transverse reinforcement”, ACI Structural Journal, Volume 115, No. 6, 2018.

27. Chun SC, Oh B, Lee SH, Naito CJ.: “anchorage strength and behavior of headed bars in exterior beam-column joints”, ACI Structural Journal, Volume 106, No. 5, 2009.

28. Wong HF, Kuang JS.: “effects of beam—column depth ratio on joint seismic behaviour”. Proceedings of the Institution of Civil Engineers-Structures and Buildings. 2008 Apr;161(2):91-101.

29. Ritter, W.: “The Hennebique construction method (in German, “Die Bauweise Hennebique”), Scweizerische Bauzeitung”, 1899, pp. 41–61.

30. Morsch E.: "Concrete Steel Construction", McGraw-Hill Book Company, New York, 1909, pp. 368.

31. Schlaich, J., Schafer, K., Jennewein, M.: "towards a consistent design of structural concrete", PCI Journal Vol. 32, May-June 1987.

32. Schlaich, J., Schafer, K.: "design and detailing of structural concrete using strut and tie models", The Structural Engineer, Vol. 69, No. 6, March 1991, pp. 113-125.

33. Collins M. P. and Mitchell D.: "Prestressed Concrete Structures", Prentice Hall, Englewood Cliffs, New Jersey 07362, 1991, pp. 766-.

34. BROWN, M. D., SANKOVICH, C. L., BAYRAK O., J. J. O., BREEN, J. E. & WOOD, S. L.: “Design for Shear in Reinforced Concrete Using Strut-and-Tie Models, in Examination of the AASHTO LRFD Strut and Tie Specification”, Texas Dept. of Transportation and U.S Dept. of Transportation, The University of Texas: Austin.1, 2005.

35. CEB-FIP: "Model Code for Concrete Structures, CEB-FIP International Recommendations", 1990.

36. Hwang, S.J. and Lee, H.J.: “Strength prediction for discontinuity regions by softened strut-and-tie model”, Journal of Structural Engineering, Volume 128, No. 12, 2002, pp.1519-1526.

37. Hwang, S.J. and Lee, H.J.: “Analytical model for predicting shear strengths of exterior reinforced concrete beam-column joints for seismic resistance”, ACI Structural Journal, 1999, pp.846-857.

38. Hwang SJ, Tsai RJ, Lam WK, Moehle JP.: “Simplification of softened strut-and-tie model for strength prediction of discontinuity regions”, ACI Structural Journal, Volume 114, No. 5, 2017.

39. Vollum R, Parker D.: “External beam–column joints: design to Eurocode 2”, Magazine of concrete research, Volume 60, No. 7, 2008, pp.511-21.

40. CAMPANA, S., RUIZ, M. F., ANASTASI, A. & MUTTONI, A.: “Analysis of shear-transfer actions on one-way RC members based on measured cracking pattern and failure kinematics”, Magazine of Concrete Research, Volume 65, 2013, pp.386-404.

41. WALRAVEN, J. C.: “Aggregate interlock: a theoretical and experimental analysis”, TU Delft, Delft University of Technology, 1980.

42. LI, N., MAEKAWA, L. & OKAMURA, H.: “Contact density model for stress transfer across cracks in concrete”, Journal of the Faculty of Engineering, University of Tokyo, 1989, pp. 9-52.

43. WALRAVEN, J. & REINHARDT, H.: “Theory and experiments on the mechanical behaviour of cracks in plain and reinforced concrete subjected to shear loading”, 26. HERON, 1981.

44. HAMADI, Y. & REGAN, P.: “Behaviour of normal and lightweight aggregate beams with shear cracks”, The Structural Engineer, 58B-4, 1980, pp.71-79.

45. BAZANT, Z. P. & GAMBAROVA, P. G.: “Rough crack models in reinforced concrete”, Journal of Structural Engineering, Journal of the Structural Division, Volume 106, No. 4, 1980, pp.819-842.

46. GAMBAROVA, P. & KARAKOÇ, C.: “A new approach to the analysis of the confinement role in regularly cracked concrete elements”, Transactions of the 7. international conference on structural mechanics in reactor technology. Vol. H, 1983, pp. 251–261.

47. PAULAY, T. & LOEBER, P.: “Shear transfer by aggregate interlock”, Special Publication, Volume 42, 1974, pp.1-16.

48. SOLTANI, M.: “Micro computational approach to post cracking constitutive laws of reinforced concrete and applications to nonlinear finite element analysis”, University of Tokyo, 2002.

49. SIGRIST, V. Zum: “Verformungsvermögen von Stahlbetonträgern (In German)”, Birkhäuser, 1995.

50. CAVAGNIS, F., FERNÁNDEZ RUIZ, M. & MUTTONI, A.: “An analysis of the shear-transfer actions in reinforced concrete members without transverse reinforcement based on refined experimental measurements”. Structural Concrete, Vol 16. 2017.

51. CAVAGNIS, F., FERNÁNDEZ RUIZ, M. & MUTTONI, A.: “Shear failures in reinforced concrete members without transverse reinforcement: An analysis of the critical shear crack development on the basis of test results”. Engineering Structures, 103, 2015, pp.157-173.

52. ELWAKEEL, A., FANG, L., ABDELSALAM, M. & VOLLUM, R. L.: “Contribution of the Shear Transfer Actions in Short Span Beams”, fib Bulletin 85: Towards a rational understanding of shear in beams and slabs, 85, 15, 2018.

53. HUBER, T., HUBER, P. & KOLLEGGER, J.: “Influence of aggregate interlock on the shear resistance of reinforced concrete beams without stirrups”, Engineering Structures, Volume 186, 2019. pp.26-42.

54. LaVision: “Product Manual for DaVis 8.3”, LaVision GmbH: Gottingen, Germany, 2017.

55. LaVision: “Product Manual for StrainMaster.”, LaVision GmbH: Gottingen, Germany, 2015.

56. Elwakeel, Abobakr.: “Shear Enhancement in RC Beams Loaded on the Tension Face.”, Civil and Environmental Engineering, Imperial College London, 2020, Print.

57. Cervenka, V., Cervenka, J., Janda, Z., and Pryl, D.: “ATENA Program Documentation, Part 8: User's Manual for ATENA-GiD Interface”, Cervenka Consulting: Prague, 2014.

58. Cervenka, V., Jendele, L., and Cervenka, J.: “ATENA Program Documentation, Part 1: Theory”, Cervenka Consulting: Prague, 2013.

59. van Mier, J.G.M.: “Multiaxial strain-softening of concrete”, Materials and Structures, Volume 19, No. 3, 1986, pp.179-190.

60. KUPFER, H., HILSDORF, H.K., RÜSCH, H.: “ Behavior of Concrete under Biaxial Stress”, Journal ACI, Volume 66, No.8, 1969, pp.656-666.

61. Menetrey, P. and Willam, K.J.: “Triaxial Failure Criterion for Concrete and its Generalization”. ACI Structural Journal, Volume 92, NO. 3, 1995, pp.311-318.

62. HORDIJK, D.A.: “Local Approach to Fatigue of Concrete, Doctor dissertation”, Delft University of Technology, The Netherlands, ISBN 90/9004519-8, 1991.

63. VECCHIO, F. J. & COLLINS, M. P.: “The modified compression-field theory for reinforced concrete elements subjected to shear”. ACI Structural Journal, Volume 83, 1986, pp.219-231.

64. NGO, D. & SCORDELIS, A. C.: “Finite Element Analysis of Reinforced Concrete Beams”, Journal Proceedings, Volume 64, No. 3, 1967, pp. 152-163.

65. Cervera M, Chiumenti M.: “Mesh objective tensile cracking via a local continuum damage model and a crack tracking technique”, Computer methods in applied mechanics and engineering, Volume 196, No. 1-3, 2006, pp.304-20.

66. de Borst, R., Remmers, J.J.C., Needleman, A., and Abellan, M.A.: “Discrete vs smeared crack models for concrete fracture: bridging the gap”, International Journal for Numerical and Analytical Methods in Geomechanics, Volume 28, No. 78, 2004, p. 583-607.

67. RASHID, Y.: “Ultimate strength analysis of prestressed concrete pressure vessels”, Nuclear engineering and design, Volume 7, No. 4, 1968, pp.334-344.

68. Bazant, Z.P. and Planas, J.: “Fracture and size effect in concrete and other quasibrittle materials”, Vol.ume16, 1997.

69. CRISFIELD, M.A., WILLS, J.: “The Analysis of Reinforced Concrete Panels Using Different Concrete Models”, Journal of engineering mechanics, Volume 115, No. 3, 1989, pp.578-597.

70. KOLMAR, W.: “Beschreibung der Kraftuebertragung über Risse in nichtlinearen Finite-Element-Berechnungen von Stahlbetontragwerken", Dissertation, T.H. Darmstadt, 1986 , p. 94.
71. Bigaj, A.J.: “Structural dependence of rotation capacity of plastic hinges in RC beams and slabs”, Delft University of Technology, 1999.

72. Wempner, G. A.: “Discrete approximations related to nonlinear theories of solids”, International Journal of Solids and Structures, Volume 7, No. 11, 1971, pp.1581-1599.

73. Riks, E.: “An incremental approach to the solution of snapping and buckling problems”, International Journal of Solids and Structures, Volume 15, No. 7, 1979, pp.529-551.

74. Kollegger, J. and Mehlhorn, G.: “Experimentelle und analytische untersuchungenzur aufstellung eines materialmodels für gerissene stahbetonscheiben”, Nr.6 Forschungsbericht, Massivbau, Gesamthochschule Kassel, 1988

75. Dyngeland, T.: “Behavior of reinforced concrete panels. Dissertation”, Doktor Ingenierafhandling (Ph. D. thesis, Institut for Betongkonstruksjoner), Trondheim, 1989.

76. Collins M.P.: “Evaluation of shear design procedures for concrete structures”, in A report prepared for the CSA Technical Committee on Reinforced Concrete Design, 2001.

Appendix: Permission to reuse figures from other publications

Page No.	Type of work:	Name of work	Source of work	Copyright holder and contact	permission requested on	I have permission yes /no	Permission note
40	figure	Figure 2-1	Taylor H. P. J.: "The behaviour of insitu concrete beam-column joints", Cement and Concrete Association, Technical Report 42.492, May 1974.	Cement and Concrete Association	10/04/2022	yes	Written permission
41	table	Table 2-1	Taylor H. P. J.: "The behaviour of insitu concrete beam-column joints", Cement and Concrete Association, Technical Report 42.492, May 1974.	Cement and Concrete Association	08/04/2022	yes	Written permission
42	table	Table 2-2	Taylor H. P. J.: "The behaviour of insitu concrete beam-column joints", Cement and Concrete Association, Technical Report 42.492, May 1974.	Cement and Concrete Association	08/04/2022	yes	Written permission
44	figure	Figure 2-2	Kordina, K.: "Bewehrungsfuhrung in Ecken und Rahmenendknoten, Deutscher Ausschuss fur Stahlbeton", Heft 354, 1984, pp. 93.	https://www.slub-dresden.de/	09/04/2022	Yes	email permission
44	table	Table 2-3	Kordina, K.: "Bewehrungsfuhrung in Ecken und Rahmenendknoten, Deutscher Ausschuss fur Stahlbeton", Heft 354, 1984, pp. 93.	https://www.slub-dresden.de/	09/04/2022	Yes	email permission
45	table	Table 2-4	Kordina, K.: "Bewehrungsfuhrung in Ecken und Rahmenendknoten, Deutscher Ausschuss fur Stahlbeton", Heft 354, 1984, pp. 93.	https://www.slub-dresden.de/	09/04/2022	Yes	email permission
46	figure	Figure 2-3	Sarsam, K.F., Phipps, M.E.: "The shear design of insitu reinforced beam-column joints subjected to monotonic loading", Magazine of Concrete Research Vol 37, No130, March 1985, pp16-28.	Magazine of Concrete Research	09/04/2022	Yes	email permission

47	table	Table 2-5	Sarsam, K.F., Phipps, M.E.: "The shear design of insitu reinforced beam-column joints subjected to monotonic loading", Magazine of Concrete Research Vol 37, No130, March 1985, pp16-28.	Magazine of Concrete Research	09/04/2022	yes	email permission
47	table	Table 2-6	Sarsam, K.F., Phipps, M.E.: "The shear design of insitu reinforced beam-column joints subjected to monotonic loading", Magazine of Concrete Research Vol 37, No130, March 1985, pp16-28.	Magazine of Concrete Research	09/04/2022	yes	email permission
50	figure	Figure 2-4	Scott, R. H.: "The effects of detailing on RC beam/column connection behaviour", The Structural Engineer, Volume 70, No. 18, 1992, pp.318-324.	The Structural Engineer	09/04/2022	yes	Written permission
51	table	Table 2-7	Scott, R. H.: "The effects of detailing on RC beam/column connection behaviour", The Structural Engineer, Volume 70, No. 18, 1992, pp.318-324.	The Structural Engineer	09/04/2022	yes	Written permission
52	table	Table 2-8	Scott, R. H.: "The effects of detailing on RC beam/column connection behaviour", The Structural Engineer, Volume 70, No. 18, 1992, pp.318-324.	The Structural Engineer	09/04/2022	yes	Written permission
55	figure	Figure 2-5	Reys de Ortiz I.: “Strut and Tie Modelling of Reinforced Concrete Short Beams and Beam–column Joints”. PhD Thesis, University of Westminster, 1993.	University of Westminster	07/04/2022	yes	Written permission
56	figure	Figure 2-6	Reys de Ortiz I.: “Strut and Tie Modelling of Reinforced Concrete Short Beams and Beam–column Joints”. PhD Thesis, University of Westminster, 1993.	University of Westminster	07/04/2022	yes	Written permission
57	figure	Table 2-9	Reys de Ortiz I.: “Strut and Tie Modelling of Reinforced Concrete Short Beams and Beam–column Joints”. PhD Thesis, University of Westminster, 1993.	University of Westminster	07/04/2022	yes	Written permission

57	figure	Figure 2-10	Reys de Ortiz I.: "Strut and Tie Modelling of Reinforced Concrete Short Beams and Beam–column Joints". PhD Thesis, University of Westminster, 1993.	University of Westminster	07/04/2022	yes	Written permission
59	figure	Figure 2-7	Parker, D.E. and Bullman, P.J.M.: "Shear strength within reinforced concrete beam-column joints". The Structural engineer, Vol 75, No. 4. 1997.	The Structural Engineer	09/04/2022	yes	Written permission
60	table	Table 2-11	Parker, D.E. and Bullman, P.J.M.: "Shear strength within reinforced concrete beam-column joints". The Structural engineer, Vol 75, No. 4. 1997.	The Structural Engineer	09/04/2022	yes	Written permission
60	table	Table 2-2	Parker, D.E. and Bullman, P.J.M.: "Shear strength within reinforced concrete beam-column joints". The Structural engineer, Vol 75, No. 4. 1997.	The Structural Engineer	09/04/2022	yes	Written permission
63	figure	Figure 2-8	Hamil, Stephen J.: "Reinforced concrete beam-column connection behaviour", Doctoral thesis, Durham University, 2000.	Durham University	07/04/2022	yes	Written permission
64	figure	Figure 2-9	Hamil, Stephen J.: "Reinforced concrete beam-column connection behaviour", Doctoral thesis, Durham University, 2000.	Durham University	07/04/2022	yes	Written permission
65	figure	Figure 2-10 & Figure 2-11	Hamil, Stephen J.: "Reinforced concrete beam-column connection behaviour", Doctoral thesis, Durham University, 2000.	Durham University	07/04/2022	yes	Written permission
66	table	Table 2-13	Hamil, Stephen J.: "Reinforced concrete beam-column connection behaviour", Doctoral thesis, Durham University, 2000.	Durham University	07/04/2022	yes	Written permission
67	table	Table 2-14	Hamil, Stephen J.: "Reinforced concrete beam-column connection behaviour", Doctoral thesis, Durham University, 2000.	Durham University	07/04/2022	yes	Written permission
68	table	Table 2-15	Hamil, Stephen J.: "Reinforced concrete beam-column connection behaviour", Doctoral thesis, Durham University, 2000.	Durham University	07/04/2022	yes	Written permission

70	figure	Figure 2-12	Hegger J, Sherif A, Roeser W.: “Nonseismic design of beam-column joints”, ACI Structural Journal, Volume 100, No. 5, 2003, pp.654-64.	ACI Structural Journal	07/04/2022	yes	Written permission
71	figure	Figure 2-13	Hegger J, Sherif A, Roeser W.: “Nonseismic design of beam-column joints”, ACI Structural Journal, Volume 100, No. 5, 2003, pp.654-64.	ACI Structural Journal	07/04/2022	yes	Written permission
71	table	Table 2-16	Hegger J, Sherif A, Roeser W.: “Nonseismic design of beam-column joints”, ACI Structural Journal, Volume 100, No. 5, 2003, pp.654-64.	ACI Structural Journal	07/04/2022	yes	Written permission
74	figure	Figure 2-14	Sperry J, Darwin D, O’Reilly M, Lequesne RD, Yasso S, Feldman L, Lepage A.: “Conventional and High-Strength Hooked Bars—Part: 1 Anchorage Tests”, American Concrete Institute, 2017.	ACI Structural Journal	07/04/2022	yes	Written permission
74	table	Table 2-17	Sperry J, Darwin D, O’Reilly M, Lequesne RD, Yasso S, Feldman L, Lepage A.: “Conventional and High-Strength Hooked Bars—Part: 1 Anchorage Tests”, American Concrete Institute, 2017.	ACI Structural Journal	07/04/2022	yes	Written permission
76	table	Table 2-18	ACI-ASCE Committee 352: "Recommendations for the design of beam-column joints in monolithic reinforced concrete structures", ACI Journal, Proceedings V.82, No. 3, May-June 1985, pp. 266-283.	ACI Structural Journal	07/04/2022	yes	Written permission
77	table	Table 2-19	ACI-ASCE Committee 352R-02: “Recommendations for the Design of Beam–column Joints in Monolithic Reinforced Concrete Structures”. American Concrete Institute, Detroit, ACI Manual of Concrete Practice, Technical Documents, 2002, pp.38.	ACI Structural Journal	07/04/2022	yes	Written permission
81	table	Table 2-20	Hegger J, Sherif A, Roeser W.: “Nonseismic design of beam-column joints”, ACI Structural Journal, Volume 100, No. 5, 2003, pp.654-64.	ACI Structural Journal	07/04/2022	yes	Written permission
86	figure	Figure 2-16(a)	Wong HF, Kuang JS. Effects of beam—column depth ratio on joint seismic behaviour. Proceedings of the Institution of Civil Engineers-Structures and Buildings. 2008 Apr;161(2):91-101.	Institution of Civil Engineers-	09/04/2022	yes	email

				Structures and Buildings			
86	figure	Figure 2-16(b)	Hegger J, Sherif A, Roeser W.: “Nonseismic design of beam-column joints”, ACI Structural Journal, Volume 100, No. 5, 2003, pp.654-64.	ACI Structural Journal	07/04/2022	yes	Written permission
87	figure	Figure 2-17	Schlaich, J., Schafer, K., Jennewein, M.: "Towards a consistent design of structural concrete", PCI Journal Vol. 32, May-June 1987.	PCI Journal	09/04/2022	yes	email permission
87	figure	Figure 2-17	Schlaich, J., Schafer, K.: "Design and detailing of structural concrete using strut and tie models", The Structural Engineer, Vol. 69, No. 6, March 1991, pp. 113-125.	The Structural Engineer	09/04/2022	yes	email permission
88	figure	Figure 2-18	Gao X, Xiang D, He Y, Li J.: “Shear deformation and force transfer of exterior beam-column joints”, ACI Structural Journal, Volume 117, No. 6, 2020, pp.253-67.	ACI Structural Journal	07/04/2022	yes	Written permission
90	figure	Figure 2-19	Collins M. P. and Mitchell D.: "Prestressed Concrete Structures", Prentice Hall, Englewood Cliffs, New Jersey 07362, 1991, pp. 766.	Prentice Hall	08/04/2022	yes	Written permission
92	figure	Figure 2-20	Schlaich, J., Schafer, K.: "Design and detailing of structural concrete using strut and tie models", The Structural Engineer, Vol. 69, No. 6, March 1991, pp. 113-125.	The Structural Engineer	09/04/2022	yes	email permission
93	figure	Figure 2-21	BROWN, M. D., SANKOVICH, C. L., BAYRAK O., J. J. O., BREEN, J. E. & WOOD, S. L.: “Design for Shear in Reinforced Concrete Using Strut-and-Tie Models, in Examination of the AASHTO LRFD Strut and Tie Specification”, Texas Dept. of Transportation and U.S Dept. of Transportation, The University of Texas: Austin.1, 2005.	Texas Dept. of Transportation and U.S Dept. of Transportation	10/04/2022	yes	email permission

94	figure	Figure 2-22	Reys de Ortiz I.: "Strut and Tie Modelling of Reinforced Concrete Short Beams and Beam–column Joints". PhD Thesis, University of Westminster, 1993.	University of Westminster	07/04/2022	yes	Written permission
96	figure	Figure 2-23	Hwang, S.J. and Lee, H.J.: "Analytical model for predicting shear strengths of exterior reinforced concrete beam-column joints for seismic resistance", ACI Structural Journal, 1999, pp.846-857.	ACI Structural Journal	07/04/2022	yes	Written permission
96	figure	Figure 2-24	Hwang, S.J. and Lee, H.J.: "Analytical model for predicting shear strengths of exterior reinforced concrete beam-column joints for seismic resistance", ACI Structural Journal, 1999, pp.846-857.	ACI Structural Journal	07/04/2022	yes	Written permission
100	figure	Figure 2-26	Vollum R, Parker D.: "External beam–column joints: design to Eurocode 2", Magazine of concrete research, Volume 60, No. 7, 2008, pp.511-21.	Magazine of concrete research (ICE)	09/04/2022	yes	Email permission
101/102	figure	Figure 2-27 & Figure 2-28	WALRAVEN, J. C.: "Aggregate interlock: a theoretical and experimental analysis", TU Delft, Delft University of Technology, 1980.	Delft University of Technology	10/04/2022	yes	email permission
103	figure	Figure 2-29 & Figure 2-30	WALRAVEN, J. C.: "Aggregate interlock: a theoretical and experimental analysis", TU Delft, Delft University of Technology, 1980.	Delft University of Technology	10/04/2022	yes	email permission
104	figure	Figure 2-31	BAZANT, Z. P. & GAMBAROVA, P. G.: "Rough crack models in reinforced concrete. Journal of Structural Engineering", Journal of the Structural Division, Volume 106, No. 4, 1980, pp.819-842.	Journal of the Structural Division	10/04/2022	yes	email permission
107	figure	Figure 2-32 & Figure 2-33	SIGRIST, V. Zum: "Verformungsvermögen von Stahlbetonträgern (In German)", Birkhäuser, 1995.	Birkhäuser	10/04/2022	yes	Written permission
109	figure	Figure 2-34	HUBER, T., HUBER, P. & KOLLEGGER, J.: "Influence of aggregate interlock on the shear resistance of reinforced concrete beams without stirrups", Engineering Structures, Volume 186, 2019. pp.26-42.	Engineering Structures	10/04/2022	yes	Written permission

109	figure	Figure 2-35	CAVAGNIS, F., FERNÁNDEZ RUIZ, M. & MUTTONI, A.: "An analysis of the shear-transfer actions in reinforced concrete members without transverse reinforcement based on refined experimental measurements". Structural Concrete, Vol 19. 2018.	Structural Concrete	09/04/2022	yes	Written permission
127	figure	Figure 3-12	CAMPANA, S., RUIZ, M. F., ANASTASI, A. & MUTTONI, A.: "Analysis of shear-transfer actions on one-way RC members based on measured cracking pattern and failure kinematics", Magazine of Concrete Research, Volume 65, 2013, pp.386-404.	Magazine of Concrete Research	09/04/2022	yes	email permission
151	figure	Figure 4-6	EN 1992-1-1, "Eurocode 2: Design of Concrete Structures-Part 1-1: General Rules and Rules for Buildings," CEN, Brussels, Belgium, 2004.	CEN national Members	10/04/2022	yes	Written permission
210	figure	Figure 5-1	Cervenka, V., Jendele, L., and Cervenka, J.: "ATENA Program Documentation, Part 1: Theory", Cervenka Consulting: Prague, 2013.	Cervenka Consulting	07/04/2022	yes	Written permission
211	figure	Figure 5-2 & Figure 5-3	Cervenka, V., Jendele, L., and Cervenka, J.: "ATENA Program Documentation, Part 1: Theory", Cervenka Consulting: Prague, 2013.	Cervenka Consulting	07/04/2022	Yes	Written permission
212	figure	Figure 5-4	Cervenka, V., Jendele, L., and Cervenka, J.: "ATENA Program Documentation, Part 1: Theory", Cervenka Consulting: Prague, 2013.	Cervenka Consulting	07/04/2022	yes	Written permission
213	figure	Figure 5-5	Menetrey, P. and Willam, K.J.: "Triaxial Failure Criterion for Concrete and its Generalization". ACI Structural Journal, Volume 92, NO. 3, 1995, pp.311-318.	ACI Structural Journal	10/04/2022	yes	Written permission
214	figure	Figure 5-6	Cervenka, V., Jendele, L., and Cervenka, J.: "ATENA Program Documentation, Part 1: Theory", Cervenka Consulting: Prague, 2013.	Cervenka Consulting	07/04/2022	yes	Written permission
214	figure	Figure 5-7	Cervenka, V., Jendele, L., and Cervenka, J.: "ATENA Program Documentation, Part 1: Theory", Cervenka Consulting: Prague, 2013.	Cervenka Consulting	07/04/2022	yes	Written permission

215/216	figure	Figure 5-8 & Figure 5-9	Cervenka, V., Jendele, L., and Cervenka, J.: "ATENA Program Documentation, Part 1: Theory", Cervenka Consulting: Prague, 2013.	Cervenka Consulting	07/04/2022	yes	Written permission
217	figure	Figure 5-10	Cervenka, V., Jendele, L., and Cervenka, J.: "ATENA Program Documentation, Part 1: Theory", Cervenka Consulting: Prague, 2013.	Cervenka Consulting	07/04/2022	yes	Written permission
218	figure	Figure 5-11	Cervenka, V., Jendele, L., and Cervenka, J.: "ATENA Program Documentation, Part 1: Theory", Cervenka Consulting: Prague, 2013.	Cervenka Consulting	07/04/2022	yes	Written permission
218	figure	Figure 5-12	de Borst, R., Remmers, J.J.C., Needleman, A., and Abellan, M.A., Discrete vs smeared crack models for concrete fracture: bridging the gap. International Journal for Numerical and Analytical Methods in Geomechanics, 2004. 28(78): p. 583-607.	International Journal for Numerical and Analytical Methods in Geomechanics	10/04/2022	yes	https://secure.wiley.com/AGENT-confirmation-page
219/220	figure	Figure 5-13 & Figure 5-14	Cervenka, V., Jendele, L., and Cervenka, J.: "ATENA Program Documentation, Part 1: Theory", Cervenka Consulting: Prague, 2013.	Cervenka Consulting	07/04/2022	yes	Written permission
221	figure	Figure 5-15	Cervenka, V., Jendele, L., and Cervenka, J.: "ATENA Program Documentation, Part 1: Theory", Cervenka Consulting: Prague, 2013.	Cervenka Consulting	07/04/2022	yes	Written permission
222	figure	Figure 5-16	Cervenka, V., Jendele, L., and Cervenka, J.: "ATENA Program Documentation, Part 1: Theory", Cervenka Consulting: Prague, 2013.	Cervenka Consulting	07/04/2022	yes	Written permission
223	figure	Figure 5-17	Cervenka, V., Jendele, L., and Cervenka, J.: "ATENA Program Documentation, Part 1: Theory", Cervenka Consulting: Prague, 2013.	Cervenka Consulting	07/04/2022	yes	Written permission
223	table	Table 5-1	Cervenka, V., Jendele, L., and Cervenka, J.: "ATENA Program Documentation, Part 1: Theory", Cervenka Consulting: Prague, 2013.	Cervenka Consulting	07/04/2022	yes	Written permission
224	figure	Figure 5-18	Cervenka, V., Jendele, L., and Cervenka, J.: "ATENA Program Documentation, Part 1: Theory", Cervenka Consulting: Prague, 2013.	Cervenka Consulting	07/04/2022	yes	Written permission

225	figure	Figure 5-19	Cervenka, V., Jendele, L., and Cervenka, J.: “ATENA Program Documentation, Part 1: Theory”, Cervenka Consulting: Prague, 2013.	Cervenka Consulting	07/04/2022	yes	Written permission
226	figure	Figure 5-20	Cervenka, V., Jendele, L., and Cervenka, J.: “ATENA Program Documentation, Part 1: Theory”, Cervenka Consulting: Prague, 2013.	Cervenka Consulting	07/04/2022	yes	Written permission
227	figure	Figure 5-21	Cervenka, V., Jendele, L., and Cervenka, J.: “ATENA Program Documentation, Part 1: Theory”, Cervenka Consulting: Prague, 2013.	Cervenka Consulting	07/04/2022	yes	Written permission
284	figure	Figure 6-7	Collins M. P. and Mitchell D.: "Prestressed Concrete Structures", Prentice Hall, Englewood Cliffs, New Jersey 07362, 1991, pp. 766.	Prentice Hall	08/04/2022	yes	Written permission
285	figure	Figure 6-9	Collins M. P. and Mitchell D.: "Prestressed Concrete Structures", Prentice Hall, Englewood Cliffs, New Jersey 07362, 1991, pp. 766.	Prentice Hall	08/04/2022	yes	Written permission